Faculty of Science and Engineering

Centre for Marine Science and Technology

Measurement and Simulation of Ship Under-Keel Clearance in Port Approach Channels

Jeong Hun Ha

This thesis is presented for the Degree of
Doctor of Philosophy
of
Curtin University

April 2018

Declaration

To the best of my knowledge and belief this thesis contains no material previously published by any other person except where due acknowledgment has been made.

This thesis contains no material which has been accepted for the award of any other degree or diploma in any university.

Jeong Hun Ha

Signature:  Date: 13/04/2018

Abstract

The main objective of this thesis is to provide a comprehensive guideline to ship under-keel clearance (UKC) based on numerical modelling, model-scale and full-scale measurements. To achieve this, simulations and full-scale trials of vertical ship motions in port approach channels are undertaken, with particular focus on the effects of ship squat and wave-induced motions on overall UKC assessment. This study will contribute to the better understanding of vertical ship motions in shallow water or port approach channels, and bring practical support to UKC management in ports.

Several theoretical methods and extensive model-scale test data are used to test ship squat (sinkage and trim) in a wide range of ship hull forms in shallow open waterways, dredged channels and canals. Sinkage coefficients are developed for 13 published ship hull forms, of types mainly used for container ships, oil tankers, bulk carriers and LNG carriers, and a guideline for making a choice of the sinkage coefficient, corresponding to the ship types, and channel and canal configurations, is suggested. Particular attention is paid to the dynamic sinkage and trim of modern container ships in shallow water or port approach channels. Two potential flow methods, the slender-body method and the Rankine-source method, are discussed in detail with reference to available model-scale test results. Slender-body theory is seen to give good predictions of dynamic sinkage and trim in wide canals or open water, whereas the Rankine-source method offers a more accurate solution in the particular case of ships at high speed in narrow canals.

Because high-quality data from full-scale trials will play an important role in this study, undertaking full-scale measurement campaigns to measure dynamic ship motions, including squat and wave-induced motions, in port approach channels is a vital part of this study. They are undertaken for container ship transits at the Port of Fremantle, and bulk carrier transits at the Port of Geraldton, using high-accuracy GNSS receivers on board with a fixed reference station. These trial results, which include diverse ship operating conditions and environmental conditions, are applied for ship squat comparisons and validations as well as for ship wave-induced motion comparisons and validations at full scale.

Slender-body shallow-water theory, as implemented in the computer code *SlenderFlow*, is applied to predict the measured sinkage and trim of the ship transits. It is shown that the theory is able to predict ship squat with reasonable accuracy for both bulk carriers and container ships at full scale in open dredged channels. An empirical correction may be only required for cases that are underpredicted by the theory, as a conservative method. The best way to empirically correct sinkage and trim predictions at full scale is an area of ongoing research.

A linear strip method, as implemented in the computer code *OCTOPUS*, is applied to predict the ship wave-induced motions. The method is seen to provide a reasonably accurate estimate of heave, roll and pitch responses of container ships at full scale in open dredged channels. Measured roll response in particular is used to assess the suitability of existing roll damping methods at full scale. Large-amplitude long-period roll motions are observed in some of the container ship trials, and unexpected harmonic pitch motions are observed in others. Further research into these seemingly non-linear effects is recommended.

Acknowledgements

For the record:

I wish to thank all the marine pilots and staff at Mid West Ports Authority and Fremantle Ports for their assistance, support and enthusiasm in conducting the full-scale trials discussed in this thesis. I would also like to acknowledge the following people and organizations for their contributions to this research: all the shipping operators who provided access to and hull information for the ships under study; the GNSS Research Group, Curtin University, which provided the GNSS equipment; the coastal infrastructure team of the Western Australian Department of Transport, who provided measured wave data and authorisation to use the *W@ves21* software; Flanders Hydraulics Research and Ghent University, Belgium, who provided hull data for FHR Ships D, F and G; the Federal Waterways Engineering and Research Institute (BAW), Germany, who provided hull data for the JUMBO and MEGA-JUMBO; and the Korean Research Institute Ships and Ocean Engineering (KRISO), who provided hull data for the KVLCC 1, KVLCC2 and KLNG. Tremarfon Pty Ltd provided measured tide and wave data; and OMC International provided surveyed depth data for the channels. The contribution of an Australian Government Research Training Program Scholarship in supporting this research is acknowledged. This thesis was professionally edited by Dr Margaret Johnson of The Book Doctor, in accordance with the guidelines established by the Institute of Professional Editors and the Deans and Directors of Graduate Studies.

Off the record:

It all comes down to the fact that I met my main supervisor, Dr Tim Gourlay, who has provided abundant and up-to-date resources on this topic as well as earnest and enthusiastic support of my PhD project. Most of the work during my PhD has been a collaboration with him: in particular, the full-scale trials of bulk carriers and container ship motions, were dangerous, difficult and finicky, and were only carried out with his most active participation. Needless to say, this thesis would not have been possible without him. I am greatly indebted to him, and I hope one day to be in the fortunate position of being able to reciprocate.

I must also express my heartfelt thanks to Dr Alec Duncan for his contributions and efforts as my new supervisor; the Director of Centre for Marine Science and Technology (CMST), Dr Christine Erbe, for her willingness to help ensure a smooth and successful launch; and Professor Do Sam Kim from the Korea Maritime and Ocean University for his generous advice at all times. I would also like to thank all staff and postgraduates of the CMST.

Thanks go to my close friends in South Korea, who make my time enjoyable time whenever I return; to my previous colleagues from DY Engineering, KS D. C. I and ERE E&C for their friendly and professional companionship; and my ‘Australian’ friends, including Ethan, Gianna and Gino, for the pleasant and precious time they share with me that allows me to be free of PhD stress for a while. Special thanks also go to fellow students Hasan and Xing, who spent much time with me in Room 109, Building 120, Curtin Uni.

My family and in-laws have suffered from my absence but their constant encouragement has been the impetus for completing this challenge. No matter where I am and what I do, I know they will always stand by my side. I wish to thank them all for their understanding. I lost my father during my PhD years, and this thesis is dedicated to him; he would be very proud of his son if he were alive. Now, my appreciation for my mother’s presence has become stronger. I love you, Mum.

Finally, sure enough, I send my biggest thanks to Mina, my wife, for everything from her understanding and patience to her love. We will always make a perfect combination. You are my best friend and soul mate. We will be together every single step of our life.

List of Publications

Ha, J. H., & Gourlay, T. P. (2018a). Full-scale measurements and method validation of container ship wave-induced motion at the Port of Fremantle. Accepted, to appear in *Journal of Waterway, Port, Coastal, and Ocean Engineering*.

Ha, J. H., & Gourlay, T. P. (2018b). Validation of container ship squat modelling using full-scale trials at the Port of Fremantle. *Journal of Waterway, Port, Coastal, and Ocean Engineering*, *144*(1). doi: 10.1061/(ASCE)WW.1943-5460.0000425

Ha, J. H., & Gourlay, T. P. (2017). Bow and stern sinkage coefficients for cargo ships in shallow open water. *Third-place winner of the 2017 PIANC De Paepe-Willems Award, PIANC Yearbook 2017*. Brussels, Belgium: World Association for Waterborne Transport Infrastructure.

Ha, J. H., Gourlay, T. P., & Nadarajah, N. (2016). Measured ship motions in Port of Geraldton approach channel. *Proceedings of the 4th International Conference on Ship Manoeuvring in Shallow and Confined Water*, *MASHCON 2016*, *Hamburg*, *Germany*, 236–250.

Ha, J. H., & Gourlay, T. P. (2016a). Ship motion measurements for ship under-keel clearance in the Port of Fremantle. *CMST Report 2016–07*, Centre for Marine Science and Technology, Curtin University, Bentley, WA.

Ha, J. H., & Gourlay, T. P. (2016b). Ship motion measurements for ship under-keel clearance in the Port of Geraldton. *CMST Report 2016-28*, Centre for Marine Science and Technology, Curtin University, Bentley, WA.

Gourlay, T. P., **Ha, J. H.**, Mucha, P., & Uliczka, K. (2015). Sinkage and trim of modern container ships in shallow water. *Proceedings of the Coasts and Ports 2015 Conference*, *Auckland*, *New Zealand*.

Table of Contents

Chapter 3
Container Ship Squat Prediction Using Model-Scale Tests

Chapter 4
Full-Scale Measurement Campaigns

Chapter 5

Ship Squat Comparisons and Validations Using Full-Scale Trials

Chapter 6

Ship Wave-Induced Motion Comparisons and Validations Using Full-Scale Trials

Nomenclature

Abbreviations	**Description**
AHD	Australian Height Datum
ANTT	Australian National Tide Tables
AP	Aft Perpendicular
AWAC	Acoustic Wave And Current profiler
AWST	Australian Western Standard Time
BAW	Federal Waterways Engineering and Research Institute, Germany
BoM	Australian Government Bureau of Meteorology
CD	Chart Datum
CFD	Computational Fluid Dynamics
CMST	Centre for Marine Science and Technology, Curtin University, Western Australia
DST	Development Centre for Ship Technology and Transport Systems, Germany
DTC	Duisburg Test Case
DWC	Deep Water Channel
DWT	DeadWeight Tonnage
FFT	Fast Fourier Transform
FHR	Flanders Hydraulics Research, Belgium
FL	Front Lead light
FP	Forward Perpendicular
FPSO	Floating Production Storage and Offloading
FS	Free Surface
GNSS	Global Navigation Satellite System
HAT	Highest Astronomical Tide
HTC	Hamburg Test Case
ICORELS	International COmmission for the REception of Large Ships
IGES	Initial Graphics Exchange Specification
ITTC	International Towing Tank Conference
JBC	Japan Bulk Carrier
KCS	KRISO Container Ship
KLNG	KRISO Liquefied Natural Gas carrier

KRISO	Korean Research Institute Ships and Ocean engineering
KVLCC	KRISO Very Large Crude oil Carrier
LAT	Lowest Astronomical Tide
LCB	Longitudinal Centre of Buoyancy
LCF	Longitudinal Centre of Floatation
LCG	Longitudinal Centre of Gravity
LNG	Liquefied Natural Gas
LPG	Liquefied Petroleum Gas
MAPE	Mean Absolute Percentage Error
MARAD	U.S. MARitime ADministration
MDT	Mean Dynamic Topography
MEM	Maximum Entropy Method
MSL	Mean Sea Level
MWPA	Mid West Ports Authority, Western Australia
NGA	U.S. National Geospatial-Intelligence Agency
NM	North Mole
NMRI	National Maritime Research Institute, Japan
NOAA	U.S. National Oceanic and Atmospheric Administration
NTU	National Tide Unit, Australian Government BoM
PIANC	The World Association for Waterborne Transport Infrastructure, Belgium
RANS	Reynolds-Averaged Navier-Stokes
RAO	Response Amplitude Operator
RMS	Root-Mean-Square
Ro-Ro	Roll-on / Roll-off
RPM	Revolution Per Minute
SM	South Mole
SOG	Speed Over Ground
SSA	Significant Single Amplitude
SST	Sea Surface Topography
STW	Speed Through Water
SVA	Schiffbau-Versuchsanstalt Potsdam, Germany
TEU	Twenty-foot Equivalent Unit
UKC	Under-Keel Clearance
VTS	Vessel Traffic Service
VWS	Versuchsanstalt für Wasserbau und Schiffbau, Germany
WA DoT	Western Australian Department of Transport

Roman Symbols	**Description**
a_{33}	Heave added mass
a_{44}	Roll added moment of inertia
a_{55}	Pitch added moment of inertia
$A_{1/3}$	Significant amplitude
A_c	Channel wetted cross-sectional area
A_{max}	Maximum amplitude
A_s	Ship submerged cross-sectional area (amidships)
A_{WP}	Ship waterplane area
B	Ship beam (breadth)
B_{44E}	Eddy making roll damping coefficient
B_{44F}	Frictional roll damping coefficient
B_{44K}	Bilge keel roll damping coefficient
B_{44L}	Lift roll damping coefficient
B_{44S}	Correction on the potential roll damping coefficient due to forward speed (or wave damping at forward speed)
B_{44V}	Total viscous roll damping coefficient
B_{max}	Maximum ship beam (breadth)
$B(x)$	Ship waterline beam (breadth) at position x
c	Dynamic trim correction
C_B	Block coefficient
C_F	Correction factor for ship shape (Römisch)
C_s	Sinkage coefficient in open water
C_{s_bow}	Bow sinkage coefficient
C_{s_LCF}	LCF sinkage coefficient
C_{s_max}	Maximum sinkage coefficient
C_{s_mid}	Midship sinkage coefficient
C_{s_stern}	Stern sinkage coefficient
C_V	Correction factor for ship speed (Römisch)
C_θ	Trim coefficient
C_ϕ	Ship turning coefficient
f	Frequency
F_h	Depth-based Froude number
F_r	Froude number
g	Acceleration due to gravity

G_{FS}	GNSS height relative to instantaneous static free surface
G_{LAT}	GNSS height relative to LAT
$G_{measured}$	Raw GNSS height (ellipsoid height)
G_{MSL}	GNSS height relative to MSL
GM	Metacentric height
GM_f	Metacentric height, corrected for free surface effect
GM_L	Longitudinal metacentric height
GM_T	Transverse metacentric height
h	Water depth (or channel depth)
h_o	Water depth outside channel
h_1	Water depth outside channel
h_T	Channel trench depth
H_s	Significant wave height
I_W	Second moment of waterplane area
k	Fourier transform variable
k_{xx}	Roll radius of gyration
k_{yy}	Pitch radius of gyration
K	Channel coefficient (Barrass)
K_1	Corrected channel coefficient (Huuska/Guliev)
K_s	Correction factor for channel width (Huuska/Guliev)
KG	Height of the ship's centre of gravity above keel
l_R	Heel moment arm due to ship turning
L	Ship submerged length
L_{OA}	Ship length overall
L_{OS}	Ship length overall submerged
L_{PP}	Ship length between perpendiculars
m_n	n-th order spectral moment
M	Ship weight
n	Canal-to-ship hull cross-sectional area ratio
N	Geoid undulation
p	Hydrodynamic pressure (pressure above hydrostatic)
R_C	Steady turning radius
S	Blockage factor ($= A_s / A_c$)
S_1	Corrected blockage factor (Huuska/Guliev)
S_{bow}	Sinkage at forward perpendicular
S_{LCF}	Sinkage at LCF
S_{max}	Maximum sinkage

S_{mid}	Sinkage at midships
S_{stern}	Sinkage at aft perpendicular
S_w	Wave energy spectrum
$S(x)$	Ship submerged cross-sectional area at position x
S_η	Motion response spectrum
t	Instantaneous tidal height
t_{mean}	Mean tidal height (difference between MSL and LAT)
T	Ship draught
T_{01}	Mean period
T_{02}	Average zero-crossing period
T_m	Mean period
T_p	Spectral peak period
T_s	Significant period
T_z	Ship natural heave period
T_θ	Ship natural pitch period
T_ϕ	Ship natural roll period
U	Ship speed (= free stream speed in body-fixed reference frame)
U_C	Ship speed at steady turning
V	Ship speed (in m/s, Römisch)
V_{cr}	Critical ship speed (in m/s, Römisch)
V_e	Enhanced ship speed (in m/s, Yoshimura)
V_K	Ship speed (in knots, Barrass)
V_s	Ship speed (in m/s, Yoshimura)
w	Channel width (to the toe of slope)
w_{ch}	Effective channel width
x	Longitudinal coordinate
x_{LCF}	Position of longitudinal centre of floatation
x_{mid}	Position of midships
y	Transverse coordinate
Y	Ship motion RAO
z	Vertical coordinate
Z	Hydrodynamic vertical force on ship
$Z_{1/3}$	Significant heave amplitude
Z_{max}	Maximum heave amplitude

Greek Symbols	Description
α	Absolute wave direction
θ	Stern-down change in trim due to squat
$\theta_{1/3}$	Significant pitch angle amplitude
θ_{max}	Maximum pitch angle amplitude
λ	Transverse decay parameter
ρ	Fluid density
ϕ	Disturbance velocity potential
$\phi_{1/3}$	Significant roll angle amplitude
ϕ_C	Heel angle due to ship turning
ϕ_{max}	Maximum roll angle amplitude
ϕ_R	Maximum heel angle due to ship turning

Mathematical Symbols	Description
∇	Ship displacement volume

Software	Description
AutoCAD 2017	https://www.autodesk.com
MATLAB R2016a	https://www.mathworks.com
MAXSURF Modeler Advanced 20.00.05.47	http://www.maxsurf.net
Microsoft Excel	https://www.microsoft.com
OCTOPUS	http://www.abb.com
PDSTRIP	http://pdstrip.source forge.net
Rhino 5	http://www.rhino3d.com
SlenderFlow	https://www.perthhydro.com
Trimble Business Centre v3.50	https://www.trimble.com
W@ves21	http://www.datawell.nl

Chapter 1

General Introduction

1.1 Background and motivation

The basic aim of approach channels is to provide safe passage to all ships requiring to move into port from the sea to the berthing area. Approach channels should, therefore, be planned to achieve requirements for the safe navigation of ships, easy manoeuvring, and the harmony of bathymetric and marine conditions.

The development of shipbuilding skills has led to the ability to build mega-ships for the better economy of shipping, and now even ultra-large container ships with lengths over 366 m, and LNG carriers over 300 m, have become common in ports (Eloot & Vantorre, 2011). However, this international trend to increase in ship size in the past few decades means that determining the necessary channel depth, which is generally determined by under-keel clearance (UKC), becomes increasingly important as the main cause of ships' grounding is insufficient depth in the port or coastal water area where the ship must manoeuvre (Li, 2010). Many ports are contemplating deepening existing channels or planning new approach channels that can safely accommodate the new generation of cargo ships.

Much of this work is dredging, which is essentially an excavating operation, and the determination of the correct depth of channels is mainly governed by UKC, or the difference between the lowest part of the ship's hull and the seabed. However, as shown in Figure 1.1, two kinds of UKC, static and nett (or dynamic, real time, or actual), have clear and distinct specific applications. Static UKC is the difference between the available water depth and the ship's draught (Gourlay, 2014b), whereas nett UKC reflects the dynamic interactions of squat, heel and wave-induced motions, all of which act to decrease the clearance between keel and seabed. To ensure the safety of any ship transit in approach channels, nett UKC must always be greater than a predetermined safety tolerance (PIANC, 2014).

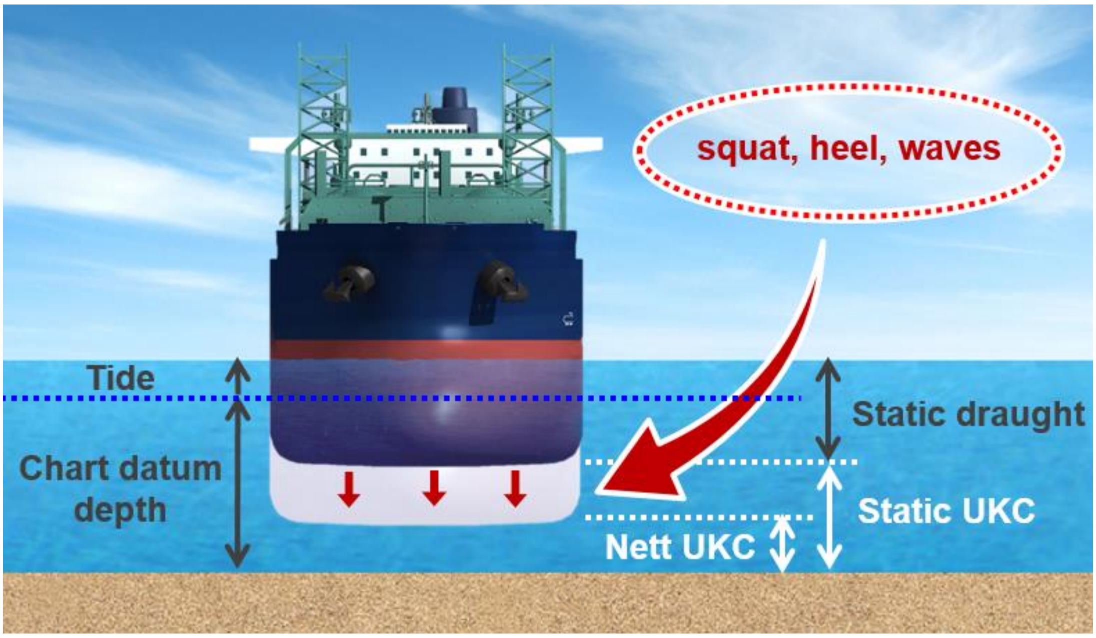

Figure 1.1. Important components for calculating UKC of a ship in port approach channels

In terms of ship manoeuvrability, or specific manoeuvres of the pilot or ship without assistance of tugs, a different safety margin should be satisfied. When the distance between the seabed and the ship's hull decreases, the ship manoeuvrability at the design speed also decreases. PIANC (1985) introduced the Manoeuvrability Margin (MM), i.e., the minimum clearance between the ship's hull and the manoeuvrability-governing depth, which ensures that there is adequate water flow around the ship and over the rudder for the ship to be safely controlled. The MM is used to define the time-averaged clearance under the ship, and its minimum value depends on ship type, ship traffic (one-way or two-way), channel configuration and whether the ship has tug assistance. For most ship sizes, types and channel types, a minimum MM of 5% of draught or 0.6 m, whichever is greater, has been found to be sufficient for proper manoeuvrability, and another minimum MM of 0.5 m is generally considered for tug-assisted operations, regardless of draught (PIANC, 2014). The calculation for minimum MM should never be confused with the calculation for nett UKC that includes wave response allowance. A more detailed description of the MM, e.g., its requirements, calculations and applications, can be found in PIANC (2014).

When a ship is underway in shallow calm water (or an approach channel with calm wind and low swell conditions), it experiences a downward sinkage and dynamic trim change, collectively called 'ship squat'. Ocean waves may also cause vertical motions of a ship travelling in an approach channel, exemplified by wave-induced heave, roll and pitch. Such motions in shallow water are significant concerns for large monohull ships like bulk carriers and container ships, because they often operate at small UKC.

Some of the grounding incidents in approach channels have been attributed to ship squat and wave-induced motions (Gourlay, 2015): for example, the grounding of oil tankers *Capella Voyager* and *Eastern Honour* during their approach to the Port of Whangarei, New Zealand, in 2003, was a result of wave-induced motions (Transport Accident Investigation Commission, 2003a; 2003b); and the most widely reported of ship grounding due to squat, the cruise ship *Queen Elizabeth II* in Vineyard Sound, USA, in 1992, was caused by its high speed induced squat (Marine Accident Investigation Branch, 1993). The oil tankers *Tasman Spirit* grounded in Karachi Harbour, Pakistan, in 2003 and *Iran Noor* in Ningbo Port, China, in 2004 (Barrass, 2004a). A more recent grounding was of the oil tanker *Desh Rakshak* in the entrance to Port Philip, Australia, in 2006 (Australian Transport Safety Bureau, 2007). All these cases are attributable to the combined effect of ship squat and wave-induced motions.

Such groundings demonstrate that accurate predictions of ship motion in shallow water or port approach channels are indispensable for safe UKC management, and can also play a vital role in supporting the economic and environmental issues inherent in planning a new approach channel or deepening existing channels. For these reasons, in-depth studies of the clearance between moving ships and the seabed and thus of UKC, consideration of various navigational environments such as sea conditions; ship size, speed, loading conditions; among other factors, need to be actively undertaken.

1.2 Ship under-keel clearance (UKC) and factors affecting it

As mentioned, an optimum dredging depth for an approach channel is determined by the application of a ship's UKC and the factors affecting it: that is, water level-related factors including tidal effect, ship-related factors including static draught and vertical motions, and bottom-related factors (PIANC, 2014). Of the ship-related factors, dynamic vertical motions like ship squat, heel, and wave-induced motions are significant factors affecting UKC requirements.

Ship squat is the change in a ship's vertical position when underway. It is commonly characterised by a bodily sinkage and a dynamic change in trim (PIANC, 2014). In particular, when a ship travels in shallow water (or port approach channels), water flow along the sides and underneath the ship is faster than in open water. This causes a change in the hydrodynamic force between the seabed and the ship's keel, resulting in a reduction in pressure: the so-called Bernoulli effect. This reduction leads to the ship dropping vertically (a downward sinkage) into its own wave trough, plus a moment about the transverse axis (change in trim). The combination of the bodily sinkage and the dynamic change in trim is called 'ship squat'; it brings the ship closer to the seabed. An example of an occasion in which ship squat occurred is shown in Figure 1.2.

(a)

(b)

Figure 1.2. An example of ship squat: (a) Freight Ro-Ro at draught of 6.5 m, speed of 10 knots and UKC of approximately 8 m; (b) The same ship at speed of 20 knots and UKC of 10 m [photos by John Clandillon-Baker FNI (United Kingdom Maritime Pilots' Association, 2008)]

Generally both bow and stern sink deeper as the ship's speed increases, but not equally. Typically, maximum sinkage occurs at the bow for ships with a high block coefficient (full-form), such as bulk carriers and tankers; fine-form ships like passenger liners and container ships, which usually tend to travel faster than full-form ships, do not always experience their maximum sinkage at the bow: sometimes it occurs at the stern (PIANC, 2014). For large modern bulk carriers or container ships, maximum sinkage, regardless of whether it occurs at bow or stern, can be in the order of 1−2 m. This may cause the ship to run aground if it is moving too fast in shallow water (PIANC, 2014).

A number of theoretical and experimental studies have been undertaken in an effort to better predict the squat effect (see PIANC, 2014 for an overview). Initial attempts to calculate ship squat were made in the 1930s. Kreitner (1934) considered a one-dimensional hydraulic theory of a block ship and Havelock (1939) of an elliptical hull form in infinitely deep water. Constantine (1960) studied the relationship between subcritical, critical and supercritical speed regimes in the case of a ship travelling in a shallow and narrow channel. Slender-body theory, a method to calculate flow around ships whose beam and draught are small compared to their length, was originally developed by several researchers (Joosen, 1964; Maruo, 1962; Newman, 1964; Newman & Tuck, 1964). Tuck (1966) developed a slender-body shallow-water theory to predict the vertical force on slender ships in shallow water at both subcritical and supercritical speeds; these showed a reasonable correlation with the model-scale test results presented by Graff, Kracht, and Weinblum in 1964 (Duffy, 2008). Tuck's (1966) theory was developed by himself and others, Tuck (1967) for shallow water of finite width, Beck, Newman, and Tuck (1975) for dredged channels, and Tuck and Taylor (1970). Dand and Ferguson (1973) presented a semi-empirical method for squat prediction in shallow water with model-scale and full-scale measurement data. Naghdi and Rubin (1984) studied the squat problem using a two-dimensional hydraulics theory, and Cong and Hsiung (1991) made a similar approach combining the thin ship and flat ship theory to solve the same problem for transom stern ships (Lataire, Vantorre, & Delefortrie, 2012). Gourlay (2000) applied the slender-body theory to predict squat with arbitrary bottom conditions. An overview of the slender-body theory was provided by Gourlay (2008b).

These techniques were so complicated that they were of little practical use to mariners, and since then several empirical methods of predicting squat have been developed, based on numerical approaches or model-scale tests, to deal with the need for a simpler, more handy expression (Ankudinov, Daggett, Huval, & Hewlett, 1996; Barrass, 1979; Eryuzlu, Cao, & D'Agnolo, 1994; Hooft, 1974; Huuska, 1976; Millward, 1992; Römisch, 1989; Stocks, Dagget, & Pagé, 2002; Yoshimura, 1986). These methods, developed in different conditions and dealing with different hull forms, channel configurations and speed ranges, have shown good agreement with the cases that they were designed for, but may show variable results for other types of ships and channels.

More recent research activities have focused on the validation of numerical models and existing methods for determining ship squat, including scale model tests (Delefortrie, Vantorre, Eloot, Verwilligen, & Lataire, 2010; Mucha, el Moctar, & Böttner, 2014; Uliczka, Kondziella, & Flügge, 2004; Yun, Park, & Yeo, 2014) and full-scale tests (Gourlay, 2008a; Uliczka & Kondziella, 2006) for container ships; scale model tests (Lataire, Vantorre, & Delefortrie, 2012; Yun, Park, & Park, 2014) and full-scale tests (Beaulieu, Gharbi, Ouarda, & Seidou, 2009) for oil tankers; and scale model tests (Duffy, 2008; Gourlay, 2011) and full-scale tests (Ha, Gourlay, & Nadarajah, 2016; Härting, Laupichler, & Reinking, 2009; Moes, 2007) for bulk carriers.

Ocean waves are a demonstrable cause of vertical ship motions, which are an intricate combination of heave, roll and pitch, and which have the potential to cause the largest reduction in UKC if a port is directly open to the ocean and its approach channel is exposed to long-period swells. However, very few studies on ship wave-induced motions in port approach channels have been conducted; most studies in this area have focused on the motions of offshore structures (Faltinsen & Michelsen, 1974; Skandali, 2015; Standing, Brendling, & Jackson, 1993; van Dijk, Quiniou-Ramus, & Le-Marechal, 2003) or of moored ships (Van Oortmerssen, 1976; Veen, 2003). Campbell and Zwamborn (1984) and Van Wyk and Zwamborn (1988) conducted model-scale tests on wave-induced motions of bulk carriers under conditions representative of some major South African ports; and another set of wave-induced motion studies was made using numerical modelling to confirm the suitability of existing channels in the United States (Briggs, Demirbilek, & Lin, 2014; Briggs & Henderson, 2011). For measurements and validations at full scale, Van Wyk (1982) carried out trials on some bulk carriers using a simple photogrammetric technique. In 1980, Wang conducted full-scale measurements of motion characteristics for 29 ship transits, including oil tankers, bulk carriers and container ships, in the Columbia River entrance channel, using an instrumentation package called the Ship Motion and Positioning System (SMPS). Validation of a numerical model for predicting ship UKC using full-scale measurements of some container ship transits (McCollum & Ankudinov, 2000) was also made by Briggs, Silver, Kopp, Santangelo, and Mathis (2013).

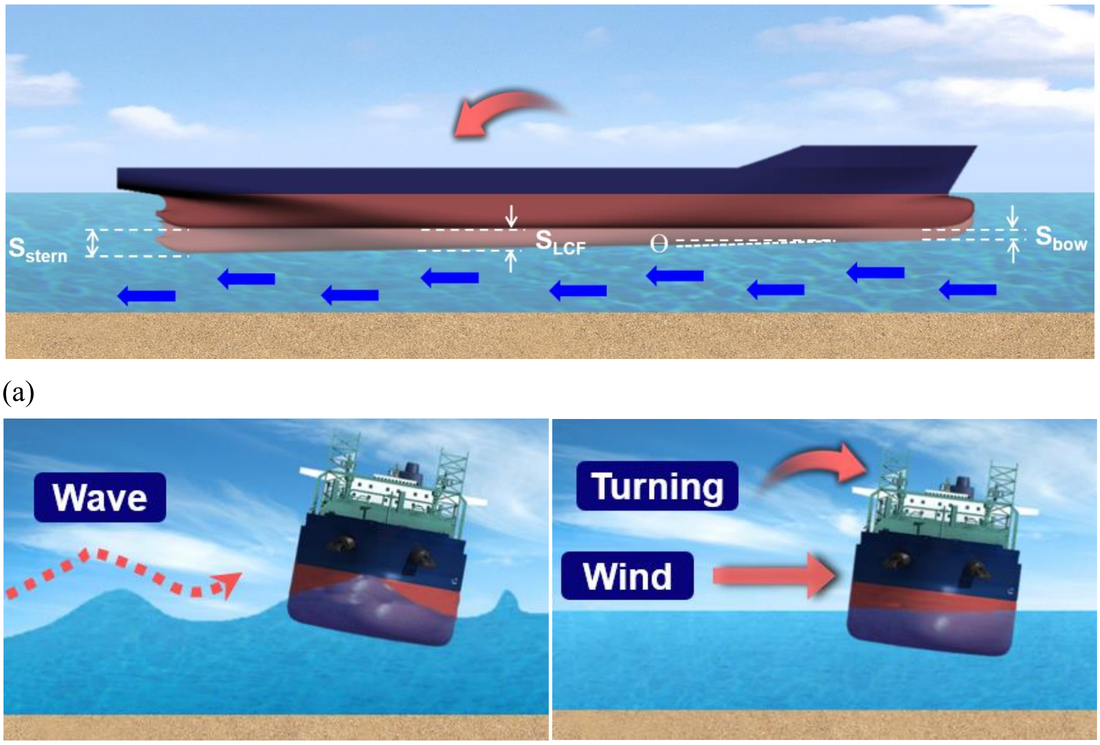

(a)

(b) (c)

Figure 1.3. Factors affecting UKC: (a) Squat (a case of trim by stern); (b) Wave-induced motions; (c) Heel due to turning and wind

Heel caused by wind or turning is another important factor affecting UKC. Container ships generally experience large heel arising from turning and wind: heel angles of the order of 1−2° were measured in container ships in Hong Kong (Gourlay, 2008a). In contrast, bulk carriers have a relatively large displacement-to-length ratio, a low vertical centre of gravity above keel (KG) and a small above-water profile area, which translates into smaller heel angles caused by wind and turning, generally of up to 0.5° (Ha, Gourlay, & Nadarajah, 2016). This means that dynamic heel may be a more important consideration for container ships than for bulk carriers, bringing their bilge corners closest to the seabed. Figure 1.3 illustrates the three main factors of squat, wave-induced motions and heel, each of which has a great influence on UKC.

1.3 Objectives and significance

The primary objective of this study is to provide fundamental data and information for a comprehensive UKC guideline based on numerical modellings plus model-scale and full-scale measurement data. Accurate and practical prediction techniques of vertical ship motions in port approach channels can give an appropriate UKC allowance for dynamic factors such as squat, wave-induced motions and heel, and cannot be overemphasised. This thesis will mostly describe the contributions of squat and wave-induced motions to UKC because standard methods already exist for calculating heeling moments due to turning and wind (PIANC, 2014). The objectives of this study may be condensed into the following:

- to develop a technique to predict ship squat in shallow water or port approach channels that is applicable to a wide range of ship hull forms and channel configurations, and results in a guideline on UKC

- to perform full-scale measurements to obtain high-quality data on vertical ship motions in port approach channels, including squat and wave-induced motions, which may be used in practical tests of numerical UKC modelling

- to validate current UKC practices using model-scale and full-scale test results

- to identify limitations in existing methods and suggest improvements to them based on the results of full-measurement case studies

The numerical methods, suggested guidelines and improvements arising from this study can be extended to a wide range of applications to ensure the most efficient and safe UKC management in ports. A better understanding of ship UKC will facilitate

- the safety of ship transits by ensuring a consistently low grounding risk in all environmental conditions

- less dredging, cutting costs and minimising the environmental impacts inherent in dredging works

- more cargo, as existing ships can load deeper and make the most of their carrying capacity in port approach channels more efficient shipping operations as larger ships can be accommodated in ports, increasing fuel economy

This study will also produce reliable data that engineers may utilise in the design of approach channels, especially at stages in which the dredging depth has to be determined, to ensure the optimum design of channel sections and the capacity of existing channels to accommodate larger ships.

1.4 Methodology

In this thesis, 13 published representative ship hull forms are developed from supplied IGES files and the published lines plans. These models, which fall into the categories of container ships, bulk carriers, oil tankers and membrane LNG carriers, are used to recommend guidelines when making a choice of sinkage coefficients. To capture the effect of different channel or canal configurations on the sinkage coefficients, 24 channel cases of varying width, depth and side depth are applied to each hull model.

Model-scale tests, in a controlled environment, remain the method of choice for benchmarking studies (Mucha, el Moctar, & Böttner, 2014; Gourlay, von Graefe, Shigunov, & Lataire, 2015), with appropriate allowance for scale effects (Deng et al., 2014; Graff, Kracht, & Weinblum, 1964). For analysis of sinkage and trim of modern container ships in shallow water, model-scale test data, e.g., tests for the Duisburg Test Case (DTC) (Mucha & el Moctar, 2014b; Mucha, el Moctar, & Böttner, 2014), KRISO Container Ship (KCS) (Gronarz, Broß, Mueller-Sampaio, Jiang, & Thill, 2009; Mucha & el Moctar, 2014a), JUMBO (Uliczka, Kondziella, & Flügge, 2004) and MEGA-JUMBO (Uliczka, Kondziella, & Flügge, 2004), are extensively used and discussed with theoretical methods. A review of changing container ship hull designs to the present time is made with regard to the modelled hulls. Two additional container ship hull forms, the Hamburg Test Case (HTC) and S-175, are considered for comparative purposes.

Measurements and validations at full scale will have a decisive effect on this study. The progressively increasing accuracy of Global Navigation Satellite System (GNSS) receivers allow full-scale measurements in actual sea conditions. Full-scale trials measuring the dynamic sinkage, trim and heel of 11 bulk carrier transits at the Port of Geraldton (Ha & Gourlay, 2016b) and 16 container ship transits at the Port of Fremantle (Ha & Gourlay, 2016a), were successfully performed. The measurements were carried out using high-accuracy GNSS receivers on board each ship and at a fixed base station for an external reference (Feng & O'Mahony, 1999; Gourlay & Klaka, 2007). At the same time, video footage was taken to capture each ship's manoeuvring during a turn. Figure 1.4 shows the photos of the GNSS receiver and video capture device taken during the full-scale trials at the Port of Geraldton channel.

Figure 1.4. GNSS receiver and video capture device setups on bridge wing

Measured ship motion data was post-processed using relevant software, e.g., *MATLAB R2016a* (https://www.mathworks.com), *AutoCAD 2017* (https://www.autodesk.com) and *Trimble Business Centre v3.50* (https://www.trimble.com) software, to identify the sinkage at the forward, aft and transverse extremities of the keel that would be a point of concern about running aground. Sinkage, trim and heel were calculated by comparing the vertical motions of the ship underway to those at berth allowing for tidal changes. Wave-induced heave, roll and pitch motions are derived by applying a low-pass filter to remove the effects of near-steady components, that is, of squat and heel caused by wind and turning. The measured squat and wave-induced motions at full scale are both compared with the theoretical predictions.

Environmental data, such as wave data from wave rider buoys and tide records from tide gauges, were provided by Mid West Ports Authority (MWPA), Fremantle Ports, and the coastal infrastructure team from the WA Department of Transport (WA DoT). Detailed survey data for channel bathymetry were also provided through collaboration with MWPA, Fremantle Ports and OMC International. Wave data analysis in particular needs to be taken into account because several wave parameters, including wave height and period, are important in understanding wave-induced ship motions and, hence, UKC calculations in port approach channels. Full measured wave time series data, which covered the entire period of the ship transits, was used for the wave spectral analysis.

Spectral analysis is conducted to produce heave, roll and pitch motion response spectra of each ship, which later are compared with those from predictions to provide method validation of ship wave-induced motions in port approach channels at full scale.

1.5 Overview of the thesis

This thesis is composed of five chapters. Each reviews the current state of ship motion predictions, including ship squat and wave-induced motions, and attempts to identify an appropriate approach that will improve UKC predictions. A brief summary of each chapter is as follows:

Chapter 2: Sinkage Coefficients for Ship Squat Prediction Using Numerical Modelling

In Chapter 2, sinkage coefficients are developed for cargo ships in shallow open water (or port approach channels) with minimal transverse restrictions. The sinkage coefficients are calculated using slender-body shallow-water theory (Beck, Newman, & Tuck, 1975; Tuck, 1966; 1967) applied to 13 published ship hull forms. Results are condensed into sinkage coefficient ranges for container ships, oil tankers, bulk carriers and membrane LNG carriers. Because the sinkage coefficients are significantly affected by different channel configurations or by blockage effects of canals, limitations on the use of the coefficients are suggested considering both ship and channel dimensions.

Chapter 3: Container Ship Squat Prediction Using Model-Scale Tests

Chapter 3 concerns the dynamic sinkage and trim of modern container ships in shallow water (or port approach channels) in detail. A review is made of the changes to container ship hull designs to the present, together with available model test data (Gronarz, Broß, Mueller-Sampaio, Jiang, & Thill, 2009; Mucha & el Moctar, 2014a; 2014b; Mucha, el Moctar, & Böttner, 2014; Uliczka, Kondziella, & Flügge, 2004) for sinkage and trim. Two potential flow methods, the slender-body method (Tuck, 1966; 1967) and the Rankine-source method (von Graefe, 2014a), are discussed with reference to the model test results. Several empirical methods (Barrass, 2004b; Huuska, 1976; Römisch, 1989; Stocks, Dagget, & Pagé, 2002; Yoshimura, 1986), as given in the PIANC guidelines (2014), are also compared, against both the model test results and the theoretical methods.

Chapter 4: Full-Scale Measurement Campaigns

Chapter 4 presents results from a series of recent full-scale trials measuring dynamic sinkage, trim and heel of 11 bulk carrier transits at the Port of Geraldton (Ha & Gourlay, 2016b) and of 16 container ship transits at the Port of Fremantle (Ha & Gourlay, 2016a). Measurements were carried out using high-accuracy GNSS receivers on board and a fixed reference station. Measured sinkage, together with ship speed and channel bathymetry, are shown. Additional comparisons of dynamic trim and heel between the ship transits are also given. The results are used to produce squat comparisons and validations (Chapter 5) and wave-induced motion comparisons and validations (Chapter 6).

Chapter 5: Ship Squat Comparisons and Validations Using Full-Scale Trials

In Chapter 5, selected results are presented from the two sets of full-scale trials, including bulk carrier trials at the Port of Geraldton and container ship trials at the Port of Fremantle (Chapter 4). The measured dynamic sinkage, trim and heel of three sample bulk carrier and five sample container ship transits, are discussed in more detail. Maximum dynamic sinkage and dynamic draught, as well as elevations of each ship's keel relative to chart datum, are calculated. A theoretical method using slender-body shallow-water theory (Beck, Newman, & Tuck, 1975; Tuck, 1966) is applied to calculate sinkage and trim of the example ship transits. A comparison between measured and predicted results is made to validate the software used to make the UKC predictions.

Chapter 6: Ship Wave-Induced Motion Comparisons and Validations Using Full-Scale Trials

The validation of the numerical models of ship wave-induced motions in port approach channels is performed in Chapter 6. A selected set of high-quality data from the full-scale trials of the vertical motions of container ship transits at the Port of Fremantle is used (Chapter 4). Measured wave-induced heave, roll and pitch motions of six example container ship transits are discussed in detail, together with descriptions of in-situ wave measurements and wave spectral analysis. A linear strip method, as implemented in a computer code *OCTOPUS* (Journée, 2001; Journée & Adegeest, 2003), is applied to predict the wave-induced motions. A comparison is made between measured and predicted motion responses to validate the ship motion software; and particular attention is paid to roll motion response to assess the suitability of existing roll damping methods (Himeno, 1981; Ikeda, Himeno, & Tanaka, 1978) at full scale.

Chapter 7 summarises the conclusions of each chapter and identifies limitations of the approaches used in this thesis. Recommendations and research directions for future work are also outlined.

Chapter 2

Sinkage Coefficients for Ship Squat Prediction Using Numerical Modelling

In this chapter, sinkage coefficients are developed for cargo ships in shallow open water (or port approach channels) with minimal transverse restrictions. These sinkage coefficients may be used for UKC management by ports, pilots and deck officers. The coefficients are calculated using slender-body shallow-water theory applied to 13 published ship hull forms. Results are condensed into sinkage coefficient ranges for container ships, oil tankers, bulk carriers and membrane LNG carriers. It is shown that the coefficient in open water varies from ship hull to ship hull, but distinguishing characteristics according to ship types are observed. Because the coefficients are significantly affected by varying width, depth and side depth of dredged channels or by blockage effects of canals, limitations on their use are suggested, based on ship and navigation channel dimensions. Examples of an assessment are also given for container ships, bulk carriers and LNG carriers in Australian ports, which may be used to determine whether a particular ship and channel configuration might be classed as open water, or whether a specific narrow-channel analysis is required.

2.1 Introduction

Information on suitable squat allowances for different types of channels and ships is addressed in the recent guidelines for port approach channels by the World Association for Waterborne Transport Infrastructure (PIANC, 2014). Several semi-empirical methods (Hooft, 1974; Huuska, 1976; International Commission for the Reception of Large Ships, 1980; Millward, 1992) are based on the slender-body analysis of Tuck (1966) for ships in shallow open water. According to that theory, the midship (midway of L_{PP}), bow and stern sinkage of a ship should be given by

$$S_{mid} = C_{s\_mid} \frac{\nabla}{L_{PP}{}^2} \frac{F_h{}^2}{\sqrt{1-F_h{}^2}} \tag{2.1}$$

$$S_{bow} = C_{s\_bow} \frac{\nabla}{L_{PP}{}^2} \frac{F_h{}^2}{\sqrt{1-F_h{}^2}} \tag{2.2}$$

$$S_{stern} = C_{s\_stern} \frac{\nabla}{L_{PP}{}^2} \frac{F_h{}^2}{\sqrt{1-F_h{}^2}} \tag{2.3}$$

F_h is then defined by

$$F_h = \frac{U}{\sqrt{gh}} \tag{2.4}$$

Eqs. (2.1), (2.2) and (2.3) suggest a semi-empirical method to predict ship sinkage: that is, to perform model testing to calculate the sinkage coefficients experimentally, then apply them to predict sinkage in full-scale ships. A problem with this approach is that model tests are necessarily performed in a finite-width tank, for which sinkage coefficients are not constant, but also depend on the tank width, water depth and ship speed. The linear finite-width theory of Tuck (1967) suggests that sinkage will increase as channel width decreases. In addition, non-linear effects become increasingly important as channel width decreases. These effects mean that sinkage coefficients are found not to be constant for each ship. As an example, the MEGA-JUMBO container ship model (Uliczka, Kondziella, & Flügge, 2004) was found to have midship sinkage coefficients (C_{s_mid}) ranging from 1.40−1.76 in the widest channel configuration tested, and 2.02−2.20 in the narrowest channel configuration tested (Gourlay, Ha, Mucha, & Uliczka, 2015).

Why not use smaller-scale models in shallow-water model tests, to minimise the tank width effect? This approach was taken by Graff, Kracht and Weinblum (1964), who used 6-m models for deep-water tests and 3-m models for shallow-water tests. Unfortunately, the smaller-scale models showed an increase in viscous scale effect, which is important for dynamic trim; choosing an appropriate scale is a compromise between minimising tank width effect and minimising scale effect. Needless to say, wide tanks, such as the 10-m wide Duisburg tank, are highly sought after for shallow-water tests.

Some authors have tried to capture the dependence on channel width through empirical corrections to the sinkage coefficients (PIANC, 2014). While this might work well in ship models and channels used to develop the correction, the physics might not be captured adequately enough to enable the application of these methods to a wide range of ships. It is, therefore, recommended that complete numerical simulations be performed for ships in channels. For example, the linear slender-body theory of Tuck (1967) may be used for moderate-width channels; the non-linear Rankine-source method (e.g., von Graefe, 2014a) for narrow channels; and the non-linear hydraulic theory of Gourlay (1999) for very narrow channels. Reynolds-Averaged Navier-Stokes (RANS) methods are becoming increasingly common for modelling ship sinkage and trim, especially in confined waterways (Mucha, el Moctar, & Böttner, 2014).

This chapter pays particular attention to developing sinkage coefficients for waterways with minimal transverse restrictions, such as open waterways or dredged channels, which are common port approach channels on the Australian continental shelf. The coefficients are calculated using the slender-body theory of Tuck (1966) for open water, Tuck (1967) for canals, and Beck, Newman and Tuck (1975) for dredged channels, generalised in Gourlay (2008b). The methods are implemented in the computer code '*SlenderFlow*' (http://www.perthhydro.com), which uses linearised hull and free-surface boundary conditions. For wide channels, the slender-body theory has been shown to give good results for container ships at model scale (Gourlay, Ha, Mucha, & Uliczka, 2015); container ships at full scale (Gourlay, 2008a; Ha & Gourlay, 2018b); bulk carriers and tankers at model scale (Gourlay, 2006; Gourlay, Lataire, & Delefortrie, 2016); and bulk carriers and tankers at full scale (Gourlay, 2008c; Ha, Gourlay, & Nadarajah, 2016).

2.2 Cargo ship types and representative ship models

While lines plans for merchant cargo ships are generally confidential, many ship hull forms for research objectives have been developed over the years. Here, 13 published representative ship models were chosen for analysis, including all of container ships, bulk carriers, oil tankers and membrane LNG carriers. Oil tankers and bulk carriers will be grouped when interpreting simulation results, due to parallels in their hull shapes.

Ships carrying different types of cargo have evolved to have different hull shapes. Shipping containers are fairly low density and need to be transported quickly; so container ships tend to have low block coefficient (C_B), to maximise waterplane area for their displacement and give an efficient hull shape. Bulk carriers and tankers have high-density cargo with less requirement for speed; their hull shapes tend to have high C_B to maximise deadweight capacity at the expense of hull efficiency. Membrane LNG carriers are generally between container ships and tankers in terms of hull shape and C_B, but have shallower draught because of their low-density cargo.

In this chapter the focus will be on container ships, bulk carriers, oil tankers and membrane LNG carriers, the various hull types to be analysed. The results will not be directly applicable to other cargo ship types such as Ro-Ro vessels, car carriers, livestock carriers, Moss LNG carriers, LPG carriers or warships.

The container ships modelled are as follows:

'Duisburg Test Case' ('DTC', 355-m L_{PP}), designed by the University of Duisburg-Essen, Germany, in 2012, is representative of a 14,000-TEU Post-Panamax container ship (el Moctar, Shigunov, & Zorn, 2012).

'KRISO Container Ship' ('KCS', 230-m L_{PP}), designed by Korean Research Institute Ships and Ocean Engineering (KRISO) in 1997, is representative of a 3,600-TEU Panamax container ship (Lee, Koh, & Lee, 2003).

'JUMBO' (320-m L_{PP}), designed by SVA, Potsdam, Germany, in 1995, is representative of a 5,500-TEU Post-Panamax container ship (Uliczka, Kondziella, & Flügge, 2004).

'MEGA-JUMBO' (360-m L_{PP}), designed by VWS, Berlin, Germany, in 2001, is the design ship for the Jade Weser Port in Germany, and is representative of a 12,000-TEU Post-Panamax container ship (Uliczka, Kondziella, & Flügge, 2004).

'FHR Ship D' (291.13-m L_{PP}), designed by Flanders Hydraulics Research and Ghent University, Belgium, in 1996 - 2000, is representative of a Post-Panamax container ship (Gourlay, von Graefe, Shigunov, & Lataire, 2015; Vantorre & Journée, 2003).

'FHR Ship F' (190-m L_{PP}), designed by Flanders Hydraulics Research and Ghent University, Belgium, in 1996 - 2000, is representative of a Panamax container ship (Gourlay, von Graefe, Shigunov, & Lataire, 2015; Vantorre & Journée, 2003).

The oil tankers modelled are as follows:

'KRISO Very Large Crude Oil Carrier' ('KVLCC' 320-m L_{PP}), designed by Korean Research Institute Ships and Ocean Engineering (KRISO) in 1997, is representative of a 300,000-DWT oil tanker (Larsson, Stern, & Bertram, 2003; Van et al., 1998).

'KRISO Very Large Crude Oil Carrier 2' ('KVLCC2', 320-m L_{PP}), designed by Korean Research Institute Ships and Ocean Engineering (KRISO) in 1997, is representative of a 300,000-DWT oil tanker, and is the second version of the KVLCC with more U-shaped stern frame-lines (Larsson, Stern, & Bertram, 2003; Van et al., 1998).

The bulk carriers modelled are as follows:

'Japan 1704B standard series' (6-m model L_{PP}), designed by National Maritime Research Institute (NMRI, former Ship Research Institute of Japan), is representative of a Panamax bulk carrier (Yokoo, 1966).

'Japan Bulk Carrier' ('JBC', 280-m L_{PP}), designed by National Maritime Research Institute (NMRI, former Ship Research Institute of Japan), Yokohama National University and Ship Building Research Centre of Japan, is representative of a Post-Panamax bulk carrier (National Maritime Research Institute, 2015).

‘FHR Ship G’ (180-m L_{PP}), designed by Flanders Hydraulics Research and Ghent University, Belgium, in 1996 - 2000, is representative of a Panamax bulk carrier (Gourlay, von Graefe, Shigunov, & Lataire, 2015; Vantorre & Journée, 2003).

‘MARAD Ship G’ (6.096-m model L_{PP}), designed by Maritime Administration (MARAD), U.S. Department of Transportation, is a full-form cargo ship model from the MARAD series (Roseman, 1987).

The membrane LNG carrier modelled is as follows:

‘KRISO Liquefied Natural Gas Carrier’ (‘KLNG’, 266-m L_{PP}), designed by Korean Research Institute Ships and Ocean Engineering (KRISO) in 2003, is representative of a 138,000-m^3 membrane LNG carrier (Van et al., 2003; 2006).

The hull shapes of these 13 ships were developed from supplied IGES files and published lines plans, using *Rhino 5* (http://www.rhino3d.com), *AutoCAD 2017* (http://www.autodesk.com) and *MAXSURF Modeler Advanced 20.00.05.47* (http://www.maxsurf.net). Calculated details of the modelled ships are given in Table 2.1. Note that LCB and LCF are given as a percentage (%) of L_{PP} forward of AP. Some of the particulars were calculated from the modelled ships and are approximate. Dimensions of the Japan 1704B and MARAD Ship G are at model scale because no full-scale dimensions are specified.

Significant differences in hydrostatic characteristics between the ship hulls are identified in Table 2.1. For example, the block coefficient (C_B) ranges from 0.60 to 0.72 for the container ships, 0.77 to 0.86 for the oil tankers/bulk carriers, and 0.75 for the LNG carrier. LCB ranges from 47.05 to 49.97 % for the container ships, 51.53 to 54.93 % for the oil tankers/bulk carriers, and 49.97 % for the LNG carrier. LCF is aft of the LCB by on average 2.8 % of the L_{PP} for the container ships, 3.6 % for the oil tankers/bulk carriers, and 2.3 % for the LNG carrier.

Table 2.1. Details of the ship hull forms used for numerical calculations

Ships		L_{PP} L_{OA}* L_{OS}† (m)	B (m)	T (m)	∇ (m^3)	C_B (-)	Max. A_s (m^2)	LCB (%)	LCF (%)
Container ships	DTC	355.00 372.81* 366.93†	51.00	14.50	173,337	0.660	730.02	49.04	45.38
	KCS	230.00 243.84* 239.41†	32.20	10.80	52,013	0.650	342.42	48.52	44.33
	JUMBO	320.00 336.90* 336.90†	40.00	14.50	133,901	0.721	564.22	49.30	45.84
	MEGA-JUMBO	360.00 377.65* 365.85†	55.00	16.00	215,775	0.681	867.53	49.97	49.12
	FHR Ship D	291.13 301.51* 301.51†	40.25	15.00	106,226	0.604	593.13	47.05	44.54
	FHR Ship F	190.00 198.64* 198.64†	32.00	11.60	42,338	0.600	365.02	47.74	45.43
Oil tankers	KVLCC1	320.00 333.58* 333.58†	58.00	20.80	312,738	0.810	1,203.80	53.48	49.75
	KVLCC2	320.00 333.58* 333.58†	58.00	20.80	312,622	0.810	1,203.80	53.52	50.02
Bulk carriers	Japan 1704B	6.000 6.335* 6.061†	0.923	0.334	1.482	0.801	0.306	54.93	52.16
	JBC	280.00 290.96* 290.96†	45.00	16.50	178,370	0.858	741.11	52.53	49.30
	FHR Ship G	180.00 188.24* 188.24†	33.00	11.60	57,806	0.839	381.69	53.36	51.09
	MARAD Ship G	6.096 6.604* 6.604†	1.219	0.406	2.318	0.768	0.492	51.53	45.33
LNG carrier	KLNG	266.00 277.54* 270.60†	42.60	11.30	95,940	0.749	473.53	49.97	47.65

[Note: T is ship's design draught; C_B is the ratio of ∇ to ($L_{PP} \cdot B \cdot T$); Max. A_s is maximum cross-sectional area of ship's hull]

Table 2.1 also shows that each ship hull exhibits features typical of its type. Slower full-form ships, such as tankers or bulk carriers, for example, tend to have their LCB well forward of amidships, whereas fine-form ships, such as container ships and LNG carriers, have their LCB slightly aft of amidships (PIANC, 2014).

Comparative body plans of the 13 ship hull forms are shown in Figure 2.1 to Figure 2.4. These body plans illustrate 50 evenly-spaced stations from the transom to the front of the bulb. The body plans of the Japan 1704B and MARAD ship G have a different scale to the others (see Table 2.1).

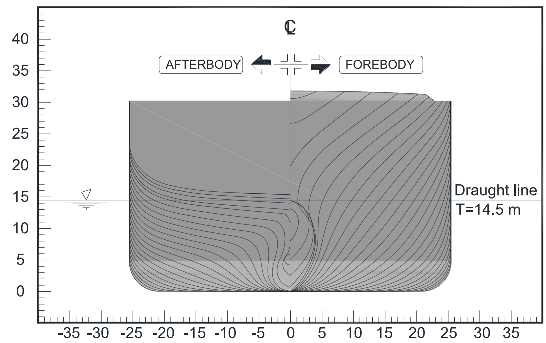

(a) DTC

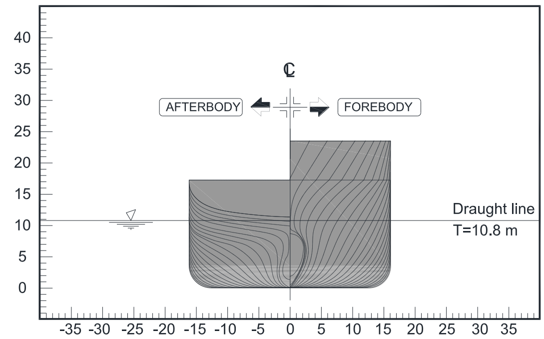

(b) KCS

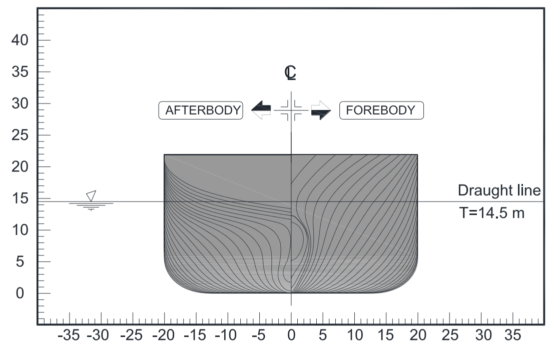

(c) JUMBO

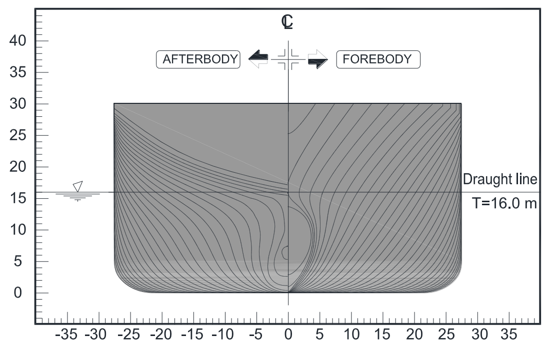

(d) MEGA-JUMBO

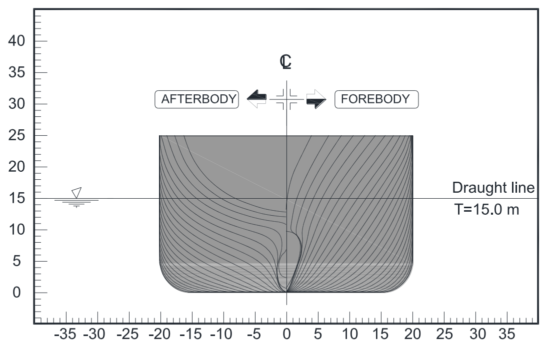

(e) FHR Ship D

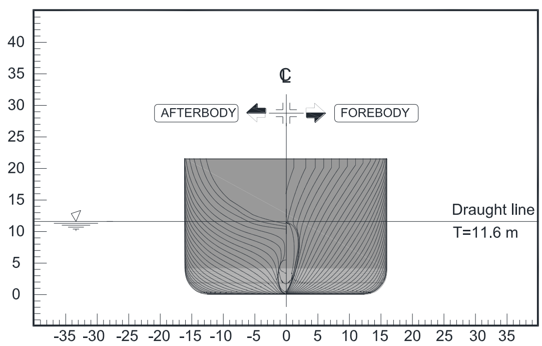

(f) FHR Ship F

Figure 2.1. Body plans of the container ship hulls

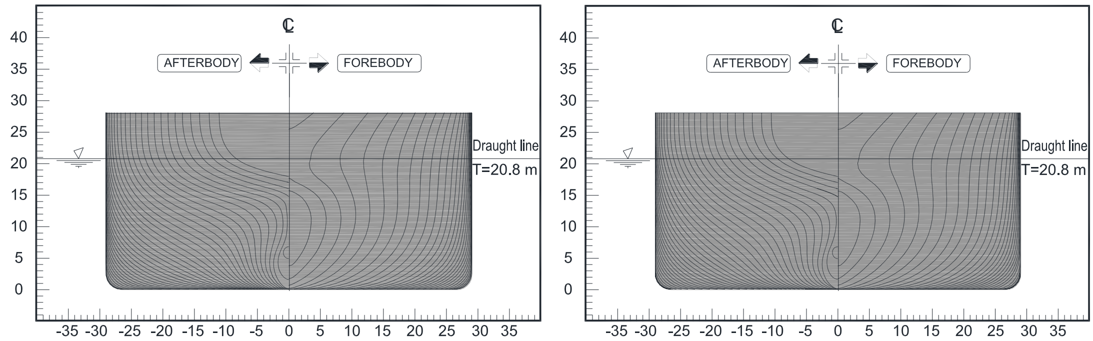

(a) KVLCC1 (b) KVLCC2

Figure 2.2. Body plans of the oil tanker hulls

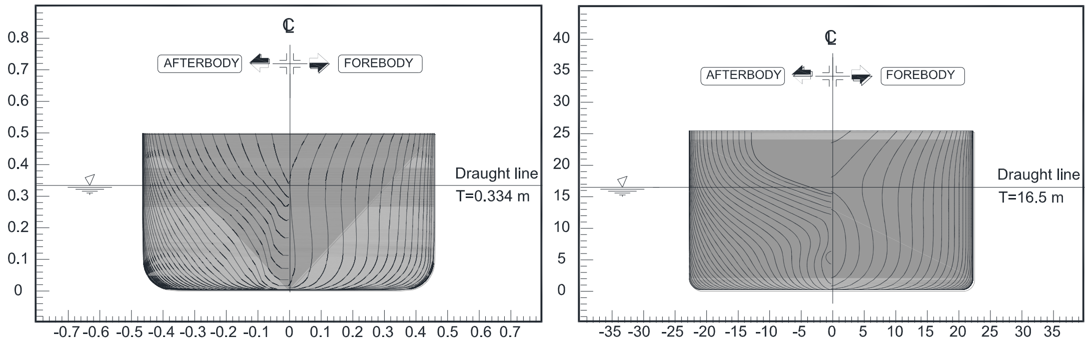

(a) Japan 1704B (b) JBC

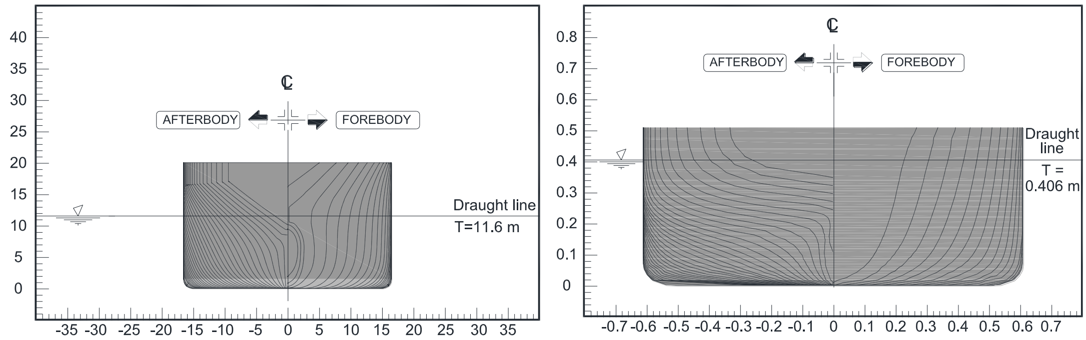

(c) FHR Ship G (d) MARAD Ship G

Figure 2.3. Body plans of the bulk carrier hulls

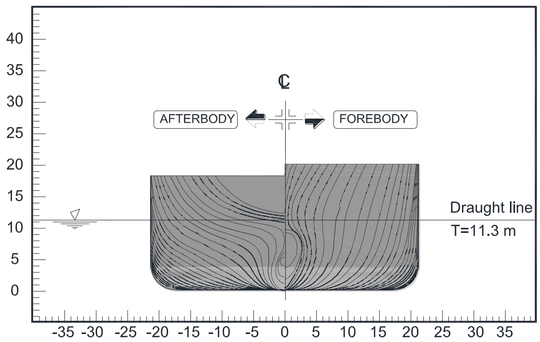

Figure 2.4. Body plan of the LNG carrier hull (KLNG)

Figure 2.1 to Figure 2.4 indicate that significant differences in hull shape exist between different ship types. The distinctive characteristics for the container ships are:

- a pronounced bow bulb
- a wide and nearly flat-bottomed transom stern and aft sections, which are close to horizontal at the waterline

For the oil tankers and bulk carriers, distinctive characteristics in hull shape are:

- forward sections almost vertical at the waterline
- aft sections not far from vertical at the waterline
- smaller transoms and sharper bow bulbs than the container ships

The hull shape of the KLNG is generally between those of the container ships and the oil tankers.

Appendix A shows the bow, stern, profile, bottom and perspective views of the modelled ships. These figures emphasise the features of each ship type's hull shape.

2.3 Theoretical methods

The theoretical method used to calculate open-water sinkage coefficients for the 13 ship hulls is the slender-body shallow-water theory of Tuck (1966). To identify the effect of transverse restrictions, e.g., the width and trench depth of dredged channels, or canal effect, on the sinkage coefficients, the resulting open-water sinkage coefficients should be compared to channel and canal sinkage coefficients, which are calculated based on the slender-body shallow-water theory of Beck, Newman and Tuck (1975), and Tuck (1967), respectively. Gourlay (2008b) compiled and modified these theories to make them more applicable to ships with transom sterns and to cater for arbitrary transverse bathymetry. In this thesis, the theoretical methods are implemented in *SlenderFlow*, a computer code for calculating the flow of water around a slender ship in shallow water developed at Perth Hydro (http://www.perthhydro.com); it is the improved version of '*ShallowFlow*' (Gourlay, 2014a). A more detailed description of the methods, i.e., Tuck (1966) for open water of constant depth, Tuck (1967) for rectangular canals, and Beck, Newman and Tuck (1975) for dredged channels, can be found in Gourlay (2008b; 2011). Note that other conditions are also able to be modelled by *SlenderFlow*, such as arbitrary cross-sectional canals (Gourlay, 2008b), non-linear narrow canals (Gourlay, 1999) and trans-critical monohulls and catamarans (Gourlay, 2008b; Gourlay & Tuck, 2001).

The following is a brief description of the computation methods.

2.3.1 Open water of constant depth

The theoretical methods are valid under assumptions (Gourlay, 2008b; 2014a), which are:

The flow is inviscid, irrotational and incompressible; thus, viscous effects are restricted to a slender boundary layer near the ship's hull and barely affect the pressure distribution around the hull, except possibly at the stern.

The ship's beam is quite small compared to its length; so wave amplitudes are small compared to the ship's length, and allow linearisation of the free surface boundary condition and a series solution in increasing powers of the ship's beam/ship's length (B/L) ratio.

The water depth is quite small compared to the ship's length; hence, horizontal flow velocities overwhelm vertical flow velocities, i.e., two-dimensional flow.

The ship is moving along the centreline of canal or channel configuration, and the bathymetry is assumed symmetric either side of the ship's centreline; thus, cross-flow beneath the ship is ignored.

To describe the flow around a ship, a ship-fixed coordinate system should be defined appropriately, as illustrated in Figure 2.5, which describes:

longitudinal coordinate x centred at midships and positive towards the stern; i.e., $x = 0$ at midships, and the bow of the ship at $x = -L/2$ and stern at $x = L/2$

transverse coordinate y centred at the ship's centreline and positive to starboard; i.e., $y = 0$ at the ship's centreline

vertical coordinate z centred at the height of the undisturbed free surface and positive upwards; i.e., $z = 0$ at the free surface and $z = -h$ at the seabed

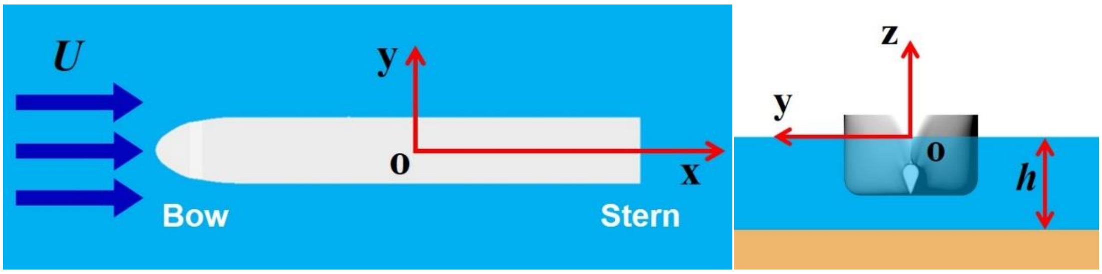

(a) Plan view (b) Section view

Figure 2.5. Ship-fixed coordinate system

Based on the earlier assumptions and coordinate system, considering a slender vertical strut extending from bottom to top of a shallow stream of depth h and infinite width, Michell (1898) showed that the leading-order disturbance velocity potential ϕ is nearly horizontal and satisfies the linearised shallow-water equation

$$(1-F_h{}^2)\frac{\partial^2\phi}{\partial x^2}+\frac{\partial^2\phi}{\partial y^2}=0 \tag{2.5}$$

where F_h = depth-based Froude number in which U is the free stream speed, equal to the ship speed in a conventional earth-fixed coordinate system (refer to Eq. (2.4)). For a slender ship with a general cross-sectional shape, Tuck (1966) solved the problem of defining the kinematic boundary condition on the hull, using matched asymptotic expansions, and Eq. (2.5) is to be solved subject to a boundary condition of the form:

$$\frac{\partial\phi}{\partial y}=\pm\frac{U}{2h}S'(x) \text{ on } y=0_{\pm} \tag{2.6}$$

where $S(x)$ is the ship's submerged cross-sectional area with respect to position x, and the prime denotes the derivative dS/dx. Another boundary condition, which is the far-field boundary condition, is

$$\frac{\partial \phi}{\partial x}, \frac{\partial \phi}{\partial y} \to 0 \text{ as } y \to \pm\infty \text{ for subcritical flow } (F_h < 1) \tag{2.7}$$

or else behaves like an outward wave for supercritical flow ($F_h > 1$). By considering the velocity potential for a line of moving sources in the (x, y) horizontal plane with source strength proportional to the rate of change of ship cross-sectional area at each position x (Gourlay, 2011; Tuck, 1966) so that the boundary condition Eq. (2.6) is satisfied, expressions for the velocity potential and resulting pressure field, including direct integration of a singular integral, were found by Tuck (1966).

Gourlay (2008b) proposed an alternative solution using Fourier transforms. By taking the Fourier transform of Eq. (2.5) and solving subject to boundary condition (2.6), the velocity potential for subcritical flow can be written

$$\phi = -\frac{U}{4\pi h\sqrt{1-F_h^{\,2}}} \int_{-\infty}^{\infty} \frac{\overline{S'}(k)}{|k|} e^{-\sqrt{1-F_h^{\,2}}\,|k|\,y} e^{-ikx} dk \tag{2.8}$$

$\overline{S}(k)$ is the Fourier transform of the derivative of the ship's cross-sectional area $S(x)$ at position x, and $\overline{B}(k)$ is the Fourier transform of the ship's waterline breadth $B(x)$ at position x, namely

$$\overline{S'}(k) = \int_{-\infty}^{\infty} S'(x) e^{ikx} dx \tag{2.9}$$

$$S'(x) = \frac{dS}{dx} \tag{2.10}$$

$$\overline{B^*}(k) = \int_{-\infty}^{\infty} B(x) e^{-ikx} dx \tag{2.11}$$

$$\overline{xB^*}(k) = \int_{-\infty}^{\infty} (x - x_{LCF}) B(x) e^{-ikx} dx \tag{2.12}$$

where $\overline{xB}(k)$ is the Fourier transform of $\overline{xB}(x)$ and the asterisk denotes complex conjugate. $S'(x)$ is used here to allow transom-stern ships (Gourlay, 2008b).

Hydrodynamic pressure, vertical force and trim moment (about transverse axis) can then be calculated as described in Gourlay (2008b). For a ship held vertically at its static draught and trim, for instance, the upward vertical force Z may be written in the form:

$$Z = -\frac{\rho U^2}{4\pi h\sqrt{1-F_h^2}} \int_{-\infty}^{\infty} i\bar{S}'(k)\overline{B^*}(k)\,\mathrm{sgn}(k)\,dk \tag{2.13}$$

By switching $\bar{B}(k)$ into $\overline{xB}(k)$, the bow-down trim moment is calculated, and the sign function is

$$\mathrm{sgn}(k) = \begin{cases} -1 & k < 0 \\ 0 & k = 0 \\ 1 & k > 0 \end{cases} \tag{2.14}$$

A substitute method for calculating the vertical force and trim moment is given by the Fourier integral representation (2.13), considering computational efficiency with a non-singular integrand. Once the vertical force and trim moment are calculated, the sinkage and trim then follow by hydrostatics (Gourlay, 2008b), as described in Tuck (1966). The resulting midship, bow and stern sinkage are given hydrostatically by Eqs. (2.1), (2.2) and (2.3), respectively, and the LCF sinkage can also be written in the following form (Tuck & Taylor, 1970):

$$S_{LCF} = C_{s\_LCF}\frac{\nabla}{L_{PP}^2}\frac{F_h^2}{\sqrt{1-F_h^2}} \tag{2.15}$$

The LCF sinkage coefficient (C_{s_LCF}) then satisfies

$$C_{s\_LCF} = \frac{L_{PP}^2}{4\pi A_{WP}\nabla}\int_{-\infty}^{\infty} i\bar{S}'(k)\overline{B^*}(k)\,\mathrm{sgn}(k)\,dk \tag{2.16}$$

where the ship's waterplane area (A_{WP}) is given by

$$A_{WP} = \int_{-\infty}^{\infty} B(x)dx \tag{2.17}$$

Similarly, the change in stern-down trim angle in radians due to squat θ may be written as follows (Hooft, 1974; Huuska, 1976):

$$\theta = C_\theta \frac{\nabla}{L_{PP}{}^3} \frac{F_h{}^2}{\sqrt{1-F_h{}^2}} \tag{2.18}$$

where the trim coefficient (C_θ) is calculated from

$$C_\theta = \frac{L_{PP}{}^3}{4\pi I_W \nabla} \int_{-\infty}^{\infty} i\bar{S}'(k)\overline{xB^*}(k)\operatorname{sgn}(k)dk \tag{2.19}$$

where the second moment of waterplane area (I_W) is given by

$$I_W = \int_{-\infty}^{\infty} (x - x_{LCF})^2 B(x)dx \tag{2.20}$$

In addition, assuming the ship hull to be rigid, the midship sinkage can be obtained by its geometric relationship with the LCF sinkage, written as

$$S_{mid} = S_{LCF} + \frac{(x_{mid} - x_{LCF})\theta}{L_{PP}} \tag{2.21}$$

Therefore, the midship sinkage coefficient (C_{s_mid}) can also be calculated by

$$C_{s\_mid} = C_{s\_LCF} + \frac{(x_{mid} - x_{LCF})C_\theta}{L_{PP}} \tag{2.22}$$

Theoretically, in open water the non-dimensional sinkage coefficients C_{s_mid}, C_{s_bow} and C_{s_stern} are predicted to be constant for each ship, regardless of ship speed or water depth; they should also be independent of scale. However, the trim coefficient C_θ is quite sensitive to hull shape, e.g., longitudinal section area and waterline beam distribution, which may be partly explained by the LCB and LCF (Gourlay, 2008a). A significant effect of hull shape on trim will be described in Chapter 3.

2.3.2 Canal of constant depth and width

One of the earlier assumptions was that the ship is travelling along the centreline of a canal so that cross-flow beneath the ship is ignored, as illustrated in Figure 2.6.

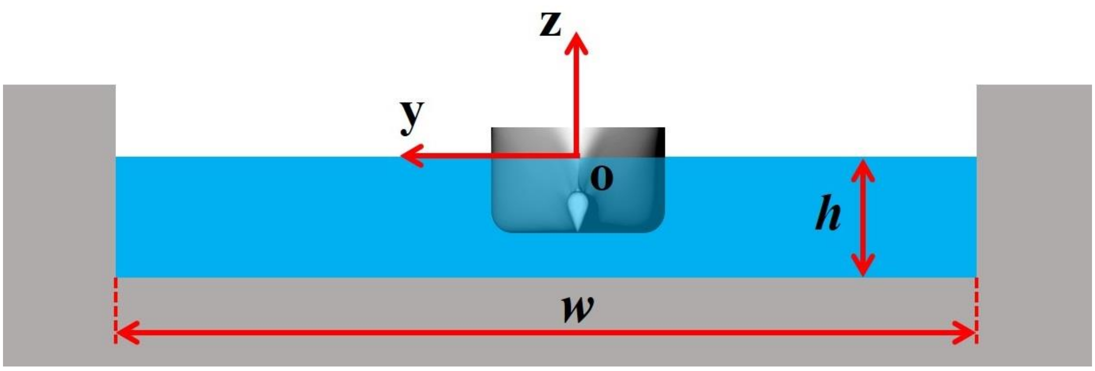

Figure 2.6. Cross-section of a ship in a canal of constant depth and width

The governing Eq. (2.5) and hull boundary condition (2.6) are still valid in this situation. A wall boundary condition is employed by replacing the second boundary condition (2.7) used in open water. The method for this problem was provided by Tuck (1967) using Fourier transforms. He found that the percentage increase of midship sinkage and trim in a rectangular canal over open-water values was governed by the width parameter

$$\bar{w} = \frac{w}{L}\sqrt{1 - F_h^{\ 2}} \tag{2.23}$$

In the study by Tuck (1967), integration by parts was used for the hull boundary condition (2.6), and the ship's cross-sectional area at the bow and stern were assumed to equal zero. However, this assumption cannot be applied to modern ships with transom sterns, and the flow cannot close immediately after the transom for certain speeds; that is, there is some flow separation in the stern section (Terziev et al., 2018). Gourlay (2008b) therefore proposed that $S'(x)$ in Eq. (2.9) should be taken as zero ahead of and behind the ship, to use the hull boundary condition (2.6) in its original form. This method ensures smooth flow detachment from the transom even at high speeds and, hence, can allow for Tuck's (1967) theory to be applicable to modern transom-stern ships.

For both cruiser and transom sterns, the resulting alternative solution was given by Gourlay (2008b):

$$Z = -\frac{\rho U^2}{4\pi h\sqrt{1-F_h^{\ 2}}}\int_{-\infty}^{\infty} i\overline{S}'(k)\overline{B^*}(k)\coth\left(\frac{w}{2}\sqrt{1-F_h^{\ 2}}\,k\right)dk \qquad (2.24)$$

No assumption of zero section area at the stern is required in this solution. In a similar manner as when in open water, the vertical force and trim moment can be calculated using the Fourier integral representation (2.24); the sinkage and trim then follow from hydrostatics.

2.3.3 Dredged channel

For a dredged channel with a step depth change on either side, as shown in Figure 2.7, a ship is again considered to be travelling along the centreline of the channel. Beck, Newman and Tuck (1975) solved this problem using Fourier transforms. The same governing Eq. (2.5) and hull boundary condition (2.6), as well as the assumption of zero section area at the ship's stern, were applied.

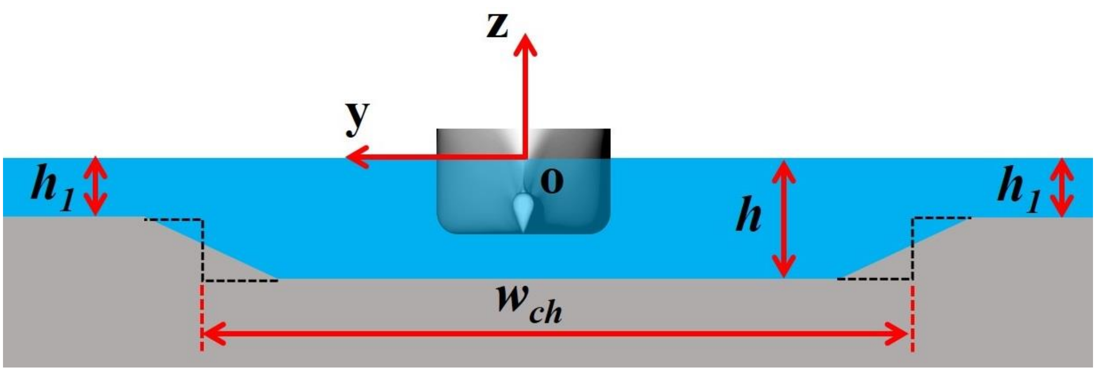

Figure 2.7. Cross-section of a ship in a dredged channel

Gourlay (2008b) rederived the solution with the derivative of the section area $S'(x)$, which may be written in the form

$$Z = -\frac{\rho U^2}{4\pi h\sqrt{1-F_h^{\ 2}}}\int_{-\infty}^{\infty} i\overline{S}'(k)\overline{B^*}(k)K(k)dk \qquad (2.25)$$

The function $K(k)$ is given by

$$K(k) = \frac{\cosh\left(\left(\frac{w_{ch}}{2}\right)\sqrt{1-F_h^2}\,k\right) + \left(\frac{h_1\lambda}{h}\sqrt{1-F_h^2}\,k\right)\sinh\left(\left(\frac{w_{ch}}{2}\right)\sqrt{1-F_h^2}\,k\right)}{\sinh\left(\left(\frac{w_{ch}}{2}\right)\sqrt{1-F_h^2}\,k\right) + \left(\frac{h_1\lambda}{h}\sqrt{1-F_h^2}\,k\right)\cosh\left(\left(\frac{w_{ch}}{2}\right)\sqrt{1-F_h^2}\,k\right)} \tag{2.26}$$

where

$$\lambda = \begin{cases} \sqrt{1-F_1^2}\,|k|, & F_1 < 1 \\ -i\sqrt{F_1^2-1}\,k & F_1 > 1 \end{cases} \tag{2.27}$$

$$F_1 = \frac{U}{\sqrt{gh_1}} \tag{2.28}$$

For the special case when $F_1 = 1$, the function $K(k)$ is given by

$$K(k) = \coth\left(\left(\frac{w_{ch}}{2}\right)\sqrt{1-F_h^2}\,k\right) \tag{2.29}$$

According to Gourlay (2008b), a dredged channel with a slope on its sides can be modelled as a step depth change from h to h_1 half-way along the slope on each side of the channel (see Figure 2.7) because the most important factors influencing sinkage and trim are the channel's cross-sectional area, depth in the vicinity of the ship and waterline width.

2.4 Open-water sinkage coefficients

Now open-water sinkage coefficients for the 13 ship hulls should be calculated using Tuck's (1966) slender-body theory for open water. The theoretical sinkage coefficient for each ship type, as calculated using Eqs. (2.1), (2.2) and (2.3), is shown in Table 2.2.

From Table 2.2, hull shape is seen to be the most important factor for these results.

The bow sinkage coefficient for the group of the oil tankers and bulk carriers, which ranges between 1.91 and 2.04 on average, is 26 % larger than that of the container ships', and 22 % larger than that of the LNG carrier's value. The midship sinkage coefficient ranges from 1.17 for the JUMBO of the container ship type through to 1.41 for the KLNG. The difference between C_{s_bow} and C_{s_stern} for the ships and, thus, their dynamic trim, indicates that dynamic trim is negative (bow-down) for all the ships except the MEGA-JUMBO. Dynamic trim for the container ships is generally quite small compared with the oil tankers/bulk carriers, but some trim quite strongly bow-down, like the KCS and JUMBO. Similar results were found in full-scale measurements on 16 container ships in Hong Kong (Gourlay & Klaka, 2007).

Table 2.2. Calculated bow, stern and midship sinkage coefficients for open water

Ships		Draught (m)	Sinkage coefficient (C_S)			Trim (+, stern down)
			Bow (C_{S_bow})	Midship (C_{S_mid})	Stern (C_{S_stern})	
Container ships	DTC	14.5	1.647	1.242	0.908	(−)
	KCS	10.8	1.830	1.273	0.806	(−)
	JUMBO	14.5	1.721	1.174	0.633	(−)
	MEGA-JUMBO	16.0	1.260	1.400	1.523	(+)
	FHR Ship D	15.0	1.495	1.278	1.065	(−)
	FHR Ship F	11.6	1.409	1.361	1.314	(−)
Overall		–	**1.26−1.83** **1.30−1.98***	**1.17−1.40** **1.30−1.49***	**0.63−1.52** **0.70−1.57***	
Oil tankers	KVLCC1	20.8	2.035	1.198	0.371	(−)
	KVLCC2	20.8	2.018	1.204	0.400	(−)
Bulk carriers	Japan 1704B	0.334	1.906	1.277	0.649	(−)
	JBC	16.5	1.946	1.236	0.536	(−)
	FHR Ship G	11.6	1.939	1.255	0.586	(−)
	MARAD Ship G	0.406	2.035	0.964	0.198	(−)
Overall		–	**1.91−2.04** **1.95−2.39***	**0.96−1.28** **1.13−1.37***	**0.20−0.65** **0.23−0.66***	
LNG carriers	KLNG	11.3	1.611 1.668*	1.410 1.459*	1.211 1.254*	(−)

[Note: *These ranges are based on Eqs. (2.1), (2.2) and (2.3) using L_{OS} instead of L_{PP}]

It should be noted that the sinkage coefficients are calculated using Eqs. (2.1), (2.2) and (2.3) and, hence, the ships' L_{PP} for the usual practice (see Table 2.1). However, ship length overall submerged (L_{OS}), the distance from the foremost part of the submerged hull, which includes the front of the bulb (for modern container ships), to the aftmost part of the submerged hull, is used for the numerical calculations in which the underwater dimension is relevant. Therefore, the calculated sinkage coefficients can be increased to some extent, as marked with asterisks in Table 2.2, depending on the ratio of L_{PP} to L_{OS}. For example, the MARAD Ship G has no bulbous bow but long stern overhang submerged, which translates into an increase in the range of its sinkage coefficients. The average ratio of L_{PP} / L_{OS} is 0.96, with the minimum value of 0.92 for the MARAD Ship G and the maximum value of 0.99 for the Japan 1704B.

As previously mentioned, the sinkage coefficient in open water is constant for each ship, regardless of the ship speed or water depth, but does depend on hull shape. Therefore, based on Table 2.2, a guideline for making a choice of the sinkage coefficient corresponding to different ship types should be offered. These recommended sinkage coefficients are shown in Table 2.3. Calculated sinkage coefficients with using L_{OS} are also shown.

Table 2.3. Recommended sinkage coefficients regarding ship types in open water

Ship types	**Sinkage coefficient (C_S)**		
	Bow (C_{S_bow})	**Stern (C_{S_stern})**	**Max. (C_{S_max})**
Container ships	1.3−1.8 1.3−2.0*	0.6−1.5 0.7−1.6*	1.8 2.0*
Oil tankers & Bulk carriers	1.9−2.0 2.0−2.4*	0.2−0.7 0.2−0.7*	2.0 2.4*
LNG carriers	1.6 1.7*	1.2 1.3*	1.6 1.7*

[Note: *These ranges are based on Eqs. (2.1), (2.2) and (2.3) using L_{OS} instead of L_{PP}]

2.5 Limitations on using sinkage coefficients for different bathymetries

Because the sinkage coefficients are affected by channel or canal configurations, e.g., channel width, channel depth and side depth, limitations on using the sinkage coefficients should be clearly indicated with varying channel dimensions. As shown in Figure 2.8, three idealised types of approach channel, as defined in PIANC (2014), were considered for providing the limitations.

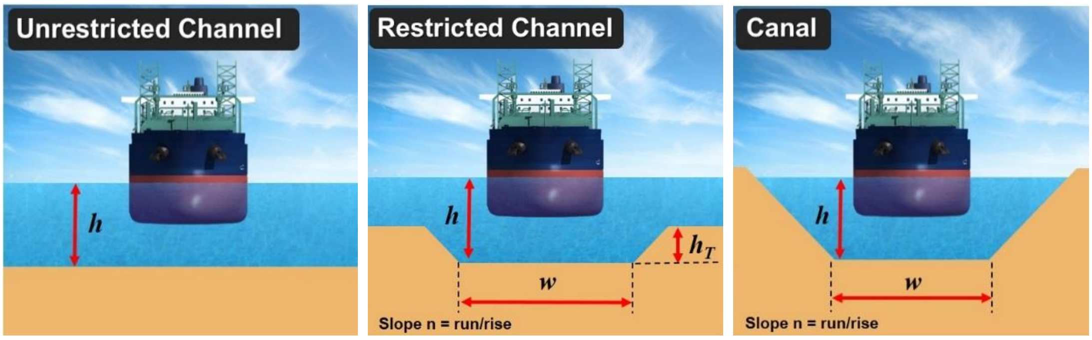

(a) (b) (c)

Figure 2.8. Channel configurations: (a) Unrestricted (open water); (b) Restricted (dredged channel); (c) Canal

Figure 2.9 illustrates relevant parameters for calculating sinkage coefficients of the ship travelling at 12 knots in the dredged channel. A 4H: 1V slope, which is typical of channels dredged through surficial sandy seabeds in Western Australia, was applied to both the dredged channel and canal configurations (Gourlay, 2013b). The depth in the channel (including tide) and canal was set for shallow-water condition of h/T = 1.2 (Jachowski, 2008; Vantorre, 2003), with varying trench depth (h_T) for the dredged channel. As explained previously, the channel width was modelled as a step depth change from channel depth (h) to outer water depth (h_o) at half-way along the slope on each side of the channel, as described in Gourlay (2008b).

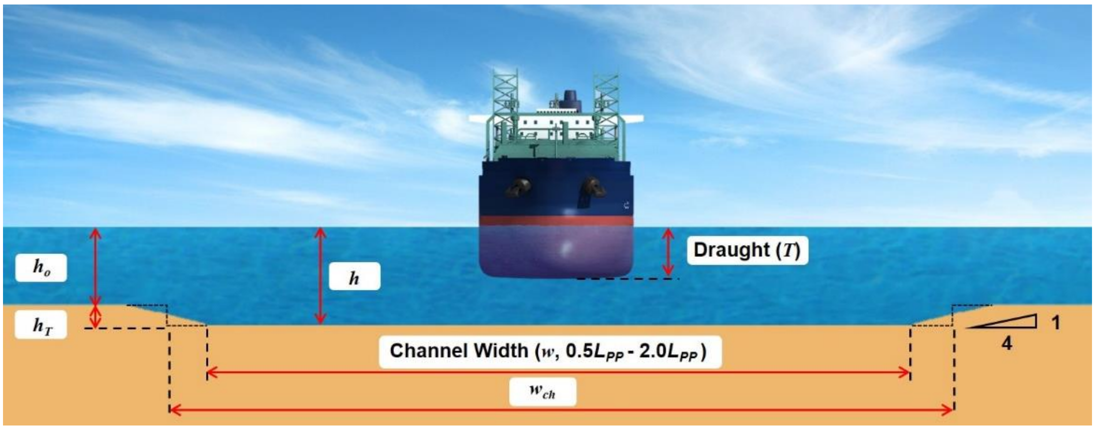

Figure 2.9. Channel configuration modelled and important parameters

The effect of different bathymetries, such as channel width (to the toe of slope) and trench depth (h_T) ranging from h_T / h of 0.1 to 0.5, is shown in Figure 2.10 to Figure 2.11. Here, channel and canal sinkage coefficients were calculated using the slender-body theory of Beck, Newman and Tuck (1975) for dredged channels, and Tuck (1967) for canals, respectively. The results plotted are the ratio of C_{s_max} to C_s in open water, regardless of whether it is C_{s_bow} and C_{s_stern}.

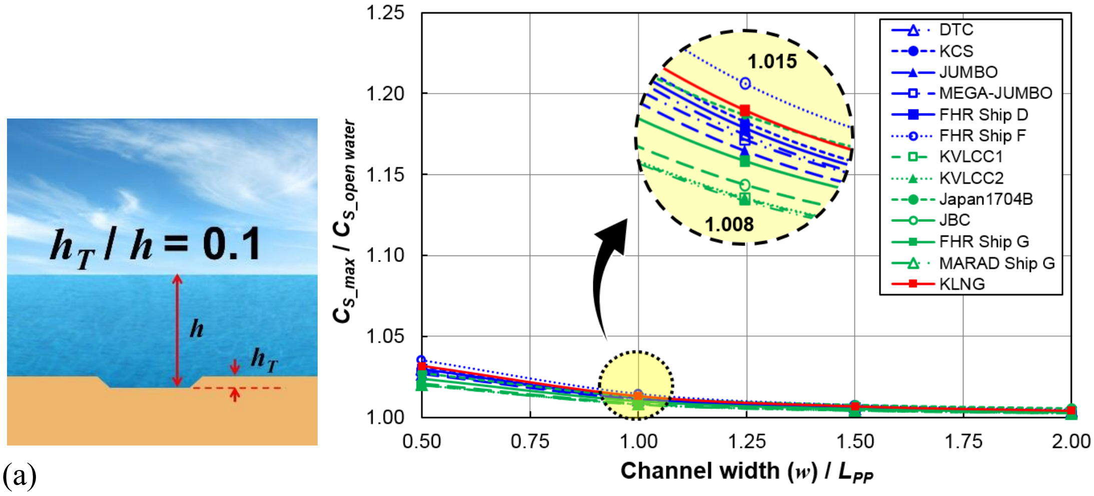

(a)

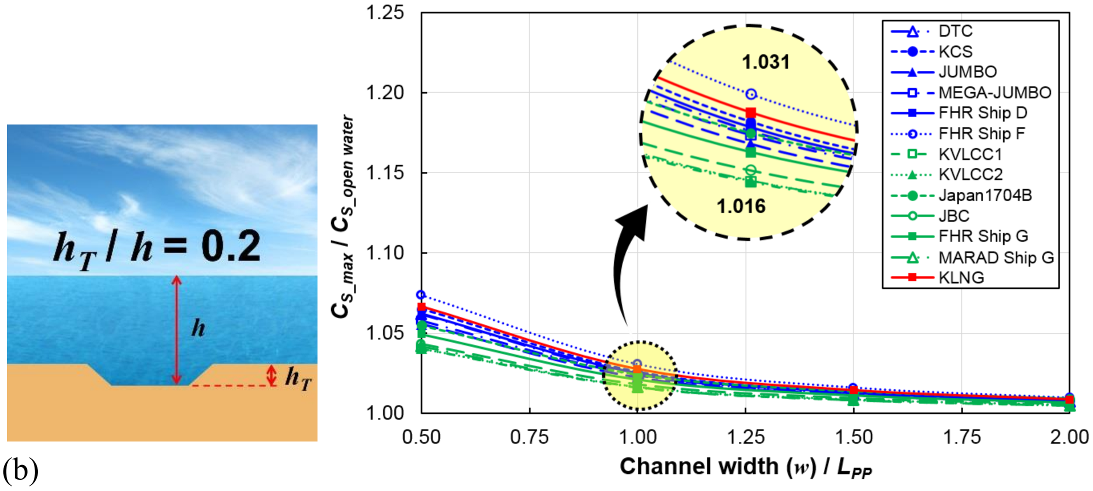

(b)

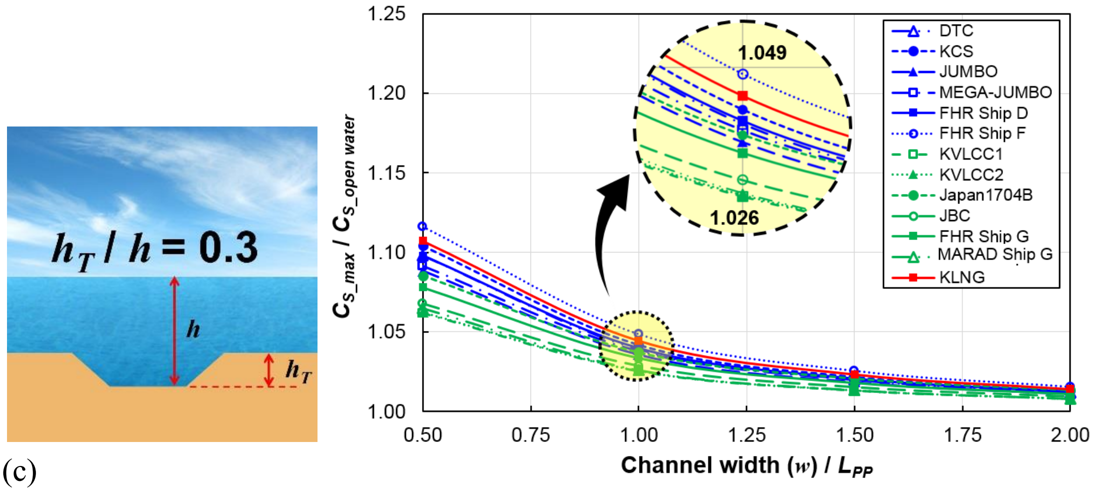

(c)

Figure 2.10. Effect of transverse bathymetry on predicted sinkage coefficient: (a) h_T/h = 0.1; (b) h_T/h = 0.2; (c) h_T/h = 0.3

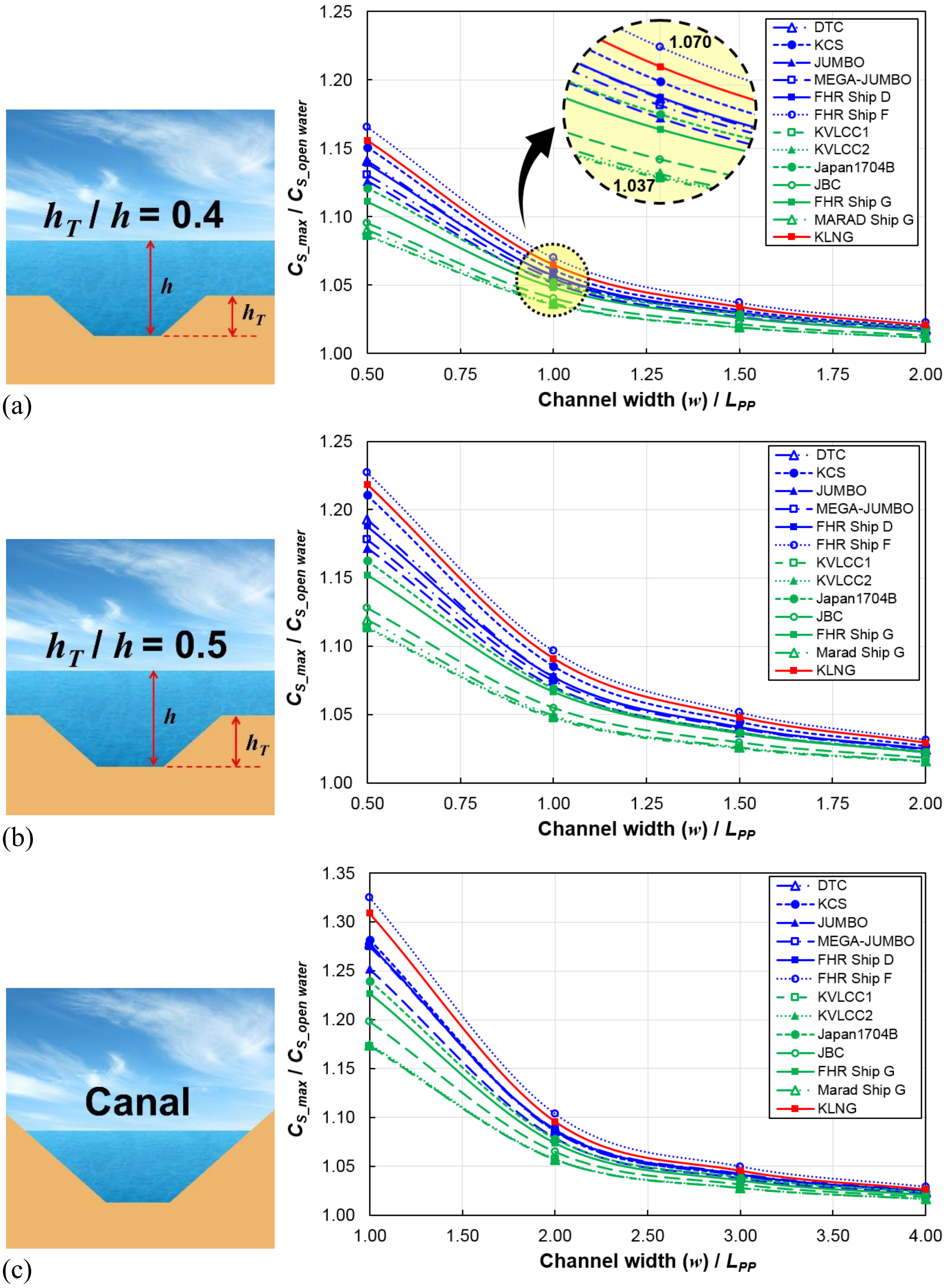

Figure 2.11. Effect of transverse bathymetry on predicted sinkage coefficient: (a) h_T/h = 0.4; (b) h_T/h = 0.5; (c) Canal

It is shown that the channel and canal sinkage coefficients are all larger than the open-water value, by an amount that depends on the channel bathymetry. For example, in the most restricted case in the dredged channels (w / L_{PP} = 0.5 and h_T / h =0.5) (see

Figure 2.11(b)), the maximum sinkage coefficient for the container ships is on average 19 % larger than in open water, whereas that for the oil tankers/bulk carriers is on average 13 %, and for KLNG 21 %, larger than the open-water value. The difference is mainly because that the transverse restriction increases the midship sinkage but not the dynamic trim (Gourlay, Ha, Mucha, & Uliczka, 2015).

Figure 2.10(a, b and c) and Figure 2.11(a and b) can be used to determine whether a particular ship and channel configuration may be classed as open water, or whether a specific narrow-channel analysis is required. For instance, if the channel sinkage coefficient is within 5 % of the open-water value, it may be acceptable to use open-water theory. Table 2.4 shows this assessment for port approach channels in Western Australia, used here as examples. Note that the calculations were done at lowest astronomical tide.

Table 2.4. Variation from open-water conditions

Particulars	**Fremantle (Deep Water Channel)**	**Geraldton**	**Barrow Island**
	Dredged channel (chart AUS112)	**Dredged channel (chart AUS81)**	**Dredged channel (chart AUS66)**
Channel width (w)	300 m	180 m	260 m
Dredged depth (h)	16.4 m	14.0 m	13.5 m
Approximate trench depth (h_T)	1.1 m	3.0 m	6.0 m
h_T / h	0.07	0.21	0.44
Example ship	Post-Panamax container ship	Panamax iron ore carrier	KLNG membrane LNG carrier
L_{PP}	260 m	215 m	266 m
Channel width (w) / L_{PP}	1.15	0.84	0.98
Maximum sinkage coefficient (variation from open-water value)	~ 1 %	~ 3 %	~ 8 %

Based on Table 2.4, the Fremantle and Geraldton channels may be classed as open water for predicting ship sinkage and trim, whereas a specific narrow-channel analysis would be recommended for the Barrow Island channel.

The sinkage coefficient for the canal is considerably higher than that for open water, as presented in Figure 2.11(c). However, when the canal width is equal to or greater than three times the L_{PP}, canal effects are minimal, as the Tuck (1967) results are within 5 % of the open water (Tuck, 1966) results.

2.6 Conclusions

For UKC management, sinkage coefficients were developed for use in open waterways, dredged channels and canals. The ship hull forms considered in this chapter for calculating the sinkage coefficients were of a broad range of ship hulls: the DTC, KCS, JUMBO, MEGA-JUMBO, FHR Ship D and FHR Ship F for container ships; the KVLCC1 and KVLCC2 for oil tankers; the Japan 1704B, JBC, FHR Ship G and MARAD Ship G for bulk carriers; and the KLNG for membrane LNG carriers. Significant differences in hydrostatic characteristics between hulls were identified, but each exhibited features typical of their type.

Theoretical methods using the slender-body shallow-water theory of Tuck (1966) for open water, Tuck (1967) for canals, and Beck, Newman and Tuck (1975) for dredged channels were applied to calculate sinkage coefficients. The sinkage coefficient in open water varied from ship hull to ship hull, but distinguishing characteristics for each ship type were observed. The bow sinkage coefficients were larger than the stern sinkage coefficients in most cases, regardless of type. The midship sinkage coefficient ranged between 1.17 and 1.40 for the container ships, 0.96 and 1.28 for the oil tankers/bulk carriers, and 1.41 for the KLNG.

A guideline for choosing a sinkage coefficient corresponding to the three categories of ship types was suggested, with a maximum sinkage coefficient of 1.8 for container ships, 2.0 for oil tankers/bulk carriers, and 1.6 for LNG carriers. These sinkage coefficients may be used for UKC management by ports.

It was found of the dredged channels that the sinkage coefficients were affected by varying channel width, depth and side depth. The maximum channel sinkage coefficient of each ship model for the most restricted case (w / L_{PP} = 0.5 and h_T / h =

0.5) was in the order of 11–23 % larger than the open-water value. An assessment was made to see whether a particular ship and channel configuration might be classed as open water, or whether a specific narrow-channel analysis is required. Examples were provided for a Post-Panamax container ship, Panamax iron ore carrier and membrane LNG carrier (KLNG) in port approach channels in Western Australia.

Blockage effects on the ships were found to be significant in canals, but minimal when the canal width was equal to or greater than three times the L_{PP}.

Chapter 3

Container Ship Squat Prediction Using Model-Scale Tests

This chapter concerns dynamic sinkage and trim of modern container ships in shallow water (or port approach channels) in detail. A review is made of changes in container ship hull designs to the present time, together with available model test data for sinkage and trim. Two potential flow methods, the slender-body and the Rankine-source method, are discussed with reference to the model test results. It is shown that slender-body theory is able to give good predictions of dynamic sinkage and trim in wide canals or open water, and the Rankine-source method offers an accurate solution, particularly for ships at high speed in narrow canals. Additionally, results of the comparison and validation of simple empirical methods for predicting dynamic sinkage and trim of container ships, as given in the PIANC guidelines, are also presented.

3.1 Introduction

There is a trend internationally towards higher-capacity container ships, and many ports are considering what maximum size they take in the future. The largest ships will invariably be draught-restricted, so squat and wave-induced motions may cause them to run aground if not correctly allowed for. Dredging has environmental implications on water quality, underwater noise, tidal streams and coastal wave climate, and both costs and effects must go into any analysis of channel deepening; but notwithstanding this, channel deepening is on the wish-list of many ports.

Because larger ships tend to have smaller wave-induced motions but more considerable squat than smaller ships, especially in shallow and restricted fairways, the new generation of larger ships has brought new challenges in safely managing

UKC in ports. It is therefore timely to review the state-of-the-art in ship squat prediction for modern container ships.

3.2 Container ship hull shapes

As discussed in Chapter 2, a number of container ship research hull forms have been developed that are representative of designs of their time, such as the DTC (el Moctar, Shigunov, & Zorn, 2012), KCS (Lee, Koh, & Lee, 2003), JUMBO (Uliczka, Kondziella, & Flügge, 2004) and MEGA-JUMBO (Uliczka, Kondziella, & Flügge, 2004). In this chapter, two additional container ship hull forms are considered for comparative purposes:

- ‘Hamburg Test Case’ (‘HTC’, 153.7-m L_{PP}), a model of the container ship ‘Teresa del Mar’ built by Bremer Vulkan, Germany, in 1986 and still in service (Gietz & Kux, 1995).

- ‘S-175’ (175-m L_{PP}), a somewhat simplified hull shape used as a model testing benchmark (International Towing Tank Conference, 1987).

Variations between these ships in hull shape may have an effect on their sinkage and trim characteristics. Because changing hull shape has a significant effect on trim but a relatively small effect on sinkage (Uliczka & Kondziella, 2006), particular attention will be given to the effect of hull shape on dynamic trim.

As mentioned in Chapter 2, the hull shapes of the DTC, KCS, JUMBO and MEGA-JUMBO were developed from supplied IGES files (see Figure 2.1). For this chapter, the hull shapes of the HTC and S-175 were digitised from the published lines plans, using the stations given in Gietz and Kux (1995) and the International Towing Tank Conference (ITTC, 1987), respectively. Calculated details of the modelled container ships are shown in Table 3.1.

The KCS design draught is 10.8 m (Lee, Koh, & Lee, 2003), but it was modelled at 10.0-m draught for comparing model test results (Gronarz, Broß, Mueller-Sampaio, iang, & Thill, 2009; Mucha & el Moctar, 2014a). For the DTC, the ship hull was modelled at three different draughts: 13.0, 14.0 and 14.5 m, as used for model testing (Mucha & el Moctar, 2014b; Mucha, el Moctar, & Böttner, 2014). The different hull geometry of each case, e.g., displacement volume (∇), block coefficient (C_B) and waterplane area (A_{WP}), can presumably affect their sinkage and trim.

Table 3.1. Details of the container ship hulls

Ships	L_{PP} L_{OA}* L_{OS}† (m)	B (m)	T (m)	A_{WP} (m²)	∇ (m³)	∇/ L_{PP}^3 (-)	C_B (-)	LCB (m, %)	LCF (m, %)
DTC	355.00 372.81* 356.78†	51.00	13.00	14,604	150,910	0.00337	0.641	175.64 (49.48)	166.19 (46.81)
	355.00 372.81* 363.28†		14.00	15,058	165,746	0.00370	0.654	174.65 (49.20)	162.86 (45.88)
	355.00 372.81* 366.93†		14.50	15,302	173,337	0.00387	0.660	174.09 (49.04)	161.08 (45.38)
KCS	230.00 243.84* 233.88†	32.20	10.00	5,891	47,197	0.00388	0.637	112.46 (48.89)	104.61 (45.48)
JUMBO	320.00 336.90* 336.90†	40.00	14.50	11,426	133,901	0.00409	0.721	157.77 (49.30)	146.67 (45.84)
MEGA-JUMBO	360.00 377.65* 365.85†	55.00	16.00	15,658	215,775	0.00462	0.681	179.89 (49.97)	176.83 (49.12)
HTC	153.70 163.15* 158.15†	27.50	10.30	5,577	28,332	0.00780	0.651	75.97 (49.43)	71.59 (46.58)
S-175	175.00 186.45* 178.25†	25.40	9.50	3,152	24,053	0.00449	0.570	84.99 (48.56)	80.45 (45.97)

[Note: Block coefficient (C_B) is the ratio of ∇ to (L_{PP}·B·T); LCB and LCF are given in both metres and % of L_{PP} forward of AP]

In Table 3.1, a significant variation in block coefficient (C_B), which ranges between 0.570 and 0.721, is confirmed. Note that the typical range of C_B is around 0.50–0.65 for fine-form hulls, 0.65–0.75 for moderate hulls and 0.75–0.85 for full-form hulls (Yaakob, 2008). LCB is slightly aft of midships for all the hulls, from 48.56 % for the S-175 with a relatively short L_{PP} through to 49.97 % for the MEGA-JUMBO. In the MEGA-JUMBO the LCF and LCB are virtually at the same position, whereas the LCFs for the others are aft of the LCB by approximately 3 % of L_{PP}.

Body plans of the container ships are shown in Figure 3.1. The comparison reveals significant changes in container ship design over the years; for instance, the S-175 (International Towing Tank Conference, 1987) has a relatively small and low bow bulb, no stern bulb, and sections that are not far from vertical at the waterline; the modern DTC (el Moctar, Shigunov, & Zorn, 2012) has a high bow bulb, pronounced stern bulb, and aft sections that are close to horizontal at the waterline. The JUMBO (Uliczka, Kondziella, & Flügge, 2004) has an immersed transom at its design draught. More detailed views of the DTC, KCS, JUMBO and MEGA-JUMBO can be found in Chapter 2 and Appendix A.

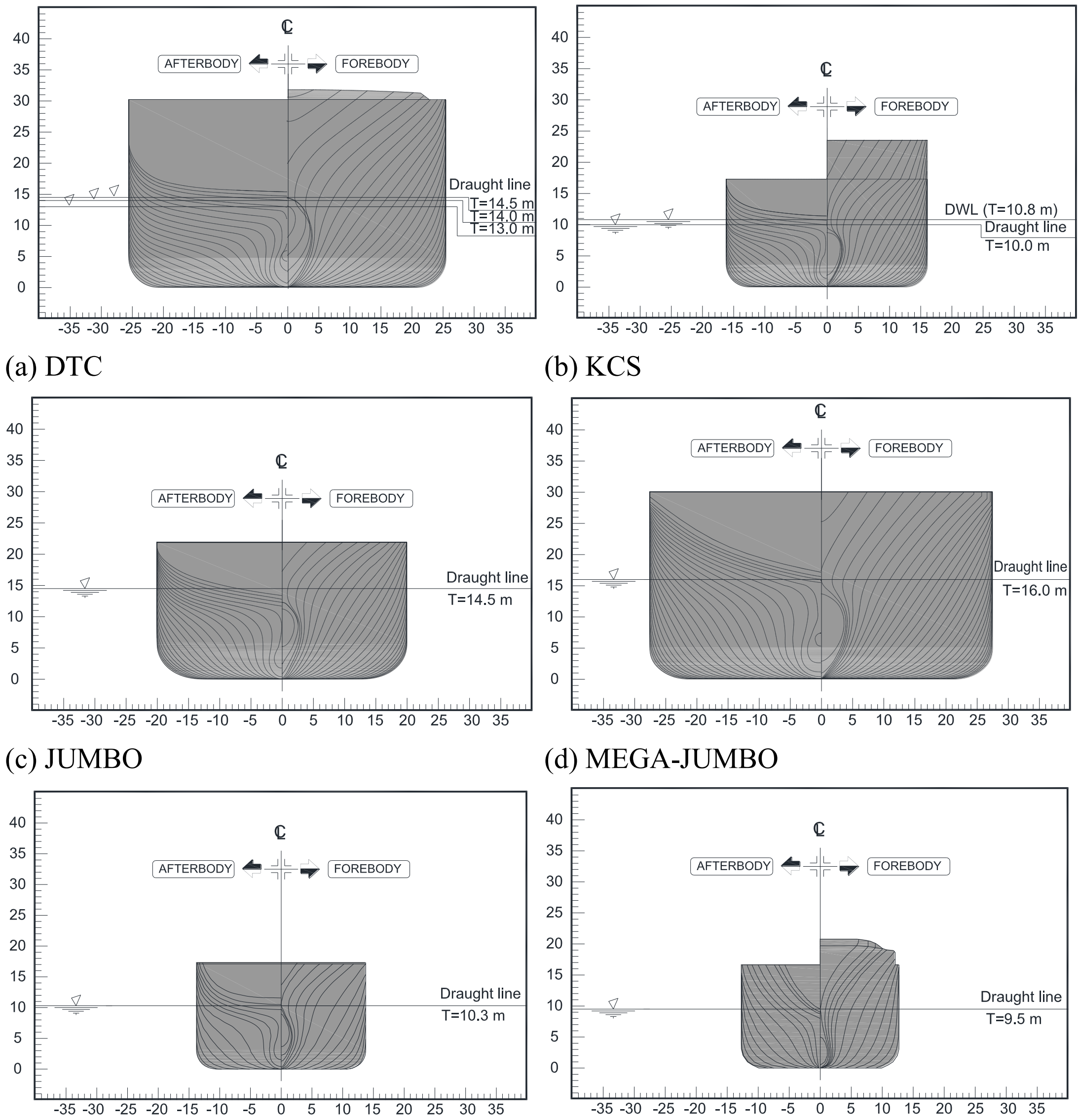

(a) DTC (b) KCS

(c) JUMBO (d) MEGA-JUMBO

(e) HTC (f) S-175

Figure 3.1. Body plans of the container ship hulls [Note: (a) DTC, (b) KCS, (c) JUMBO and (d) MEGA-JUMBO show 50 evenly-spaced stations from transom to the front of the bulb; (e) HTC shows its stations given in (Gietz & Kux, 1995); (f) S-175 shows its stations 0, 0.25, .., 1, 1.5, .., 9, 9.25, ..,10 (International Towing Tank Conference, 1987)]

Figure 3.2 shows profiles, waterplanes and midship sections of all container ships, scaled against L_{PP} in each case.

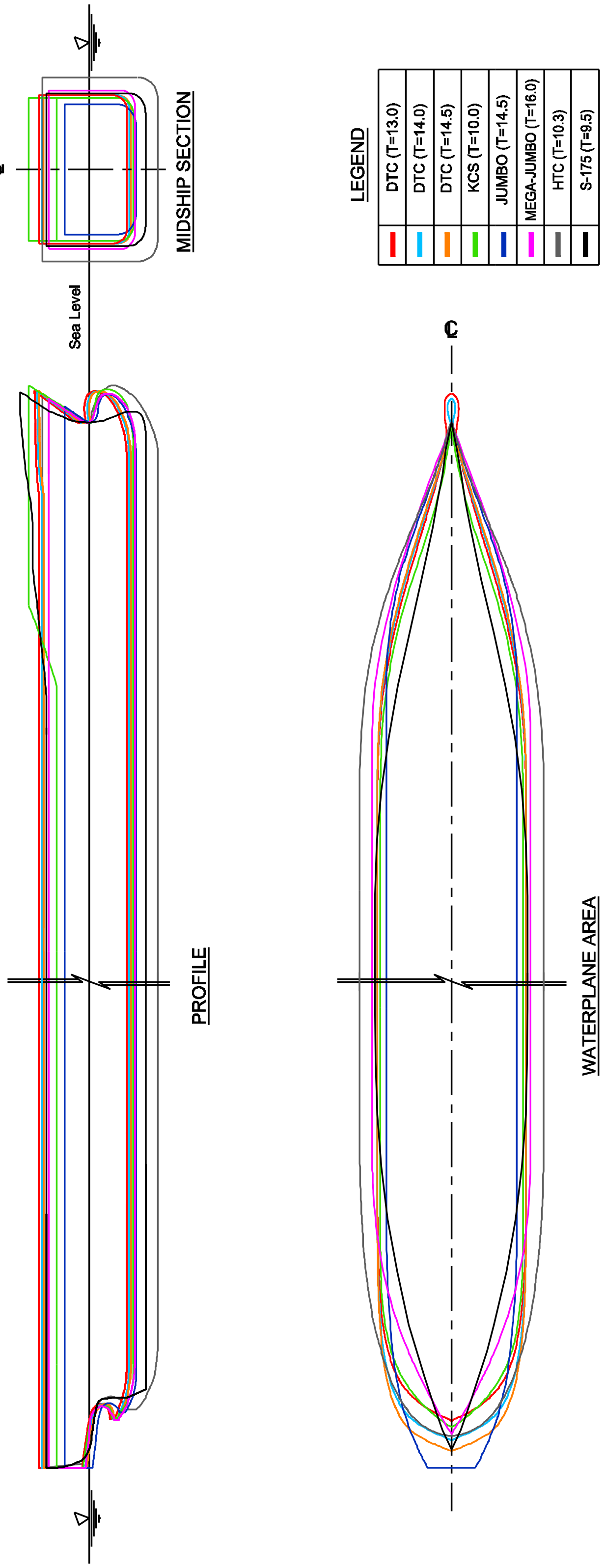

Figure 3.2. Ship profiles, waterplanes and midship sections of the modelled container ship hulls

Significant differences in stern waterplane shape between the ship hulls, which has an important effect on dynamic trim, are observed. For the DTC, the changing draught also has a significant effect on the waterplane near the bow and stern.

A comparison of the non-dimensionalised hull sectional area curves is shown in Figure 3.3.

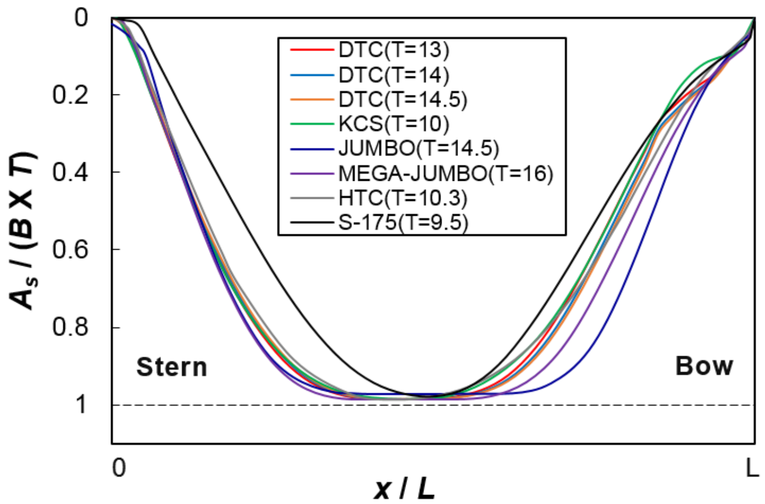

Figure 3.3. Comparative sectional area curves for the ship hulls [Note: Aft submerged extremity is at x = 0; forward submerged extremity is at $x = L$]

It is seen that some of the hulls, for instance those of the JUMBO and MEGA-JUMBO, have long parallel midbodies reminiscent of bulk carriers, with rapidly-varying section areas near the bow. The S-175 has a sectional area curve with a rather gradual slope near the stern and a comparatively short parallel midbody.

3.3 Model test results for sinkage and trim

3.3.1 Model test conditions

The DTC, KCS, JUMBO and MEGA-JUMBO have been extensively model tested in recent years for shallow-water sinkage and trim, as follows:

Tests on a 1:40 scale towed model of the KCS were carried out at the Development Centre for Ship Technology and Transport Systems (DST) in Duisburg, Germany, in the standard rectangular tank cross-section (Gronarz, Broß, Mueller-Sampaio, Jiang, & Thill, 2009; Mucha & el Moctar, 2014a).

Tests on a 1:40 scale self-propelled model of the DTC were performed at DST in the standard rectangular tank cross-section (Mucha & el Moctar, 2014b; Mucha, el Moctar, & Böttner, 2014). Tests on the same model were undertaken at the Federal Waterways Engineering and Research Institute (BAW) in Hamburg, Germany, in an asymmetric trapezoidal canal of similar cross-section area to the Duisburg tank.

Tests on 1:40 scale self-propelled models of the JUMBO and MEGA-JUMBO were carried out at BAW, in canals with 3H:1V sloping banks and varying widths (Uliczka, Kondziella, & Flügge, 2004). Results from the largest and smallest canal widths will be discussed in this chapter.

Comparative channel conditions for all model tests are shown in Table 3.2.

Table 3.2. Channel conditions used in model testing

Test cases	T (m)	Canal width / L_{PP}	Canal width / Ship beam	Canal : Hull cross-sectional area ratio (n)	Canal depth / Ship draught	Note
DTC	13.0	1.13	7.84	9.79	1.23	Rec. tank (at DTC)
	14.0			9.08	1.14	
	14.5			8.77	1.10	
	13.0	1.55	10.78	10.33	1.23	Non-rec. tank (at BAW)
	14.0			9.58	1.14	
	14.5			9.25	1.10	
KCS	10.0	1.74	12.42	14.53	1.15	h = 11.5 m
				16.42	1.30	h = 13.0 m
				20.21	1.60	h = 16.0 m
JUMBO	14.5	1.65	13.21	14	1.14	Smallest canal width
		3.90	31.16	35		Largest canal width
MEGA-JUMBO	16.0	1.49	9.75	10	1.13	Smallest canal width
		3.50	22.89	25		Largest canal width

[Note: Values for the KCS are represented for test depth of 11.5, 13.0 and 16.0 m]

Figure 3.4 has been created to promote understanding of Table 3.2, showing comparative channel configurations for all model tests at full scale.

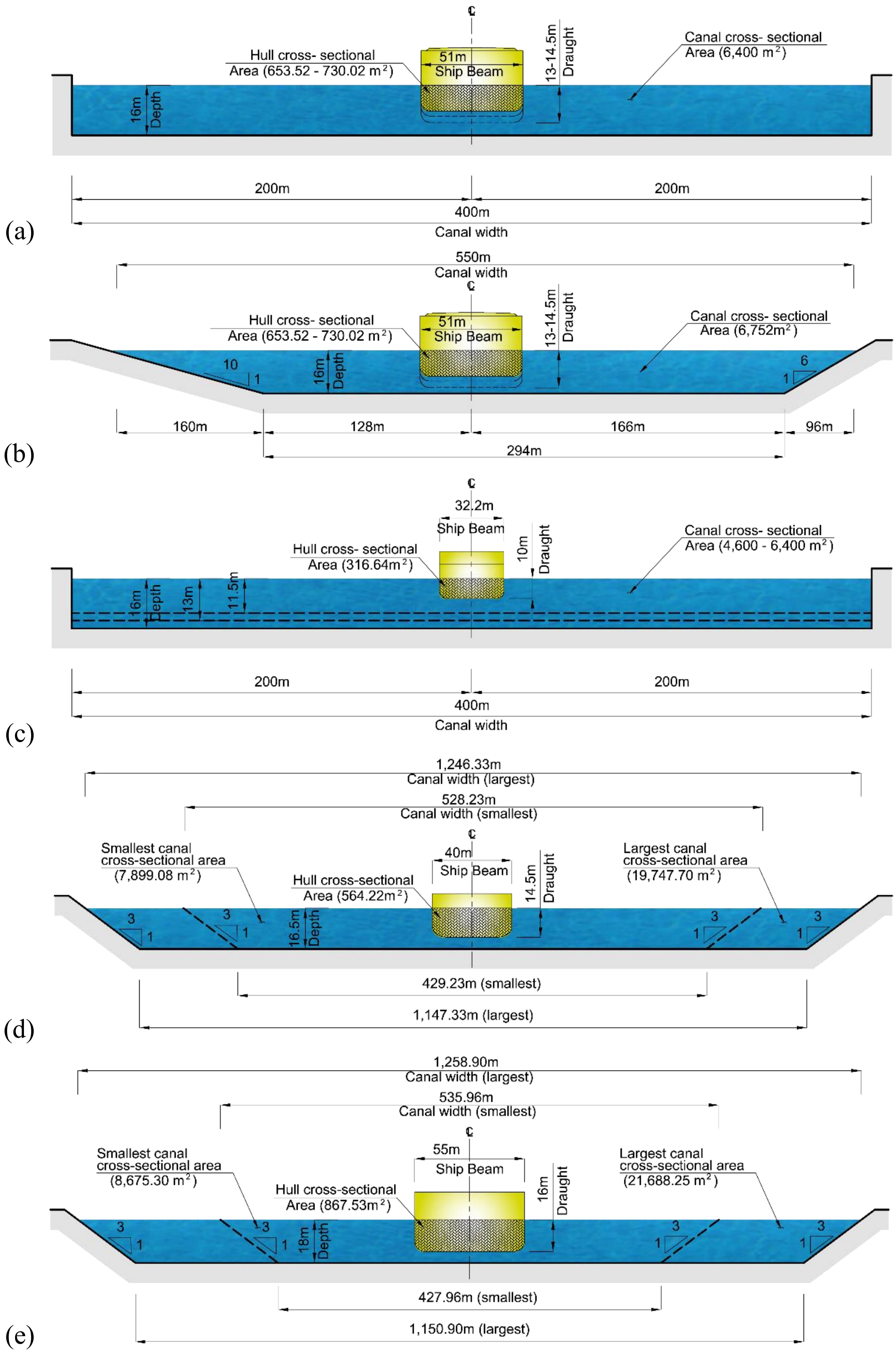

Figure 3.4. Cross sections of the channels tested: (a) Rectangular tank at DST for the DTC; (b) Non-rectangular tank at BAW for the DTC; (c) Rectangular tank at DST for the KCS; (d) Trapezoidal tank at BAW for the JUMBO; (e) Trapezoidal tank at BAW for the MEGA-JUMBO [Note: Dimensions of the ships and channels are at full scale]

3.3.2 Measured dynamic sinkage

Figure 3.5 shows the scaled midship sinkage (S_{mid} / L_{PP}) as measured in the model tests. This result is plotted against the non-dimensional depth-based Froude number (F_h): see Eq. (2.4). As an example, a container ship travelling in 16-m water depth (including tide) at a speed of 12 knots, corresponds to F_h = 0.49. Depth Froude numbers (F_h) typically range from 0.3–0.6 in port approach channels. As shown in Table 3.2, the KCS tests were performed at three different depths: h = 11.5 m, h = 13.0 m and h = 16.0 m; but all collapse onto a single line with this scaling, as predicted by slender-body theory.

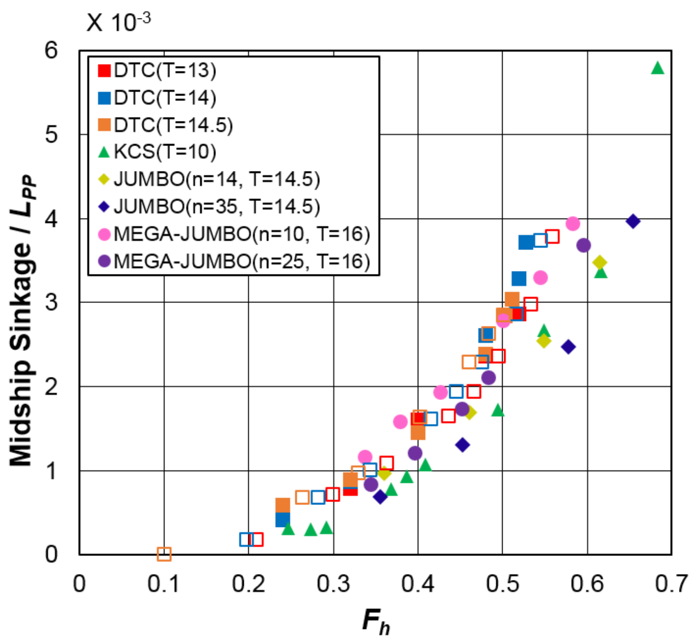

Figure 3.5. Measured midship sinkage (positive downward) [Note: Unfilled squares are represented for the DTC in the non-rectangular canal (at BAW)]

In general, the DTC (T = 14.5) has the highest value at a given depth Froude number (F_h), nearly the same as in the case of the MEGA-JUMBO (n = 10), followed by the DTC (T = 14), DTC (T = 13), MEGA-JUMBO (n = 25), JUMBO (n = 14), KCS and JUMBO (n = 35). Such an order does not seem to correlate with either the block coefficient (C_B) or volumetric coefficient (∇ / L_{PP}^3). For instance, at F_h = 0.5, the scaled midship sinkage for the DTC (T = 14.5) is 64 % larger than that for the KCS, despite their similar block and volumetric coefficients (see Table 3.1) under the same channel conditions (at DST); but note that this difference may be at least partly due to the effect of self-propulsion (Delefortrie, Vantorre, Eloot, Verwilligen, & Lataire, 2010; Duffy, 2008; Tahara, Wilson, Carrica, & Stern, 2006) in the tests with the self-propelled model of the DTC and the towed model of the KCS.

From Figure 3.5, it can be confirmed that canal width is important for these results, with the JUMBO and MEGA-JUMBO having significantly larger sinkage in the narrow-canal cases. For example, the scaled midship sinkage (S_{mid} / L_{PP}) of the JUMBO in the narrow-canal case (n = 14) is approximately 17 % larger than in the wide-canal case (n = 35); the MEGA-JUMBO also has a value in the narrow-canal case (n = 10) about 21 % larger than in the wide-canal case (n = 25) (refer to Table 3.2 and Figure 3.4).

3.3.3 Measured dynamic trim

Results of dynamic trim for the container ship test cases are shown in Figure 3.6. Dynamic trim is quite small for all container ships, with some ships bow-down and some stern-down: for example, the DTC and MEGA-JUMBO generally trim stern-down, and the KCS and JUMBO bow-down. This is in line with the full-scale measurements of 16 deep-draught container ships in Hong Kong (Gourlay and Klaka, 2007), which show that around half trimmed bow-down and half stern-down. The effect of hull shape on full-scale measurements of dynamic trim is discussed in Uliczka and Kondziella (2006).

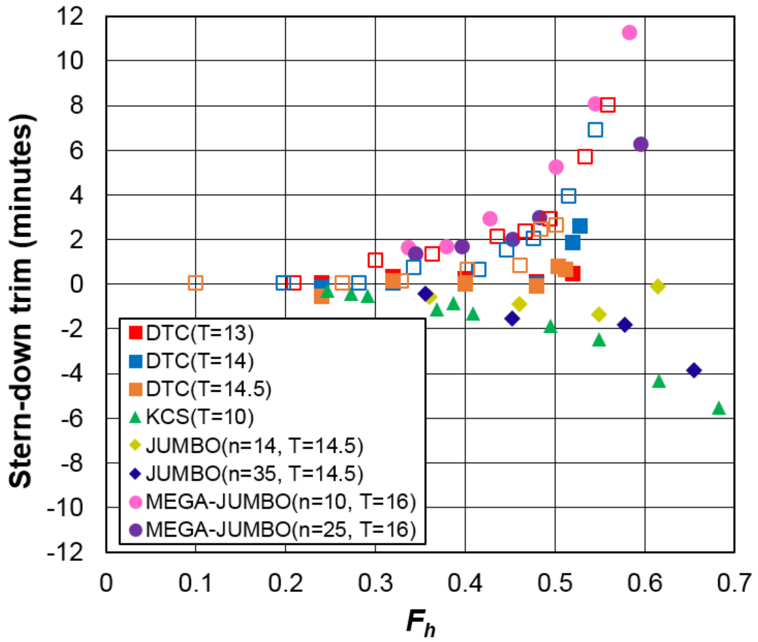

Figure 3.6. Measured dynamic trim (positive stern-down) [Note: Unfilled squares are represented for the DTC in the non-rectangular canal (at BAW)]

Although dynamic trim is often said to correlate with block coefficient (C_B), as witnessed by the tendency of high-block-coefficient bulk carriers to trim strongly bow-down (PIANC, 2014), no such correlation is seen in the container ships analysed here. For example, the DTC and KCS have similar C_B, as do the JUMBO and MEGA-JUMBO (see Table 3.1), but these groups show conflicting results for dynamic trim.

The JUMBO and MEGA-JUMBO results in Figure 3.6 indicate that canal width has little effect on dynamic trim, with the narrow canal giving a slight stern-down correction for both container ships, of around 1.2 minutes for the JUMBO and 2.3 minutes for the MEGA-JUMBO. The DTC is seen to have a more stern-down trim in the asymmetric (non-rectangular) canal than in the rectangular canal; this is apparently caused by higher propeller RPM in the asymmetric canal tests (Mucha & el Moctar, 2014b), as shown in Table 3.3.

.

Table 3.3. Comparison for propeller RPM in the DTC tests

Test cases	Rectangular canal (DST Tank) *		Non-rectangular canal (BAW Tank) #	
	Ship speed (knots)	**RPM**	**Ship speed (knots)**	**RPM**
DTC (T=13.0m)	5.83	30.60	7.08	38
	7.78	39.60	8.76	48
	9.72	51.00	10.58	62
	11.66	64.30	11.28	69
	12.64	70.30	12.03	77
	-	-	12.92	89
DTC (T=14.5m)	5.83	34.3	6.4	38
	7.78	43.4	8	48
	9.72	55.8	9.7	62
	11.66	71.9	11.2	77
	12.25	77.5	11.8	84
	12.44	84.3	12.2	89

[Note: *These details can be found in Mucha and el Moctar (2014b); #Dr Uliczka provided these details in an email (personal communication, May 22, 2015)]

3.4 Comparison of measured ship squat with theoretical methods

Now a comparison of the model test results with predictions from two potential-flow methods, in this case the slender-body and Rankine-source methods, should be made. The slender-body theory is based on the rectangular-canal slender-body theory of Tuck (1967), implemented in the computer program *SlenderFlow* (refer to Chapter 2). The Rankine-source code *GL Rankine* (von Graefe, 2014a) uses source patches on the hull and free surface, and exact hull and free-surface boundary conditions.

3.4.1 Comparison of measured and predicted sinkage

Figure 3.7 shows a comparison of the scaled midship sinkage (S_{mid} / L_{PP}) as measured in the model tests with the predictions of the Tuck (1967) and Rankine-source (von Graefe, 2014a) methods.

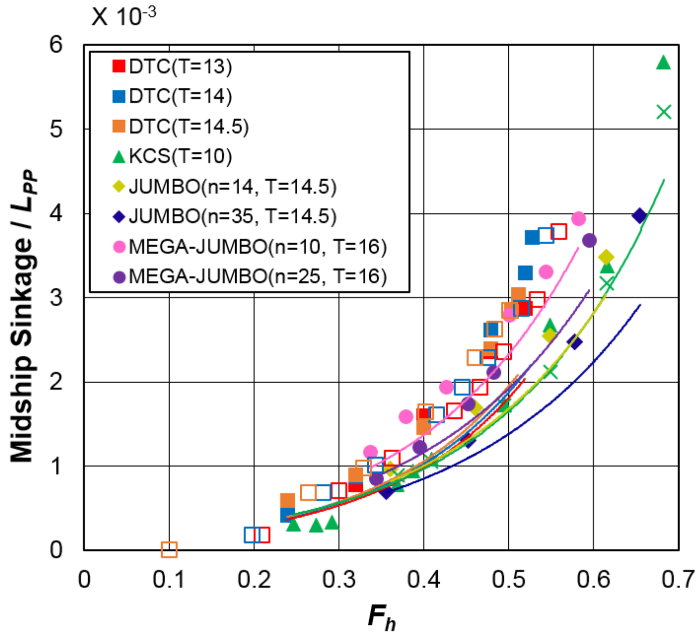

Figure 3.7. Measured and calculated midship sinkage (positive downward) [Note: Unfilled squares are represented for the DTC in the non-rectangular canal (at BAW); solid lines for Tuck's method (1967) for canals; × for Rankine-source method]

For ease of comparison across the speed range, results can be shown in terms of the midship sinkage coefficient C_{s_mid} (Tuck, 1966) defined by

$$\frac{S_{mid}}{L_{PP}} = C_{s\_mid} \frac{\nabla}{L_{PP}^{\ 3}} \frac{F_h^{\ 2}}{\sqrt{1-F_h^{\ 2}}} \tag{3.1}$$

A comparison between the measured and calculated midship sinkage coefficients is shown in Figure 3.8. In the wide-canal cases of the JUMBO (n = 35) and MEGA-JUMBO (n = 25), at low speeds, the Tuck (1967) and Rankine-source predictions are very close to the model test results. In these cases, channel effects are seen to be minimal because the Tuck (1967) results are very close to the open-water (Tuck, 1966) results.

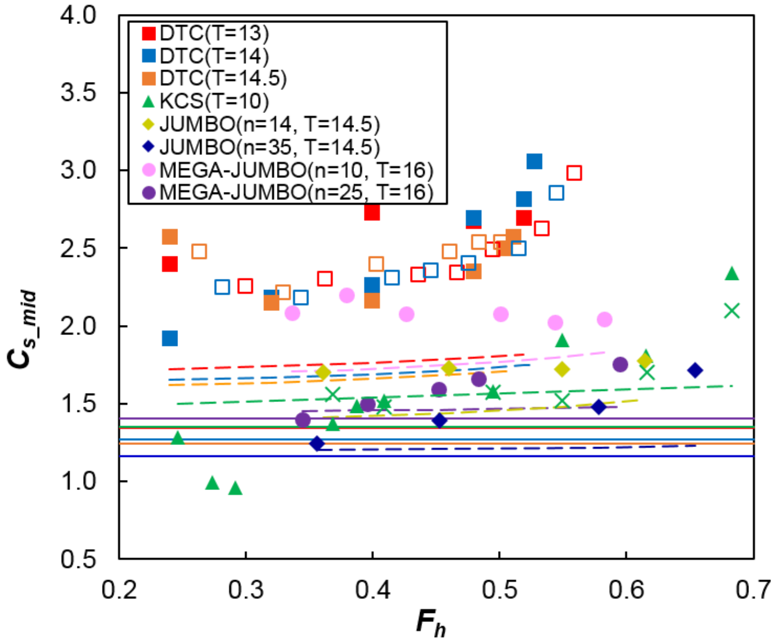

Figure 3.8. Measured and calculated midship sinkage coefficient (C_{s_mid}) [Note: Unfilled squares are represented for the DTC in the non-rectangular canal (at BAW); solid lines for Tuck's method (1966) for open water; dashed lines for Tuck's method (1967) for canals; × for Rankine-source method]

As the depth Froude number (F_h) increases above 0.6 for the wide-canal cases, or the canal becomes narrower: that is, the DTC (n = 8.77–10.33), JUMBO (n = 14) and MEGA-JUMBO (n = 10), the Tuck (1967) method starts to significantly underpredict the sinkage. It is thought that this is due to the increasingly recognised importance of non-linear effects at all speeds in narrow canals, or at high speed in wide canals. The Rankine-source method is seen to be closer to the model test results for the KCS at $F_h > 0.6$, than the Tuck (1967) method.

Figure 3.9 shows percentage difference between the measurements and predictions (Tuck, 1967) for the midship sinkage in the model tests. The Tuck method is seen to generally underpredict the sinkage of the container ships at model scale; similar results are found in Gourlay (2006; 2013a; 2014a). This is principally due to the linearisation of the free surface boundary condition, coupled with the low pressure produced ahead of the propeller (Gourlay, 2014a). Regardless of F_h and, hence, across all speeds, and regardless of draught and channel conditions, the mean absolute percentage error (MAPE) for each test case is 29.88 % for the DTC in the rectangular canal (at DST); 27.88 % for the DTC in the non-rectangular canal (at BAW); 21.74 % for the KCS;

15.55 % for the JUMBO; and 12.37 % for the MEGA-JUMBO. The midship sinkage for the wide-canal cases, the JUMBO (n = 35), the MEGA-JUMBO (n = 25) and the KCS, at $0.3 < F_h < 0.5$, were predicted to be within ± 10 %.

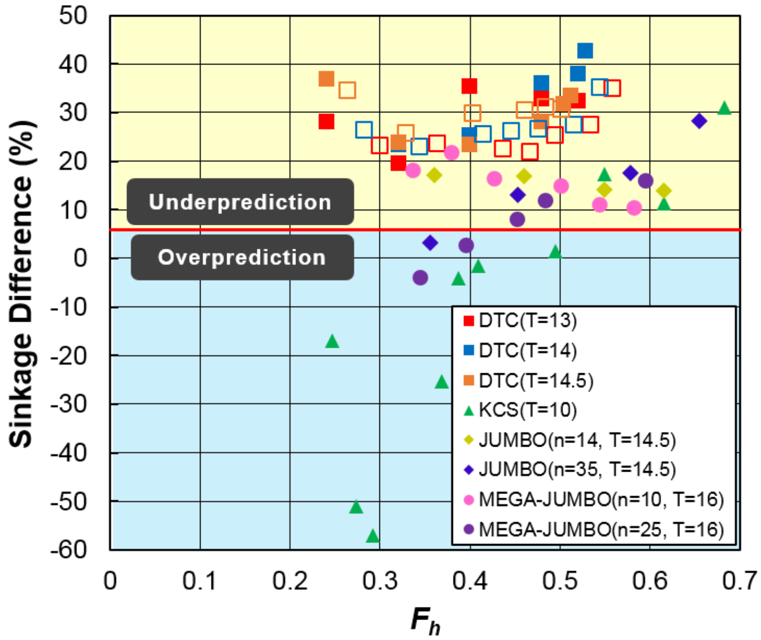

Figure 3.9. Percentage difference between measured and calculated midship sinkage (Tuck, 1967) [Note: Unfilled squares are represented for the DTC in the non-rectangular canal (at BAW)]

3.4.2 Comparison of measured and predicted trim

A comparison between measured and predicted dynamic trim is shown in Figure 3.10. It is shown that the theories generally predict a trim that is slightly more bow-down than the model test results. This is thought to be due to neglecting the effect of the viscous boundary layer thickening towards the stern, and of the low-pressure area forward of the propeller, both of which tend to make the trim more stern-down than the predictions suggest.

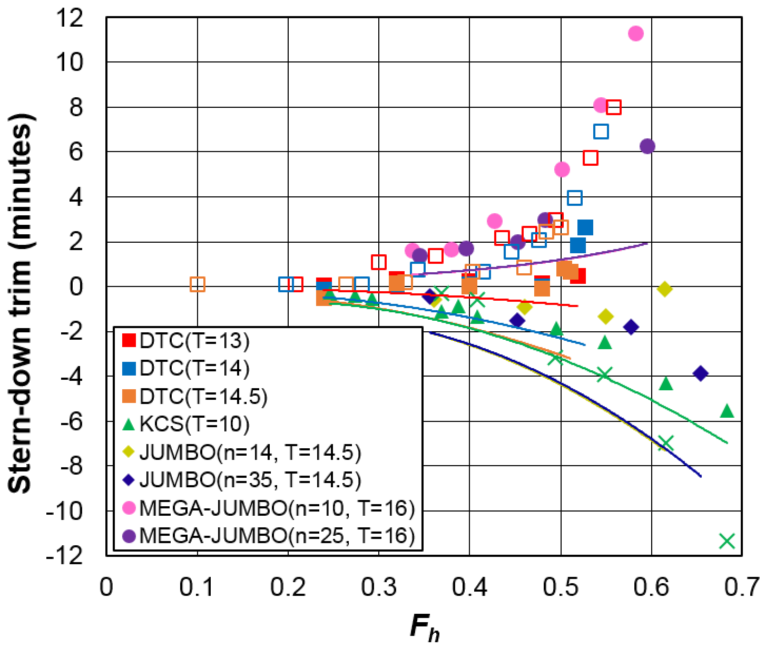

Figure 3.10. Measured and calculated dynamic trim (positive stern-down) [Note: Unfilled squares are represented for the DTC in the non-rectangular canal (at BAW); solid lines for Tuck's method (1967) for canals; × for Rankine-source method]

Comparative hydrodynamic pressure along the hulls, for all ships and test cases, are shown in Figure 3.11, calculated using the Tuck theory (1967).

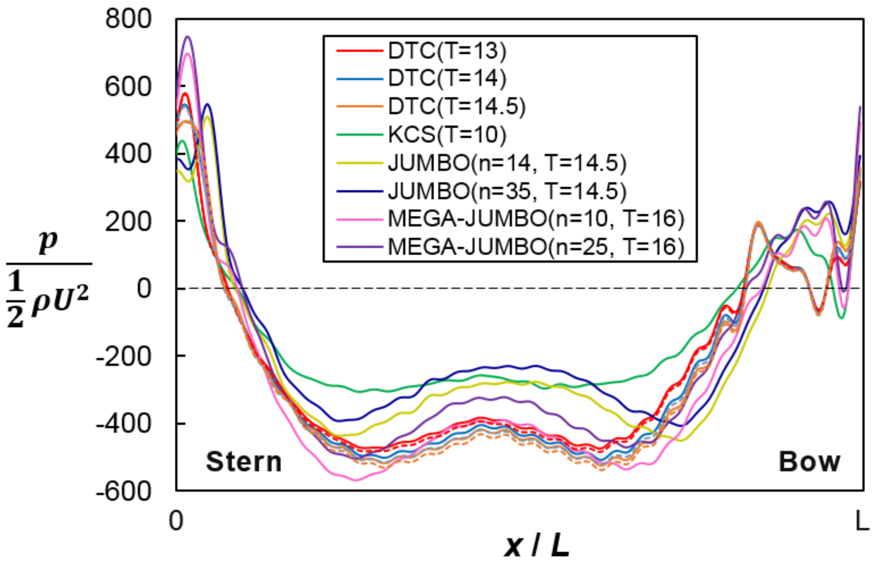

Figure 3.11. Pressure above hydrostatic (non-dimensional) along the ship hulls at F_h = 0.5 [Note: Front of bulb is at x = L, and stern at x = 0, at tested depth; dashed lines are represented for the DTC in the non-rectangular canal (at BAW)]

The hull pressure is characterised by deep low-pressure regions at the forward and aft shoulders. The effect of these on dynamic trim can be seen from the vertical force per unit length *f*, which is plotted in Figure 3.12.

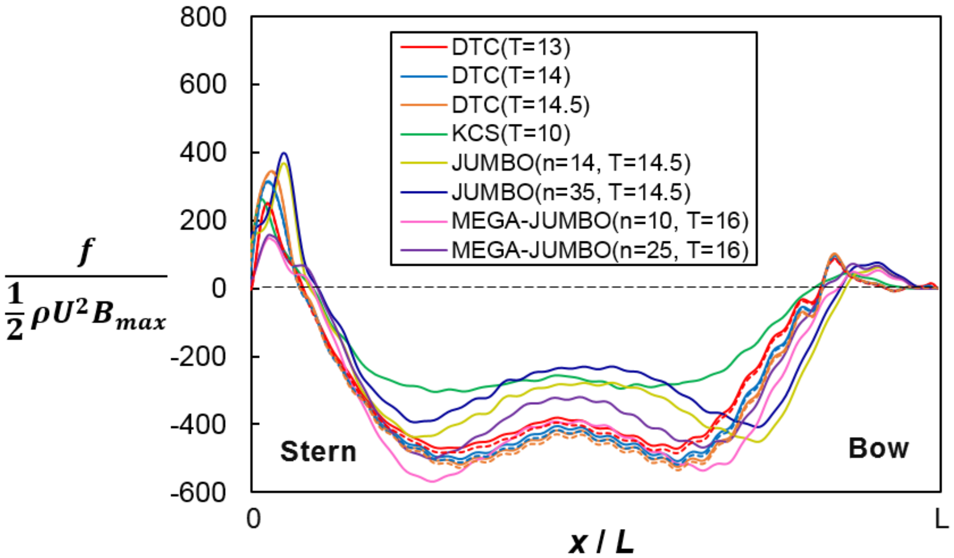

Figure 3.12. Vertical force per unit length $f = pB$ at $F_h = 0.5$ [Note: Front of bulb is at $x = L$, and stern at $x = 0$, at tested depth; dashed lines are represented for the DTC in the non-rectangular canal (at BAW)]

If the centroid of this vertical force is ahead of the LCF, the ship will trim bow-down, and if aft, the ship will trim stern-down. Examples of both stern-down and bow-down trim appear in Figure 3.13. As described previously, no clear correlation between dynamic trim and block coefficient (C_B) was confirmed in the model test results; Figure 3.12 and Figure 3.13 help to explain why. The dynamic trim is caused by the difference between large amounts of force, the downward force at the forward and aft shoulder, and the upward force at the bow and stern. Small changes in hull shape will change the balance between these; and it is anticipated that good container ship design will minimise dynamic trim to minimise any adverse effects of resistance. This explains the small dynamic trim values measured in model tests and predicted theoretically.

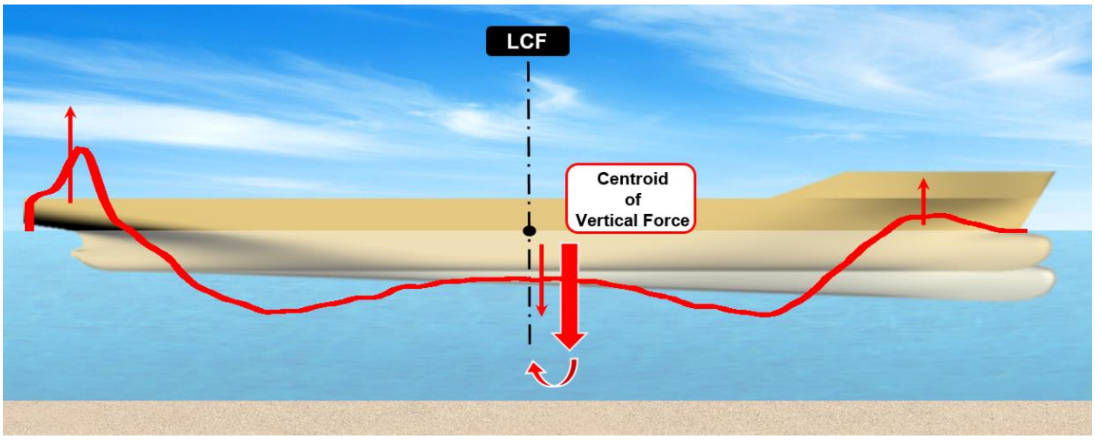

(a) Bow-down trim

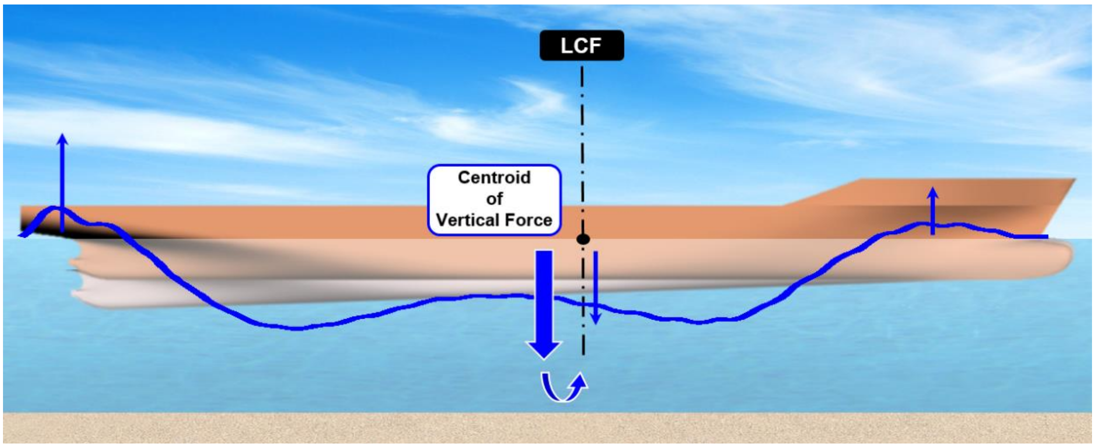

(b) Stern-down trim

Figure 3.13. Examples of dynamic trim: (a) Bow-down; (b) Stern-down

3.5 An empirical correction for dynamic trim?

Tuck's (1967) theory is an inviscid theory, in that it does not include the effect of boundary-layer thickening near the ship's stern, nor does it take into account the low-pressure region ahead of the ship's propeller. These effects in the theory are seen to give a model trim that is more stern-down than the predictions in the test cases studied here.

Viscous effects on dynamic trim are scale-dependent and may be expected to be less important at full scale when the Reynolds number is large and the flow more closely approximates an inviscid flow. According to RANS-CFD calculations (Deng et al., 2014) for the DTC container ship at 14-m draught, dynamic trim was predicted to be 2.9 minutes more stern-down at model scale than at full scale, at 12 knots in 16-m water depth (F_h = 0.49). This difference is of similar magnitude to the difference between the model tests and slender-body predictions (Tuck, 1967), so that the slender-body predictions may quite closely approximate the dynamic trim at full scale.

For comparison, the difference in dynamic trim between towed and self-propelled models of the DTC (Mucha & el Moctar, 2014b) was around 0.5 minutes more stern-down for the self-propelled model at F_h = 0.5.

To provide a more accurate prediction of the dynamic trim at model scale, a small stern-down empirical correction to the dynamic trim can be made. A dynamic trim correction (in minutes stern-down) may take the form:

$$\Delta\theta = cF_h^2 \tag{3.2}$$

From an analysis of the theoretical and model test results, the constant c is found to have an average value of 12.21 and standard deviation of 6.81.

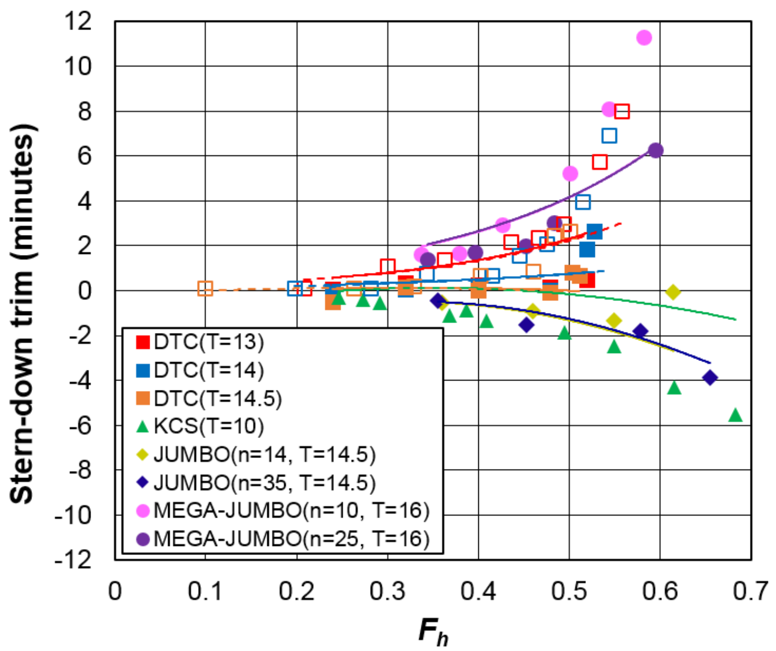

Figure 3.14. Measured and calculated dynamic trim applying the empirical correction

Figure 3.14 shows a comparison between measured and predicted dynamic trim using Tuck's (1967) method with the dynamic trim correction of c =12.21 (in minutes stern-down) in Eq. (3.2). Compared with Figure 3.10, the predicted dynamic trim for all container ships is more close to the model test results, especially in the range F_h = 0.2−0.5. At F_h = 0.49, the correction is 2.7 minutes, very close to the RANS-calculated difference between model scale and full scale (Deng et al., 2014) discussed previously. While this empirical correction may be applied to match model test results more closely, it is recommended that no such correction be applied at full scale.

3.6 Comparison of measured ship squat with empirical methods in the PIANC guidelines

The recent guidelines for port approach channels (PIANC, 2014) report information on suitable squat allowances for different types of channels and ships and provide several semi-empirical methods, including

Stocks, Dagget and Pagé (2002): A version of Tuck (1966)

Huuska/Guliev (Huuska, 1976)

ICORELS (International Commission for the Reception of Large Ships, 1980)

Barrass3 (Barrass, 2004b)

Eryuzlu2 (Eryuzlu, Cao, & D'Agnolo, 1994)

Römisch (1989)

Yoshimura (1986)

In this chapter, five methods in the PIANC guidelines will be used for further comparisons: the Stocks, Dagget and Pagé (2002), Huuska/Guliev (Huuska, 1976), Barrass3 (Barrass, 2004b), Römisch (1989) and Yoshimura (1986). The ICORELS (International Commission for the Reception of Large Ships, 1980) and Eryuzlu2 (Eryuzlu, Cao, & D'Agnolo, 1994) will not be considered at this stage; they are not recommended for the canal-type channel, which is the type of channel model tested and being applied to the numerical modelling, as shown in Figure 3.4.

The midship sinkage and trim of the container ships have been taken into account in comparing and validating the theoretical methods. However, the focus should now lie on the ship's maximum sinkage so that it is directly comparable to results from the five empirical methods listed in PIANC. For information only, the Römisch (1989) method gives a prediction for sinkage at both bow and stern, and the others make no such distinction. A more detailed description of each method can be found in PIANC (2014).

The five methods are defined by Eq. (3.3)–Eq. (3.16).

Stocks, Dagget and Pagé (2002): A version of Tuck (1966):

$$S_{\max} = 1.46 \frac{\nabla}{L_{PP}^{2}} \frac{F_h^{2}}{\sqrt{1-F_h^{2}}} K_s + 0.5 L_{PP} \sin\left\{ \frac{\nabla}{L_{PP}^{3}} \frac{F_h^{2}}{\sqrt{1-F_h^{2}}} K_s \right\} \tag{3.3}$$

Huuska/Guliev (Huuska, 1976):

$$S_{\max} = C_s \frac{\nabla}{L_{PP}^{2}} \frac{F_h^{2}}{\sqrt{1-F_h^{2}}} K_s \tag{3.4}$$

Note that C_s = 2.4 is typically used, and the depth-based Froude number (F_h) was previously defined (see Eq. (2.4)). The non-dimensional correction factor for channel width (K_s) is

$$K_s = \begin{cases} 7.45 S_1 + 0.76 & S_1 > 0.03 \\ 1.0 & S_1 \le 0.03 \end{cases} \tag{3.5}$$

with the non-dimensional corrected blockage factor S_1 for the three types of channel configuration: unrestricted (U), restricted (R) and canal (C) (refer to Figure 2.8); these are given by

$$S_1 = \begin{Bmatrix} 0.03 & U \\ \dfrac{S}{K_1} & R \\ S & C \end{Bmatrix} \tag{3.6}$$

where the blockage factor S is a proportion of a cross-sectional area of a ship (A_s) and of a channel (A_c), defined as

$$S = \frac{A_s}{A_c} \tag{3.7}$$

Barrass3 (Barrass, 2004b):

$$S_{\max} = \frac{C_B V_K^2}{100/K} \tag{3.8}$$

where V_K = ship speed in knots; and K = channel coefficient, given by

$$K = 5.74 S^{0.76} \quad 1 \le K \le 2 \tag{3.9}$$

Römisch (1989):

$$S_{bow} = C_V C_F K_{\Delta T} T \tag{3.10}$$

$$S_{stern} = C_V K_{\Delta T} T \tag{3.11}$$

where C_V = correction factor for ship speed; C_F = correction factor for ship shape; and $K_{\Delta T}$ = correction factor for squat at ship critical speed. These non-dimensional coefficients are defined as

$$C_V = 8\left(\frac{V}{V_{cr}}\right)^2 \left[\left(\frac{V}{V_{cr}} - 0.5\right)^4 + 0.0625\right] \tag{3.12}$$

$$C_F = \left(\frac{10 C_B}{L_{PP}/B}\right)^2 \tag{3.13}$$

$$K_{\Delta T} = 0.155\sqrt{\frac{h}{T}} \tag{3.14}$$

Yoshimura (1986):

$$S_{\max} = \left[\left(0.7 + 1.5 \frac{1}{h/T} \right) \left(\frac{C_B}{L_{PP}/B} \right) + 15 \frac{1}{h/T} \left(\frac{C_B}{L_{PP}/B} \right)^3 \right] \frac{V_e^2}{g} \tag{3.15}$$

where V_e = modified ship speed defined as

$$V_e = \begin{cases} V_s & U \\ \dfrac{V_s}{(1-S)} & R,C \end{cases} \tag{3.16}$$

Figure 3.15 shows comparisons between the measured and calculated maximum sinkage for the DTC case at draughts of 13.0, 14.0 and 14.5 m. The blue circles represent the results from the numerical calculations using Tuck (1967), as previously discussed.

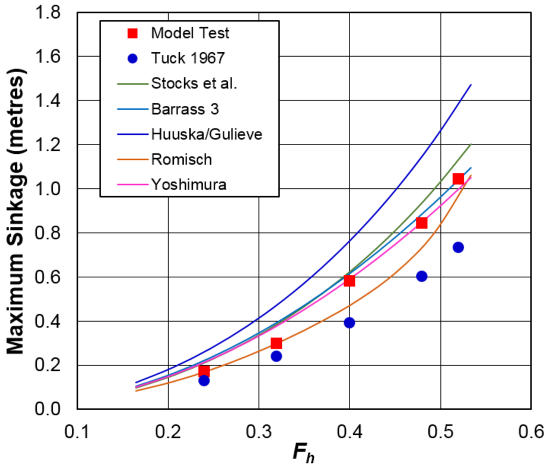

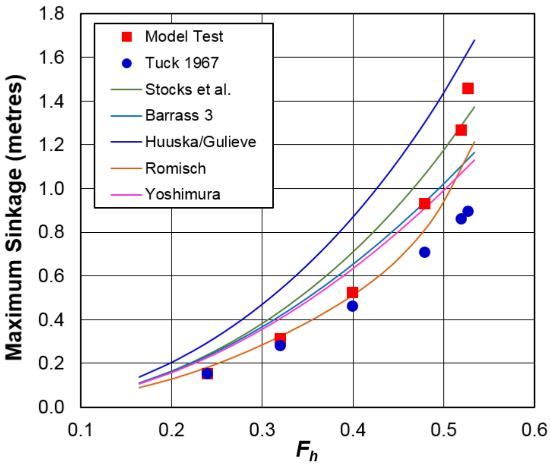

(a) T = 13.0 m (b) T = 14.0 m

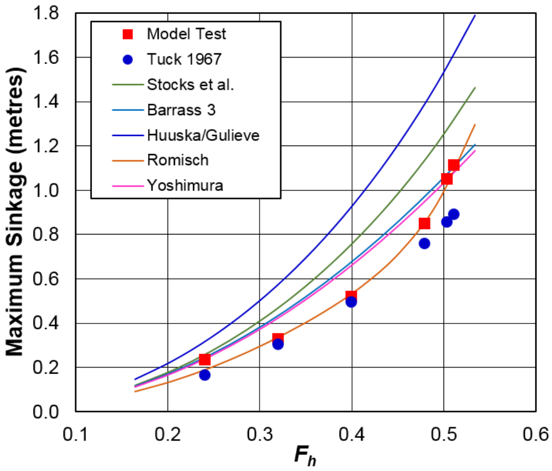

(c) T = 14.5 m

Figure 3.15. Comparison of the empirical methods in the PIANC guidelines with the model test results for the DTC

The five methods in the PIANC guidelines overpredict sinkage for the DTC on the whole, whereas Tuck (1967) tends to underpredict it. The Huuska/Guliev (1976) method is seen to significantly overpredict the measurements, in that the predicted maximum sinkage is on average 33 % larger than the model test results. The Stocks, Dagget and Pagé (2002), Barrass3 (Barrass, 2004b) and Yoshimura (1986) methods slightly overpredict the maximum sinkage at low speeds (F_h < 0.45), but make predictions closer to the measured sinkage at F_h > 0.45: that is, when ship speed is over 11 knots.

The Römisch (1989) prediction is found to be in a good agreement with the measured values for all DTC test cases across all speeds and draught conditions, particularly for the test at a draught of 14.5 m (see Figure 3.15(c)). In this case, the Römisch (1989) predicted the maximum sinkage at the stern; e.g., the calculated sinkage at the stern was approximately 18 % greater than that at the bow, as in the model tests, which showed that the DTC (T = 14.5) trimmed stern-down (see Figure 3.6). The Tuck (1967) method is very close to the model test results at low speeds irrespective of the DTC's draughts, but underpredicts sinkage at high speeds.

Comparisons between the empirical methods in the PIANC guidelines and the Tuck (1967) method, together with the model test results for the KCS at test depths of 11.5, 13.0 and 16.0 m, are shown in Figure 3.16. Again, the Römisch (1989) method seems to be as accurate as the Tuck (1967) prediction for the KCS case, although, interestingly, it predicts the maximum sinkage at the stern (stern-down); but the model tests show conflicting results with the KCS having a negative trim (bow-down) (see Figure 3.6). The Stocks, Dagget and Pagé (2002) method might be a useful tool for predicting the maximum sinkage in this case.

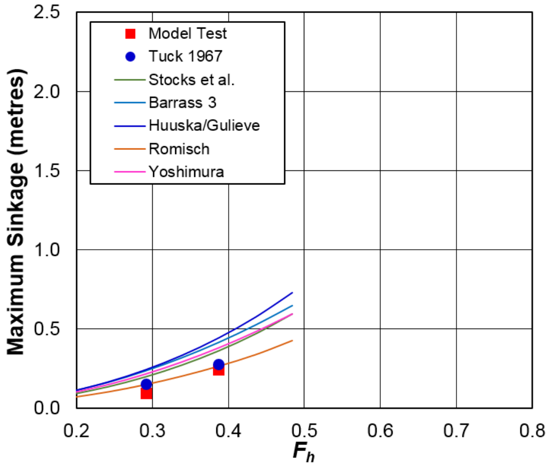

(a) h = 11.5 m

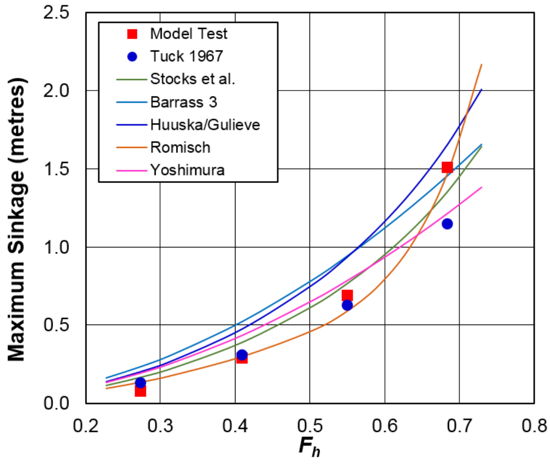

(b) h = 13.0 m

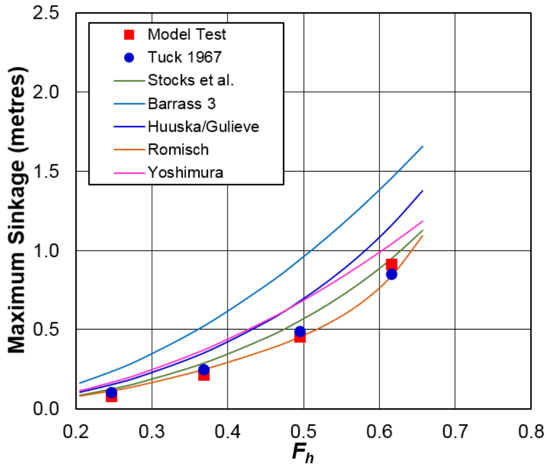

(c) h = 16.0 m

Figure 3.16. Comparison of the empirical methods in the PIANC guidelines with the model test results for the KCS

Figure 3.17 shows comparisons for the JUMBO in the smallest (n = 14) and largest (n = 35) channel widths. The 'n' values, canal-to-ship hull cross-sectional area ratio, is an important factor in these results. The Huuska/Guliev (1976) method noticeably overpredicts the measured maximum sinkage in the smallest channel width (n = 14), and the Römisch (1989) method underpredicts the test results in the largest channel width (n = 35). The maximum sinkage in the narrow-canal case (n = 14) and wide-canal case (n = 35) are reasonably well predicted by the Yoshimura (1986) and Stocks, Dagget and Pagé (2002) methods, respectively. It is expected that the Römisch (1989) method will be significantly affected by the ship's high speed in the narrow canal considering that its prediction shows a rapidly-increasing slope at $F_h > 0.5$, as seen in Figure 3.17(a).

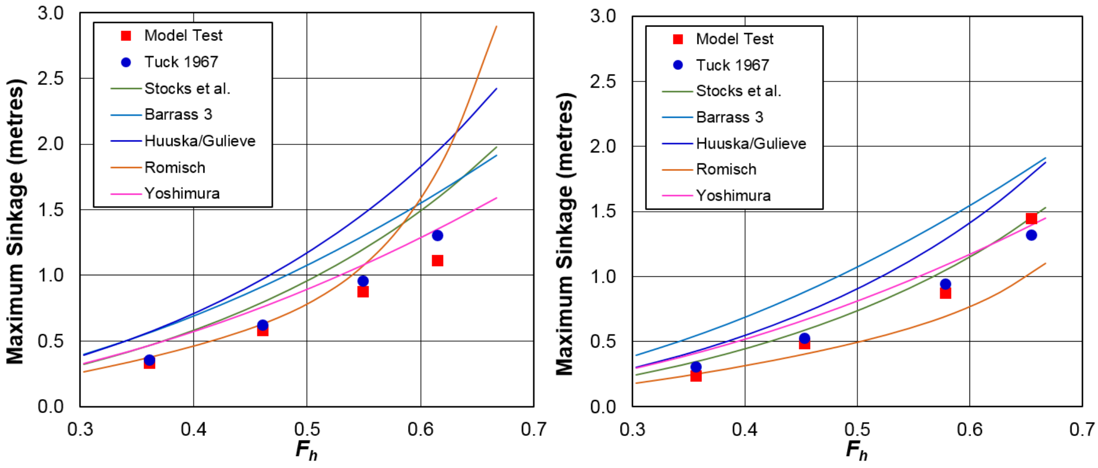

(a) n = 14 (b) n = 35

Figure 3.17. Comparison of the empirical methods in the PIANC guidelines with the model test results for the JUMBO [Note: n is canal-to-hull cross-sectional area ratio]

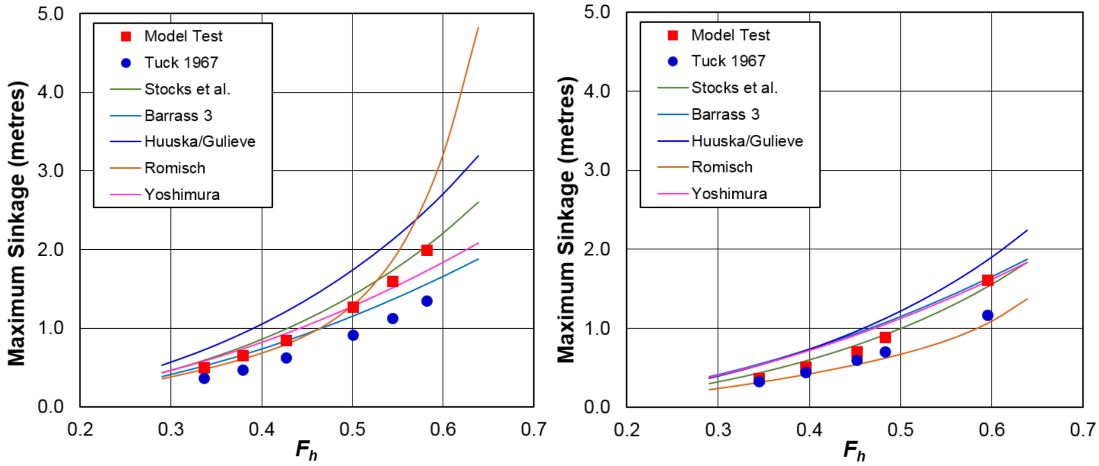

(a) n = 10 (b) n=25

Figure 3.18. Comparison of the empirical methods in the PIANC guidelines with the model test results for the MEGA-JUMBO [Note: n is canal-to-hull cross-sectional area ratio]

Figure 3.18 also shows comparisons for the MEGA-JUMBO in the smallest (n = 10) and largest (n = 25) channel widths. Good agreement between the Stocks, Dagget and Pagé (2002) method and the model test results are observed for both the narrow- (n = 10) and wide-canal cases (n = 25) across all speed ranges. This, and the results for the JUMBO (see Figure 3.17(a)), confirm that the blockage effect is important for the Römisch (1989) prediction, in that sinkage is considerably overpredicted as the depth Froude number (F_h) increases above 0.5 in the narrow canal (n = 10) and is generally underpredicted in the wide canal (n = 25). The maximum sinkage from the

Barrass3 (Barrass, 2004b) and Yoshimura (1986) methods appears to give good agreement with those from the model tests in the narrow-canal case (n = 10).

Percentage differences (average across all speeds) of the maximum sinkage between the measurements and predictions applying the five methods in the PIANC guidelines are given in Table 3.4. These results can be used for choosing an efficient method for general use in container ships. Note that the Tuck (1967) results are also given for comparative purposes.

Table 3.4. Percentage difference (average across all speeds) between measured and predicted maximum sinkage

Test cases		Tuck (1967)	Stocks, Dagget & Pagé (2002)	Barrass3 (2004)	Huuska /Gulieve (1976)	Römisch (1989)	Yoshimura (1986)
DTC	T = 13.0 m	27.02	15.07	13.81	40.90	8.76	10.81
	T = 14.0 m	19.45	25.89	24.26	50.59	11.62	23.20
	T = 14.5 m	15.12	28.05	13.43	56.80	5.00	11.68
KCS	h = 11.5 m	38.17	78.99	110.04	119.18	34.07	92.87
	h = 13.0 m	25.27	38.31	75.56	62.93	20.92	54.63
	h = 16.0 m	15.20	27.56	123.78	56.19	16.07	60.20
JUMBO	n = 14	9.99	38.15	54.28	69.17	26.12	27.90
	n = 35	13.51	21.33	74.44	48.57	17.61	34.02
MEGA-JUMBO	n = 10	28.57	12.57	8.67	37.84	12.92	9.49
	n = 25	17.00	11.05	28.95	33.36	24.07	26.27
Overall		**20.93**	**29.70**	**52.72**	**57.55**	**17.71**	**35.11**

The most efficient analysis of container ships in this chapter was via the Römisch (1989) method. However, this tends to underpredict the model test results in the wide-canal cases, including the KCS (h = 16 m), JUMBO (n = 35) and MEGA-JUMBO (n = 25), which means that Römisch may not work so well for unrestricted channels. This tendency was witnessed in full-scale trials on two container ships in the rivers Elbe and Weser in Germany (Briggs, Debaillon, Uliczka, & Dietze, 2009), which showed that the Römisch prediction worked well for the restricted channel only. The second-best method is that of Stocks, Dagget and Pagé (2002), followed by Yoshimura's (1986); both seem to be able to predict squat for container ships with reasonable accuracy. The Barrass3 (Barrass, 2004b) and Huuska/Guliev (1976) methods both appear to be subject to the blockage effect, but show conflicting trends. For the Barrass3 (Barrass, 2004b) method, the predicted sinkage in the narrow-canal cases, i.e., all cases of the DTC, JUMBO (n = 14) and MEGA-JUMBO (n = 10), was closer to the measured sinkage than the predictions for the wide-canal cases. In contrast, the Huuska/Guliev (1976) method was more accurate for the wide-canal cases, with the KCS (h = 16 m), JUMBO (n = 35) and MEGA-JUMBO (n = 25), than for the narrow-canal cases.

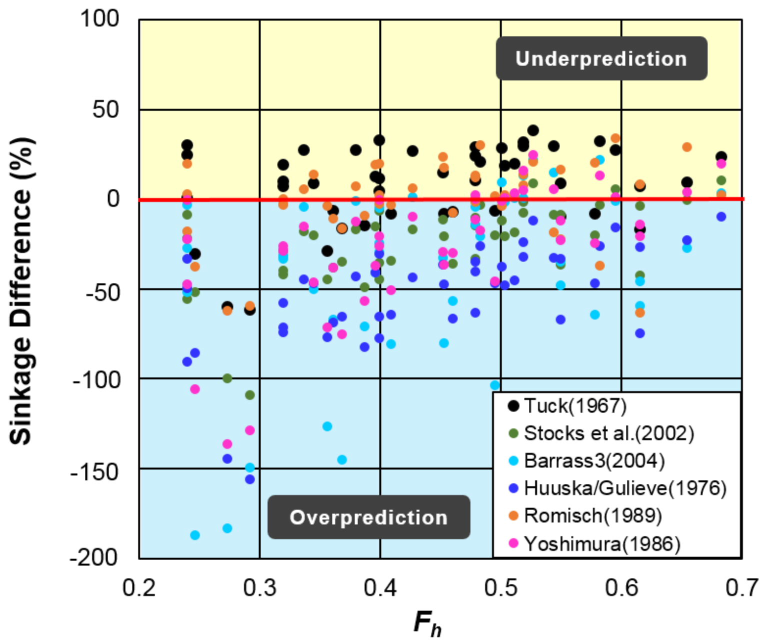

Figure 3.19. Percentage difference between measured and predicted maximum sinkage for all test cases

Figure 3.19 shows percentage differences between the measured and predicted maximum sinkage, regardless of the channel conditions or hulls being tested. In general, the Tuck (1976) method is seen to underpredict the maximum sinkage of the container ships analysed here, whereas the five empirical methods overpredict it. The percentage difference for the Römisch (1989) method ranges from around (+) 20 to (-) 60 %, but generally is within (±) 20 % of the measured value; the value of the Barrass3 (Barrass, 2004b) method is spread throughout the overprediction area; the Stocks, Dagget and Pagé (2002) and Yoshimura (1986) methods have a similar trend in their distributions; the Huuska/Guliev (1976) method is distributed along (-) 50 % on the whole.

Because only the canal type has been considered in this chapter, these results are not directly applicable to the other channel types such as unrestricted and restricted channels (see Figure 2.8). It is also recommended that ship squat should be predicted using more than one method, with consideration of ship hulls, channel configurations and methodological constraints. The effect of channel configurations on the empirical methods in the PIANC guidelines can be found in Briggs, Debaillon, Uliczka and Dietze (2009), and Briggs, Kopp, Ankudinov and Silver (2013).

3.7 Conclusions

A comparison and analysis of the dynamic sinkage and trim of several modern container ship hulls in shallow water or port approach channels was performed, including available model test data. The container ship hull forms considered in this chapter were the DTC, KCS, JUMBO, MEGA-JUMBO, HTC and S-175.

A review was made of changes in container ship hull designs to the present time. Significant changes were captured, from the HTC and S-175 having a relatively small and low bow bulb and no stern bulb to the modern container ships with a tendency to high bulbous bows and broad and flat transoms. Important differences in stern waterplane shape, which has an important effect on dynamic trim, were also observed.

Extensive model test data are available for the analysis of sinkage and trim in modern container ship hull forms, such as those if the DTC, KCS, JUMBO and MEGA-JUMBO, in shallow water.

Two potential flow methods, the slender-body and Rankine-source methods, were applied to compare with model test results for the four container ship hulls. It was shown that the slender-body theory can accurately predict sinkage in wide canals or open water, but underpredicts sinkage in narrow canals. The Rankine-source method provided a particularly good sinkage estimate for the KCS at high speed. Calculations for the other ship cases would be very useful in assessing this method further. Slender-body theory was also able to predict dynamic trim with reasonable accuracy at model scale (except at high speed), and potentially with good accuracy at full scale.

The five empirical methods listed in the recent guidelines for port approach channels (PIANC, 2014) were used for further comparisons with the numerical and model test results. In terms of percentage differences, the most efficient method for testing container ships was the Römisch (1989), followed by Stocks, Dagget and Pagé (2002) and Yoshimura (1986) methods; but note that all the results described in this chapter might be applicable to the canal type only.

Chapter 4

Full-Scale Measurement Campaigns

This chapter presents some results from a series of recent full-scale trials measuring the dynamic sinkage, trim and heel of 11 bulk carrier transits and 16 container ship transits entering and leaving the Port of Geraldton and the Port of Fremantle, respectively. Measurements were carried out using high-accuracy GNSS receivers on board and a fixed reference station. Measured sinkage, together with ship speed and channel bathymetry, are shown. Maximum dynamic sinkage and dynamic draught, as well as elevations of the ship's keel relative to chart datum, are also shown. Additional comparisons of dynamic trim and heel between the ship transits are given.

Raw data from each set of trials has been published as a Centre for Marine Science and Technology (CMST) report by Ha and Gourlay (2016a; 2016b). The measured results will be used for ship squat comparisons and validations (Chapter 5) as well as for ship wave-induced motion comparisons and validations (Chapter 6).

4.1 Introduction

Although model-scale tests in a controlled environment remain the method of choice for benchmarking studies (Mucha, el Moctar, & Böttner, 2014; Gourlay, von Graefe, Shigunov, & Lataire, 2015) with appropriate allowance for scale effects (Deng et al., 2014; Graff, Kracht, & Weinblum, 1964), since the 1990s full-scale measurements of dynamic ship motion in waterways have been successfully carried out by making use of the increasingly accurate Global Navigation Satellite System (GNSS) (Feng & O'Mahony, 1999; Gourlay & Klaka, 2007; Ha, Gourlay, & Nadarajah, 2016; Härting & Reinking, 2002). These trials have been valuable in furnishing accurate and reliable full-scale data that may be utilised by ports, pilots and deck officers, but conducting them involves a great deal of time and requires thorough preparation and close collaboration with pilots, port terminals, shipping agents and the port Vessel Traffic Service (VTS). Care must be taken not to interfere with port operations, nor delay normal pilotage. In addition, when validating numerical ship motion modelling at full scale, there are uncertainties in applying theoretical methods to actual transit conditions, including seabed conditions; varying bathymetry; ever-changing waves, wind and currents; as well as problems with studying commercial ships whose lines plans are confidential. Despite such difficulties in implementation and application, measurements and validations at full scale provide an important practical test of numerical under-keel clearance (UKC) modelling.

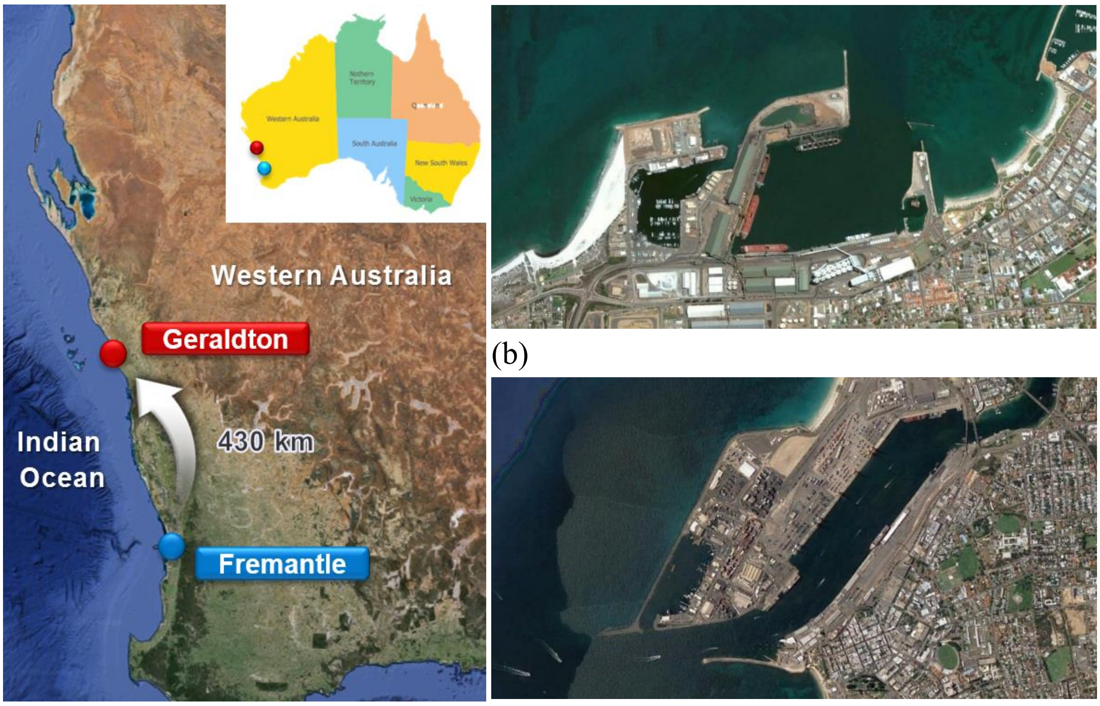

(a) (c)

Figure 4.1. (a) Map showing port locations (source: Google Earth Pro); (b) Satellite image of the Port of Geraldton (Image © 2017 TerraMetrics, Data SIO, NOAA, U.S. Navy, NGA, GEBCO); (c) Satellite image of the Port of Fremantle (Image © 2017 TerraMetrics, Data SIO, NOAA, U.S. Navy, NGA, GEBCO)

Full-scale trials of bulk carrier motions were performed in the Port of Geraldton, and of container ship motions in the Port of Fremantle. The purpose of the trials was not only to obtain high-quality data on vertical ship motions in their approach channels, including squat and wave-induced motions, but also to validate current UKC practice using the data from the measurements. The measurements were made using the shorebased receiver method, which uses high-accuracy GNSS receivers on board plus a fixed base station for an external reference (Feng & O'Mahony, 1999; Gourlay & Klaka, 2007). Maps and satellite images of the Port of Geraldton and the Port of Fremantle are shown in Figure 4.1.

4.2 Ship motion trials on bulk carriers at the Port of Geraldton

In September and October 2015, at the Port of Geraldton, located in the mid-west region of Western Australia (see Figure 4.1(a)), full-scale measurements were performed on 11 bulk carrier transits, including five inbound and six outbound transits, via the curved approach channel (see chart AUS81).

4.2.1 Description of bulk carrier motion trials

4.2.1.1 Description of the port and channel

The layout of the Port of Geraldton, including its approach channel and navigational beacons, is illustrated in Figure 4.2 (see also Figure 4.1(b)).

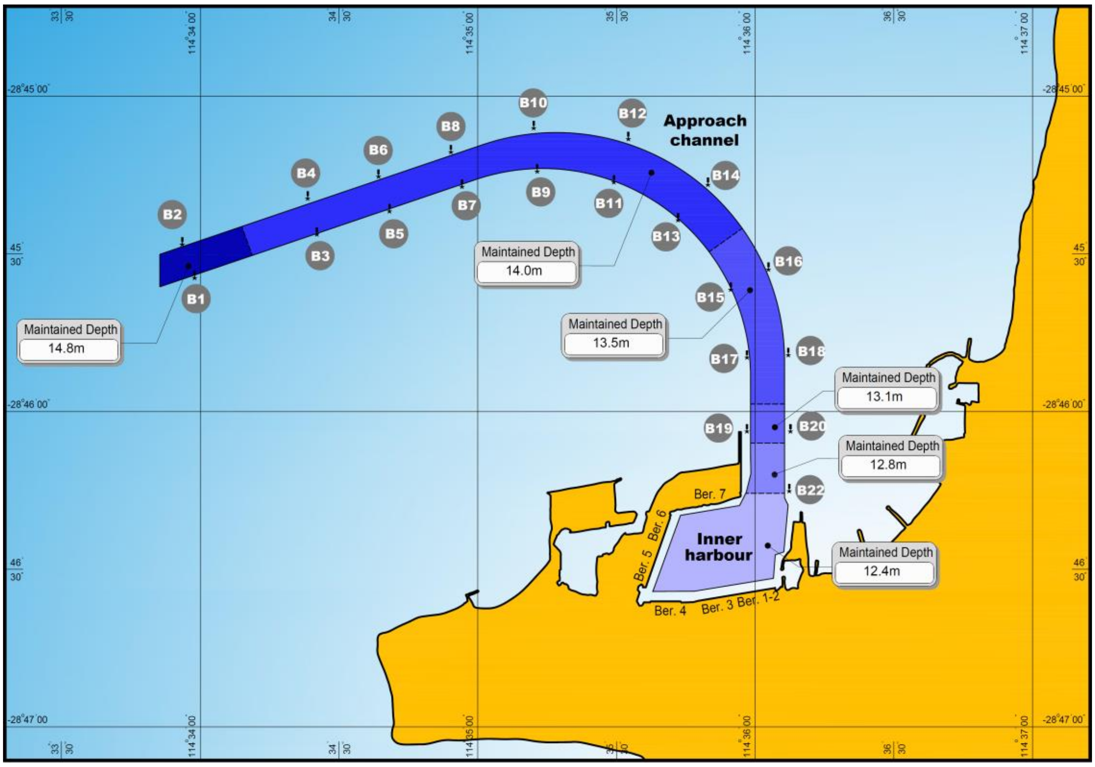

Figure 4.2. Layout of the Port of Geraldton, including its approach channel and navigational beacons

The channel is around 2.8 nautical miles in length and 180 m in width (at the toe of the bottom slope), varying in depth from 12.8 to 14.8 m based on the Chart Datum (CD), which is equal to the Lowest Astronomical Tide (LAT) and 0.547 m below the Australian Height Datum (AHD, national vertical datum for Australia). The inner harbour has a water area of approximately 33 ha with a maintained depth of 12.4 m (CD). An additional depth of up to 1.2 m can be caused by tides. Highest Astronomical Tide (HAT) and Mean Sea Level (MSL) in the port are 1.2 and 0.6 m, respectively (see chart AUS81). Details of tides can be found in the Australian National Tide Tables (ANTT; also known as AHP11).

4.2.1.2 Description of the ships (bulk carriers) and transit conditions

Measurements were undertaken on 11 bulk carrier transits on the dates shown in Table 4.1.

Table 4.1. Measurement date at the Port of Geraldton

Measurements	Ships	In / Out	Measurement date
1st set of measurements 31st Aug. − 3rd Sep. 2015 (4 days)	*HONG YUAN*	inbound	Wed. 2nd September 2015
	PETANI	inbound	Thu. 3rd September 2015
	DONNACONA	inbound	Thu. 3rd September 2015
2nd set of measurements 27th Sep. − 2nd Oct. 2015 (6 days)	*GUO DIAN 17*	outbound	Mon. 28th September 2015
	SFL SPEY	outbound	Mon. 28th September 2015
	AAL FREMANTLE	inbound	Mon. 28th September 2015
	IVS MAGPIE	outbound	Mon. 28th September 2015
	FENG HUANG FENG	outbound	Tue. 29th September 2015
	AAL FREMANTLE	outbound	Wed. 30th September 2015
	SEA DIAMOND	inbound	Thu. 1st October 2015
	SEA DIAMOND	outbound	Fri. 2nd October 2015

During each transit, the author was able to view the ship's trim and stability book and take photos of relevant operating conditions. Ship dimensions and comparative transit conditions for all the bulk carriers are shown in Table 4.2. For details of the ships, displacement and C_B are values at summer draught; C_B is the ratio of displaced volume to (L_{PP}·Beam·Draught). For details of the transit conditions, C_B is calculated based on arrival or departure draught; LCB and LCF are given as metres forward of the AP; average draught is represented for C_B, LCB and LCF.

Table 4.2. Details of the ships (bulk carriers) and transit conditions

	Particulars	*HONG YUAN*	*PETANI*	*DONNACONA*	*GUO DIAN 17*	*SFL SPEY*	*AAL FREMANTLE*	*IVS MAGPIE*	*FENG HUANG FENG*	*SEA DIAMOND*
Details of ships	**Ship size**	Panamax	Panamax	Handy	Panamax	Handy	Handy	Handy	Panamax	Panamax
	Capacity (DWT)	76,364	75,228	28,115	76,426	33,986	18,793	28,240	75,396	77,096
	Year built	2009	2008	2001	2013	2011	2011	2011	2011	2007
	L_{OA} (m)	225.00	225.00	166.30	225.00	181.00	148.60	169.37	225.00	224.99
	L_{PP} (m)	217.00	217.00	161.15	219.00	172.00	140.30	160.40	217.00	217.00
	Depth (m)	19.60	-	-	19.60	14.00	13.50	13.60	19.60	19.50
	Beam (m)	32.26	32.26	24.50	32.26	30.00	23.40	27.20	32.26	32.26
	Design draught (m)	12.20	12.50	-	12.20	9.40	8.00	-	12.20	12.24
	Summer draught (m)	14.20	14.20	10.51	14.20	9.82	9.80	9.82	14.22	14.08
	Displacement (t) at summer draught	88,500.00	87,003.00	35,407.00	89,800.80	42,884.00	26,553.30	34,766.00	88,535.90	87,782.00
	C_B (-)	0.869	0.854	0.833	0.873	0.826	0.805	0.792	0.868	0.869
Details of transit conditions	**Cargo**	Iron ore	Iron ore	Mineral sands	Iron ore	-	Zinc concentrate	Grain (wheat)	Iron ore	Iron ore
	Arrival draught (m)	Fwd. 7.34 Mid. 8.25 Aft. 9.12	Fwd. 7.30 Mid. 7.75 Aft. 8.20	Fwd. 9.18 Mid. 9.24 Aft. 9.29	-	-	Fwd. 6.02 Mid. 6.05 Aft. 6.07	-	-	Fwd. 5.65 Mid. 6.65 Aft. 7.65
	Departure draught (m)	-	-	-	Fwd. 12.15 Mid. 12.15 Aft. 12.15	Fwd. 8.22 Mid. 8.25 Aft. 8.27	Fwd. 8.75 Mid. 9.11 Aft. 9.48	Fwd. 8.78 Mid. 8.80 Aft. 8.82	Fwd. 12.18 Mid. 12.20 Aft. 12.20	Fwd. 8.91 Mid. - Aft. 10.26
	Actual displacement (t)	48,779.00	44,984.00	30,610.00	75,571.00	35,379.00	15,453.00(in), 24,482.00 (out)	30,724.00	74,788.00	38,461.00 (in), 57,427.00 (out)
	C_B (-)	0.824	0.809	0.819	0.859	0.811	0.759 (in), 0.799 (out)	0.781	0.854	0.806 (in), 0.835 (out)
	LCB (m)	116.48@8.24m	117.16@7.76m	77.06@9.20m	-	-	73.09@6.00m (in) 71.12@9.10m (out)	75.73@8.80m	113.90@12.20m	116.18@6.65m (in) 115.05@9.59m (out)
	LCF (m)	112.17@8.24m	113.76@7.76m	-	-	-	71.20@6.00m (in) 64.29@9.10m (out)	80.26@8.80m	106.80@12.20m	114.66@6.65m (in) 110.53@9.59m (out)
	KG (m)	10.11	10.58	7.89	5.90	5.64	7.86 (in), 7.63(out)	7.80	6.41	8.77 (in), 8.07 (out)
	GM_f (m)	4.13	3.86	2.55	7.11	6.71	2.44 (in), 2.29 (out)	3.08	7.10	5.04 (in), 5.93 (out)
Details of berthing	**Berth No.**	No.7	No.5	No.6	No.7	No.6	No.6	No.3	No.7	No.5
	Berthing side (port or starboard)	port-side	port-side	port-side	port-side	port-side	starboard-side	starboard-side	port-side	port-side
	Arrival berthing	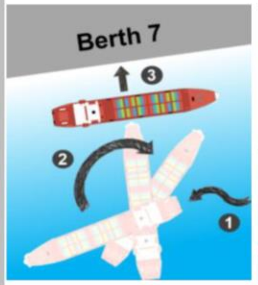			-	-	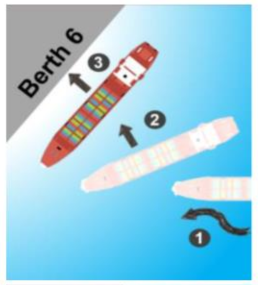	-	-	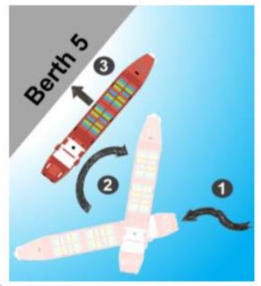
	Departure unberthing	-	-	-	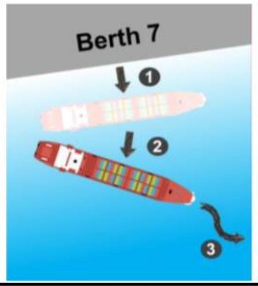	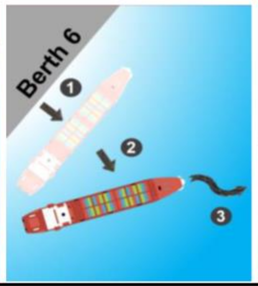		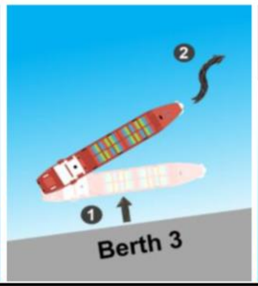	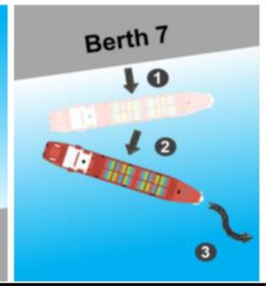	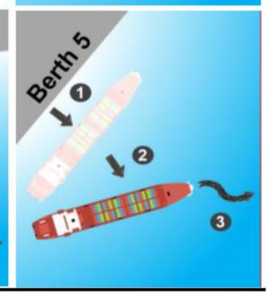

Table 4.2 additionally includes some illustrations that give information on how each ship berthing and unberthing operation was performed, and whether the ship was moored port-side or starboard-side to the quay wall. This helps to understand what happens when the tugs pull the ship off the quay wall.

4.2.1.3 Ship motion measurement equipment

Ship motions were measured using SOKKIA GSR2700 ISX (https://sokkia.com) and Trimble R10 (https://www.trimble.com) GNSS receivers for the first and second set of measurements, respectively. Four receivers were used for each set of measurements, one in each of the following locations:

Base station fixed to pilot jetty
Roving receiver fixed to ship bow
Roving receiver fixed to port bridge wing
Roving receiver fixed to starboard bridge wing

The fixed base station was used to apply differential corrections to the roving receiver results. Stated position accuracy of the SOKKIA GSR2700 ISX (SOKKIA, 2007) and Trimble R10 (Trimble, 2012) GNSS receivers is shown in Table 4.3.

Table 4.3. Accuracy of the GNSS receivers

Receivers	Image	Stated accuracy (general)
SOKKIA GSR2700 ISX		Horizontal : 10 mm + 1 ppm × (baseline length) Vertical : 20 mm + 1 ppm × (baseline length)
Trimble R10		Horizontal : 8 mm + 1 ppm × (baseline length) Vertical : 15 mm + 1 ppm × (baseline length)

An example of the GNSS equipment setup at the Port of Geraldton is shown in Figure 4.3.

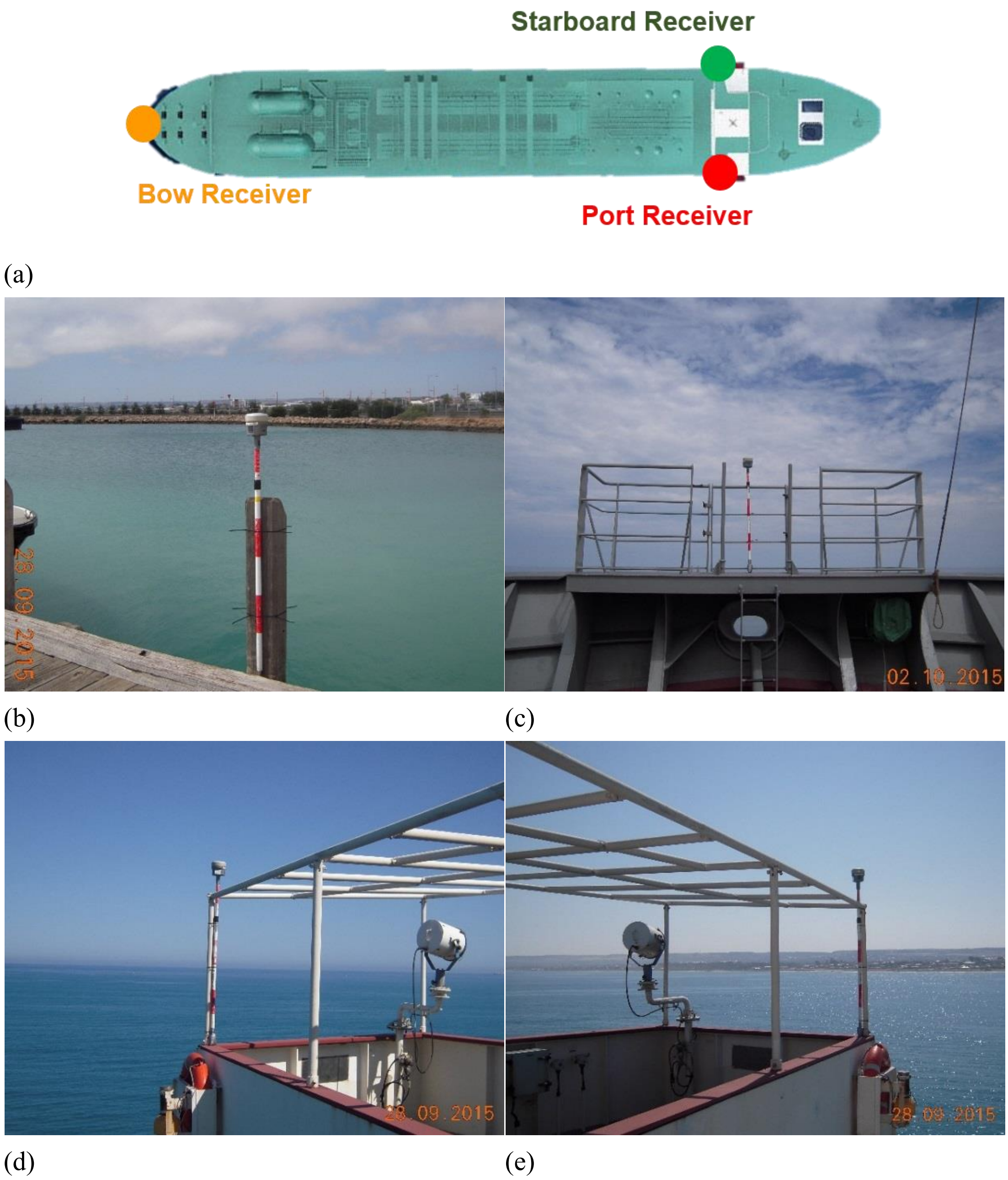

Figure 4.3. GNSS receiver setups: (a) Plan view of ship receivers; (b) Base station on pilot jetty in the *AAL FREMANTLE* (inbound) transit; (c) Bow receiver in the *SEA DIAMOND* (outbound) transit; (d) Port receiver on bridge wing in the *GUO DIAN 17* (outbound) transit; (e) Starboard receiver on bridge wing in the *GUO DIAN 17* (outbound) transit

The base station (see Figure 4.3(b)) was placed at two points on the pilot jetty for each set of trials, as shown in Figure 4.4. The blue point (28° 46.55517' S, 114° 36.13383' E) is the base station location for the first set of trials, and the red point (28° 46.55433' S, 114° 36.10567' E) for the second set of trials. As the SOKKIA GSR2700 ISX GNSS receivers (SOKKIA, 2007) have a power input, during the first set of trials the base station was set up at the blue point where mains power was available. However, as the Trimble R10 GNSS receivers (Trimble, 2012) used for the second set of trials do not have a power input, the base station was moved to the red point, which is in a more open area providing more reliable GNSS satellite coverage.

Figure 4.4. Base station location on pilot jetty (Image © 2016 TerraMetrics, Data SIO, NOAA, U.S. Navy, NGA, GEBCO)

4.2.1.4 Description of trial procedure

The procedure for the ship transits was:

- Set up a GNSS receiver for a fixed base station on the pilot jetty
- Board the vessel with the pilot
- Set up GNSS receivers on the bow and both port and starboard bridge wings (symmetric positions)
- Maintain data recording throughout the pilotage
- Remove equipment and disembark with the pilot

Data recording covered a period of time before departure or after arrival to include a stationary reading at the berth. Data recording commenced before leaving the berth for the outbound transits, and continued until after all mooring work had been completed for the inbound transits; the at-berth measurements were then used as a reference value for comparing the vertical height measurements while underway. Figure 4.5 shows photos of each step of the procedure, taken during the trials at the Port of Geraldton.

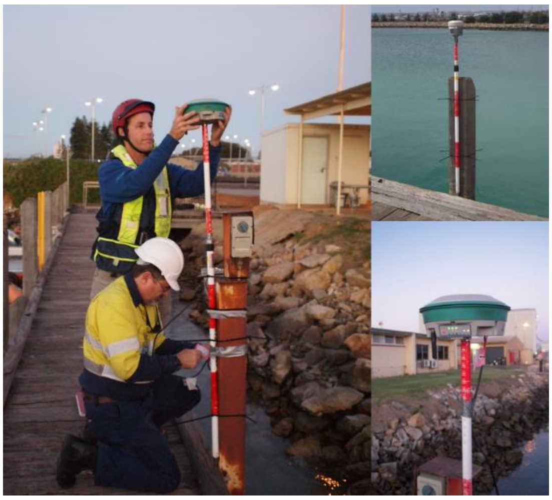

(a)

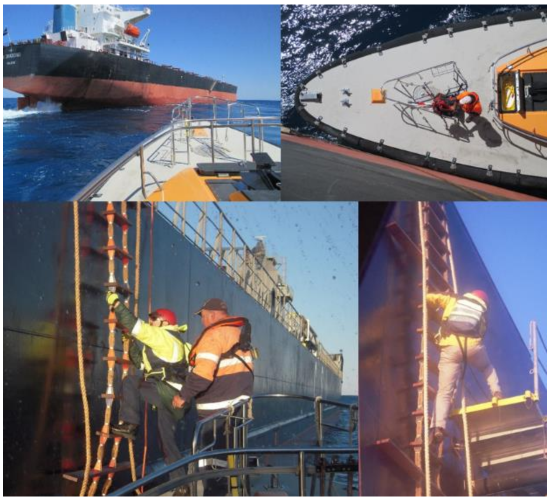

(b)

(c)

(d)

(e)

Figure 4.5. Trials procedure: (a) Set up a fixed base station; (b) CMST researchers board vessel with pilot; (c) Set up GNSS receivers on board; (d) Data recording throughout pilotage; (e) Remove equipment and disembark with pilot

4.2.2 Environmental data

Tidal data in the form of raw sea surface elevations as measured at Berth 3–4 (28° 46.60000' S, 114° 35.76667' E) (see also Figure 4.2) in the Port of Geraldton was provided by the Mid West Ports Authority (MWPA). The independent local tide for each transit was extracted from the raw sea surface data, using a low-pass filter with a cutoff period of 5 minutes, and then applied to calculate the dynamic sinkage of the bulk carriers, which will be explained subsequently. The tidal data covering the period of an example transit (*HONG YUAN*, inbound) is shown in Figure 4.6(a).

***HONG YUAN* (inbound)**

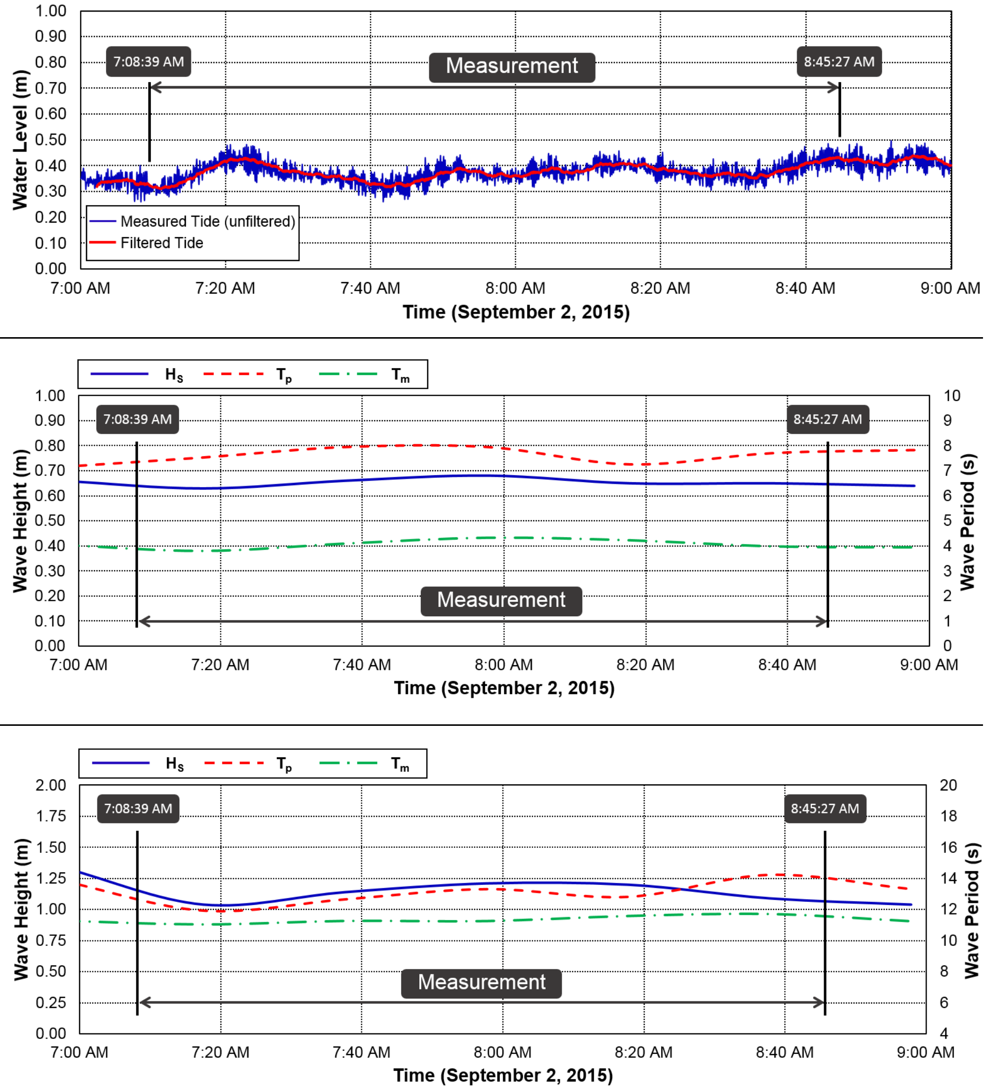

(a) Tide

(b) Sea

(c) Swell

Figure 4.6. (a) Measured tidal data; (b) Measured wave (sea) data; (c) Measured wave (swell) data during the *HONG YUAN* (inbound) transit [Note: Sea/swell cutoff period is 8 seconds; H_s = significant wave height; T_p = spectral peak wave period; T_m = mean wave period]

Wave data from the Acoustic Wave And Current Profiler (AWAC) at Beacon 2 (B2) (28° 45.47000' S, 114° 33.93167' E), located at the end of the channel (see Figure 4.2), were also provided by MWPA. Figure 4.6(b and c) shows such data for the *HONG YUAN* (inbound) transit by way of example. Wave heights and periods are presented as sea and swell components, and the sea/swell cutoff period is 8 seconds. The full set of the tidal and wave data for all the bulk carrier transits can be found in Appendix B (B.1).

During the trials, waves were measured by AWAC at Beacon 2 (B2), and also by 10 pressure sensors at all starboard-hand beacons: Beacon 1 (B1), Beacon 3 (B3), Beacon 5 (B5), …, and Beacon 19 (B19), which are shown as red circles in Figure 4.7. The full measured wave time series data may be used to study wave-induced motions in the channel in future work.

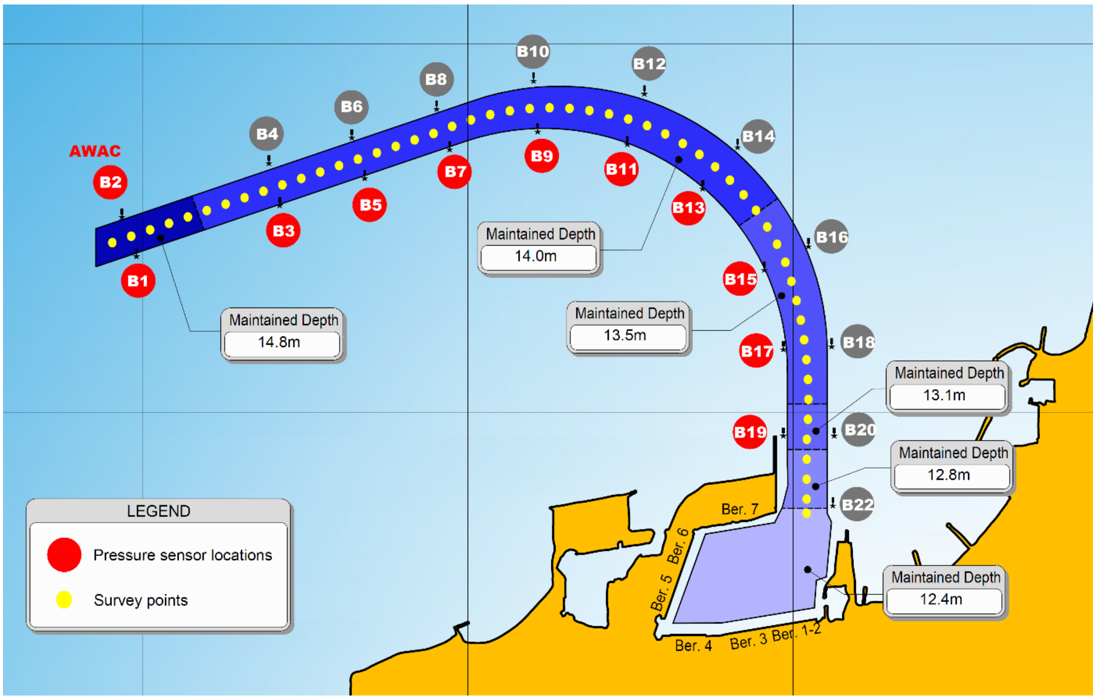

Figure 4.7. Wave pressure sensor locations and actual survey points

No particular observations on wind speeds and directions were made for the measurements in the Port of Geraldton. The full measured wind data can be obtained from the Australian Government Bureau of Meteorology (BoM) if required.

4.2.3 Bathymetric data

To give keel heights relative to the seabed, it is helpful to have more accurate bathymetric data than the given water depths on the nautical chart (AUS81). Fifty-three survey points for the channel were provided by OMC International, and are shown as yellow points in Figure 4.7. A comparison between the bathymetry based on AUS81 and the survey points is presented in Figure 4.8. The flat and dashed seabed line is based on the charted depth on AUS81, and the fluctuating seabed line is the actual survey line, provided by OMC International.

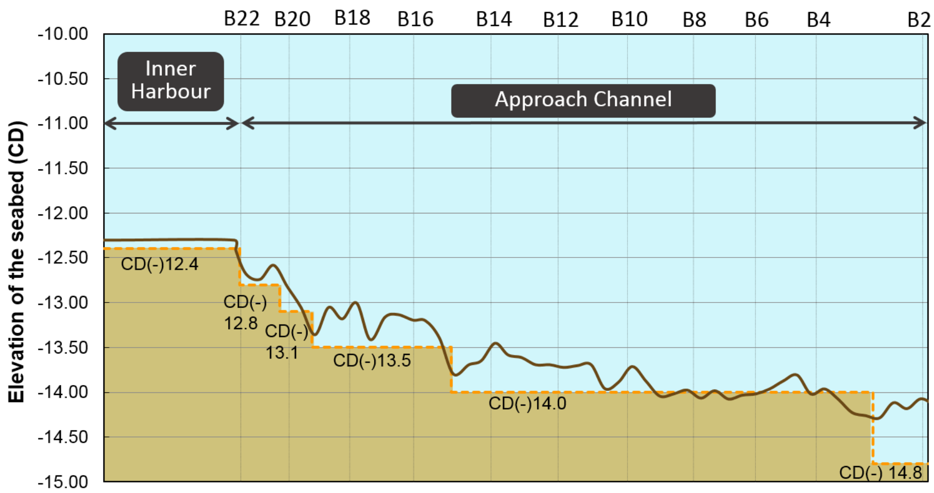

Figure 4.8. Comparison of the seabed lines based on the chart and survey

4.2.4 Data processing

In the present trials, all data were recorded at 1.0 Hz. Data processing techniques discussed here followed those described in Feng and O'Mahony (1999), and Gourlay and Klaka (2007).

Because raw GNSS heights are referenced to an ellipsoid (the WGS84 ellipsoid), and not to chart datum, some height components had to be converted from ellipsoidal heights to heights with respect to the local static waterline: e.g., a local port datum or LAT. To relate the raw GNSS heights to sea level, the geoid undulation (or geoid height) (N), which is the difference between the geoid and the ellipsoid, was first considered to transfer between the raw GNSS heights and the orthometric (geoid) heights; the Earth Gravitational Model 2008 (EGM2008), which is a spherical harmonic model of the Earth's gravitational potential (Pavlis, Holmes, Kenyon, &

Factor, 2012) released by the US National Geospatial-Intelligence Agency (NGA), was used to indicate orthometric heights relative to the Mean Sea Level (MSL). These heights may be a best fit to a vertical datum in a global sense, but are only approximations to the real MSL surface in an area. For this study, at the coastline, it was assumed that the geoid and actual MSL surfaces are essentially the same (Fraczek, 2003); an error analysis in using the geoid model (EGM2008) will be discussed in Chapter 5.

Important height components for calculating sinkage from raw GNSS height measurements are shown in Figure 4.9, and Table 4.4 identifies their generic relationships.

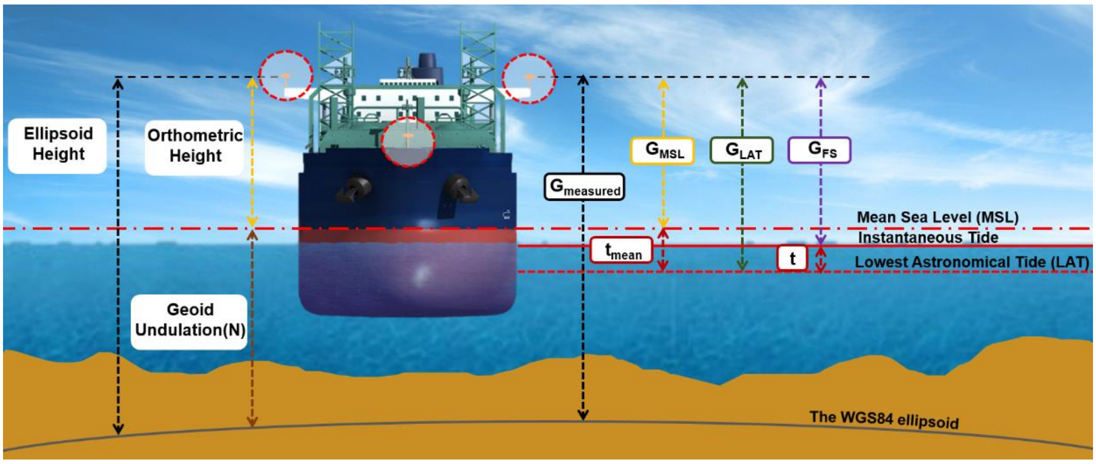

Figure 4.9. Components for calculating sinkage from GNSS height measurements

Table 4.4. Steps for calculating sinkage with height components

Steps	Calculations	Note
1	$G_{measured}$	Raw GNSS height, Ellipsoid height
2	$G_{measured} - N$ (Geoid undulation) $= G_{MSL}$	Orthometric height (using EGM 2008)
3	$G_{MSL} + t_{mean} = G_{LAT}$	t_{mean} = MSL – LAT
4	$G_{LAT} - t = G_{FS}$ $((G_{measured} - N)_{GMSL} + t_{mean})_{GLAT} - t = G_{FS}$	t = Instantaneous tidal height
5	Sinkage $= (G_{FS})_{static} - (G_{FS})_{underway}$ $(G_{measured} - N + t_{mean} - t)_{static}$ $- (G_{measured} - N + t_{mean} - t)_{underway}$	Sinkage at each receiver

To obtain the height of a GNSS receiver above the instantaneous static free surface (G_{FS}) around a ship, several calculation steps using such height components should be made in the sequence shown in Table 4.4 (Steps 1 to 4). Sinkage is ultimately calculated by the vertical height differences between the static floating position at the berth and when underway (Step 5).

By accurately calculating the sinkage of the three GNSS receivers, i.e., bow, port and starboard receivers (see Figure 4.3(a)), with respect to the local static free surface, and assuming the ship to be rigid, it is possible to obtain sinkage at other points of concern of running aground on bulk carriers: the Forward Perpendicular (FP), Aft Perpendicular (AP), and forward and aft shoulders of the bilge corners, shown in Figure 4.10. Dynamic trim and heel can then be calculated by comparing trim and heel angles relative to the static floating position (Gourlay, 2008a). No additional hogging or sagging of the ship while underway is considered.

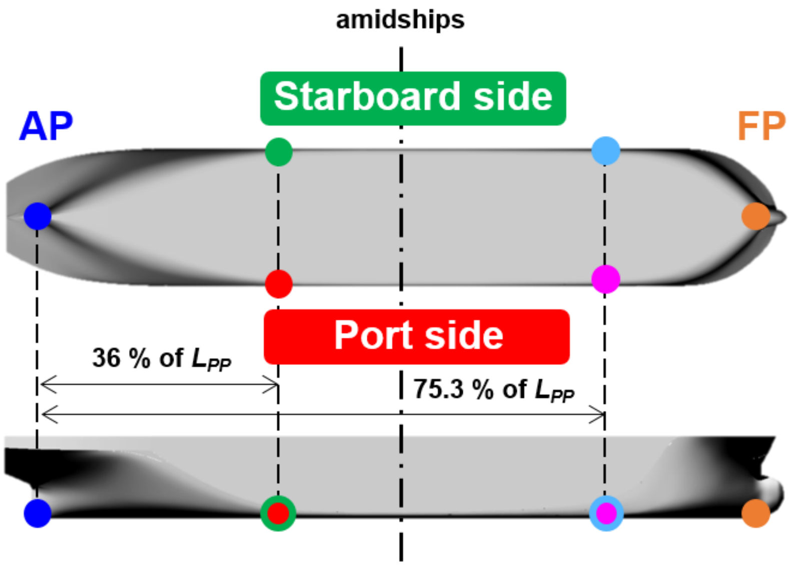

Figure 4.10. Hull extremities for bulk carriers

4.2.5 Results

4.2.5.1 Measured ship tracks

Measured midship tracks of the five inbound and six outbound ship transits are illustrated in Figure 4.11 and Figure 4.12.

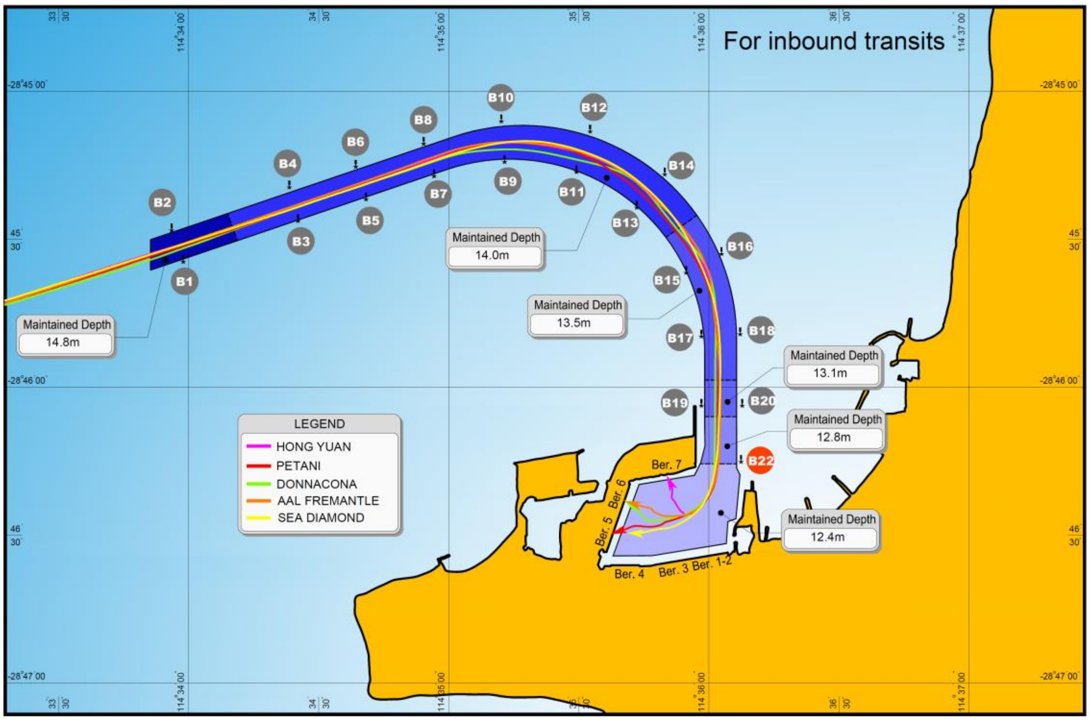

Figure 4.11. Measured midship tracks for the five inbound transits

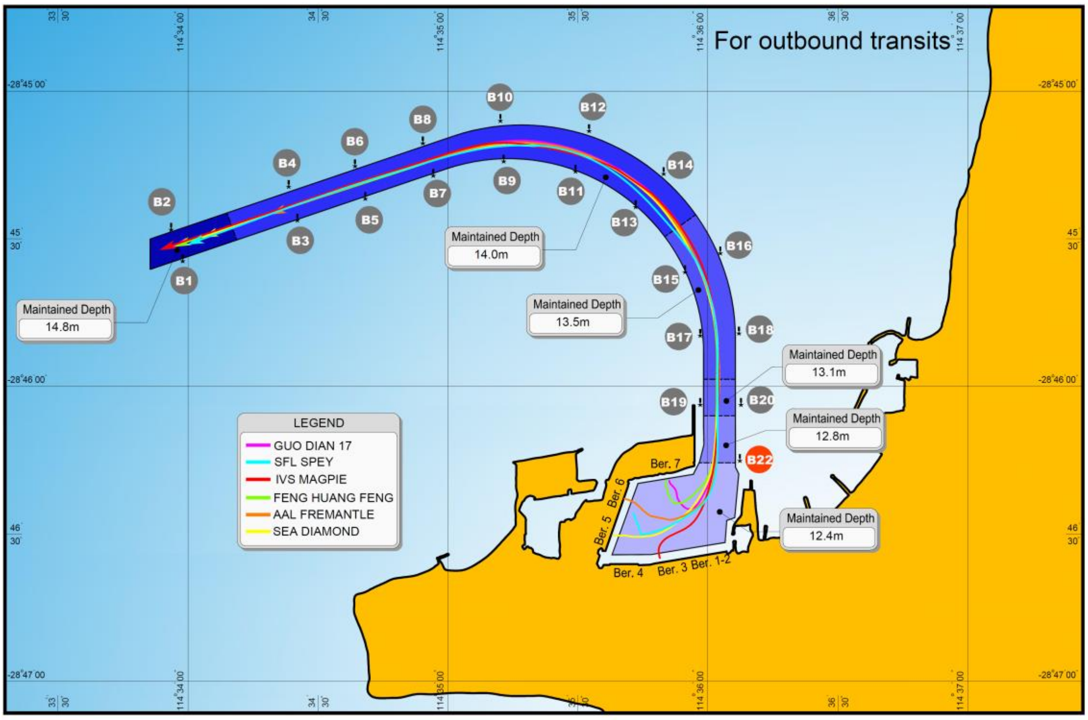

Figure 4.12. Measured midship tracks for the six outbound transits

The measurements for the inbound transits were made from the moment all onboard receivers were set up, always before the ships moved into the channel (or passed B1 and B2), and continued until all mooring work was completed at the berth. For the outbound ship transits, the measurements were made before leaving the berth until the ships passed the last beacons (B1 and B2) at the end of the channel.

4.2.5.2 Individual measurement results

Raw GNSS heights of the bow, port and starboard receivers above the local static free surface, plus ship speed and detailed at-berth measurement results (in an example transit (*HONG YUAN*, inbound)), are shown in Figure 4.13. As mentioned previously, sinkage is then calculated by the vertical height differences between the static floating position at the berth and when underway. The static floating position at the berth is captured based on 3-minute-averaged values of the ship's vertical motion after the end of the mooring works for the inbound transits, and prior to the beginning of unberthing for the outbound transits.

***HONG YUAN* (inbound)**

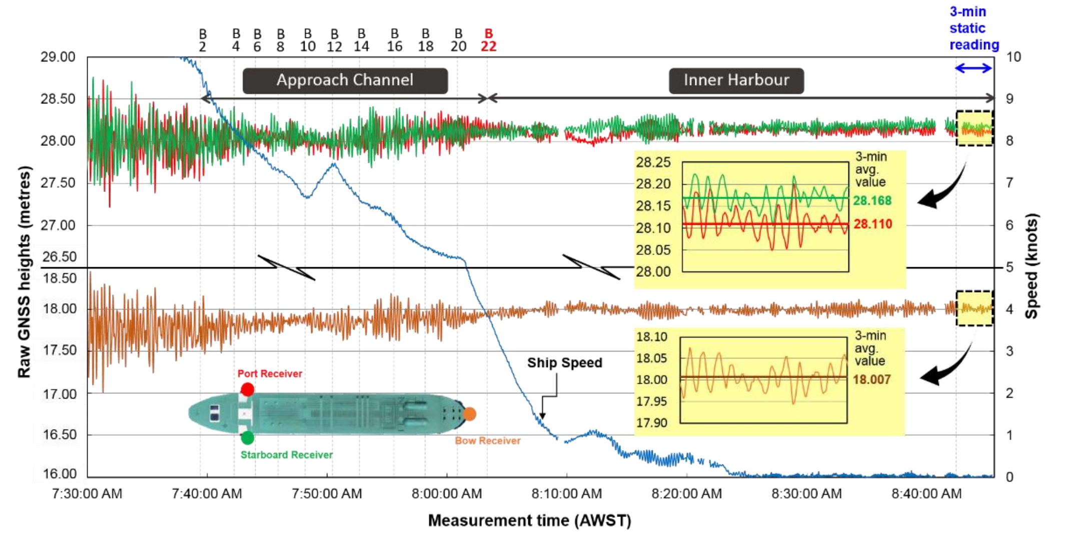

Figure 4.13. Raw GNSS heights above the local static free surface for the *HONG YUAN* (inbound) transit

Measured sinkage results, together with ship speed and channel bathymetry along the channel, for the example transit (*HONG YUAN*, inbound) is shown in Figure 4.14(a). Appendix C (C.1) shows the complete set of the measured sinkage results for all the bulk carrier transits. Here, dynamic sinkage means the total sinkage (positive downward), relative to the static floating position at the berth, and includes a near-steady component due to the Bernoulli effect known as squat; an unsteady component caused by wave-induced heave, pitch and roll; and a slowly-varying heel due to wind and turning.

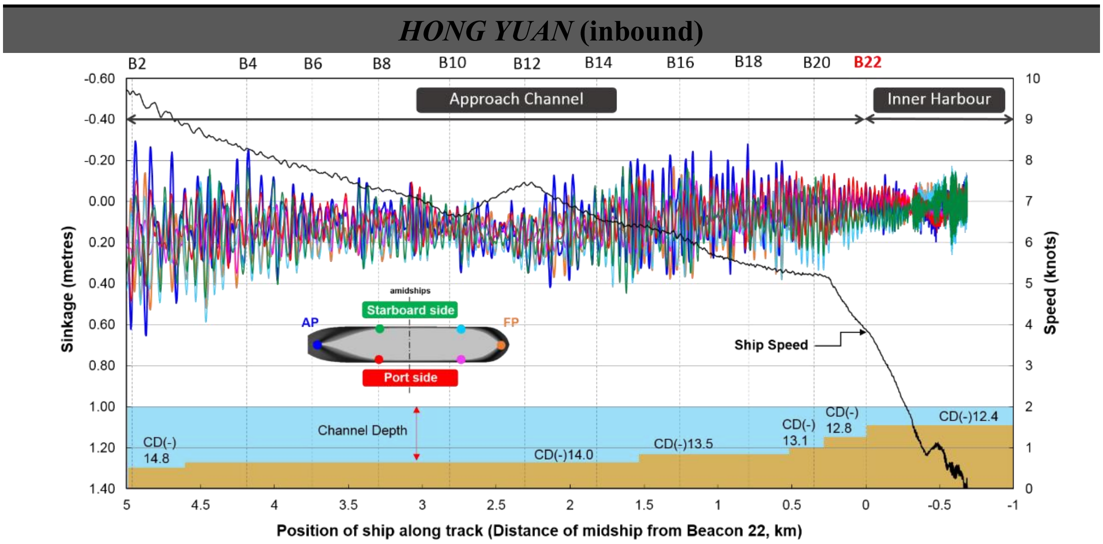

(a) Measured sinkage

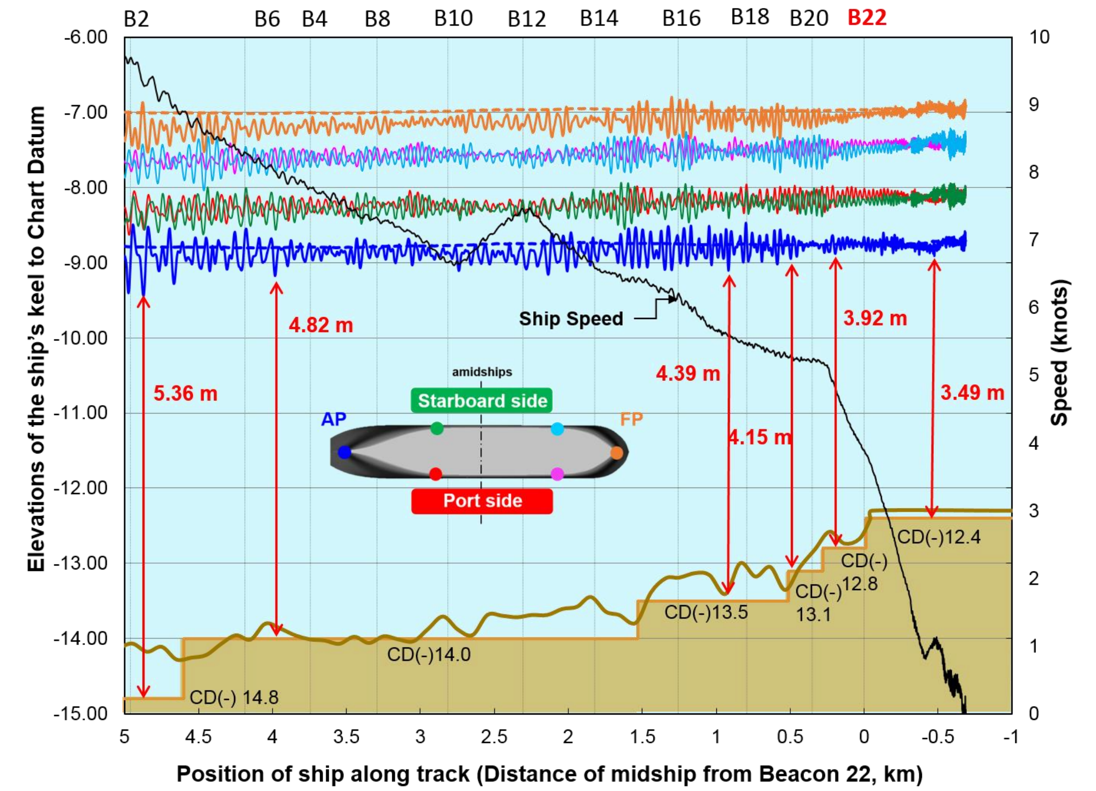

(b) Elevations of the ship's keel

Figure 4.14. (a) Measured sinkage (positive downward) at six points [Note: Chart datum depths (not to scale) also shown]; (b) Elevations of the ship's keel relative to chart datum [Note: Dashed lines near the top of the figure are elevations of the FP (orange) and AP (blue), including changes in tide only; i.e., their static position, not including squat and wave-induced motions; the flat seabed line is based on the charted depth on AUS81; the fluctuating seabed line is the actual survey line provided by OMC International]

With the positions of the FP and AP, the forward and aft shoulders of the bilge corners are also plotted in Figure 4.14 because they can be particularly vulnerable to grounding, considering the combined effects of dynamic trim and heel, and the ships' long parallel midbodies. A parallel body line from the deck and profile drawing for *SEA DIAMOND* was used to determine the positions of the forward and aft shoulders of the bilge corners: approximately 75.3 and 36.0 % of L_{PP} forward of the AP, respectively (see Figure 4.10). These proportions were applied to all the bulk carriers. For the transverse positions of the bilge corners, distances of 89, 91 and 88 % of the half-beam away from the centreline of the ships were taken from the sections of the general arrangement plan for *GUO DIAN 17*, *FENG HUANG FENG* and *SEA DIAMOND*, respectively. An estimated 90 % of that was, therefore, applied to all the bulk carriers uniformly.

It is more effective to see measured vertical motions of the ship against the same horizontal axis, using a cumulative distance from a fixed point. Pilots normally state their position in the channel using the beacons; so Beacon 22 (B22), shown as a red circle in Figure 4.11 and Figure 4.12, was used as the fixed point. The sinkage results were plotted against the cumulative distance from B22, and vertical lines are shown for B20, B18, B16, …, and B2.

For practical UKC management, the ship's vertical position should be plotted relative to chart datum, so that the port may know the actual real-time clearance from the seabed. Figure 4.14(b) shows these vertical elevation changes (see Appendix C (C.1) for all transits). The minimum real-time clearance in each section of varying water depth was captured.

Sinkage results for the bulk carrier transits are summarised in Table 4.5.

Nearly half of the bulk carrier transits had maximum sinkage at the stern, and the other half at the bow. However, for ships with static stern-down trim, e.g., *DONNACONA* (inbound), *AAL FREMANTLE* (outbound) and *SEA DIAMOND* (outbound) (see Table 4.2), the FP or forward shoulder of the bilge corners with maximum sinkage may not be the closest point to the seabed: the stern can still have a maximum dynamic draught due to its already close proximity to the seabed. Here, the dynamic draught at each location on the ship can be found by adding the static draught at that point to the sinkage at that point. The point on the ship with the maximum dynamic draught is the point most likely to hit the bottom: the AP for *DONNACONA* (inbound), the FP for *FENG HUANG FENG* (outbound) and the port forward shoulder of the bilge corners for *IVS MAGPIE* (outbound).

Table 4.5. Measured maximum sinkage and dynamic draught, and dynamic draught increase for the bulk carrier transits

Ships	In/Out	Maximum sinkage				Maximum dynamic draught		Dynamic draught increase	
		(m)	point	(% of L_{PP})	(% of static draught)	(m)	point	(m)	(% of static draught)
HONG YUAN	in	0.65	AP	0.30	7.16	9.77	AP	0.65	7.16
PETANI	in	0.65	AP	0.30	7.94	8.85	AP	0.65	7.94
DONNACONA	in	0.43	Stbd Fwd Bilge	0.27	4.72	9.70	AP	0.41	4.37
AAL FREMANTLE	in	0.90	AP	0.64	14.88	6.97	AP	0.90	14.88
SEA DIAMOND	in	0.80	AP	0.37	10.42	8.45	AP	0.80	10.42
*GUO DIAN 17**	out	0.77	FP	0.35	6.31	12.92	FP	0.77	6.31
SFL SPEY	out	1.05	FP	0.61	12.79	9.27	FP	1.05	12.79
IVS MAGPIE	out	0.98	Port Fwd Bilge	0.61	11.16	9.77	Port Fwd Bilge	0.98	11.16
*FENG HUANG FENG**	out	0.56	FP	0.26	4.57	12.74	FP	0.56	4.57
AAL FREMANTLE	out	0.58	FP	0.41	6.66	9.89	AP	0.41	4.30
*SEA DIAMOND**	out	0.94	FP	0.43	10.60	11.10	AP	0.84	8.22

[Note: *These transits are discussed in detail in Chapter 5.2]

The static trim of a ship may also have affected maximum sinkage because LCF moves depending on the waterplane area, which varies with draughts at the AP and FP, and displacement. For example, *AAL FREMANTLE* (outbound) had static stern-down trim and deeper draught than in its inbound transit with level static trim (see Table 4.2), and its LCB and LCF were farther aft of amidships. This change in LCF position may have caused larger pitching moment at the FP and resulted partly in a higher probability of the FP having maximum sinkage; the axis of dynamic pitch is time-varying but expected to be located near LCF (Papanikolaou, 2014). A similar trend was found in the *SEA DIAMOND* (outbound) transit.

In Table 4.5, dynamic draught increase is defined as the difference between the maximum dynamic draught and its static draught (Gourlay & Klaka, 2007). Because the points on the ship hull having maximum sinkage and maximum dynamic draught can differ, dynamic draught increase is required to show the extent of the difference between the maximum dynamic draught and its static draught. This leads directly to a decrease in UKC, and is the most important consideration in avoiding grounding. Maximum sinkage and dynamic draught increase are also expressed as a percentage of the static draught of the ship to enable comparison of the results with conventional information on ship UKC or navigation.

As shown in Figure 4.14(b) for the *HONG YUAN* (inbound) transit and Appendix C (C.1) for all transits, the minimum real-time clearance in each section of varying water depth was captured. Table 4.6 summarises calculated minimum real-time clearance in the inner harbour and approach channel, as well as the keel point at which that occurs. Tide ranges while underway in each section are also shown so that tidal contributions to the minimum UKC can be roughly identified (see Appendix B (B.1)).

Generally, for the ships trimmed by the stern at departure or arrival time (see Table 4.2), the AP was the closest point to the seabed in both the inner harbour and approach channel, but the ships with almost level static trim, like *GUO DIAN 17* (outbound), *SFL SPEY* (outbound) and *IVS MAGPIE* (outbound), had their minimum UKC at the FP or the forward shoulder of the bilge corners in the channel.

Table 4.6. Calculated minimum UKC for the bulk carrier transits

Ship transits	**In/ Out**	**Inner harbour (charted depth: 12.4 m)**				**Approach channel (charted depth: 12.8−14.8 m)**			
		(m)	**point**	**(% of static draught)**	**tide ranges (m)**	**(m)**	**point**	**(% of static draught)**	**tide ranges (m)**
HONG YUAN	in	3.49	AP	38.23	0.35-0.43	3.92	AP	42.93	0.31-0.43
PETANI	in	4.49	AP	54.74	0.38-0.43	4.85	AP	59.13	0.39-0.45
DONNACONA	in	3.43	AP	36.95	0.41-0.48	3.83	AP	41.17	0.43-0.47
AAL FREMANTLE	in	6.72	Port Aft Bilge	111.02	0.54-0.63	7.07	AP	116.41	0.60-0.68
SEA DIAMOND	in	4.99	AP	65.17	0.40-0.46	5.22	AP	68.26	0.37-0.47
*GUO DIAN 17**	out	0.80	Stbd Fwd Bilge	6.61	0.68-0.75	1.01	FP	8.35	0.71-0.77
SFL SPEY	out	4.70	AP	56.87	0.73-0.76	4.93	FP	59.97	0.71-0.78
IVS MAGPIE	out	3.92	AP	44.43	0.53-0.60	4.34	Stbd Fwd Bilge	49.34	0.54-0.64
*FENG HUANG FENG**	out	0.90	Stbd Aft Bilge	7.40	0.79-0.85	1.30	AP	10.64	0.75-0.83
AAL FREMANTLE	out	3.53	AP	37.19	0.72-0.74†	3.89	AP	40.99	0.74-0.76†
*SEA DIAMOND**	out	2.25	AP	21.94	0.30-0.42	2.62	AP	25.57	0.29-0.42

[Note: *These transits are discussed in detail in Chapter 5.2; †No measured tidal data was acquired for the *AAL FREMANTLE* (outbound) transit; instead tide range using predicted hourly tidal data (Australian Government Bureau of Meteorology, n. d. a) is presented]

4.2.5.3 Comparisons between the bulk carrier transits

Along with the dynamic sinkage at the six points of the bulk carriers (see Figure 4.10), dynamic trim and heel of all bulk carrier transits were also calculated. Figure 4.15 and Figure 4.16 show these dynamic trim and heel results by the direction of transit.

Inbound transits

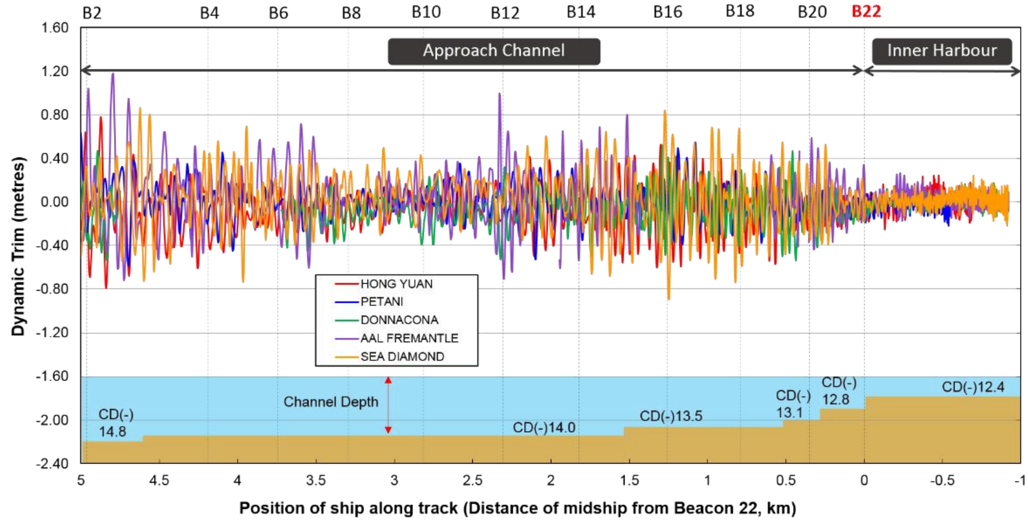

(a) Measured dynamic trim

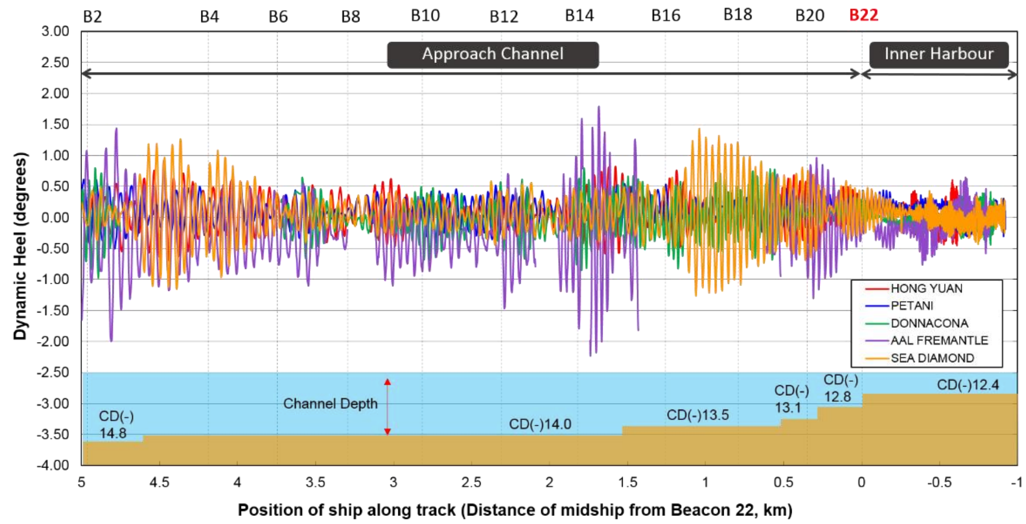

(b) Measured dynamic heel

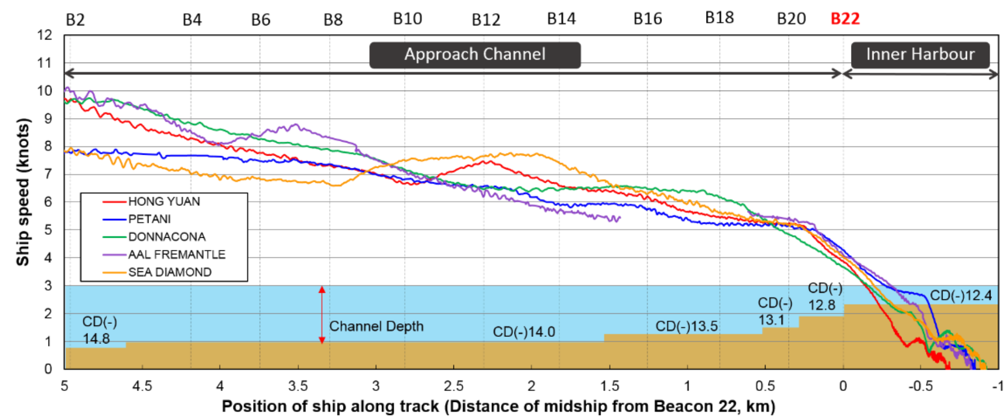

(c) Measured ship speed

Figure 4.15. (a) Measured dynamic trim (positive stern-down); (b) Measured dynamic heel (positive to starboard); (c) Measured ship speed, for the inbound ship transits [Note: Chart datum depths (not to scale) also shown]

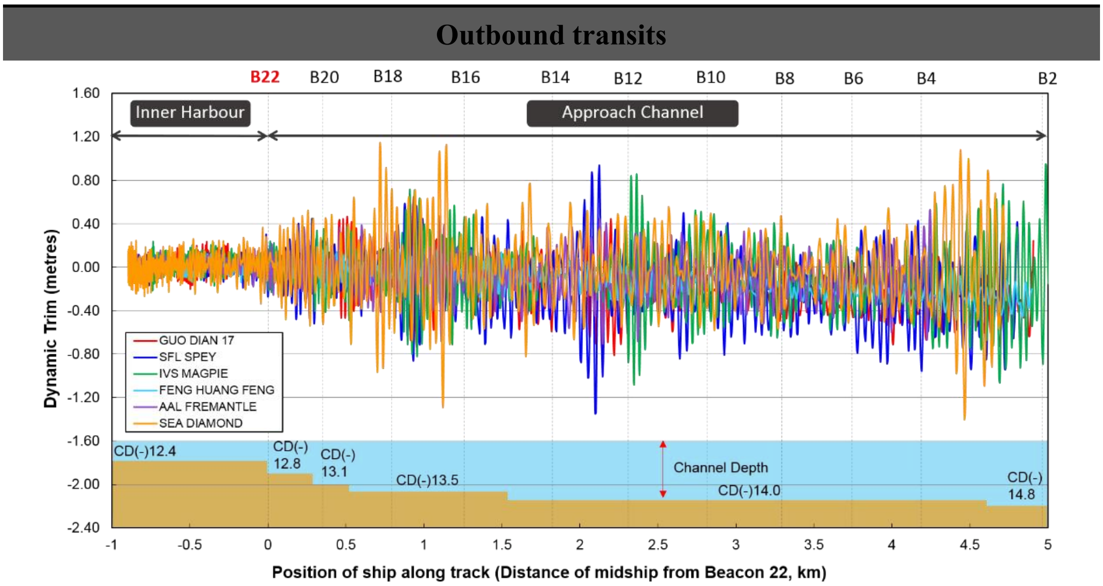

(a) Measured dynamic trim

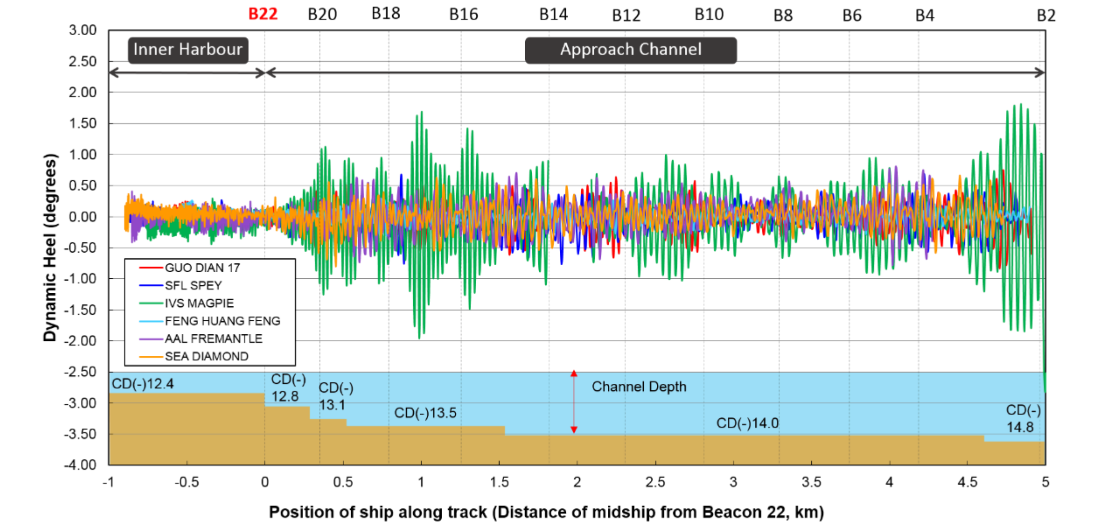

(b) Measured dynamic heel

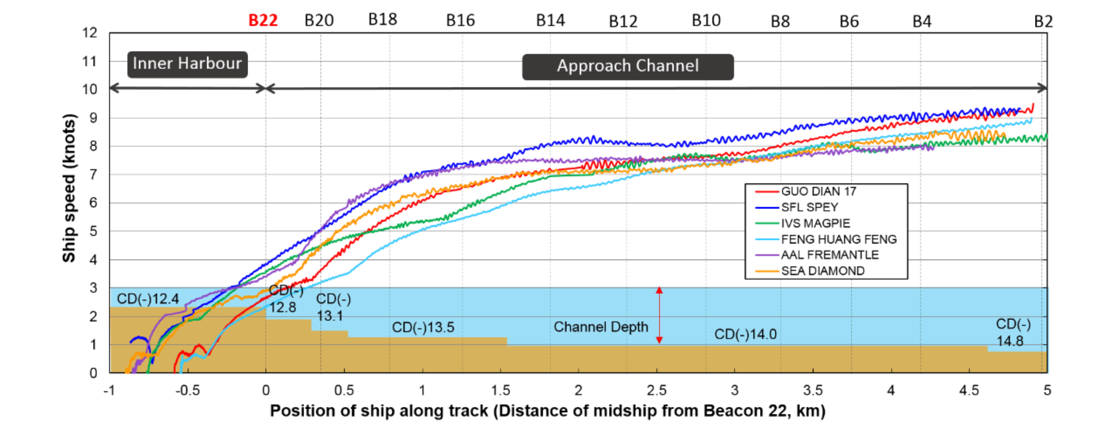

(c) Measured ship speed

Figure 4.16. (a) Measured dynamic trim (positive stern-down); (b) Measured dynamic heel (positive to starboard); (c) Measured ship speed, for the outbound ship transits [Note: Chart datum depths (not to scale) also shown]

Dynamic trim means, here, the ship's total change in trim (positive stern-down) relative to the static floating position at the berth, and includes wave-induced pitch; it is given in metres based on the difference between the FP and AP. Dynamic heel is the ship's total change in heel (positive to starboard), relative to the static floating position at the berth, which includes wave-induced roll, and is given in degrees.

Dynamic heel may be affected by the types of cargo on board: whether iron ore, mineral sands or grain (see Table 4.2), as a ship's GM varies with the concentration of weight distribution. For example, much larger heel angles were observed for *IVS MAGPIE* (outbound) carrying a low density cargo of wheat which gave it a low GM (metacentric height) and high KG (vertical centre of gravity above keel). In contrast, two iron ore carriers, *SEA DIAMOND* (outbound) and *SFL SPEY* (outbound), had pitch angles similar to those of *IVS MAGPIE* (outbound), but smaller heel angles due to their high GM and low KG.

Table 4.7. Calculated natural roll period and measured wave data during each transit

Ships	**In/ Out**	**GM_f (m)**	**Natural roll period (T_ϕ, sec)**	**Measured wave data (swell)**		
				H_s (m)	**T_p (sec)**	**T_m (sec)**
HONG YUAN	in	4.13	12.70	1.04-1.34	11.9-14.2	11.0-11.7
PETANI		3.86	13.14	0.73-0.88	10.7-12.3	10.7-11.4
DONNACONA		2.55	12.27	0.73-0.90	10.1-13.0	11.1-12.2
AAL FREMANTLE		2.44	11.98	0.86-1.15	9.7-13.8	11.3-12.0
SEA DIAMOND		5.04	11.50	1.19-1.61	11.1-13.1	11.6-12.2
*GUO DIAN 17**	out	7.11	9.68	0.92-1.30	9.2-14.2	11.0-11.9
SFL SPEY		6.71	9.27	0.92-1.15	11.9-14.2	11.4-11.8
IVS MAGPIE		3.08	12.40	0.80-1.05	11.5-14.0	11.2-11.8
*FENG HUANG FENG**		7.10	9.69	0.42-0.50	10.8-13.5	11.0-11.5
AAL FREMANTLE		2.29	12.37	0.58-0.75	10.0-18.6	11.0-11.5
*SEA DIAMOND**		5.93	10.60	1.29-1.77	13.1-15.1	13.0-14.0

[Note: *These transits are discussed in detail in Chapter 5.2]

For a better understanding of dynamic heel, the natural roll period of ship transits should be calculated and compared with the wave data measured during each transit, as shown in Table 4.7.

Large dynamic heel can occur in a ship when the wave encounter period is close to the ship's natural roll period. The natural roll period (T_ϕ) according to Ohgushi (1961) is approximately

$$T_\phi = 0.8 \frac{B}{\sqrt{GM_f}} \tag{4.1}$$

The wave data in Table 4.7 and Appendix B (B.1; see also Figure 4.6) are from the same source. More accurate calculations of the natural roll period and wave-induced motions will be discussed in Chapter 6.

4.3 Ship motion trials on container ships at the Port of Fremantle

In April 2016, at the Port of Fremantle, Western Australia's largest general cargo port, full-scale measurements were performed on 16 container ship transits, including seven inbound and nine outbound transits, via its Deep Water Channel, Entrance Channel and Inner Harbour (see chart AUS112 and 113).

4.3.1 Description of container ship motion trials

4.3.1.1 Description of the port and channels

The layout of the Port of Fremantle, including its approach channels and navigational buoys, is illustrated in Figure 4.17 (see also Figure 4.1(c)).

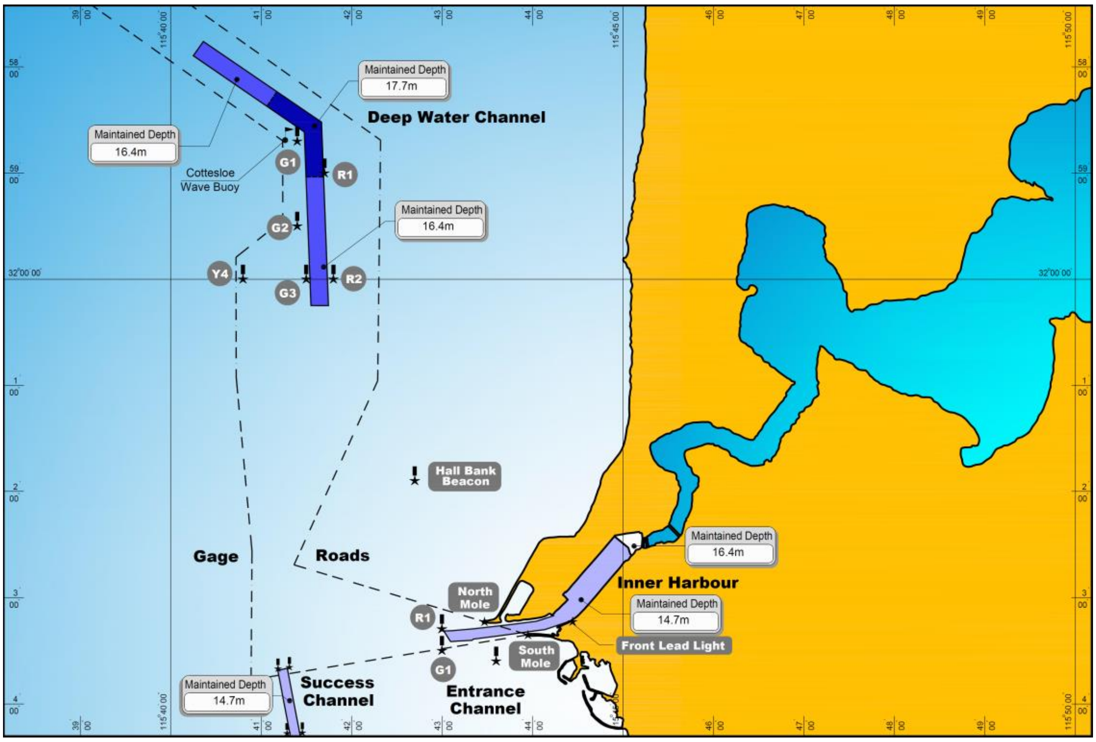

Figure 4.17. Layout of the Port of Fremantle, including its approach channels and navigational buoys

The Port of Fremantle is operated with a marine section that is largely divided into four parts: the Deep Water Channel (DWC), around 3 nautical miles in length and 300 m in width; the Entrance Channel, around 1 nautical mile from Front Lead light (FL) to Green No.1 Buoy (G1) and 170 m wide; the Inner Harbour with a water area of approximately 82 ha; and the unmaintained section, between the Deep Water Channel and Entrance Channel. The channels vary in depth from 14.7 to 17.7 m based on the Chart Datum (CD), which is approximately the level of LAT and 0.756 m below the AHD. An additional depth of up to 1.3 m can be caused by tides. HAT and MSL in the Port of Fremantle are 1.3 and 0.7 m, respectively (see chart AUS112). Details of tides can be found in the ANTT. Actual surveyed depth data for the Deep Water Channel, Entrance Channel, and Inner Harbour were provided by Fremantle Ports; no detailed bathymetric survey data for the unmaintained section is available. Approximate water depth in the unmaintained section can be found in charts AUS 112 and 113, in which the charted depth in that section is between 15 and 20 m.

4.3.1.2 Description of the ships (container ships) and transit conditions

Measurements were undertaken on 16 container ship transits on the dates shown in Table 4.8.

Table 4.8. Measurement date at the Port of Fremantle

Measurements	Ships	In / Out	Measurement date
Set of measurements 16th - 25th Apr. 2016 (10 days)	*MSC ILONA*	outbound	Sat. 16th April 2016
	OOCL HOUSTON	outbound	Sat. 16th April 2016
	SEAMAX STAMFORD	inbound	Sun. 17th April 2016
	SEAMAX STAMFORD	outbound	Sun. 17th April 2016
	CMA CGM CHOPIN	inbound	Mon. 18th April 2016
	MOL EMISSARY	inbound	Mon. 18th April 2016
	CMA CGM CHOPIN	outbound	Mon. 18th April 2016
	MOL EMISSARY	outbound	Tue. 19th April 2016
	SAFMARINE MAKUTU	inbound	Wed. 20th April 2016
	MOL PARAMOUNT	inbound	Thu. 21st April 2016
	SAFMARINE MAKUTU	outbound	Thu. 21st April 2016
	CMA CGM LAMARTINE	outbound	Fri. 22nd April 2016
	MOL PARAMOUNT	outbound	Fri. 22nd April 2016
	OOCL BRISBANE	inbound	Sun. 24th April 2016
	CMA CGM WAGNER	inbound	Mon. 25th April 2016
	OOCL BRISBANE	outbound (partial pilotage)	Mon. 25th April 2016

Ship dimensions and comparative transit conditions for all the container ships are shown in Table 4.9.

Table 4.9. Details of the ships (container ships) and transit conditions

	Particulars	_MSC ILONA_	_OOCL HOUSTON_	_SEAMAX STAMFORD_	_CMA CGM CHOPIN_	_MOL EMISSARY_	_SAFMARINE MAKUTU_	_MOL PARAMOUNT_	_CMA CGM LAMARTINE_	_OOCL BRISBANE_	_CMA CGM WAGNER_
Details of ships	**Ship size**	Post-Panamax	Panamax	Post-Panamax	Post-Panamax	Panamax	Panamax	Post-Panamax	Post-Panamax	Panamax	Post-Panamax
	Capacity (TEU)	6,750	4,578	4,896	5,782	5,100	4,154	6,350	6,574	4,578	5,782
	Year built	2001	2007	2015	2004	2009	2007	2005	2009	2009	2004
	L_{OA} (m)	300.00	260.05	250.00	277.28	294.13	292.08	293.19	299.20	260.05	277.28
	L_{PP} (m)	286.56	244.80	238.35	263.00	283.20	277.00	276.00	286.70	244.80	263.00
	Depth (m)	24.20	19.30	19.60	24.30	22.10	21.70	24.30	24.60	19.30	24.30
	Beam (m)	40.00	32.25	37.30	40.00	32.20	32.25	40.00	40.00	32.25	40.00
	Design draught (m)	12.00	11.00	11.50	12.50	12.00	12.20	-	12.00	11.00	12.50
	Summer draught (m)	14.50	12.60	13.00	14.50	13.65	13.50	14.02	14.52	12.60	14.52
	Displacement (t)	112,639.60	67,248.80	79,702.00	96,757.00	87,855.00	82,287.00	99,620.00	110,445.10	67,248.80	96,997.00
	C_B (-)	0.661	0.660	0.673	0.619	0.689	0.666	0.628	0.647	0.660	0.620
Details of transit conditions	**Pilot**	Trevor Bozoky	Trevor Bozoky	Hamish MacAdie (in), Stuart Proctor (out)	Hamish MacAdie (in), John Ball (out)	John Ball (in), John Ball (out)	Stuart Proctor (in), John Hoogewaard (out)	Jeremy Parkin (in), Raymond Alfreds (out)	Rory Main	John Hoogewaard (in), Hamish MacAdie (out)	Andrew Davison
	Arrival draught (m)	-	-	Fwd. 10.40 Mid. - Aft. 11.25	Fwd. 11.65 Mid. - Aft. 11.70	Fwd. 10.90 Mid. 11.40 Aft. 12.10	Fwd. 12.60 Mid. - Aft. 12.60	Fwd. 11.39 Mid. - Aft. 11.39	-	Fwd. 11.02 Mid. 11.54 Aft. 12.06	Fwd. 10.00 Mid. - Aft. 11.50
	Departure draught (m)	Fwd. 12.35 Mid. - Aft. 12.35	Fwd. 11.60 Mid. - Aft. 11.60	Fwd. 12.35 Mid. 12.42 Aft. 12.49	Fwd. 10.00 Mid. - Aft. 11.10	Fwd. 9.80 Mid. 10.50 Aft. 11.50	Fwd. 11.00 Mid. - Aft. 11.40	Fwd. 13.04 Mid. - Aft. 12.99	Fwd. 11.20 Mid. - Aft. 11.50	Fwd. 10.00 Mid. 10.20 Aft. 10.40	-
	Actual displacement (t)	-	58,228.80	62,584.00 (in), 75,034.00 (out)	70,279.00 (in), 61,863.00 (out)	69,605.00 (in), 63,557.30 (out)	73,593.00 (in), 63,732.00 (out)	73,926.90 (in), 88,769.00 (out)	77,453.00	60,301.40 (in), 51,131.20 (out)	63,569.00
	C_B (-)	-	0.620	0.634 (in), 0.663 (out)	0.558 (in), 0.544 (out)	0.648 (in), 0.638 (out)	0.638 (in), 0.621 (out)	0.574 (in), 0.603 (out)	0.581	0.646 (in), 0.619 (out)	0.548
	LCB (m)	-	116.17@11.60m	117.79@10.85m (in) 116.45@12.45m (out)	128.03@11.65m (in) 129.08@10.55m (out)	137.01@11.40m (in) 137.62@10.50m (out)	132.65@12.60m (in) 134.10@11.20m (out)	133.06@11.40m (in) 131.42@13.00m (out)	-	116.29@11.50m (in) 117.70@10.20m (out)	-
	LCF (m)	-	105.56@11.60m	111.68@10.85m (in) 107.45@12.45m (out)	118.64@11.65m (in) 122.20@10.55m (out)	130.08@11.40m (in) 132.68@10.50m (out)	121.22@12.60m (in) 125.90@11.20m (out)	126.05@11.40m (in) 119.62@13.00m (out)	-	105.89@11.50m (in) 109.97@10.20m (out)	-
	GM_t (m)	-	1.34	3.88 (in), 2.96 (out)	2.93 (in), 3.32 (out)	1.28 (in), 1.55 (out)	0.81 (in), 1.49 (out)	3.87 (in), 3.20 (out)	2.99	1.00 (in), 1.11 (out)	4.51
Details of berthing	**Berth No. (North Quay)**	NQ No.7	NQ No.7	NQ No.9	NQ No.5	NQ No.7	NQ No.9	NQ No.7	NQ No.5	NQ No.9	NQ No.5
	Berthing side (port or starboard)	port-side	port-side	port-side	starboard-side	port-side	port-side	port-side	starboard-side	port-side	starboard-side
	Arrival berthing	-	-	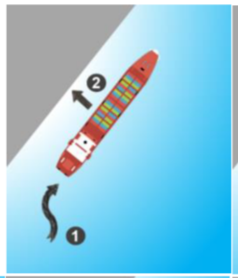			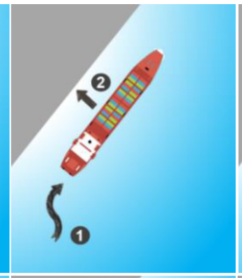	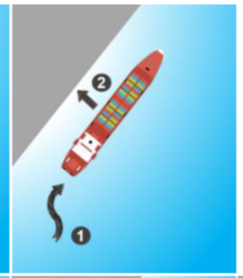	-	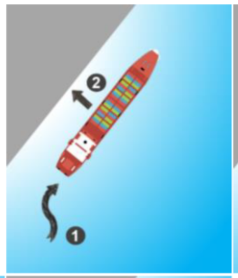	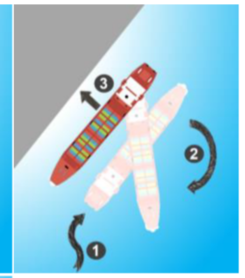
	Depature unberthing	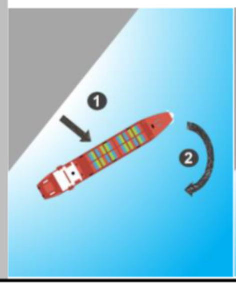	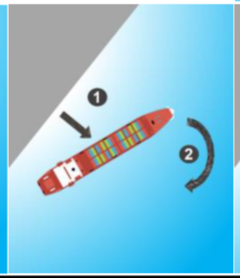		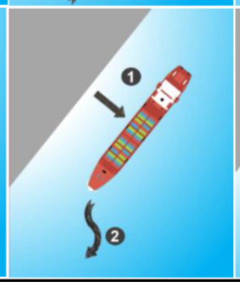				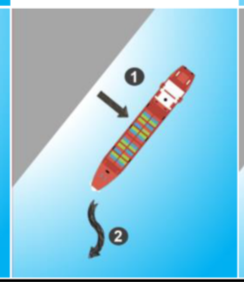	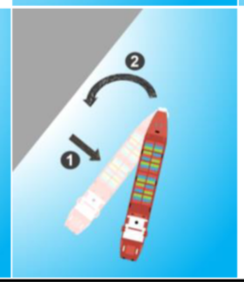	-

4.3.1.3 Ship motion measurement equipment

Instead of the GNSS receivers used for the bulk carrier motion trials at the Port of Geraldton (see Table 4.3), JAVAD Triumph-1 and Triumph-2 GNSS receivers (https://www.javad.com) were used for the container ship motion trials at the Port of Fremantle. Four receivers were used for each set of measurements, one in each of the following locations:

Base station fixed to pilot jetty
Roving receiver fixed to ship bow
Roving receiver fixed to port bridge wing
Roving receiver fixed to starboard bridge wing

The fixed base station was used to apply differential corrections to the roving receiver results, as mentioned in 4.2.1.3. Stated position accuracy of the receivers is shown in Table 4.10, as specified in JAVAD (2012) and JAVAD (2015).

Table 4.10. Accuracy of the GNSS receivers (source: JAVAD (2012; 2015))

Receivers	Image	Stated accuracy (general)
JAVAD Triumph-1		Horizontal : 10 mm + 1 ppm × (baseline length) Vertical : 15 mm + 1 ppm × (baseline length)
JAVAD Triumph-2		Horizontal : 10 mm + 1 ppm × (baseline length) Vertical : 15 mm + 1 ppm × (baseline length)

A typical GNSS equipment setup at the Port of Fremantle is shown in Figure 4.18.

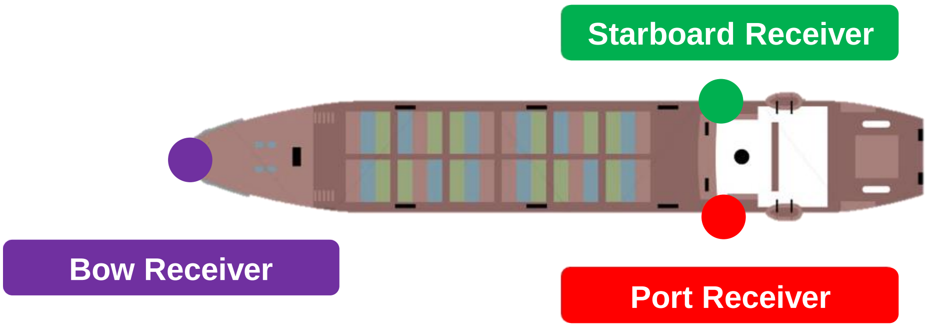

(a)

(b)

(c)

(d)

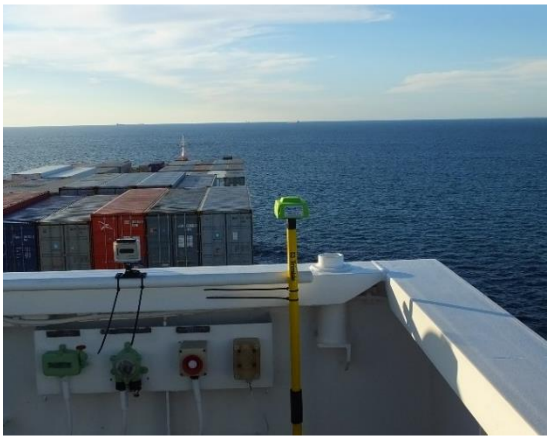

(e)

Figure 4.18. GNSS receiver setups: (a) Plan view of ship receivers; (b) Base station on pilot jetty in the *CMA CGM LAMARTINE* (outbound) transit; (c) Bow receiver in the *MOL PARAMOUNT* (outbound) transit; (d) Port receiver on bridge wing in the *SAFMARINE MAKUTU* (outbound) transit; (e) Starboard receiver on bridge wing in the *SAFMARINE MAKUTU* (outbound) transit

The base station (see Figure 4.18(b)) was placed at the same point (32° 2.52236' S, 115° 45.19799' E) on the pilot jetty for all the container ship transits, as shown in Figure 4.19.

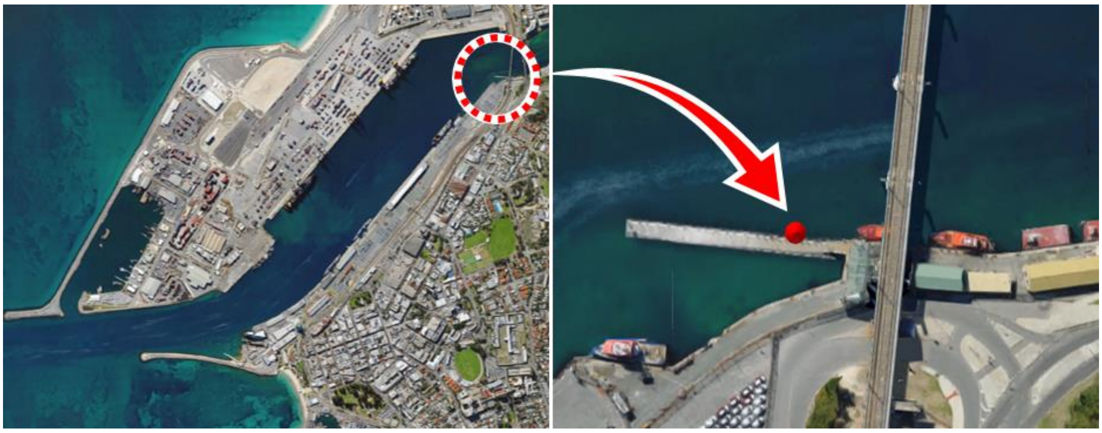

Figure 4.19. Base station location on pilot jetty (Imagery ©2016 Google, Data SIO, NOAA, U.S. Navy, NGA, GEBCO, Map data © 2016 Google)

4.3.1.4 Description of trial procedure

The same trial procedure used for the bulk carrier transits in the Port of Geraldton was applied to the container ship transits in the Port of Fremantle. Details on the trial procedure are found in 4.2.1.4.

4.3.2 Environmental data

Measured tide in the Inner Harbour (32° 3.258' S, 115° 44.3718' E) in the Port of Fremantle was provided by Fremantle Ports (http://www.fremantleports.com.au) and applied to calculate dynamic sinkage of the container ships. The tidal datum is the same as the chart datum used in charts AUS112 and 113, LAT at the Port of Fremantle. The tidal data covering the period of an example transit (*SEAMAX STAMFORD*, inbound) is shown in Figure 4.20(a).

Wave data, measured at 1.28 Hz by the Cottesloe wave buoy (31° 58.74333' S, 115° 41.39833' E) near Green No.1 Buoy (G1) in the Deep Water Channel (see Figure 4.17), was provided through collaboration with the coastal infrastructure team from the Western Australian Department of Transport (WA DoT). The full measured wave time series data will be used to study wave-induced motions in the channel (Chapter 6). The wave data during the *SEAMAX STAMFORD* (inbound) transit is presented in Figure

4.20(b and c) as an example. The full set of tidal and wave data for all container ship transits can be found in Appendix B (B.2).

SEAMAX STAMFORD **(inbound)**

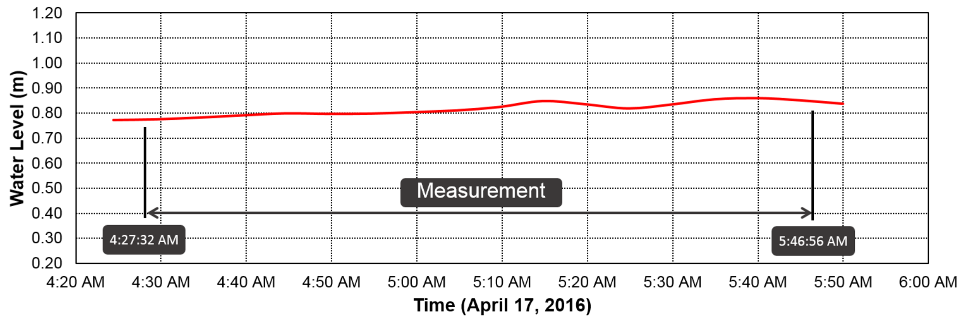

(a) Tide

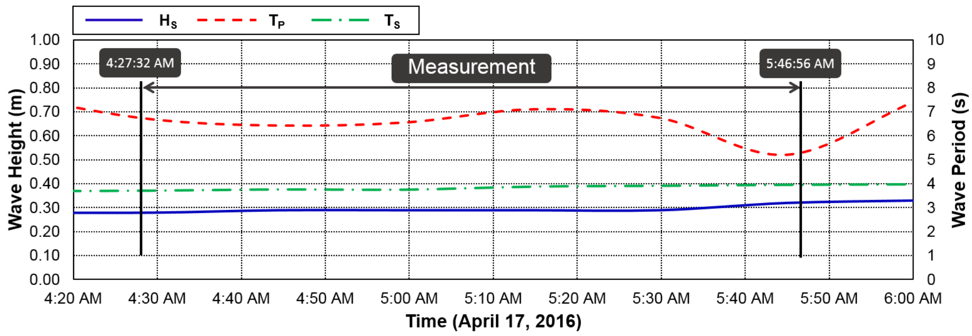

(b) Sea

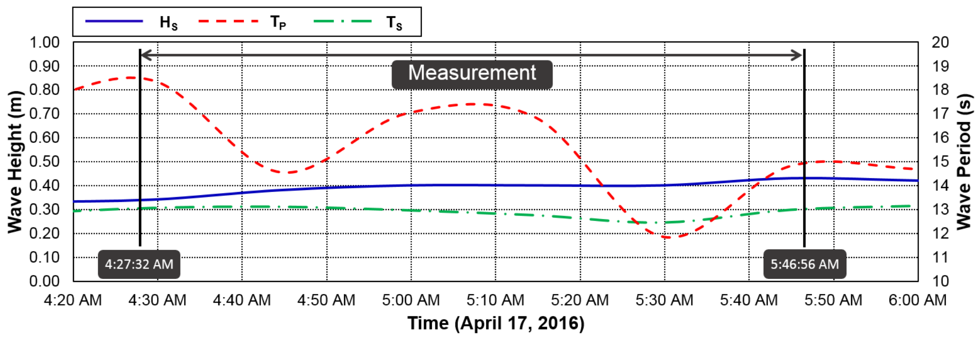

(c) Swell

Figure 4.20. (a) Measured tidal data; (b) Measured wave (sea) data; (c) Measured wave (swell) data during the *SEAMAX STAMFORD* (inbound) transit [Note: Sea/swell cutoff period is 8 seconds; H_s = significant wave height; T_p = spectral peak wave period; T_s = significant wave period]

Photos of the Cottesloe wave buoy, which were taken during the trials, are shown in Figure 4.21.

To capture wind conditions, visual observations of wind speeds and directions were made and recorded by the author during each ship transit, as shown in Table 4.11. The full measured wind data can be obtained from the Australian Government BoM if required.

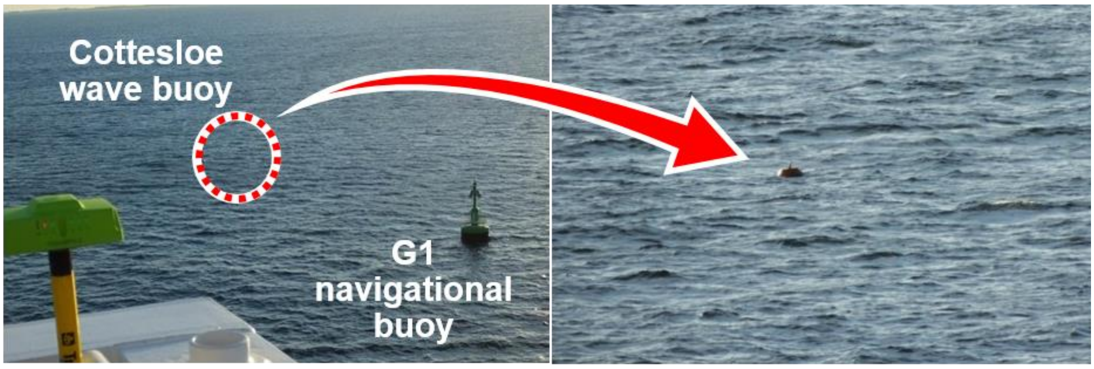

Figure 4.21. Cottesloe wave buoy and its location (refer to Figure 4.17)

Table 4.11. Details of the observed wind conditions

Ships		Wind speed	Wind direction
OOCL HOUSTON	(inbound)	5 knots	Northerly
SEAMAX STAMFORD	(inbound)	Calm	Calm
CMA CGM CHOPIN	(inbound)	Not recorded	Not recorded
MOL EMISSARY	(inbound)	10 knots	Westerly
CMA CGM CHOPIN	(outbound)	10 knots	Westerly
MOL EMISSARY	(outbound)	15 knots	South-westerly
SAFMARINE MAKUTU	(inbound)	15 knots	South-westerly
MOL PARAMOUNT	(inbound)	10 knots	Easterly
SAFMARINE MAKUTU	(outbound)	10 knots	Easterly
CMA CGM LAMARTINE	(outbound)	10 knots	Easterly
MOL PARAMOUNT	(outbound)	5 knots	Easterly
OOCL BRISBANE	(inbound)	5 - 10 knots	North-westerly
CMA CGM WAGNER	(inbound)	10 - 15 knots	North-westerly

The currents are usually quite weak. In Gage Roads (see Figure 4.17), the currents move southward across the Entrance Channel for approximately 14 hours and northward for about 10 hours; they generally attain a rate of 1 knot, but during the winter months (June through August), may reach 2 knots (National Geospatial-

Intelligence Agency, 2017; United States Naval Research Laboratory, n.d.). Note that no measurements of currents were made during the container ship trials at the Port of Fremantle.

Water density can vary from the area of the Entrance Channel and Inner Harbour to the Deep Water Channel because of the port's location in the Swan River estuary, but density in the Inner Harbour is generally stated to be 1.025 g/cm^3 at all tides (Fremantle Ports, 2011), which means there may be a delicate difference in water density inside and outside the port most of the time. Heavy rainfall can change the density in the Inner Harbour and Entrance Channel, but such a situation did not arise during the measurements.

4.3.3 Bathymetric data

The detailed survey data for the Deep Water Channel, Entrance Channel and Inner Harbour provided by Fremantle Ports were used with the bathymetric data from AUS112. These data are originally from Fremantle Ports' annual hydrographic survey of September and October 2015, and comprise 144,150 survey points for the Entrance Channel and Inner Harbour and 90,566 points for the Deep Water Channel. Figure 4.22 shows the survey points in the channels, together with an example ship track (*SEAMAX STAMFORD*, inbound).

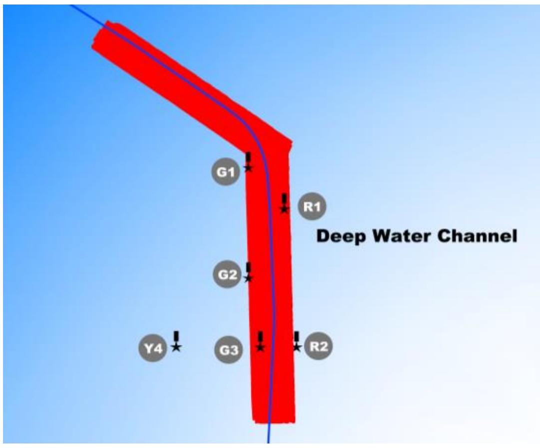

(a)

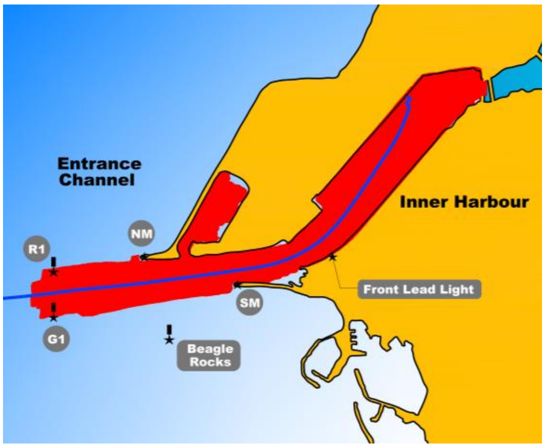

(b)

Figure 4.22. Bathymetric data from Fremantle Ports' annual hydrographic survey: (a) The Deep Water Channel; (b) The Entrance Channel and Inner Harbour

To more accurately compare the ship's keel heights and the seabed, water depths along the track should be taken from the bathymetric data. The Z-values of the survey points that are the closest points to the track on the plane were extracted using *MATLAB R2016a* (https://www.mathworks.com), Microsoft *Excel* (https://www.microsoft.com) and *AutoCAD 2017* (https://www.autodesk.com) software. A comparison between the bathymetry based on AUS112 and that extracted is shown in Figure 4.23. The flat and dashed seabed line is based on the charted depth on AUS112, and the fluctuating seabed line is the actual survey line provided by Fremantle Ports.

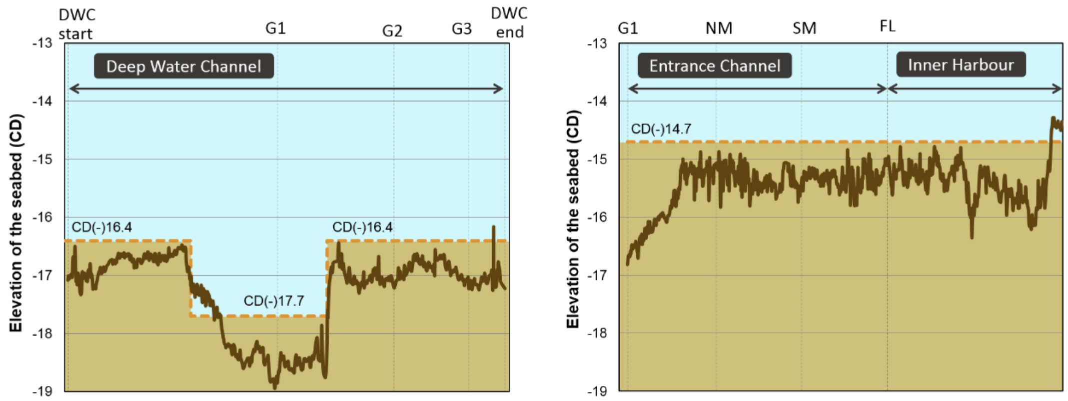

(a) (b)

Figure 4.23. Comparison of the seabed lines based on the chart and survey: (a) The Deep Water Channel; (b) The Entrance Channel and Inner Harbour [Note: DWC = Deep Water Channel; G1, G2, G3 = Green No.1, 2 and 3 buoys; NM = North Mole; SM = South Mole; FL = Front Lead light]

4.3.4 Data processing

All data were recorded at 1.0 Hz and post-processed using the *Trimble Business Centre v3.50* (https://www.trimble.com) software. Measurement results for the container ship transits at the Port of Fremantle were obtained using the same data processing techniques detailed in 4.2.4.

As mentioned in 4.2.4, EGM2008 geoid (Pavlis, Holmes, Kenyon, & Factor, 2012) used for the bulk carrier transits at the Port of Geraldton can only approximate local MSL surface, which is more precisely referenced to a local port datum or LAT. Because the AHD remains the official vertical datum in Australia (Featherstone et al., 2011) and most of the tide stations in Australia have AHD heights in metres above the stations' LAT, e.g., LAT at the Port of Fremantle is 0.756 m below the AHD

(Fremantle Ports, 2011), AUSGeoid09 (Brown, Featherstone, Hu, & Johnston, 2011; Featherstone et al., 2011), the Australia-wide gravimetric quasigeoid model, was applied instead of EGM2008. This approach gives a practical product for the more direct transformation of GNSS heights to AHD heights (Brown, Featherstone, Hu, & Johnston, 2011). More station details, including AHD height, latitude, longitude, monitoring equipment, etc., are available on the Bureau of Meteorology webpage (http://www.bom.gov.au) if required.

The raw GNSS results for each receiver were combined to give the sinkage at the forward, aft and transverse extremities of the keel that would be points of concern of running aground on container ships, as shown in Figure 4.24 (compare this with Figure 4.10).

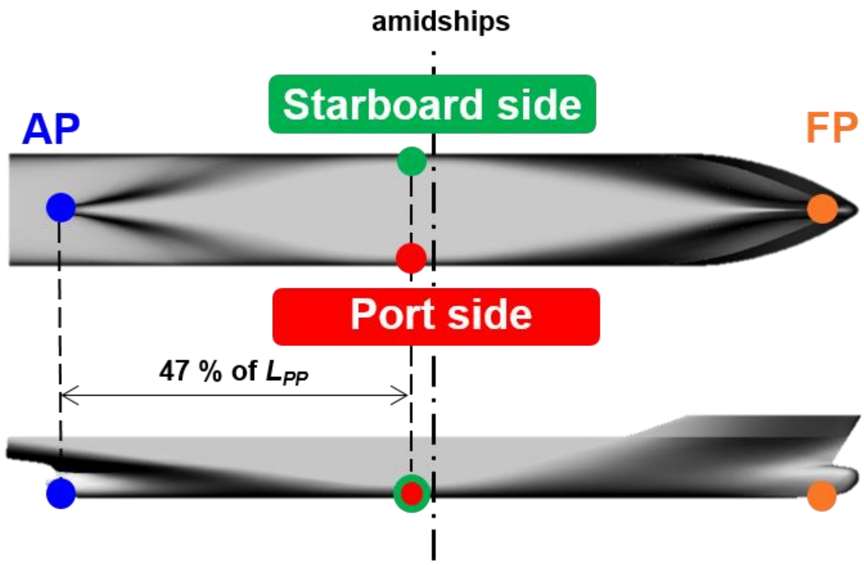

Figure 4.24. Hull extremities for container ships

4.3.5 Results

4.3.5.1 Measured ship tracks

Measured midship tracks of the seven inbound and six outbound ship transits are illustrated in Figure 4.25 and Figure 4.26.

For the inbound ships, the measurements were made from the moment all onboard receivers were set up, which was always before the ships moved into the Deep Water Channel (‘DWC start’ in Figure 4.25), until all mooring work was completed at the berth. For the outbound ships, the measurements were made before leaving the berth until the ships passed the last buoy (Green No.1 (G1)) at the curved section in the Deep Water Channel.

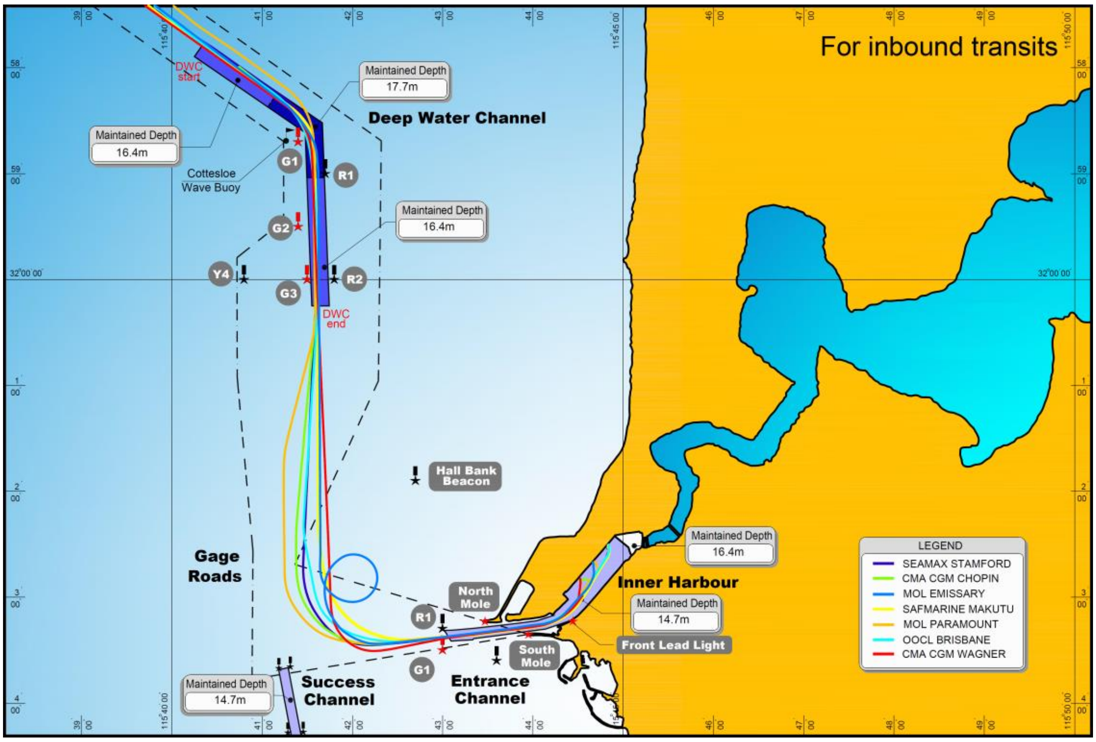

Figure 4.25. Measured midship tracks for the seven inbound transits

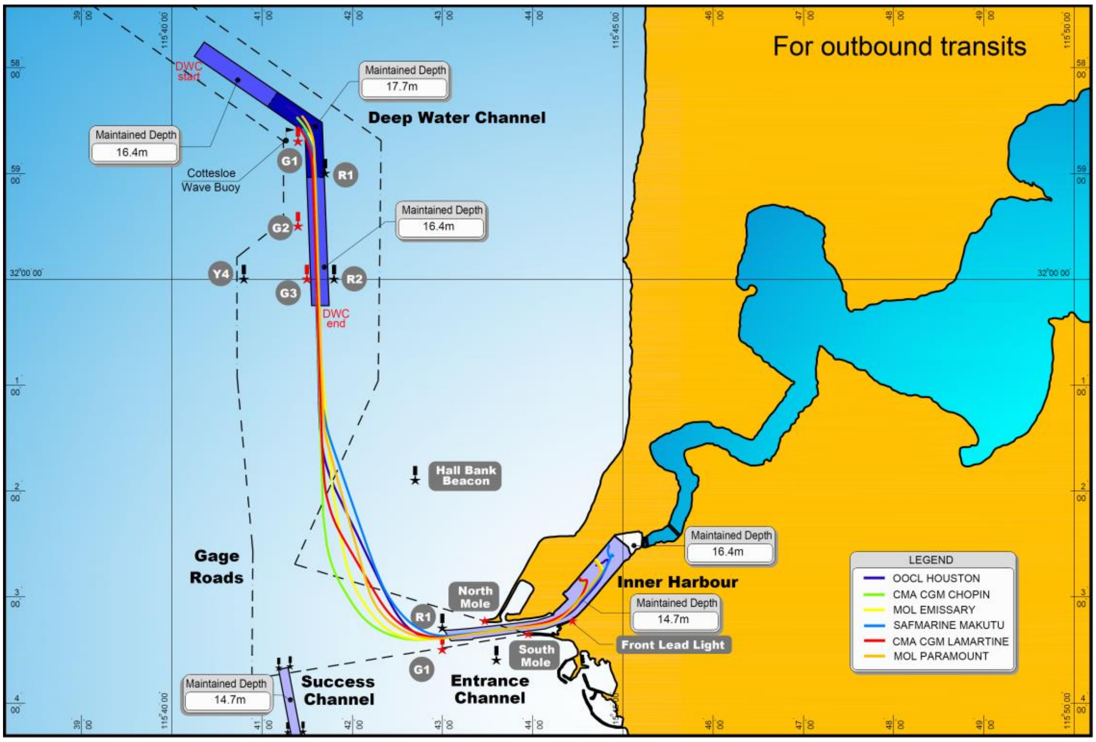

Figure 4.26. Measured midship tracks for the six outbound transits

4.3.5.2 Individual measurement results

Raw GNSS heights of the bow, port and starboard receivers above the local static free surface, together with ship speed and detailed at-berth measurement results, for an example transit (*SEAMAX STAMFORD*, inbound) are shown in Figure 4.27. As mentioned in 4.2.5.2, sinkage is then calculated by the vertical height differences between the static floating position at the berth and when underway. 3-minute-averaged values of the ship's vertical motion after the end of the mooring works or prior to the beginning of unberthing are used for the static floating position at the berth.

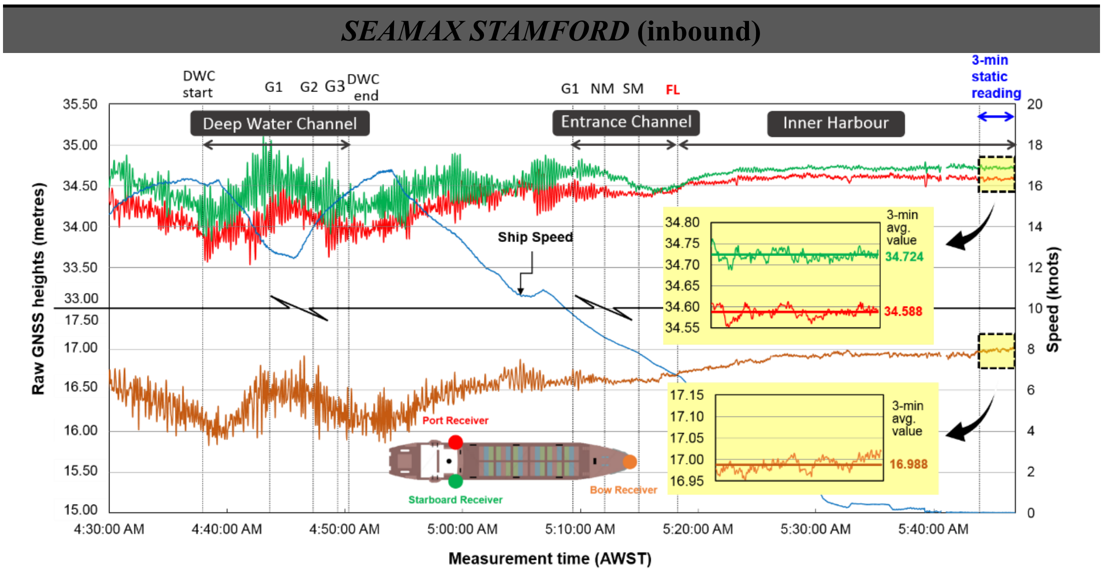

Figure 4.27. Raw GNSS heights above the local static free surface for the *SEAMAX STAMFORD* (inbound) transit

The measured sinkage result, plus ship speed and channel bathymetry, in the example transit (*SEAMAX STAMFORD*, inbound) is shown in Figure 4.28(a). Elevations of the ship's keel relative to chart datum are shown in Figure 4.28(b). Appendix C (C.2) shows the complete set of these results for all the container ship transits. The results are plotted against a cumulative distance from the Front Lead light (FL) (32° 3.22728' S, 115° 44.45048' E). Vertical lines are shown for the South Mole (SM), North Mole (NM) and Green No.1 Buoy (G1) in the Entrance Channel. In the Deep Water Channel (DWC), vertical lines are shown at the starting point, Green No.1 Buoy (G1), Green No.2 Buoy (G2), Green No.3 Buoy (G3) and the end point. All vertical lines are marked in red in Figure 4.25 and Figure 4.26. Sinkage is given at the FP, AP, and port and starboard bilge corners (refer to Figure 4.24), and defined as being positive downward.

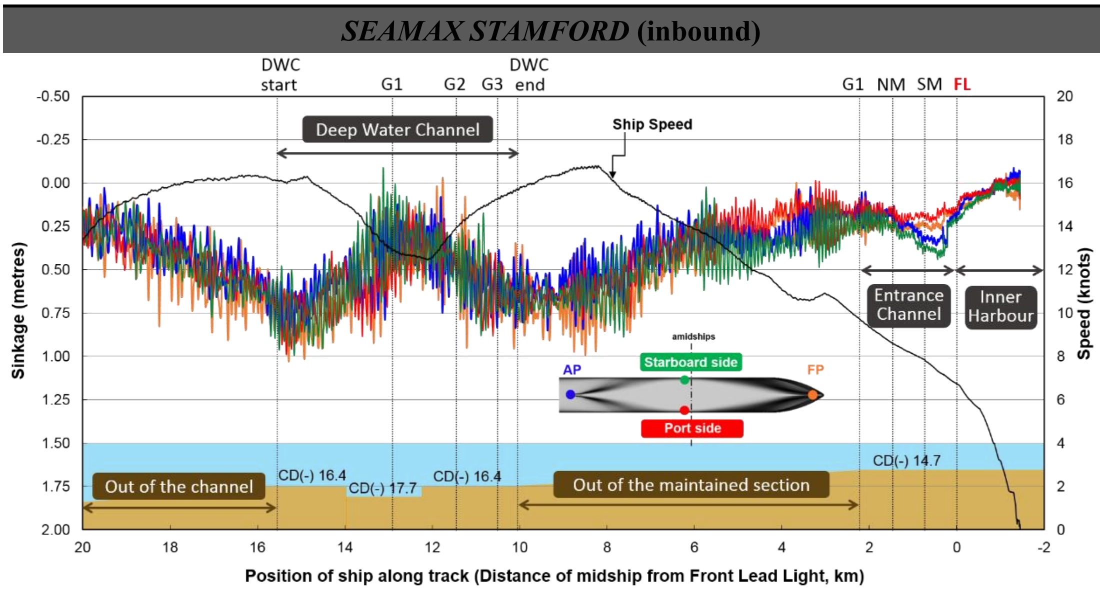

(a) Measured sinkage

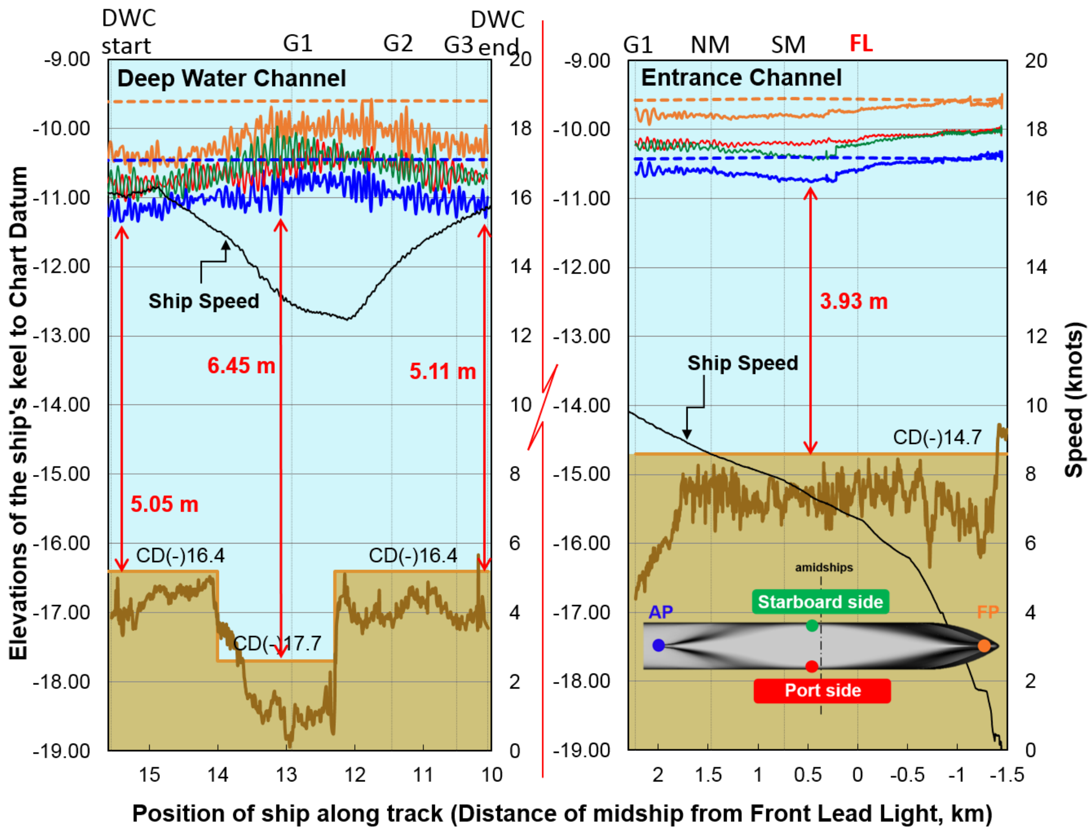

(b) Elevations of the ship's keel

Figure 4.28. (a) Measured sinkage (positive downward) at four points [Note: Chart datum depths (not to scale) also shown]; (b) Elevations of the ship's keel relative to chart datum [Note: Dashed lines near the top of the figure are elevations of the FP (orange) and AP (blue), including changes in tide only; i.e., their static position, not including squat and wave-induced motions; the flat seabed line is based on the charted depth on AUS112; the fluctuating seabed line is the actual survey line provided by Fremantle Ports]

As shown in Figure 4.24, the vulnerable extremities of container ships differ from those of bulk carriers (see Figure 4.10), which have relatively longer parallel midbodies. The positions of the port and starboard bilge corners of the container ships should, therefore, be defined properly as the widest points of the ship's keel at which maximum sinkage could occur. The widest points were captured to be a little aft of amidships, approximately 47 % of L_{PP} forward of the AP (see Figure 4.24), from the deck and profile drawing for *SEAMAX STAMFORD*. This proportion was applied to all the container ships.

For the transverse positions of the bilge corners, a distance of 78 % of the half-beam away from the centreline of the ship was taken from the body plans of the KCS (Lee, Koh, & Lee, 2003) and FHR Ship D (Gourlay, von Graefe, Shigunov, & Lataire, 2015; Vantorre & Journée, 2003) hulls, and 82 % for the DTC hull (el Moctar, Shigunov, & Zorn, 2012). All these hulls are considered representative of container ship hulls, as explained previously (see Chapter 2). In addition a distance of 82 % of the half-beam away from the centreline of the ship was taken from the section of the general arrangement plan for *CMA CGM WAGNER*. The transverse positions of the bilge corners were therefore taken as being 80 % of the half-beam away from the ship centreline in all the container ships.

Sinkage results for the container ship transits are summarised in Table 4.12.

Nearly half of the container ship transits had maximum sinkage at the bilge corners, and the other half at the bow. This is different from the sinkage results for the bulk carrier transits in the Port of Geraldton (see Table 4.5), which showed half had maximum sinkage at the bow and half at the stern. For ships with static stern-down trim, like *SEAMAX STAMFORD* (inbound), *CMA CGM CHOPIN* (outbound) and *MOL EMISSARY* (inbound/outbound) (see Table 4.9), the FP or bilge corners having maximum sinkage may not be the closest point to the seabed. The stern can still have maximum dynamic draught because of its already close proximity to the seabed. Definitions of dynamic draught and dynamic draught increase, as well as their applications, are described in 4.2.5.2.

Table 4.12. Measured maximum sinkage and dynamic draught, and dynamic draught increase for the container ship transits

Ships	In/ Out	Maximum sinkage				Maximum dynamic draught		Dynamic draught increase	
		(m)	point	(% of L_{PP})	(% of static draught)	(m)	point	(m)	(% of static draught)
*SEAMAX STAMFORD**	in	1.03	FP	0.43	9.91	12.14	AP	0.89	7.87
CMA CGM CHOPIN		1.32	FP	0.50	11.34	12.97	FP	1.32	11.34
MOL EMISSARY		1.27	FP	0.45	11.66	12.77	AP	0.67	5.54
*SAFMARINE MAKUTU**		1.17	Stbd Bilge	0.42	9.28	13.77	Stbd Bilge	1.17	9.28
*MOL PARAMOUNT**		0.91	Stbd Bilge	0.33	7.96	12.30	Stbd Bilge	0.91	7.96
*OOCL BRISBANE**		1.24	Port Bilge	0.51	10.73	12.92	AP	0.86	7.14
*CMA CGM WAGNER**		1.27	Stbd Bilge	0.48	11.81	12.38	AP	0.88	7.62
OOCL HOUSTON	out	1.11	Port Bilge	0.45	9.53	12.71	Port Bilge	1.11	9.53
CMA CGM CHOPIN		0.95	FP	0.36	9.53	11.93	AP	0.83	7.45
MOL EMISSARY		1.12	FP	0.40	11.43	12.45	AP	0.95	8.24
SAFMARINE MAKUTU		1.45	FP	0.52	13.22	12.48	Port Bilge	1.27	11.33
CMA CGM LAMARTINE		1.11	Port Bilge	0.39	9.78	12.47	Port Bilge	1.11	9.78
MOL PARAMOUNT		0.98	FP	0.36	7.50	14.02	FP	0.98	7.50

[Note: *These transits are discussed in detail in Chapter 5.3]

Calculated minimum real-time clearance in the Deep Water Channel, Entrance Channel and Inner Harbour, together with the keel point at which that occurs, are shown in Table 4.13. Tide ranges while underway in each section are also shown so that tidal contributions to the minimum UKC can be roughly identified (see Appendix B (B.2)).

Table 4.13. Calculated minimum UKC for the container ship transits

Ship transits	In/ Out	Entrance Channel & Inner Harbour (charted depth: 14.7 m)				Deep Water Channel (charted depth: 16.4−17.7 m)			
		(m)	point	(% of static draught)	tide ranges (m)	(m)	point	(% of static draught)	tide ranges (m)
*SEAMAX STAMFORD**	in	3.93	AP	34.97	0.82-0.86	5.05	AP	44.90	0.78-0.80
CMA CGM CHOPIN		3.54	Port Bilge	30.33	0.79-0.86	4.33	FP	37.21	0.82-0.83
MOL EMISSARY		3.30	AP	27.29	0.97-1.05	4.63	AP	38.25	0.99-1.00
*SAFMARINE MAKUTU**		2.47	Stbd Bilge	19.57	0.75-0.83	3.62	FP	28.72	0.77-0.77
*MOL PARAMOUNT**		3.67	Stbd Bilge	32.26	0.64-0.67	4.75	Stbd Bilge	41.68	0.63-0.65
*OOCL BRISBANE**		3.22	AP	26.70	0.86-0.93	4.38	AP	36.34	0.85-0.87
*CMA CGM WAGNER**		3.82	AP	33.20	0.89-0.96	4.92	AP	42.76	0.88-0.90
OOCL HOUSTON	out	3.33	FP	28.66	0.80-0.85	4.77	Stbd Bilge	41.08	0.82-0.83
CMA CGM CHOPIN		4.10	AP	36.94	1.00-1.04	5.45	AP	49.13	0.97-0.98
MOL EMISSARY		3.76	AP	32.68	0.82-0.90	4.97	AP	43.21	0.81-0.84
SAFMARINE MAKUTU		3.38	AP	29.64	0.55-0.59	4.51	FP	40.96	0.56-0.57
CMA CGM LAMARTINE		3.35	AP	29.13	0.56-0.66	4.61	AP	40.11	0.60-0.62
MOL PARAMOUNT		2.05	FP	15.72	0.65-0.72	3.28	FP	25.12	0.70-0.71

[Note: *These transits are discussed in detail in Chapter 5.3]

The AP was the closest point to the seabed in both channels for most of the container ships trimmed by the stern at departure or arrival time (see Table 4.9) such as *SEAMAX STAMFORD* (inbound), *CMA CGM WAGNER* (inbound), *CMA CGM CHOPIN* (outbound) and *MOL EMISSARY* (outbound). However, the container ships with almost level static trim had their minimum UKC at the FP or bilge corners: for example, at the port bilge corner and FP for *CMA CGM CHOPIN* (inbound), the starboard bilge corner and FP for *SAFMARINE MAKUTU* (inbound), and the FP and starboard bilge corner for *OOCL HOUSTON* (outbound).

Note that the points closest to the seabed can be different in Table 4.12 and Table 4.13 because the maximum sinkage and dynamic draught for each container ship were captured through its entire transit, including the unmaintained section of the channels, whereas the minimum UKC for each container ship was calculated within the channels.

4.3.5.3 Comparisons between the container ship transits

With the dynamic sinkage at the four points of the container ships (see Figure 4.24), dynamic trim and heel of all container ship transits were also calculated. Figure 4.29 and Figure 4.30 show these dynamic trim and heel results, for inbound and outbound transits separately.

As stated in 4.2.5.3, dynamic trim and heel refer to a ship's total change in trim (positive stern-down) and heel (positive to starboard), relative to its static floating position at the berth. Dynamic trim is given in metres, based on the difference between the FP and AP, and dynamic heel is in degrees.

Inbound transits

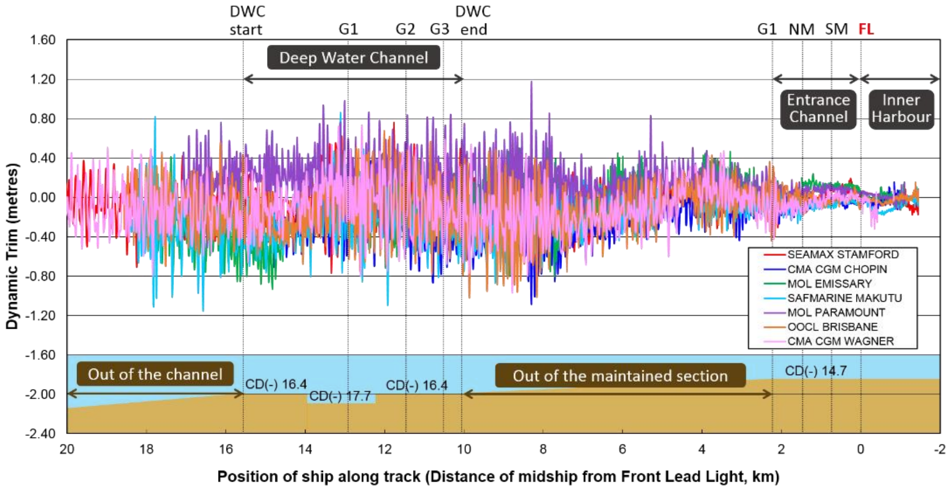

(a) Measured dynamic trim

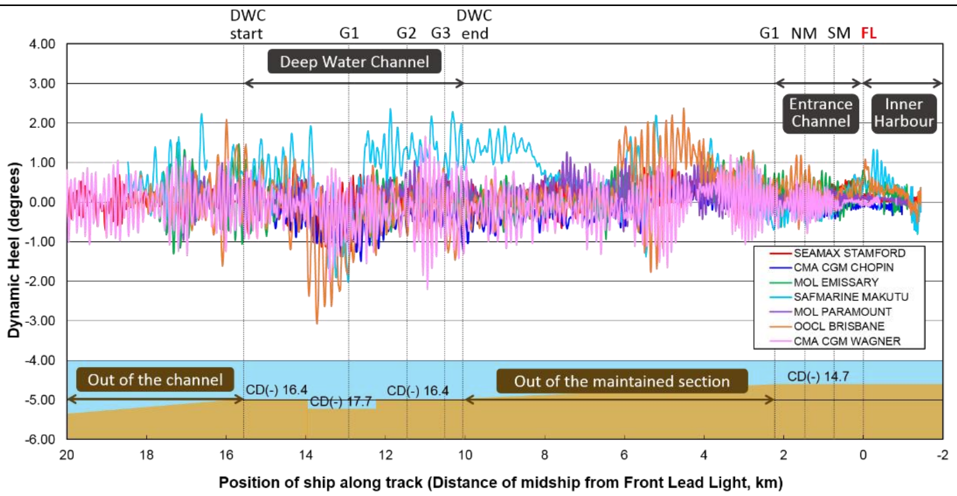

(b) Measured dynamic heel

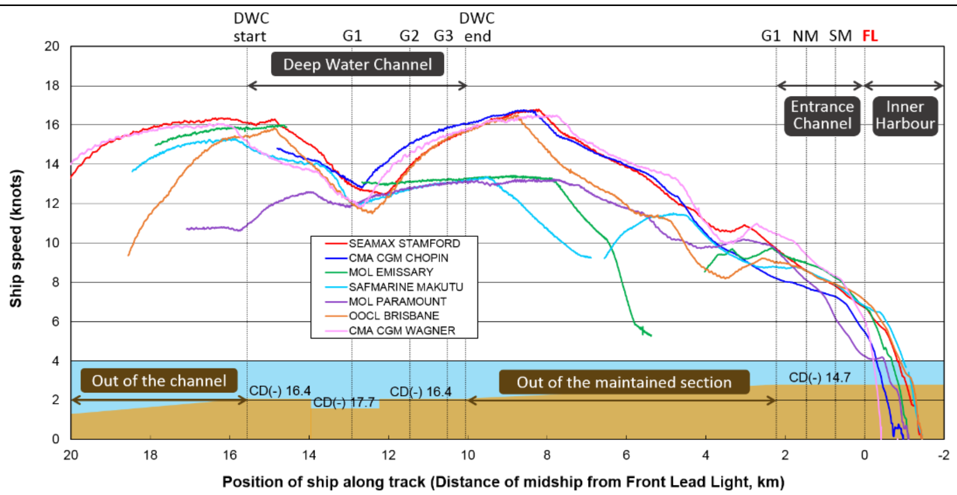

(c) Measured ship speed

Figure 4.29. (a) Measured dynamic trim (positive stern-down); (b) Measured dynamic heel (positive to starboard); (c) Measured ship speed, for the inbound ship transits [Note: Chart datum depths (not to scale) also shown]

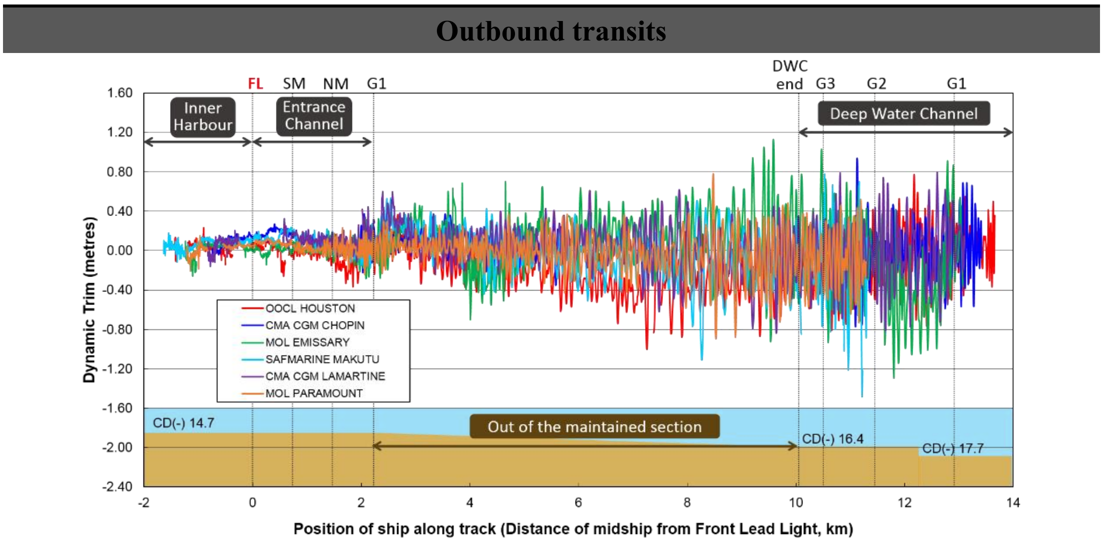

(a) Measured dynamic trim

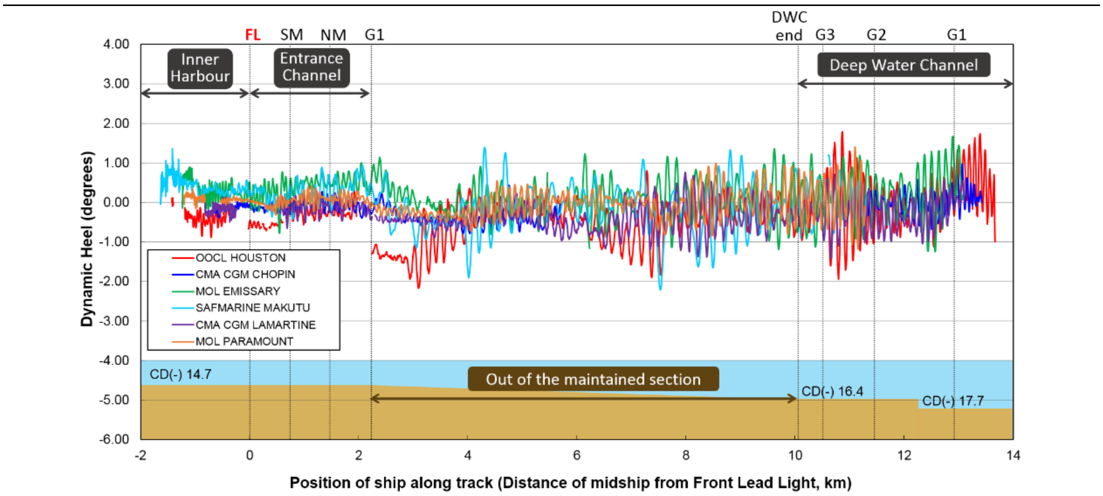

(b) Measured dynamic heel

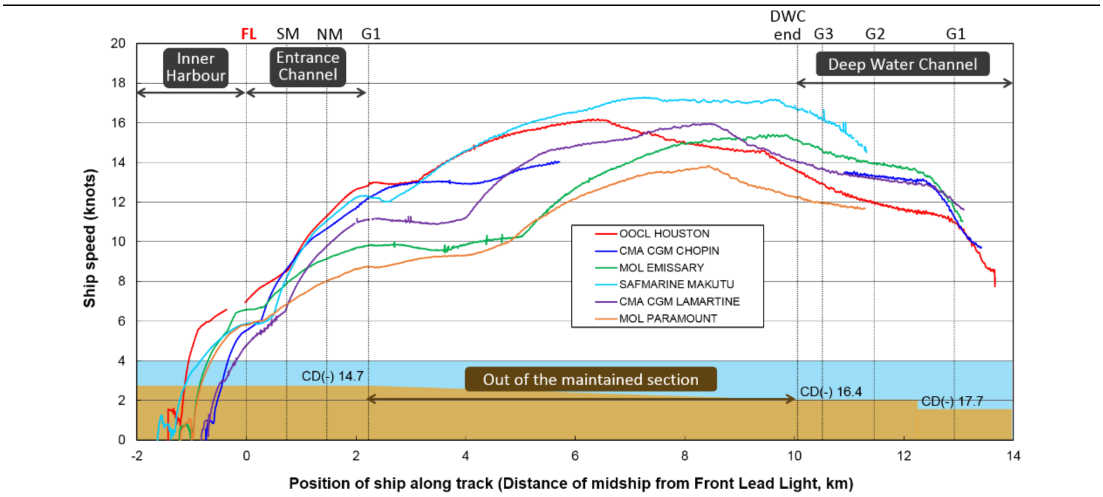

(c) Measured ship speed

Figure 4.30. (a) Measured dynamic trim (positive stern-down); (b) Measured dynamic heel (positive to starboard); (c) Measured ship speed, for the outbound ship transits [Note: Chart datum depths (not to scale) also shown]

The natural roll period (T_ϕ) for each container ship transit can be approximated by Eq. (4.1). As shown in Table 4.14, this can be compared with the wave data measured during each transit for speculating on the likelihood of large dynamic heel caused by resonant rolling.

Table 4.14. Calculated natural roll period and measured wave data during each transit

Ships	In/ Out	GM_f (m)	Natural roll period (T_ϕ, sec)	Measured wave data (swell)		
				H_s (m)	T_p (sec)	T_s (sec)
*SEAMAX STAMFORD**	in	3.88	15.15	0.33-0.43	11.9-18.4	12.5-13.2
CMA CGM CHOPIN		2.93	18.69	0.40-0.46	12.9-16.0	13.2-13.7
MOL EMISSARY		1.28	22.77	0.47-0.61	11.4-15.4	12.3-12.9
*SAFMARINE MAKUTU**		0.81	28.67	0.30-0.35	12.0-13.9	11.9-12.5
*MOL PARAMOUNT**		3.87	16.27	0.24-0.29	12.8-13.8	11.9-12.4
*OOCL BRISBANE**		1.00	25.80	0.48-0.54	11.4-14.3	11.4-12.0
*CMA CGM WAGNER**		4.51	15.07	0.52-0.62	12.3-17.6	12.4-13.7
OOCL HOUSTON	out	1.34	22.29	0.33-0.38	11.9-17.8	12.2-12.6
CMA CGM CHOPIN		3.32	17.56	0.56-0.61	11.4-14.7	12.2-12.7
MOL EMISSARY		1.55	20.69	0.40-0.48	13.1-14.7	11.9-12.4
SAFMARINE MAKUTU		1.49	21.14	0.38-0.42	11.1-12.2	11.2-11.5
CMA CGM LAMARTINE		2.99	18.51	0.49-0.50	12.1-16.8	11.7-12.0
MOL PARAMOUNT		3.20	17.89	0.49-0.53	15.8-17.0	12.1-12.7

[Note: *These transits are discussed in detail in Chapter 5.3]

The wave data in Table 4.14 and Appendix B (B.2, see also Figure 4.20) are from the same source.

4.4 Conclusions

High-quality data for vertical ship motions in port approach channels were obtained from recent full-scale trials measuring dynamic sinkage, trim and heel of 11 bulk carrier transits entering and leaving the Port of Geraldton and 16 container ship transits entering and leaving the Port of Fremantle. The trial results will be made publicly available so they can be used for validating current UKC practice by ports and as a set of benchmarking data that can be used internationally.

Measurements were carried out using high-accuracy GNSS receivers on board and a fixed reference station. Measured sinkage, together with ship speed and channel bathymetry, were shown. Maximum dynamic sinkage and dynamic draught, as well as elevations of the ship's keel relative to chart datum, were also shown. Additional comparisons of dynamic trim and heel between the inbound and outbound transits were given. Three container ship transits, of the *MSC ILONA* (outbound), *SEAMAX STAMFORD* (outbound) and *OOCL BRISBANE* (outbound), were excluded from this study because there were suspicious data and ambiguity problems in their measurement results (see Appendix B (B.2) for more information).

A comprehensive environmental investigation was performed to support the measured ship motion results, including tide, wave, bathymetry and wind. The full measured tide and wave time series data covering the period of the ship transits; and the bathymetric data from the actual hydrographic survey were secured in collaboration with MWPA, Fremantle Ports and the coastal infrastructure team from the WADoT.

Raw data from each set of trials has been published as a Centre for Marine Science and Technology (CMST) report (Ha & Gourlay, 2016a; 2016b). The trials results will be applied for ship squat validations at full scale (Chapter 5), and for ship wave-induced motion validations at full scale (Chapter 6).

Chapter 5

Ship Squat Comparisons and Validations Using Full-Scale Trials

In this chapter, selected results are presented from two sets of full-scale trials measuring dynamic sinkage, trim and heel in bulk carrier transits at the Port of Geraldton and container ship transits at the Port of Fremantle (see Chapter 4). Measured dynamic sinkage, trim and heel of three example bulk carrier and five container ship transits are discussed in detail. Maximum dynamic sinkage and dynamic draught, as well as elevations of the ship's keel relative to chart datum, are calculated. A theoretical method using slender-body shallow-water theory is applied to calculate sinkage and trim for the ship transits, and a comparison is made between measured and predicted results to validate the ship motion software used for the UKC prediction. It is shown that slender-body theory is able to predict ship squat (steady sinkage and trim) with reasonable accuracy for both bulk carriers and container ships at full scale in open dredged channels.

5.1 Introduction

From the full-scale trials of bulk carrier and container ship motions in the approach channels of the Port of Geraldton and Fremantle (refer to Chapter 4), two sets of high-quality data on vertical ship motions and environmental conditions have been secured. With these data sets, the validation of numerical ship squat modelling may be achieved at full scale.

The dynamic sinkage, trim and heel of, for example, bulk carriers and container ships over their entire transits can be calculated by comparing their vertical motions when underway to their stationary condition at the berth. The dynamic draught at each point of each ship in the approach channels is found using the dynamic sinkage results and its static draught. For practical UKC management, UKC is also calculated by comparing elevations of the ship's keel relative to the seabed. The nett UKC and risk of running aground are then governed by the maximum dynamic draught over all the most vulnerable hull extremities, which are the FP, AP, and forward and aft shoulders of the bilge corners for bulk carriers (see Figure 4.10), and the FP, AP, and port and starboard bilge corners for container ships (see Figure 4.23). Such an accumulation of full-scale measurements will be important to develop the comprehensive guidelines for minimum UKC.

5.2 Validation of bulk carrier squat modelling

For bulk carrier squat modelling, the full-scale measurement results of the bulk carrier transits in the Port of Geraldton approach channel were used. General information on the full-scale trials is presented in Chapter 4.2.

5.2.1 Description of the bulk carriers and transit conditions

The following criteria have been taken into account in choosing example ship transits for further analysis:

A transit should have no suspicious data or ambiguity problems in any measurement results; it should be a set of high-quality data.

Hydrostatic data at an actual transit draught should be obtained during trials to assist with ship motion validation. These data are obtained from the ship's trim and stability book.

To validate ship motion predictions, there should be a published representative ship model that has characteristics similar to those of the actual ship. All ships should be fairly modern so that analysis can keep pace with contemporary trends in ship design.

Relevant environmental data, such as waves, wind and tides, should be obtained.

On this basis, three bulk carrier transits at the Port of Geraldton were selected from the total of eleven. Table 5.1 presents the pertinent details of these ships: *GUO DIAN 17*, built in 2013, a 76,000-DWT Panamax bulk carrier; *FENG HUANG FENG*, built in 2011, a 75,000-DWT Panamax bulk carrier; and *SEA DIAMOND*, built in 2007, a 77,000-DWT Panamax bulk carrier. They have similar hull dimensions and a high block coefficient (C_B). More details about them and their transit conditions can be found in Table 4.2.

Table 5.1. Details of the bulk carriers

Particulars	***GUO DIAN 17***	***FENG HUANG FENG***	***SEA DIAMOND***
Ship size	Panamax	Panamax	Panamax
L_{OA} (m)	225.00	225.00	224.99
L_{PP} (m)	219.00	217.00	217.00
Beam (m)	32.26	32.26	32.26
Summer draught (m)	14.20	14.22	14.08
Displacement (t)	89,800.80	88,535.90	87,782.00
C_B (-)	0.873	0.868	0.869

[Note: Displacement and C_B are values at summer draught; C_B is the ratio of displaced volume to (L_{PP}·Beam·Draught)]

Table 5.2. Details of the bulk carrier transit conditions

Particulars	***GUO DIAN 17***	***FENG HUANG FENG***	***SEA DIAMOND***
Date / Time (AWST)	28/09/2015 09:18 - 10:13 a.m.	29/09/2015 21:41 - 22:53 p.m.	02/10/2015 09:52 - 10:58 a.m.
Direction	outbound	outbound	outbound
Draught fwd. (m)	12.15	12.18	8.91
Draught aft. (m)	12.15	12.20	10.26
Actual displacement (t)	75,571.00	74,788.00	57,427.00
C_B (-)	0.859 @ 12.15 m	0.854 @ 12.20 m	0.835 @ 9.59 m
LCB (m)	-	113.9 @ 12.20 m	115.05 @ 9.59 m
LCF (m)	-	106.80 @ 12.20 m	110.53 @ 9.59 m
GM_f(m)	7.11	7.10	5.93

[Note: C_B is calculated based on actual departure draught; LCB and LCF are given as metres forward of the AP; average draught is represented for C_B, LCB and LCF; dates and times are in Australian Western Standard Time (AWST)]

Because each ship may have travelled under vastly different conditions, all available relevant operating conditions need to be taken into account. Comparative transit conditions for the three bulk carriers are shown in Table 5.2. Details for *GUO DIAN 17* and *FENG HUANG FENG* are based on the data from ‘Application for Berth’, submitted to the Port of Geraldton no later than 2 hours prior to their actual departure. For the *SEA DIAMOND* transit, a loading condition report was provided by the shipping agent when the author disembarked after taking the measurements. Hydrostatic data was obtained from the ship’s trim and stability book during the *FENG HUANG FENG* and *SEA DIAMOND* transits.

GUO DIAN 17 and *FENG HUANG FENG* had a nearly fully-loaded draught with almost level static trim, whereas *SEA DIAMOND* had a comparatively shallower draught and was trimmed by the stern at departure time. All of these were outbound transits.

5.2.2 Description of the port, channel and measured ship tracks

The layout of the Port of Geraldton, including its approach channel and navigational beacons, together with tracks of the three outbound bulk carriers, are illustrated in Figure 5.1.

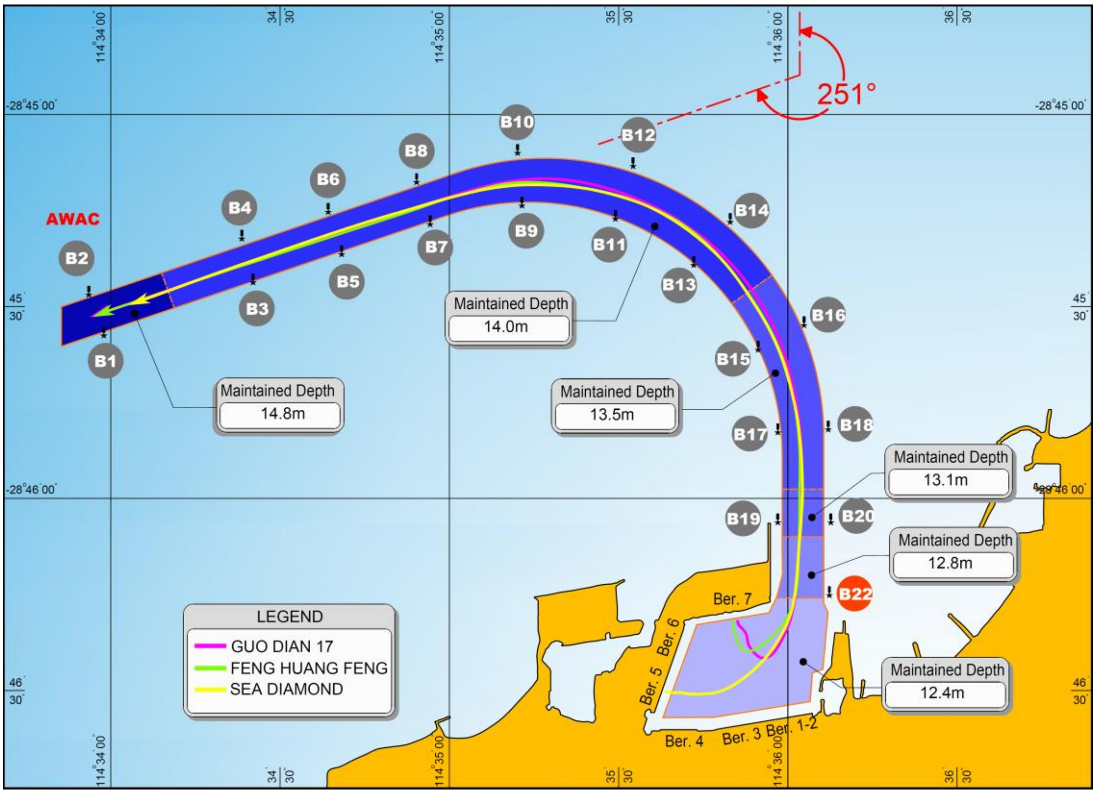

Figure 5.1. Port of Geraldton approach channel and measured midship tracks

As mentioned in Chapter 4.2.2, tidal data in the form of raw sea surface elevations, as measured at Berth 3–4 (28° 46.60000' S, 114° 35.76667' E) with a sampling frequency of 0.5 Hz, was provided by MWPA. Independent local tide for each transit was extracted from the raw sea surface data using a low-pass filter with a cutoff period of 5 minutes. The tidal data covering the period of the three bulk carrier transits is shown in Figure 5.2.

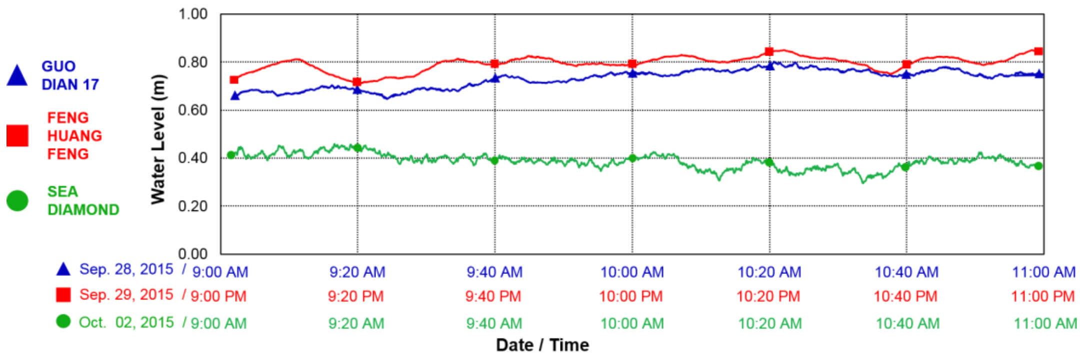

Figure 5.2. Measured tidal data during the transits

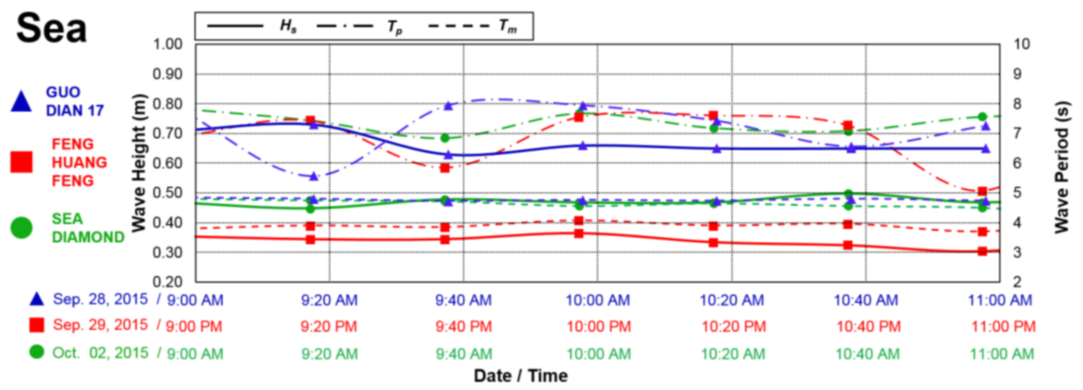

(a)

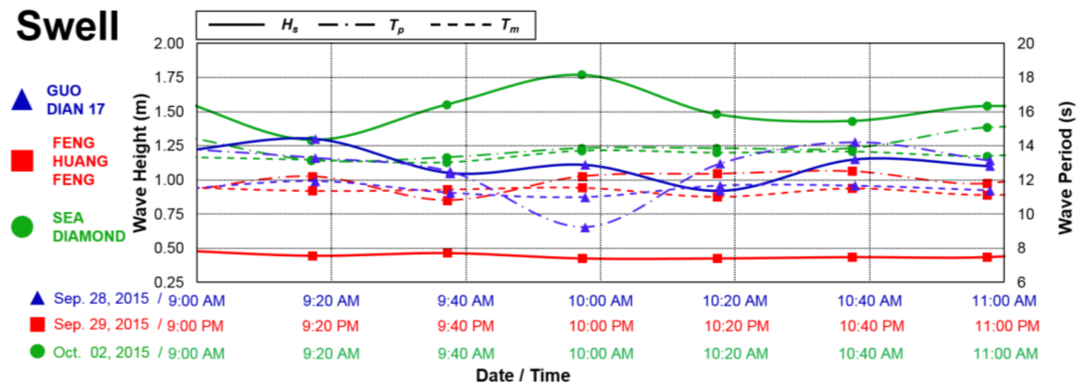

(b)

Figure 5.3. Measured wave data during the transits: (a) Sea; (b) Swell [Note: Sea/swell cutoff period is 8 seconds; H_s = significant wave height; T_p = spectral peak wave period; T_m = mean wave period]

Because the Port of Geraldton is exposed to long-period swells, which cause wave-induced motions of ships in the channel, measured dynamic sinkage includes wave-induced heave, roll and pitch caused by the swells. Wave data from the AWAC at Beacon 2 (B2) (28° 45.47000' S, 114° 33.93167' E) (see Figure 5.1), was provided by MWPA. Figure 5.3 shows the measured wave data for the bulk carrier transits.

More details on the port, channels and environmental conditions in the port can be found in Chapter 4.2.1 and 4.2.2, and bathymetric data in Chapter 4.2.3.

5.2.3 Measured dynamic sinkage, trim and heel

5.2.3.1 Error analysis

The vertical position accuracy of the SOKKIA GSR2700 ISX and Trimble R10 receivers are specified as within 20 mm + 1 ppm × (baseline length) and 15 mm + 1 ppm × (baseline length), respectively, in the manuals (SOKKIA, 2007; Trimble, 2012).

Expected vertical root-mean-square (RMS) errors for the transits were captured in the baseline processing of the *Trimble Business Centre v3.50* software. These were in the range of 0.010 and 0.012 m, and the RMS error in the GNSS receiver's vertical position was estimated to be less than 0.012 m.

As stated in Chapter 4.2.4, raw GNSS heights are referenced to an ellipsoid, and geoid undulation (N) is required to convert ellipsoidal heights to orthometric heights. The Earth Gravitational Model 2008 (EGM2008), a spherical harmonic model of the Earth's gravitational potential (Pavlis, Holmes, Kenyon, & Factor, 2012), was applied to transfer between the raw GNSS heights and orthometric (geoid) heights. The value of geoid undulation (N) is negative in which the geoid lies below the ellipsoid and vice versa. Because values of N are given by a regular grid, N *values at specific points* along the tracks of the three bulk carrier transits were taken from interpolation in the 2.5-minute grid of EGM2008, which ranged between (-) 24.872 and (-) 25.015 m with a standard deviation of 0.034 m for *GUO DIAN 17*, 0.042 m for *FENG HUANG FENG*, and 0.043 m for *SEA DIAMOND*. The RMS error in obtaining geoid undulation (N) may be an estimate of the standard deviation of those N values and is less than 0.043 m.

The stationary reading at the berth was based on 3-minute-averaged values of the ship's vertical motion prior to the beginning of unberthing for departure. However, the static floating position of the ships still had some residual vertical movement from seiches in the inner harbour. The RMS error from each receiver on the ships for the first 3 minutes after all onboard receivers were set up, and which had the least impact from the unberthing operations, ranged from 0.019 to 0.057 m. The RMS error in the static reading was, therefore, estimated to be less than 0.057 m.

Equipment error in the tide gauge should also be considered as an error component in calculating dynamic sinkage. Measurement uncertainty, i.e., sensor uncertainty of the tide gauge, is stated to be within ± 0.010 m (Australian Government Bureau of Meteorology, n. d. b).

As previously mentioned, the local tide data recorded at 2-second intervals (0.5 Hz), provided by MWPA, was filtered to remove harbour oscillations. The tidal data filtered was applied to the dynamic sinkage of the ships measured at 1-second intervals; a linear interpolation method was used to find tidal elevation at a particular point, i.e., at 1.0 Hz. The RMS error in the method was found to be extremely small, so that it can be considered a negligible error for the three bulk carrier transits. Note that tidal data filtered to remove harbour seiche effects cannot quantify error from actual tide.

The tidal data as measured at Berth 3–4 in the Port of Geraldton (see Figure 5.1) was used for the entire transit, even though the end of the channel is approximately 2 nautical miles away from the inner harbour as the crow flies. By comparing measured tidal data from other stations near the Port of Geraldton, an error in tidal elevation due to sea surface slope can be estimated (Gourlay & Klaka, 2007); however, the most proximate tide stations are about 35 nautical miles south (Port Denison) and west (Pelsaert Island) of the port, so their data may not be an appropriate source in this case. Ha and Gourlay (2018b) showed that an error in the discrepancy of tidal elevation may be less than 0.010 m for a distance of 6.5 nautical miles in the Port of Fremantle. Assuming the Port of Geraldton has a similar sea surface slope, the RMS error in the discrepancy of tidal elevation application is zero near the inner harbour and less than 0.003 m in the approach channel.

The RMS errors inherent in calculating the dynamic sinkage of the bulk carrier transits in the channel are summarised in Table 5.3. For the final dynamic sinkage results, all height components, including the previously mentioned sources, are added or subtracted (refer to Chapter 4.2.4); the total RMS error is the square root of the sum of the squares of the error for each factor (Gourlay, 2008c): 0.074 m in the channel and 0.073 m in the inner harbour.

Table 5.3. Estimated RMS errors in calculating dynamic sinkage

Error factors	Approach channel (m)	Inner harbour (m)
Error in the GNSS receivers	0.012	0.012
Error in Geoid undulation N (EGM2008)	0.043	0.043
Error in the static reading at the berth	0.057	0.057
Error in the tide gauge	0.010	0.010
Error in interpolating to find tidal elevation at a particular point (at 1.0 Hz)	-	-
Error in the discrepancy of tidal elevation due to sea surface slope	0.003	-
Total	**0.074**	**0.073**

If a large number of trials were performed in the same conditions, the total RMS error would be the standard deviation of the measured dynamic sinkage (Gourlay, 2008c). The errors depend on assuming a distribution to be normal (or Gaussian), so about 95 % of the actual dynamic sinkage usually falls within two standard deviations of the mean. Therefore, with 95 % confidence, the actual dynamic sinkage will lie within the margin of error of ± 0.148 m in the approach channel, and ± 0.146 m in the inner harbour.

5.2.3.2 Dynamic sinkage

Measured sinkage, ship speed and channel bathymetry for the three example bulk carrier transits are shown in Figure 5.4. The positions of the FP and AP, the forward and aft shoulder of the bilge corners, are plotted (see Figure 4.10). Further information on the way to determine the positions of the six points of the bulk carriers can be found in Chapter 4.2.5.2.

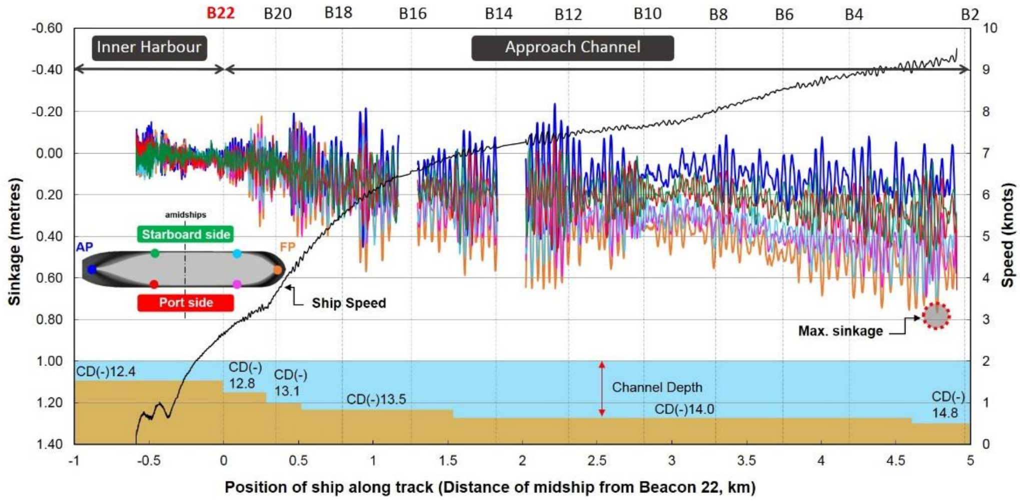

(a) *GUO DIAN 17*

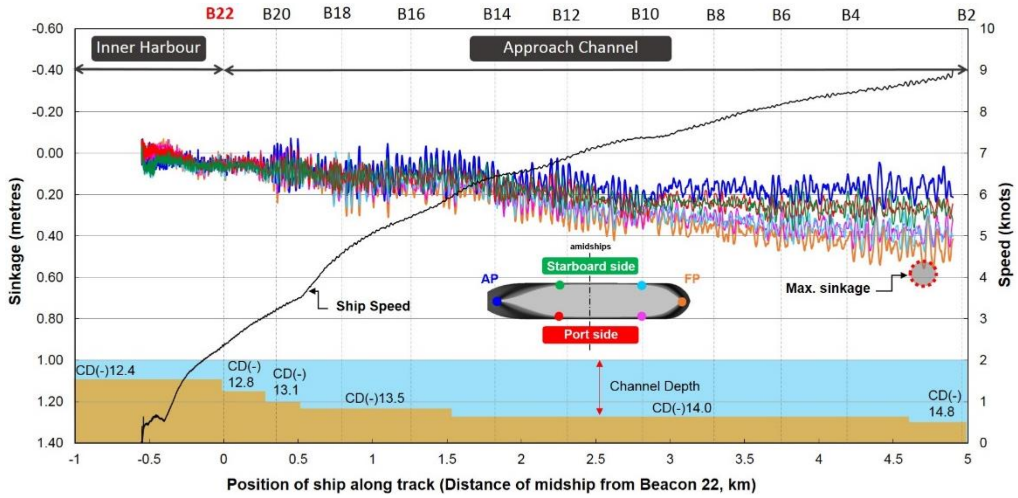

(b) *FENG HUANG FENG*

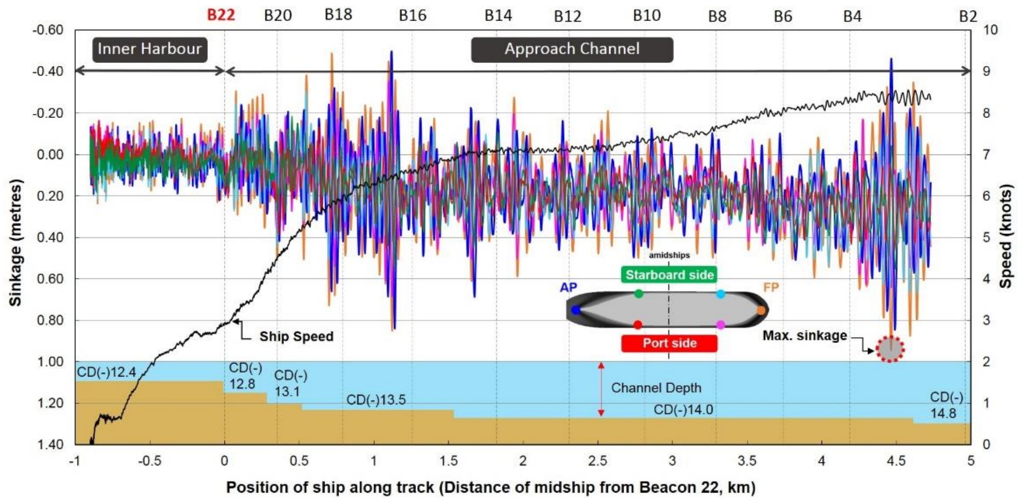

(c) *SEA DIAMOND*

Figure 5.4. Measured sinkage (positive downward) at six points: (a) *GUO DIAN 17*; (b) *FENG HUANG FENG*; (c) *SEA DIAMOND* [Note: Chart datum depths (not to scale) also shown]

As mentioned previously, dynamic sinkage means the total sinkage (positive downward) relative to the still water level, as compared to the static floating position at the berth, and includes a near-steady component due to squat; an unsteady component due to wave-induced heave, pitch and roll; and a slowly-varying heel due to wind and turning. Particularly when swell waves are present, dynamic sinkage of the ship will be more intricate, with its wave-induced motion that is a combination of heaving, pitching and rolling. For example, because the *SEA DIAMOND* transit was undertaken in large, long period swell conditions (see Figure 5.3(b)), its vertical motions are seen to be highly oscillatory (see Figure 5.4(b)) due to the wave-induced heave, pitch and roll.

Based on Chart AUS81, outbound transits are on a heading of 0° (North) from B20 to B18, then there is an approximately 1,200 m-radius turn to port, steadying on a heading of 251° from B8 to the end of the channel (see Figure 5.1). By comparing this to the directions of the prevailing swells in Table 5.4, it is expected that the bulk carrier transits were in port beam seas near B18 and in head seas near B4.

Table 5.4. Measured swell data at Beacon 2 during the transits

Ship transits	AWST	H_s (m)	T_p (sec)	T_m (sec)	Dir (◦)
GUO DIAN 17	28/09/2015 9:18	1.30	13.3	11.9	247
	28/09/2015 9:38	1.05	12.5	11.3	242
	28/09/2015 9:58	1.11	9.2	11.0	244
	28/09/2015 10:18	0.92	13.0	11.7	243
	28/09/2015 10:38	1.15	14.2	11.7	243
	28/09/2015 10:58	1.10	13.1	11.4	246
	28/09/2015 11:18	1.15	13.7	11.8	244
FENG HUANG FENG	29/09/2015 21:18	0.44	12.2	11.3	249
	29/09/2015 21:38	0.46	10.8	11.4	240
	29/09/2015 21:58	0.42	12.2	11.5	248
	29/09/2015 22:18	0.42	12.3	11.0	248
	29/09/2015 22:38	0.43	12.5	11.5	251
	29/09/2015 22:58	0.43	11.8	11.1	240
	29/09/2015 23:18	0.50	13.5	11.5	240
SEA DIAMOND	2/10/2015 9:18	1.29	13.1	13.2	247
	2/10/2015 9:38	1.55	13.3	13.0	249
	2/10/2015 9:58	1.77	13.8	13.7	245
	2/10/2015 10:18	1.48	13.8	13.6	246
	2/10/2015 10:38	1.43	13.8	13.6	248
	2/10/2015 10:58	1.54	15.1	13.4	252
	2/10/2015 11:18	1.47	14.8	14.0	245

[Note: The time of each record is the time at the end of the 20 minutes, in which the data was recorded; wave data in Figure 5.3(b) and Table 5.4 are from the same source]

As shown in Figure 5.4, maximum sinkage was observed at the bow in the vicinity of B2: that is, near the end of the channel; but significant oscillations also occurred when the bulk carriers were travelling between B20 and B12. This was common to all the bulk carrier transits, and might be referable to the combined effects of dynamic trim and heel changes caused by turning manoeuvres and beam waves in this severely curved section. The maximum sinkage is 0.77 m (0.35 % of L_{PP}) for *GUO DIAN 17*, 0.56 m (0.26 % of L_{PP}) for *FENG HUANG FENG* and 0.94 m (0.44 % of L_{PP}) for *SEA DIAMOND*.

With swell present, maximum dynamic draught may occur at the forward shoulders of the bilge corners (Gourlay, 2007). The forward shoulders of the bilge corners had a greater sinkage than the bow at some instances in the cases of the *GUO DIAN 17* and *SEA DIAMOND* transits; but because *SEA DIAMOND* used the static stern-down trim of 1.35 m on her departure (see Table 5.2), the stern still had the maximum dynamic draught (refer to Figure C.11 in Appendix C). No significant wave-induced heave, pitch and roll in the *FENG HUANG FENG* transit were seen, with calm wind and low swell conditions. These sinkage results for the three bulk carrier transits can be found in Table 4.5.

In Appendix C (C.1), Figure C.6(b) for *GUO DIAN 17*, Figure C.9(b) for *FENG HUANG FENG* and Figure C.11(b) for *SEA DIAMOND* show elevations of the ship's keel relative to chart datum, as well as elevations of the FP and AP, including changes in tide only; that is, their static position not including squat and wave-induced motions. This shows how much of the vertical movement was due to tide changes.

Table 5.5. Example calculation of sinkage and real-time UKC for *SEA DIAMOND*

<table>
<tr><th>Calculations</th><th colspan="2">Components</th><th>FP</th><th>AP</th><th>Note</th></tr>
<tr><td rowspan="8">Sinkage calculation</td><td>A</td><td>Static draught</td><td>8.91 m</td><td>10.26 m</td><td>-</td></tr>
<tr><td>B</td><td>Tide elevation at berth</td><td>(+) 0.39 m CD</td><td>(+) 0.39 m CD</td><td>-</td></tr>
<tr><td>C</td><td>Keel elevation at berth</td><td>(-) 8.52 m CD</td><td>(-) 9.87 m CD</td><td>B-A</td></tr>
<tr><td>D</td><td>Bow GNSS receiver elevation at berth</td><td>(+) 16.40 m CD</td><td>-</td><td>-</td></tr>
<tr><td>E</td><td>Bow GNSS receiver elevation underway</td><td>(+) 15.46 m CD</td><td>-</td><td>-</td></tr>
<tr><td>F</td><td>Bow sinkage relative to chart datum</td><td>0.94 m</td><td>-</td><td>D-E</td></tr>
<tr><td>G</td><td>Tide elevation underway</td><td>(+) 0.39 m CD</td><td>(+) 0.39 m CD</td><td>-</td></tr>
<tr><td>H</td><td>Sinkage relative to free surface water level</td><td>0.94 m</td><td>0.84 m</td><td>F+G-B</td></tr>
<tr><td rowspan="3">Real-time UKC calculation</td><td>I</td><td>Dynamic draught</td><td>9.85 m</td><td>11.10 m</td><td>A+H</td></tr>
<tr><td>J</td><td>Water depth underway</td><td>(-) 14.00 m CD</td><td>(-) 14.00 m CD</td><td>-</td></tr>
<tr><td>K</td><td>Real-time UKC</td><td>4.54 m</td><td>3.30 m</td><td>(G-I)-J</td></tr>
</table>

Table 5.5 shows an example calculation of sinkage and real-time UKC for *SEA DIAMOND* at the time of maximum measured sinkage, showing its FP (see Table 4.5) between B4 and B2 with the water depth of 14.0 m (see Figure 5.4). When compared

with Table 4.5, it confirms that maximum sinkage at the FP does not give maximum dynamic draught because the AP has a larger static draught. Because the sinkage at the AP, for comparative purposes in Table 5.5, was calculated from the raw GNSS results of each receiver, some elevations for it cannot be shown: as in the D, E and F components of Table 5.5.

Calculated minimum real-time clearance in the inner harbour and approach channel, as well as the keel point in which that occurs, can be found in Table 4.6. Minimum real-time clearances are captured of 0.80 m for *GUO DIAN 17*, 0.90 m for *FENG HUANG FENG* and 2.25 m for *SEA DIAMOND* (see Appendix C (C.1)). The starboard forward shoulder of the bilge corners for *GUO DIAN 17* and the starboard aft shoulder of the bilge corners for *FENG HUANG FENG* are the closest points to the seabed over their entire transits, and are observed in the inner harbour. This is primarily due to heel, because tugs pulled the ships to starboard during the unberthing operations. For *SEA DIAMOND*, with the static stern-down trim, the AP is the closest point to the seabed through the whole transit.

5.2.3.3 Dynamic trim

Bulk carriers with level static trim tend to have dynamic trim by the bow when underway; see Dand and Ferguson (1973) for model-scale tests, and Härting, Laupichler and Reinking (2009) for full-scale tests. This large bow-down trim means that the bow can be the point on the ship most vulnerable to grounding.

Figure 5.5 shows results of dynamic trim for the three bulk carrier transits. Dynamic trim is, here, the ship's total change in trim (positive stern-down), relative to the static floating position at the berth, and includes wave-induced pitch. Steadily increasing trim by the bow is observed in all three cases, but is swamped by wave-induced pitching in *SEA DIAMOND*. So that trim is not swamped by wave-induced pitch, a low-pass filter with a cutoff period of 5 minutes was applied to the dynamic trim results. Note that dynamic trim, given in metres, is based on the difference between the FP and AP, and the filtered results are displayed in the same colour as the measured, but thicker lines for each transit.

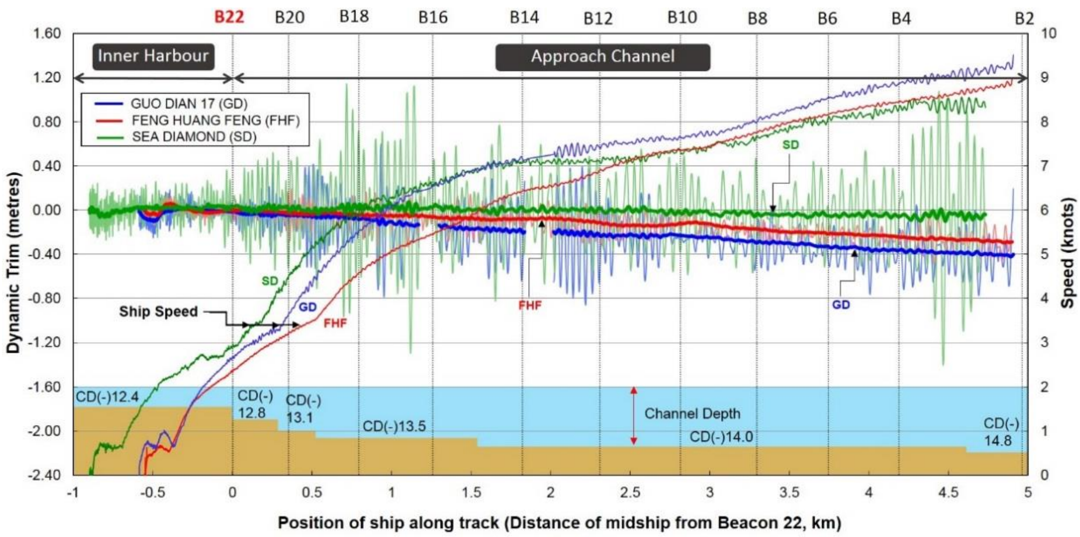

Figure 5.5. Measured dynamic trim (positive stern-down) for the three bulk carrier transits [Note: Chart datum depths (not to scale) also shown]

By looking at the oscillations of dynamic sinkage for each transit (see Figure 5.4), it is seen that dynamic trim is more likely to affect maximum sinkage for bulk carriers than dynamic heel, which will be discussed subsequently. This situation is different from that of container ships, in which dynamic heel may be the most important factor governing maximum sinkage (Gourlay & Klaka, 2007).

According to full-scale tests made by Ferguson and McGregor (1986), and Hatch (1999), acceleration and deceleration influence dynamic trim. *GUO DIAN 17* and *SEA DIAMOND* quickly accelerated to speeds up to 6 knots while passing between B22 and B18. Some significant oscillations in dynamic trim are seen in *SEA DIAMOND* near B18, B16 and the end of the channel. This may be explained by the operating conditions of a comparatively larger swell (see Table 5.4 and Figure 5.3(b), mostly head sea condition) but lighter displacement (see Table 5.2).

The maximum unfiltered dynamic trims are 0.86, 0.49 and 1.40 m (0.39, 0.23 and 0.65 % of the L_{PP}) by the bow for the *GUO DIAN 17*, *FENG HUANG FENG* and *SEA DIAMOND* transit, respectively. The maximum filtered dynamic trims are 0.42 m for *GUO DIAN 17*, 0.29 m for *FENG HUANG FENG*, and 0.10 m for *SEA DIAMOND*. These values correspond to 0.19, 0.13 and 0.05 % of their L_{PP}, respectively.

5.2.3.4 Dynamic heel

Dynamic heel may cause the bilge corners to be the closest points to the seabed. For ports exposed to long-period swell, large dynamic heel occurs when the wave encounter period is close to a ship's natural roll period. Calculated natural roll periods (T_ϕ) of the bulk carriers using Eq. (4.1), together with the wave data measured during each transit, can be found in Table 4.7. *SEA DIAMOND* has a smaller GM_f and, hence, a longer natural roll period compared to the other two. More accurate calculations of the natural roll period and wave-induced motions will be made in Chapter 6.

Measured dynamic heel for the three bulk carrier transits is shown in Figure 5.6. In this chapter, dynamic heel means the ship's total change in heel (positive to starboard), relative to its static floating position at the berth, and includes wave-induced roll (Gourlay, 2008a). Results are also shown with a low-pass filter, which is applied to remove the effect of wave-induced roll.

Larger heel oscillations are seen in the *GUO DIAN 17* and *SEA DIAMOND* transits, which may be due to the ship's natural roll period close to the wave encounter period for *GUO DIAN 17*, and due to the relatively larger wave height for *SEA DIAMOND*. *FENG HUANG FENG* travelled in low swell conditions, and has small roll angles.

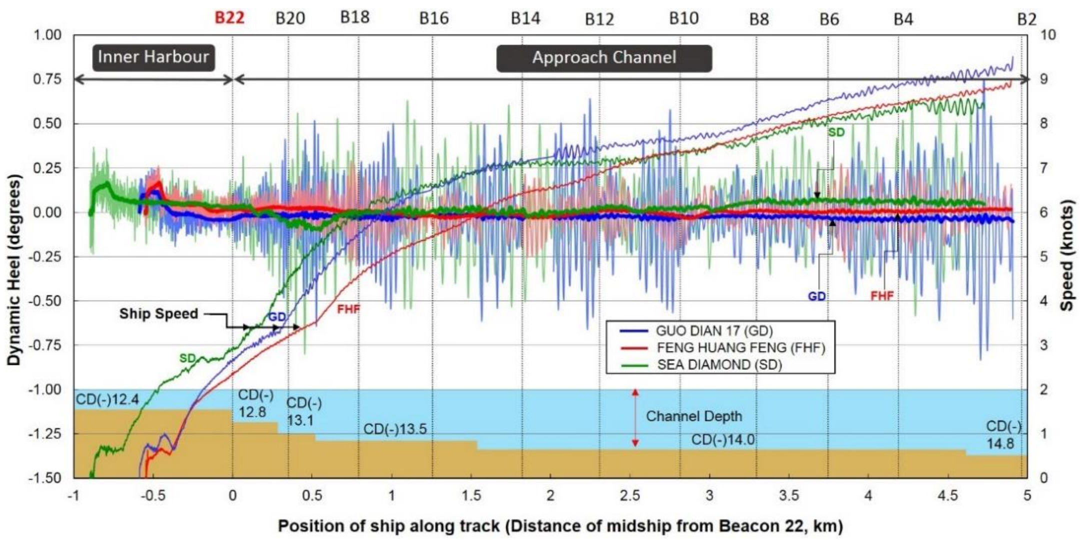

Figure 5.6. Measured dynamic heel (positive to starboard) for the three bulk carrier transits [Note: Chart datum depths (not to scale) also shown]

An oscillation pattern in dynamic heel between each beacon in the curved section of the channel (between B18 and B10) was observed equally in all three bulk carrier transits. This repetitive pattern may be partly attributable to rudder-induced heel caused by turning manoeuvres. Such a pattern may be studied further in future work, with reference to the measured rudder changes and calculated wave-induced motions. As mentioned in 5.2.3.2, the action of tugs during unberthing operations created a considerable heel to starboard, observed in the inner harbour (before B22), for all bulk carriers.

Container ships with level static trim generally have significant heel arising from wind and turning in calm water. For example, heel angles of the order 1 to 2° were measured in container ships in Hong Kong (Gourlay, 2008a). However, bulk carriers have a relatively large displacement-to-length ratio, low KG and small above-water profile area, which translate into smaller heel angles caused by wind and turning.

5.2.4 Theoretical squat predictions

As the Port of Geraldton approach channel is a typically dredged channel in channel configurations, a differential between channel depth and the depths on either side is observed in the bathymetric data on the nautical chart (see chart AUS81): e.g., the depths on the side of the channel are approximately 3 m shallower than in the dredged channel in the longest section, with a maintained depth of 14.0 m (see Figure 5.1); a conceptual cross section of this is shown in Figure 5.7.

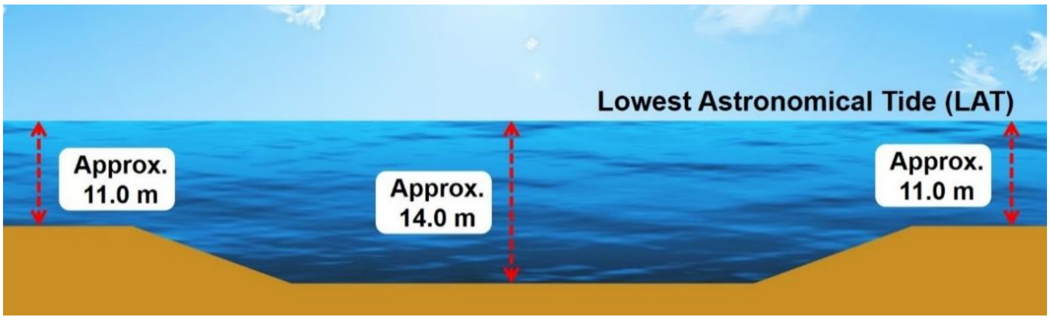

Figure 5.7. Conceptual cross section of the Port of Geraldton approach channel [Note: This view is for illustration only (not to scale)]

In Chapter 2, some port approach channels in Western Australia, including the Port of Geraldton approach channel, were assessed to see whether a particular ship and channel configuration might be classed as open water, or whether a specific narrow-channel analysis is required. For a Panamax carrier with an L_{PP} of 215 m, the sinkage coefficient for the Port of Geraldton channel was predicted within 3 % of the open-water value using the slender-body theory (see Table 2.4). For predicting ship sinkage and trim, therefore, the bulk carrier transits can be classed as open water conditions because the effect of transverse bathymetries, such as channel width and trench depth, on ships with L_{PP} of 217 and 219 m, is seen to be minimal (see Figure 2.10(b)).

5.2.4.1 Theoretical method

A theoretical method used in this chapter to compare measured sinkage and trim is based on the slender-body shallow-water theory of Tuck (1966) for open water, implemented in the computer code *SlenderFlow*. Eqs. (2.1), (2.2) and (2.3) were used to predict ship sinkage, and Eq. (2.17) dealt with the change in stern-down trim angle in radians due to squat θ. A much more detailed description of the theoretical method can be found in Chapter 2.

5.2.4.2 Ship hull forms modelled

Because stability and hydrostatic data were obtained for each ship, but not lines plans or hull offsets, a representative hull, which has similar characteristics to the practical hulls, should be chosen and modified to match the main hull parameters. For minimum modification, the other dimensionless parameters, such as C_B and LCB, should also be reasonably similar. There are a number of publicly available bulk carrier hull forms which can be used, including the Japan 1704B (Yokoo, 1966), JBC (National Maritime Research Institute, 2015), FHR Ship G (Gourlay, von Graefe, Shigunov, & Lataire, 2015; Vantorre & Journée 2003) and MARAD Ship G (Roseman, 1987). Details of the candidate ship hull forms can be found in Chapter 2.2.

The principal details of these candidates and the three bulk carriers measured are shown in Table 5.6.

Table 5.6. Details of the bulk carriers measured and candidate ship hull forms

Cases	Ships & hulls	L_{PP} (m)	Beam (m)	Draught (m)	C_B (-)	LCB (%)	LCF (%)
Bulk carriers measured	*GUO DIAN 17*	219.00	32.26	14.20 (at summer)	0.873	-	-
				12.15 (at actual)	0.859	-	-
	FENG HUANG FENG	217.00	32.26	14.22 (at summer)	0.868	-	-
				12.20 (at actual)	0.854	52.49	49.22
	SEA DIAMOND	217.00	32.26	14.08 (at summer)	0.869	51.78	48.57
				9.59 (at actual)	0.835	53.02	50.94
Candidate bulk carrier hull forms	Japan 1704B	6.00	0.923	0.334	0.801	54.93	52.16
	JBC	280.00	45.00	16.50	0.858	52.53	49.30
	FHR Ship G	180.00	33.00	11.60	0.839	53.36	51.09
	MARAD Ship G	6.096	1.219	0.406	0.768	51.53	45.33

[Note: Block coefficient (C_B) represents values at summer and actual draught for each bulk carriers measured, and at design draught for the candidate ship hull forms; LCB and LCF are given as a percentage of L_{PP} forward of the AP]

5.2.4.3 Modelling at reduced draught

Modification of the reference hull should be made to match the main hull parameters at the ship's actual transit conditions and, hence, at reduced draught. A general procedure for the modifications can be made as follows:

A representative hull is chosen, with similar ship dimensions as well as dimensionless parameters, such as C_B and LCB to each ship being modelled, e.g., the FHR Ship G.

The selected hull is scaled to the same length (L_{PP}), beam and midships draught as the ship being modelled.

Parametric transformation is done using *MAXSURF Modeler Advanced 20.00.05.47* to match the desired hull parameters and hydrostatic properties by filling out the volume fore and aft.

Based on the actual load and ballast conditions (see Table 5.2 and Table 5.6) as well as the previously mentioned procedure, two kinds of the modified FHR Ship G model were made from the supplied IGES files, one for *SEA DIAMOND* and the other for both *GUO DIAN 17* and *FENG HUANG FENG*, given the resemblance in their transit conditions (see Table 5.6). The body plan of the FHR ship G is shown in Figure 2.3(c) and its bow, stern, profile, bottom and perspective views in Figure A.10 (Appendix A).

5.2.5 Results

Comparisons between measured and calculated sinkage at midships, together with ship speed and channel bathymetry, are shown in Figure 5.8. Measured sinkage results are also shown with a low-pass filter, which is applied to remove the effect of wave-induced motions.

It is known that the theoretical method (Tuck, 1966) tends to underpredict the sinkage of cargo ships in finite-width canal model tests, especially in very narrow canals (Gourlay, 2013a; Gourlay, Lataire, & Delefortrie, 2016). No model tests approximating open-water dredged channels are available to compare with data produced in this research. In the present full-scale trials, given that the transits involved significant speed and depth changes along the channel, the overall performance of the theoretical method is quite good; but the theory (Tuck, 1966) is still seen to slightly underpredict the sinkage. The predicted midship sinkage, for speeds above 7 knots, is on average 3 % less than the filtered measurements for *GUO DIAN 17*, 11 % for *FENG HUANG FENG* and 9 % for *SEA DIAMOND*, but the measurements are swamped by wave-induced heave for *SEA DIAMOND*. However, an exact comparison is not possible because of the many uncertainties involved in applying the theory to the full-scale measurements, such as the complex bathymetry, the condition of the seabed (e.g., mud, sand, rock, seagrass or corals) and the effect of the approximated hull geometry. All these factors complicate the application of the theory.

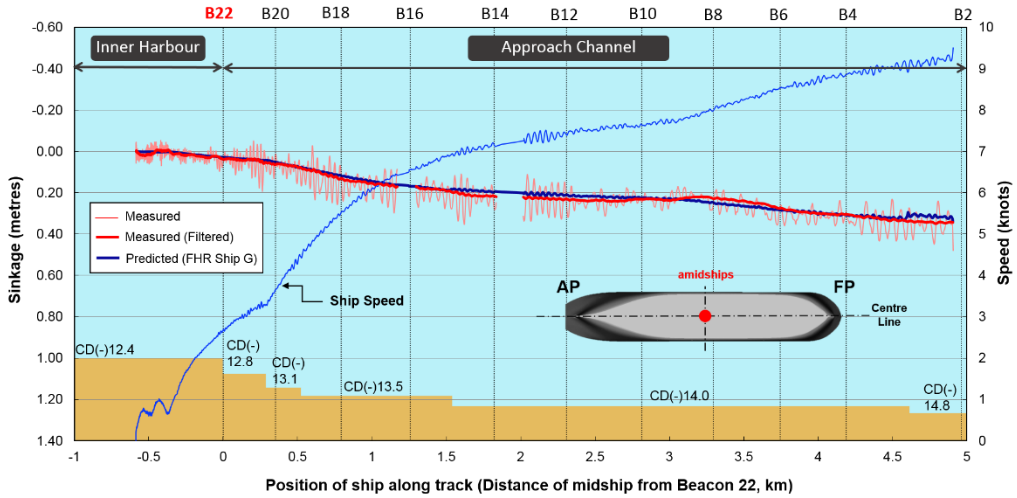

(a) *GUO DIAN 17*

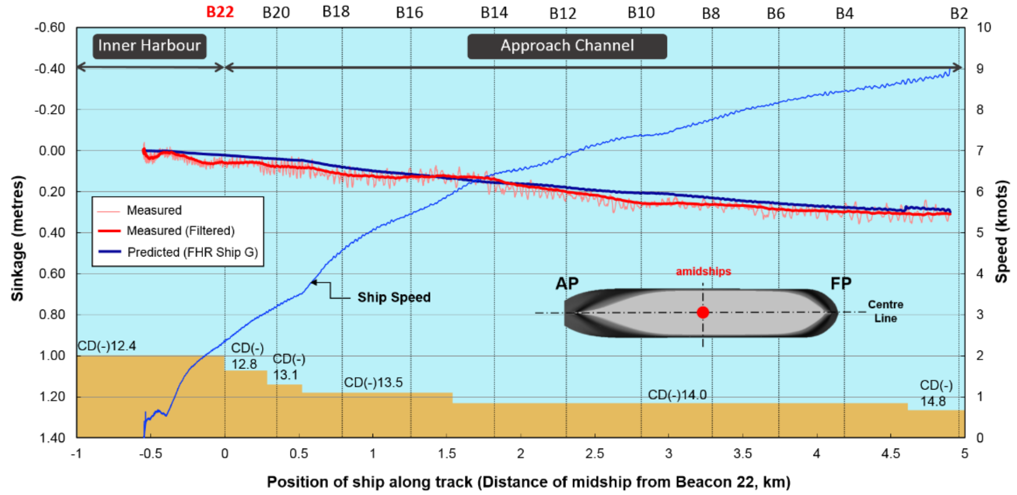

(b) *FENG HUANG FENG*

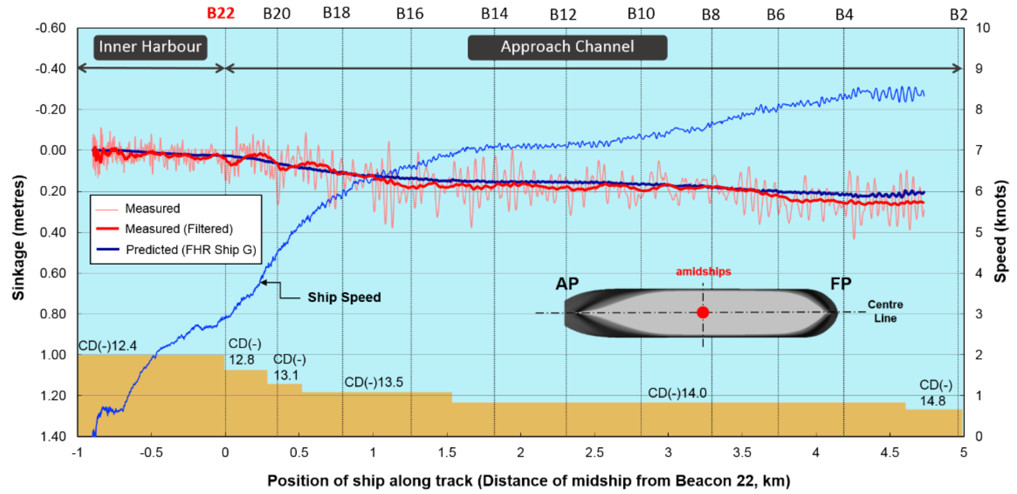

(c) *SEA DIAMOND*

Figure 5.8. Measured and calculated sinkage (positive downward) at midships: (a) *GUO DIAN 17*; (b) *FENG HUANG FENG*; (c) *SEA DIAMOND* [Note: Calculations do not include wave-induced motions; chart datum depth (not to scale) also shown]

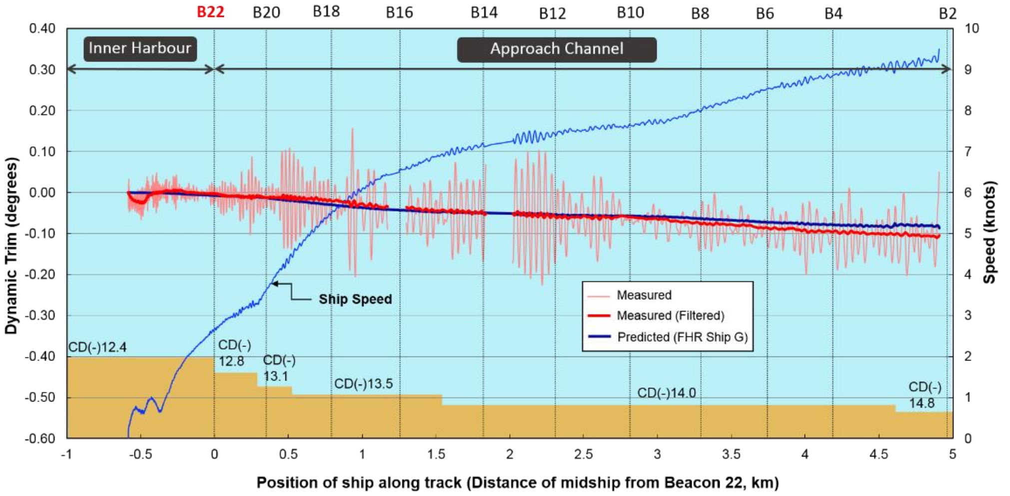

(a) *GUO DIAN 17*

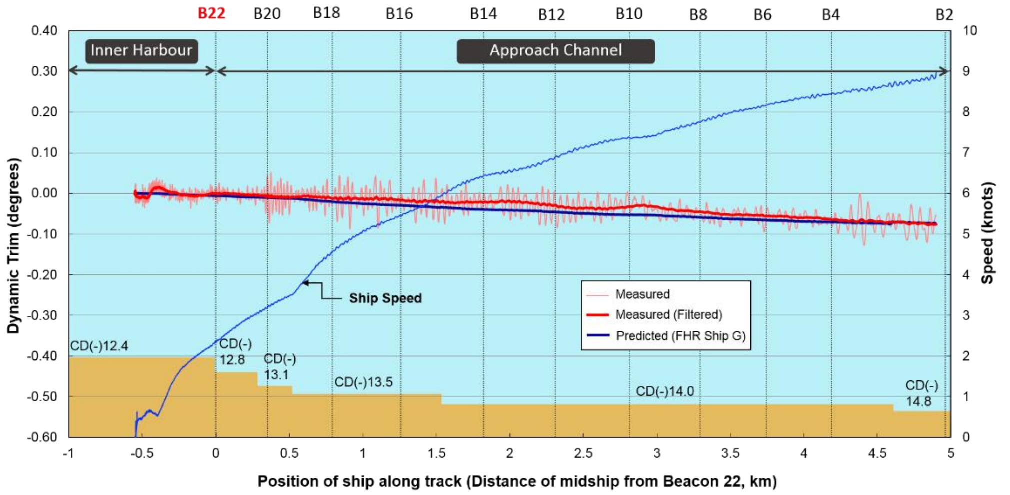

(b) *FENG HUANG FENG*

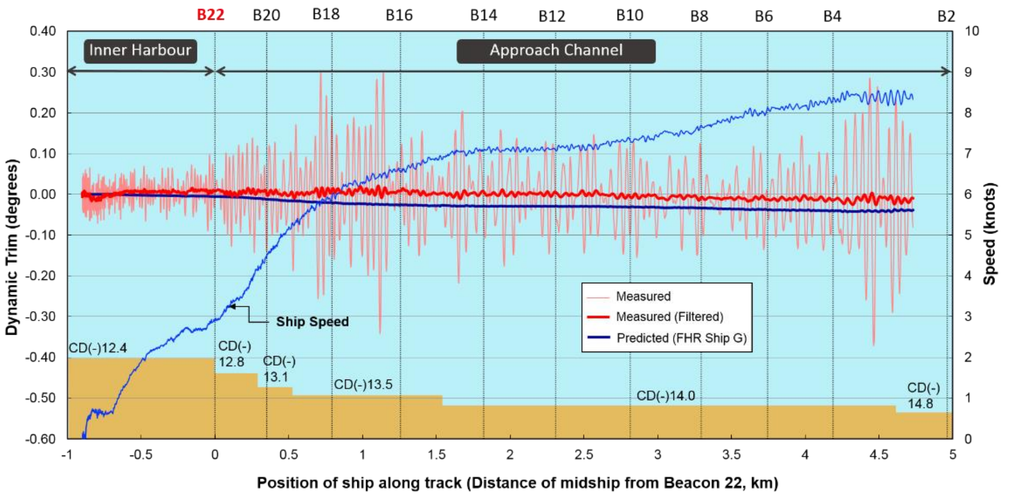

(c) *SEA DIAMOND*

Figure 5.9. Measured and calculated dynamic trim (positive stern-down): (a) *GUO DIAN 17*; (b) *FENG HUANG FENG*; (c) *SEA DIAMOND* [Note: Calculations do not include wave-induced motions; chart datum depth (not to scale) also shown]

Dynamic trim is more difficult to predict than sinkage as it is caused by the difference between large quantities: the downward force at the forward and aft shoulder, and the upward force at the bow and stern. Small changes in hull shape will change the balance between each of these. The effect of hull shape on dynamic trim is discussed in Gourlay, Ha, Mucha and Uliczka (2015). Figure 5.9 shows comparisons between measured and predicted dynamic trim. Dynamic trim is given here in degrees (°). Measured trim results are also shown with a low-pass filter, which is applied to remove the effect of wave-induced pitch.

The predicted dynamic trim is negative, so bow-down for all the bulk carrier transits using the FHR Ship G hull. In comparison with the measurements, the predicted dynamic trim for *FENG HUANG FENG* and *SEA DIAMOND* are slightly more bow-down (or less stern-down) than were measured, whereas *GUO DIAN 17* shows a predicted dynamic trim of less bow-down (or more stern-down). Considering the previously mentioned approximations of the modelled hull forms, it is found that the theoretical prediction quite closely estimates dynamic trim at full scale.

5.3 Validation of container ship squat modelling

For container ship squat modelling, the full-scale measurement results for the container ship transits in the Port of Fremantle approach channels were used. The general information about these trials is detailed in Chapter 4.3.

5.3.1 Description of the container ships and transit conditions

From on the criteria listed in 5.2.1, three Post-Panamax and two Panamax container ship transits were chosen from the total 16 container ship measurements at the Port of Fremantle: *SEAMAX STAMFORD*, built in 2015, is a Post-Panamax container ship with a capacity of 4,896 TEU; *MOL PARAMOUNT*, built in 2005, is a Post-Panamax container ship with a capacity of 6,350 TEU; *CMA CGM WAGNER*, built in 2004, is a Post-Panamax container ship with a capacity of 5,782 TEU; *SAFMARINE MAKUTU*, built in 2007, is a Panamax container ship with a capacity of 4,154 TEU; and *OOCL BRISBANE*, built in 2009, is a Panamax container ship with a capacity of 4,578 TEU.

Details of these container ships are shown in Table 5.7. Two Post-Panamax container ships, MOL PARAMOUNT and CMA CGM WAGNER, and two Panamax container ships, SAFMARINE MAKUTU and OOCL BRISBANE, have similar ship dimensions, respectively, and slightly lower CB than SEAMAX STAMFORD. Details of the five container ships and their transit conditions can be found in Table 4.9.

Table 5.7. Details of the container ships

Particulars	*SEAMAX STAMFORD*	*MOL PARAMOUNT*	*CMA CGM WAGNER*	*SAFMARINE MAKUTU*	*OOCL BRISBANE*
Ship size	Post-Panamax	Post-Panamax	Post-Panamax	Panamax	Panamax
L_{OA} (m)	250.00	293.19	277.28	292.08	260.05
L_{PP} (m)	238.35	276.00	263.00	277.00	244.80
Beam (m)	37.30	40.00	40.00	32.25	32.25
Summer draught (m)	13.00	14.02	14.52	13.52	12.60
Displacement (t)	79,702.00	99,620.00	96,997.00	82,287.00	67,248.80
C_B (-)	0.673	0.628	0.620	0.665	0.660

[Note: Displacement and C_B are values at summer draught; C_B is the ratio of displaced volume to (L_{PP}·Beam·Draught)]

Comparative transit conditions for the five container ships are shown in Table 5.8. *MOL PARAMOUNT* and *SAFMARINE MAKUTU* had level static trim, whereas *SEAMAX STAMFORD*, *CMA CGM WAGNER* and *OOCL BRISBANE* statically trimmed stern-down on their arrival, by 0.85, 1.50 and 1.04 m each.

Table 5.8. Details of the container ship transit conditions

Particulars	Post-Panamax			Panamax	
	SEAMAX STAMFORD	***MOL PARAMOUNT***	***CMA CGM WAGNER***	***SAFMARINE MAKUTU***	***OOCL BRISBANE***
Date / Time (AWST)	17/04/2016 04:27-05:47	21/04/2016 03:11-04:32	25/04/2016 04:12-05:31	20/04/2016 20:56-22:09	24/04/2016 21:05-22:16
Direction	inbound	inbound	inbound	inbound	inbound
Draught fwd. (m)	10.40	11.39	10.00	12.60	11.02
Draught aft. (m)	11.25	11.39	11.50	12.60	12.06
Arrival Disp. (t)	62,584.00	73,926.90	63,569.00	73,593.00	60,301.40
C_B (-)	0.634	0.574	0.548	0.638	0.646
LCB (m)	117.79	133.06	-	132.65	116.29
LCF (m)	111.68	126.05	-	121.22	105.89
GM_f(m)	3.88	3.87	4.51	0.81	1.00

[Note: C_B is calculated based on actual arrival draught; LCB and LCF are given as metres forward of the AP; average draught is represented for C_B, LCB and LCF; dates and times are in Australian Western Standard Time (AWST)]

5.3.2 Description of the port, channels and measured ship tracks

The layout of the Port of Fremantle, including its approach channels and navigational buoys, together with tracks of the five inbound container ships, are illustrated in Figure 5.10.

All tracks look almost analogous to each other within the Deep Water Channel, but each took a different path to the Entrance Channel and required a different turning radius to enter. Different pilotage sequences may have been required, depending on diverse loading conditions as well as changing environmental conditions. Because each pilotage was conducted by different pilots, different techniques could have also been applied.

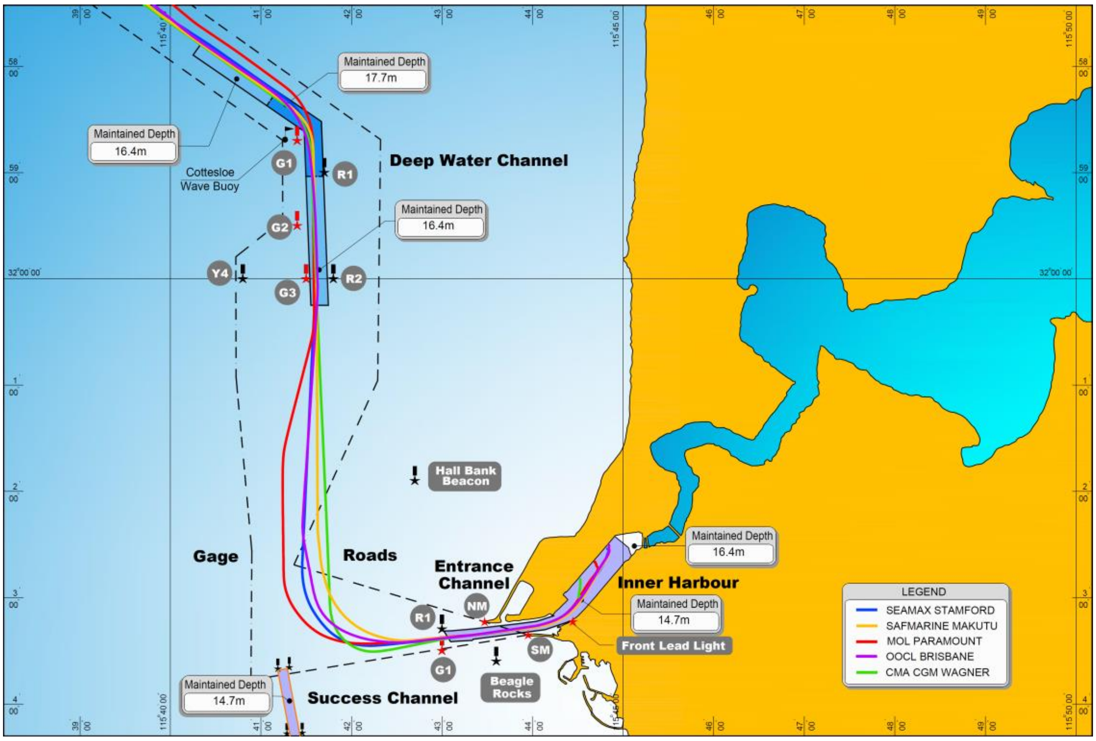

Figure 5.10. Port of Fremantle approach channels and measured midship tracks

As previously mentioned in Chapter 4.3.2, the measured tide in the Inner Harbor (32° 3.258' S, 115° 44.3718' E) of the Port of Fremantle was provided by Fremantle Ports and used to calculate the dynamic sinkage of the five container ships. The tidal datum is the same as the chart datum used in charts AUS112 and AUS113; hence, LAT at the Port of Fremantle. The tidal data covering the period of the five container ship transits is shown in Figure 5.11.

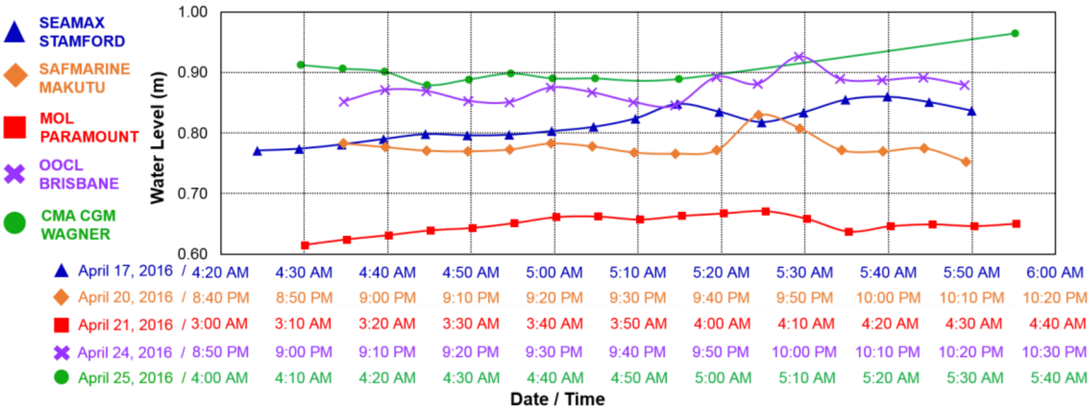

Figure 5.11. Measured tidal data during the transits

Wave data, measured at 1.28 Hz by the Cottesloe wave buoy near the G1 buoy in the Deep Water Channel (see Figure 4.17 and Figure 5.10), was provided from collaboration with the coastal infrastructure team from WADoT. Figure 5.12 shows the measured wave data for the container ship transits.

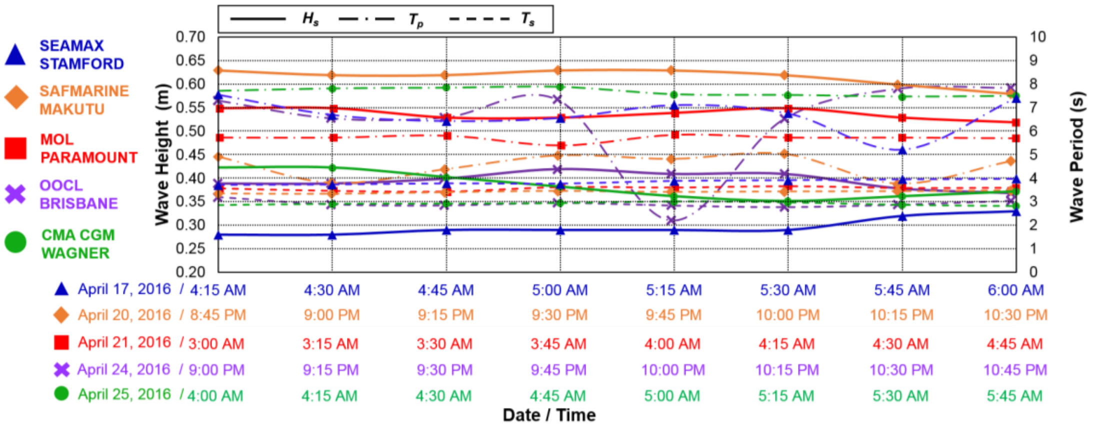

(a) Sea

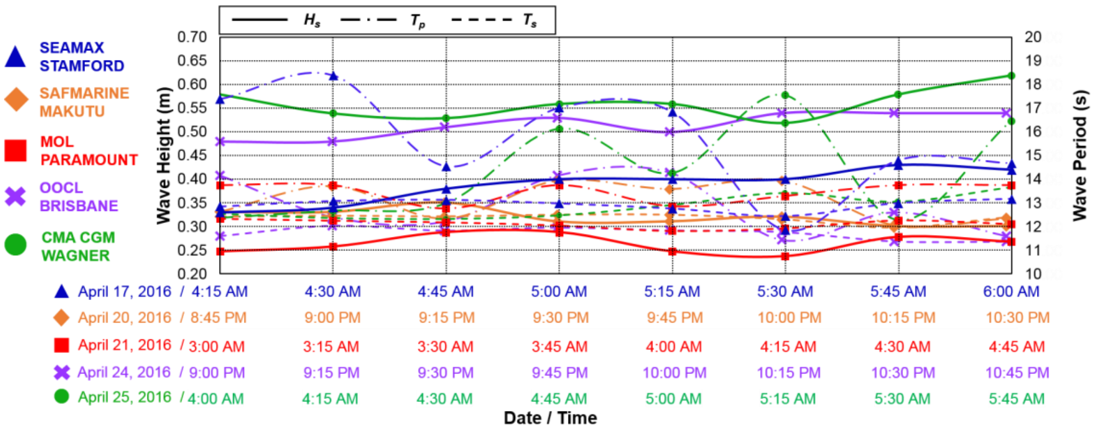

(b) Swell

Figure 5.12. Measured wave data during the transits: (a) Sea; (b) Swell [Note: Sea/swell cutoff period is 8 seconds; H_s = significant wave height; T_p = spectral peak wave period; T_s = significant wave period]

More details on the port, channels and environmental conditions, including wind, currents and water density, in the Port of Fremantle can be found in Chapter 4.3.1 and 4.3.2, and bathymetric data in Chapter 4.3.3.

5.3.3 Measured dynamic sinkage, trim and heel

5.3.3.1 Error analysis

The vertical position accuracy of the JAVAD GNSS Triumph-1 and Triumph-2 receivers is specified to be within 15 mm + 1 ppm × (baseline length) in JAVAD GNSS (2012; 2015). Expected vertical RMS errors for the container ship transits were captured in the baseline processing of the *Trimble Business Centre v3.50* software.

These were in the range of 0.011 and 0.012 m; the RMS error in the GNSS receiver's vertical position was estimated to be less than 0.012 m.

To determine geoid undulation (N) for the bulk carrier transits at the Port of Geraldton, EGM2008 geoid (Pavlis, Holmes, Kenyon, & Factor, 2012) was used with respect to WGS 84. However, for the container ship trials at the Port of Fremantle, GDA94 (the Geocentric Datum of Australia) and AUSGeoid09 (the Australia-wide gravimetric quasigeoid model) were applied to transfer between the raw GNSS heights and the AHD heights; AUSGeoid09 may be practical for determining orthometric (geoid) heights from GNSS heights in the continent of Australia, due to the coastal geodetic levelling networks (refer to Chapter 4.3.4). According to Featherstone et al. (2011), and Brown, Featherstone, Hu and Johnston (2011), an RMS error of ± 0.030 m was found when using AUSGeoid09.

The stationary reading at the berth was based on 3-minute-averaged values of the ship's vertical motion after the end of the mooring works. As was the case at the Port of Geraldton, the ships at that time still had some residual vertical movement caused by seiches in the Inner Harbour. The RMS error from each receiver on the container ships, for the last 3 minutes after completion of mooring operations, ranged from 0.009 to 0.024 m. The RMS error in the static reading was, therefore, estimated to be less than 0.024 m.

Likewise, the expected RMS error in tide gauges themselves, which is the equipment error of the tide gauge, is typically 0.010 m (Gourlay & Klaka, 2007; Verstraete, 2001).

The local tide data recorded at 5-minute intervals was linearly interpolated to find tidal elevation at 1.0 Hz, so that the resulting tidal data could be applied to the dynamic sinkage of the container ships measured at 1-second intervals. The RMS error in the interpolation method ranged between 0.006 and 0.017 m for the five container ships, and was estimated to be less than 0.017 m.

Although the end of the Deep Water Channel is approximately 6.5 nautical miles away from the gauge, the tidal data from the tide gauge in the Inner Harbour (32° 3.258' S, 115° 44.372' E) of the Port of Fremantle was used for the entire transit, including a section of the Deep Water Channel. By comparing measured tidal data from other stations near the Port of Fremantle, any error in tidal elevation due to sea surface slope can be estimated (Gourlay & Klaka, 2007). Hourly tidal observations in Hillarys Boat Harbour (31° 49.536' S, 115° 44.316' E), located about 13.5 nautical miles away from the Port of Fremantle, were provided by the National Tidal Unit (NTU) of the Australian Government Bureau of Meteorology. Because the tidal data from each tide gauge has been referenced to different vertical datums, a temporary datum should be made for putting these time series of tide observations together. It is assumed that the level of local MSL based on each datum will be the same. The difference in tidal elevation between the two stations can then be found using the level of the local MSL as a common datum.

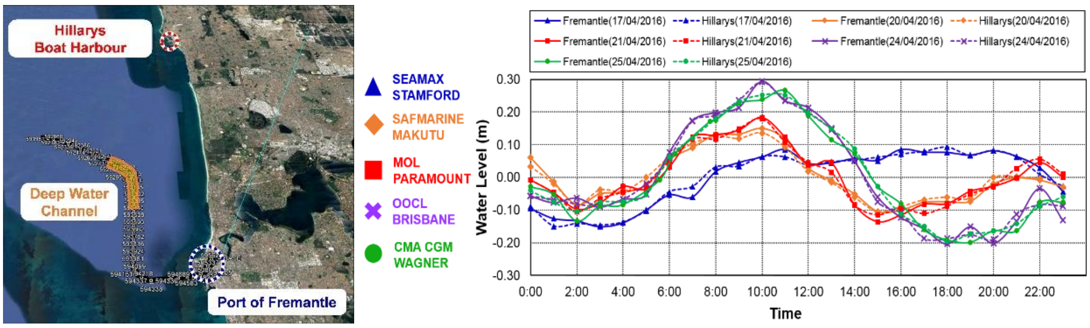

(a) (b)

Figure 5.13. Measured tidal data during the transits: (a) Geographical location of the Port of Fremantle, Hillarys Boat Harbour and Deep Water Channel (©2016 Google, Image ©2016 DigitalGlobe, Data SIO, NOAA, U.S. Navy, NGA, GEBCO); (b) Tidal elevation relative to local MSL for the Port of Fremantle and Hillarys Boat Harbour

As shown in Figure 5.13, tidal elevation relative to the local MSL for the Port of Fremantle and Hillarys Boat Harbour were compared to estimate the error. For the 5 days of the container ship trials, the RMS error of the observed tidal data from the two stations ranged from 0.013 to 0.021 m. Assuming the Deep Water Channel lies halfway between the Port of Fremantle and Hillarys Boat Harbour, the RMS error in the discrepancy of tidal elevation application is zero near the Inner Harbour and Entrance Channel, and less than 0.010 m in the Deep Water Channel.

The total estimated RMS errors inherent in calculating the dynamic sinkage of the container ship transits are 0.046 m in the Deep Water Channel and 0.045 m in the Entrance Channel and Inner Harbour, as summarised in Table 5.9.

Table 5.9. Estimated RMS errors in calculating dynamic sinkage

Error factors	**Deep Water Channel (m)**	**Entrance Channel & Inner Harbour (m)**
Error in the GNSS receivers	0.012	0.012
Error in Geoid undulation N (AUSGeoid09)	0.030	0.030
Error in the static reading at the berth	0.024	0.024
Error in the tide gauge	0.010	0.010
Error in interpolating to find tidal elevation at a particular point (at 1.0 Hz)	0.017	0.017
Error in the discrepancy of tidal elevation due to sea surface slope	0.010	-
Total	**0.046**	**0.045**

With a 95 % confidence, the actual dynamic sinkage will lie within the margin of error of ± 0.092 m in the Deep Water Channel, and ± 0.090 m in the Entrance Channel and Inner Harbour. Compared with the errors in the bulk carrier transits in the Port of Geraldton channel (see Table 5.3), a decrease in total error, mainly attributed to the error in the static reading at the berth, is found.

5.3.3.2 Dynamic sinkage

Measured sinkage, together with ship speed and channel bathymetry, for the five example container ship transits are shown in Figure 5.14 and Figure 5.15. Sinkage is given at the FP, AP, and port and starboard bilge corners (see Figure 4.24). More details on the sinkage results, e.g., the definition of the dynamic sinkage and the way for determining the positions of the four points of the container ships, can be found in Chapter 4.3.5.2.

Note that gaps in the results of some transits, like *SAFMARINE MAKUTU* (see Figure 5.15(a)), are because some GNSS fixes were of insufficient quality and have been rejected (see Appendix C for more information).

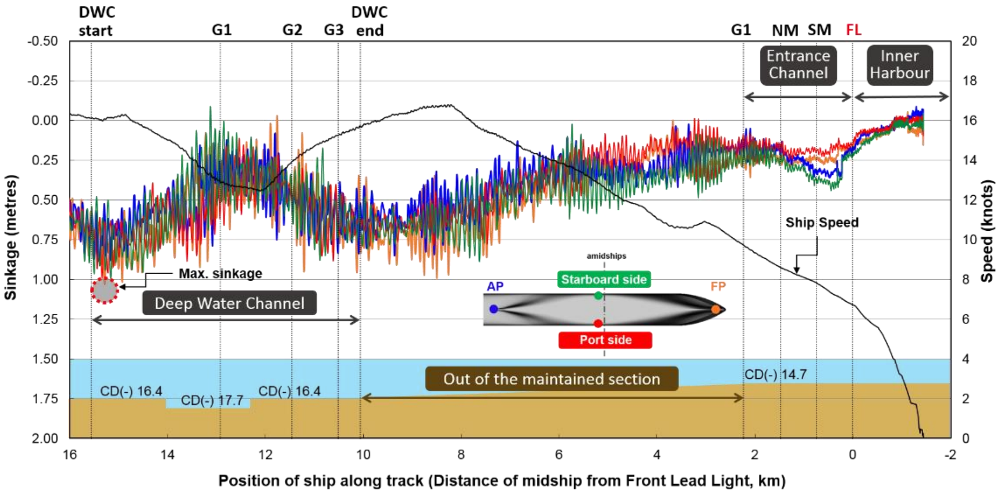

(a) *SEAMAX STAMFORD*

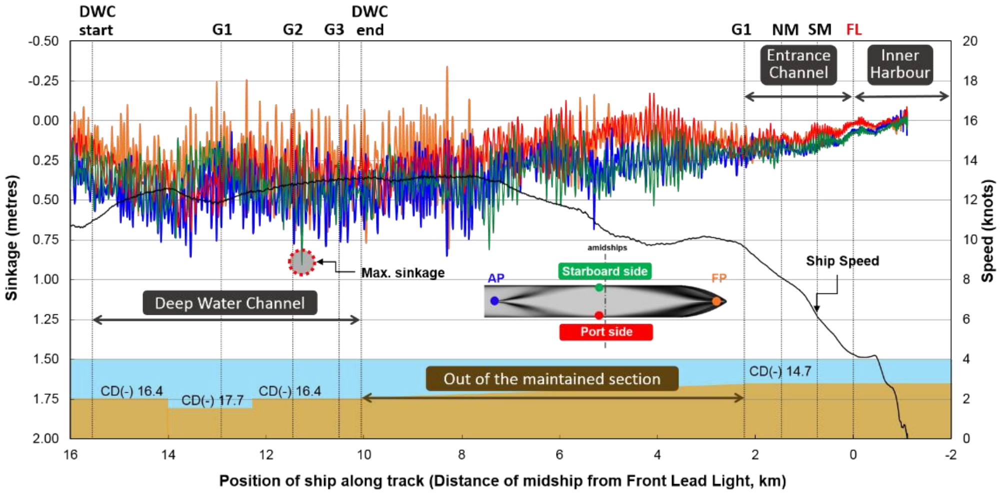

(b) *MOL PARAMOUNT*

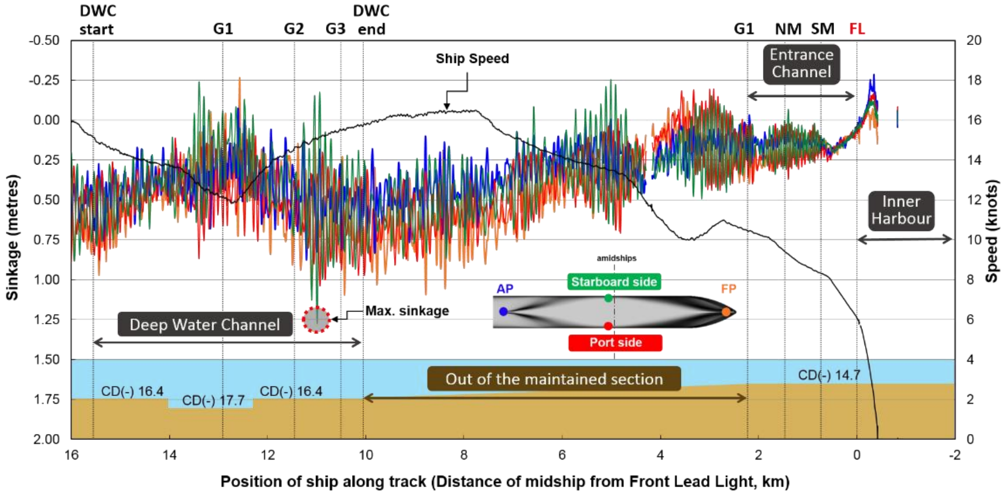

(c) *CMA CGM WAGNER*

Figure 5.14. Measured sinkage (positive downward) at four points for the three Post-Panamax container ships: (a) *SEAMAX STAMFORD*; (b) *MOL PARAMOUNT*; (c) *CMA CGM WAGNER* [Note: Chart datum depths (not to scale) also shown]

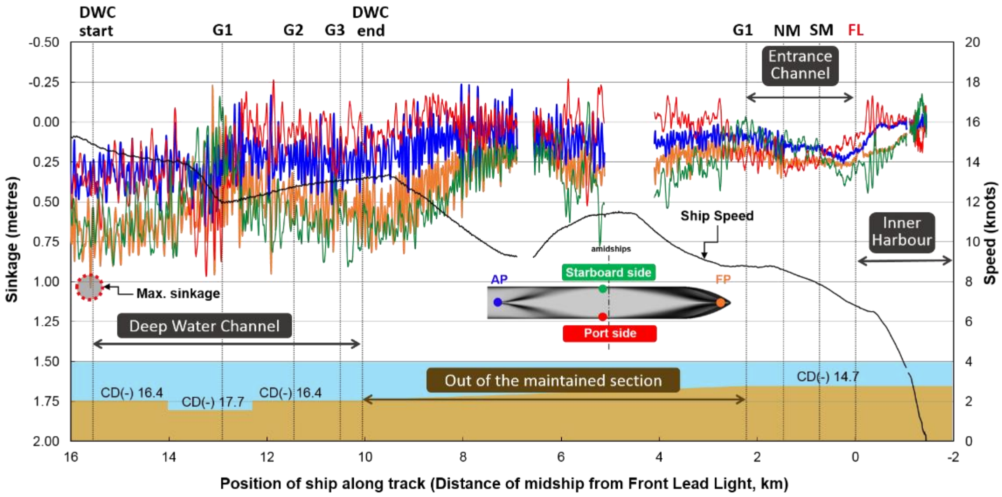

(a) *SAFMARINE MAKUTU*

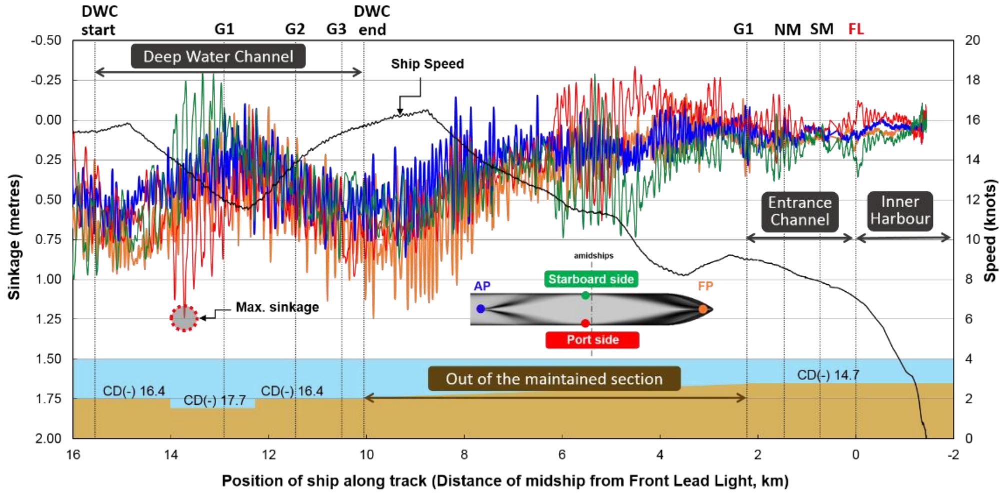

(b) *OOCL BRISBANE*

Figure 5.15. Measured sinkage (positive downward) at four points for the two Panamax container ships: (a) *SAFMARINE MAKUTU*; (b) *OOCL BRISBANE* [Note: Chart datum depths (not to scale) also shown]

Figure 5.14 and Figure 5.15 clearly show the effect of ship speed on sinkage. However, in the trials at the Port of Fremantle, the speed of the five container ships and the water depth decreased simultaneously in the deepest part of the Deep Water Channel, around the G1 buoy; this meant that another important correlation between the sinkage and water depth is not independently captured. The container ships all may have required decreasing their speed for turning manoeuvres in this curved section of the channel (see also Figure 5.10). As mentioned in Chapter 4.3.1.1, water depth in the unmaintained section (between the Deep Water Channel and Entrance Channel) is uncertain, and no detailed bathymetric survey data is available. According to charts AUS 112 and 113, water depth in that section is seen to be quite erratic, ranging from about 15 to 20 m, so no interpretation of the correlation between the sinkage and water depth in the section can be made.

Maximum sinkage was observed at the starboard bilge corner in the area between the G2 and G3 buoys of the Deep Water Channel for *MOL PARAMOUNT* and *CMA CGM WAGNER*. Maximum sinkage occurred at the bow near the starting point of the Deep Water Channel for *SEAMAX STAMFORD* and *SAFMARINE MAKUTU*. *SEAMAX STAMFORD* and *SAFMARINE MAKUTU* also had large sinkage and oscillations, close to their maximum values, near the G2 buoy. This may result from the combined effect of residual heel oscillations caused by rudder application and rate of turn (Gourlay, 2008a), and dynamic trim caused by acceleration (Ferguson & McGregor, 1986; Hatch, 1999), because a change in rudder application, as well as an acceleration in ship speed, were made in this part of the channel at the end of the turn (see Figure 5.10). *OOCL BRISBANE* had its maximum sinkage at the port bilge corner around the G1 buoy in the Deep Water Channel due to a relatively larger heel angle during her turning, which will be explained subsequently.

The *SEAMAX STAMFORD*, *CMA CGM WAGNER* and *OOCL BRISBANE* transits had similar ship speeds during their pilotage and a similar trend in their vertical motions. Because the *CMA CGM WAGNER* and *OOCL BRISBANE* transits took place in a relatively larger and longer period of swell conditions (see Figure 5.12(b)), highly oscillatory vertical motions due to their wave-induced motions are seen in the result. Sinkage results for the container ship transits can be found in Table 4.12.

SEAMAX STAMFORD had a maximum sinkage at the bow, and the other four at the bilge corners. However, for a ship with static stern-down trim, like *SEAMAX STAMFORD*, *CMA CGM WAGNER* and *OOCL BRISBANE* (see Table 5.8), the FP or bilge corners with the maximum sinkage may not be the closest point to the seabed. The stern can still have maximum dynamic draught as it is already close to the seabed. The point on the ship with the maximum dynamic draught is the point most likely to hit the bottom: the AP for S*EAMAX STAMFORD*, *CMA CGM WAGNER* and *OOCL BRISBANE*, and the starboard bilge corner for *MOL PARAMOUNT* and *SAFMARINE MAKUTU*, as shown in Table 4.12. Definitions of the dynamic draught and dynamic draught increase, as well as their applications, can be found in Chapter 4.2.5.2.

For practical UKC management, in Appendix C (C.2), Figure C.12(b) for *SEAMAX STAMFORD*, Figure C.15(b) for *SAFMARINE MAKUTU*, Figure C.16(b) for *MOL PARAMOUNT*, Figure C.17(b) for *OOCL BRISBANE* and Figure C.18(b) for *CMA CGM WAGNER* show the ships' vertical positions relative to the chart datum, so that the port may know the actual real-time clearance from the seabed. In addition, Table 5.10 shows an example calculation of sinkage and real-time UKC for *SEAMAX STAMFORD* at the time of maximum measured sinkage, showing its FP (see Table 4.12) in the section of the Deep Water Channel with the water depth of 16.4 m (see Figure 5.10 and Figure 5.14(a)). Again, it is confirmed that maximum sinkage at the FP does not give maximum dynamic draught because the AP has a larger static draught.

Table 5.10. Example calculation of sinkage and real-time UKC for *SEAMAX STAMFORD*

Calculations		Components	FP	AP	Note
Sinkage calculation	A	Static draught	10.40 m	11.25 m	-
	B	Tide elevation at berth	(+) 0.85 m CD	(+) 0.85 m CD	-
	C	Keel elevation at berth	(-) 9.55 m CD	(-)10.40 m CD	B-A
	D	Bow GNSS receiver elevation at berth	(+) 17.71 m CD	-	-
	E	Bow GNSS receiver elevation underway	(+) 16.61 m CD	-	-
	F	Bow sinkage relative to chart datum	1.10 m	-	D-E
	G	Tide elevation underway	(+) 0.78 m CD	(+) 0.78 m CD	-
	H	Sinkage relative to free surface water level	1.03 m	0.88 m	F+G-B
Real-time UKC calculation	I	Dynamic draught	11.43 m	12.13 m	A+H
	J	Water depth underway	(-) 16.40 m CD	(-) 16.40 m CD	-
	K	Real-time UKC	5.75 m	5.05 m	(G-I)-J

The minimum real-time clearance in each section of varying water depth can then be captured by the earlier calculation. Calculated minimum real-time clearance in the

Deep Water Channel, Entrance Channel and Inner Harbour, as well as the keel point at which it occurs, can be found in Table 4.13.

For the ships trimmed by the stern at arrival time, the *SEAMAX STAMFORD*, *CMA CGM WAGNER* and *OOCL BRISBANE*, the AP is the closest point to the seabed in both channels; but *MOL PARAMOUNT* and *SAFMARINE MAKUTU*, with level static trim (see Table 5.8) have their minimum UKC at the starboard bilge corner or FP.

5.3.3.3 Dynamic trim

Here, the dynamic trim is the ship's total change in trim (positive stern-down) relative to the static floating position, which includes wave-induced pitch (Gourlay, 2008a). So that trim is not swamped by wave-induced pitch, a low-pass filter with a cutoff period of 5 minutes was applied to the dynamic trim results. Measured dynamic trim for the five container ship transits is shown in Figure 5.16.

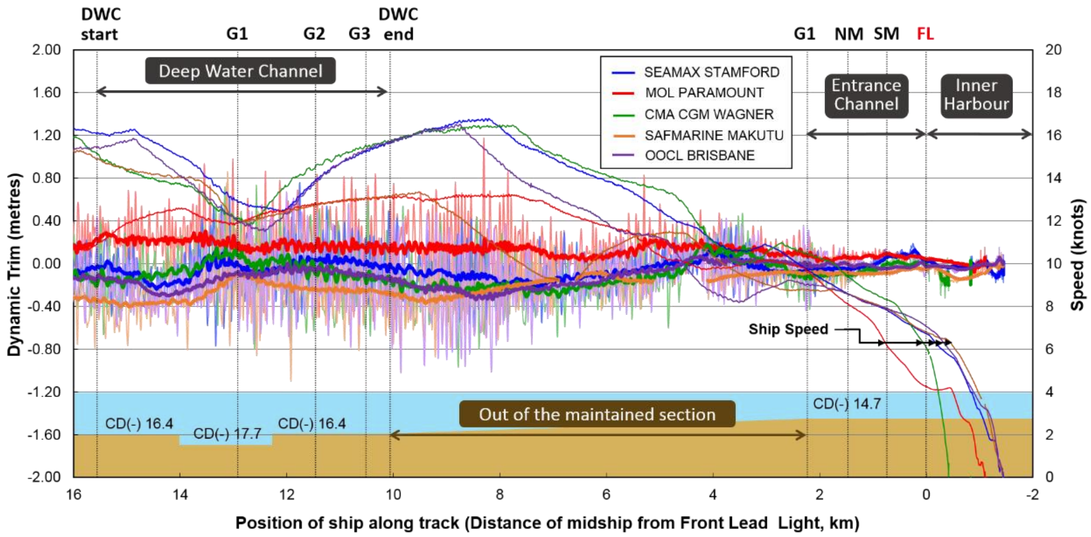

Figure 5.16. Measured dynamic trim (positive stern-down) for the five container ship transits [Note: Chart datum depths (not to scale) also shown]

Model-scale tests (Dand & Ferguson, 1973; Gourlay, 2006; Gourlay, Lataire, & Delefortrie, 2016) and full-scale tests (Gourlay, 2008c; Ha, Gourlay, & Nadarajah, 2016; Härting, Laupichler, & Reinking, 2009) show that bulk carriers have a tendency to trim by the bow when underway. No such tendency in trim is seen in container ships, e.g., Gourlay, Ha, Mucha and Uliczka (2015) and Uliczka and Kondziella (2006) for model-scale test results; Gourlay (2008a), and Gourlay and Klaka (2007) for full-scale test results, around half of which trimmed bow-down and half stern-down. In the full-scale trials at the Port of Fremantle, *SEAMAX STAMFORD*, *CMA CGM WAGNER*, *SAFMARINE MAKUTU* and *OOCL BRISBANE* generally trimmed bow-down, and *MOL PARAMOUNT* stern-down. The maximum unfiltered dynamic trims are 0.77 m by the bow for *SEAMAX STAMFORD*, 1.17 m by the stern for *MOL PARAMOUNT*, 0.97 m by the bow for *CMA CGM WAGNER*, 1.16 m by the bow for *SAFMARINE MAKUTU* and 1.02 m by the bow for *OOCL BRISBANE*. These values correspond to 0.32, 0.42, 0.37, 0.42 and 0.42 % of their L_{PP}, respectively.

Gourlay and Klaka (2007) showed that container ships that are full-scale tested have little dynamic trim in most cases. This is evidenced by comparing the results of dynamic trim in 5.2.3.3, based on the full-scale measurements of the bulk carriers. For example, an average dynamic trim for the three bulk carriers at their speeds between 8 and 9 knots was approximately 0.21 m (see Figure 5.5), whereas that of the five container ships in the Port of Fremantle trials in the same speed range was 0.04 m, which was the average absolute value of the filtered data. However, container ships tend to travel faster than bulk carriers. The maximum filtered results of the Post-Panamax container ships are 0.24 m at the speed of 16 knots for *SEAMAX STAMFORD*, 0.30 m at the speed of 12 knots for *MOL PARAMOUNT* and 0.31 m at the speed of 15 knots for *CMA CGM WAGNER*. For the other Panamx container ships, the near-steady component due to squat was comparatively larger than those of the Post-Panamax ships: e.g., maximum filtered value of 0.40 m at the speed of 14 knots for *SAFMARINE MAKUTU* and 0.34 m at the speed of 16 knots for *OOCL BRISBANE*.

Dynamic trim seems to be affected by turning manoeuvres: the *SEAMAX STAMFORD*, *CMA CGM WAGNER*, *SAFMARINE MAKUTU* and *OOCL BRISBANE* cases showed increases in dynamic stern-down trim when the turn was made, near the G1 buoy in the Deep Water Channel and around 2 km away from the G1 buoy of the Entrance Channel. This effect was also witnessed in Hong Kong container ship trials (Gourlay, 2008a). As explained earlier, however, the measured dynamic trim in the vicinity of the G1 buoy in the Deep Water Channel was affected by changes in both ship speed and water depth.

5.3.3.4 Dynamic heel

Figure 5.17 presents measured dynamic heel for the five container ship transits. Again, dynamic heel means the ship's total change in heel (positive to starboard), relative to the static floating position, which includes wave-induced roll (Gourlay, 2008a). Results are also shown with the low-pass filter applied to remove the effect of wave-induced roll.

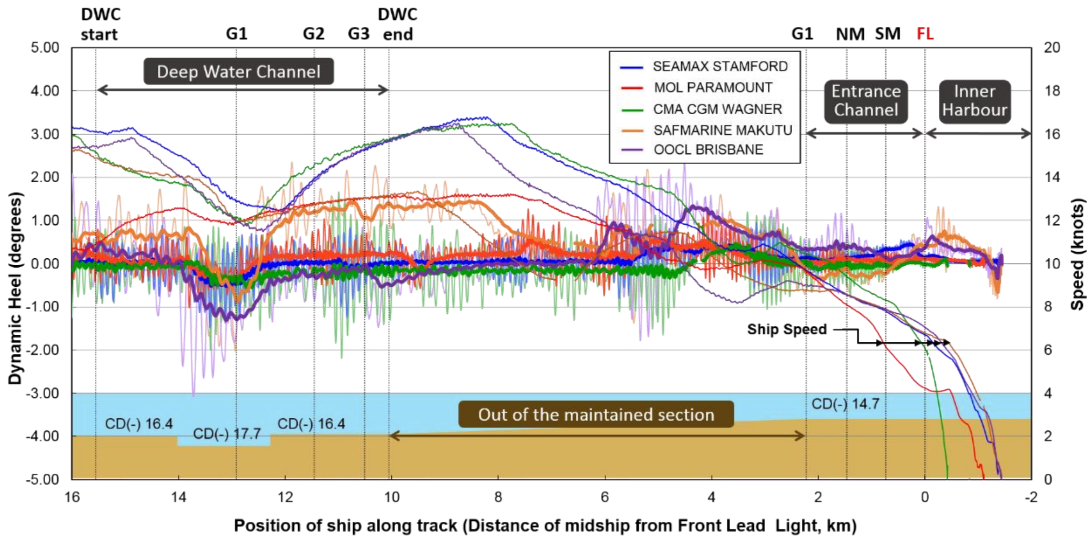

Figure 5.17. Measured dynamic heel (positive to starboard) for the five container ship transits [Note: Chart datum depths (not to scale) also shown]

Because container ships generally have a small displacement-to-length ratio, high KG and low GM, large heel angles are caused by turning and wind (Gourlay & Klaka, 2007). Furthermore, resonant rolling can occur if the wave encounter period is close to a ship's natural roll period. This means that dynamic heel may be the most important factor governing maximum sinkage for container ships, as it can bring the bilge corners closest to the seabed. Calculated natural roll periods (T_ϕ) of the container ships using Eq. (4.1), together with the wave data measured during each transit, can be found in Table 4.14.

For the container ships measured here, it can be confirmed that the influence of dynamic heel on the sinkage overwhelms that of dynamic trim by comparing the results of dynamic heel with the measured dynamic sinkage (see Figure 5.14 for the Post-Panamax ships and Figure 5.15 for the Panamax ships). *SEAMAX STAMFORD* and *MOL PARAMOUNT* had heel angles generally of the order 0.5–1.5°, the range of which can cause one of the bilge corners to be closer to the seabed by 0.16–0.49 m for *SEAMAX STAMFORD* with the beam of 37.3 m, and 0.17–0.52 m for *MOL PARAMOUNT* with the beam of 40 m. Of the Post-Panamax ship transits, *CMA CGM WAGNER* travelled in the largest swell conditions (see Figure 5.12) and had the largest heel oscillation angle, more than 2°. A measured maximum heel angle of 2.2° brings the bilge corner 0.77 m closer to the seabed for the 40-metre beam *CMA CGM WAGNER*. Much larger heel angles are seen in the two Panamax container ship transits. For example, *OOCL BRISBANE* with the beam of 32.25 m had significant dynamic heel angles up to 3.1°, which can draw the bilge corner 0.87 m closer to the seabed. This is primarily due to the combined effects of heel changes caused by turning manoeuvres and its wave-induced roll. The *SAFMARINE MAKUTU* case had had an initial heel angle of on average 0.6° to starboard before the ship entered the Deep Water Channel.

The effect of turning manoeuvres on dynamic heel was confirmed by the measurements. All transits had considerable heel angles to port when the ships turned to starboard around the G1 buoy in the Deep Water Channel, and another set of larger heel angles to starboard when they made turns to port before entering the Entrance Channel. Because *SAFMARINE MAKUTU* and *OOCL BRISBANE* had low GM on their arrival (see Table 5.8), much larger heel angles caused by turning manoeuvres were observed. The PIANC guidelines (2014) offer standard methods for calculating heel angles due to turning (ϕ_R) and wind (ϕ_W). The heel angle due to ship turning (ϕ_C) according to PIANC (2014) is estimated by

$$\phi_C = \frac{l_R {U_C}^2}{g R_C \overline{GM}} \tag{5.1}$$

where l_R = heel moment arm due to ship turning; U_C = ship speed at steady turning; and R_C = steady turning radius. The maximum heel angle due to ship turning (ϕ_R) is then given as

$$\phi_R = \phi_{MAX} = C_\phi \phi_C \tag{5.2}$$

where the coefficient (C_ϕ) depends on the magnitude of rudder angle and ranges between 1.3 and 1.7 for turning with rudder angle of 10 to 20°, respectively.

To create a comparison and validation of this method with the measured dynamic heel, a maximum heel angle during each transit's turning around the G1 buoy in the Deep Water Channel was captured from the filtered results excluding the effect of wave-induced roll (refer to thicker lines in Figure 5.17). Most of the container ship transits were travelled with calm wind conditions (see Table 4.11) at the full-scale trials, so heel angle due to ship turning (ϕ_R) would have made the dominant contribution to the total heel angle with little contribution from wind; heel angle due to wind (ϕ_W) will not be considered at this stage. Comparisons between measured and calculated maximum heel angles due to ship turning (ϕ_R) are shown in Table 5.11.

Table 5.11. Measured and calculated heel angle due to turning manoeuvres

Max. heel angle (ϕ_R)	Post-Panamax			Panamax	
	SEAMAX STAMFORD	*MOL PARAMOUNT*	*CMA CGM WAGNER*	*SAFMARINE MAKUTU*	*OOCL BRISBANE*
Measurement	0.52°	0.37°	0.56°	1.38°	1.31°
Prediction	0.59°	0.61°	0.62°	2.49°	1.44°

[Note: Maximum values are calculated and captured for ship turning around the G1 buoy in the Deep Water Channel; Measured heel angles are results with the low-pass filter]

In general, the method in the PIANC guidelines slightly overpredicts the maximum heel angle due to turning manoeuvres, but is seen to offer good predictions as a conservative method, in that the predicted maximum heel angles are on average 36 % larger than the measured results. Note that measured turning radius for each transit was used in the calculation: 1,140 m for *SEAMAX STAMFORD*; 1,240 m *MOL PARAMOUNT*; 1,130 m for *CMA CGM WAGNER*; 1,030 m for *SAFMARINE MAKUTU*; and 1,500 m for *OOCL BRISBANE*.

A more detailed description of each method, i.e., heel angle due to ship turning (ϕ_R) and wind forces (ϕ_W), can be found in PIANC (2014).

5.3.4 Theoretical squat predictions

Because the Deep Water Channel and the Entrance Channel have different channel depths, depths on the side of the channel and channel width, the relevant channel dimensions for predicting sinkage and trim need to be taken into account.

Chapter 2 showed how sinkage coefficients are affected by varying channel width, channel depth and side depth. Based on the results in Chapter 2 (see Figures 2.10 and 2.11), with a Post-Panamax container ship (L_{PP} 260m), as in the ships analysed in this chapter, the maximum sinkage coefficient for the Deep Water Channel was predicted within 1 % of the open-water value (see Table 2.4), whereas that for the Entrance Channel was predicted to be within 10–15 % of the open-water value. For theoretical squat predictions, therefore, the transits can be classed as open-water conditions for the Deep Water Channel and dredged channel conditions for the Entrance Channel. Conceptual cross-sections of the channels are shown in Figure 5.18.

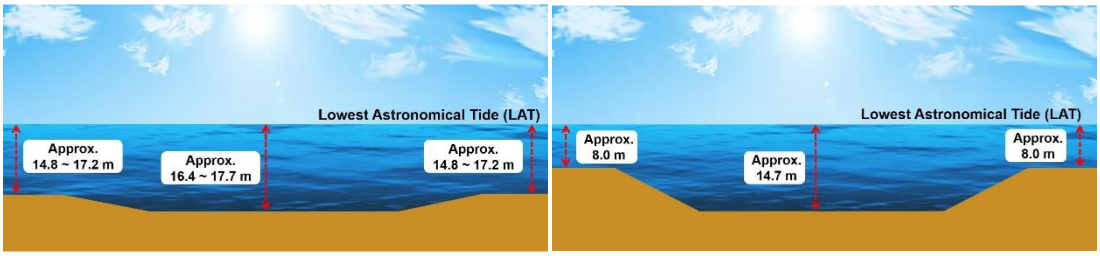

(a) (b)

Figure 5.18. Conceptual cross section: (a) Deep Water Channel; (b) Entrance Channel [Note: These views are for illustration only (not to scale)]

5.3.4.1 Theoretical method

The sinkage at midships (midway of L_{PP}) and the change in stern-down trim due to squat are predicted using the slender-body shallow-water theory of Tuck (1966) for open water and Beck, Newman and Tuck (1975) for dredged channels, generalised in Gourlay (2008b) and implemented in the computer code *SlenderFlow*. A detailed description of the theoretical methods can be found in Chapter 2. For wide channels, the slender-body theory has been shown to give good results for container ships at both model scale (Gourlay, Ha, Mucha, & Uliczka, 2015) and full scale (Gourlay, 2008a).

5.3.4.2 Ship hull forms modelled

Without lines plans or exact hull offsets, published representative ship models that have characteristics similar to the practical hulls should be selected for the theoretical predictions. There are a number of publicly available container ship hull forms, including the DTC (el Moctar, Shigunov, & Zorn, 2012), KCS (Lee, Koh, & Lee, 2003), JUMBO (Uliczka, Kondziella, & Flügge, 2004), MEGA-JUMBO (Uliczka, Kondziella, & Flügge, 2004), FHR Ship D and FHR Ship F (Gourlay, von Graefe, Shigunov, & Lataire, 2015; Vantorre & Journée 2003). Details of the candidate ship hull forms can be found in Chapter 2.2.

The principal details of these candidates and the five container ships measured are shown in Table 5.12.

Table 5.12. Details of the container ships measured and candidate ship hull forms

Cases	Ships & hulls	L_{PP} (m)	Beam (m)	Draught (m)	C_B (-)	LCB (%)	LCF (%)
Container ships measured	*SEAMAX STAMFORD*	238.35	37.30	13.00 (at summer)	0.673	48.64	44.75
				10.83 (at actual)	0.634	49.42	46.86
	MOL PARAMOUNT	276.00	40.00	14.02 (at summer)	0.628	47.17	42.87
				11.39 (at actual)	0.574	48.21	45.67
	CMA CGM WAGNER	263.00	40.00	14.52 (at summer)	0.620	-	-
				10.75 (at actual)	0.548	-	-
	SAFMARINE MAKUTU	277.00	32.25	13.52 (at summer)	0.665	47.50	42.99
				12.60 (at actual)	0.638	47.89	43.76
	OOCL BRISBANE	244.80	32.25	12.60 (at summer)	0.660	46.97	42.62
				11.54 (at actual)	0.646	47.50	43.26
Candidate container ship hull forms	DTC	355.00	51.00	14.50	0.660	49.04	45.38
	KCS	230.00	32.20	10.80	0.650	48.52	44.33
	JUMBO	320.00	40.00	14.50	0.721	49.30	45.84
	MEGA-JUMBO	360.00	55.00	16.00	0.681	49.97	49.12
	FHR Ship D	291.13	40.25	15.00	0.604	47.05	44.54
	FHR Ship F	190.00	32.00	11.60	0.600	47.74	45.43

[Note: Block coefficient (C_B) represents values at summer and actual draught for each container ship measured, and at design draught for the candidate ship hull forms; LCB and LCF are given as a percentage of L_{PP} forward of the AP]

The KCS was chosen for the *SEAMAX STAMFORD*, *SAFMARINE MAKUTU* and *OOCL BRISBANE* transits, and the FHR Ship D for both the *MOL PARAMOUNT* and *CMA CGM WAGNER* transits. A minimum modification was a priority in selecting the reference hull for each transit. Changing ship hull shape has a significant effect on trim but a relatively small effect on sinkage (Gourlay, Ha, Mucha, & Uliczka, 2015; Ha & Gourlay, 2017; Uliczka & Kondziella, 2006).

Modifications of the selected reference hulls were made to match the main hull parameters at the ships' actual load and ballast conditions (see Table 5.8 and Table 5.12). As a result, five ship models were made from the supplied IGES files: three model ships using the KCS for *SEAMAX STAMFORD*, *SAFMARINE MAKUTU* and *OOCL BRISBANE*; and two different model ships using the FHR Ship D for *MOL PARAMOUNT* and *CMA CGM WAGNER*. A detailed procedure for the modifications can be found in 5.2.4.3. Body plans of the KCS and FHR ship D are shown in Figures 2.1(b) and (e), respectively; and their bow, stern, profile, bottom and perspective views are shown in Figures A.2 and A.5 in Appendix A.

5.3.5 Results

Comparisons between measured and calculated sinkage at midships, together with ship speed and channel bathymetry, are shown in Figure 5.19 and Figure 5.20. Measured sinkage results are also shown with a low-pass filter, which is applied to remove the effect of wave-induced motions.

According to Gourlay, Ha, Mucha and Uliczka (2015), the rectangular-canal slender-body theory (Tuck, 1967) predicts the sinkage very close to the model test results for the wide-canal cases in which channel effects are minimal, but underpredicts it in narrow canals. Note that no model tests approximating open-water dredged channels are available for comparison. In this thesis, the predictions with the full-scale test results show that the measured midship sinkage agrees quite well with the predicted midship sinkage, especially, in the Deep Water Channel which is classed as open water. For example, the predicted midship sinkage for the two Panamax container ship transits (see Figure 5.20) was very consistent with the filtered measurements; the average overprediction of less than 1 % was found for each transit.

However, Tuck's (1966) theory is seen to slightly overpredict sinkage for the three Post-Panamax container ship transits on the whole. The predicted midship sinkage within the Deep Water Channel is, on average, 7 % larger than the filtered measurements for *SEAMAX STAMFORD*, 5 % for *MOL PARAMOUNT*, 14 % for *CMA CGM WAGNER*. This is contrary to the results in Gourlay (2008a), in which the theoretical method (Tuck, 1966) generally underpredicts the sinkage. That underprediction was at least partly due to depth variations transverse to the ships' track that were not accounted for.

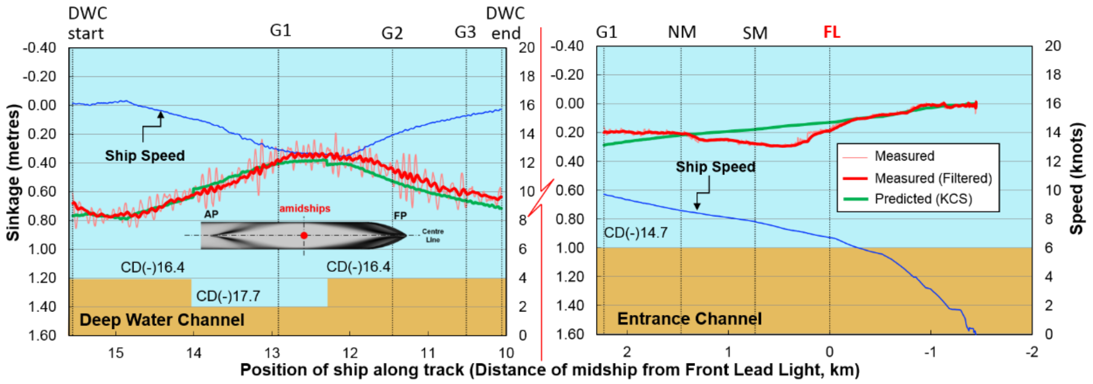

(a) *SEAMAX STAMFORD*

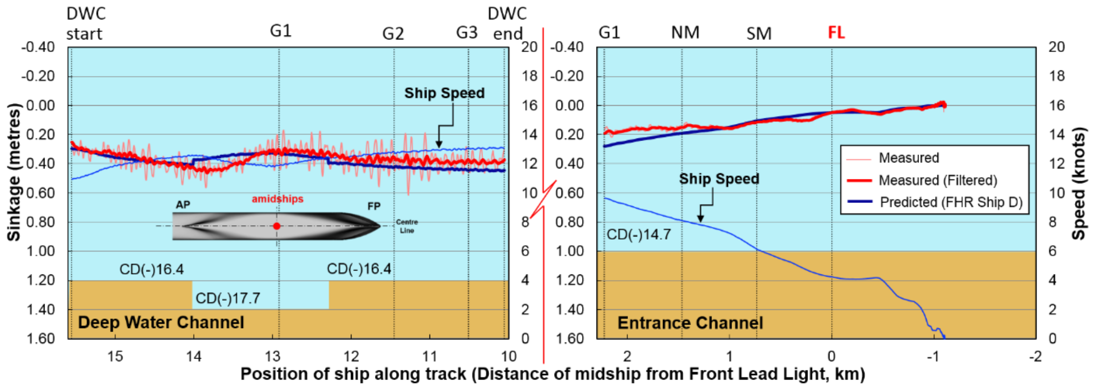

(b) *MOL PARAMOUNT*

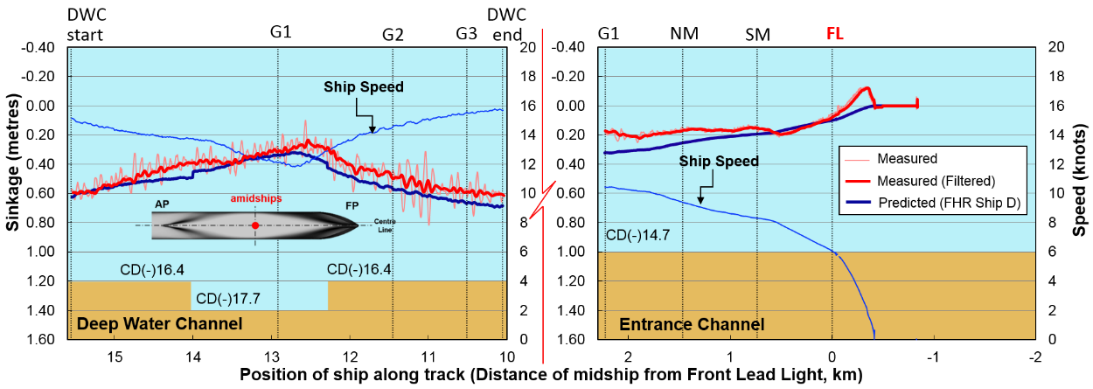

(c) *CMA CGM WAGNER*

Figure 5.19. Measured and calculated sinkage (positive downward) at midships for the three Post-Panamax container ships: (a) *SEAMAX STAMFORD*; (b) *MOL PARAMOUNT*; (c) *CMA CGM WAGNER* [Note: Calculations do not include wave-induced motions; chart datum depth (not to scale) also shown]

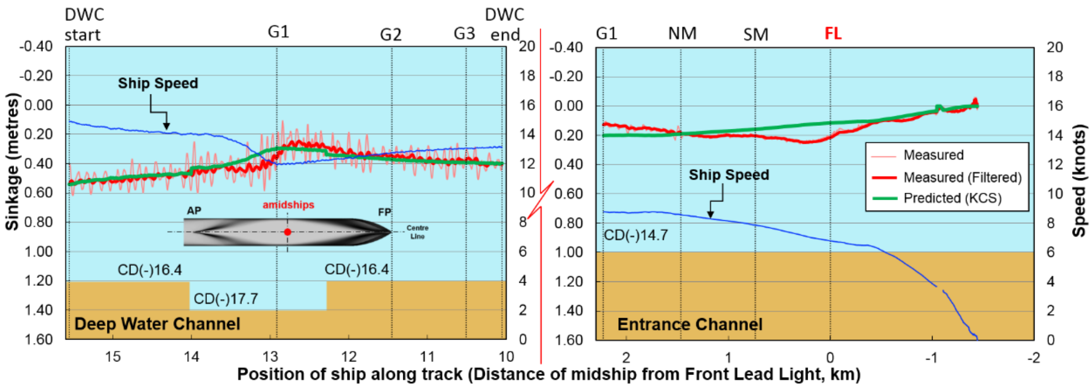

(a) *SAFMARINE MAKUTU*

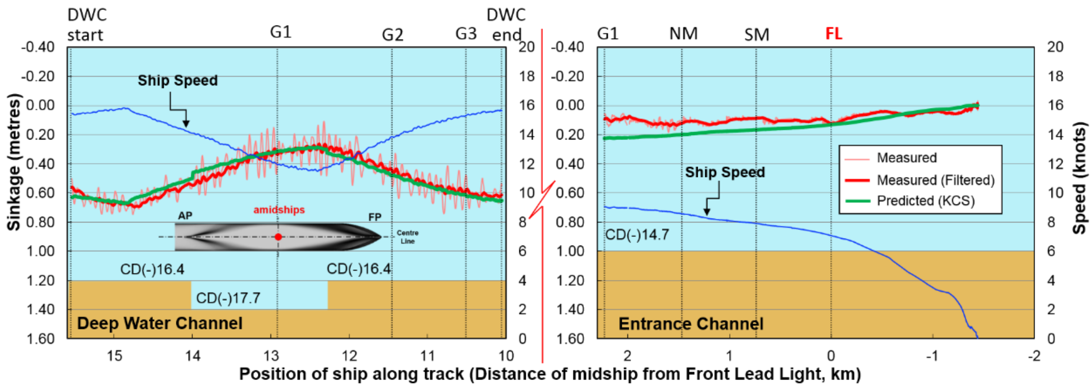

(b) *OOCL BRISBANE*

Figure 5.20. Measured and calculated sinkage (positive downward) at midships for the two Panamax container ships: (a) *SAFMARINE MAKUTU*; (b) *OOCL BRISBANE* [Note: Calculations do not include wave-induced motions; chart datum depth (not to scale) also shown]

Figure 5.21 and Figure 5.22 show comparisons between measured and predicted dynamic trim. Dynamic trim is given here in degrees (°). Measured trim results are also shown with a low-pass filter, which is applied to remove the effect of wave-induced pitch. The predicted dynamic trim is generally negative (bow-down) for *SEAMAX STAMFORD*, *SAFMARINE MAKUTU* and *OOCL BRISBANE* using the KCS hull, and positive (stern-down) for both *MOL PARAMOUNT* and *CMA CGM WAGNER* using the FHR Ship D hull.

Compared with the measurements, the predicted dynamic trim for S*EAMAX STAMFORD* and *MOL PARAMOUNT* are more bow-down (or less stern-down) than the measured, whereas *CMA CGM WAGNER*, *SAFMARINE MAKUTU* and *OOCL BRISBANE* show predicted dynamic trim that are slightly less bow-down (or more stern-down). Because the modelled hull forms are approximate for the predictions, the dynamic trim is reasonably well predicted by the theoretical method at full scale.

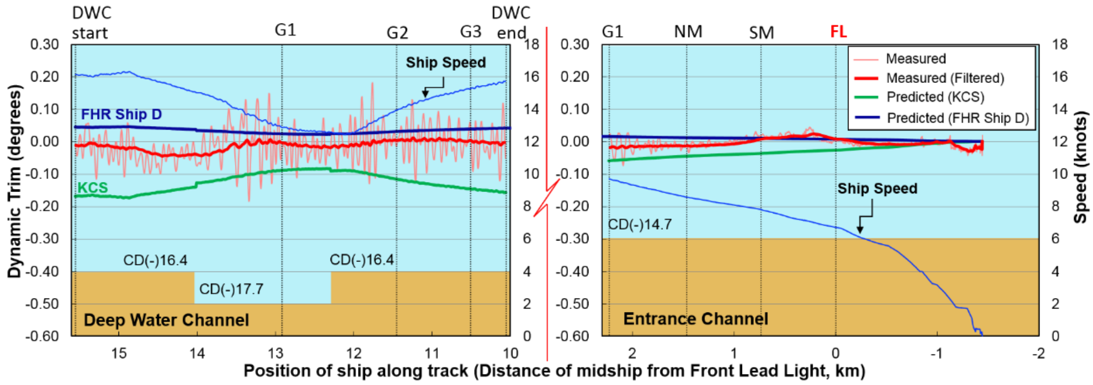

(a) *SEAMAX STAMFORD*

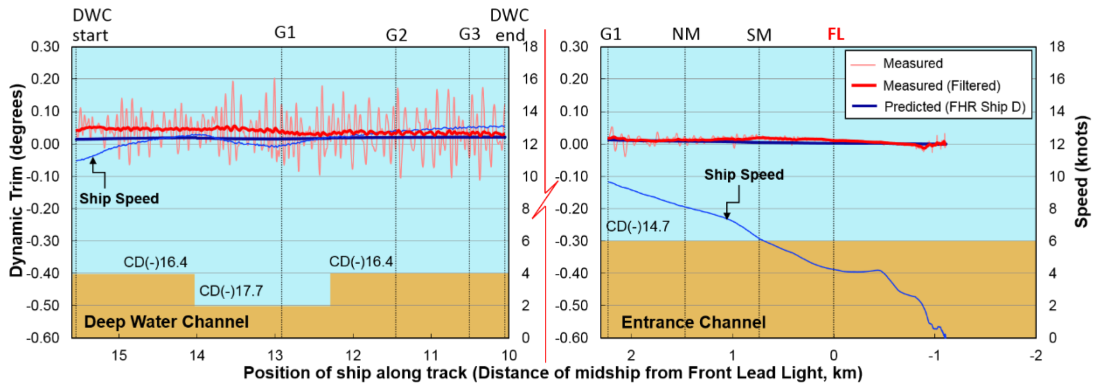

(b) *MOL PARAMOUNT*

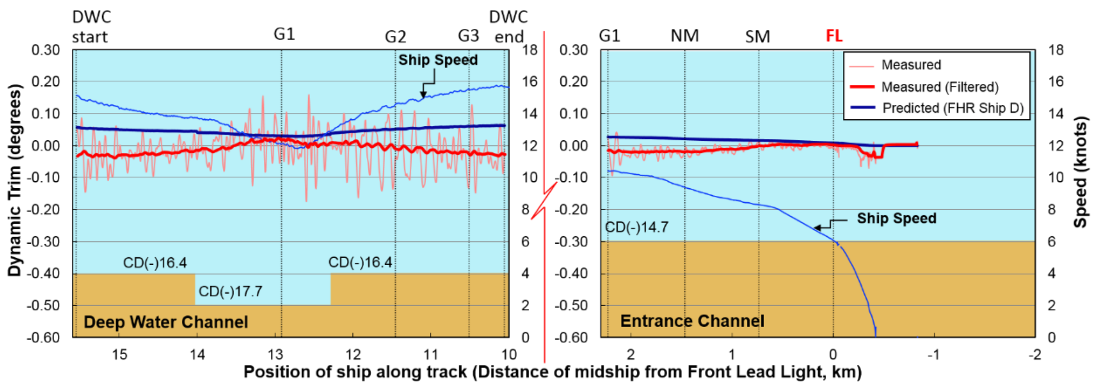

(c) *CMA CGM WAGNER*

Figure 5.21. Measured and calculated dynamic trim (positive stern-down) for the three Post-Panamax container ships: (a) *SEAMAX STAMFORD*; (b) *MOL PARAMOUNT*; (c) *CMA CGM WAGNER* [Note: Calculations do not include wave-induced motions; chart datum depth (not to scale) also shown]

Additionally, as shown in Figure 5.21(a), the two modelled ship hulls, i.e., the KCS and FHR Ship D, were applied to the *SEAMAX STAMFORD* case to see the effect of hull geometry on dynamic trim. The two modelled ships have been modified to match the *SEAMAX STAMFORD*’s hull parameters at its actual transit conditions, and they should have similar hull characteristics such as block coefficient (C_B) and LCB.

However, they show conflicting results for dynamic trim, with the KCS having a negative trim (bow-down) and the FHR Ship D a positive trim (stern-down). This epitomises how sensitive dynamic trim is to hull shape, and the importance of acquiring a ship's full lines plans or exact hull offsets for predictions. Note that less modification was made for the KCS because of its original resemblance to the *SEAMAX STAMFORD* hull.

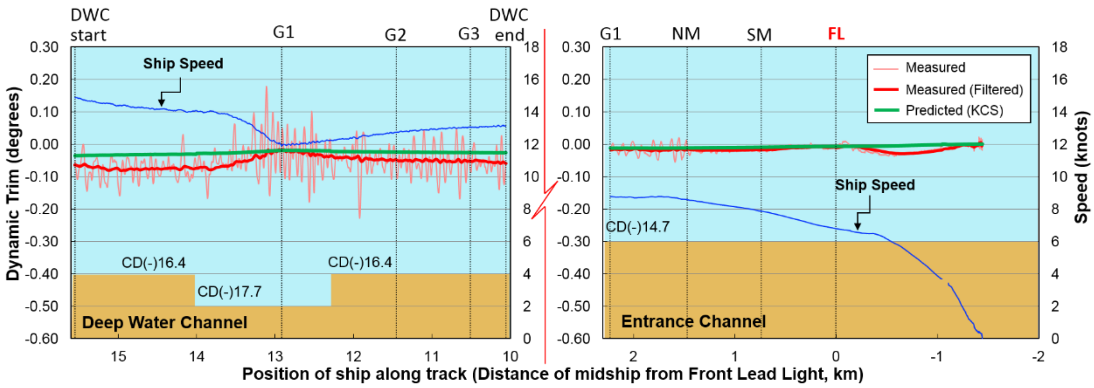

(a) *SAFMARINE MAKUTU*

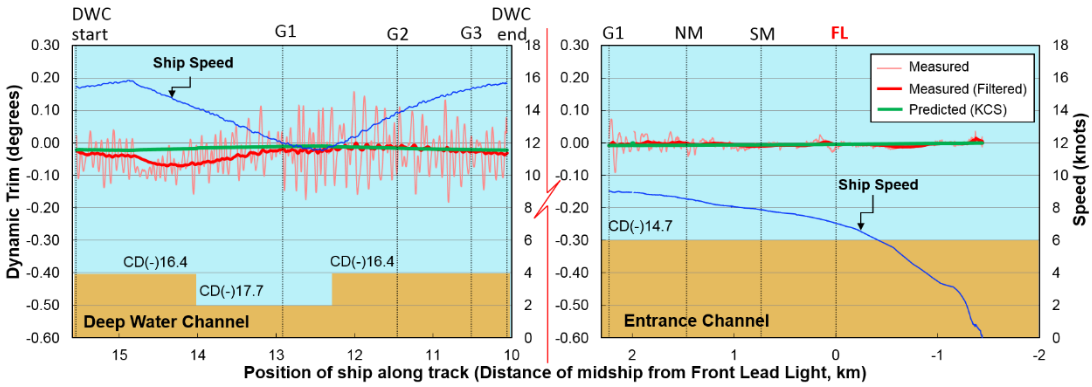

(b) *OOCL BRISBANE*

Figure 5.22. Measured and calculated dynamic trim (positive stern-down) for the two Panamax container ships: (a) *SAFMARINE MAKUTU*; (b) *OOCL BRISBANE* [Note: Calculations do not include wave-induced motions; chart datum depth (not to scale) also shown]

5.4 Conclusions

The full-scale trials of bulk carriers and container ships in the Geraldton and Fremantle approach channels produced dependable data sets on vertical ship motions. The dynamic sinkage, trim and heel of three example bulk carrier and five container ship transits were analysed in more detail. In particular, three bulk carrier transits were chosen for case studies, of a transit in low swell (*FENG HUANG FENG*), a transit in large swell (*SEA DIAMOND*), and a transit in medium swell (*GUO DIAN 17*).

Estimated errors involved in calculating dynamic sinkage were analysed, including the effects of the GNSS receivers' error, geoid undulation (N) error, static reading error and tide-related errors. The total RMS error in downward sinkage of each point on the hull was estimated to be around 0.074 m in the Port of Geraldton channel. In the Port of Fremantle trials, total RMS errors of 0.046 m were estimated in the Deep Water Channel, and 0.045 m in the Entrance Channel and Inner Harbour. The decrease in total error was mainly due to the error in the static reading at the berth.

Maximum sinkage, including the effects of squat and wave-induced motions, occurred at the bow, with ranges between 0.26 and 0.43 % of L_{PP}; 4.57 and 10.60 % of the static draught for the three bulk carriers (*GUO DIAN 17*, *FENG HUANG FENG* and *SEA DIAMOND*). For the five container ships analysed in this chapter (*SEAMAX STAMFORD*, *MOL PARAMOUNT*, *CMA CGM WAGNER*, *SAFMARINE MAKUTU* and *OOCL BRISBANE*), four transits (*MOL PARAMOUNT*, *CMA CGM WAGNER*, *SAFMARINE MAKUTU* and *OOCL BRISBANE*) had maximum sinkage at the bilge corners, and the other (*SEAMAX STAMFORD*) at the bow, ranging between: 0.33 and 0.51 % of L_{PP}; 7.96 and 11.81 % of the static draught. A bulk carrier transit (*SEA DIAMOND*) and three container ship transits (*SEAMAX STAMFORD*, *CMA CGM WAGNER* and *OOCL BRISBANE*) showed that the stern could have maximum dynamic draught due to its already close proximity to the seabed.

An increase in dynamic draught on the point on the ship with the maximum dynamic draught ranged from 4.57 and 8.22 % of the static draught for the bulk carrier transits and 7.14 to 9.28 % for the container ship transits. Elevations of the ship's keel relative to chart datum were calculated for practical UKC management, and the minimum real-time clearance in each section of varying water depth was also captured (see Appendix C).

Steadily increasing dynamic trim by the bow was observed in the bulk carriers, but no clear trend was found in the full-scale measurements of the container ships at the Port of Fremantle, with four transits (*SEAMAX STAMFORD*, *CMA CGM WAGNER*, *SAFMARINE MAKUTU* and *OOCL BRISBANE*) trimming bow-down and the other (*MOL PARAMOUNT*) trimming stern-down. For Panamx container ships (*SAFMARINE MAKUTU* and *OOCL BRISBANE*), the near-steady component due to squat was comparatively larger than those of the Post-Panamax ships at their speeds between 12 and 16 knots. The overall dynamic trim of the container ships was much less than that of the bulk carriers at full scale.

Because the bulk carriers had a relatively large displacement-to-length ratio, low KG and small above-water profile area, smaller heel angles caused by wind and turning were observed: a maximum heel angle of up to 0.75°, and heel angles generally of the order 0 to 0.5°. For the three container ships, the effect of dynamic heel on the sinkage generally overwhelmed that of dynamic trim. The effect of turning manoeuvres on dynamic heel was confirmed by the measurements. A maximum heel angle of more than 2° and heel angles generally of the order 0.5 to 1.5° were measured for the three Post-Panamax container ships (*SEAMAX STAMFORD*, *MOL PARAMOUNT* and *CMA CGM WAGNER*). Much larger heel angles up to 3.1° were seen in the two Panamax container ship transits (*SAFMARINE MAKUTU* and *OOCL BRISBANE*). A Standard method offered by the recent guidelines for port approach channels (PIANC, 2014) was used for further comparisons with the measured maximum heel angles due to ship turning.

A theoretical method using slender-body shallow-water theory was applied to predict the measured sinkage and trim of the ship transits. The slender-body theory was able to predict squat (steady sinkage and trim) with reasonable accuracy for both bulk carriers and container ships at full scale in open dredged channels. The theoretical method (Tuck, 1966) was seen to slightly underpredict the sinkage for all the bulk carrier transits; thus, a small empirical correction to the theory might be advisable for better UKC predictions. The theory (Tuck, 1966) also slightly overpredicted the sinkage for all the container ship transits on the whole; an empirical correction for the container ship trials may not be necessary as a conservative method.

Chapter 6

Ship Wave-Induced Motion Comparisons and Validations Using Full-Scale Trials

The validation of the numerical models of ship wave-induced motions in port approach channels is performed in this chapter. A selected set of high-quality data from full-scale trials measuring vertical motions of container ship transits entering and leaving the Port of Fremantle is used (refer to Chapter 4.3). Measured wave-induced heave, roll and pitch motions of six example container ship transits are discussed in detail, together with descriptions of in-situ wave measurements and wave spectral analysis. A linear strip method, as implemented in the computer code *OCTOPUS*, is applied to predict the ship wave-induced motions. A comparison is made between measured and predicted ship motion responses to validate the ship motion software; measured roll response can be particularly useful in assessing the suitability of existing roll damping methods at full scale. The method is seen to give predictions of heave, roll and pitch responses with reasonable accuracy for container ships at full scale in open dredged channels. Large-amplitude long-period roll motions are observed in some of the container ship trials, and unexpected harmonic pitch motions are also observed in other cases. Further research is recommended to study these seemingly non-linear effects.

6.1 Introduction

Dynamic vertical ship motions such as squat, heel and wave-induced motions are significant factors affecting UKC requirements. A number of approaches have been taken to better predict the squat effect, including model-scale tests (Dand & Ferguson, 1973; Lataire, Vantorre, & Delefortrie, 2012) and full-scale tests (Ha, Gourlay, & Nadarajah, 2016; Härting, Laupichler, & Reinking, 2009) for bulk carriers; and model-scale tests (Gronarz, Broß, Mueller-Sampaio, Jiang, & Thill, 2009; Mucha, el Moctar,

& Böttner, 2014) and full-scale tests (Gourlay, 2008a; Uliczka & Kondziella, 2006) for container ships. Standard methods exist to calculate heeling moments caused by turning and wind (PIANC, 2014). Wave-induced heave, roll and pitch motions have the potential to result in the largest reduction in ship UKC in a case where the port is directly open to the ocean and its approach channel is exposed to long-period swells. However, few studies of ship wave-induced motions in approach channels have been conducted. For bulk carriers, model-scale tests were performed by Van Wyk and Zwamborn (1988), and full-scale tests by Wang (1980) and Van Wyk (1982). For container ships, numerical modellings were undertaken by Briggs, Demirbilek and Lin (2014), and full-scale tests by Wang (1980) and Briggs, Silver, Kopp, Santangelo and Mathis (2013).

Ship wave-induced motions are the most complicated UKC effect to model, partly due to the complexity of analysis and partly to the large number of variables, including ship dimensions, weight distribution, heading and speed; water depth; and wave-related parameters (wave height, period, direction and spreading) (PIANC, 2014). Therefore, obtaining a reliable data set on vertical ship motions together with in-situ wave measurement data is of great importance to study the ship wave-induced motions, especially at full scale in port approach channels.

The successful performance of full-scale trials of container ship motions in the Port of Fremantle approach channels (refer to Chapter 4.3) produced a set of high-quality data on both vertical ship motions and in-situ directional wave measurements. In this chapter, method validation of container ship wave-induced motions in port approach channels using such a data set is performed, and some noticeable results are discussed. Since validations of ship wave-induced motions in port approach channels using full-scale high-quality data do not appear to have been published before, the results may be useful for developing UKC management in ports.

6.2 Full-scale measurements of container ship motions

In this chapter, the full-scale measurement results of container ship transits at the Port of Fremantle were used to study the wave-induced motion characteristics in the port approach channels. The general process of the full-scale measurements are detailed in Chapter 4.

6.2.1 Choosing a suitable data set for analysis of ship wave-induced motions

It would be better to perform full-scale trials on ship wave-induced motions with many wave buoys. As mentioned in 4.2.2, during the bulk carrier trials in the Port of Geraldton channel, waves were measured by the AWAC at B2 and by 10 pressure sensors at all the starboard-hand beacons, B1, B3, B5, …, B19 (see Figure 4.7). The ship motions measured along the channel, together with the full measured wave time series data, may be used to study wave-induced motions. However, such a prospective study, using the wave data from the eleven beacons, will not yield the most relevant results because of short transit times which cannot give statistically significant motion measurements.

Criteria should also be made to select a better fitting ship transit for the analysis of wave-induced motions in the port channels:

A ship transit should include a straight course and, hence, a consistent and continuous ship heading.

The straight transit course should be of at least ten minutes' duration, to allow statistically significant motion measurements. Assuming an individual wave has a period of 10 or 15 seconds, the ship may experience about 40 or 60 waves affecting its motions in ten minutes.

Since some of the container ship transits in the Port of Fremantle channels satisfy the above criteria, using the measurement results of container ship transits at the Port of Fremantle may be appropriate for studying the ship wave-induced motions in the channels. Further explanations for selecting specific ship transits will be made subsequently.

6.2.2 Description of the port, its channels and measured ship tracks

Figure 6.1 shows the layout of the Port of Fremantle, including its approach channels and navigational buoys, and tracks of six example container ship transits. Criteria applied in choosing these six transits is discussed below.

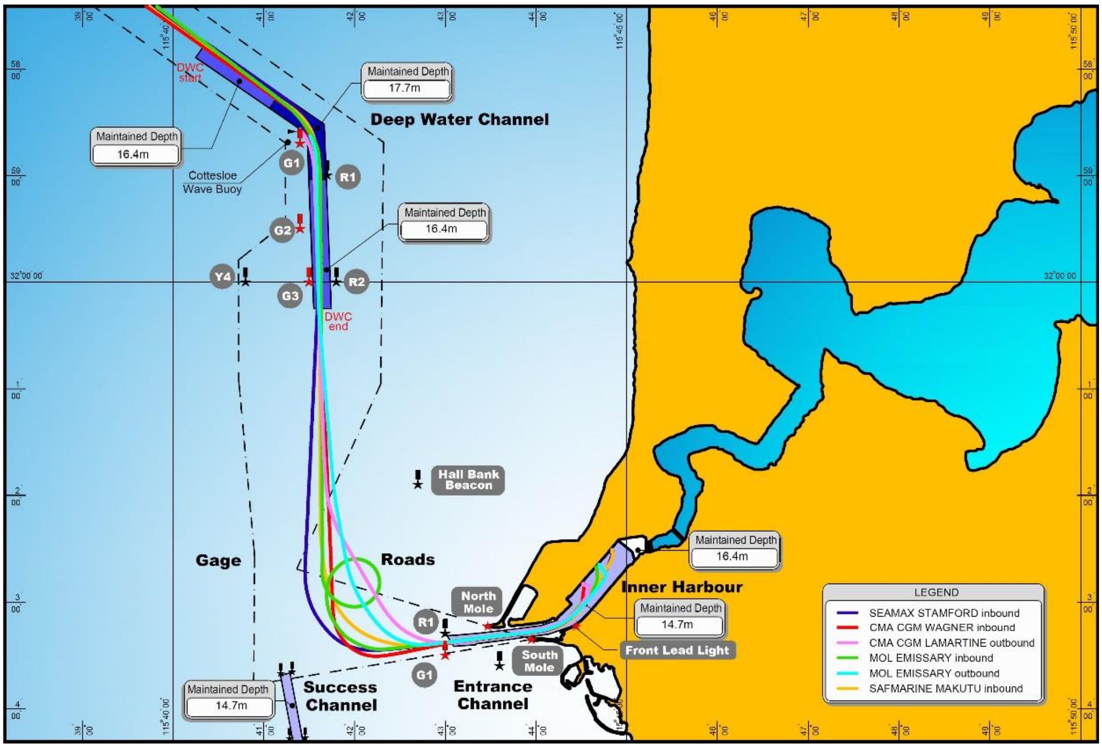

Figure 6.1. Layout of the Port of Fremantle, including its approach channels and navigational buoys, and measured midship tracks

Based on Chapter 4.3, the environmental conditions in the Port of Fremantle are summarised as follows:

The currents move southward and northward in Gage Roads (see Figure 6.1) across the Entrance Channel, generally at a rate of 1 knot, and up to 2 knots in the winter months (June through August) (National Geospatial-Intelligence Agency, 2017; United States Naval Research Laboratory, n. d.). According to advice from Fremantle Ports, the currents in the area are mainly wind-driven. At the time of the full-scale trials, light winds were generally observed (refer to Table 4.11), so it is expected that the currents would have been minimal.

Water density in the Inner Harbour is stated to be 1.025 g/cm^3, generally, at all tides (Fremantle Ports, 2011); a heavy rainfall may cause a variation in water density in the Inner Harbour and Entrance Channel due to the port's geographic location in an estuary (Swan River Estuary), but this did not arise during the measurements.

The tidal datum is the same as the chart datum in charts AUS112 and AUS113 and, hence, LAT at the Port of Fremantle. The range of measured tide in the Inner Harbour (32° 3.258' S, 115° 44.3718' E), as provided by Fremantle Ports, varied between each transit, from around 0.5 to 1.1 m.

During the trials, wind speeds of up to 15 knots were recorded by the author's visual observations (see Table 4.11).

More details on the port, channels and environmental conditions in the port can be found in Chapter 4.3.2.

6.2.3 Description of the ships and transit conditions

On the basis of some underlying criteria (see Chapter 5.2.1) that are preferentially applied to filter out non-conforming ship transits, like ship transits with poor GNSS signals and noise, as well as the additional criteria mentioned in 6.2.1, six container ship transits were selected for analysis of wave-induced motions, listed in Table 6.1. Here, details of MOL EMISSARY are represented for both its inbound and outbound transits.

Table 6.1. Details of the container ships

Particulars	*SEAMAX STAMFORD*	*CMA CGM WAGNER*	*CMA CGM LAMARTINE*	*MOL EMISSARY*	*SAFMARINE MAKUTU*
Ship size	Post-Panamax	Post-Panamax	Post-Panamax	Panamax	Panamax
L_{OA} (m)	250.00	277.28	299.20	294.13	292.08
L_{PP} (m)	238.35	263.00	286.70	283.20	277.00
Beam (m)	37.30	40.00	40.00	32.20	32.25
Summer draught (m)	13.00	14.52	14.52	13.65	13.52
Displacement (t)	79,702.00	96,997.00	110,455.10	87,855.00	82,287.00
C_B (-)	0.673	0.620	0.647	0.689	0.665

[Note: Displacement and C_B are values at summer draught; C_B is the ratio of displaced volume to (L_{PP}·Beam·Draught)]

For ship motion validation, hydrostatic data at the ships' actual transit draught were acquired from the ships' trim and stability book. Transverse GM_f data was taken from the loading plan. Comparative details of transit conditions for all the container ships are shown in Table 6.2.

.

Table 6.2. Details of the transit conditions

Particulars	Post-Panamax			Panamax		
	SEAMAX STAMFORD	***CMA CGM WAGNER***	***CMA CGM LAMARTINE***	***MOL EMISSARY***	***MOL EMISSARY***	***SAFMARINE MAKUTU***
Date/Time (AWST)	17/04/2016 04:27-05:47	25/04/2016 04:12-05:31	22/04/2016 14:20-15:12	18/04/2016 18:24-19:51	19/04/2016 21:55-23:21	20/04/2016 20:56-22:09
Direction	inbound	inbound	outbound	inbound	outbound	inbound
Draught fwd. (m)	10.40	10.00	11.20	10.90	9.80	12.60
Draught aft. (m)	11.25	11.50	11.50	12.10	11.50	12.60
Actual Disp. (t)	62,584.00	63,569.00	77,453.00	69,605.00	63,557.30	73,593.00
C_B (-)	0.634	0.548	0.581	0.648	0.638	0.638
GM_f (m)	3.88	4.51	2.99	1.28	1.55	0.81

[Note: C_B is calculated based on average draught at arrival or departure; dates and times are in Australian Western Standard Time (AWST)]

6.2.4 Determination of the transit courses for analysis

By applying the specific criteria, the six example transits were chosen for their straight courses, illustrated in Figure 6.2. Diverse loading conditions, changing environmental conditions and different pilotage techniques by different pilots could have led to the transits showing different paths to the Entrance Channel (see also Figure 6.1) and, hence, varying lengths and headings for each straight course.

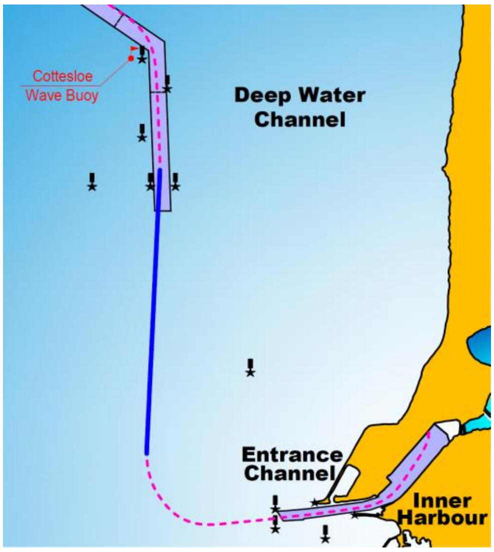

(a) *SEAMAX STAMFORD* (inbound)

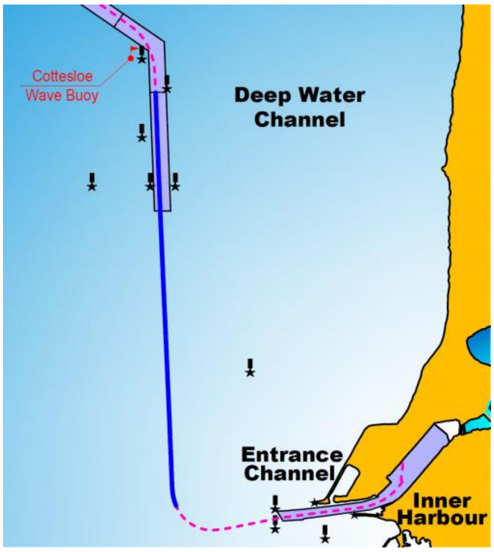

(b) *CMA CGM WAGNER* (inbound)

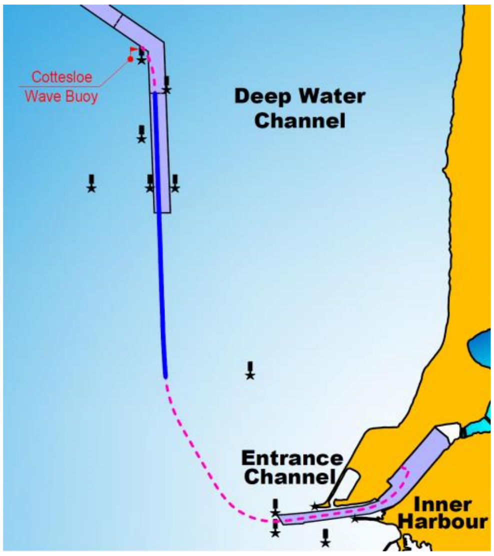

(c) *CMA CGM LAMARTINE* (outbound)

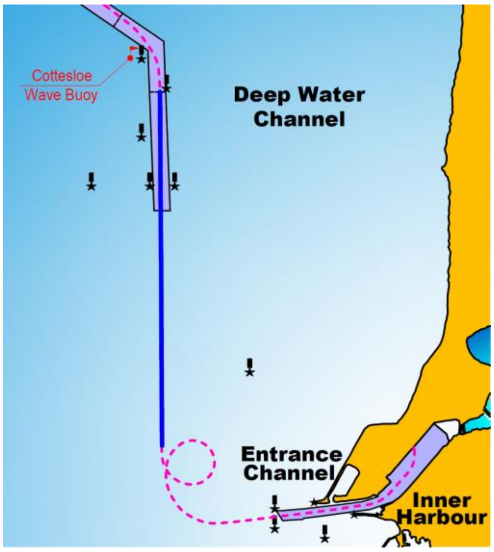

(d) *MOL EMISSARY* (inbound)

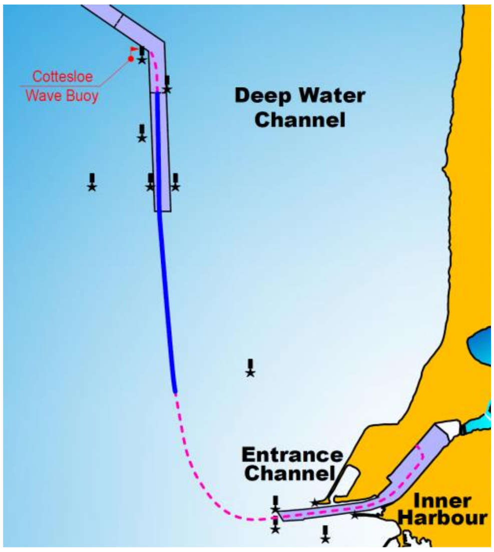

(e) *MOL EMISSARY* (outbound)

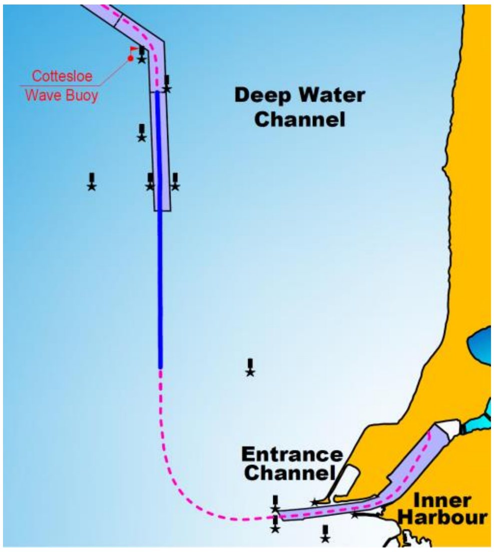

(f) *SAFMARINE MAKUTU* (inbound)

Figure 6.2. Determined straight courses (as illustrated in solid lines)

Table 6.3 shows details of the straight courses. Ship's heading is measured in degrees clockwise from the north line (0°).

Table 6.3. Details of the straight courses

Particulars	Post-Panamax			Panamax		
	SEAMAX STAMFORD (inbound)	*CMA CGM WAGNER* (inbound)	*CMA CGM LAMARTINE* (outbound)	*MOL EMISSARY* (inbound)	*MOL EMISSARY* (outbound)	*SAFMARINE MAKUTU* (inbound)
Ship heading (◦)	183	178	358	179	357	180
Avg. speed (knots)	15.35	14.89	14.38	12.70	14.47	11.90
Avg. water depth (m)	17.90	18.00	17.70	18.10	17.95	17.90
Avg. tide (m)	0.80	0.89	0.60	0.99	0.84	0.77

The straight courses include an unmaintained section between the Deep Water Channel and Entrance Channel (see Figure 6.2 and Appendix C (C.2)) whose depth ranges from approximately 15 to 20 m. Based on the ratio of water depth (h) to ship draught (T) (PIANC, 2014), it is considered that the container ships travelled in the Deep Water Channel under shallow water conditions ($h / T < 1.5$) and in the unmaintained section, generally, under shallow water conditions ($h / T < 1.5$) but sometimes under medium conditions ($1.5 < h / T < 2.0$).

Water depths along the ships' tracks in the unmaintained section are estimated to be in the range of 17 and 18 m. These are averaged with the 16.4-m water depth of the Deep Water Channel (see Figure 6.1) to give a consistent depth, so the definitive water depth contains one value only for ship wave-induced motion modelling. The average water depth, which includes local tidal effects (see Table 6.3), was then used in *OCTOPUS*, e.g., an average water depth of 17.90 m for the *SEAMAX STAMFORD* (inbound) transit. Details on the tidal data can be found in Appendix B (B.2).

6.3 Wave measurements and analysis

Because studies of ship motions in waves presuppose knowledge of the sea state, identifying wave characteristics has important applications in dealing with ship wave-induced motions. During the container ship trials in the Port of Fremantle, waves were measured using a Datawell Directional Waverider buoy (Datawell BV, 2014a), and full measured wave time series data was used for wave spectral analysis (see Appendix B (B.2) for the full set of wave data for all the container ship transits).

6.3.1 Description of the in-situ wave measurements

Wave data from the Cottesloe wave buoy was provided by the coastal infrastructure team from the WA DoT. The buoy is located at 31° 58.74333' South, 115° 41.39833' East, chart datum depth of 16–17 m, near Green No.1 Buoy (G1) in the Deep Water Channel (see Figure 6.1 and Figure 6.2). The buoy measured raw north, west and vertical displacement at a rate of 1.28 Hz (Datawell BV, 2014a), and the raw data was read and postprocessed using *W@ves21* software (Datawell BV, 2014b), the data acquisition and processing software developed by the buoy manufacturer Datawell BV (http://www.datawell.nl). Figure 6.3 presents an example of the processing results, that is measured wave height and period during the *SAFMARINE MAKUTU* (inbound) transit.

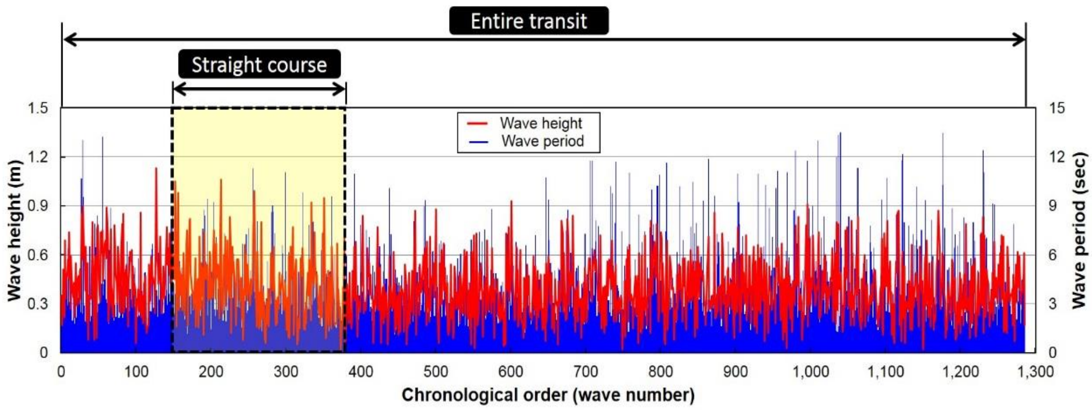

Figure 6.3. An example of wave data from the Cottesloe wave buoy: Measured wave height and period during the *SAFMARINE MAKUTU* (inbound) transit

6.3.2 Consideration of wave data from a single buoy

For studying the ship wave-induced motions in the Port of Fremantle approach channels, wave data from a single buoy (the Cottesloe wave buoy), which is located some distance from the end points of each straight course (see Figure 6.2), is only available. There may be changes and differences in wave characteristics while underway and moving away from the buoy, for example in wave height, direction and spreading arising from bathymetry and winds; but the sea state between the buoy and a ship's moving point on the straight course is expected to be similar for several reasons:

The buoy and transit courses are both located in the open sea with no adjacent island.

From the standpoint of wave analysis, the buoy and the end points of the straight courses are not far apart from each other (up to 4.5 nautical miles), but they each is far from the coast.

No significant changes in charted bathymetry along the ship transits, including the fixed location of the buoy, are seen in charts AUS 112 and 113.

The full-scale trials on the container ship motions were performed in weak winds and wind direction changes.

Based on these conditions, it is assumed that the wave refraction, diffraction and reflection, which can change the wave characteristics, did not occur between the two areas (the fixed location of the buoy and a ship's moving point within its straight course) during the container ship trials. This approach also had to be a compromise between statistical and geographic issues: thus, a ship transit course should be of at least ten minutes' duration, to give statistically significant motion measurements, and should not deviate from the local area, to be covered by the wave buoy.

6.3.3 Wave energy spectra

In *W@ves21*, fast Fourier transform (FFT) is applied to obtain a buoy's heave spectrum and, hence, wave power spectral density. Wave directions are derived from the co-spectral and quadrature spectral densities of heave, north and west displacement signals. The Maximum Entropy Method (MEM) is used to convert the raw data into wave directional distributions, that is, the wave power spectral density as a function of both wave frequency and wave direction (Datawell BV, 2012).

The spectral processing routine in *W@ves21* is devised such that every 200 seconds a total of 256 heave samples are used to compute a spectrum in the frequency range 0.025 to 0.58 Hz (64 frequencies in total), with a resolution of 0.005 Hz for frequencies from 0.025 to 0.1 Hz (16 frequencies) and a resolution of 0.01 Hz between 0.11 and 0.58 Hz (48 frequencies) (Datawell BV, 2014a). Resulting directional or non-directional wave spectra from *W@ves21* need to be compared with those from other software to ensure its suitability. An in-house *MATLAB* code was employed to obtain non-directional wave spectra using the same wave measurement data. It used a Bartlett window with half-window overlaps (Press, Teukolsky, Vetterling, & Flannery, 1992), and the number of points in each segment was set at 256.

Measured non-directional and directional wave spectra during the container ship transits are shown in Figure 6.4. According to the manual of the buoy (DWR-MKIII), the buoy can measure wave height for wave periods between 1.6 and 30 seconds with an accuracy of 0.5 % of measured value (Datawell BV, 2014a), which means that the buoy cannot effectively measure waves with periods longer than 30 seconds because its inertial system is prone to low-frequency drift. Therefore, a cutoff frequency of 0.033 Hz (or a cutoff period of 30 seconds) might be considered as a lower limit for the measured wave spectra (Jeans, Bellamy, de Vries, & Van Weert, 2003; Lenain & Melville, 2014). The time period of the measured wave data corresponds to the time period of each straight course. The non-directional wave spectra from *W@ves21* appear to give good agreement with those from the in-house *MATLAB* code.

In Figure 6.4, the wave spectra show a clear distinction between the sea and swell parts in the Port of Fremantle approach channels. Generally, the peak wave frequency for each transit lies between 0.05 and 0.1 Hz and, hence, the peak period of between 10 and 20 seconds, with the dominant wave directions between 225 (south-west) and 315° (north-west). The wave spectra during *CMA CGM WAGNER* (inbound), *MOL EMISSARY* (outbound) and *SAFMARINE MAKUTU* (inbound) show relatively larger contributions of the sea part to the total wave energy.

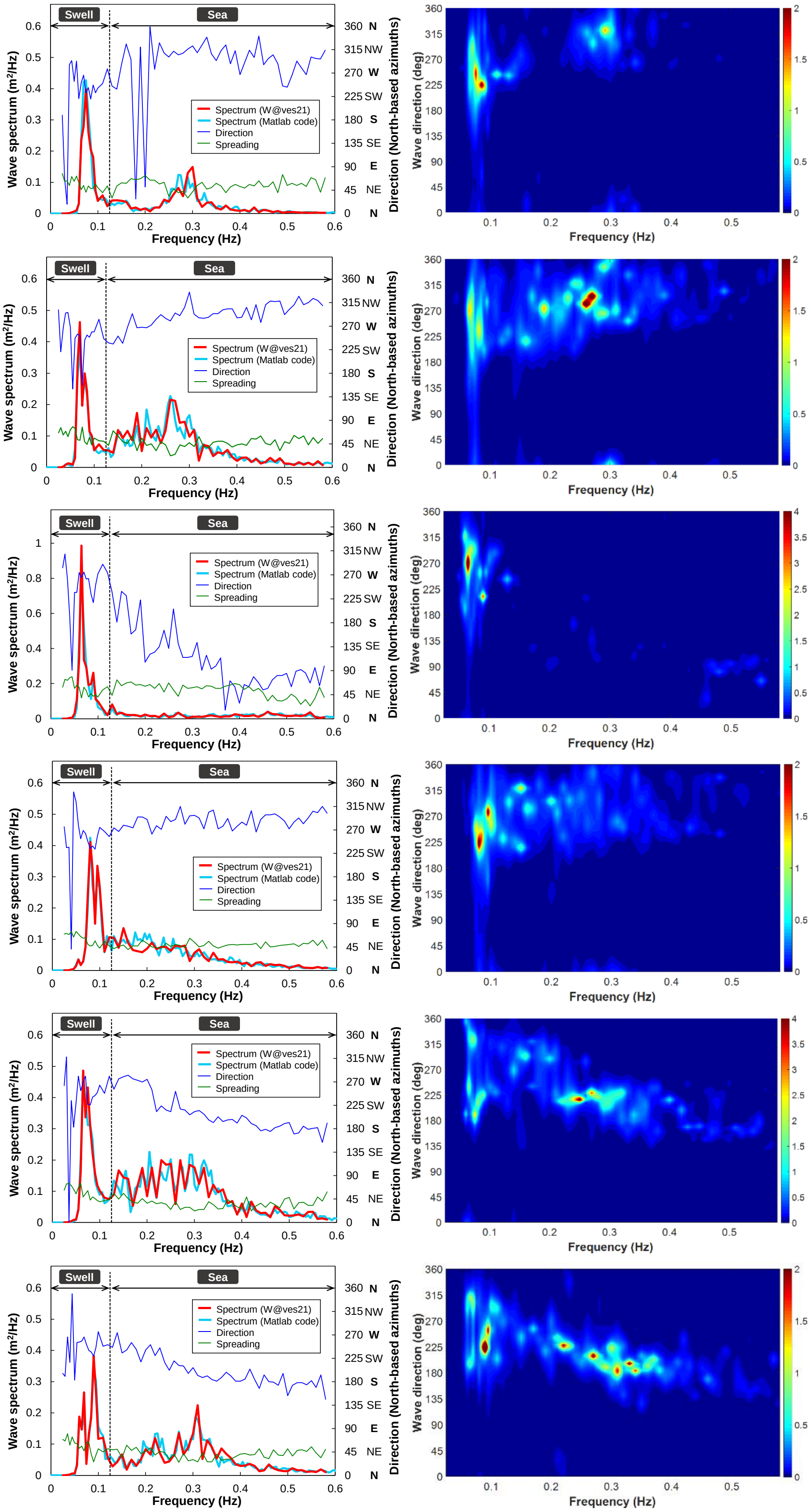

(a)
SEAMAX STAMFORD
(inbound)

(b)
CMA CGM WAGNER
(inbound)

(c)
CMA CGM LAMARTINE
(outbound)

(d)
MOL EMISSARY
(inbound)

(e)
MOL EMISSARY
(outbound)

(f)
SAFMARINE MAKUTU
(inbound)

Figure 6.4. Non-directional (left) and directional (right) wave spectra measured during the container ship transits

The wave spectrum showing the sea state during each transit can be described by the most commonly used parameters: the significant wave height, and mean and peak wave periods. The significant wave height (H_s), and mean (T_{01}) and average zero-crossing (T_{02}) wave periods are defined as

$$H_s = 4\sqrt{m_0} \tag{6.1}$$

$$T_{01} = \frac{m_0}{m_1} \tag{6.2}$$

$$T_{02} = \sqrt{\frac{m_0}{m_2}} \tag{6.3}$$

where n-th order spectral moment (m_n) is given by

$$m_n = \int_0^\infty S(f) f^n df \qquad n = 0, 1, 2, \ldots \tag{6.4}$$

where $S(f)$ is the spectral density at a frequency f. The peak wave period (T_p) is defined as the wave period with the largest wave energy.

Important wave parameters derived from the wave spectra are summarised in Table 6.4. The sea and swell separation frequency is 0.125 Hz (or a period of 8 seconds); hence, for example, the significant wave height for the swell part can be calculated by the area under the wave spectral curve (m_0) for frequencies from 0 to 0.125 Hz.

Table 6.4. Details of the wave parameters during the transits

Parameters		Post-Panamax			Panamax		
		SEAMAX STAMFORD (inbound)	*CMA CGM WAGNER* (inbound)	*CMA CGM LAMARTINE* (outbound)	*MOL EMISSARY* (inbound)	*MOL EMISSARY* (outbound)	*SAFMARINE MAKUTU* (inbound)
Total	H_s (m)	0.58	0.80	0.63	0.72	0.92	0.74
	T_p (sec)	13.33	14.29	15.38	12.50	15.38	11.11
	T_{01} (sec)	5.21	4.50	5.98	4.96	4.34	4.24
	T_{02} (sec)	4.42	3.96	4.44	4.25	3.81	3.71
Swell	H_s (m)	0.39	0.42	0.50	0.44	0.47	0.42
	T_p (sec)	13.33	14.29	15.38	12.50	15.38	11.11
	Direction at peak (◦)	232	252	265	234	270	229
	Spreading at peak (◦)	41	52	39	47	49	26
Sea	H_s (m)	0.43	0.68	0.37	0.56	0.79	0.61
	T_p (sec)	3.33	3.85	7.69	6.67	4.35	3.23
	Direction at peak (◦)	322	280	237	279	224	192
	Spreading at peak (◦)	42	22	44	49	38	26

6.4 Wave-induced vertical ship motions: heave, roll and pitch responses

The overall vertical motion of a ship in a port approach channel with waves present is considered a combination of its heave, roll and pitch motions. To understand the complicated mixture of these, each motion of the ship should be individually investigated and analysed in a particular environmental condition. Spectral analysis is used to produce the vertical motions of the ship in the frequency domain and, hence, its heave, roll and pitch motion response spectra. Ultimately, measured motion response spectra will be compared with those from predictions for method validation.

6.4.1 Data processing

A specific process was launched to obtain pure wave-induced heave, roll and pitch motions of the ships from the raw ship motion measurement data, divided into three steps:

Sinkage at the FP, AP, and port and starboard bilge corners of each ship, are given from calculations of the raw GNSS results of each receiver (see Appendix C (C.2) for all the container ship transits).

Dynamic sinkage (at midships), trim and heel are calculated by assuming the ship to be rigid and comparing trim and heel angles relative to the static floating position (see Figures 4.27 and 4.28 for the dynamic trim and heel results).

Pure wave-induced heave, roll and pitch motions are derived by applying a low-pass filter to remove the effects of near-steady components, like squat, and heel caused by wind and turning.

Figure 6.5 shows such a process for an example transit (*SEAMAX STAMFORD*, inbound). The results are plotted against the cumulative distance from the Front Lead Light (FL) (32° 3.22728' S, 115° 44.45048' E). Vertical lines are shown for the starting point, Green No.1 Buoy (G1), Green No.2 Buoy (G2), Green No.3 Buoy (G3) and the end point in the Deep Water Channel (DWC). In the Entrance Channel, vertical lines are shown at Green No.1 Buoy (G1), North Mole (NM) and South Mole (SM) (refer to Figure 6.1). The position of the straight course in the entire transit is also shown. Regarding Figure 6.5(a), sinkage is given at the FP, AP, and port and starboard bilge corners (positive downward). Ship speed is the ship's Speed Over Ground (SOG) based on the GNSS results, but the ship's Speed Through Water (STW) cannot be measured independently from the measurements. As the currents in Gage Roads (see Figure 6.1) move southward for approximately 14 hours and northward for 10 hours at a rate of 1 knot, but sometimes 2 knots in unsettled weather during winter (National Geospatial-Intelligence Agency, 2017; United States Naval Research Laboratory, n.d.); the ship's STW may be considered to be within ± 1 knot of the ship's SOG. In Figure 6.5(b), dynamic trim and heel are the ship's total change in trim (positive stern-down) and in heel (positive to starboard), respectively.

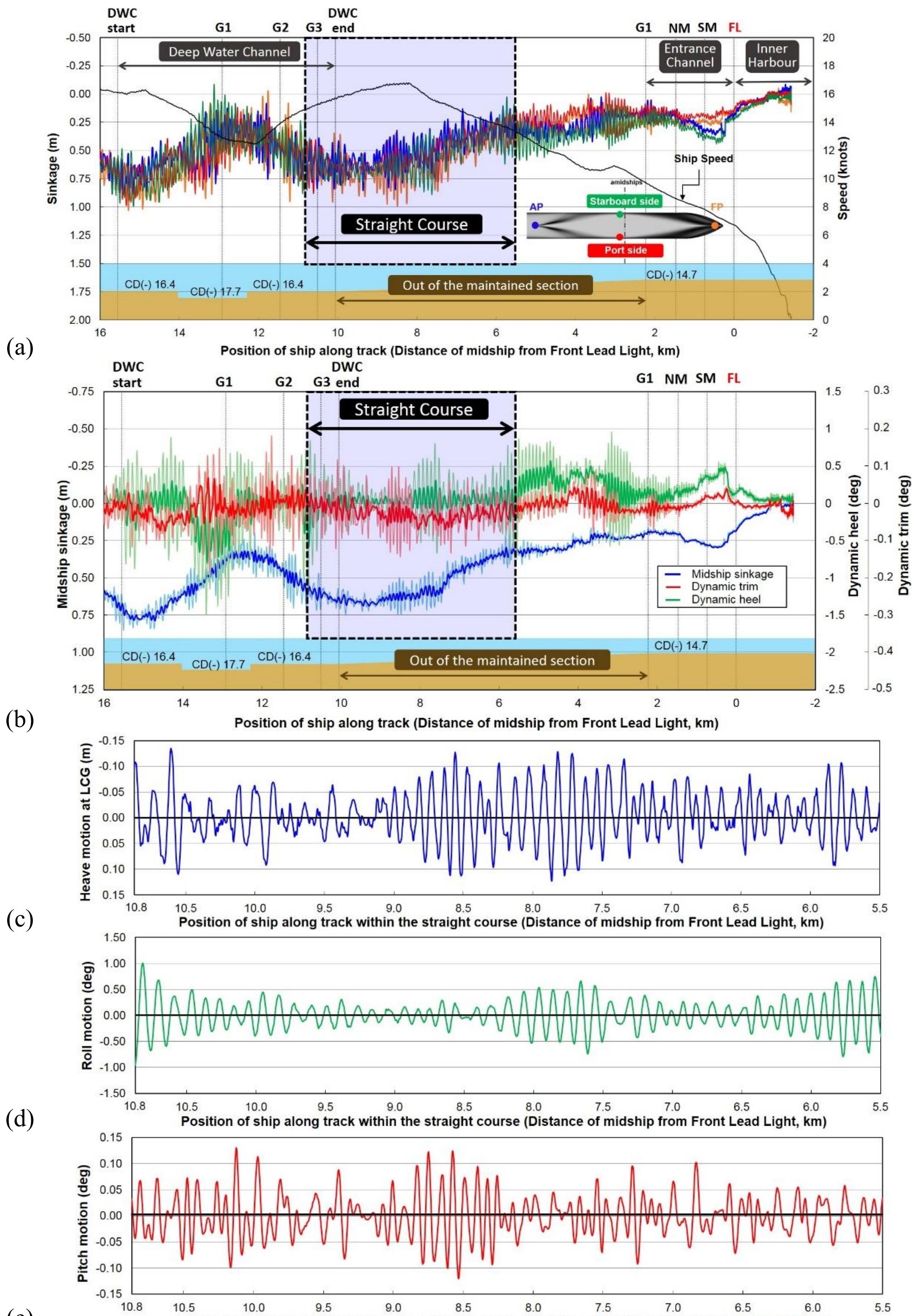

Figure 6.5. (a) Measured sinkage at four points (FP, AP, and port and starboard bilge corners); (b) Measured midship sinkage, dynamic trim and dynamic heel with their filtered results (thicker lines) [Note: Chart datum depth (not to scale) also shown]; (c) Pure heave motion at LCG (positive downward); (d) Pure roll motion (positive to starboard); (e) Pure pitch motion (positive stern-down), for the *SEAMAX STAMFORD* (inbound) transit

As shown in Figure 6.5(a and b), the effect of ship squat, a bodily sinkage and a dynamic change in trim, was observed to be caused by changes in ship speed and water depth (PIANC, 2014). A large, slowly-varying heel due to wind or turning is not seen in the straight course. Detailed information on squat and heel of some container ship transits discussed in this chapter, e.g., *SEAMAX STAMFORD* (inbound) and *CMA CGM WAGNER* (inbound), appear in Chapter 5.3. A low-pass filter with a cutoff period of 40 seconds was applied to remove quasi-steady effects from the measured dynamic sinkage, trim and heel results. The extracted heave, roll and pitch motions in the time domain (see Figure 6.5(c, d, and e)) represent the characteristics induced by the given wave conditions (refer to Figure 6.4(a) and Table 6.4) within the straight course. Here, the heave motion is measured at the LCG of the ship.

6.4.2 Measured wave-induced heave, roll and pitch response spectra

Heave, roll and pitch motion response spectra of the transits were obtained in the same manner as the wave analysis described before. Fast Fourier transform (FFT), as implemented in the in-house *MATLAB* code, was again applied to transform the measured heave, roll and pitch motions in the time domain to the frequency domain. Figure 6.6 shows the measured wave-induced heave, roll and pitch response spectra for the six transits. The non-directional wave spectrum during each transit (see Figure 6.4(left)) is also shown for comparative purposes.

Because each transit was operated under different conditions of ship speed, heading, size, and hull shape (see Tables 6.1, 6.2 and 6.3) and sea state (see Table 6.4), a certain degree of difference in their spectral shapes, including peak frequencies, was identified. Distinguishing features observed in the present trials are as follows:

Measured heave responses show relatively wide-band spectra with multiple peaks, and their spectral shapes are usually similar to the wave spectral shapes.

Measured roll response spectra have different peaks according to ship size, such as a peak of between 0.05−0.1 Hz for the Post-Panamax ships (*SEAMAX STAMFORD* (inbound), *CMA CGM WAGNER* (inbound) and *CMA CGM*

LAMARTINE (outbound)); and a peak of less than 0.05 Hz for the Panamax ships (*MOL EMISSARY* (inbound and outbound) and *SAFMARINE MAKUTU* (inbound)); they are fairly narrow-banded near the ships' natural roll frequencies (see Table 6.5).

Measured pitch responses show double-peaked spectra in general, whereas the spectrum of the *SAFMARINE MAKUTU* (inbound) case has multiple peaks.

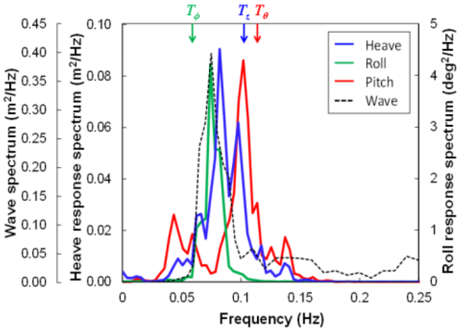

(a) *SEAMAX STAMFORD* (inbound)

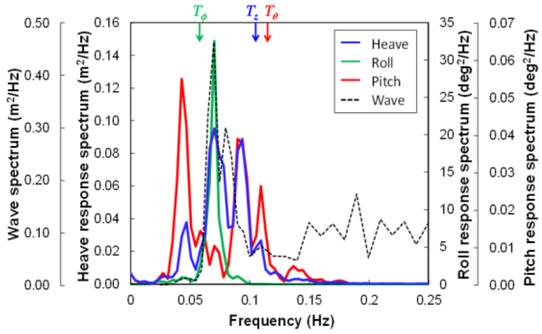

(b) *CMA CGM WAGNER* (inbound)

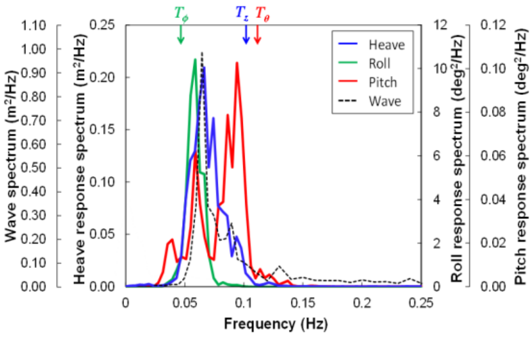

(c) *CMA CGM LAMARTINE* (outbound)

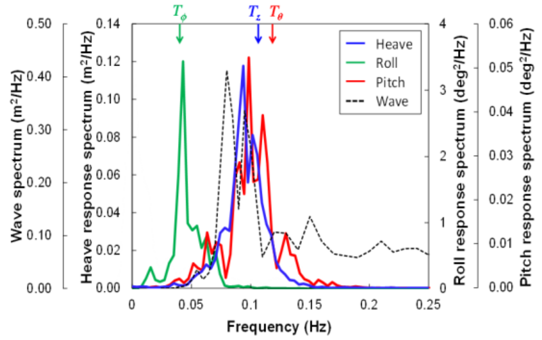

(d) *MOL EMISSARY* (inbound)

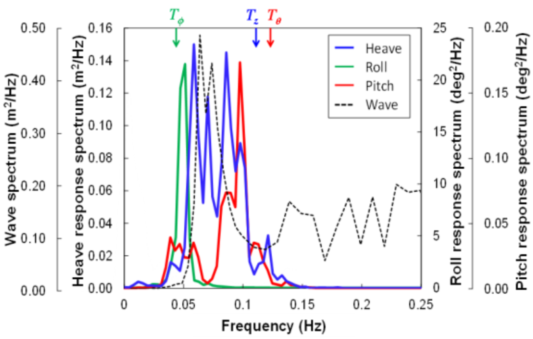

(e) *MOL EMISSARY* (outbound)

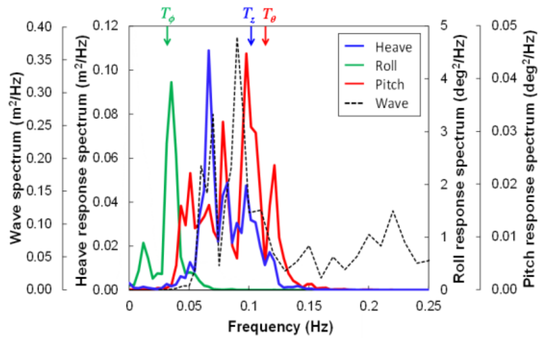

(f) *SAFMARINE MAKUTU* (inbound)

Figure 6.6. Measured heave, roll and pitch response spectra with corresponding non-directional wave spectra

In Figure 6.6, arrows at the top of the figures represent natural heave (T_z), roll (T_ϕ) and pitch (T_θ) periods for each ship transit, which can be obtained by

$$T_z = 2\pi\sqrt{\frac{(M + a_{33})}{\rho \cdot g \cdot A_{WP}}} \tag{6.5}$$

$$T_\phi = 2\pi\sqrt{\frac{(M \cdot k_{xx}^2 + a_{44})}{M \cdot g \cdot GM_T}} \tag{6.6}$$

$$T_\theta = 2\pi\sqrt{\frac{(M \cdot k_{yy}^2 + a_{55})}{M \cdot g \cdot GM_L}} \tag{6.7}$$

Note that a_{33}, a_{44} and a_{55} are calculated using a computer code *OCTOPUS* (http://www.abb.com) over the full frequency range, and Eqs. (6.5), (6.6) and (6.7) are iterated until the correct periods are obtained. Calculated natural heave, roll and pitch periods using ship models are summarised in Table 6.5. Explanations for selecting such ship models, and further modelling procedures, will be made subsequently (see also Chapter 2).

Table 6.5. Calculated natural heave, roll and pitch period (frequency)

Particulars	Post-Panamax			Panamax		
	***SEAMAX STAMFORD* (inbound)**	***CMA CGM WAGNER* (inbound)**	***CMA CGM LAMARTINE* (outbound)**	***MOL EMISSARY* (inbound)**	***MOL EMISSARY* (outbound)**	***SAFMARINE MAKUTU* (inbound)**
Modelled hull	KCS	FHR Ship D	FHR Ship D	KCS	KCS	KCS
Natural heave period (T_z)	9.69 sec (0.103 Hz)	9.54 sec (0.105 Hz)	9.85 sec (0.102 Hz)	9.31 sec (0.107 Hz)	9.01 sec (0.111 Hz)	9.82 sec (0.102 Hz)
Natural roll period (T_ϕ)	16.97 sec (0.059 Hz)	17.10 sec (0.058 Hz)	21.47 sec (0.047 Hz)	24.64 sec (0.041 Hz)	22.71 sec (0.044 Hz)	31.47 sec (0.032 Hz)
Natural pitch period (T_θ)	8.81 sec (0.114 Hz)	8.72 sec (0.115 Hz)	8.93 sec (0.112 Hz)	8.39 sec (0.119 Hz)	8.16 sec (0.123 Hz)	8.77 sec (0.114 Hz)

Having created the heave, roll and pitch motion response spectra, as shown in Figure 6.6, important ship motion parameters such as the significant single amplitude (SSA), and mean and peak periods can be deduced from the motion response spectra. For example, if m_0 is the area under the heave spectral curve for a ship, the significant heave amplitude ($Z_{1/3}$), which is the average of the one third-highest motion amplitudes, can be written

$$Z_{1/3} = 2\sqrt{m_0} \tag{6.8}$$

where the zeroth order spectral moment (m_0) is given by Eq. (6.4). The mean (T_{01}) and average zero-crossing (T_{02}) heave periods can also be calculated by Eqs. (6.2) and (6.3), respectively.

Significant roll ($\phi 1/3$) and pitch ($\theta 1/3$) amplitudes, as well as T01 and T02 for each motion spectrum, were achieved in the same manner as the heave response spectrum. The trapezoidal rule was used for approximating the area under the spectral curve.

Table 6.6 summarises the maximum and significant amplitudes, and relevant response periods for the container ship transits. Maximum amplitude for each transit is captured by finding the largest absolute amplitude in the straight course.

Table 6.6. Measured maximum and significant amplitudes, and peak (T_p), mean (T_{01}) and average zero-crossing (T_{02}) response periods

Parameters		Post-Panamax			Panamax		
		SEAMAX STAMFORD (inbound)	*CMA CGM WAGNER* (inbound)	*CMA CGM LAMARTINE* (outbound)	*MOL EMISSARY* (inbound)	*MOL EMISSARY* (outbound)	*SAFMARINE MAKUTU* (inbound)
Heave	Z_{max}	0.134 m	0.253 m	0.235 m	0.203 m	0.280 m	0.155 m
	$Z_{1/3}$	0.099 m	0.121 m	0.151m	0.110 m	0.145 m	0.104 m
	T_p	12.19 sec	14.22 sec	15.06 sec	10.67 sec	17.07 sec	15.06 sec
	T_{01}	11.62 sec	12.58 sec	14.39 sec	10.52 sec	12.64 sec	12.42 sec
	T_{02}	11.26 sec	12.04 sec	14.01 sec	10.28 sec	12.16 sec	11.99 sec
Roll	ϕ_{max}	1.004°	1.855°	0.965°	0.887°	1.199°	0.794°
	$\phi_{1/3}$	0.502°	1.065°	0.797°	0.449°	0.951°	0.467°
	T_p	13.47 sec	14.22 sec	17.07 sec	23.27 sec	19.69 sec	28.45 sec
	T_{01}	13.08 sec	14.64 sec	17.03 sec	20.80 sec	20.36 sec	29.60 sec
	T_{02}	12.96 sec	14.44 sec	16.80 sec	19.47 sec	20.08 sec	27.44 sec
Pitch	θ_{max}	0.130°	0.160°	0.152°	0.140°	0.201°	0.107°
	$\theta_{1/3}$	0.082°	0.090°	0.106°	0.079°	0.125°	0.081°
	T_p	9.85 sec	23.27 sec	10.67 sec	10.24 sec	10.24 sec	10.24 sec
	T_{01}	10.74 sec	12.91 sec	12.66 sec	10.08 sec	11.60 sec	11.43 sec
	T_{02}	10.26 sec	11.88 sec	12.18 sec	9.79 sec	11.14 sec	10.93 sec

The significant heave amplitudes (at LCG) in the range 0.10–0.15 m seem to be dependent on the swell heights; for example, CMA CGM LAMARTINE (outbound) has the highest value of 0.151 m due to the largest swell height of 0.50 m (see Table 6.4) followed by MOL EMISSARY (outbound) (Z1/3 of 0.145 m and Hs swell of 0.47 m). The roll and pitch angle amplitudes may be calculated to give their influences in metres using the beam and LPP of each ship. The roll angle amplitudes, in Table 6.6, can cause one of the bilge corners to be closer to the seabed by approximately 0.22–0.65 m by the maximum angle amplitude and 0.13–0.37 m by the significant angle amplitude. The significant pitch amplitudes range between 0.079 and 0.125°, and can bring either the FP or AP 0.17–0.31 m closer to the seabed. The largest maximum pitch amplitude of 0.201°, observed in *MOL EMISSARY* (outbound), can bring the FP or AP 0.50 m closer to the seabed.

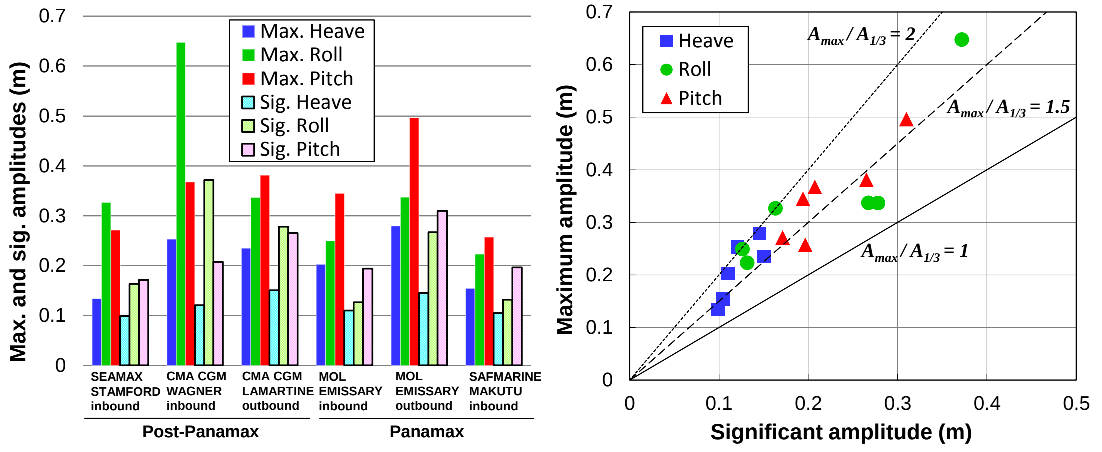

(a) (b)

Figure 6.7. (a) Comparative contributions of maximum and significant amplitudes; (b) Ratio of maximum amplitude to significant amplitude

Figure 6.7(a) shows the comparative contributions of the maximum and significant amplitudes for the container ship transits. Because the peak swell directions for all transits are very close to beam seas (see Table 6.4), the roll motion is expected to be the most significant factor governing UKC. However, in these trials the pitch motion was dominant over the heave and roll motions for the Panamax container ship transits: *MOL EMISSARY* (inbound and outbound) and *SAFMARINE MAKUTU* (inbound). This may have resulted partly from the small chance of roll resonance as their natural roll periods were far from the wave encounter periods (compare Table 6.4 and Table 6.5), and from the pitch motions arising from head, following, or oblique seas, which are possible situations considering the distributions of the wave directions (see Figure 6.4(right)). For the Post-Panamax container ship transits, the roll motion is slightly more important than the heave and pitch motions with regard to UKC.

The ratio of the maximum amplitude to the significant amplitude ($A_{max} / A_{1/3}$) shown in Figure 6.7(b) generally ranges from 1.5 to 2.0 in magnitude, and the maximum motion amplitudes for all the container ship transits are shown not to exceed twice the significant motion amplitudes.

6.5 Calculation of ship wave-induced motions

On the basis of a linear assumption of the frequency response of ship motions

(St. Denis & Pierson, 1953), the wave-induced motions of the ships can be predicted with their motion Response Amplitude Operators (RAOs) and the measured directional wave spectra. RAOs are the ratio of the response amplitude to the wave amplitude in the frequency domain, and are generally obtained with various methods such as strip theory code and radiation/diffraction panel code.

6.5.1 Calculation method

A linear strip theory method, as implemented in the computer code *OCTOPUS* with its module of *SEAWAY* (Journée, 2001; Journée & Adegeest, 2003), was used to obtain heave, roll and pitch RAOs for the ship transits. To determine the shallow-water hydrodynamic coefficients, Keil's (1974) theory was used in *OCTOPUS.* A description of the process of *OCTOPUS*'s initial seakeeping calculations to cover a full range of encountered wave conditions is found in Gourlay (2007). In the present calculations, a full range of 60 evenly-spaced wave frequencies from 0.025 to 0.25 Hz, and a full range of wave headings from 0 to 360° in 10° increments, relative to ship's heading, were chosen for the initial seakeeping calculations. The ship's heading was then used to find the RAOs in terms of wave direction. In this process, the RAOs were also interpolated to the same frequencies as the wave spectra. Having determined the motion RAOs over the full range of wave frequencies and direction combinations, the ship motion response spectra could be determined by convolution with the measured directional wave spectra (see Figure 6.4(right)) as

$$S_\eta(f,\alpha) = \left|Y(f,\alpha)\right|^2 \cdot S_w(f,\alpha) \tag{6.9}$$

Note that the earlier calculation could be expressed in terms of either the encounter frequency or the wave frequency. In this chapter the wave frequency domain has been used consistently, so the resulting motion response spectra are a function of the wave frequency. To identify such a process, Figure 6.8 complementally shows each component of Eq. (6.9), directional wave energy spectrum; motion RAO against wave direction; resulting motion response spectrum; and initial motion RAO against wave heading relative to ship, in an example transit (*SEAMAX STAMFORD*, inbound).

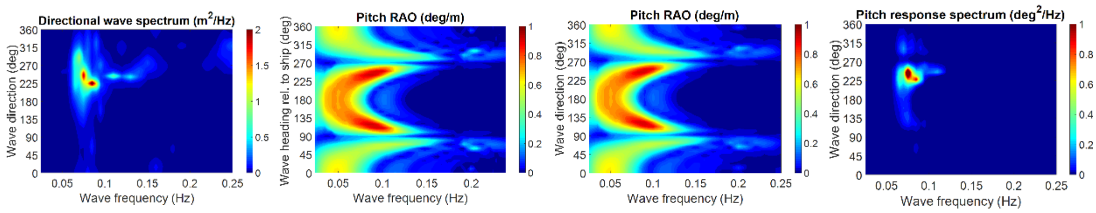

(a) (b) (c) (d)

Figure 6.8. (a) Directional wave spectrum; (b) Calculated pitch RAO against wave heading relative to ship, e.g., wave heading 0° = following seas, 90° = starboard beam seas; (c) Calculated pitch RAO against wave direction; (d) Resulting pitch response spectrum, for the *SEAMAX STAMFORD* (inbound) transit

Regarding Figure 6.8(b) and Figure 6.8(c), the RAOs initially created by *OCTOPUS* are specified for all wave headings relative to the ship, so Figure 6.8(b) cannot be matched with Figure 6.8(a), which is expressed in absolute wave directions. Figure 6.8(b) is then transformed into Figure 6.8(c) for convolution with Figure 6.8(a).

From the directional motion response spectra calculated, the non-directional motion response spectra can be found by integrating all the directional components within a single wave frequency band. These non-directional response spectra for a ship's heave, roll and pitch motions should be ultimately compared with the motion response spectra measured from the present full-scale trials. Figure 6.9 shows a methodology flowchart for the method validation of the ship wave-induced motions.

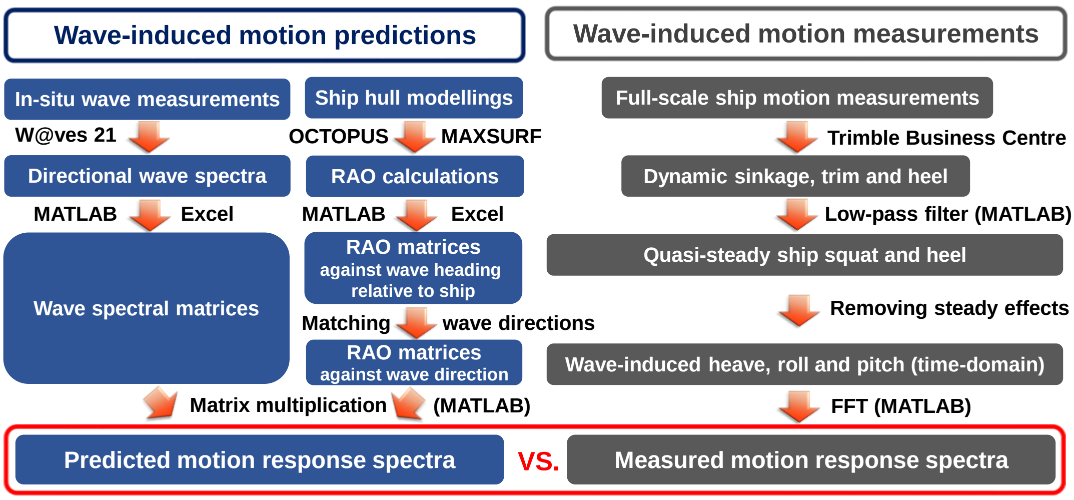

Figure 6.9. Methodology flowchart for validation of ship wave-induced motions

6.5.2 Ship hull forms modelled

To predict ship motions in a given condition, because lines plans or hull offsets for merchant container ships are usually confidential, suitable ship models should be selected from publicly available container ship hull forms for research objectives: e.g., the DTC (el Moctar, Shigunov, & Zorn, 2012), KCS (Lee, Koh, & Lee, 2003), JUMBO (Uliczka, Kondziella, & Flügge, 2004), MEGA-JUMBO (Uliczka, Kondziella, & Flügge, 2004), and FHR Ship D and FHR Ship F (Gourlay, von Graefe, Shigunov, & Lataire, 2015; Vantorre & Journée, 2003). Detailed information on the candidate ship hull forms can be found in Chapter 2.

Ships are modelled by choosing a parent hull with similar C_B, LCB and LCF to the actual ship then stretching this parent hull to the correct ship dimensions. Descriptions of the detailed procedures used in ship model selection and ship hull form modifications are presented in Chapters 2 and 5, and general geometry preparations of ship hulls for *OCTOPUS* are available in Journée (2001) and Gourlay, von Graefe, Shigunov and Lataire (2015). On the basis of these references, the KCS and FHR Ship D hulls were chosen and modified: the KCS for *SEAMAX STAMFORD* (inbound), *MOL EMISSARY* (inbound and outbound) and *SAFMARINE MAKUTU* (inbound); and the FHR ship D for *CMA CGM WAGNER* (inbound) and *CMA CGM LAMARTINE* (outbound). Body plans of the KCS and FHR ship D are shown in Figures 2.1(b) and 2.1(e); the bow, stern, profile, bottom and perspective views of the modelled ships are also shown in Appendix A.

6.5.3 Particular attention to ship roll motion

OCTOPUS calculates inviscid roll damping using standard strip theory methods. A viscous correction such as the Ikeda method (Himeno, 1981; Ikeda, Himeno, & Tanaka, 1978), a semi empirical method, can be added to this if desired. The viscous roll damping components of the Ikeda method are given by

$$B_{44V}=B_{44S}+B_{44F}+B_{44E}+B_{44L}+B_{44K} \tag{6.10}$$

The interactions between each of the components are ignored (Himeno, 1981; Ikeda, Himeno, & Tanaka, 1978).

The Ikeda method was developed and validated using small model-scale tests (Himeno, 1981; Ikeda, Himeno, & Tanaka, 1978), and publications on its validations with full-scale measurement data barely exist or have not yet been made available in the open literature. Schmitke (1978) showed that viscous roll damping might be less important in high-speed ranges. Professor Söding (personal communication, October 6, 2014) recommended no additional viscous damping for ships at substantial forward speeds when using the software *PDStrip* (Söding & Bertram, 2006), which includes hull lift effects on the roll damping. Care should, therefore, be taken to ensure the existing methods give good agreement with the full-scale roll motions of modern container ships in actual sea conditions.

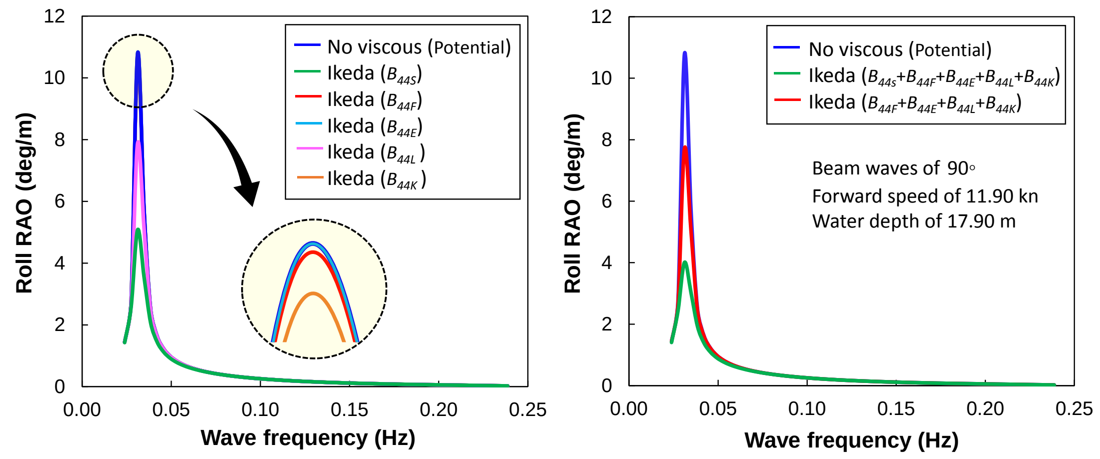

(a) (b)

Figure 6.10. Calculated roll RAOs from: (a) Different components of the Ikeda method; (b) Different approaches, for the *SAFMARINE MAKUTU* (inbound) transit

Figure 6.10(a) shows example roll RAOs calculated by the different components of the Ikeda method for the *SAFMARINE MAKUTU* (inbound) case in the given conditions (beam waves of 90°; forward speed of 11.90 knots; and water depth of 17.90 m) (see Table 6.3). For the bilge keel roll damping coefficient (B_{44K}), as the exact positions of the bilge keel for the actual ship hulls are uncertain, a bilge keel height of 0.4 m (el Moctar, Shigunov, & Zorn, 2012) and a bilge keel length of 30 % of L_{PP}, placed between 35 to 65 % of L_{PP} (*OCTOPUS* default), have been applied to all roll damping calculations.

As shown in Figure 6.10(a), the frictional damping (B_{44F}), eddy damping (B_{44E}) and bilge keel roll damping (B_{44K}) of the Ikeda method seem to have little effect on the ship's roll motion, with their roll RAOs very close to the RAO from the potential method, whereas the wave damping at forward speed (B_{44S}) appears to be the major contributing component, followed by the lift damping (B_{44L}). The frictional damping (B_{44F}) usually makes a small contribution to total roll damping, about 5–10 % of the total roll damping for a model-scale ship (Kawahara, Maekawa, & Ikeda, 2012) and 1–3 % for a full-scale ship (International Towing Tank Conference, 2011), so B_{44F} can be negligible at full scale (Himeno, 1981; Journée & Adegeest, 2003; Kawahara, Maekawa, & Ikeda, 2012). Because the eddy damping (B_{44E}) decreases with a ship's forward speed (Himeno, 1981; Ikeda, Himeno, & Tanaka, 1978; Journée & Adegeest, 2003), B_{44E} may also be ignored at full scale due to its extinction in the high-speed range (especially $F_r > 0.2$). The effect of the bilge keel on the ship's roll motion is seen to be minimal for this case because the bilge keel roll damping component is independent of forward speed according to the Ikeda method (Himeno, 1981; Ikeda, Himeno, & Tanaka, 1978).

Figure 6.10(b) shows that the Ikeda method including all five components (green line) predicts a much smaller roll RAO than the potential method (blue line). For final calculations of the roll response, an additional option (red line), the Ikeda method with no wave damping at forward speed (B_{44S}), was attempted. The Ikeda method with no B_{44S} can represent an intermediate position between the other two approaches and also represent the contribution of the lift roll damping (B_{44L}) with the small contributions from B_{44F}, B_{44E} and B_{44K} (refer to Figure 6.10(a)).

6.5.4 Results (Ship motion RAOs)

Because roll and pitch motions are strongly influenced by each of their radii of gyration, roll and pitch radii of gyration of the modelled ship should be similar to those of actual ships. However, the roll and pitch radii of gyration of the actual ships are unknown because they do not form part of normal stability calculations. For most container ships, roll and pitch radii of gyration (k_{xx} and k_{yy}) are presumed to be approximately 40 % of a ship's beam (Söding, von Graefe, el Moctar, & Shigunov, 2012; von Graefe, 2014b) and 25 % of a ship's L_{PP} (Gourlay, von Graefe, Shigunov, & Lataire, 2015; Vantorre

& Journée, 2003), respectively, so these values have been equally applied to all cases.

Calculated heave (at LCG), roll and pitch RAOs over the full range of wave directions and frequencies for two example container ship transits, *CMA CGM WAGNER* (inbound) and *CMA CGM LAMARTINE* (outbound) in the given conditions (see Table 6.3), are shown in Figure 6.11. Note that the roll RAOs are the results from the Ikeda method with no B_{44S}, by way of example. Figure D.1 in Appendix D shows these results for all six container ship transits.

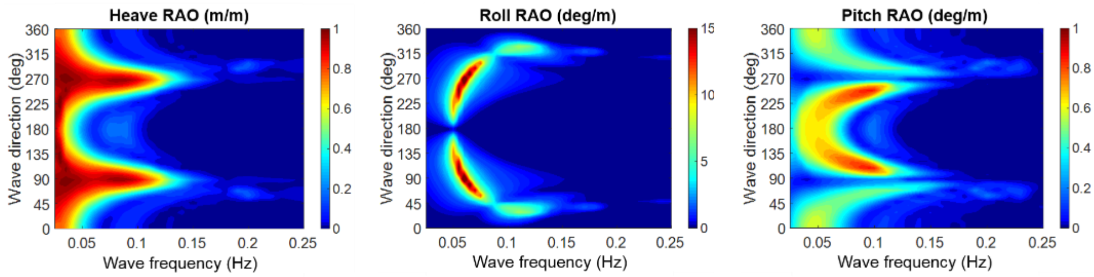

(a)

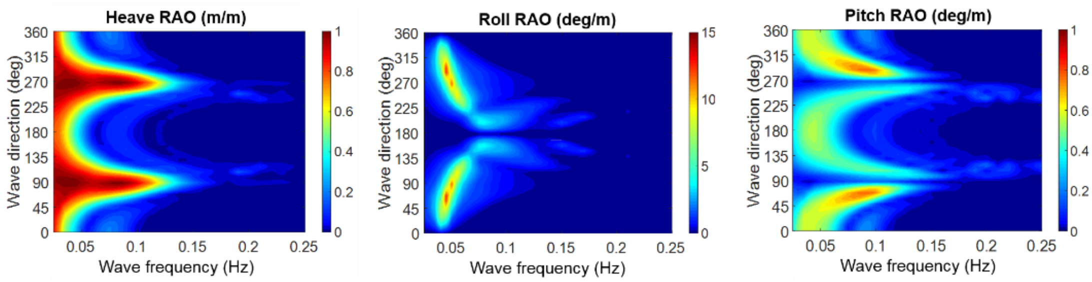

(b)

Figure 6.11. Calculated heave (left), roll (middle) and pitch (right) RAOs: (a) *CMA CGM WAGNER* inbound, 14.89 knots; (b) *CMA CGM LAMARTINE* outbound, 14.38 knots

With reference to Figure 6.10(b), Figure 6.12 additionally shows the roll RAOs from the three approaches: the potential method, the Ikeda method with no B_{44S} and the Ikeda method with all the five components, for the *CMA CGM WAGNER* (inbound) and *CMA CGM LAMARTINE* (outbound) transits. Figure D.2 in Appendix D shows these results for all six container ship transits.

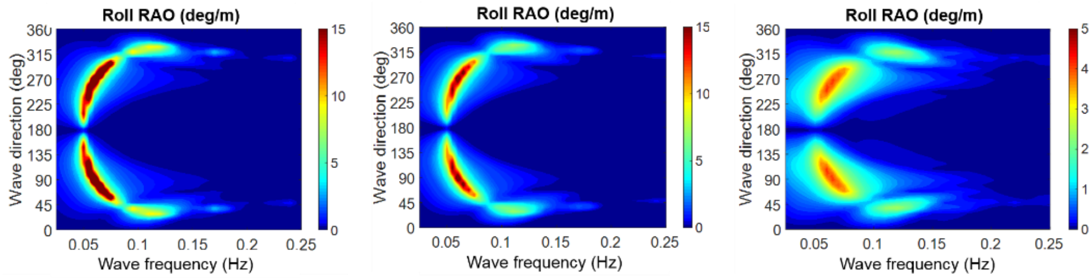

(a)

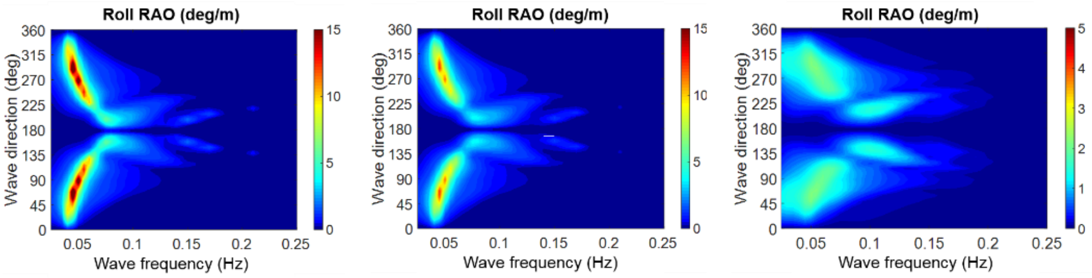

(b)

Figure 6.12. Calculated roll RAOs from the potential method (left), the Ikeda method with no B_{44S} (middle) and the Ikeda method with all five components (right): (a) *CMA CGM WAGNER* inbound, 14.89 knots; (b) *CMA CGM LAMARTINE* outbound, 14.38 knots

6.6 Method validation

Comparisons between measured and predicted heave (at LCG), roll and pitch response spectra, with the resulting significant amplitudes and peak periods, are shown in Figure 6.13, Figure 6.14 and Figure 6.15, respectively. As previously explained, the predicted non-directional response spectra were obtained from the directional response spectra by integrating all the directional components within each wave frequency band, and it must be borne in mind that the predictions given in Figure 6.13, Figure 6.14 and Figure 6.15 are only for wave buoy measurement ranges higher than 0.033 Hz, due to the low-frequency limits of the measured wave spectra. Directional heave, roll and pitch response spectra for all six container ship transits, together with corresponding directional wave spectra and their motion RAOs, are shown in Appendix E.

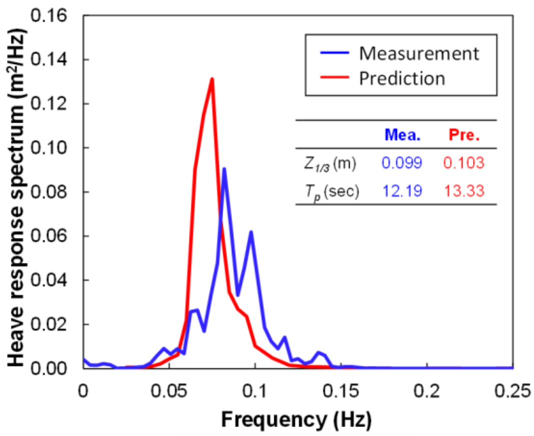

(a) *SEAMAX STAMFORD* (inbound)

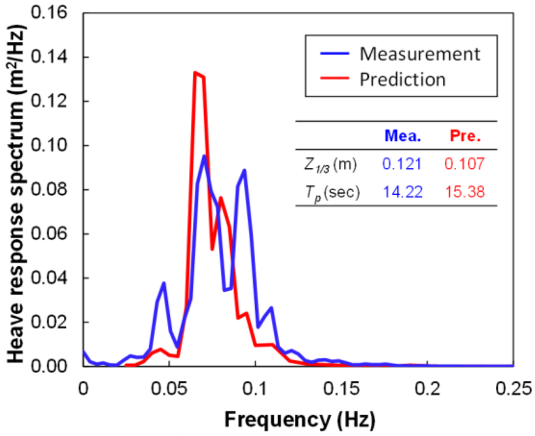

(b) *CMA CGM WAGNER* (inbound)

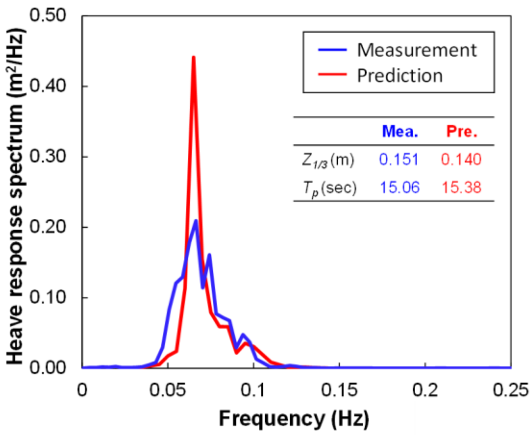

(c) *CMA CGM LAMARTINE* (outbound)

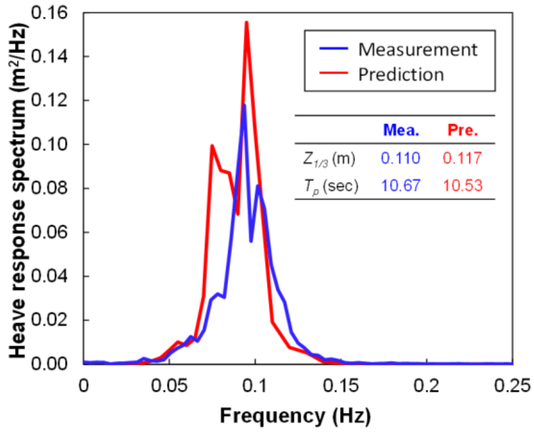

(d) *MOL EMISSARY* (inbound)

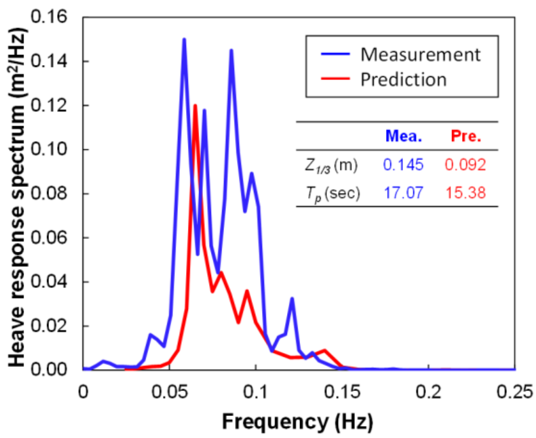

(e) *MOL EMISSARY* (outbound)

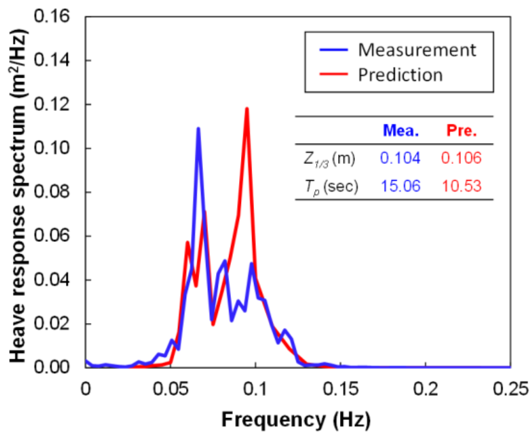

(f) *SAFMARINE MAKUTU* (inbound)

Figure 6.13. Measured and calculated heave response spectra [Note: Predictions given only for wave buoy measurement range of > 0.033 Hz]

The measured heave responses are predicted quite well by the numerical method. The average absolute error of the significant amplitude is 11.03 %, with the minimum error of 1.07 % for *SAFMARINE MAKUTU* (inbound) and the maximum error of 36.38 %

for *MOL EMISSARY* (outbound). The calculated peak periods of the heave response spectra are predicted within 10 % of the measured values, except for *SAFMARINE MAKUTU* (inbound) with a prediction error of 30.10 %. This transit occurred in erratic swells, returning a relatively wide-band spectrum with multiple peaks (see Figure 6.4(f) and Figure 6.6(f)).

Two matters in particular, need to be attended to regarding roll response. First, Figure 6.14(a, b and c) show that the full Ikeda method does not agree well with the full-scale measurements derived in the present study. This may be partly due to scale effect (Söder & Rosén, 2016). On the whole, the Ikeda method with all its components (dashed orange line) tends to significantly underpredict the roll response for the three Post-Panamax ships, *SEAMAX STAMFORD* (inbound), *CMA CGM WAGNER* (inbound) and *CMA CGM LAMARTINE* (outbound), whereas the potential method (dashed green line) gives better predictions. The Ikeda method with no B_{44S} (solid red line) may be the best tool for predicting roll response, making B_{44S}, the correction on the potential roll damping due to forward speed, unnecessary for roll motion predictions at full scale. Because frictional damping (B_{44F}), eddy damping (B_{44E}) and bilge keel damping (B_{44K}) make little contribution to the total roll damping (see Figure 6.10(a)), lift damping (B_{44L}) is the most important component for the container ship transits measured here at full scale.

As shown in Figure 6.14(d, e and f), in the Panamax container ship transits, the *MOL EMISSARY* (inbound and outbound) and *SAFMARINE MAKUTU* (inbound) transits, discrepancies between the measurements and the predictions are still conspicuous. When a ship's natural roll period is far from a typical range of wave periods (approximately 3 to 20 seconds), second-order roll motions can make the dominant contribution to the ship's total roll motions due to little potential roll damping near its natural roll period (Kim, 1992; Liu, 2003; Pinkster, 1980). In the present trials, because the Panamax container ships had natural roll periods of between about 23 and 31 seconds (see Table 6.5), a large resonant roll response from the second-order difference-frequency effect might have occurred near their natural roll periods and, hence, low frequencies in which there is very little wave energy. The linear strip method (Journée, 2001; Journée & Adegeest, 2003) used here cannot predict such non-linear phenomena, so further work is required to investigate this behaviour of container ships in the port approach channels.

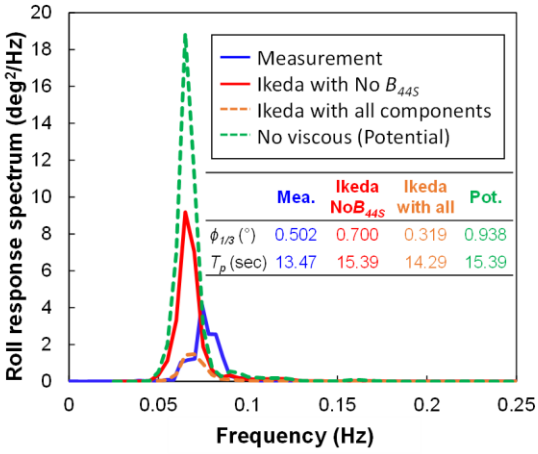

(a) *SEAMAX STAMFORD* (inbound)

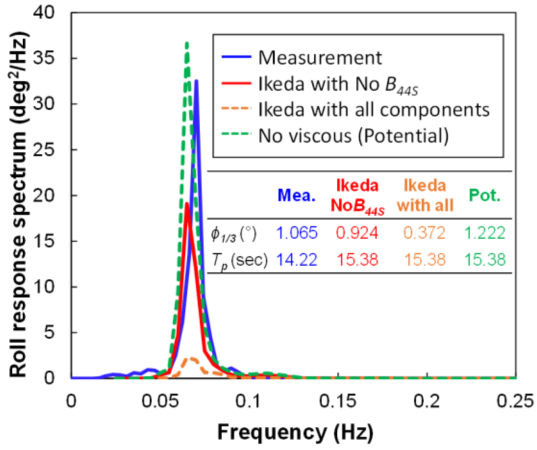

(b) *CMA CGM WAGNER* (inbound)

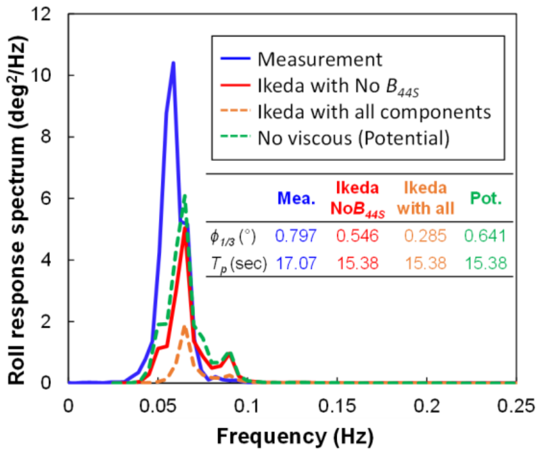

(c) *CMA CGM LAMARTINE* (outbound)

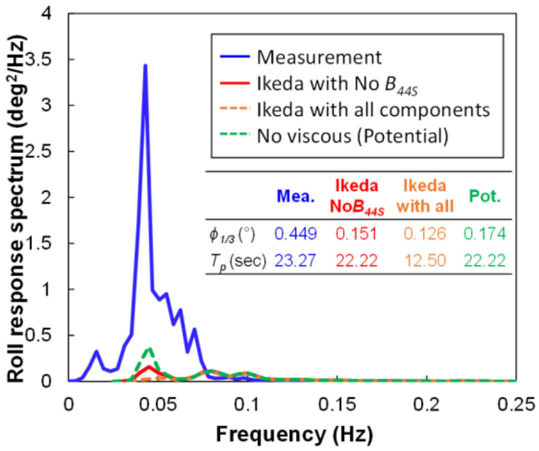

(d) *MOL EMISSARY* (inbound)

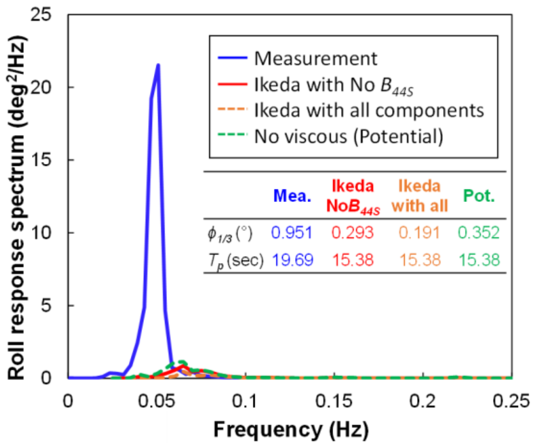

(e) *MOL EMISSARY* (outbound)

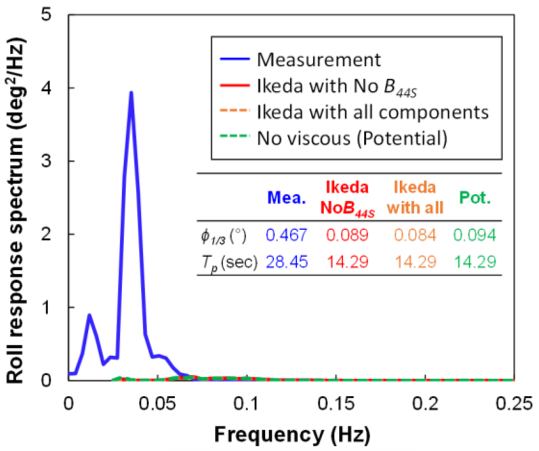

(f) *SAFMARINE MAKUTU* (inbound)

Figure 6.14. Measured and calculated roll response spectra [Note: Predictions given only for wave buoy measurement range of > 0.033 Hz]

Few studies of second-order roll motions exist, and most of these few are aimed at the motions of offshore structures or moored ships, like that of Matos, Simos and Sphaier (2011) for a semi-submersible platform with model-scale test results, and Standing, Brendling and Jackson (1991) for a FPSO (Floating Production Storage and Offloading) with full-scale test results. Therefore, the set of container ship roll motion results from the full-scale measurements presented here may provide good data for benchmarking of available numerical methods.

Figure 6.4(right), the wave directional distributions, shows a possibility of the ships' experiencing head or following seas while underway, and Table 6.4 and Table 6.5 indicate that the natural roll periods for the Panamax ship transits are about double the wave encounter periods: for example, in the peak swell period of 12.50 seconds and the natural roll period of 24.64 seconds for the *MOL EMISSARY* (inbound) transit. Considering these factors, the likelihood of the occurrence of parametric roll resonance (Froude, 1861) should not be overlooked, so it may be another possible reason for the relatively large resonant roll responses at low frequencies. As in the second-order roll motions, the parametric roll resonance cannot be captured by the linear strip method due to non-linear parametric excitations. Model-scale tests may be preferred for benchmarking studies of this phenomenon (Levadou & Gaillarde, 2003), as they can be conducted in a controlled environment, but an important practical test of numerical modelling should also be made by validations with full-scale measurement data (Galeazzi, Blanke, & Poulsen, 2013).

Regarding pitch response (see Figure 6.15), average absolute errors of 15.18 and 32.23 % are captured for the significant amplitude and peak period, respectively. Interestingly, the measured pitch response spectra are found to be double-peaked in general, which makes the predictions complicated. Whereas one of the peaks near the frequency of 0.1 Hz may be due to the ships' natural pitch frequencies (see Table 6.5), another spectral peak at the lower frequency in which little wave energy exists cannot be predicted by the linear method. Such unexpected pitch motions for the container ship transits would also be an interesting topic for future work.

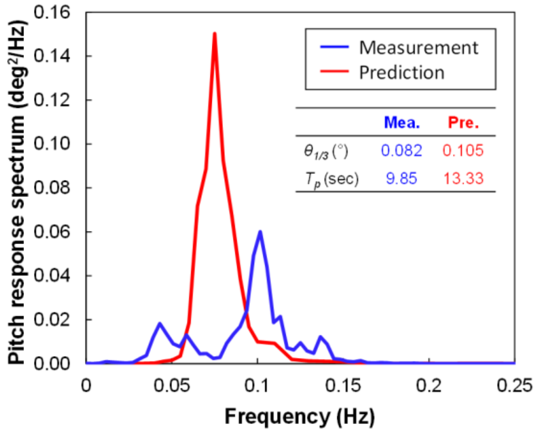

(a) *SEAMAX STAMFORD* (inbound)

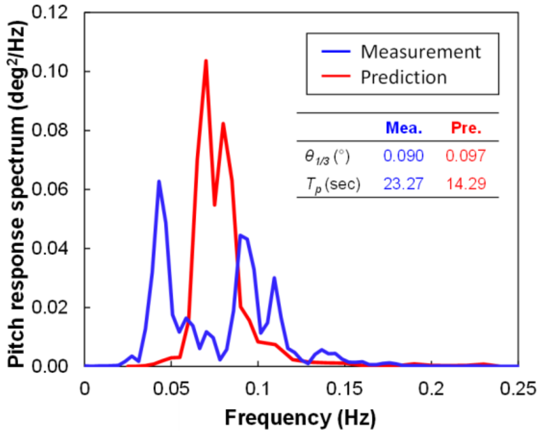

(b) *CMA CGM WAGNER* (inbound)

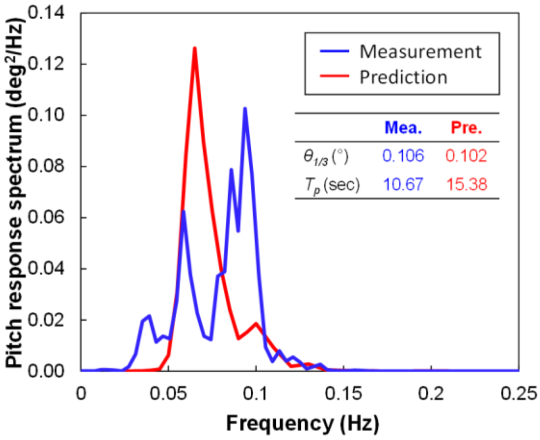

(c) *CMA CGM LAMARTINE* (outbound)

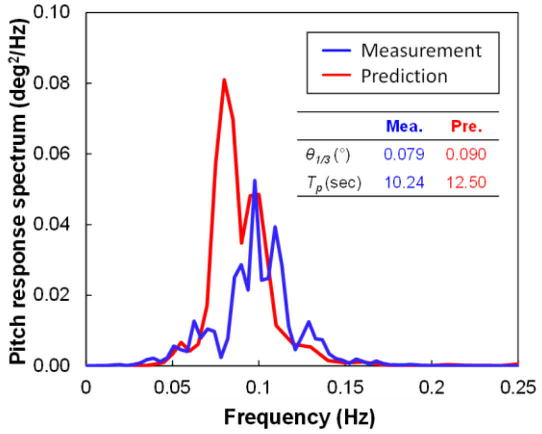

(d) *MOL EMISSARY* (inbound)

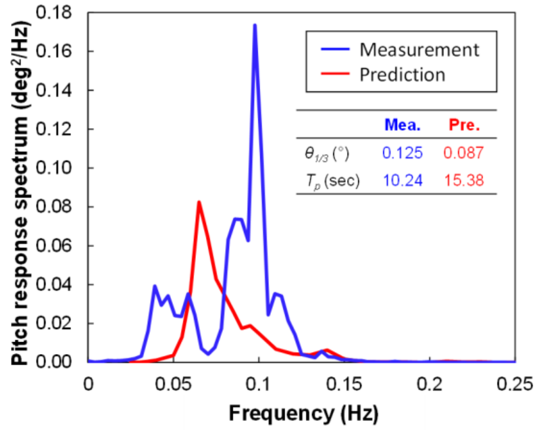

(e) *MOL EMISSARY* (outbound)

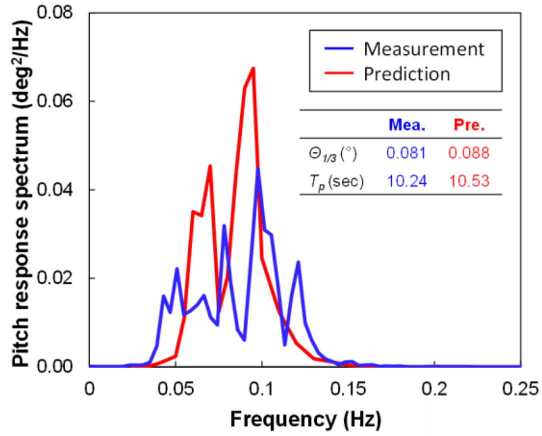

(f) *SAFMARINE MAKUTU* (inbound)

Figure 6.15. Measured and calculated pitch response spectra [Note: Predictions given only for wave buoy measurement range of > 0.033 Hz]

Figure 6.16 shows differences between the measured and calculated motion response results, which is the ratio of the predicted to the measured value: that is, *predicted value* / *measured value*. Overall, the heave responses in the given conditions at full scale are predicted well for all the transits, in that the absolute differences range from 1.1 to 36.4 % for the significant amplitude, and 1.3 to 30.1 % for the peak period. As for the roll responses, the numerical method significantly underpredicts the significant amplitudes for the Panamax container ships (*MOL EMISSARY* (inbound and outbound) and *SAFMARINE MAKUTU* (inbound)), whereas the Post-Panamax container ships (*SEAMAX STAMFORD* (inbound), *CMA CGM WAGNER* (inbound) and *CMA CGM LAMARTINE* (outbound)) are predicted with a reasonable accuracy of between 13.3 and 39.6 %. Note that the Ikeda method with no B_{44S}, having higher accuracy, is represented for the roll predictions (see Figure 6.14(a, b and c)). The predicted pitch responses also show reasonable agreement with the measurements showing the absolute differences in the range of 3.5 and 30.4 %, and 2.8 and 50.2 %, for the significant amplitude and peak period, respectively.

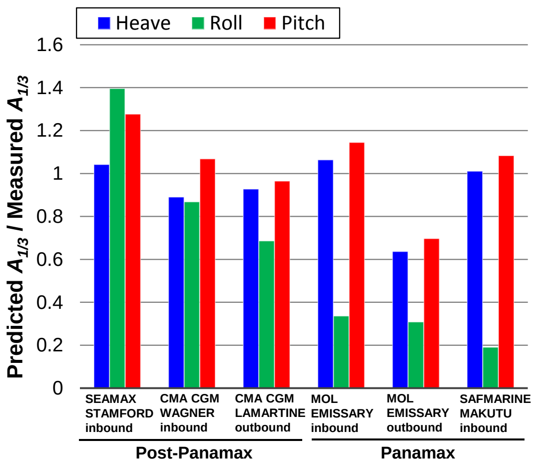

(a)

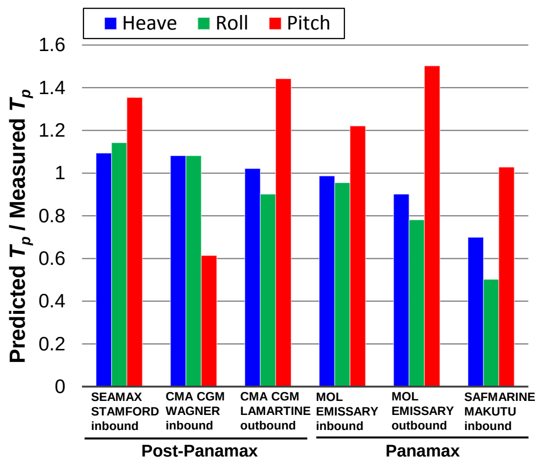

(b)

Figure 6.16. Differences between measured and calculated results for: (a) Significant amplitude; (b) Peak period

6.7 Conclusions

Having successfully performed full-scale measurements of container ships in the Port of Fremantle approach channels, a reliable data set on vertical ship motions and in-situ wave measurements was secured. Wave-induced heave, roll and pitch motions of six example container ship transits were extracted from the measured dynamic sinkage (at midships), trim and heel results. Spectral analysis of these motions was made for method validation of ship wave-induced motions in port approach channels at full scale.

Full measured wave time series data covering the entire period of the ship transits was used for the wave spectral analysis. The resulting directional wave spectra showed a clear distinction between the sea and swell parts in the Port of Fremantle approach channels. Each transit generally travelled at moderate speed (11.90–15.35 knots) in swell conditions with the significant swell heights and peak periods in the range of 0.39 and 0.50 m, and 11.11 and 15.38 seconds, respectively. The dominant wave directions of between 225 (south-west) and 315° (north-west) indicated that in general the inbound transits would travel in starboard beam or starboard bow or starboard quartering seas, and the outbound transits in port beam or port bow or port quartering seas. However, the distributions of the wave directions also showed that several transits may have travelled in head seas or following seas in some instances.

Measured heave, roll and pitch response spectra for the six container ship transits showed a certain degree of difference in the motion spectra. Heave motions had relatively wide-band response spectra with multiple peaks, and their spectral shapes were usually similar to those of the wave spectra. Roll motions showed fairly narrow-band response spectra near the ships' natural roll frequencies, and different spectral peaks for the Post-Panamax container ships (0.05–0.1 Hz) and Panamax container ships (less than 0.05 Hz). Pitch motions, interestingly, had double-peaked spectra. The significant amplitudes ranged between 0.10 and 0.15 m for the heave response, 0.449 and 1.065° for the roll response, and 0.079 and 0.125° for the pitch response. The range of the roll angle amplitude may cause one of the bilge corners to be closer to the seabed by approximately 0.13–0.37 m, and the range of the pitch angle amplitude can bring either the FP or AP 0.17–0.31 m closer to the seabed. The maximum amplitudes for all the container ship transits were shown not to exceed twice the significant amplitudes.

It is shown that the numerical method *OCTOPUS*, based on linear strip theory, was able to predict the motion responses with reasonable accuracy for full-scale container ships in the port approach channels, with an average absolute prediction error of 11.03 % for the significant heave amplitude and 15.18 % for the pitch amplitude. Regarding roll response, the original Ikeda method tended to significantly underpredict the roll response and, hence, overpredict the roll damping at full scale, but the potential method gave better predictions. The Ikeda method with no wave damping at forward speed (B_{44S}) may be the best tool for predicting the roll response here, with its higher accuracy: the average prediction error was 28.09 % for the Post-Panamax container ships (*SEAMAX STAMFORD* (inbound), *CMA CGM WAGNER* (inbound) and *CMA CGM LAMARTINE* (outbound)). This shows that B_{44S}, the correction on the potential roll damping caused by forward speed, may not be required for roll motion predictions at full scale. However, it also confirms that the linear strip program used here cannot be a proper choice when non-linear roll motions: that is, second-order roll motions and parametric roll resonance, are dominant contributors to the total roll motions. Note that if second-order effects are important, the spectral approach cannot be applied and time-domain techniques are required. These non-linear roll motions, observed in some of the present full-scale trials such as *MOL EMISSARY* (inbound and outbound) and *SAFMARINE MAKUTU* (inbound), should be investigated further. The observed double-peaked pitch responses could also be another interesting topic for future work.

Chapter 7

Conclusions and Future Work

7.1 Conclusions

In this study, sinkage coefficients were developed for cargo ships in shallow open waterways, dredged channels and canals. The coefficients were calculated using slender-body shallow-water theory (Beck, Newman, & Tuck, 1975; Tuck, 1966; 1967) applied to 13 published ship hull forms: the DTC, KCS, JUMBO, MEGA-JUMBO, FHR Ship D and FHR Ship F for container ships; the KVLCC1 and KVLCC2 for oil tankers; the Japan 1704B, JBC, FHR Ship G and MARAD Ship G for bulk carriers; and the KLNG for membrane LNG carriers. The sinkage coefficient in open water varied from hull to hull, but some distinguishing characteristics for each ship type were observed. Bow sinkage coefficients were larger than stern coefficients in most cases, regardless of ship type. A guideline for determining a sinkage coefficient corresponding to the category of ship type (container ships, oil tankers/bulk carriers, and LNG carriers), was suggested. Because the sinkage coefficients were significantly affected by the width, depth and side depth of dredged channels, or by blockage effects of canals, limitations on the use of the coefficients were also suggested, with regard to ship and navigation channel dimensions. An assessment was also made of whether a particular ship and channel configuration might be classed as open water, or whether a specific narrow-channel analysis might be required. Example assessments were provided for a Post-Panamax container ship, a Panamax iron ore carrier and a membrane LNG carrier (KLNG) in port approach channels in Western Australia.

A comparison and analysis of the dynamic sinkage and trim of several modern container ship hulls in shallow water or port approach channels was performed, together with available model-scale test data. Changes in container ship hull design to the present time were reviewed. Extensive model-scale test data exist for analysis of sinkage and trim of modern container ship hull forms, like the DTC, KCS, JUMBO and MEGA-JUMBO, in shallow water. Two potential flow methods, the slender-body method (Tuck, 1966; 1967) and the Rankine-source method (von Graefe, 2014a), were discussed with reference to the model test results, showing that the slender-body theory is accurate in its predictions of sinkage in wide canals or open water, but underpredicts sinkage in narrow canals. The Rankine-source method offers an accurate solution for this, particularly for ships at high speed in narrow canals. Calculations for the other ship hulls are recommended to assess these methods further. The slender-body theory is also able to predict dynamic trim with reasonable accuracy at model scale (except at high speed), and potentially with good accuracy at full scale. Five empirical methods (Barrass, 2004b; Huuska, 1976; Römisch, 1989; Stocks, Dagget, & Pagé, 2002; Yoshimura, 1986) listed in the recent guidelines for port approach channels (PIANC, 2014) were used for further comparisons with the numerical and model test results.

To realise measurements and validations at full scale, which can provide an important practical test of numerical UKC modelling, full-scale measurements were performed on 11 bulk carrier transits, including five inbound and six outbound transits, at the Port of Geraldton in the mid-west region of Western Australia, in September and October 2015 (Ha & Gourlay, 2016b). In April 2016, at the Port of Fremantle, Western Australia’s largest general cargo port, another set of full-scale trials measuring dynamic sinkage, trim and heel of 16 container ship transits, including seven inbound and nine outbound transits, was successfully conducted (Ha & Gourlay, 2016a). Both the measurements were made using high-accuracy GNSS receivers on board and a fixed reference station. The purpose of the trials was not only to obtain high-quality data on vertical ship motions in the port approach channels, including squat and wave-induced motions, but also to validate current UKC practice using the data from the measurements. A comprehensive environmental investigation was performed to support the measured ship motion results, including tide, wave, bathymetry and wind. Measured sinkage, together with ship speed and channel bathymetry, were shown, as were maximum dynamic sinkage and dynamic draught, and elevations of the ship’s keel relative to chart datum. Additional comparisons of dynamic trim and heel between the ship transits were given. The measured results have been used for ship squat comparisons and validations (Ha & Gourlay, 2018b) as well as for ship wave-induced motion comparisons and validations (Ha & Gourlay, 2018a), and will be made publicly available so that they can be used to validate current UKC practice by ports and as a set of benchmarking data internationally.

High-quality data for vertical ship motions in port approach channels were obtained from the two sets of the full-scale trials of bulk carriers and container ships; and the measured dynamic sinkage, trim and heel in three example bulk carrier and container ship transits, were discussed in detail. Estimated errors involved in calculating dynamic sinkage were analysed, including the effects of the GNSS receivers' error, geoid undulation error, static reading error and tide-related errors. An error in calculating geoid undulation values (N) was the main contribution to the total error, and a significant differential was found when using different geoid models like the EGM2008 and AUSGeoid09. Maximum sinkage, including the effects of squat and wave-induced motions, occurred at the bow for all three bulk carriers. Of the container ships, one transit had its maximum sinkage at the bow and the other two at the starboard bilge corner. However, several transits showed that the stern could have maximum dynamic draught due to its already close proximity to the seabed. For practical UKC management, elevations of the ship's keel relative to chart datum were calculated, and the minimum real-time clearance in each section of varying water depth was also captured. It was shown that the bulk carrier transits had a tendency to trim by the bow when underway, whereas no clear tendency in trim was found in the container ship transits. The overall dynamic trim of the container ships was much less than that of the bulk carriers at full scale. However, it was confirmed that the effect of dynamic heel on the sinkage is more important for container ships than bulk carriers, showing a maximum heel angle of up to 0.75° and heel angles generally of the order 0 to 0.5° for the three bulk carriers; and a maximum heel angle of more than 2° and heel angles generally of the order 0.5 to 1.5° for the three Post-Panamax container ships. A computer code *SlenderFlow* using slender-body shallow-water theory (Beck, Newman, & Tuck, 1975; Tuck, 1966) was applied to predict the measured sinkage and trim of the ship transits. A comparison between measured and predicted results was made to validate the ship motion software for UKC prediction. It was shown that slender-body theory is able to predict ship squat (steady sinkage and trim) with reasonable accuracy for both bulk carriers and container ships at full scale in open dredged channels.

Once a reliable data set on vertical ship motions and in-situ wave measurements from the full-scale trials of the container ships at the Port of Fremantle was obtained, validation of the numerical models of container ship wave-induced motions in the port approach channels were performed. Wave-induced heave, roll and pitch motions of six example container ship transits were extracted from the measured dynamic sinkage (at midships), trim and heel results. Spectral analysis of these motions was made, together with full measured wave time series data which covered the entire period of the container ship transits and, hence, wave spectral analysis. The resulting directional wave spectra suggested that the inbound transits were generally likely to have been in starboard beam or starboard bow or starboard quartering seas, and the outbound transits in port beam or port bow or port quartering seas; however, the distributions of the wave directions also suggested that several transits could have been made in head seas or following seas. Measured heave, roll and pitch response spectra for the six container ship transits showed a certain degree of difference. Heave motions had relatively wide-band response spectra with multiple peaks, and the spectral shapes were usually similar to those of the wave spectra. Roll motions showed a fairly narrow-band response spectra near the ships' natural roll frequencies, and different spectral peaks for the Post-Panamax (0.05-0.1 Hz) and Panamax (less than 0.05 Hz) container ships. Pitch motions, interestingly, had double-peaked spectra. The significant amplitudes ranged between 0.10 and 0.15 m for the heave response, 0.449 and 1.065° for the roll response, and 0.079 and 0.125° for the pitch response. The maximum amplitudes for all container ship transits were shown not to exceed twice the significant amplitudes.

A linear strip method, as implemented in a computer code *OCTOPUS* (Journée, 2001; Journée & Adegeest, 2003), was applied to predict the ship wave-induced motions, and a comparison was made between measured and predicted ship motion responses to validate the ship motion software. It was shown that the numerical method is able to predict the heave, roll and pitch responses with reasonable accuracy for the container ships at full scale in the port approach channels. Measured roll response in particular was used to assess the suitability of existing roll damping methods at full scale. The original Ikeda method (Himeno, 1981; Ikeda, Himeno, & Tanaka, 1978) tended to significantly underpredict the roll response and, hence, overpredict the roll damping at full scale, whereas the potential method gave better predictions. The Ikeda method with no wave damping at forward speed (B_{44S}) might be the better tool for predicting the roll response, given its higher accuracy. This result shows that B_{44S}, the correction on the potential roll damping due to forward speed, may not be required for roll motion predictions at full scale.

7.2 Future work

So far, publications concerning ship wave-induced motions in port approach channels with full-scale high-quality data do not appear to have been made available in the open literature. As a first step for providing fundamental data in this area, this thesis offers some noticeable results from container ship trials in the Port of Fremantle approach channels.

For further practical applications, other comparisons between measurements and predictions could be made with respect to the vertical motions of the six critical points for bulk carriers (see Figure 4.10) and four for container ships (see Figure 4.23). Sinkage characteristics at the vulnerable hull extremities, the FP, AP, and forward and aft shoulders of the bilge corners for bulk carriers; and the FP, AP, and port and starboard bilge corners for container ships, are of practical importance in assessing the probability of a ship grounding while underway. Understanding the composition of a ship's motions based on heave, pitch and roll may explain not only their magnitude but also the mutual phase lags between the motion modes.

Large-amplitude, long-period roll motions were observed in some cases in the full-scale trials in the Port of Fremantle channel, and double-peaked pitch responses were observed in other cases. Because the linear strip program used in this thesis cannot be a proper choice for non-linear roll motions that is, for the second-order roll motions (Kim, 1992; Liu, 2003; Pinkster, 1980) or for parametric roll resonance (Froude, 1861) and unexpected harmonic pitch motions, further research is recommended to study these seemingly non-linear effects. If nonlinearities are dominant, a linearisation method is not acceptable: hence, a spectral approach can no longer be applied, and time-domain techniques are required. The set of the container ship wave-induced motion results offered in this thesis can provide a good practical model for benchmarking of available numerical methods.

In validating ship squat modelling, the theoretical method (Tuck, 1966) is seen to generally underpredict sinkage in the example bulk carrier transits and overpredict it in the container ship transits. An empirical correction may be required in the bulk carrier transits, which were underpredicted by the prediction, as a conservative method. The best way to correct sinkage and trim predictions empirically at full scale is an area of ongoing research.

Container ships generally have significant heel arising from wind and turning in calm water. This thesis has shown that that the effect of dynamic heel on the sinkage is more important for the container ships than the bulk carriers (see Figures 5.6 and 5.16). In particular, the effect of turning manoeuvres on dynamic heel was confirmed by the container ship measurements. For example, the three Post-Panamax container ships had considerable heel angles when they made turns, e.g., a maximum heel angles of up to 2°, which includes wave-induced roll. However, such turning manoeuvres may be made in a variety of conditions that can also affect dynamic heel, such as wave actions. Dynamic heel of container ships during turning manoeuvres would be an interesting topic for future work, with reference to measured rudder changes, drift angle, rate of turn and calculated wave-induced motions.

References

Ankudinov, V. K., Daggett, C. L., Huval, C., & Hewlett, J. C. (1996). Squat predictions for manoeuvring applications. In M. S. Chislett (Ed.), *Proceedings of the International Conference on Marine Simulation and Ship Manoeuvrability, MARSIM 1996, West Terschelling, Netherlands*.

Australian Government Bureau of Meteorology. (n. d. a). *Datasheet: Hourly tides prediction for Port of Geraldton.* Melbourne, VIC. Retrieved from https://www.midwestports.com.au

Australian Government Bureau of Meteorology. (n. d. b). *Tide gauge metadata sheets for Port of Geraldton.* Melbourne, VIC. Retrieved from http://www. bom. gov. au/ntc/IDO50000/IDO50000_62290. pdf

Australian Transport Safety Bureau. (2007). *ATSB transport safety investigation report, Marine Occurrence Investigation No. 223: Independent investigation into the grounding of the Indian registered oil tanker Desh Rakshak*. Canberra, ACT: Australian Transport Safety Bureau.

Barrass, C. B. (1979). The phenomena of ship squat. *International Shipbuilding Progress*, *26*(294), 44–47.

Barrass, C. B. (2004a). *Ship design and performance for masters and mates*. Butterworth-Heinemann. UK.

Barrass, C. B. (2004b). Thirty-two years of research into ship squat. *Squat Workshop 2004*, Elsfleth/Oldenburg, Germany, 1–25.

Beck, R. F., Newman, J. N., & Tuck, E. O. (1975). Hydrodynamic forces on ships in dredged channels. *Journal of Ship Research*, *19*(3), 166–171.

Beaulieu, C., Gharbi, S., Ouarda, T. B., & Seidou, O. (2009). Statistical approach to model the deep draft ships' squat in the St. Lawrence waterway. *Journal of Waterway, Port, Coastal, and Ocean Engineering*, *135*(3), 80–90.

Briggs, M. J., Debaillon, P., Uliczka, K., & Dietze, W. (2009). Comparisons of PIANC and numerical ship squat predictions for Rivers Elbe and Weser. *Proceedings of the 3rd Squat-Workshop: Nautical Aspects of Ship Dynamics,* Elsfleth, Germany, 133–154.

Briggs, M. J., Demirbilek, Z., & Lin, L. (2014). *Vertical ship motion study for Ambrose Entrance Channel, New York (ERDC/CHL TR-14-3)*. Vicksburg, MS: US Army Engineer Research and Development Center, Coastal and Hydraulics Laboratory.

Briggs, M. J., & Henderson, W. G. (2011). *Vertical ship motion study for Savannah, GA entrance channel (ERDC/CHL TR-11-5).* Vicksburg, MS: US Army Engineer Research and Development Center, Coastal and Hydraulics Laboratory.

Briggs, M. J., Kopp, P. J., Ankudinov, V. K., & Silver, A. L. (2013). Comparison of measured ship squat with numerical and empirical methods. *Journal of Ship Research*, *57*(2), 73–85.

Briggs, M. J., Silver, A., Kopp, P. J., Santangelo, F. A., & Mathis, I. A. (2013). Validation of a risk-based numerical model for predicting deep-draft underkeel clearance. *Journal of Waterway, Port, Coastal, and Ocean Engineering*, *139*(4), 267–276.

Brown, N. J., Featherstone, W. E., Hu, G., & Johnston, G. M. (2011). AUSGeoid09: a more direct and more accurate model for converting ellipsoidal heights to AHD heights. *Journal of Spatial Science*, *56*(1), 27–37.

Campbell, N. P., & Zwamborn, J. A. (1984). Richards Bay Harbour: Port operational manual, Mark 1. *PIANC Bulletin No. 45.* Brussels, Belgium: World Association for Waterborne Transport Infrastructure.

Cong, L., & Hsiung, C. C. (1991). Computing wave resistance, wave profile, sinkage and trim of transom stern ships. *Marine and Offshore Operations*, 99–112.

Constantine, T. (1960). On the movement of ships in restricted waterways. *Journal of Fluid Mechanics*, *9*(2), 247–256.

Dand, I. W., & Ferguson, A. M. (1973). The squat of full ships in shallow water. *Transactions of the Royal Institution of Naval Architects (RINA)*, *115*, 237–255.

Datawell, BV. (2012). *Brochure W@ves21 Software*. Haarlem, Netherlands: Datawell BV. Retrieved from http://www.datawell.nl/Portals/0/Documents/Brochures/datawell_brochure_waves21_b-30-01.pdf

Datawell BV. (2014a). *Datawell Waverider Reference Manual (DWR-MKIII, DWR-G)*. Haarlem, Netherlands: Datawell BV.

Datawell BV. (2014b). *Operating Manual W@ves21 Software for Datawell Waverider Buoys (RfBuoy 2. 1. 18).* Haarlem, Netherlands: Datawell BV.

Delefortrie, G., Vantorre, M., Eloot, K., Verwilligen, J., & Lataire, E. (2010). Squat prediction in muddy navigation areas. *Ocean Engineering*, *37*(16), 1464–1476.

Deng, G. B., Guilmineau, E., Leroyer, A., Queutey, P., Visonneau, M., & Wackers, J. (2014). Simulation of container ship in shallow water at model scale & full scale. *Proceedings of the 3rd Chinese National CFD Symposium on Ship and Offshore Engineering, Dalian, China*.

Duffy, J. T. (2008). *Modelling of ship–bank interaction and ship squat for ship-handling simulation* (Doctoral dissertation, University of Tasmania, Hobart, TAS). Retrieved from https://eprints.utas.edu.au/19864

el Moctar, O., Shigunov, V., & Zorn, T. (2012). Duisburg Test Case: Post-Panamax container ship for benchmarking. *Ship Technology Research*, *59*(3), 50–64.

Eloot, K., & Vantorre, M. (2011). Ship behaviour in shallow and confined water: an overview of hydrodynamic effects through EFD. *Proceedings of RTO-AVT Specialists' Meeting on Assessment of Stability and Control Prediction Methods for Air and Sea Vehicles*, NATO. Portsdown, UK: Research and Technology Organisation (RTO).

Eryuzlu, N. E., Cao, Y. L., & D'Agnolo, F. (1994). Underkeel requirements for large vessels in shallow waterways. *Proceedings of the 28th PIANC Congress*, *Sevilla, Spain*, S-II, 17–25.

Faltinsen, O., & Michelsen, F. (1974). Motions of large structures in waves at zero Froude number. *Proceedings of the International Symposium on the Dynamics of Marine Vehicles and Structures in Waves*, *London*, *UK*.

Featherstone, W. E., Kirby, J. F., Hirt, C., Filmer, M. S., Claessens, S. J., Brown, N. J., Hu, G., & Johnston G. M. (2011). The AUSGeoid09 model of the Australian Height Datum. *Journal of Geodesy*, *85*(3), 133–150.

Feng, Y., & O'Mahony, S. (1999). Measuring ship squat, trim, and under-keel clearance using on-the-fly kinematic GPS vertical solutions. *Journal of the Institute of Navigation*, *46*(2), 109–117.

Ferguson, A. M., & McGregor, R. C. (1986). On the squatting of ships in shallow and restricted water. *Proceedings of the 20th International Conference on Coastal Engineering, Taipei, Taiwan*, 2772–2786.

Fraczek, W. (2003). Mean sea level, GPS, and the geoid. *ArcUsers Online*. Retrieved from https://www.wou.edu/las/physci/taylor/g492/geoid.pdf

Fremantle Ports. (2011). *Port Information Guide*. Fremantle, WA: Fremantle Ports. Retreived from http://www.fremantleports.com.au/sitecollectiondocuments/port%20information%20guide.pdf

Froude, W. (1861). On the rolling of ships. *Transactions of the Royal Institution of Naval Architects (RINA)*, *2*, 180–227.

Galeazzi, R., Blanke, M., & Poulsen, N. K. (2013). Early detection of parametric roll resonance on container ships. *IEEE Transactions on Control Systems Technology*, *21*(2), 489–503.

Gietz, U., & Kux, J. (1995). Flow investigations on the Hamburg Testcase model in the wind tunnel. *Bericht 550*, Technische Universität Hamburg-Harburg.

Gourlay, T. P. (1999). The effect of squat on steady nonlinear hydraulic flow past a ship in a channel. *Ship Technology Research*, *46*(4), 217–222.

Gourlay, T. P. (2000). *Mathematical and computational techniques for predicting the squat of ships* (Doctoral dissertation, University of Adelaide, Adelaide, SA). Retrieved from https://digital.library.adelaide.edu.au/dspace/handle/2440/37796

Gourlay, T. P. (2006). Flow beneath a ship at small underkeel clearance. *Journal of Ship Research*, *50*(3), 250–258.

Gourlay, T. P. (2007). Ship underkeel clearance in waves. *Proceedings of the Coasts and Ports 2007 Conference, Melbourne, VIC*.

Gourlay, T. P. (2008a). Dynamic draught of container ships in shallow water. *International Journal of Maritime Engineering*, *150*(4), 43–56.

Gourlay, T. P. (2008b). Slender-body methods for predicting ship squat. *Ocean Engineering*, 3*5*(2), 191–200.

Gourlay, T. P. (2008c). Validation of KeelClear software in Torres Strait. *CMST Report 2008–05*, Centre for Marine Science and Technology, Curtin University, Bentley, WA.

Gourlay, T. P. (2011). A brief history of mathematical ship-squat prediction, focussing on the contributions of E. O. Tuck. *Journal of Engineering Mathematics, 70*(1), 5–16.

Gourlay, T. P. (2013a). Duisburg Test Case containership squat prediction using ShallowFlow software. *Proceedings of PreSquat Workshop on Numerical Ship Squat Prediction*, *Duisburg, Germany*.

Gourlay, T. P. (2013b). Ship squat in non-uniform water depth. *Proceedings of the Coasts and Ports 2013 Conference*, *Manly, NSW*.

Gourlay, T. P. (2014a). ShallowFlow: A Program to model ship hydrodynamics in shallow water. *Proceedings of the 33rd International Conference on Ocean, Offshore and Arctic Engineering, OMAE 2014, San Francisco, CA*.

Gourlay, T. P. (2014b). *Under-keel clearance: Mind the gap*. Shipping Port International, Showcase 2014.

Gourlay, T. P. (2015). Under-keel clearance. In *Navigation accidents and their causes*. London, UK: The Nautical Institute.

Gourlay, T. P., Ha, J. H., Mucha, P., & Uliczka, K. (2015). Sinkage and trim of modern container ships in shallow water. *Proceedings of the Coasts and Ports 2015 Conference, Auckland*, *New Zealand*.

Gourlay, T. P., & Klaka, K. (2007). Full-scale measurements of containership sinkage, trim and roll. *Australian Naval Architect*, *11*(2), 30–36.

Gourlay, T. P., Lataire, E., & Delefortrie, G. (2016). Application of potential flow theory to ship squat in different canal widths. *Proceedings of the 4th International Conference on Ship Manoeuvring in Shallow and Confined Water*, *MASHCON 2016, Hamburg, Germany*, 146–155.

Gourlay, T. P., & Tuck, E. O. (2001). The maximum sinkage of a ship. *Journal of Ship Research*, *45*(1), 50–58.

Gourlay, T. P., von Graefe, A., Shigunov, V., & Lataire, E. (2015). Comparison of AQWA, GL RANKINE, MOSES, OCTOPUS, PDSTRIP and WAMIT with model test results for cargo ship wave-induced motions in shallow water. *Proceedings of the 34th International Conference on Ocean, Offshore and Arctic Engineering, OMAE 2015, St. John's, Newfoundland, Canada*.

Graff, W., Kracht, A., & Weinblum, G. (1964). Some extensions of D. W. Taylor's standard series. *Transactions of the Society of Naval Architects and Marine Engineers, 72*, 374–401.

Gronarz, A., Broß, H., Mueller-Sampaio, C., Jiang, T., & Thill, C. (2009). SIMUBIN-Modellierung und Simulation der realitaetsnahen Schiffsbewegungen auf Binnenwasserstraßen (Modelling and simulation of realistic ship movements on inland waterways). *Report 1939 B*, Development Centre for Ship Technology and Transport Systems (DST) (in German).

Ha, J. H., & Gourlay, T. P. (2016a). Ship motion measurements for ship under-keel clearance in the Port of Fremantle. *CMST Report 2016–07,* Centre for Marine Science and Technology, Curtin University, Bentley, WA.

Ha, J. H., & Gourlay, T. P. (2016b). Ship motion measurements for ship under-keel clearance in the Port of Geraldton. *CMST Report 2016-28,* Centre for Marine Science and Technology, Curtin University, Bentley, WA.

Ha, J. H., & Gourlay, T. P. (2017). Bow and stern sinkage coefficients for cargo ships in shallow open water. *Third-place winner of the 2017 PIANC De Paepe-Willems Award*, *PIANC Yearbook 2017*. Brussels, Belgium: World Association for Waterborne Transport Infrastructure.

Ha, J. H., & Gourlay, T. P. (2018a). Full-scale measurements and method validation of container ship wave-induced motion at the Port of Fremantle. To appear in *Journal of Waterway, Port, Coastal, and Ocean Engineering*.

Ha, J. H., & Gourlay, T. P. (2018b). Validation of container ship squat modelling using full-scale trials at the Port of Fremantle. *Journal of Waterway, Port, Coastal, and Ocean Engineering, 144*(1). doi: 10. 1061/(ASCE)WW. 1943-5460. 0000425

Ha, J. H., Gourlay, T. P., & Nadarajah, N. (2016). Measured ship motions in Port of Geraldton approach channel. *Proceedings of the 4th International Conference on Ship Manoeuvring in Shallow and Confined Water, MASHCON 2016, Hamburg, Germany*, 236–250.

Härting, A., Laupichler, A., & Reinking, J. (2009). Considerations on the squat of unevenly trimmed ships. *Ocean Engineering*, *36*(2), 193–201.

Härting, A., & Reinking, J. (2002). SHIPS: A new method for efficient full-scale ship squat determination. *Proceedings of the 30th PIANC Congress, Sydney, NSW,* 1805–1813.

Hatch, T. (1999). Experience measuring full scale squat of full form vessels at Australian ports. *Proceedings of the Coasts and Ports 1999 Conference, Perth*.

Havelock, T. H. (1939). Note on the sinkage of a ship at low speeds. *ZAMM-Journal of Applied Mathematics and Mechanics/Zeitschrift für Angewandte Mathematik und Mechanik*, *19*(4), 202–205.

Himeno, Y. (1981). Prediction of ship roll damping: State of the art. *Report No. 239*, Department of Naval Architecture and Marine Engineering, The University of Michigan, MI.

Hooft, J. P. (1974). The behaviour of a ship in head waves at restricted water depth. *International Shipbuilding Progress*, *21*(244), 367–378.

Huuska, O. (1976). On the evaluation of underkeel clearances in Finnish waterways. *Ship Hydrodynamics Laboratory Report No. 9*, Helsinki University of Technology, Otaniemi, Finland.

Ikeda, Y., Himeno, Y., & Tanaka, N. (1978). Components of roll damping of ship at forward speed. *Journal of the Society of Naval Architects of Japan*, *143*, 113–125.

International Commission for the Reception of Large Ships. (1980). Report of Working Group IV. *Supplement to PIANC Bulletin No. 35*.

International Towing Tank Conference. (1987). Report of the seakeeping committee, S-175 comparative model experiments. *Proceedings of the 18th International Towing Tank Conference Volume 1*, *Kobe, Japan*, 415–427.

International Towing Tank Conference. (2011). Numerical estimation of roll damping. *ITTC Recommended Procedures and Guidelines*, Procedure 7.5-02-07-04.5, Revision 00.

Jachowski, J. (2008). Assessment of ship squat in shallow water using CFD. *Archives of Civil and Mechanical Engineering*, *8*(1), 27–36.

JAVAD. (2012). *JAVAD TRIUMPH-1 Integrated GNSS Receiver Operator's Manual Version 2. 0*. San Jose, CA: JAVAD GNSS®.

JAVAD. (2015). *JAVAD TRIUMPH-2 Datasheet.* San Jose, CA: JAVAD GNSS®.

Jeans, G., Bellamy, I., de Vries, J. J., & Van Weert, P. (2003). Sea trial of the new Datawell GPS directional waverider. *Proceedings of the 7th Working Conference on Current Measurement Technology, IEEE, San Diego, CA*, 145–147.

Journée, J. M. J. (2001). User manual of SEAWAY. *TU Delft Report 1212a (Release 4. 19)*, Ship Hydromechanics Laboratory, Delft University of Technology, Delft, Netherlands.

Journée, J. M. J., & Adegeest, L. J. M. (2003). Theoretical manual of strip theory program: SEAWAY for Windows. *TU Delft Report 1370*, Ship Hydromechanics Laboratory, Delft University of Technology, Delft, Netherlands.

Joosen, W. P. A. (1964). Slender-body theory for an oscillating ship at forward speed. *Proceedings of the the 5th Symposium on Naval Hydrodynamics*, *Bergen, Norway,* 167–183.

Kawahara, Y., Maekawa, K., & Ikeda, Y. (2012). A simple prediction formula of roll damping of conventional cargo ships on the basis of Ikeda's method and its limitation. *Journal of Shipping and Ocean Engineering*, *2*(4), 201–210.

Keil, H. (1974). Die Hydrodynamische Kräfte bei der periodischen Bewegung zweidimensionaler Körper an der Oberfläche flacher Gewasser (The hydrodynamic forces of the periodic movement of two-dimensional bodies on shallow-water surface). *Bericht Nr. 305*, Institut für Schiffbau der Universität Hamburg, Deutschland (in German).

Kim, M. H. (1992). Difference-frequency wave loads on a large body in multi-directional waves. *Applied Ocean Research*, *14*(6), 353–370.

Kreitner, J. (1934). Über den Schiffswiderstand auf beschränktem Wasser. *Werft, Rederei und Hafen*, *15*, 77–82 (in German).

Larsson, L., Stern, F., & Bertram, V. (2003). Benchmarking of computational fluid dynamics for ship flows: The Gothenburg 2000 Workshop. *Journal of Ship Research*, *47*(1), 63–81.

Lataire, E., Vantorre, M., & Delefortrie, G. (2012). A prediction method for squat in restricted and unrestricted rectangular fairways. *Ocean Engineering*, *55*, 71–80.

Lee, S. J., Koh, M. S., & Lee, C. M. (2003). PIV velocity field measurements of flow around a KRISO 3600TEU container ship model. *Journal of Marine Science and Technology*, *8*(2), 76–87.

Lenain, L., & Melville, W. K. (2014). Autonomous surface vehicle measurements of the ocean's response to tropical cyclone Freda. *Journal of Atmospheric and Oceanic Technology*, *31*(10), 2169–2190.

Levadou, M., & Gaillarde, G. (2003). Operational guidance to avoid parametric roll. *Proceedings of the International Conference on Design and Operation of Container Ships, London, UK*, 75–86.

Li, L. (2010). Grounding Controlling for Ship Maneuvering in Shallow Water. *Proceedings of the 20th International Offshore and Polar Engineering Conference*, *International Society of Offshore and Polar Engineers (ISOPE), Beijing, China,* 515–522.

Liu, Y. (2003). On second-order roll motions of ships. *Proceedings of the 22nd International Conference on Ocean, Offshore and Arctic Engineering, OMAE 2003, Cancun, Mexico*.

Marine Accident Investigation Branch. (1993). *Report of the investigation into the grounding of passenger vessel Queen Elizabeth 2 on 7 August 1992*. Southampton, UK: Marine Accident Investigation Branch.

Matos, V. L. F., Simos, A. N., & Sphaier, S. H. (2011). Second-order resonant heave, roll and pitch motions of a deep-draft semi-submersible: Theoretical and experimental results. *Ocean Engineering*, *38*(17), 2227–2243.

Maruo, H. (1962). Calculation of the wave resistance of ships, the draught of which is as small as the beam. *Journal of Zosen Kiokai*, *1962*(112), 21–37.

McCollum, R. A., & Ankudinov, V. K. (2000). Measurements and predictions of wave response and vertical underkeel clearance in New York Harbor. *Proceedings of the International Conference on Marine Simulation and Ship Manoeuvrability, MARSIM 2000, Dania Beach, FL*.

Millward, A. (1992). A comparison of the theoretical and empirical prediction of squat in shallow water. *International Shipbuilding Progress*, *39*(417), 69–78.

Michell, J. H. (1898). XI. The wave-resistance of a ship. *The London, Edinburgh, and Dublin Philosophical Magazine and Journal of Science*, *45*(272), 106–123.

Moes, J. (2007). Measurement of vertical motions of bulk carriers navigating in port entrance channels. *Proceedings of the Hydrographic Conference Technical Awareness Seminar 2007, Cape Town, South Africa*.

Mucha, P., & el Moctar, O. (2014a). Numerical prediction of resistance and squat for a containership in shallow water. *Proceedings of the 17th Numerical Towing Tank Symposium, Marstrand, Sweden*.

Mucha, P., & el Moctar, O. (2014b). PreSquat: Numerische Vorhersagen von dynamischem Squat in begrenzten Gewässern (PreSquat: Numerical prediction of ship squat in restricted waters). *Bericht F005/2014*, Institut für Schiffstechnik, Universität Duisburg-Essen (in German).

Mucha, P., el Moctar, O., & Böttner, C. U. (2014). Technical note: PreSquat - Workshop on numerical prediction of ship squat in restricted waters. *Ship Technology Research*, *61*(3), 162–165.

Naghdi, P. M., & Rubin, M. B. (1984). On the squat of a ship. *Journal of Ship Research, 28*(2), 107–117.

National Geospatial-Intelligence Agency. (2017). North, west, and south coasts of Australia. *PUB. 175 sailing directions (enroute)* (13th ed.). Springfield, VA.

National Maritime Research Institute. (2015). Tokyo 2015: A Workshop on CFD in Ship Hydrodynamics. Retrieved from http://www.t2015.nmri.go.jp

Newman, J. N. (1964). A slender-body theory for ship oscillations in waves. *Journal of Fluid Mechanics*, *18*(4), 602–618.

Newman, J. N., & Tuck, E. O. (1964). Current progress in the slender body theory for ship motions. *Proceedings of the 5th Symposium on Naval Hydrodynamics*, *Bergen, Norway*, 129–165.

Ohgushi, M. (1961). *Theory of ships*, *vol. III*. Kobe, Japan: Kaibun-do Book Company (in Japanese).

Papanikolaou, A. (2014). *Ship design: methodologies of preliminary design*. Berlin, Germany: Springer.

Pavlis, N. K., Holmes, S. A., Kenyon, S. C., & Factor, J. K. (2012). The development and evaluation of the Earth Gravitational Model 2008 (EGM2008). *Journal of Geophysical Research: Solid Earth*, *117*(B4).

PIANC: The World Association for Waterborne Transport Infrastructure. (1985). *Underkeel Clearance for Large Ships in Maritime Fairways with Hard Bottoms*: *Report of Working Group II, Supplement to PIANC Bulletin No. 51*. Brussels, Belgium: World Association for Waterborne Transport Infrastructure.

PIANC: The World Association for Waterborne Transport Infrastructure. (2014). *Harbour Approach Channels Design Guidelines: PIANC Report No. 121.* Brussels, Belgium: World Association for Waterborne Transport Infrastructure.

Pinkster, J. A. (1980). *Low frequency second order wave exciting forces on floating structures* (Doctoral dissertation, Delft University of Technology, Delft, Netherlands). Retrieved from https://repository.tudelft.nl/islandora/object/uuid: d6d 42e9c-c349-47e5-8d63-5c6454196b04?collection=research

Press, W. H., Teukolsky, S. A., Vetterling, W. T., & Flannery, B. P. (1992). *Numerical recipes in C: The art of scientific computing* (2^{nd} ed.). New York, NY: Cambridge University Press.

Römisch, K. (1989). Empfehlungen zur Bemessung von Hafeneinfahrten (Recommendations for the design of harbor entrances). Wasserbauliche Mitteilungen der Technischen Universität Dresden, Heft *1*, 39–63.

Roseman, D. P. (Ed.) (1987). *The MARAD systematic series of full form ship models*. Jersey City, NJ: The Society of Naval Architects and Marine Engineers (SNAME) Publications.

Schmitke, R. T. (1978). Ship sway, roll, and yaw motions in oblique seas. *SNAME Transactions*, *86*, 26–46.

Skandali, D. (2015). *Identification of response amplitude operators for ships based on full scale measurements* (Master's thesis, Delft University of Technology, Delft, Netherlands). Retrieved from https://repository.tudelft.nl/islandora/object/uuid%3Af55f9c73-c71c-4448-b3e6-ac96dad4b269

Söder, C. J., & Rosén, A. (2016). A framework for holistic roll damping prediction. *Proceedings of the 15th International Ship Stability Workshop*, *Stockholm, Sweden*.

SOKKIA. (2007). *Sokkia GSR2700 ISX Operations Manual (58023002, Part number 750-1-0058 Rev 1)*. Olathe, KS: SOKKIA.

Söding, H., & Bertram, V. (2006). Program PDSTRIP: Public Domain Strip Method. Retrieved from https://sourceforge.net/projects/pdstrip

Söding, H., von Graefe, A., el Moctar, O., & Shigunov, V. (2012). Rankine source method for seakeeping predictions. *Proceedings of the 31st International Conference on Ocean, Offshore and Arctic Engineering, OMAE 2012, Rio de Janeiro, Brazil,* 449–460.

Standing, R. G., Brendling, W. J., & Jackson, G. E. (1991). Full-scale measured and predicted low-frequency motions of the semi-submersible support vessel 'Uncle John'. *Proceedings of the 1st International Offshore and Polar Engineering Conference, International Society of Offshore and Polar Engineers (ISOPE), Edinburgh, UK*, 434–441.

Standing, R. G., Brendling, W. J., & Jackson, G. E. (1993). *Summary report on an investigation into the correlation between full-scale measured and predicted motions of the SSSV 'Uncle John'*. London, UK: HM Stationery Office.

St. Denis, M., & Pierson, W. J. (1953). On the motion of ships in confused seas. *SNAME Transactions*, *61*, 281–357.

Stocks, D. T., Dagget, L. L., & Pagé, Y. (2002). *Maximization of ship draft in the St. Lawrence seaway, Volume 1: Squat study, Rep. No. TP 13888*. Canada: Transportation Development Centre, Transport Canada.

Tahara, Y., Wilson, R. V., Carrica, P. M., & Stern, F. (2006). RANS simulation of a container ship using a single-phase level-set method with overset grids and the prognosis for extension to a self-propulsion simulator. *Journal of marine science and technology*, *11*(4), 209-228.

Terziev, M., Tezdogan, T., Oguz, E., Gourlay, T., Demirel, Y. K., & Incecik, A. (2018). Numerical investigation of the behaviour and performance of ships advancing through restricted shallow waters. *Journal of Fluids and Structures*, 76, 185–215.

Transport Accident Investigation Commission. (2003a). *Marine Occurrence Report, Report No. 03-206, Tanker Capella Voyager, Grounding, Whangarei.* Wellington: Transport Accident Investigation Commission.

Transport Accident Investigation Commission. (2003b). *Marine Occurrence Report, Report No. 03-211, Oil Tanker Eastern Honor, Grounding, Whangarei Harbour.* Wellington: Transport Accident Investigation Commission.

Trimble. (2012). *Trimble R10 GNSS receiver User Guide: Chapter 5 Specifications (Revision A)*. Sunnyvale, CA: Trimble.

Tuck, E. O. (1966). Shallow water flows past slender bodies. *Journal of Fluid Mechanics*, *26*, 81–95.

Tuck, E. O. (1967). Sinkage and trim in shallow water of finite width. *Schiffstechnik*, *14*, 92–94.

Tuck, E. O., & Taylor, P. J. (1970). Shallow water problems in ship hydrodynamics. *Proceedings of the 8th symposium on naval hydrodynamics, Pasadena, CA,* 627–659.

Uliczka, K., & Kondziella, B. (2006). Dynamic response of very large container ships in extremely shallow water. *Proceedings of the 31st PIANC Congress*, *Estoril, Portugal*.

Uliczka, K., Kondziella, B., & Flügge, G. (2004). Dynamisches fahrverhalten sehr großer containerschiffe in seitlich begrenztem extremen Flachwasser (Dynamic behaviour of very large container ships in extremely confined and shallow water). *HANSA 141*, 1 (in German).

United Kingdom Maritime Pilots' Association. (2008). Squat: Are we out of our depth? *The Pilot 292*, 1–6.

United States Naval Research Laboratory. (n. d.). Fremantle: Tides and Currents. Retrieved from https://www.nrlmry.navy.mil/port_studies/thh-nc/australi/fremantl/text/sect6.htm

Van, S. H., Kim, W. J., Yim, D. H., Kim, G. T., Lee, C. J., & Eom, J. Y. (1998). Flow measurement around a 300K VLCC model. *Proceedings of the Annual Spring Meeting, The Society of Naval Architects of Korea (SNAK), Ulsan, Korea*, 185–188.

Van, S. H., Kim, W. J., Yoon, H. S., Lee, Y. Y., & Park, I. R. (2006). Flow measurement around a model ship with propeller and rudder. *Experiments in Fluids*, *40*(4), 533–545.

Van, S. H., Yoon, H. S., Lee, Y. Y., Park, I. R., Lee, C. J., & Kim, W. J. (2003). Measurement of flow around KRISO 138K LNG carrier model. *Journal of the Society of Naval Architects of Korea*, *40*(2), 1–10.

van Dijk, R. T., Quiniou-Ramus, V., & Le-Marechal, G. (2003). Comparison of full-scale measurements with calculated motion characteristics of a West of Africa FPSO. *Proceedings of the 22nd International Conference on Ocean, Offshore and Arctic Engineering, OMAE 2003, Cancun, Mexico*, 335–339.

Van Oortmerssen, G. (1976). *The motions of a moored ship in waves*. Netherlands Ship Model Basin (NSMB) Publication No. 510.

Vantorre, M. (2003). Review of practical methods for assessing shallow and restricted water effects. *Proceedings of the International Conference on Marine Simulation and Ship Manoeuvrability*, *MARSIM 2003, Kanazawa, Japan*.

Vantorre, M., & Journée, J. M. J. (2003). Validation of the strip theory code SEAWAY by model tests in very shallow water. *Proceedings of the Numerical Modelling Colloquium (DUT-SHL Report Nr. 1373-E)*. Antwerp, Belgium: Flanders Hydraulics Research.

Van Wyk, A. C. (1982). Wave-induced ship motions in harbour entrances: A field study. *Proceedings of the 18th International Conference on Coastal Engineering, Cape Town, South Africa*.

Van Wyk, A. C., & Zwamborn, J. A. (1988). Wave-induced ship motions in harbour approach channels. *Proceedings of the 21st International Conference on Coastal Engineering, Costa del Sol-Malaga, Spain*.

Veen, E. J. (2003). *Wave forces in directional seas: A method to include directional spreading of waves into the analysis of the behaviour of moored ships*. Faculty of Civil Engineering and Geosciences, Delft University of Technology, Delft, Netherlands.

Verstraete, J. M. (2001). *Sea-level changes and their effects: Low frequency sea level variability in the western tropical pacific 1992–1998*. Singapore: World Scientific Publishing.

von Graefe, A. (2014a). *A Rankine source method for ship–ship interaction and shallow water problems* (Unpublished doctoral dissertation). University of Duisburg-Essen, Duisburg, Germany.

von Graefe, A. (2014b). Rankine source method for seakeeping analysis in shallow water. *Proceedings of the 33rd International Conference on Ocean, Offshore and Arctic Engineering, OMAE 2014, San Francisco, CA*.

Wang, S. (1980). Full-scale measurements and statistical analyses of ship motions in a navigational channel. *Marine Technology*, *17*(4), 351–370.

Yaakob, O. B. (2008). Naval Architecture Notes. Faculty of Mechanical Engineering, Malaysia University of Technology, Johor, Malaysia. Retrieved from https://mech.utm.my/koh/wp-content/uploads/sites/98/2015/09/NA2-Chapter-1-2.pdf

Yokoo, K. (1966). Systematic series model tests in Japan concerning the propulsive performance of full ship forms. *Japan Shipbuilding and Marine Engineering*, *1*(2), 13–22.

Yoshimura, Y. (1986). Mathematical model for the manoeuvring ship motion in shallow water. *Journal of the Kansai Society of Naval Architects, Japan*, *200.*

Yun, K., Park, B., & Yeo, D. J. (2014). Experimental study of ship squat for KCS in shallow water. *Journal of the Society of Naval Architects of Korea*, *51*(1), 34–41.

Yun, K., Park, K., & Park, B. (2014). Study of ship squat for KVLCC2 in shallow water. *Journal of the Society of Naval Architects of Korea*, *51*(6), 539–547.

Appendix A - Modelled Ship Hulls

The hull shapes of the 13 cargo ships, the DTC, KCS, JUMBO, MEGA-JUMBO, FHR Ship D and FHR Ship F for container ships; the KVLCC1 and KVLCC2 for oil tankers; the Japan 1704B, JBC, FHR Ship G and MARAD Ship G for bulk carriers; and the KLNG for membrane LNG carriers (see also Table 2.1), have been modelled from supplied IGES files and the published lines plans using *Rhino 5* (www.rhino3d.com), *AutoCAD 2017* (www.autodesk.com) and *MAXSURF Modeler Advanced 20.00.05.47* (www.maxsurf.net) software.

Bow, stern, profile, bottom and perspective views of the modelled ships are shown in Figure A.1 to Figure A.10. These figures emphasise each ship type's features in hull shape. For instance, the container ship hulls have streamlined forward and aft sections, while the hulls of the oil tankers and bulk carriers are very block-like with a long parallel midbody. Note that IGES files are not available for the Japan 1704B, MARAD Ship G and KLNG, so they are not shown.

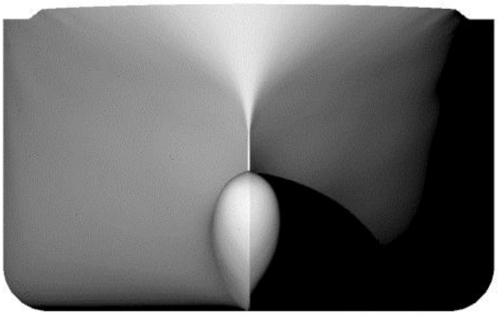

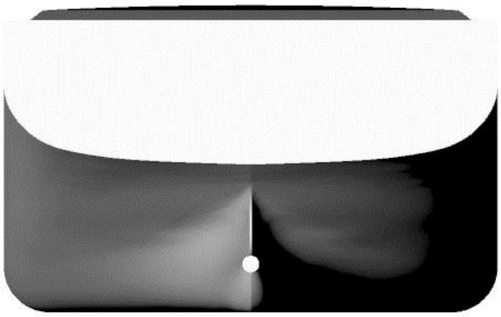

(a) Bow view (b) Stern view

(c) Profile view (starboard view)

(d) Bottom view

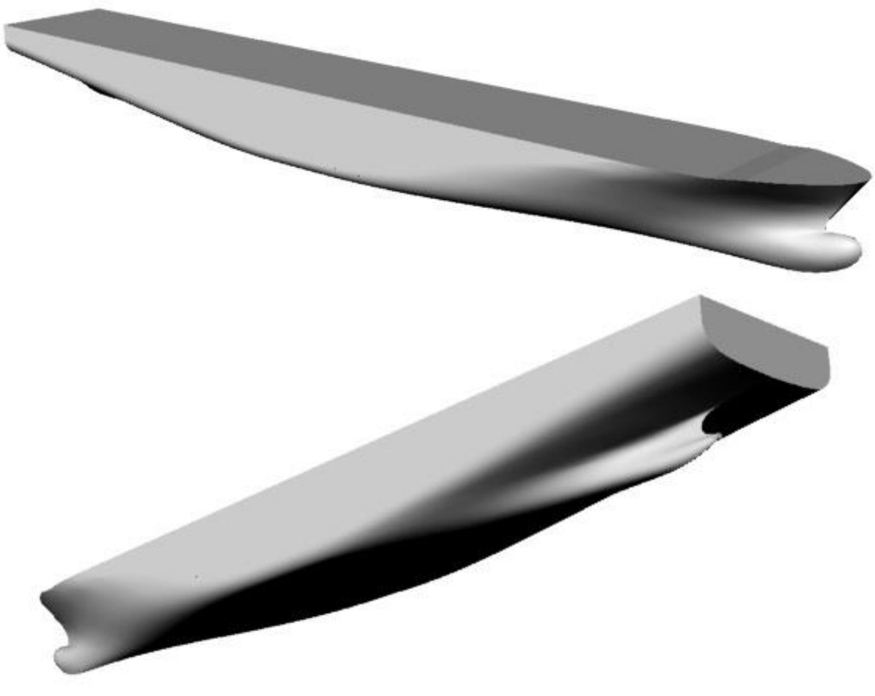

(e) Perspective view

Figure A.1. Rendered views of the DTC

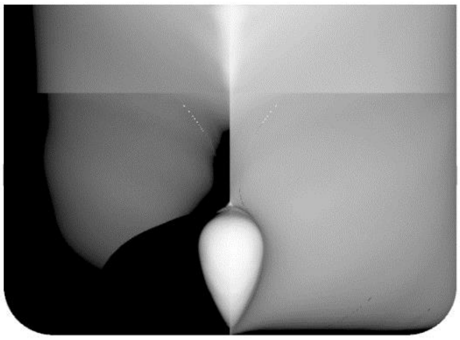

(a) Bow view

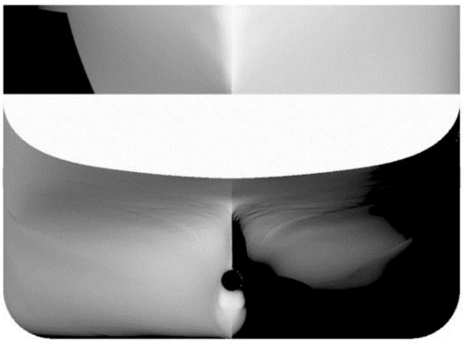

(b) Stern view

(c) Profile view (starboard view)

(d) Bottom view

(e) Perspective view

Figure A.2. Rendered views of the KCS

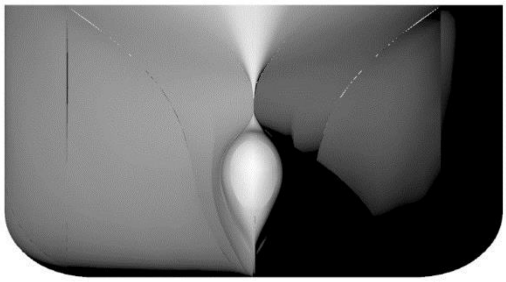

(a) Bow view

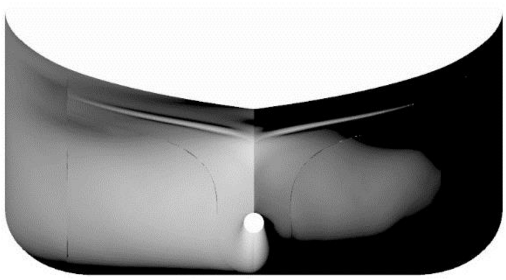

(b) Stern view

(c) Profile view (starboard view)

(d) Bottom view

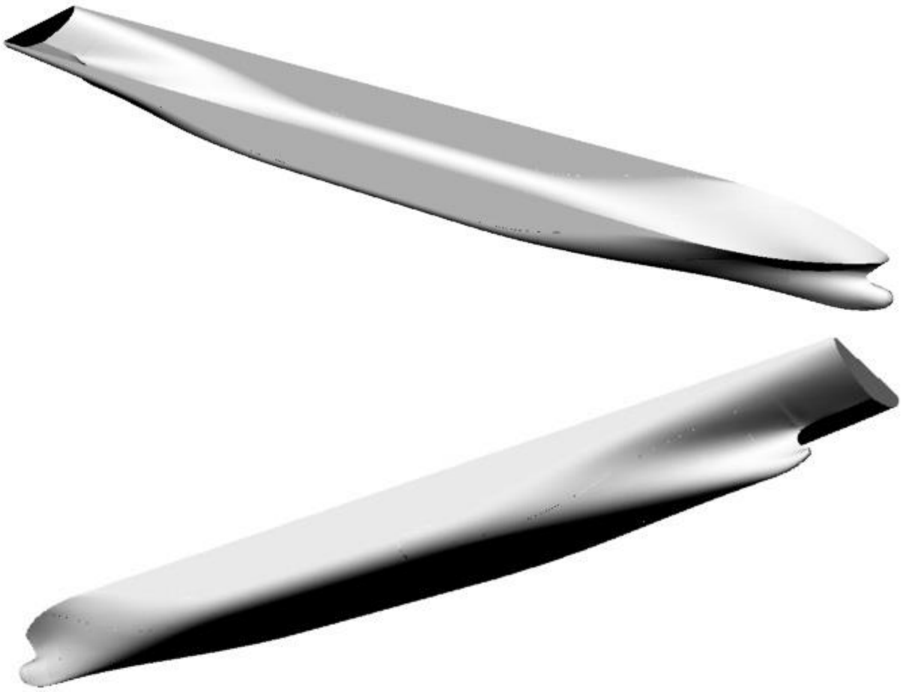

(e) Perspective view

Figure A.3. Rendered views of the JUMBO

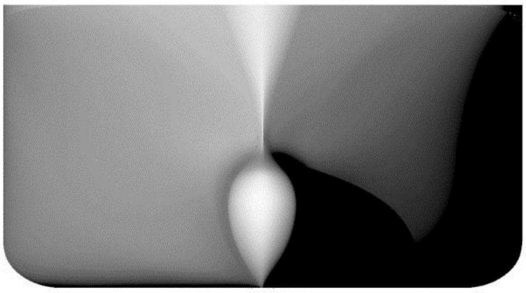

(a) Bow view

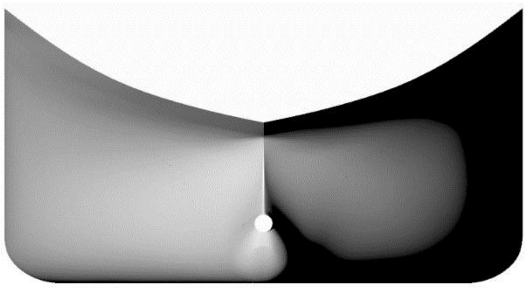

(b) Stern view

(c) Profile view (starboard view)

(d) Bottom view

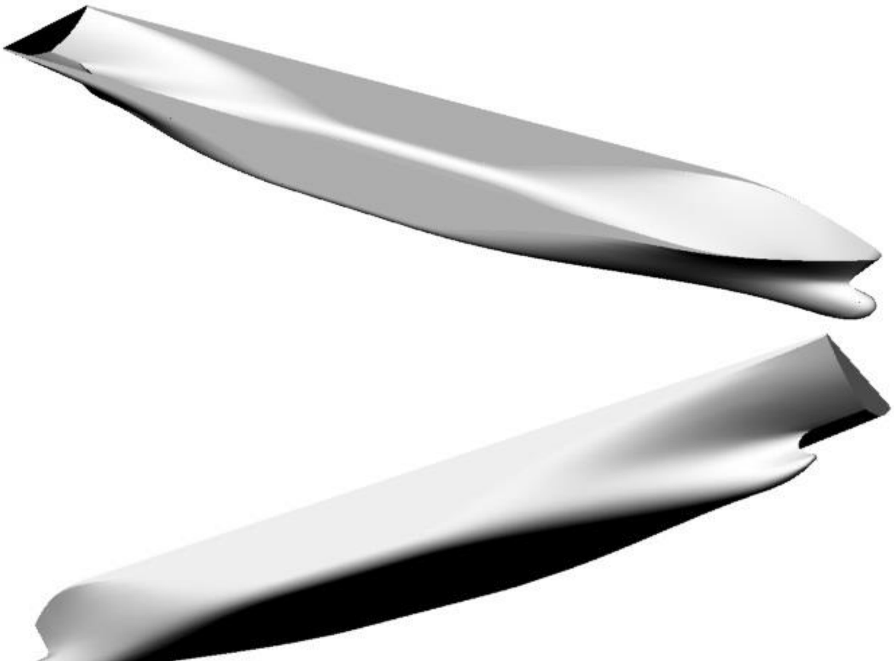

(e) Perspective view

Figure A.4. Rendered views of the MEGA-JUMBO

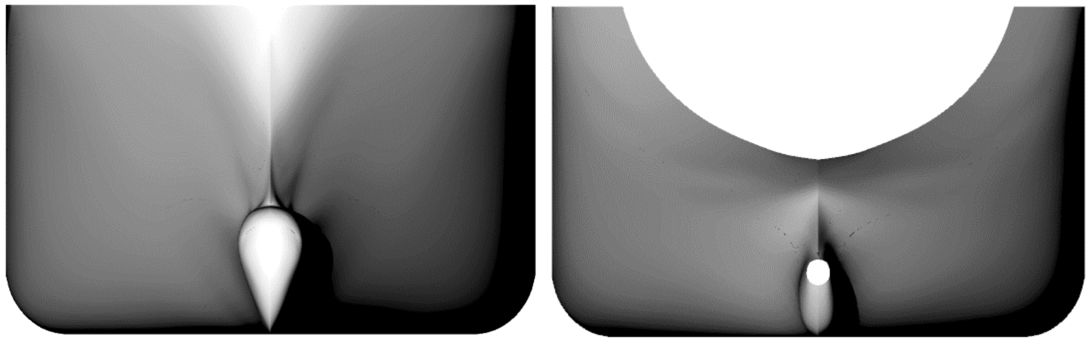

(a) Bow view (b) Stern view

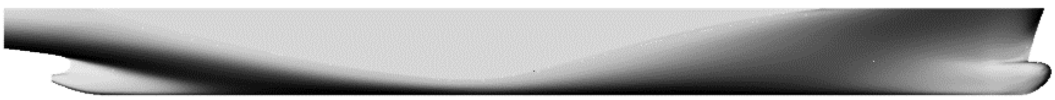

(c) Profile view (starboard view)

(d) Bottom view

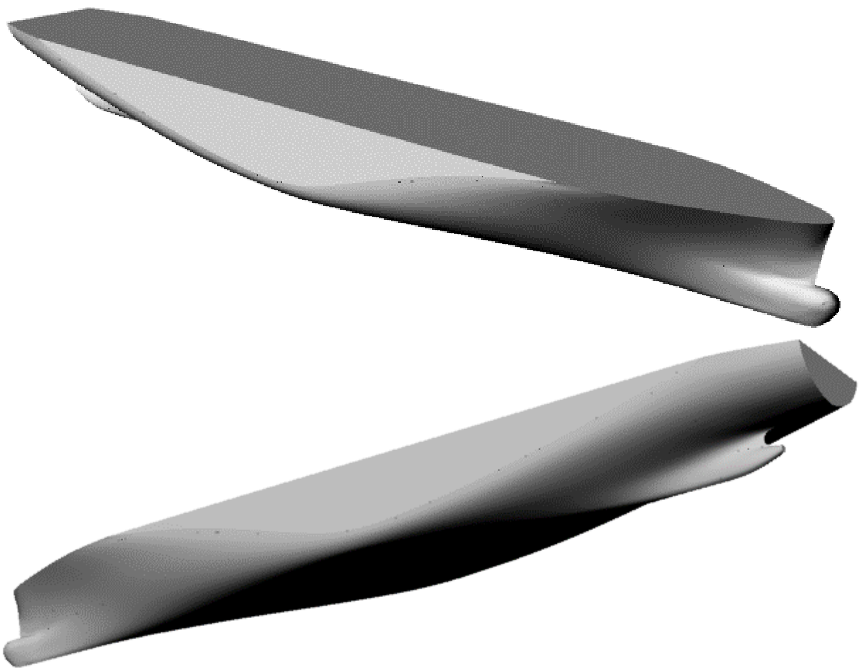

(e) Perspective view

Figure A.5. Rendered views of the FHR Ship D

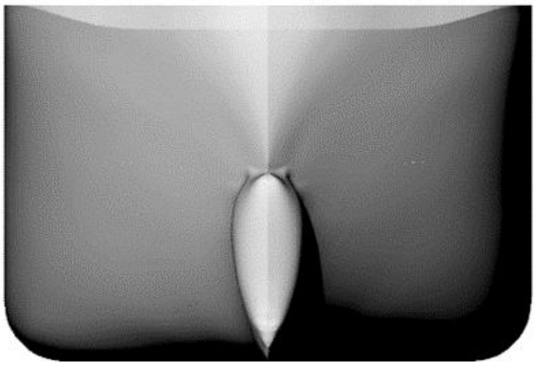

(a) Bow view

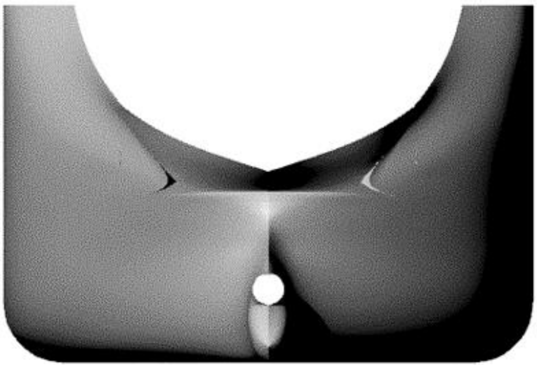

(b) Stern view

(c) Profile view (starboard view)

(d) Bottom view

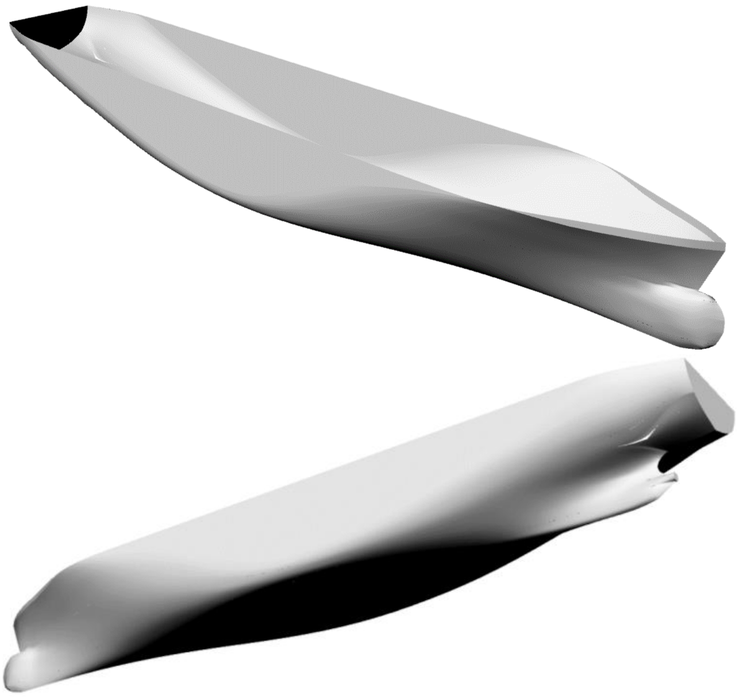

(e) Perspective view

Figure A.6. Rendered views of the FHR Ship F

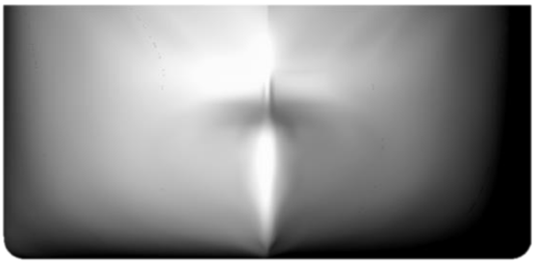

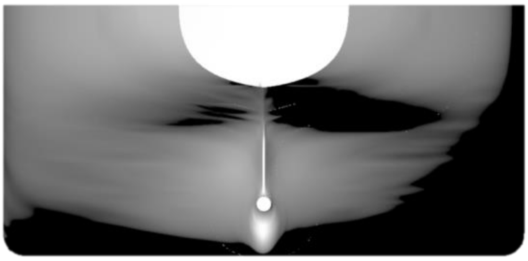

(a) Bow view (b) Stern view

(c) Profile view (starboard view)

(d) Bottom view

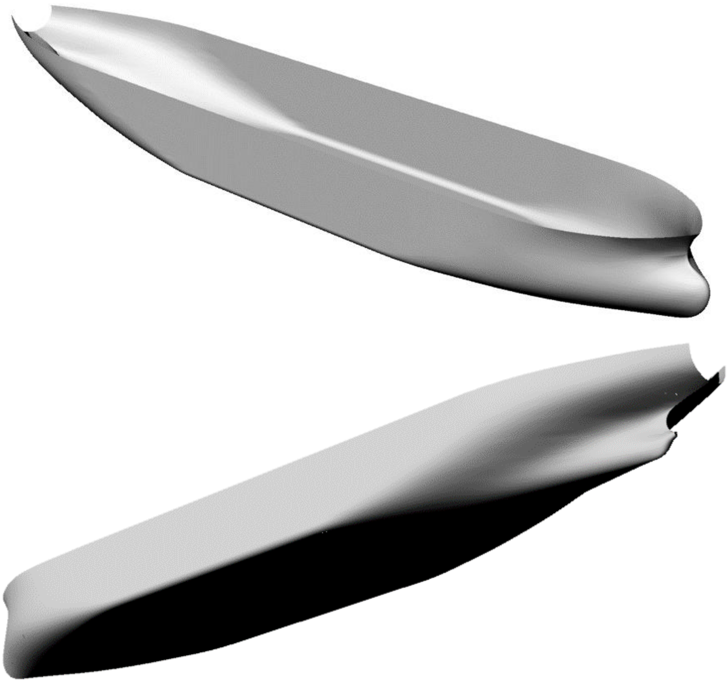

(e) Perspective view

Figure A.7. Rendered views of the KVLCC1

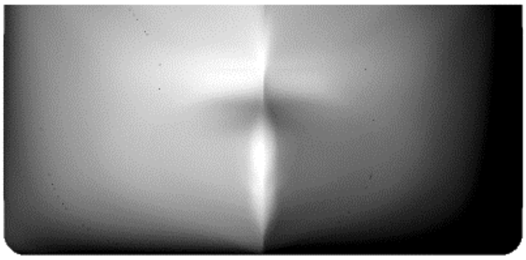

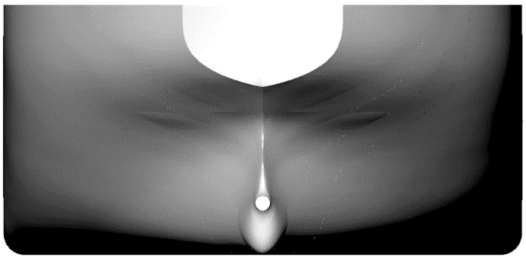

(a) Bow view (b) Stern view

(c) Profile view (starboard view)

(d) Bottom view

(e) Perspective view

Figure A.8. Rendered views of the KVLCC2

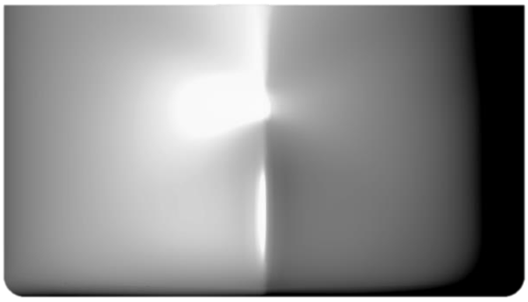

(a) Bow view

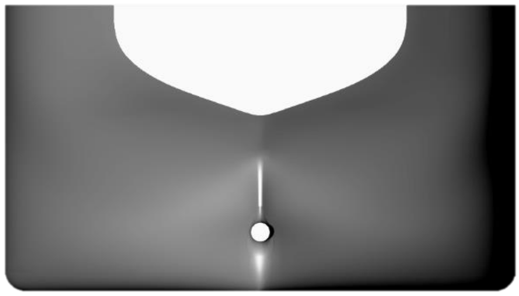

(b) Stern view

(c) Profile view (starboard view)

(d) Bottom view

(e) Perspective view

Figure A.9. Rendered views of the JBC

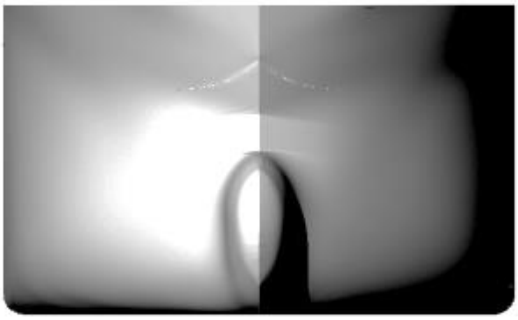
(a) Bow view

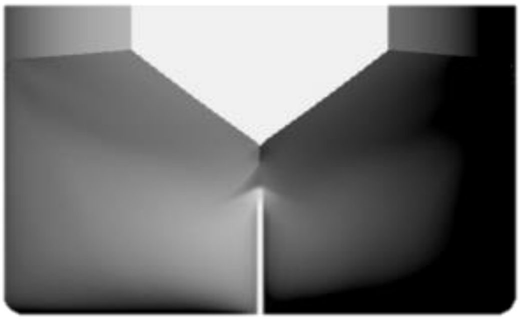
(b) Stern view

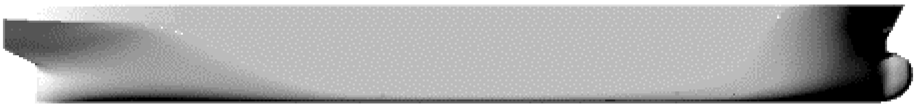
(c) Profile view (starboard view)


(d) Bottom view


(e) Perspective view

Figure A.10. Rendered views of the FHR Ship G

Appendix B - Tidal and Wave Data

B.1 Tidal and wave data measured during the bulk carrier transits at the Port of Geraldton

Tidal data in the form of raw sea surface elevations as measured at Berth 3-4 (28° 46.60000' S, 114° 35.76667' E) (see Figure 4.2) in the Port of Geraldton was provided by MWPA. The independent local tide for each transit has been extracted from the raw sea surface data using a low-pass filter with a cutoff period of five minutes. The tidal data covering the period of each bulk carrier transit is shown in Figure 4.6(a) to Figure B.11(a). No tidal data was acquired during the *AAL FREMANTLE* (outbound) transit; instead predicted hourly tidal data (Australian Government Bureau of Meteorology, n. d. a) is presented in Figure B.9(a).

Wave data from the AWAC at Beacon 2 (B2) (28° 45.47000' S, 114° 33.93167' E) (see Figure 4.7) were also provided by MWPA. Figure 4.6(b and c) - Figure B.11(b and c) show such data for all the bulk carrier transits.

Note that the tidal and wave data in Figure 4.6 to Figure B.11 are arranged in chronological order of the trials at the Port of Geraldton (see Table 4.1).

HONG YUAN (inbound)

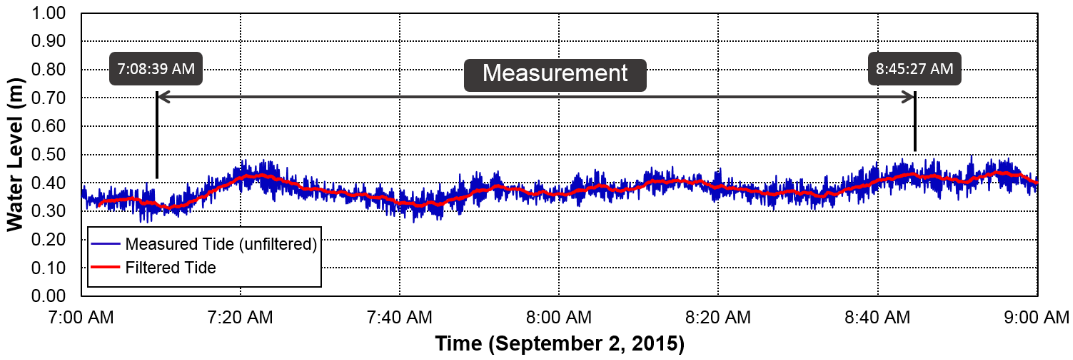

(a) Tide

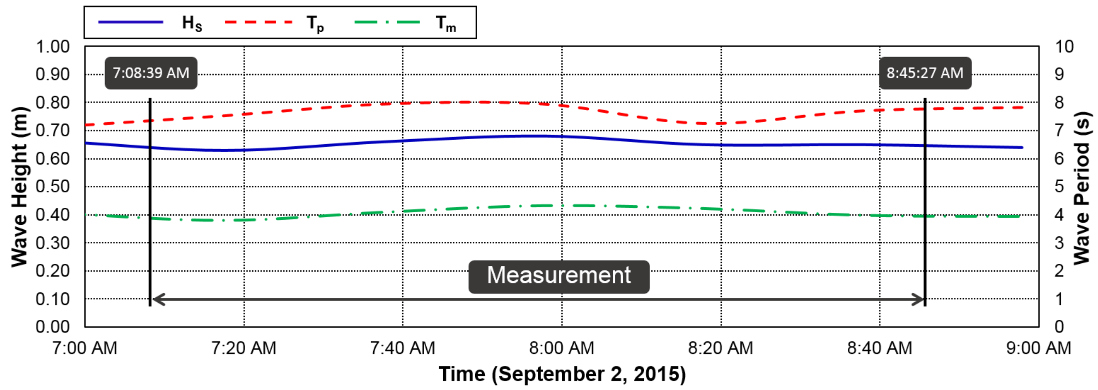

(b) Sea

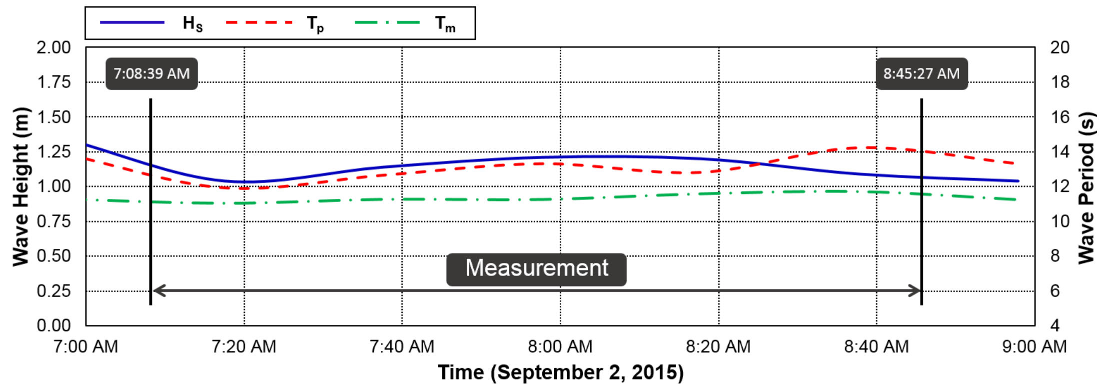

(c) Swell

Figure B.1. (a) Measured tidal data; (b) Measured wave (sea) data; (c) Measured wave (swell) data during the *HONG YUAN* (inbound) transit [Note: Sea/swell cutoff period is 8 seconds; H_s = significant wave height; T_p = spectral peak wave period; T_m = mean wave period]

PETANI (inbound)

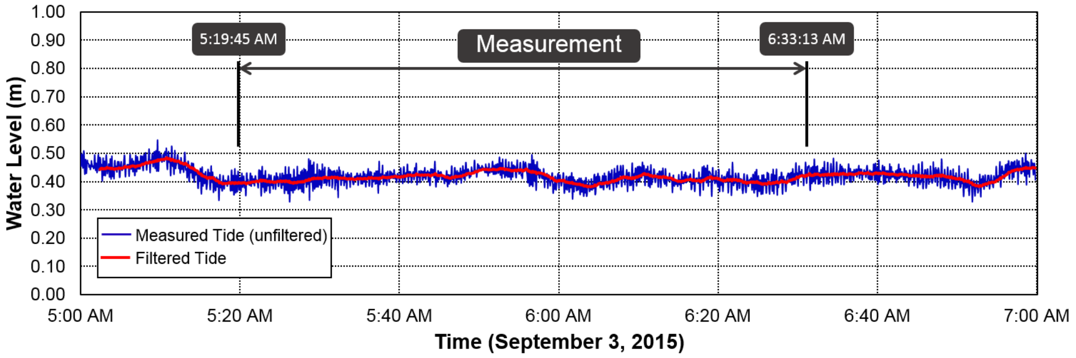

(a) Tide

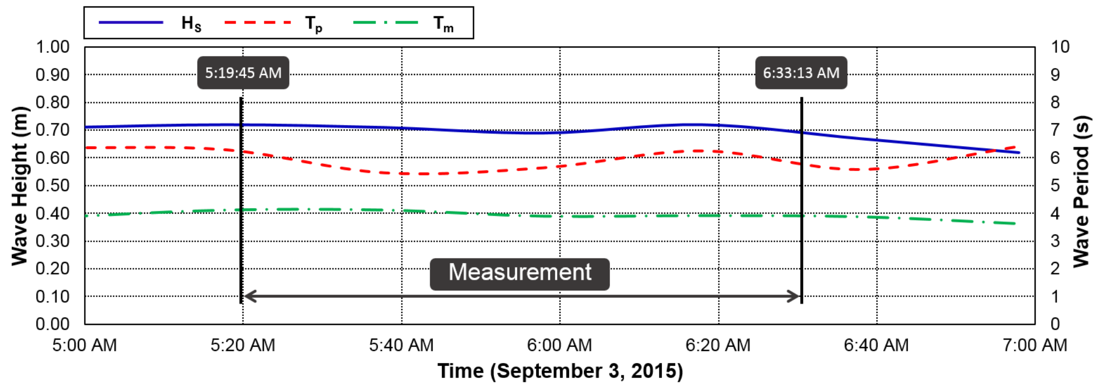

(b) Sea

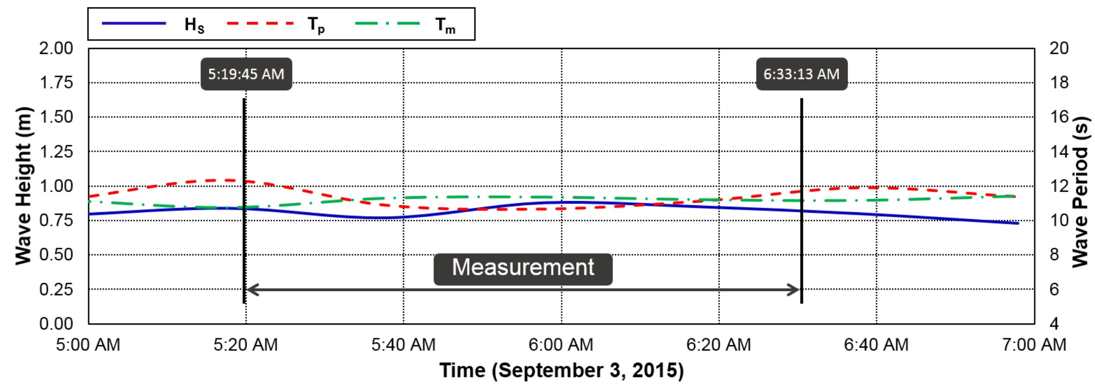

(c) Swell

Figure B.2. (a) Measured tidal data; (b) Measured wave (sea) data; (c) Measured wave (swell) data during the *PETANI* (inbound) transit [Note: Sea/swell cutoff period is 8 seconds; H_s = significant wave height; T_p = spectral peak wave period; T_m = mean wave period]

***DONNACONA* (inbound)**

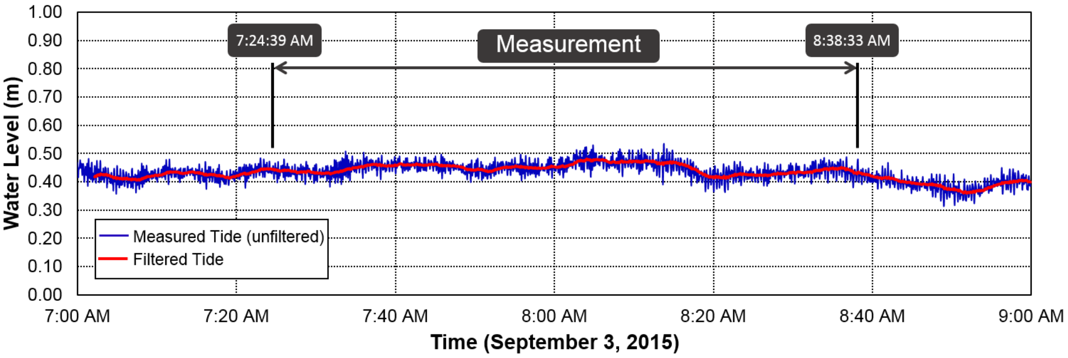

(a) Tide

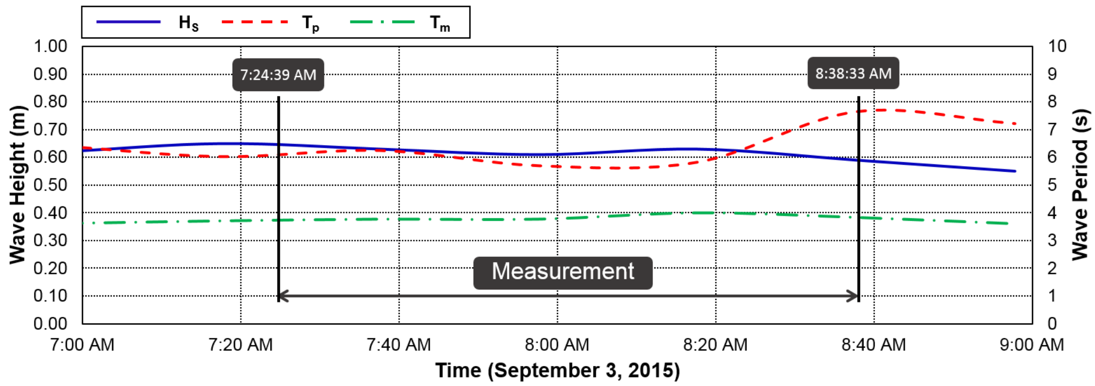

(b) Sea

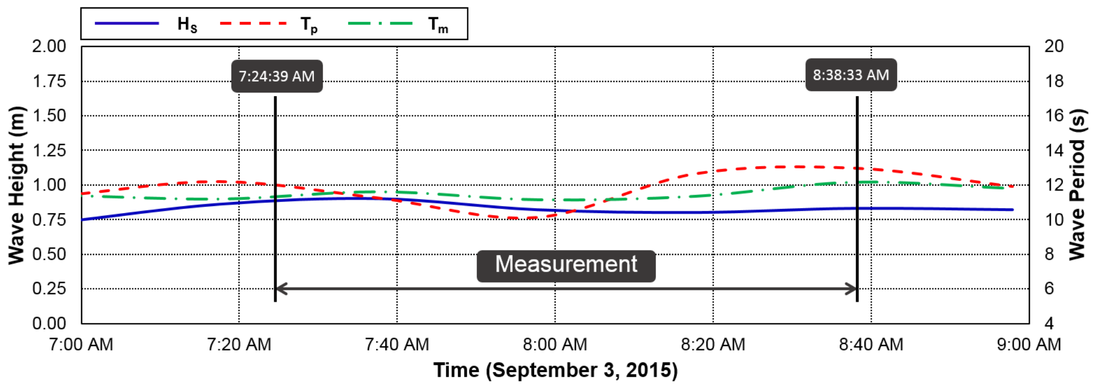

(c) Swell

Figure B.3. (a) Measured tidal data; (b) Measured wave (sea) data; (c) Measured wave (swell) data during the *DONNACONA* (inbound) transit [Note: Sea/swell cutoff period is 8 seconds; H_s = significant wave height; T_p = spectral peak wave period; T_m = mean wave period]

GUO DIAN 17 (outbound)

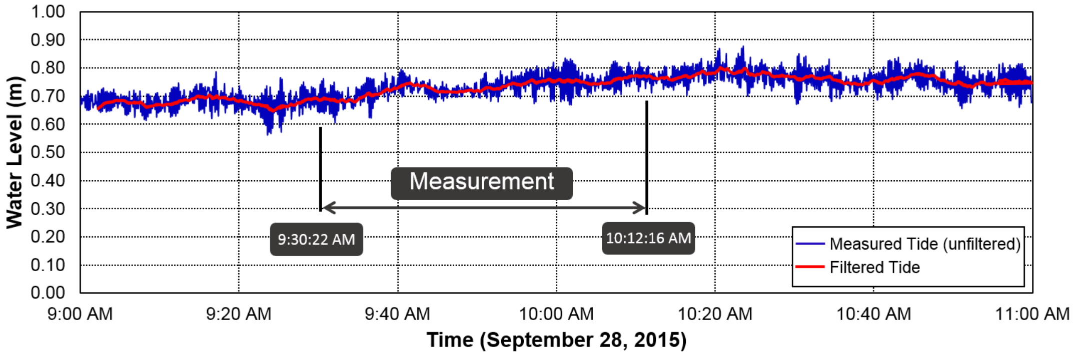

(a) Tide

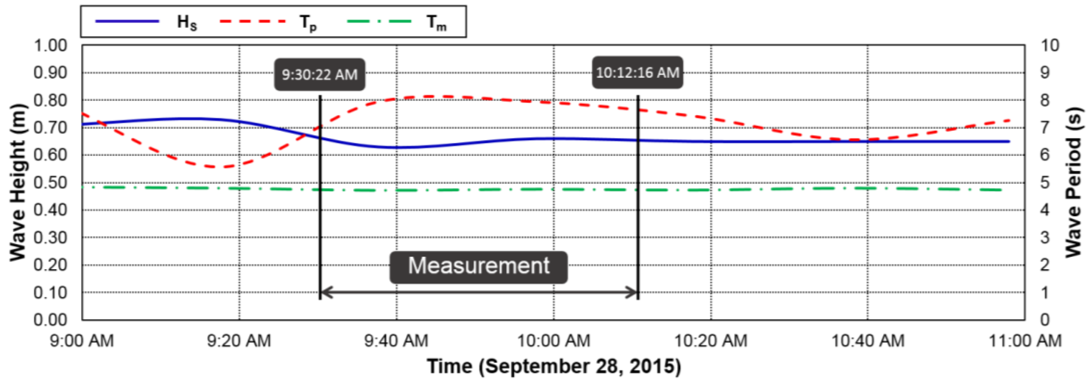

(b) Sea

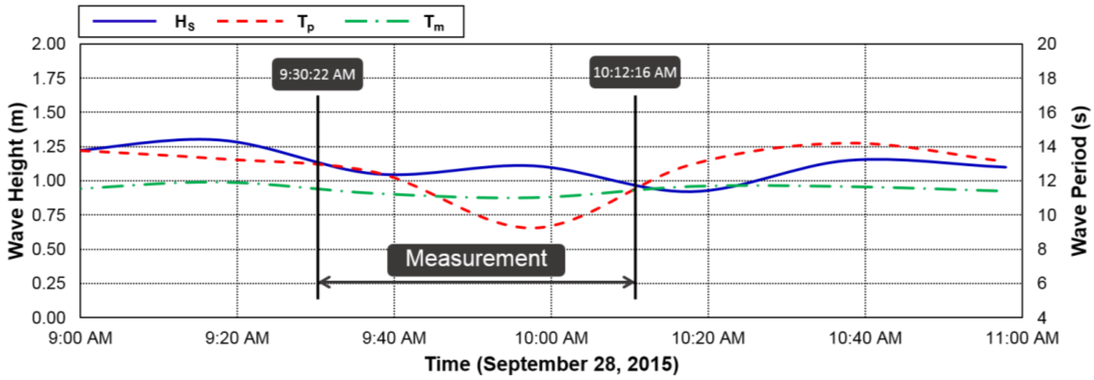

(c) Swell

Figure B.4. (a) Measured tidal data; (b) Measured wave (sea) data; (c) Measured wave (swell) data during the _GUO DIAN 17_ (outbound) transit [Note: Sea/swell cutoff period is 8 seconds; H_s = significant wave height; T_p = spectral peak wave period; T_m = mean wave period]

SFL SPEY **(outbound)**

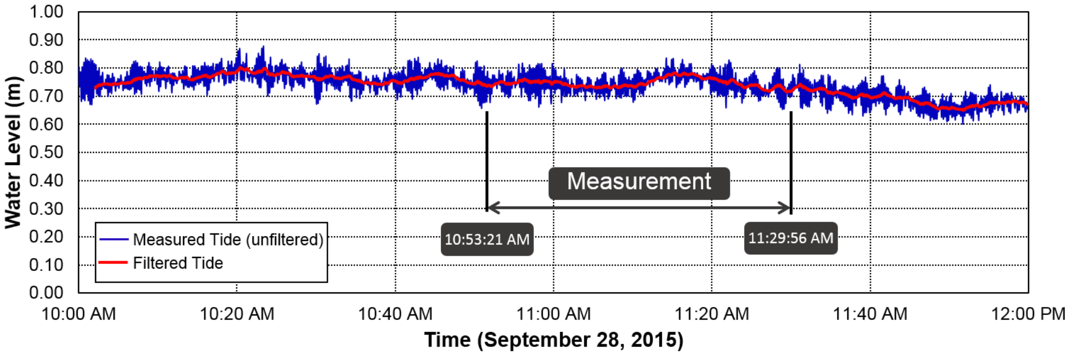

(a) Tide

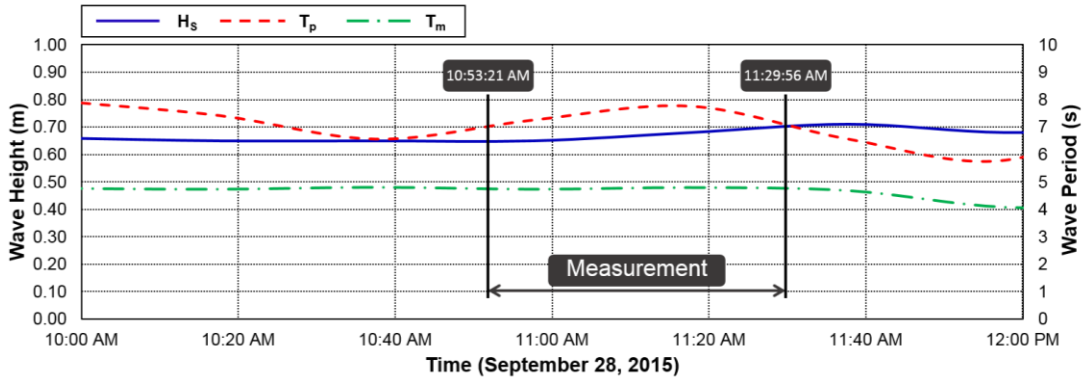

(b) Sea

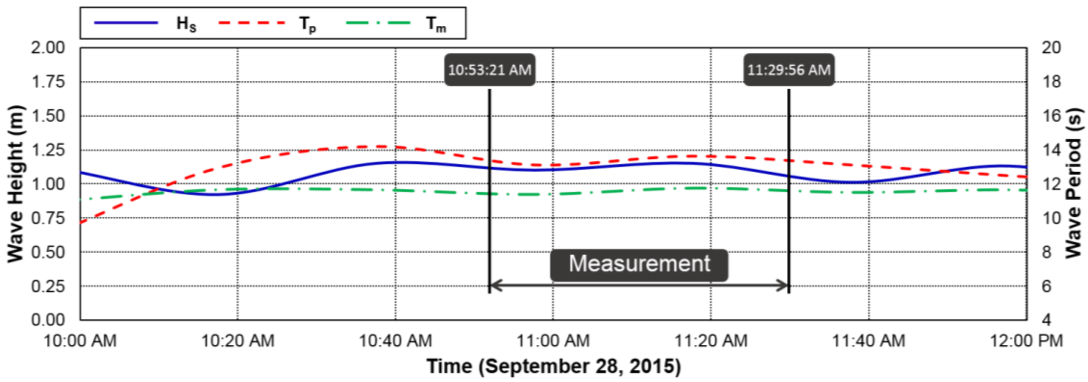

(c) Swell

Figure B.5. (a) Measured tidal data; (b) Measured wave (sea) data; (c) Measured wave (swell) data during the *SFL SPEY* (outbound) transit [Note: Sea/swell cutoff period is 8 seconds; H_s = significant wave height; T_p = spectral peak wave period; T_m = mean wave period]

***AAL FREMANTLE* (inbound)**

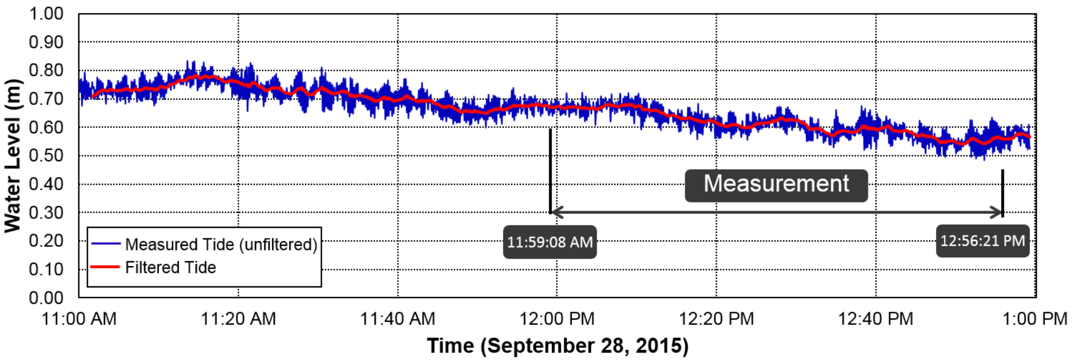

(a) Tide

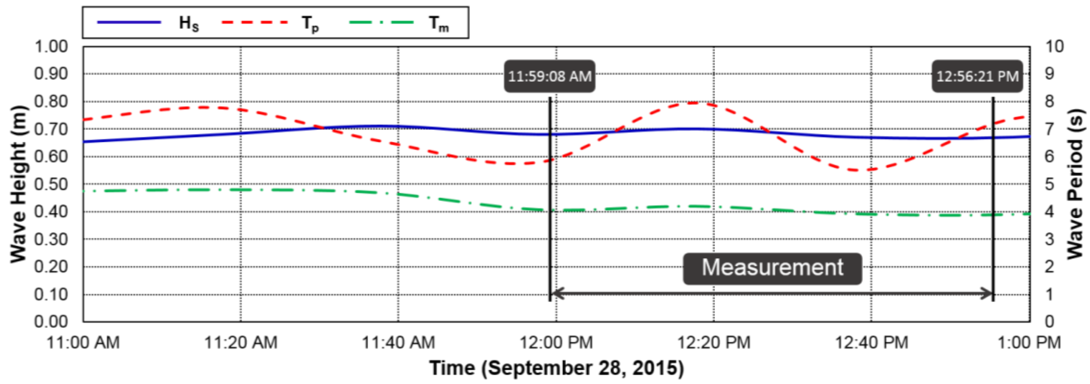

(b) Sea

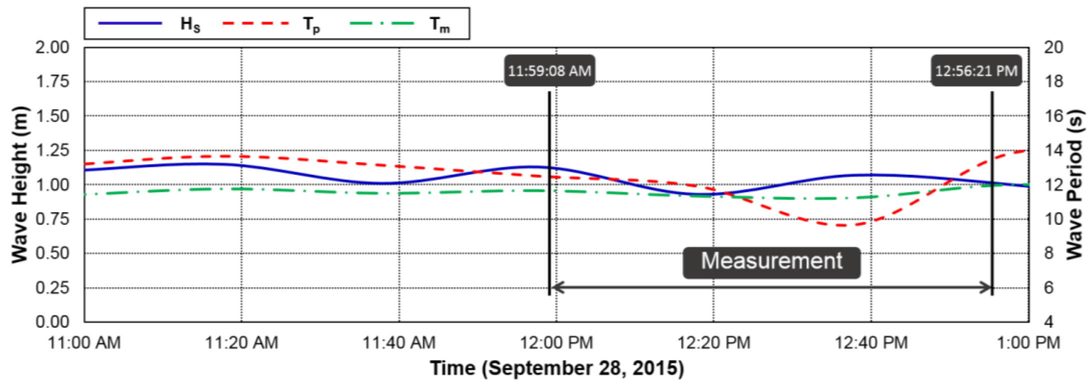

(c) Swell

Figure B.6. (a) Measured tidal data; (b) Measured wave (sea) data; (c) Measured wave (swell) data during the *AAL FREMANTLE* (inbound) transit [Note: Sea/swell cutoff period is 8 seconds; H_s = significant wave height; T_p = spectral peak wave period; T_m = mean wave period]

***IVS MAGPIE* (outbound)**

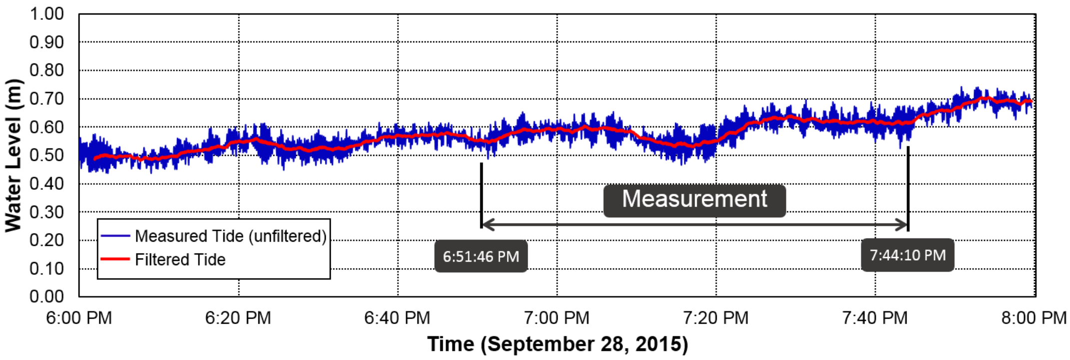

(a) Tide

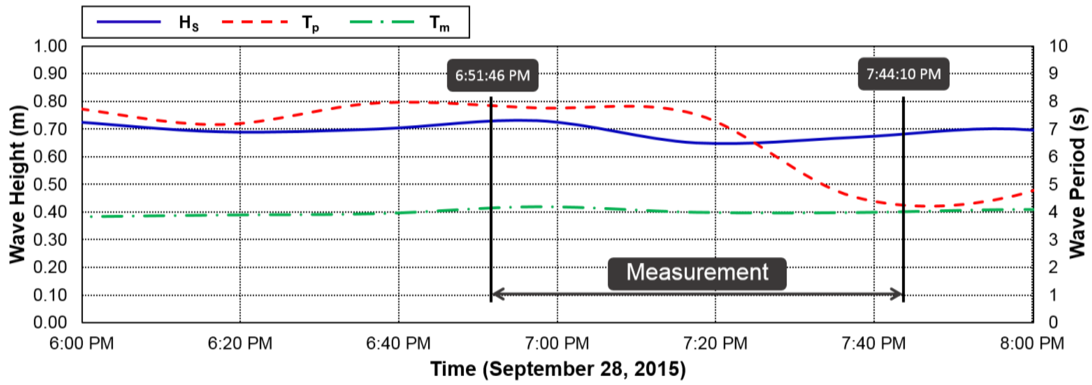

(b) Sea

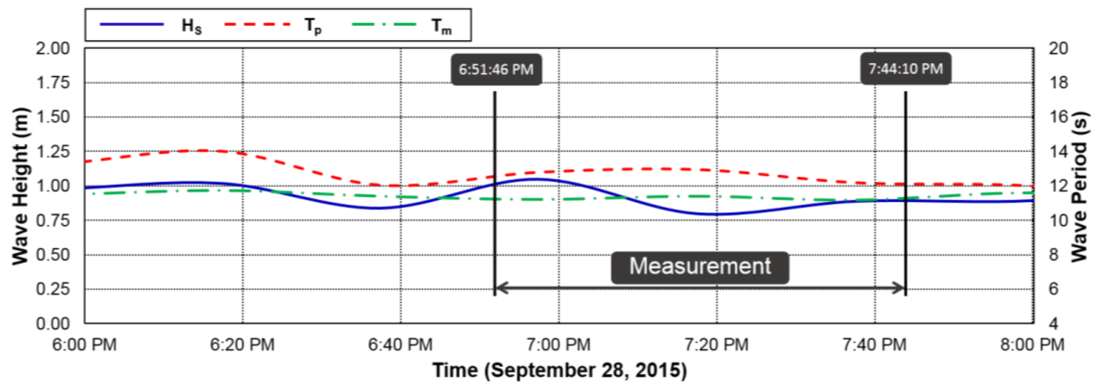

(c) Swell

Figure B.7. (a) Measured tidal data; (b) Measured wave (sea) data; (c) Measured wave (swell) data during the *IVS MAGPIE* (outbound) transit [Note: Sea/swell cutoff period is 8 seconds; H_s = significant wave height; T_p = spectral peak wave period; T_m = mean wave period]

FENG HUANG FENG (outbound)

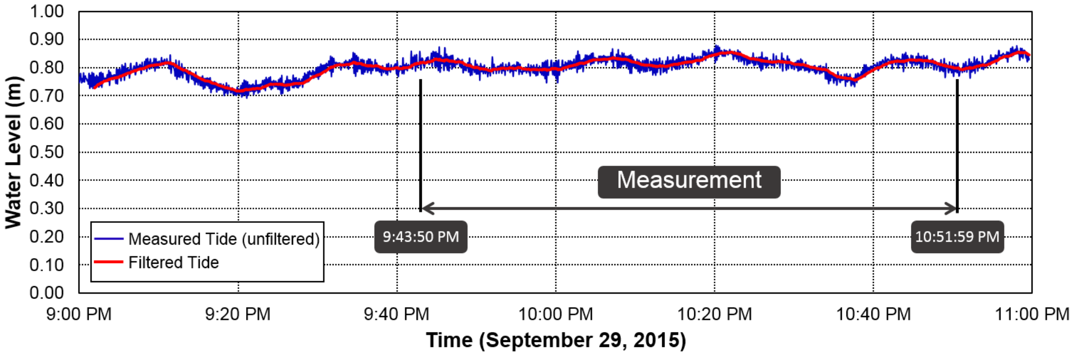

(a) Tide

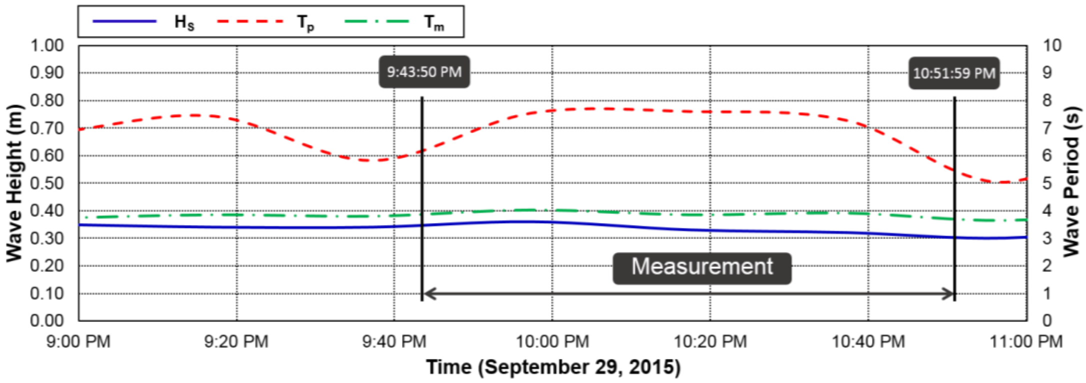

(b) Sea

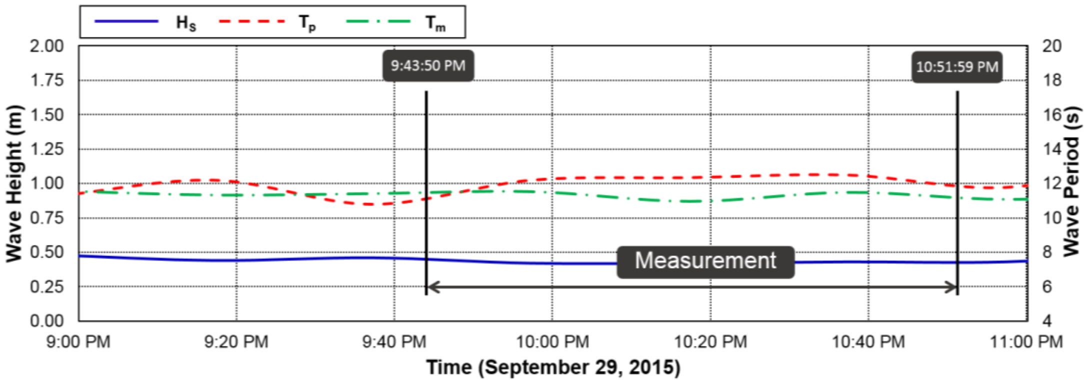

(c) Swell

Figure B.8. (a) Measured tidal data; (b) Measured wave (sea) data; (c) Measured wave (swell) data during the *FENG HUANG FENG* (outbound) transit [Note: Sea/swell cutoff period is 8 seconds; H_s = significant wave height; T_p = spectral peak wave period; T_m = mean wave period]

***AAL FREMANTLE* (outbound)**

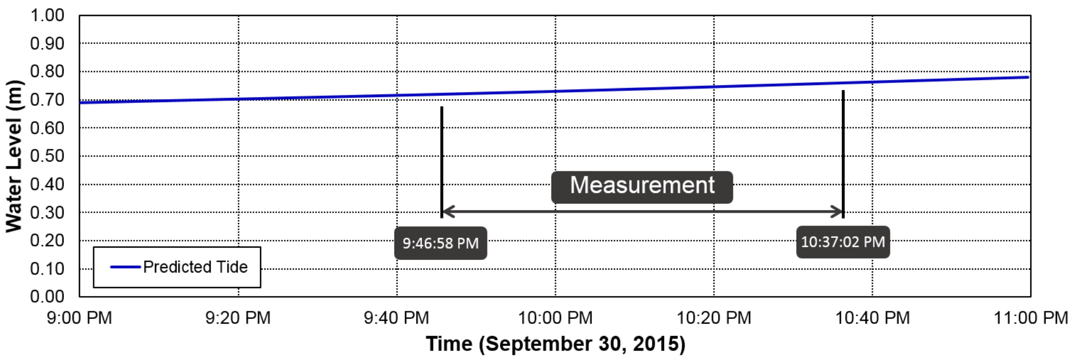

(a) Tide

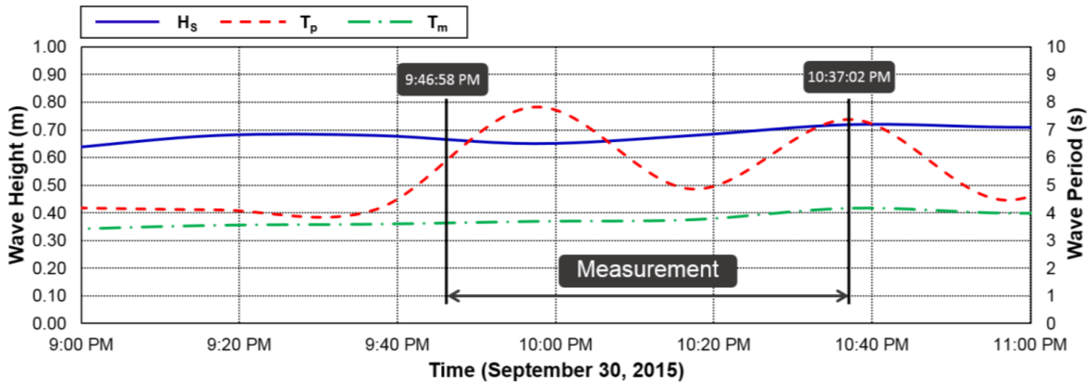

(b) Sea

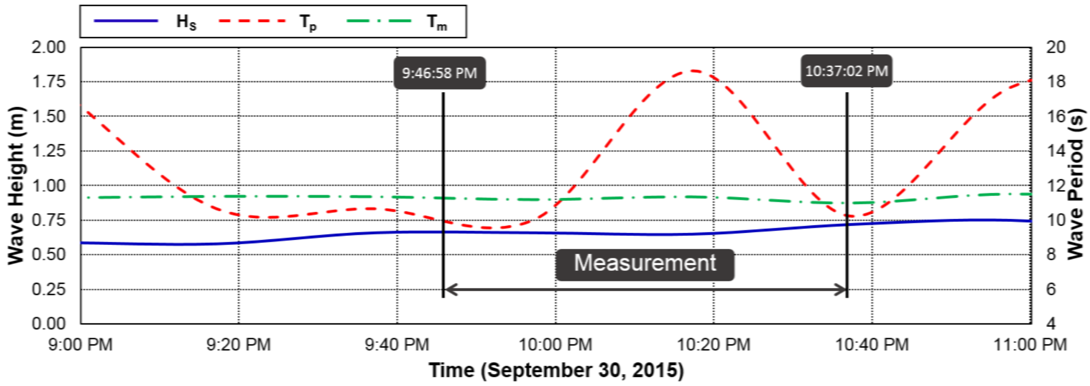

(c) Swell

Figure B.9. (a) Measured tidal data; (b) Measured wave (sea) data; (c) Measured wave (swell) data during the *AAL FREMANTLE* (outbound) transit [Note: Sea/swell cutoff period is 8 seconds; H_s = significant wave height; T_p = spectral peak wave period; T_m = mean wave period]

***SEA DIAMOND* (inbound)**

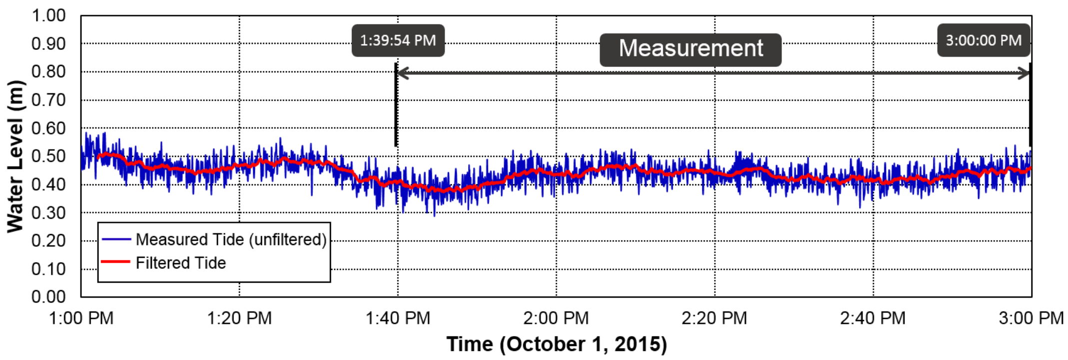

(a) Tide

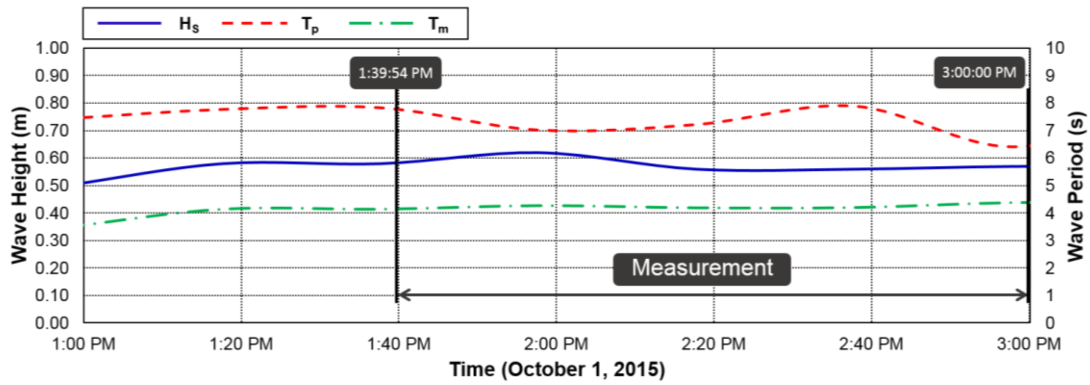

(b) Sea

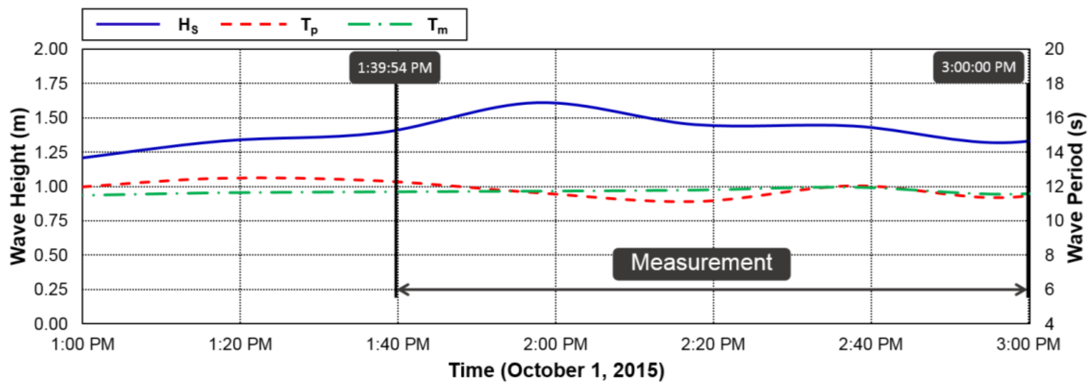

(c) Swell

Figure B.10. (a) Measured tidal data; (b) Measured wave (sea) data; (c) Measured wave (swell) data during the *SEA DIAMOND* (inbound) transit [Note: Sea/swell cutoff period is 8 seconds; H_s = significant wave height; T_p = spectral peak wave period; T_m = mean wave period]

SEA DIAMOND **(outbound)**

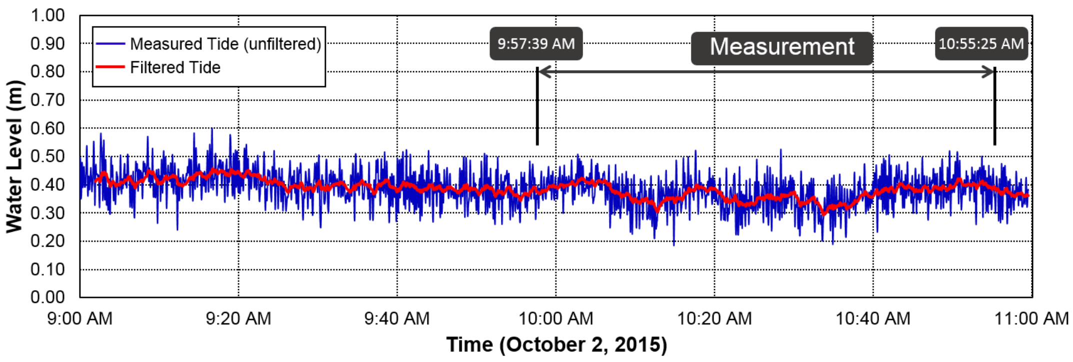

(a) Tide

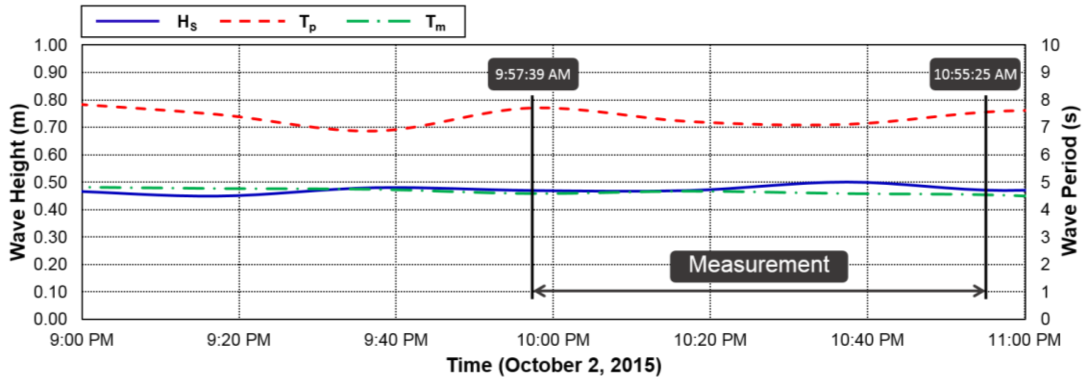

(b) Sea

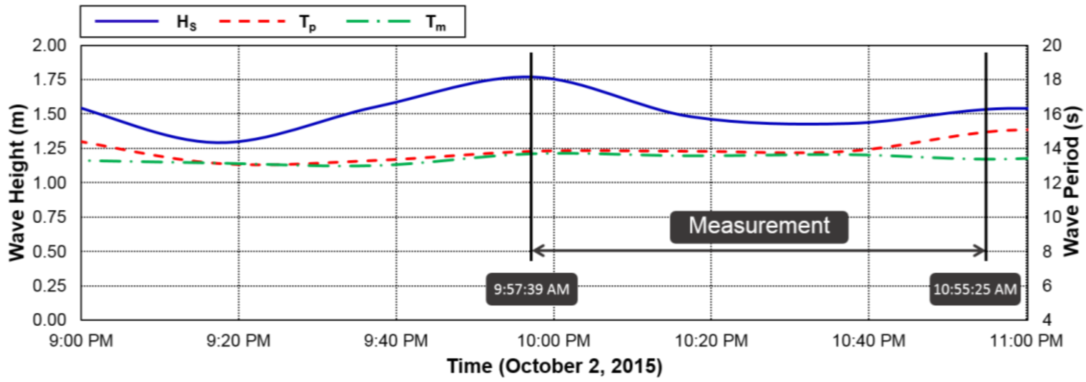

(c) Swell

Figure B.11. (a) Measured tidal data; (b) Measured wave (sea) data; (c) Measured wave (swell) data during the *SEA DIAMOND* (outbound) transit [Note: Sea/swell cutoff period is 8 seconds; H_s = significant wave height; T_p = spectral peak wave period; T_m = mean wave period]

B.2 Tidal and wave data measured during the container ship transits at the Port of Fremantle

Measured tide in the Inner Harbour (32° 3.258' S, 115° 44.3718' E) in the Port of Fremantle was provided by Fremantle Ports. The tidal datum is the same as the chart datum in charts AUS112 and 113, hence, LAT at the Port of Fremantle. The tidal data covering the period of each container ship transit is shown in Figure B.12(a) to Figure B.24(a).

Wave data, measured at 1.28 Hz by the Cottesloe wave buoy (31° 58.74333' S, 115° 41.39833' E) near Green No.1 Buoy (G1) in the Deep Water Channel (see Figures 4.16 and 4.20), have been provided with the collaboration of the coastal infrastructure team of the Western Australian Department of Transport. And are presented in Figure B.12(b and c) to Figure B.24(b and c).

Note that the tidal and wave data in Figure B.12 to Figure B.24 are arranged in chronological order of the trials at the Port of Fremantle (see Table 4.8). No tidal and wave data for the *MSC ILONA* (outbound), *SEAMAX STAMFORD* (outbound) and *OOCL BRISBANE* (outbound) transits are shown: they have been excluded from this study because of suspicious data and ambiguity problems in their measurements. For example, the *MSC ILONA* (outbound) transit has whaleback forecastle; most of the forecastle deck is shielded by steel barrier against green water. Although the bow receiver for the transit was placed at the extremity of the forecastle, in which more open area was available, but only one side was open to the atmosphere, the bow receiver may have been affected by interference from the barrier. *SEAMAX STAMFORD* (outbound) showed very poor GNSS signals in its measurement. This may be because that its bow receiver was mounted behind the green water barrier (whaleback forecastle) to achieve better GNSS satellite coverage, but it was still obscured by both multi-stacked containers and the barrier. Because the *OOCL BRISBANE* (outbound) transit was a partial transit, it has been be excluded from the study in order to avoid ambiguity.

OOCL HOUSTON **(outbound)**

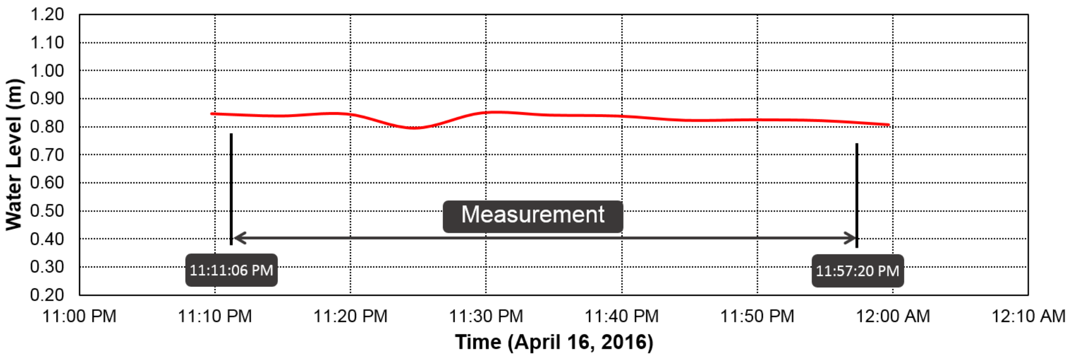

(a) Tide

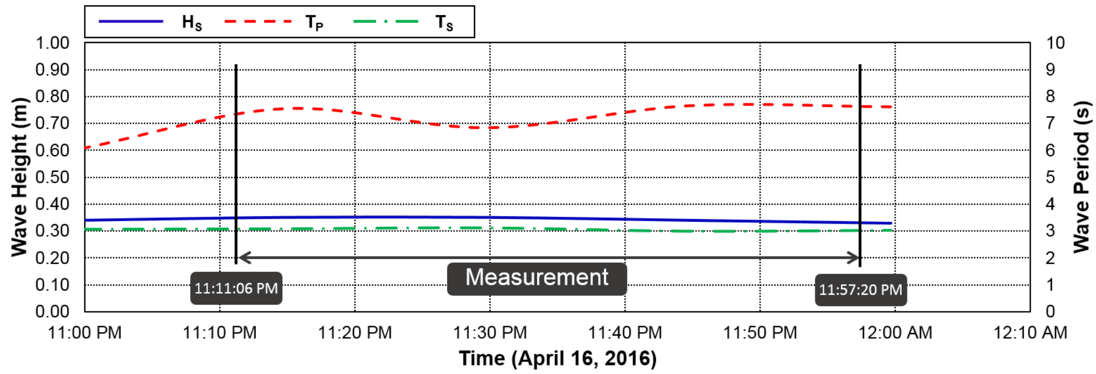

(b) Sea

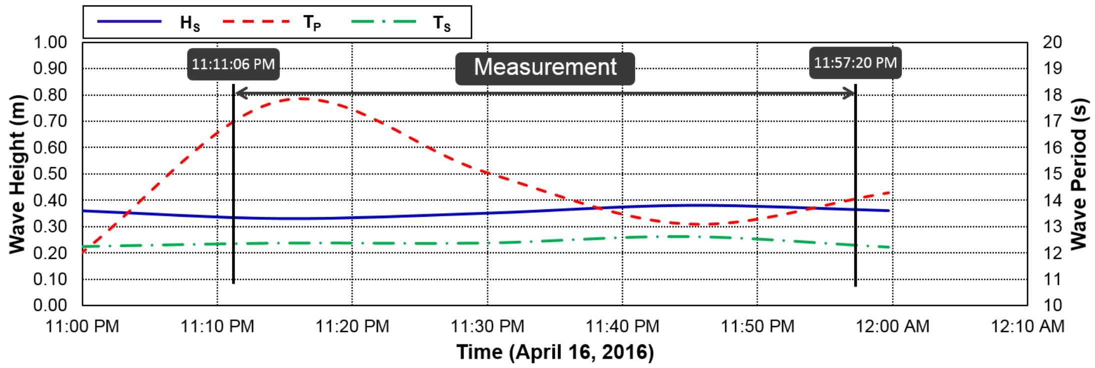

(c) Swell

Figure B.12. (a) Measured tidal data; (b) Measured wave (sea) data; (c) Measured wave (swell) data during the *OOCL HOUSTON* (outbound) transit [Note: Sea/swell cutoff period is 8 seconds; H_s = significant wave height; T_p = spectral peak wave period; T_s = significant wave period]

SEAMAX STAMFORD **(inbound)**

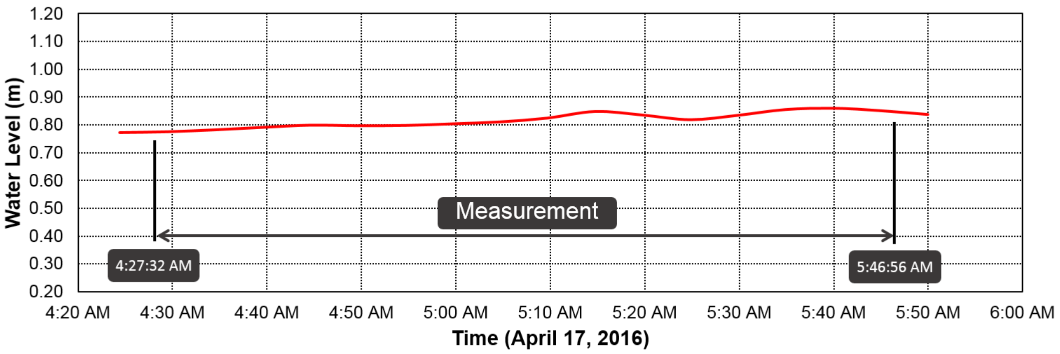

(a) Tide

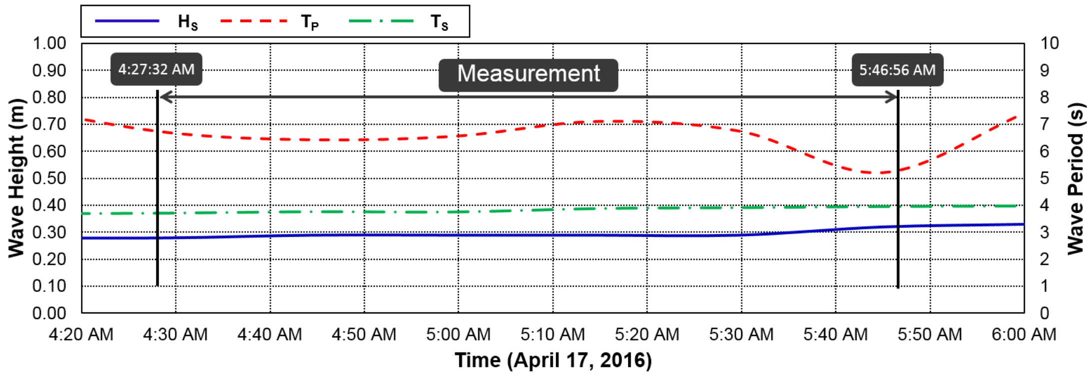

(b) Sea

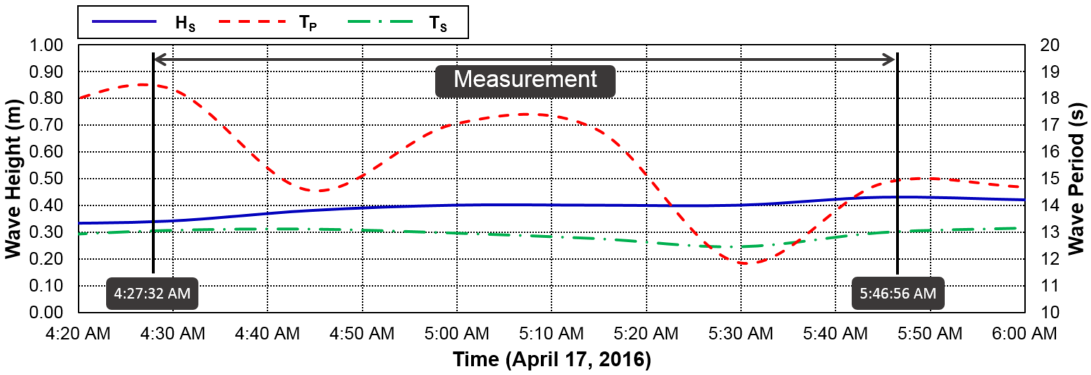

(c) Swell

Figure B.13. (a) Measured tidal data; (b) Measured wave (sea) data; (c) Measured wave (swell) data during the *SEAMAX STAMFORD* (inbound) transit [Note: Sea/swell cutoff period is 8 seconds; H_s = significant wave height; T_p = spectral peak wave period; T_s = significant wave period]

***CMA CGM CHOPIN* (inbound)**

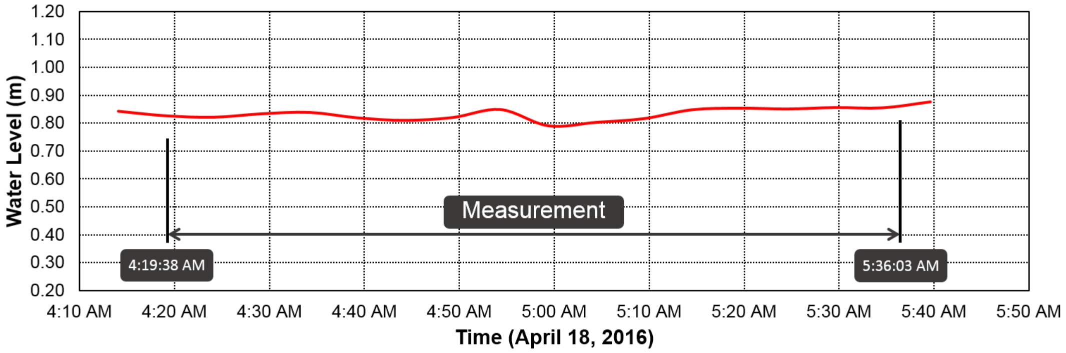

(a) Tide

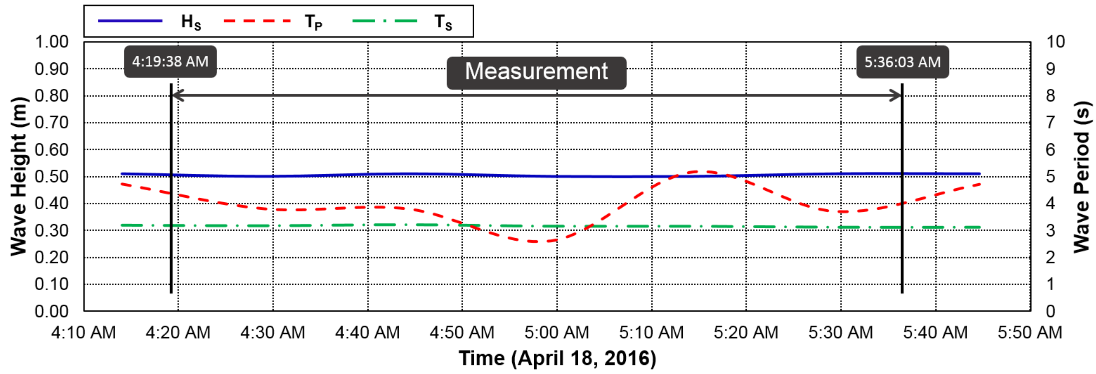

(b) Sea

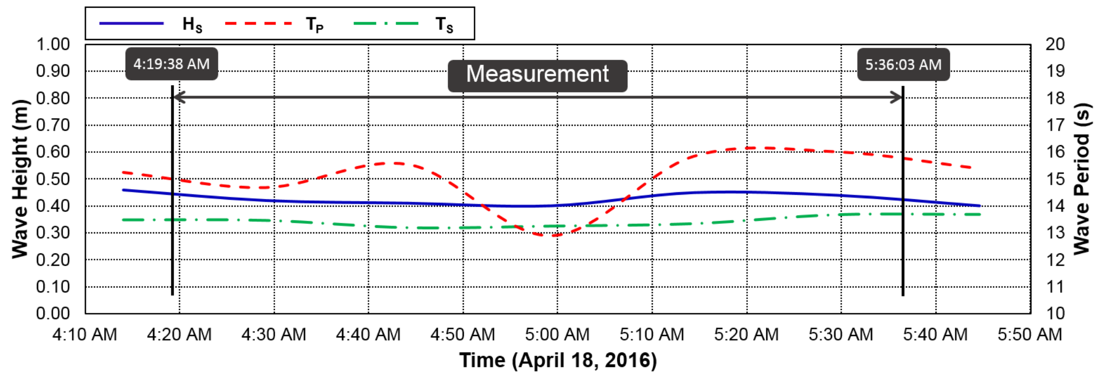

(c) Swell

Figure B.14. (a) Measured tidal data; (b) Measured wave (sea) data; (c) Measured wave (swell) data during the *CMA CGM CHOPIN* (inbound) transit [Note: Sea/swell cutoff period is 8 seconds; H_s = significant wave height; T_p = spectral peak wave period; T_s = significant wave period]

***MOL EMISSARY* (inbound)**

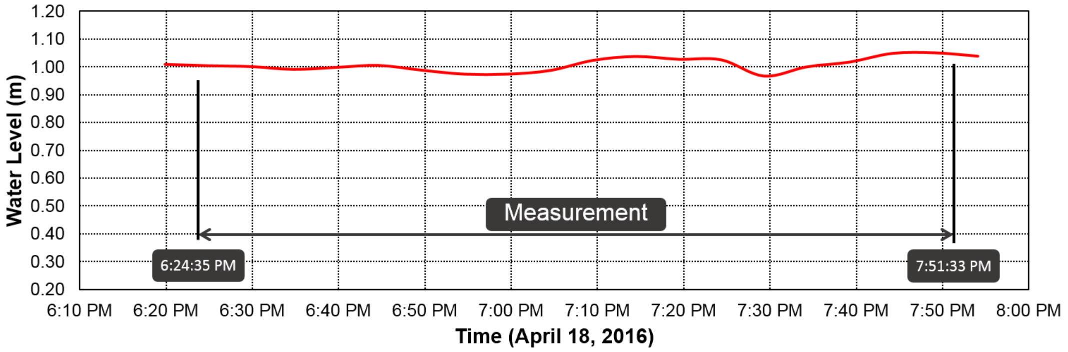

(a) Tide

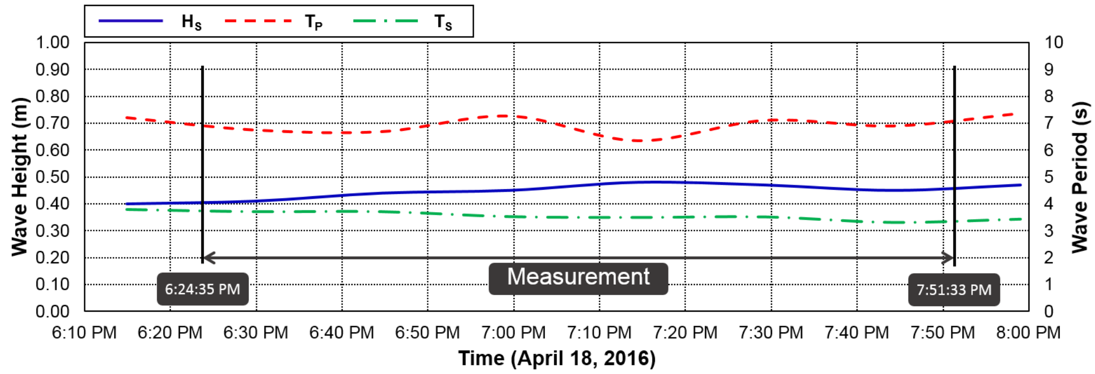

(b) Sea

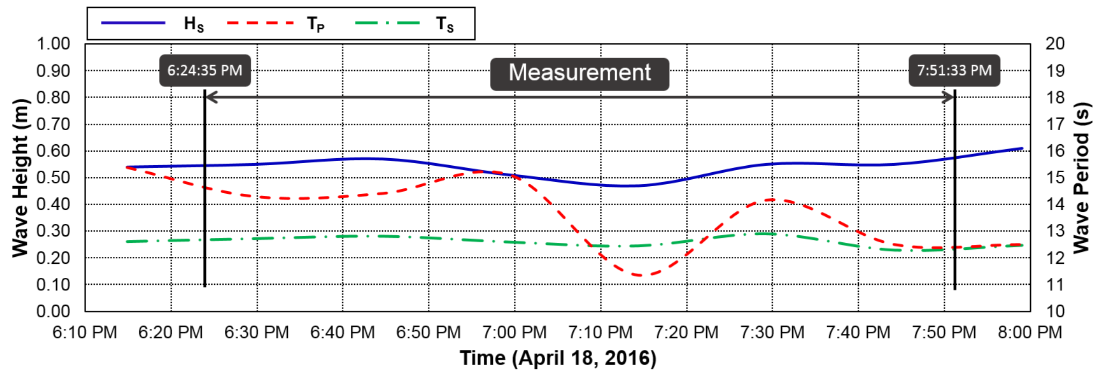

(c) Swell

Figure B.15. (a) Measured tidal data; (b) Measured wave (sea) data; (c) Measured wave (swell) data during the *MOL EMISSARY* (inbound) transit [Note: Sea/swell cutoff period is 8 seconds; H_s = significant wave height; T_p = spectral peak wave period; T_s = significant wave period]

***CMA CGM CHOPIN* (outbound)**

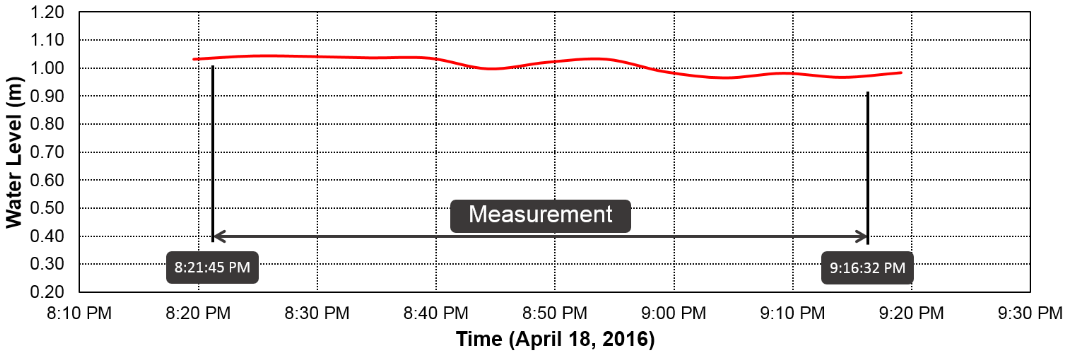

(a) Tide

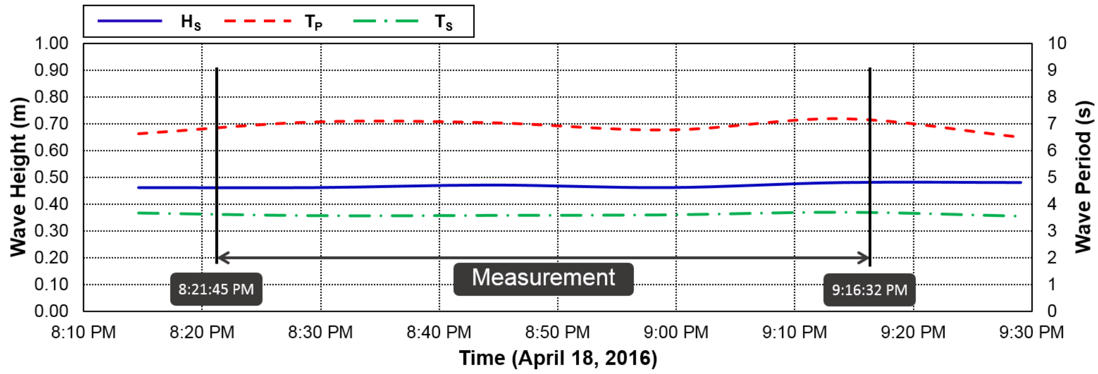

(b) Sea

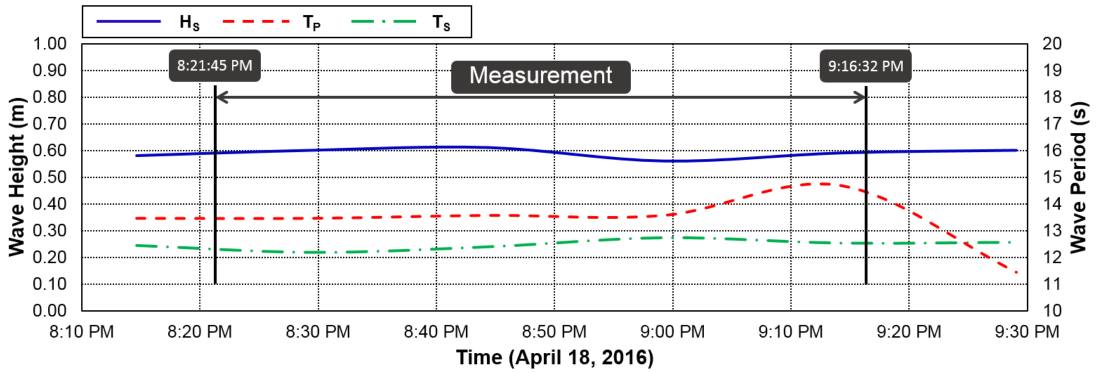

(c) Swell

Figure B.16. (a) Measured tidal data; (b) Measured wave (sea) data; (c) Measured wave (swell) data during the *CMA CGM CHOPIN* (outbound) transit [Note: Sea/swell cutoff period is 8 seconds; H_s = significant wave height; T_p = spectral peak wave period; T_s = significant wave period]

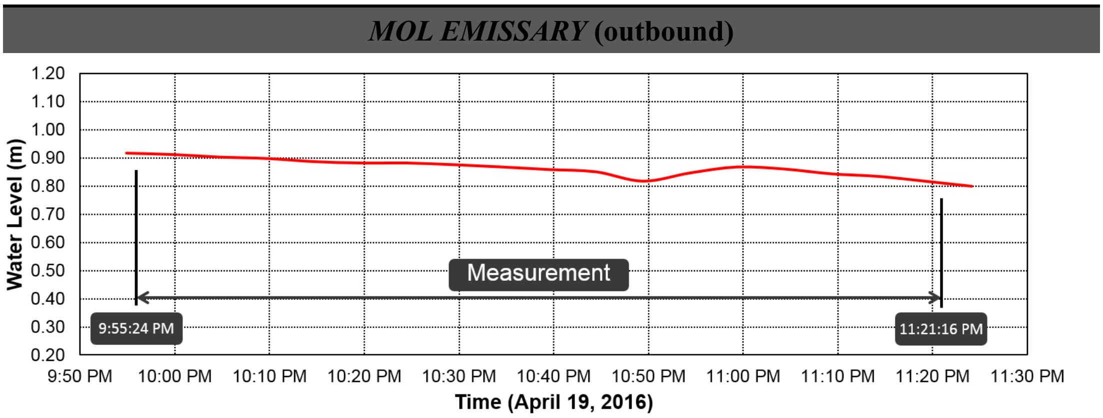

(a) Tide

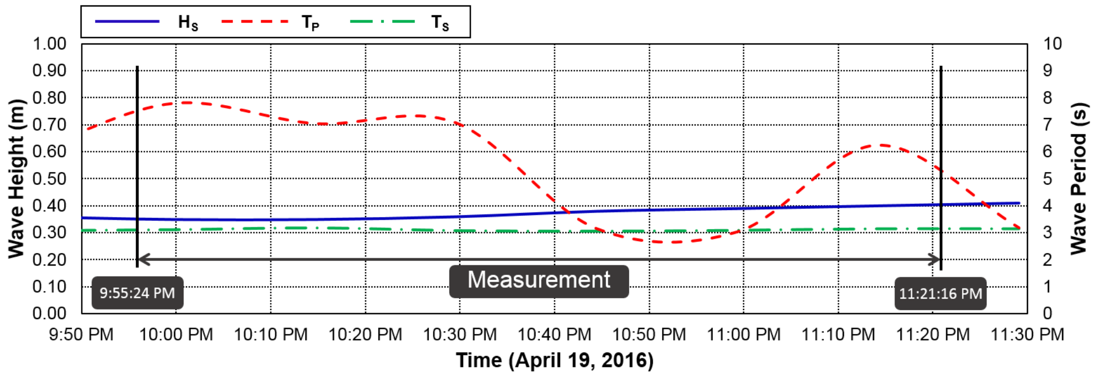

(b) Sea

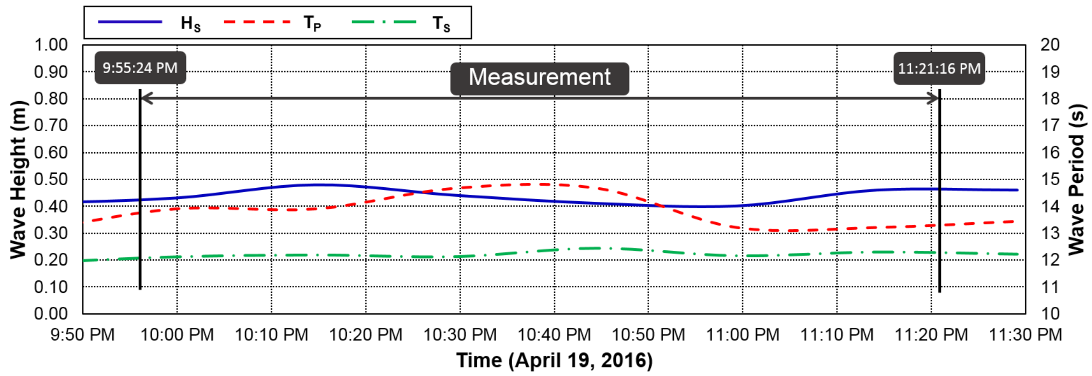

(c) Swell

Figure B.17. (a) Measured tidal data; (b) Measured wave (sea) data; (c) Measured wave (swell) data during the *MOL EMISSARY* (outbound) transit [Note: Sea/swell cutoff period is 8 seconds; H_s = significant wave height; T_p = spectral peak wave period; T_s = significant wave period]

***SAFMARINE MAKUTU* (inbound)**

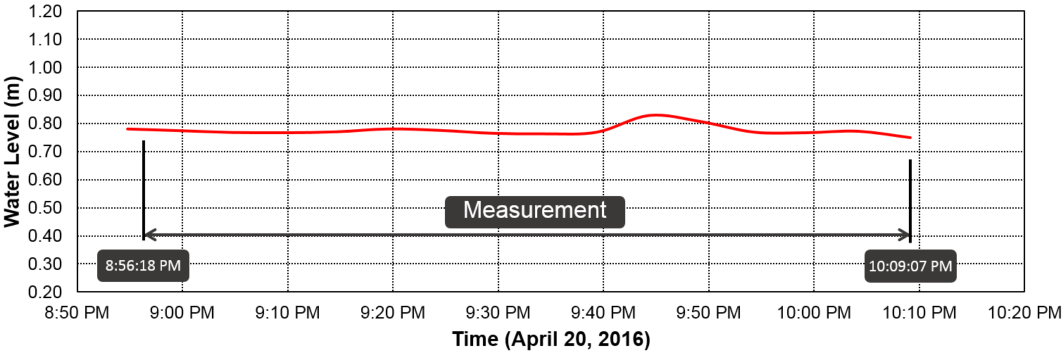

(a) Tide

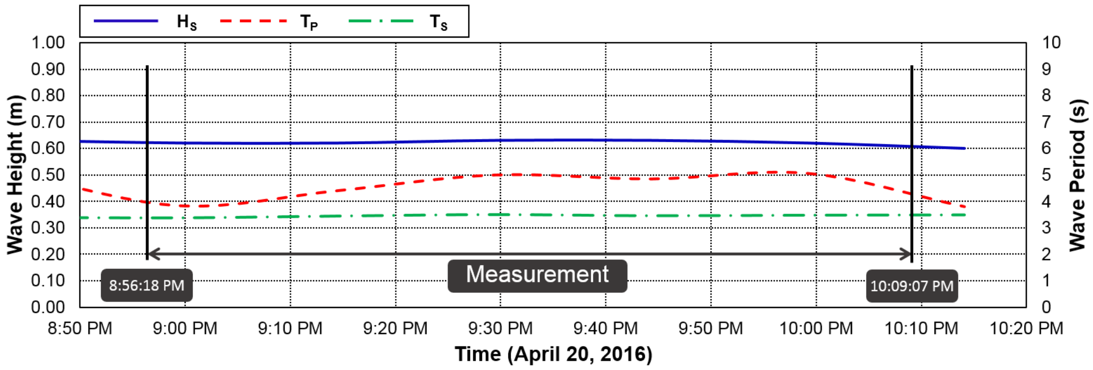

(b) Sea

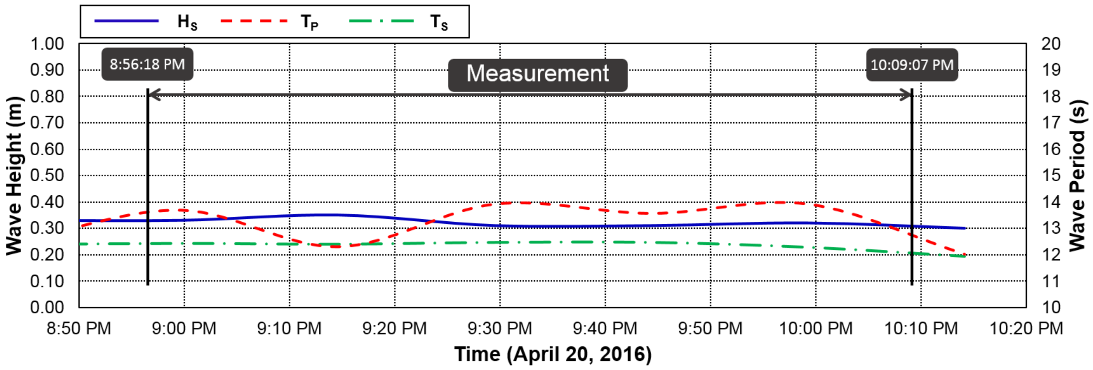

(c) Swell

Figure B.18. (a) Measured tidal data; (b) Measured wave (sea) data; (c) Measured wave (swell) data during the *SAFMARINE MAKUTU* (inbound) transit [Note: Sea/swell cutoff period is 8 seconds; H_s = significant wave height; T_p = spectral peak wave period; T_s = significant wave period]

***MOL PARAMOUNT* (inbound)**

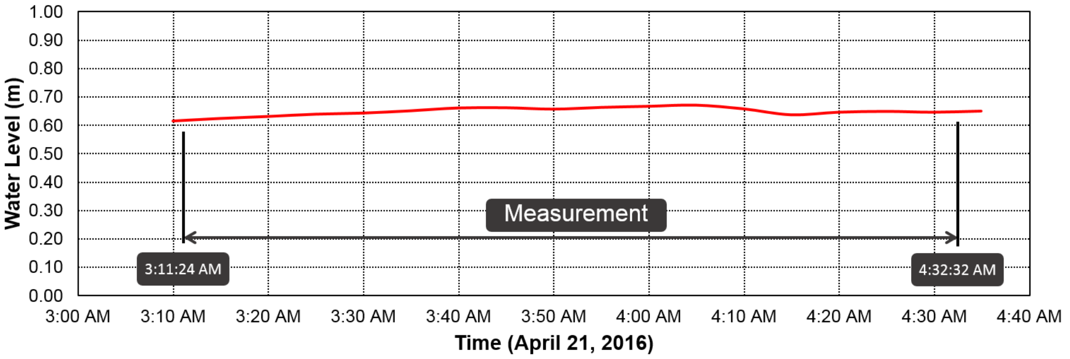

(a) Tide

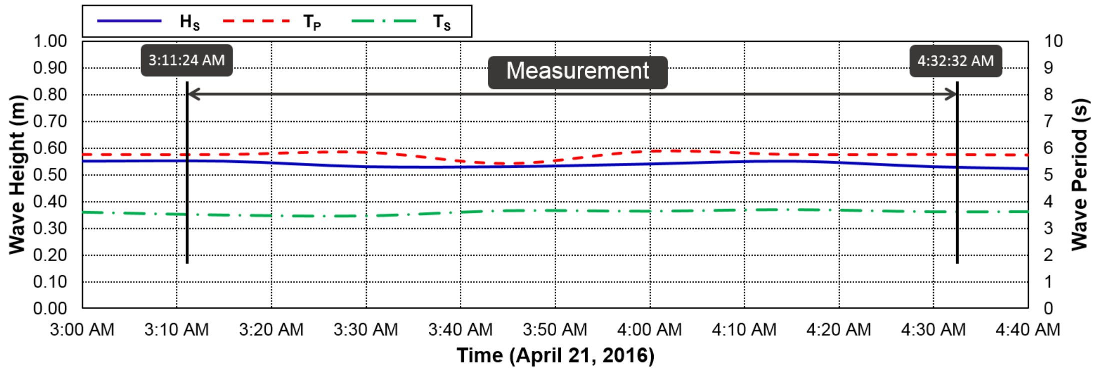

(b) Sea

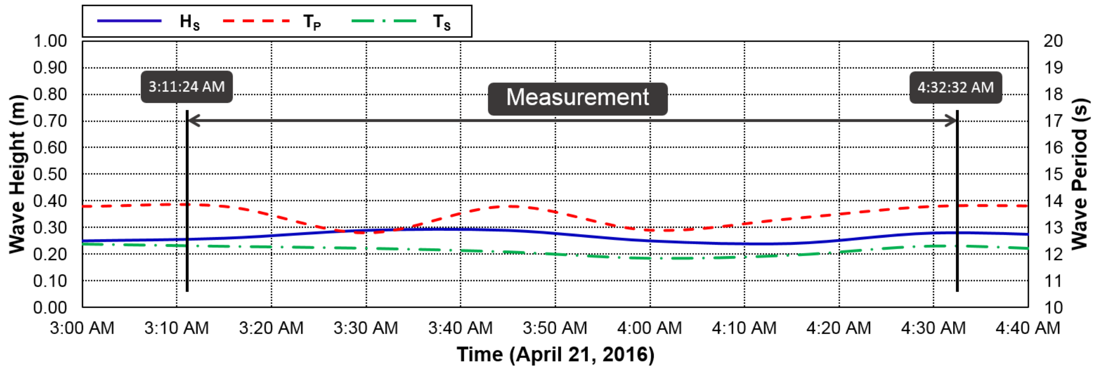

(c) Swell

Figure B.19. (a) Measured tidal data; (b) Measured wave (sea) data; (c) Measured wave (swell) data during the *MOL PARAMOUNT* (inbound) transit [Note: Sea/swell cutoff period is 8 seconds; H_s = significant wave height; T_p = spectral peak wave period; T_s = significant wave period]

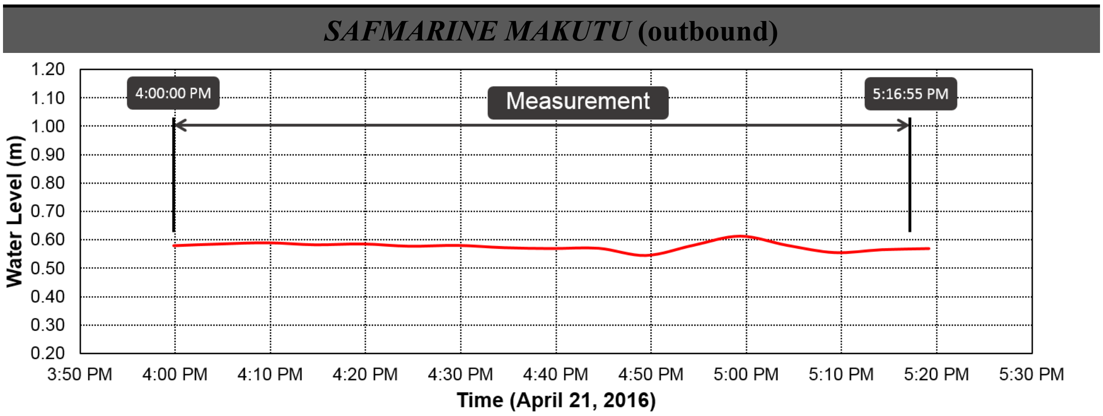

(a) Tide

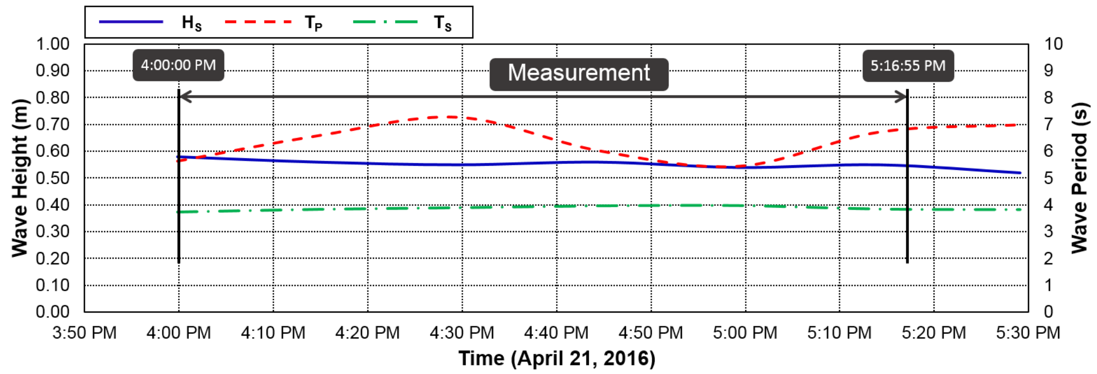

(b) Sea

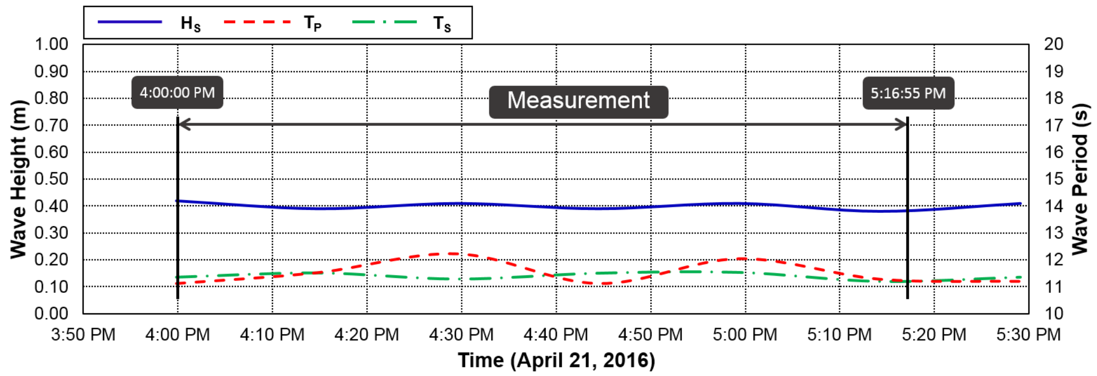

(c) Swell

Figure B.20. (a) Measured tidal data; (b) Measured wave (sea) data; (c) Measured wave (swell) data during the *SAFMARINE MAKUTU* (outbound) transit [Note: Sea/swell cutoff period is 8 seconds; H_s = significant wave height; T_p = spectral peak wave period; T_s = significant wave period]

***CMA CGM LAMARTINE* (outbound)**

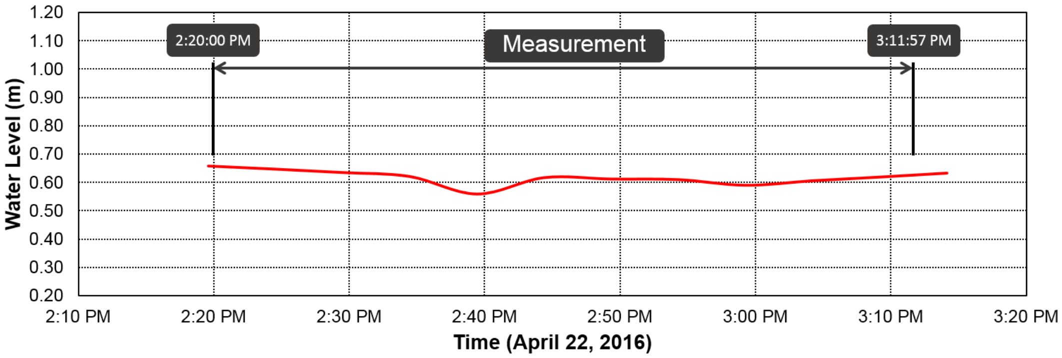

(a) Tide

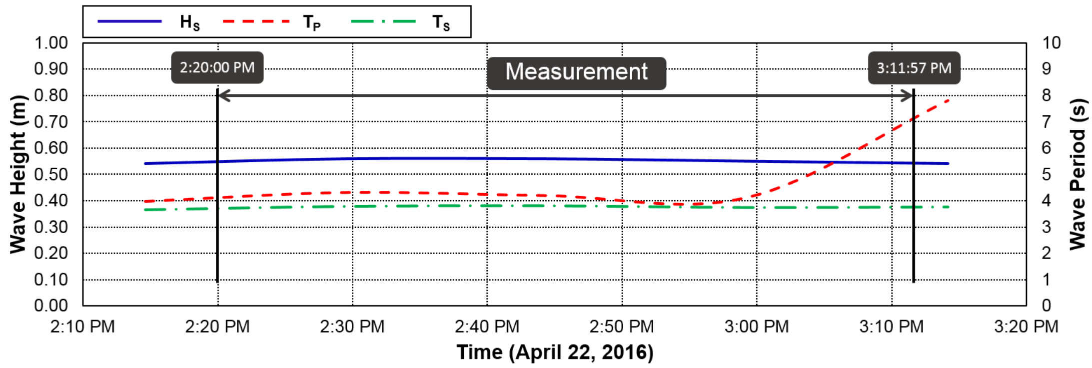

(b) Sea

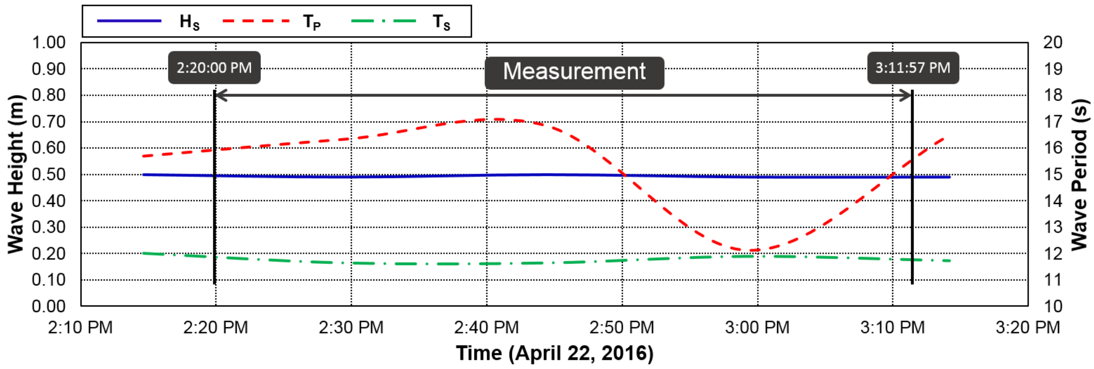

(c) Swell

Figure B.21. (a) Measured tidal data; (b) Measured wave (sea) data; (c) Measured wave (swell) data during the *CMA CGM LAMARTINE* (outbound) transit [Note: Sea/swell cutoff period is 8 seconds; H_s = significant wave height; T_p = spectral peak wave period; T_s = significant wave period]

***MOL PARAMOUNT* (outbound)**

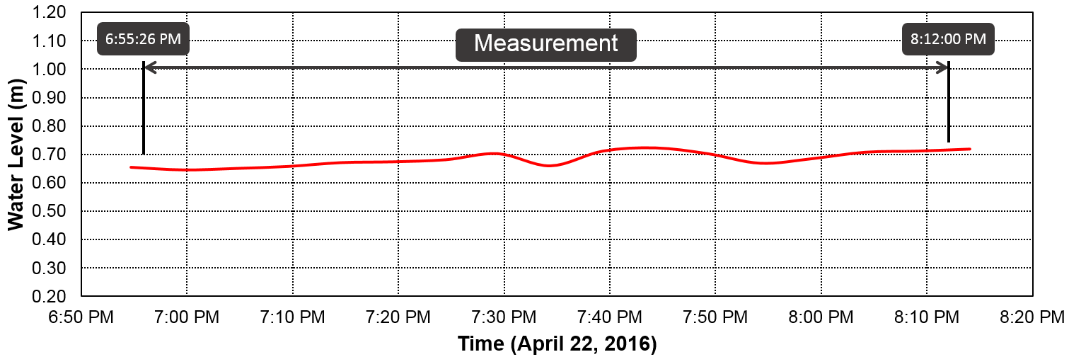

(a) Tide

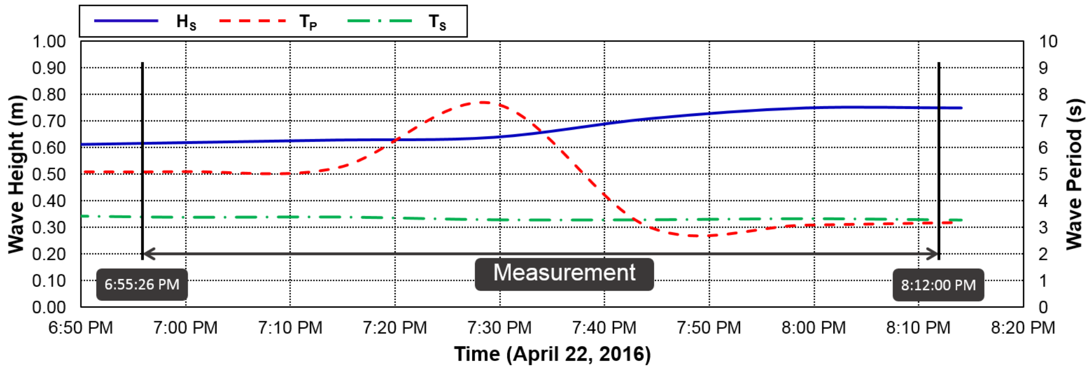

(b) Sea

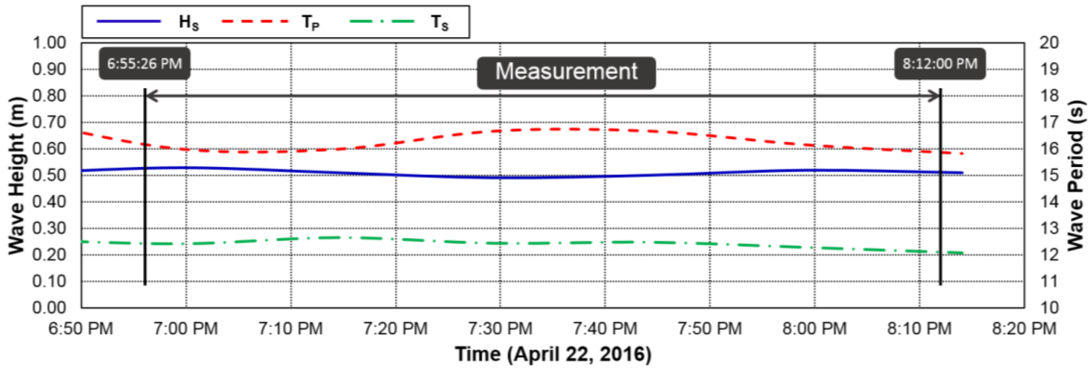

(c) Swell

Figure B.22. (a) Measured tidal data; (b) Measured wave (sea) data; (c) Measured wave (swell) data during the *MOL PARAMOUNT* (outbound) transit [Note: Sea/swell cutoff period is 8 seconds; H_s = significant wave height; T_p = spectral peak wave period; T_s = significant wave period]

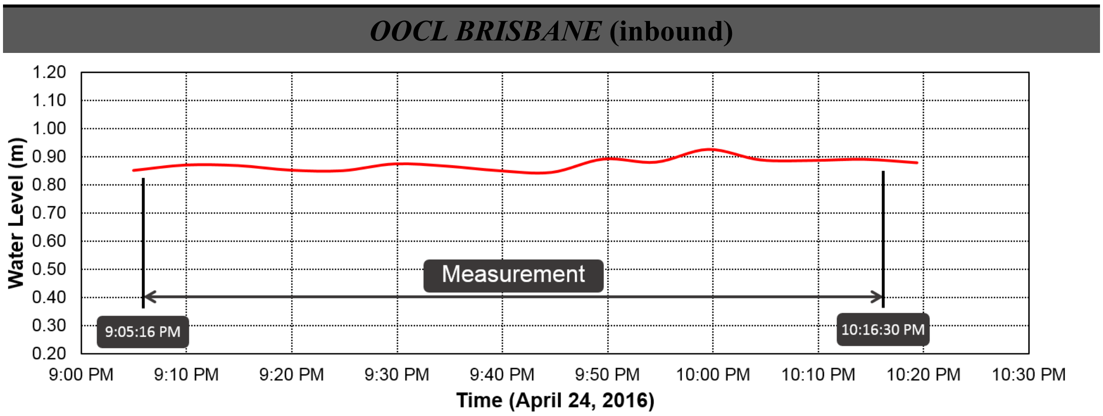

(a) Tide

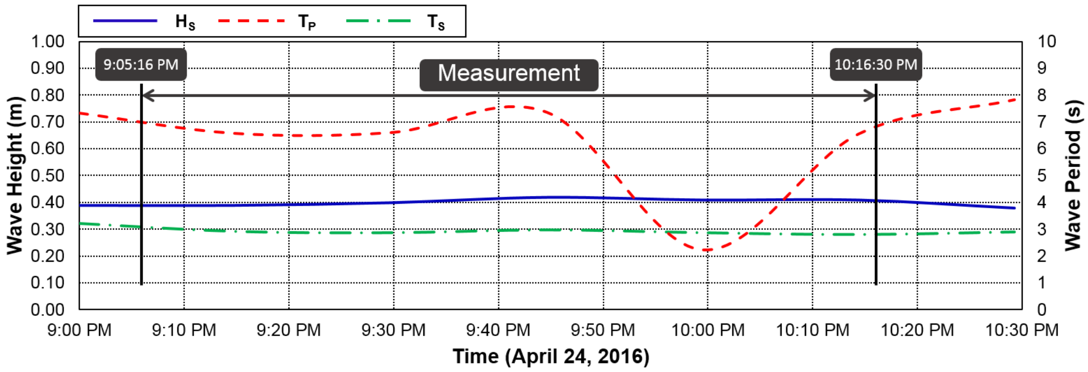

(b) Sea

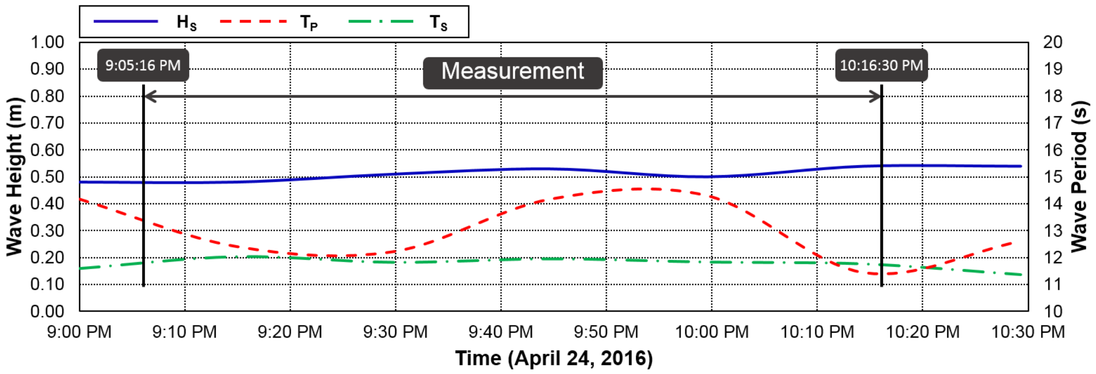

(c) Swell

Figure B.23. (a) Measured tidal data; (b) Measured wave (sea) data; (c) Measured wave (swell) data during the *OOCL BRISBANE* (inbound) transit [Note: Sea/swell cutoff period is 8 seconds; H_s = significant wave height; T_p = spectral peak wave period; T_s = significant wave period]

CMA CGM WAGNER **(inbound)**

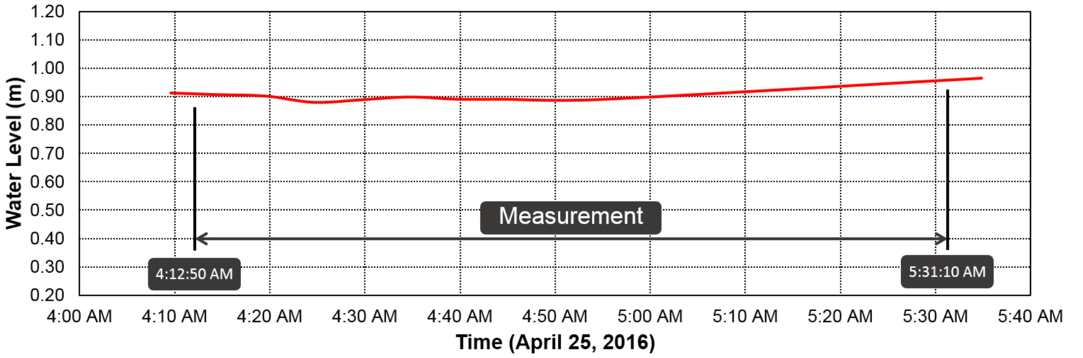

(a) Tide

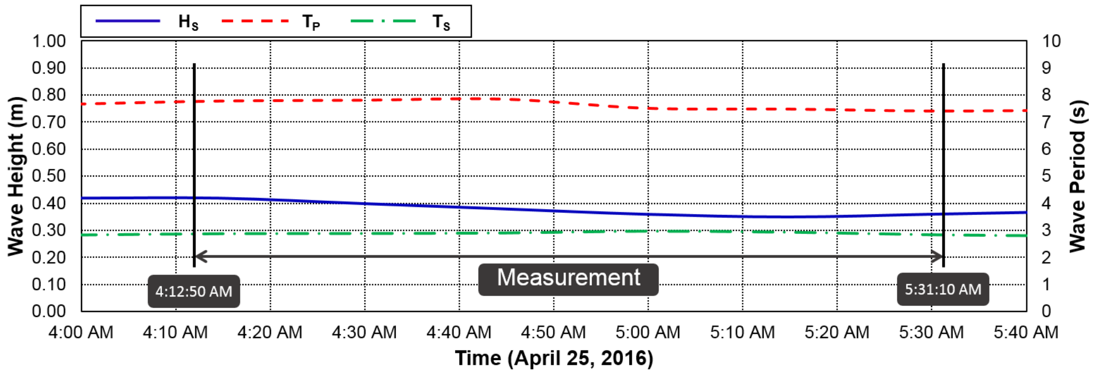

(b) Sea

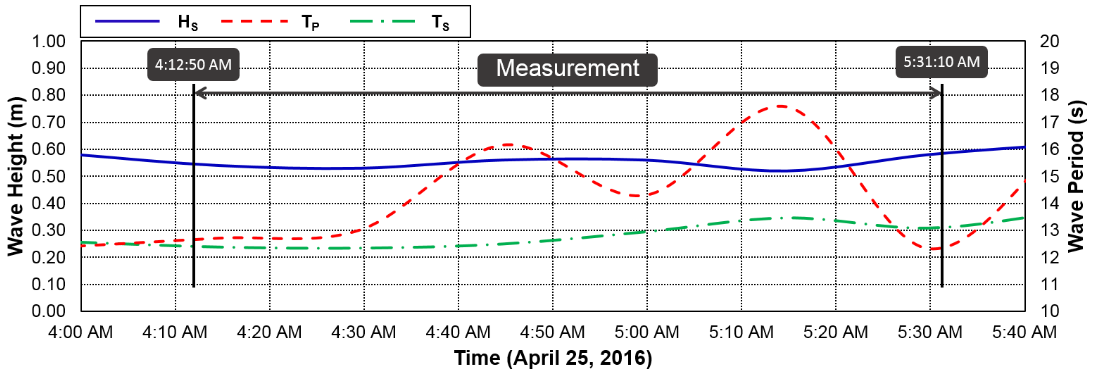

(c) Swell

Figure B.24. (a) Measured tidal data; (b) Measured wave (sea) data; (c) Measured wave (swell) data during the *CMA CGM WAGNER* (inbound) transit [Note: Sea/swell cutoff period is 8 seconds; H_s = significant wave height; T_p = spectral peak wave period; T_s = significant wave period]

Appendix C - Detailed Measurement Results

C.1 Detailed measurement results for the bulk carrier transits at the Port of Geraldton

The measured sinkage, plus ship speed and channel bathymetry along the channel for all bulk carrier transits are shown in Figure 4.14(a) to Figure C.11(a). Here, dynamic sinkage means the total sinkage (positive downward), relative to the static floating position at berth, and includes a near-steady component caused by the Bernoulli effect and known as squat; an unsteady component due to wave-induced heave, pitch and roll; and a slowly-varying heel due to wind and turning.

Figure 4.14(b) to Figure C.11(b) show elevations of the ship's keel relative to chart datum. The minimum real-time clearance in each section of varying water depth has been captured.

Results are plotted against the cumulative distance from Beacon 22 (B22); hence, distance within the inner harbour is negative. Vertical lines are shown for B20, B18, B16, …, B2 (see Figure 4.11 for the inbound transits and Figure 4.12 for the outbound). Sinkage is given at the FP, AP, and forward and aft shoulders of the bilge corners (refer to Figure 4.10), and defined as being positive downward. Note that gaps in the results of some transits are because some GNSS fixes were of insufficient quality and have been rejected. The results fall into categories of inbound and outbound transits.

***HONG YUAN* (inbound)**

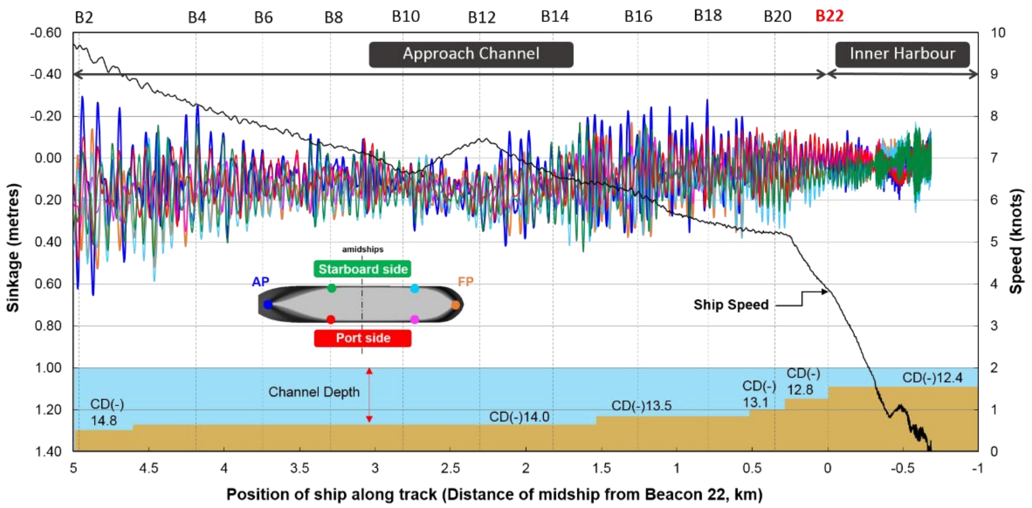

(a) Measured sinkage

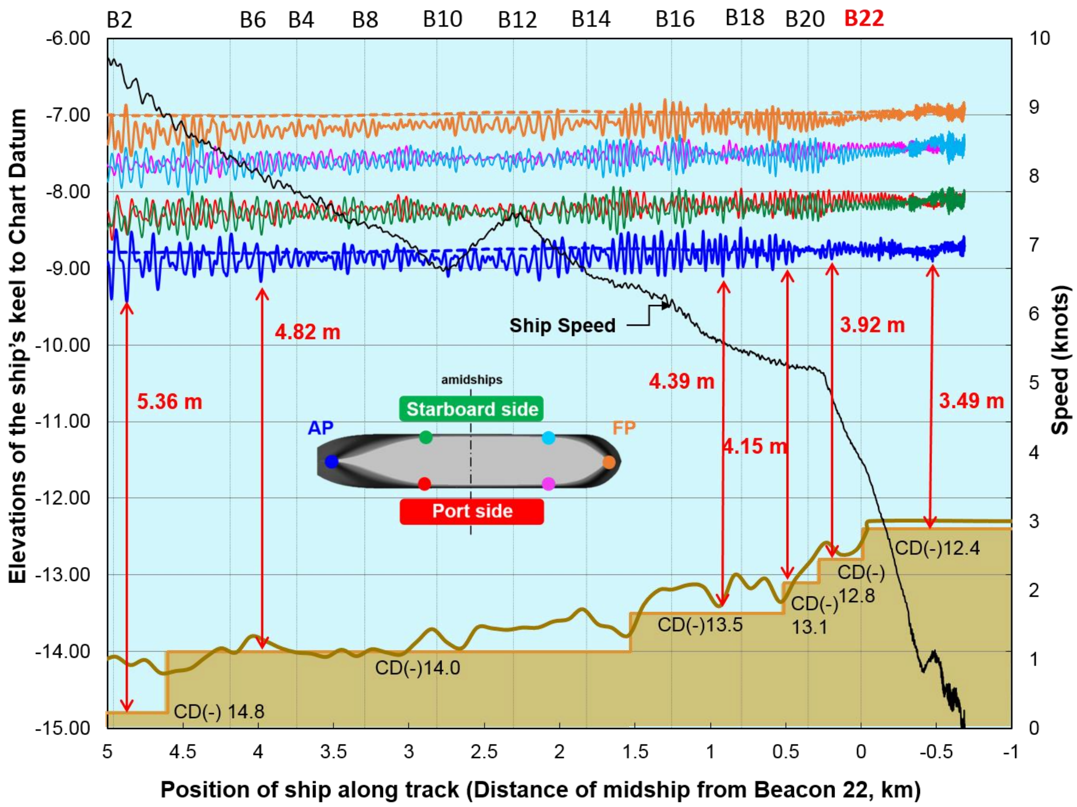

(b) Elevations of the ship's keel

Figure C.1. (a) Measured sinkage (positive downward) at six points [Note: Chart datum depths (not to scale) also shown]; (b) Elevations of the ship's keel relative to chart datum [Note: Dashed lines near the top of the figure are elevations of the FP (orange) and AP (blue), including changes in tide only; i.e., their static position, not including squat and wave-induced motions; the flat seabed line is based on the charted depth on AUS81; the fluctuating seabed line is the actual survey line provided by OMC International]

***PETANI* (inbound)**

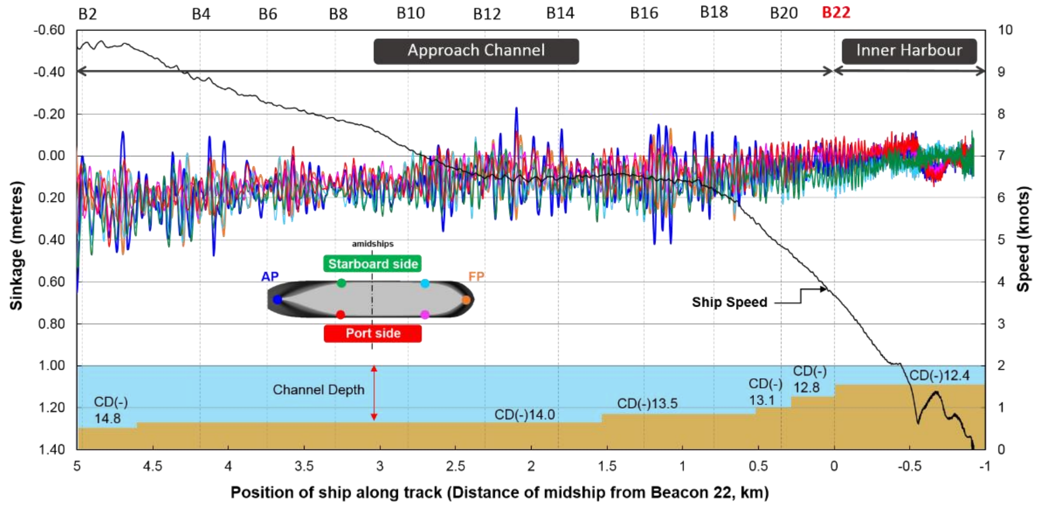

(a) Measured sinkage

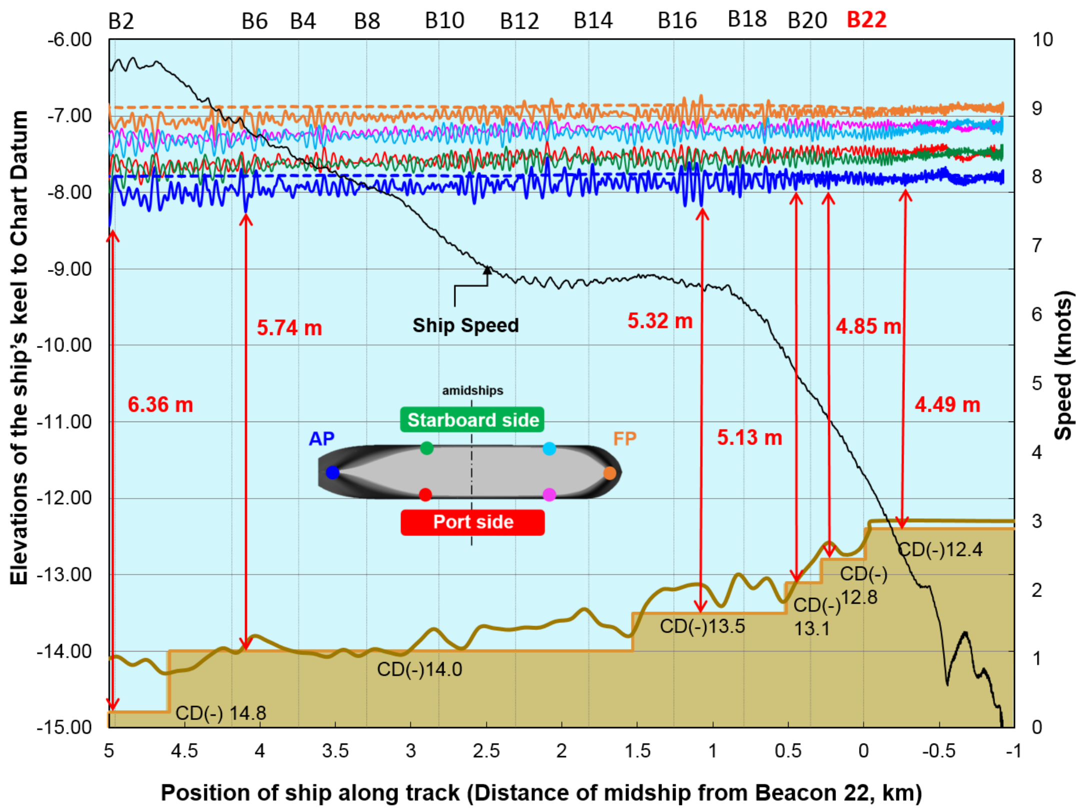

(b) Elevations of the ship's keel

Figure C.2. (a) Measured sinkage (positive downward) at six points [Note: Chart datum depths (not to scale) also shown]; (b) Elevations of the ship's keel relative to chart datum [Note: Dashed lines near the top of the figure are elevations of the FP (orange) and AP (blue), including changes in tide only; i.e., their static position, not including squat and wave-induced motions; the flat seabed line is based on the charted depth on AUS81; the fluctuating seabed line is the actual survey line provided by OMC International]

DONNACONA **(inbound)**

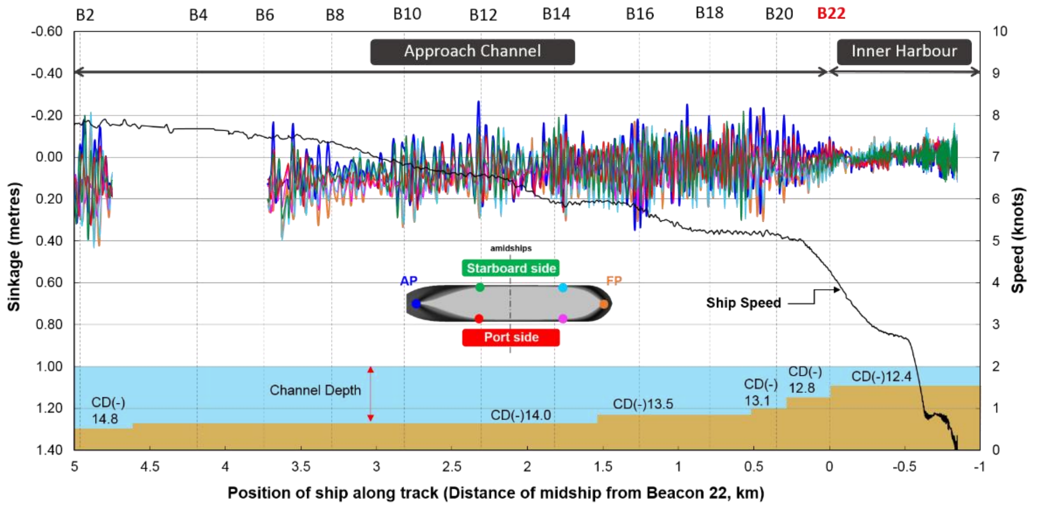

(a) Measured sinkage

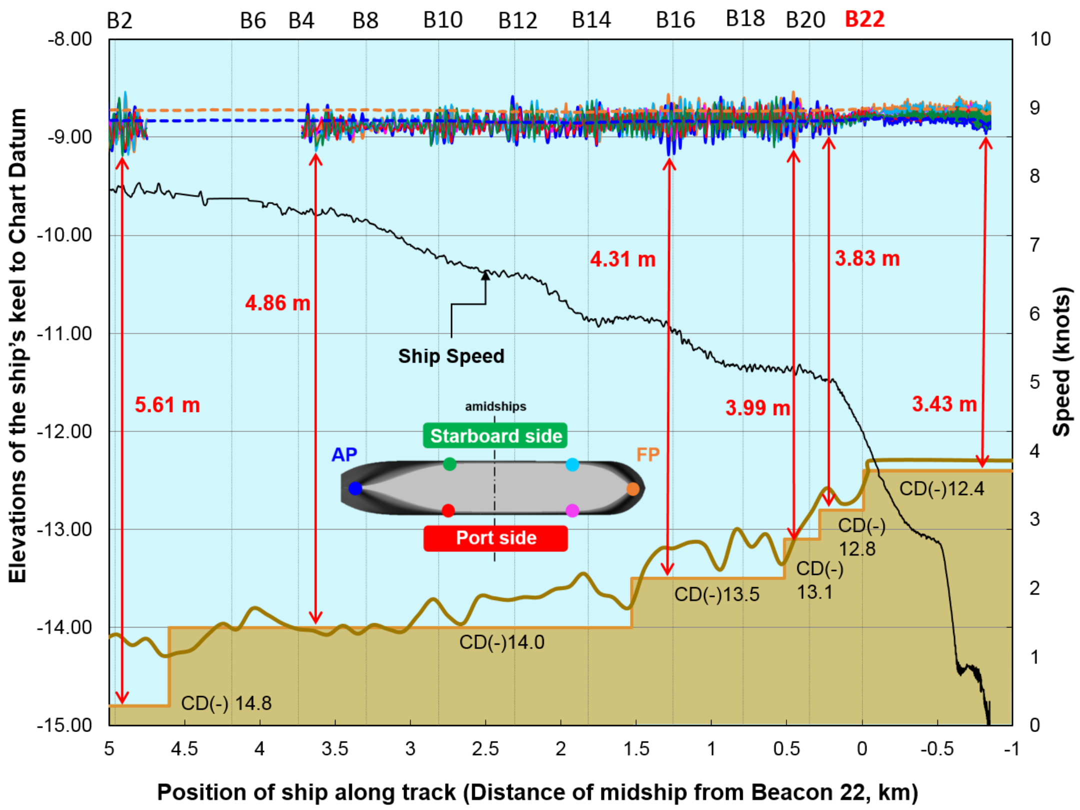

(b) Elevations of the ship's keel

Figure C.3. (a) Measured sinkage (positive downward) at six points [Note: Chart datum depths (not to scale) also shown]; (b) Elevations of the ship's keel relative to chart datum [Note: Dashed lines near the top of the figure are elevations of the FP (orange) and AP (blue), including changes in tide only; i.e., their static position, not including squat and wave-induced motions; the flat seabed line is based on the charted depth on AUS81; the fluctuating seabed line is the actual survey line provided by OMC International]

***AAL FREMANTLE* (inbound)**

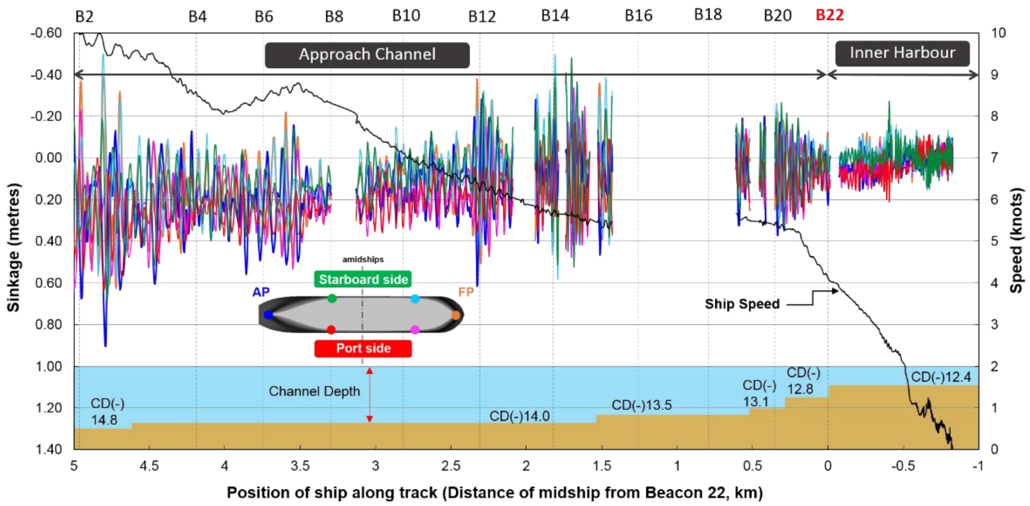

(a) Measured sinkage

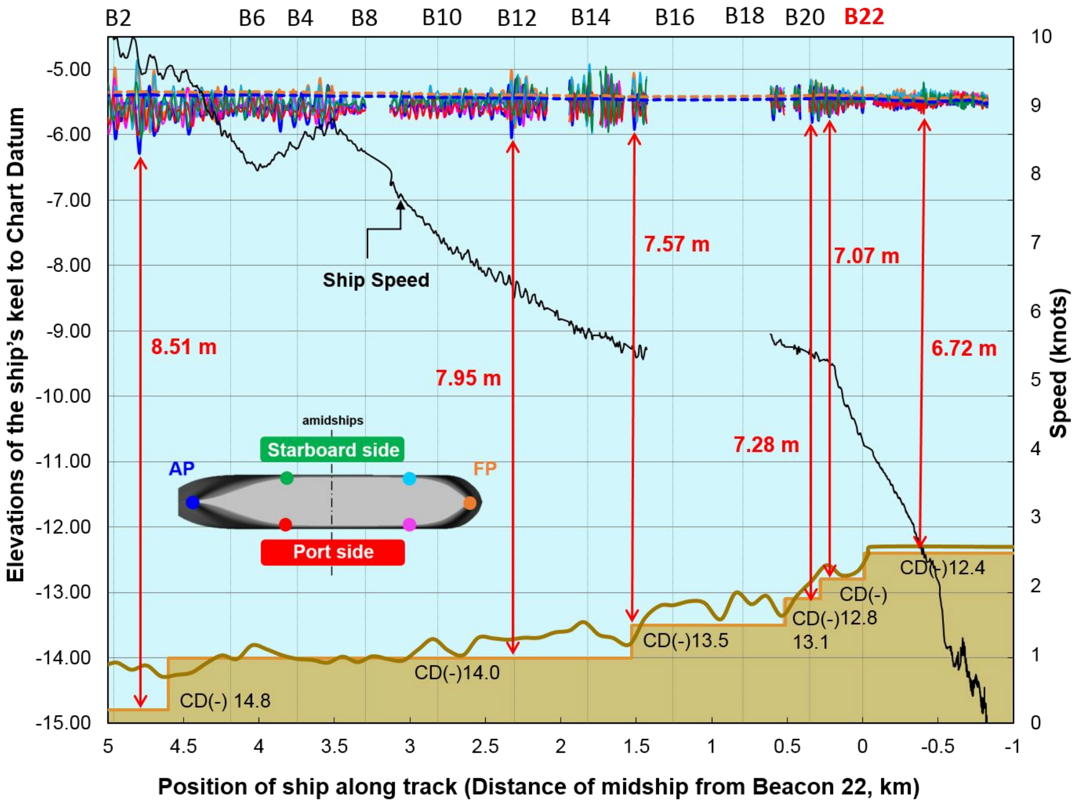

(b) Elevations of the ship's keel

Figure C.4. (a) Measured sinkage (positive downward) at six points [Note: Chart datum depths (not to scale) also shown]; (b) Elevations of the ship's keel relative to chart datum [Note: Dashed lines near the top of the figure are elevations of the FP (orange) and AP (blue), including changes in tide only; i.e., their static position, not including squat and wave-induced motions; the flat seabed line is based on the charted depth on AUS81; the fluctuating seabed line is the actual survey line provided by OMC International]

***SEA DIAMOND* (inbound)**

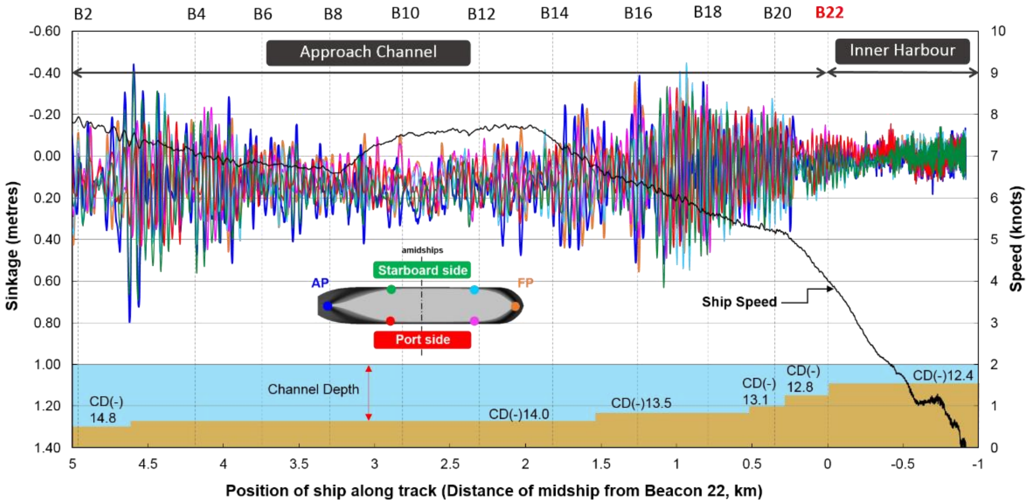

(a) Measured sinkage

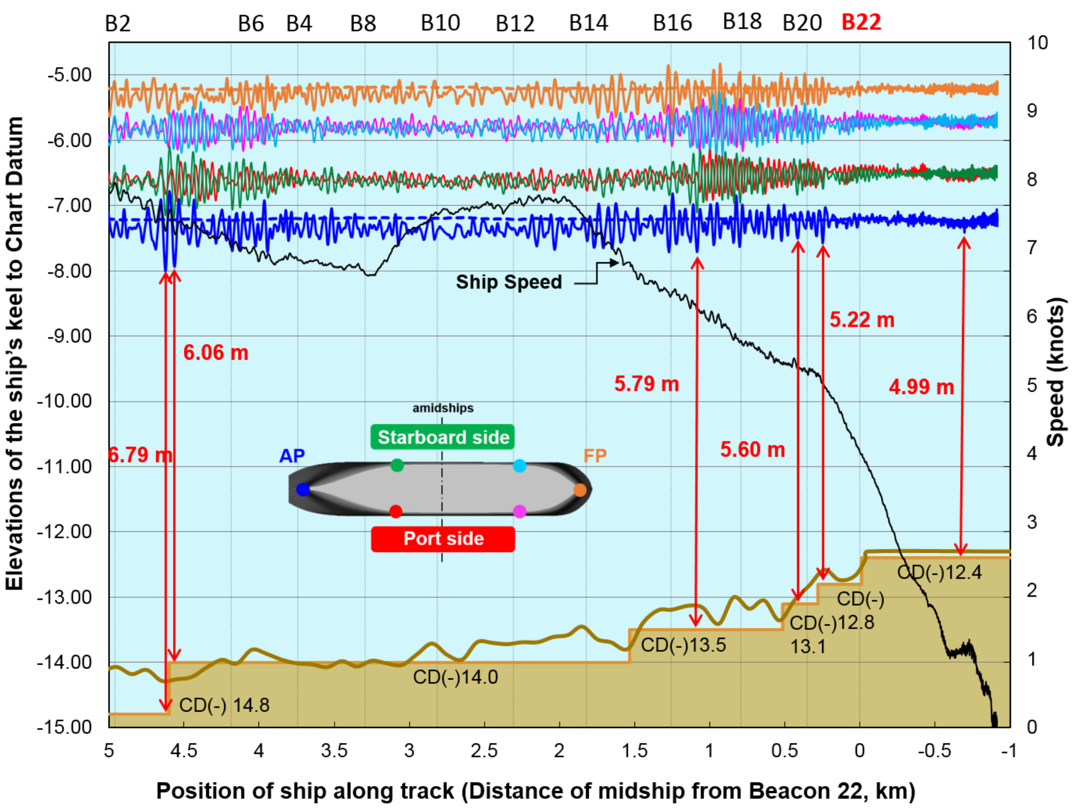

(b) Elevations of the ship's keel

Figure C.5. (a) Measured sinkage (positive downward) at six points [Note: Chart datum depths (not to scale) also shown]; (b) Elevations of the ship's keel relative to chart datum [Note: Dashed lines near the top of the figure are elevations of the FP (orange) and AP (blue), including changes in tide only; i.e., their static position, not including squat and wave-induced motions; the flat seabed line is based on the charted depth on AUS81; the fluctuating seabed line is the actual survey line provided by OMC International]

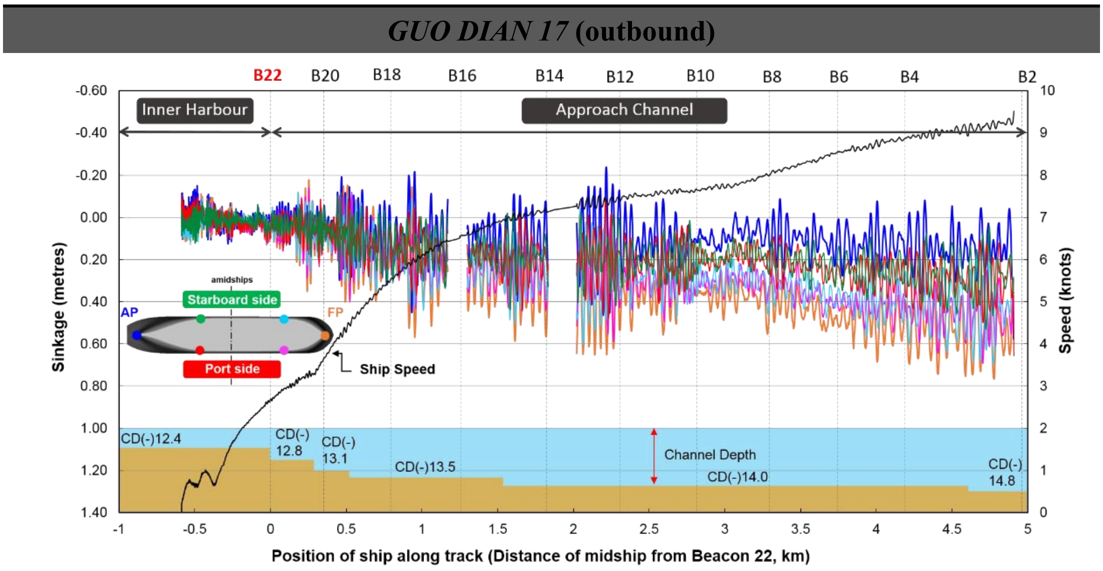

(a) Measured sinkage

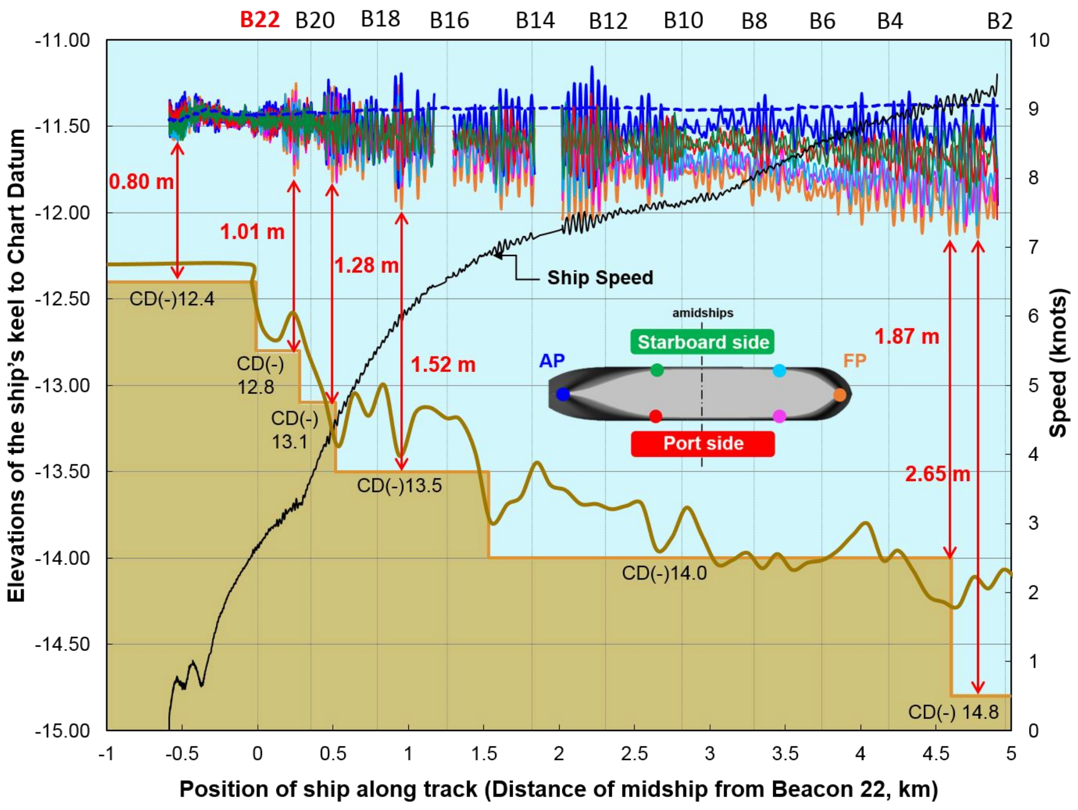

(b) Elevations of the ship's keel

Figure C.6. (a) Measured sinkage (positive downward) at six points [Note: Chart datum depths (not to scale) also shown]; (b) Elevations of the ship's keel relative to chart datum [Note: Dashed lines near the top of the figure are elevations of the FP (orange) and AP (blue), including changes in tide only; i.e., their static position, not including squat and wave-induced motions; the flat seabed line is based on the charted depth on AUS81; the fluctuating seabed line is the actual survey line provided by OMC International]

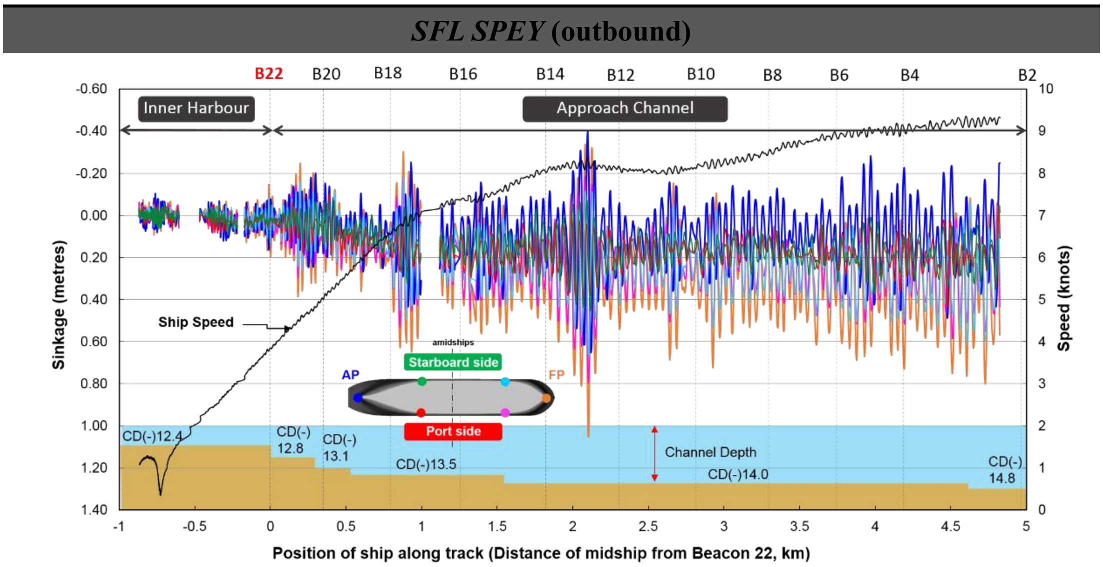

(a) Measured sinkage

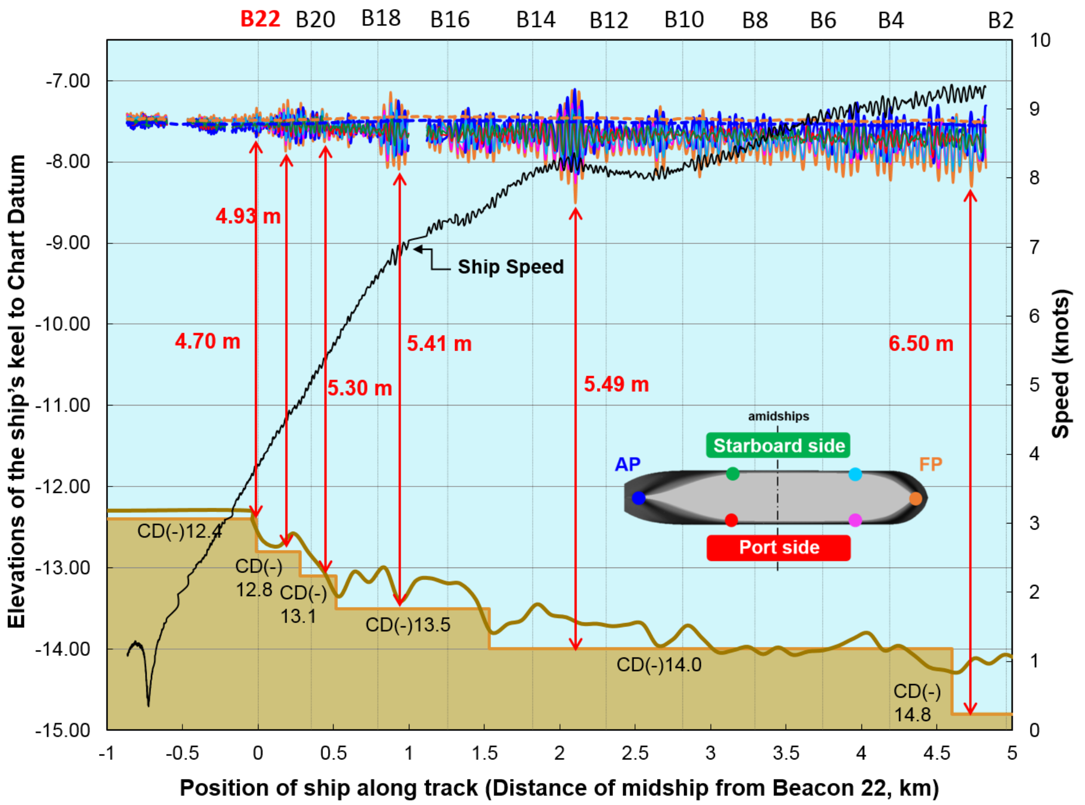

(b) Elevations of the ship's keel

Figure C.7. (a) Measured sinkage (positive downward) at six points [Note: Chart datum depths (not to scale) also shown]; (b) Elevations of the ship's keel relative to chart datum [Note: Dashed lines near the top of the figure are elevations of the FP (orange) and AP (blue), including changes in tide only; i.e., their static position, not including squat and wave-induced motions; the flat seabed line is based on the charted depth on AUS81; the fluctuating seabed line is the actual survey line provided by OMC International]

***IVS MAGPIE* (outbound)**

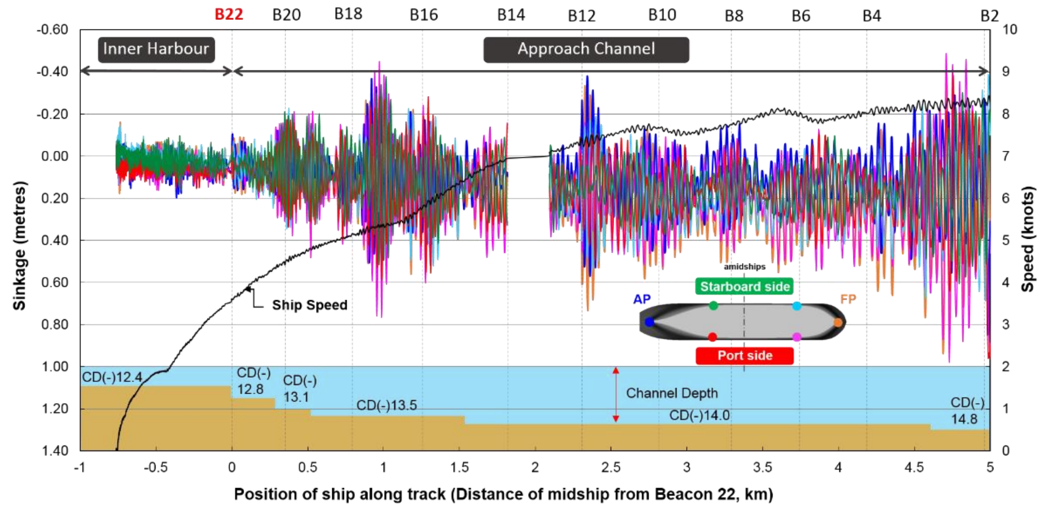

(a) Measured sinkage

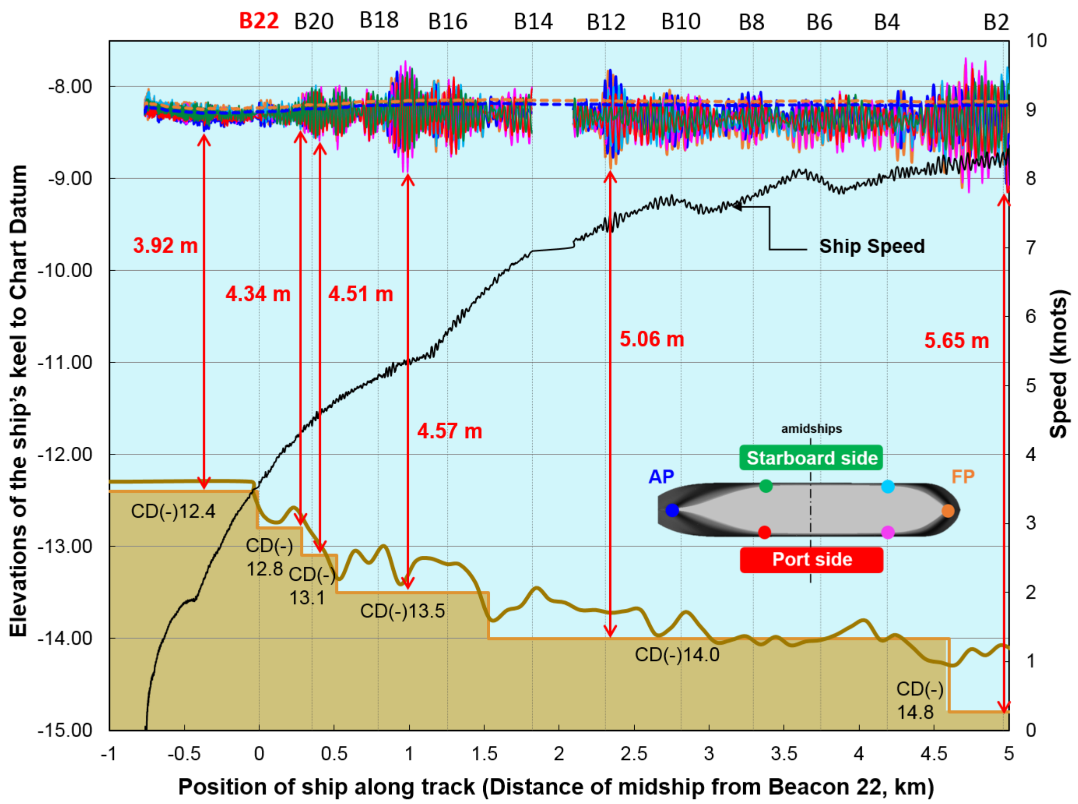

(b) Elevations of the ship's keel

Figure C.8. (a) Measured sinkage (positive downward) at six points [Note: Chart datum depths (not to scale) also shown]; (b) Elevations of the ship's keel relative to chart datum [Note: Dashed lines near the top of the figure are elevations of the FP (orange) and AP (blue), including changes in tide only; i.e., their static position, not including squat and wave-induced motions; the flat seabed line is based on the charted depth on AUS81; the fluctuating seabed line is the actual survey line provided by OMC International]

***FENG HUANG FENG* (outbound)**

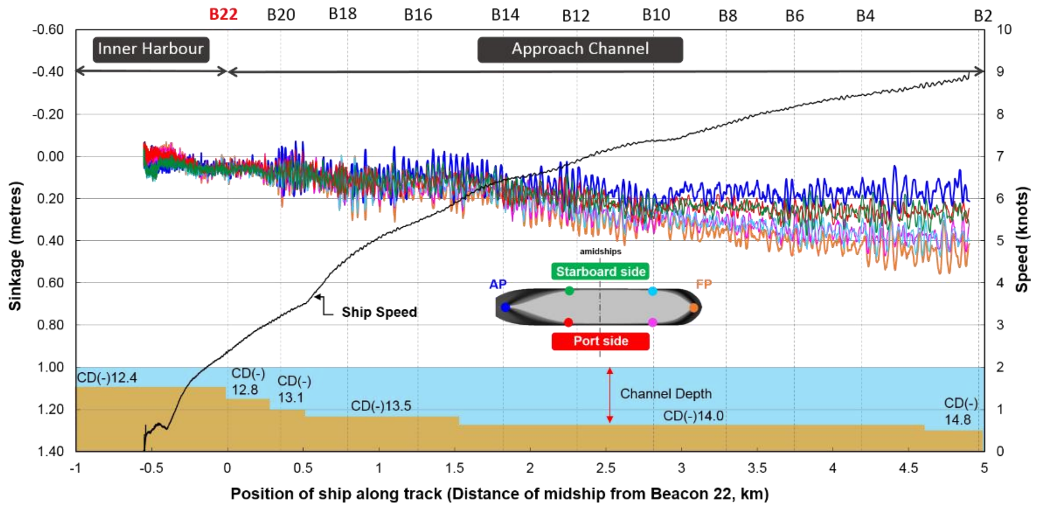

(a) Measured sinkage

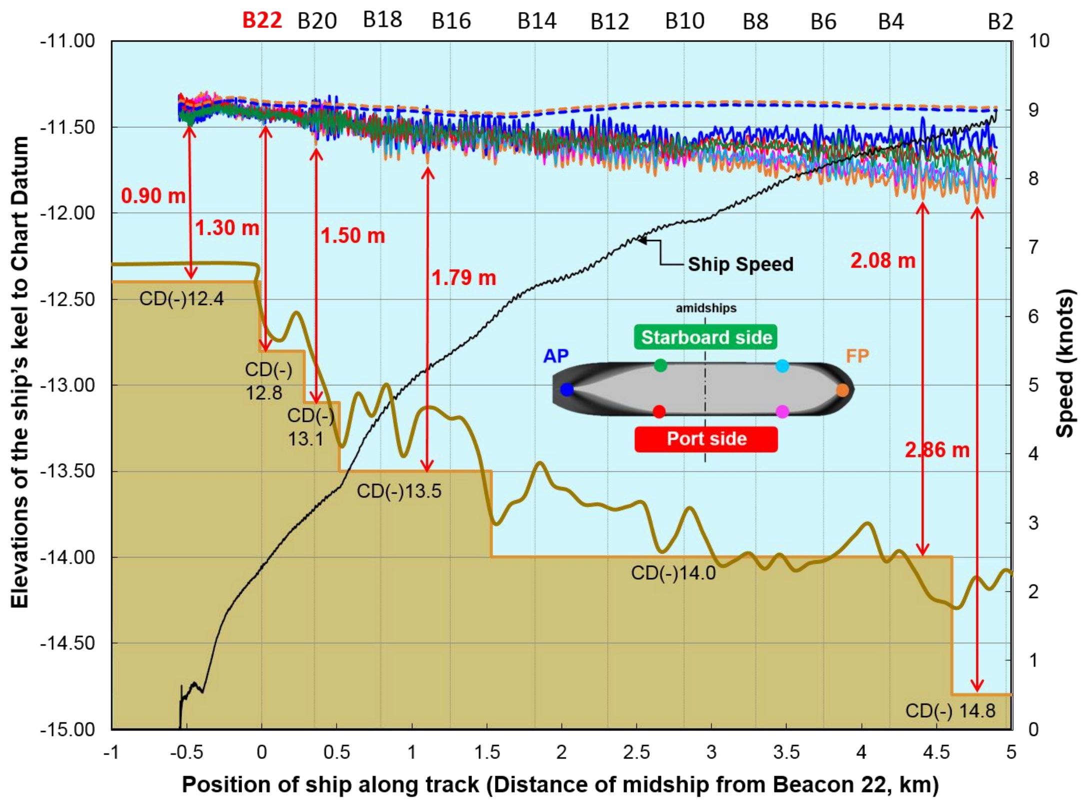

(b) Elevations of the ship's keel

Figure C.9. (a) Measured sinkage (positive downward) at six points [Note: Chart datum depths (not to scale) also shown]; (b) Elevations of the ship's keel relative to chart datum [Note: Dashed lines near the top of the figure are elevations of the FP (orange) and AP (blue), including changes in tide only; i.e., their static position, not including squat and wave-induced motions; the flat seabed line is based on the charted depth on AUS81; the fluctuating seabed line is the actual survey line provided by OMC International]

***AAL FREMANTLE* (outbound)**

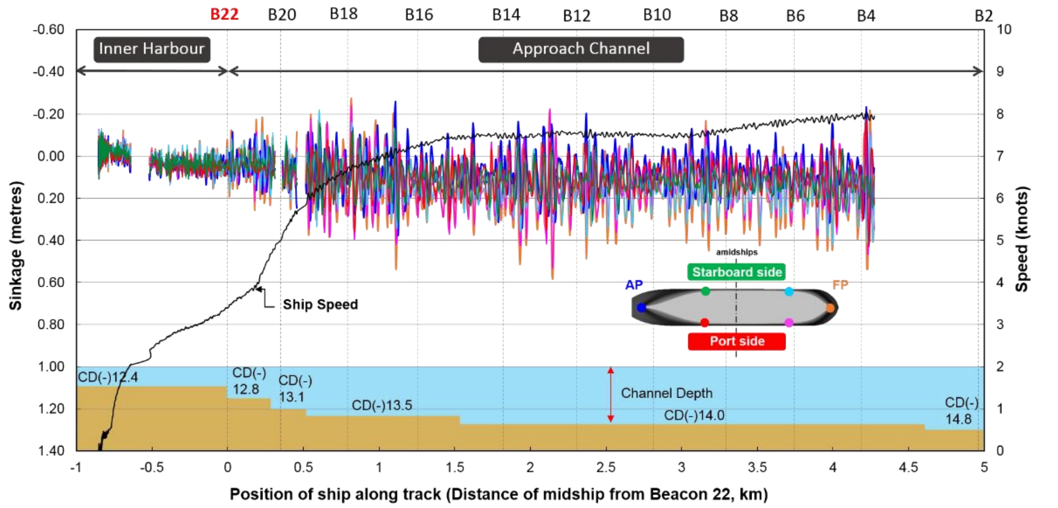

(a) Measured sinkage

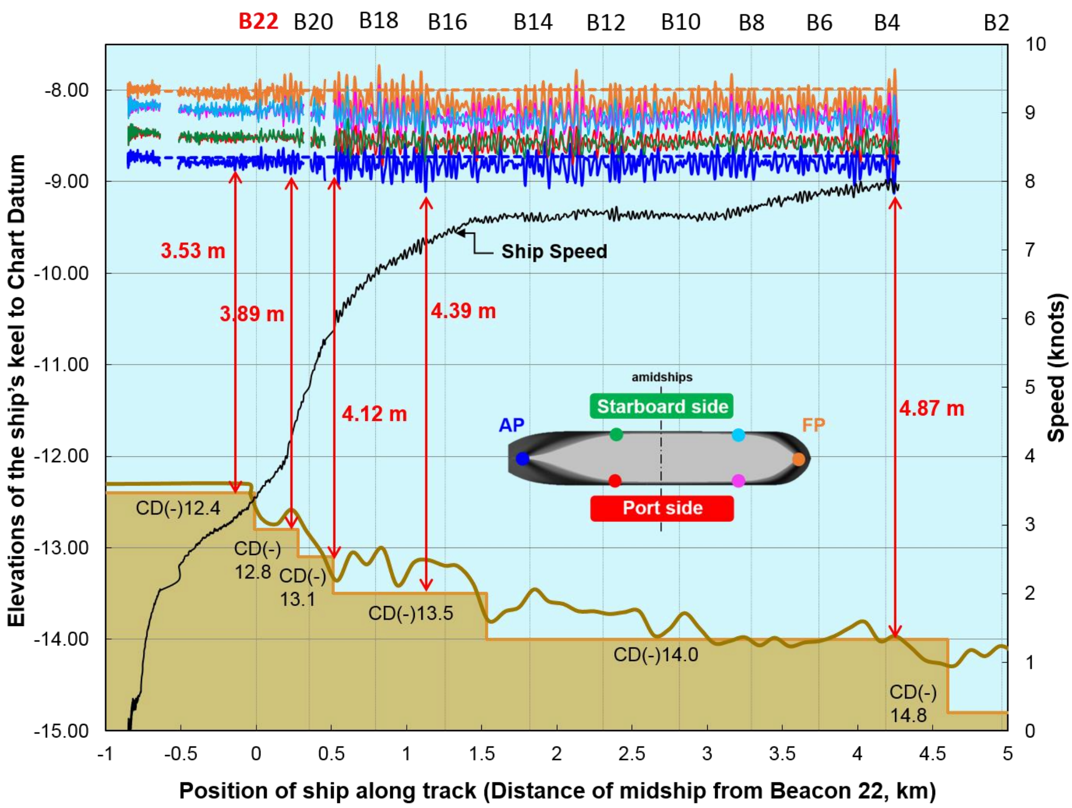

(b) Elevations of the ship's keel

Figure C.10. (a) Measured sinkage (positive downward) at six points [Note: Chart datum depths (not to scale) also shown]; (b) Elevations of the ship's keel relative to chart datum [Note: Dashed lines near the top of the figure are elevations of the FP (orange) and AP (blue), including changes in tide only; i.e., their static position, not including squat and wave-induced motions; the flat seabed line is based on the charted depth on AUS81; the fluctuating seabed line is the actual survey line provided by OMC International]

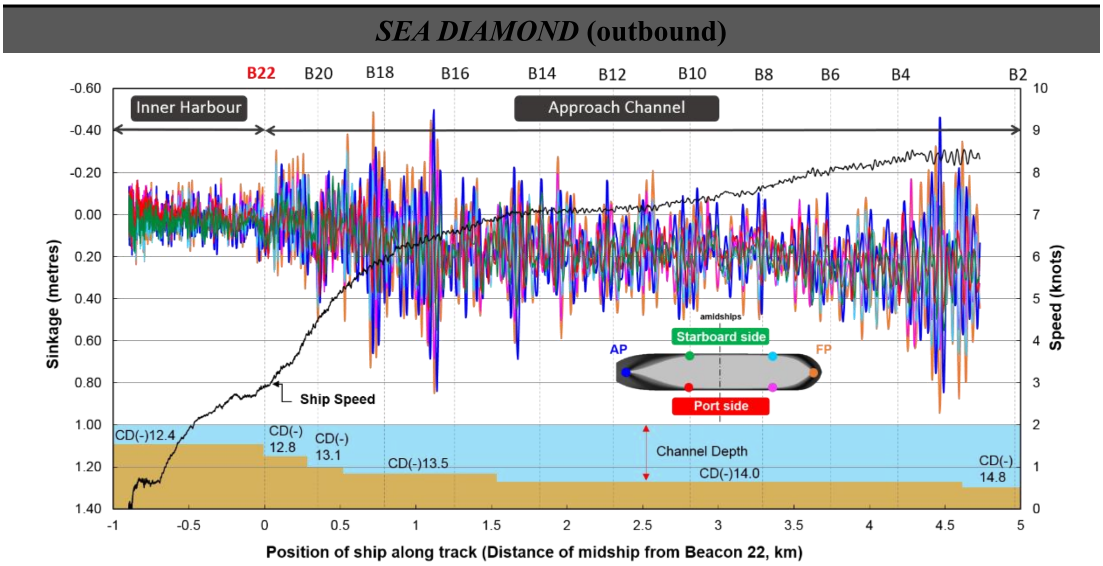

(a) Measured sinkage

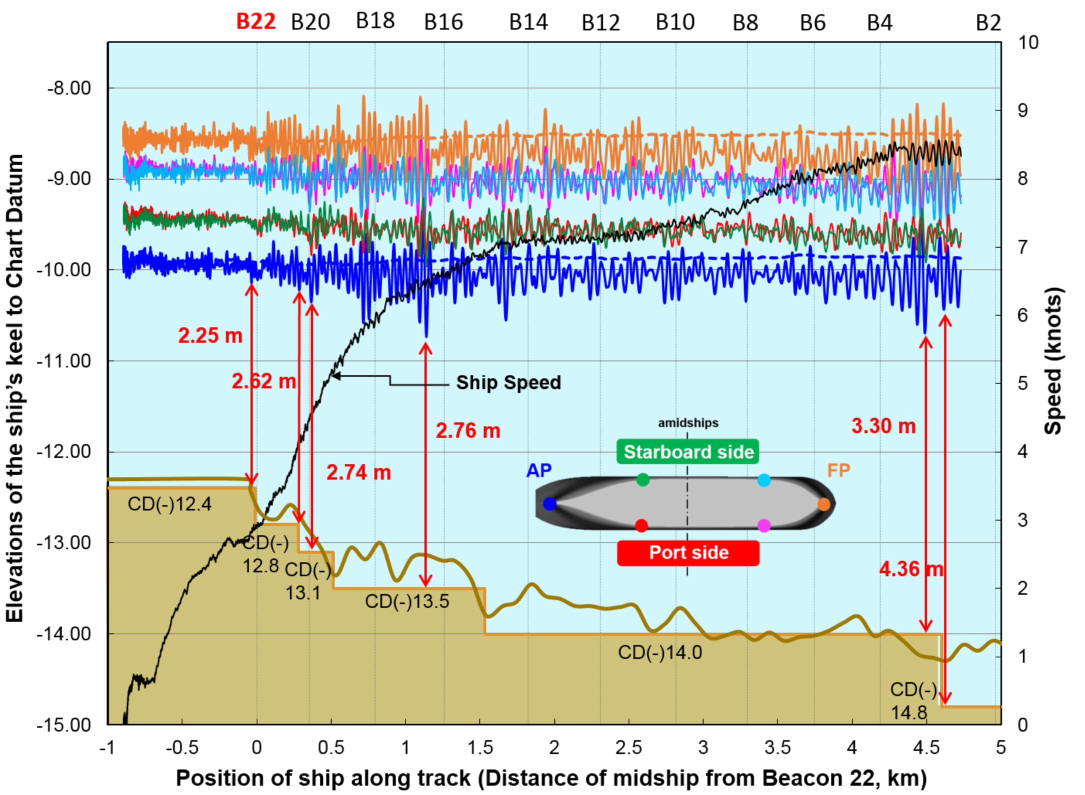

(b) Elevations of the ship's keel

Figure C.11. (a) Measured sinkage (positive downward) at six points [Note: Chart datum depths (not to scale) also shown]; (b) Elevations of the ship's keel relative to chart datum [Note: Dashed lines near the top of the figure are elevations of the FP (orange) and AP (blue), including changes in tide only; i.e., their static position, not including squat and wave-induced motions; the flat seabed line is based on the charted depth on AUS81; the fluctuating seabed line is the actual survey line provided by OMC International]

C.2 Detailed measurement results for the container ship transits at the Port of Fremantle

The measured sinkage results, together with ship speed and channel bathymetry, for all container ship transits are shown in Figure C.12(a) to Figure C.24(a). Elevations of the ship's keel relative to chart datum are also shown in Figure C.12(b) to Figure C.24(b). Results are plotted against the cumulative distance from the Front Lead light (FL) (32° 3.22728' S, 115° 44.45048' E); hence, distance within the inner harbour is negative. Vertical lines are shown for South Mole (SM), North Mole (NM) and Green No.1 Buoy (G1) in the Entrance Channel. In the Deep Water Channel (DWC), vertical lines are shown at the starting point, Green No.1 Buoy (G1), Green No.2 Buoy (G2), Green No.3 Buoy (G3) and the end point (see Figure 4.24 for the inbound transits and Figure 4.25 for the outbound). Sinkage is given at the FP, AP, and port and starboard bilge corners (refer to Figure 4.23), and defined as being positive downward.

Note that gaps in the results of some transits are because some GNSS fixes were of insufficient quality and have been rejected. As mentioned in Appendix B.2, three container ship transits, including *MSC ILONA* (outbound), *SEAMAX STAMFORD* (outbound) and *OOCL BRISBANE* (outbound), have been excluded from this study because of their poor GNSS signals. The results fall into categories of inbound and outbound transits.

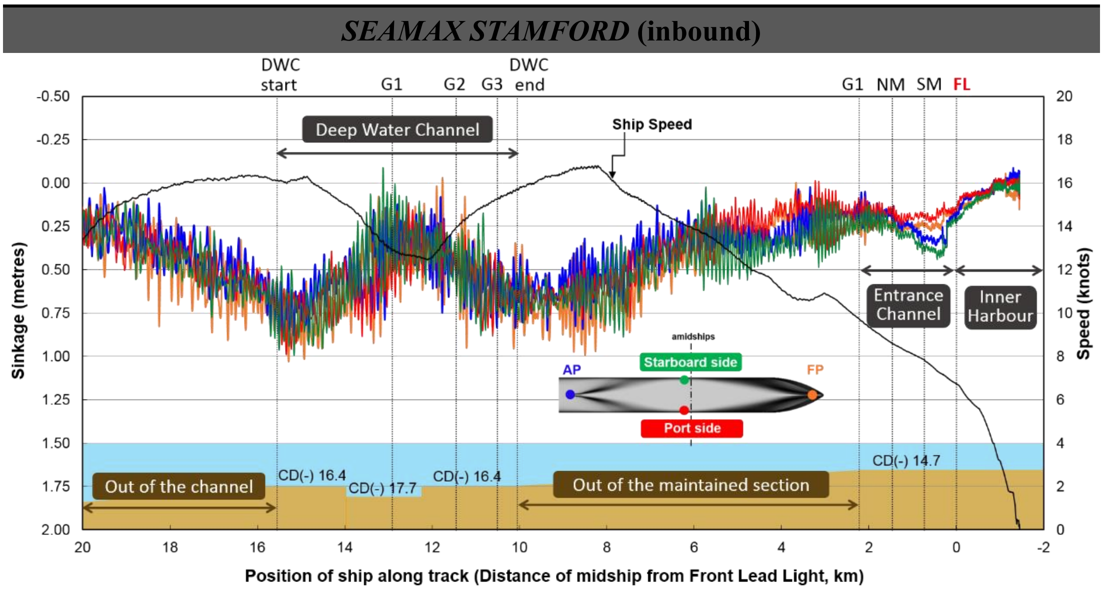

(a) Measured sinkage

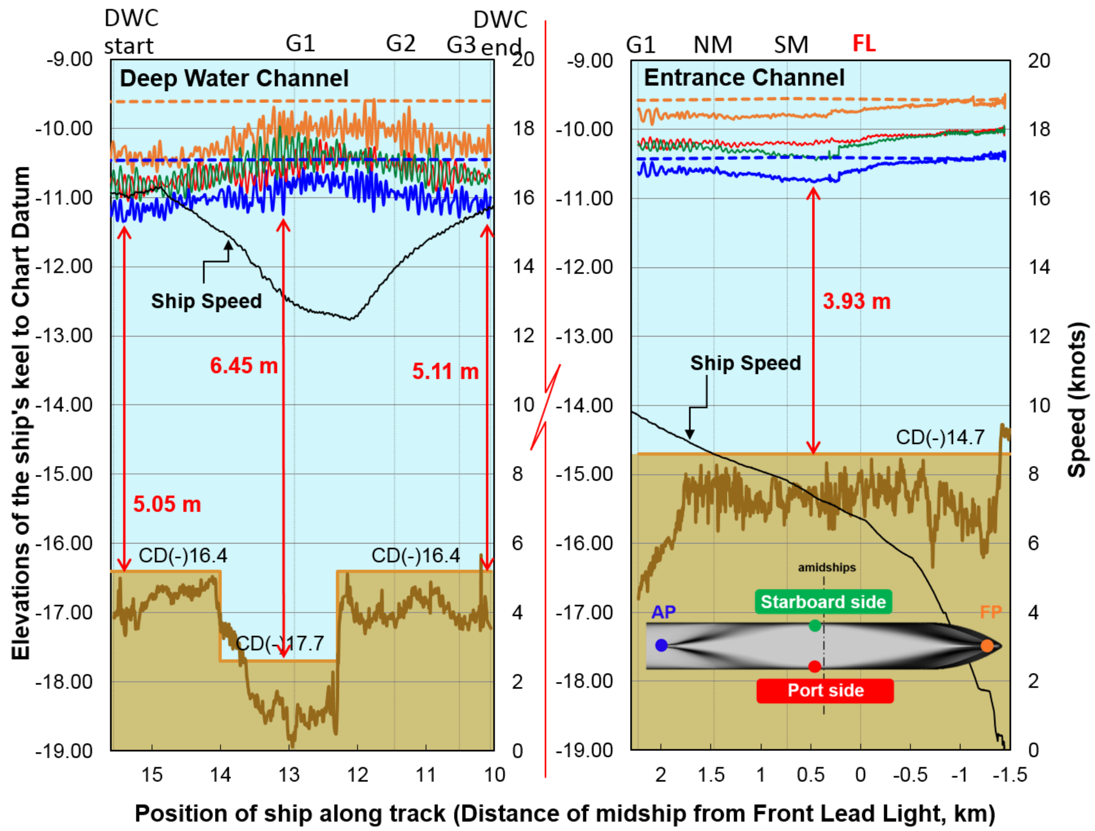

(b) Elevations of the ship's keel

Figure C.12. (a) Measured sinkage (positive downward) at four points [Note: Chart datum depths (not to scale) also shown]; (b) Elevations of the ship's keel relative to chart datum [Note: Dashed lines near the top of the figure are elevations of the FP (orange) and AP (blue), including changes in tide only; i.e., their static position, not including squat and wave-induced motions; the flat seabed line is based on the charted depth on AUS112; the fluctuating seabed line is the actual survey line provided by Fremantle Ports]

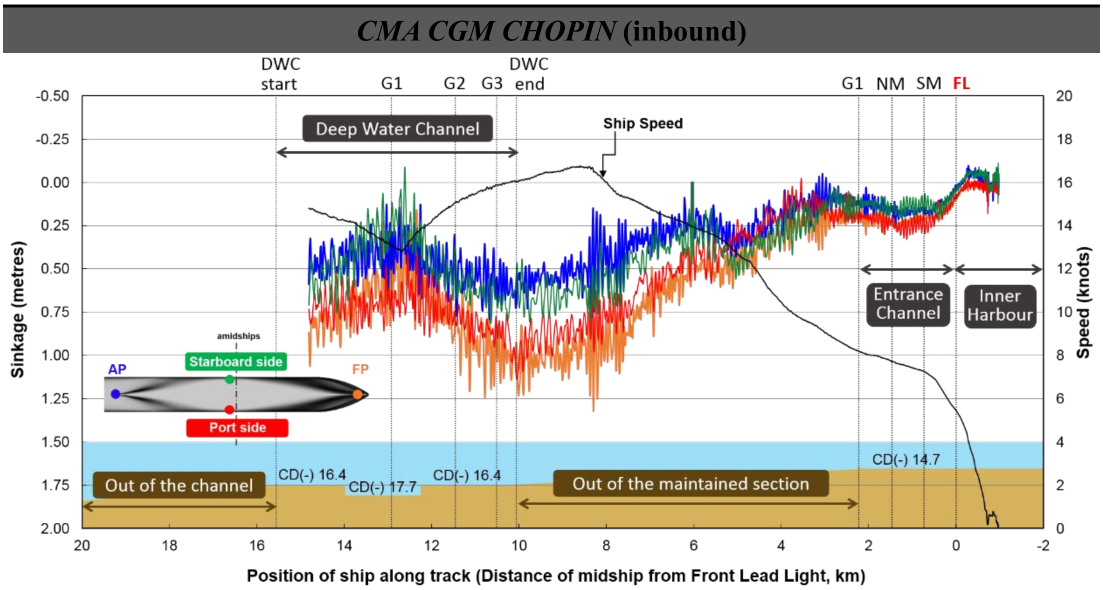

(a) Measured sinkage

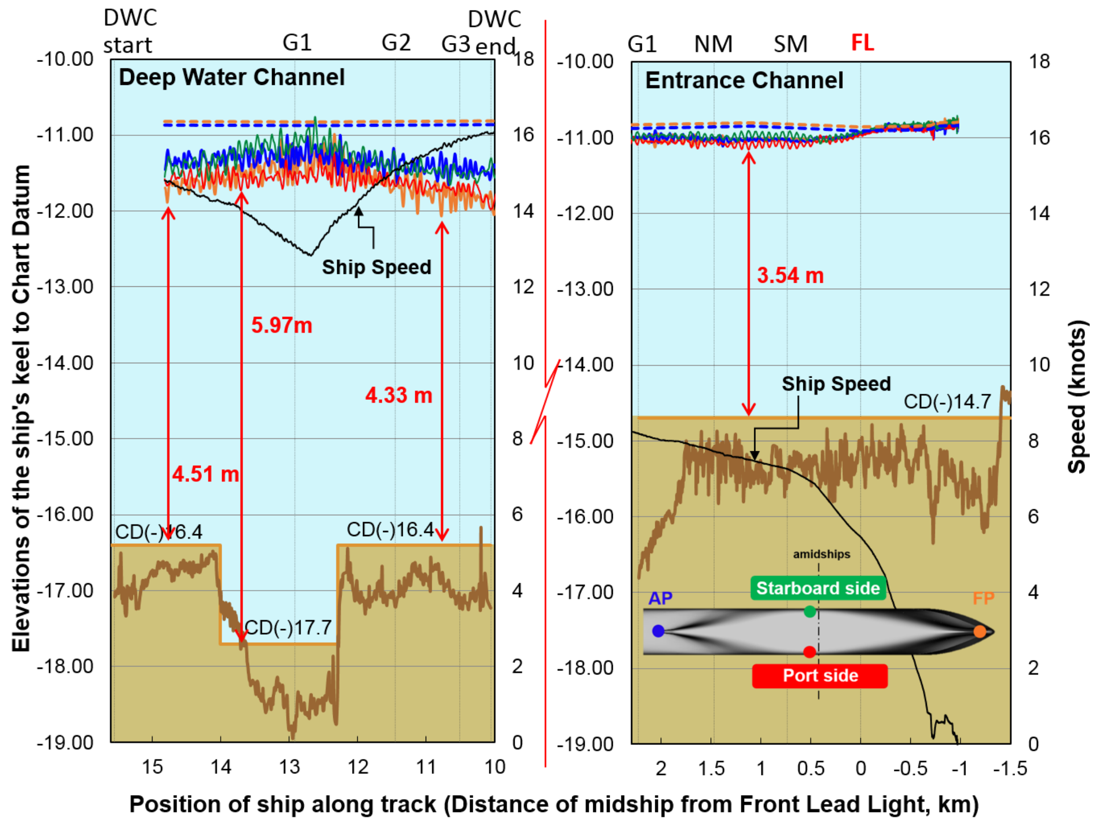

(b) Elevations of the ship's keel

Figure C.13. (a) Measured sinkage (positive downward) at four points [Note: Chart datum depths (not to scale) also shown]; (b) Elevations of the ship's keel relative to chart datum [Note: Dashed lines near the top of the figure are elevations of the FP (orange) and AP (blue), including changes in tide only; i.e., their static position, not including squat and wave-induced motions; the flat seabed line is based on the charted depth on AUS112; the fluctuating seabed line is the actual survey line provided by Fremantle Ports]

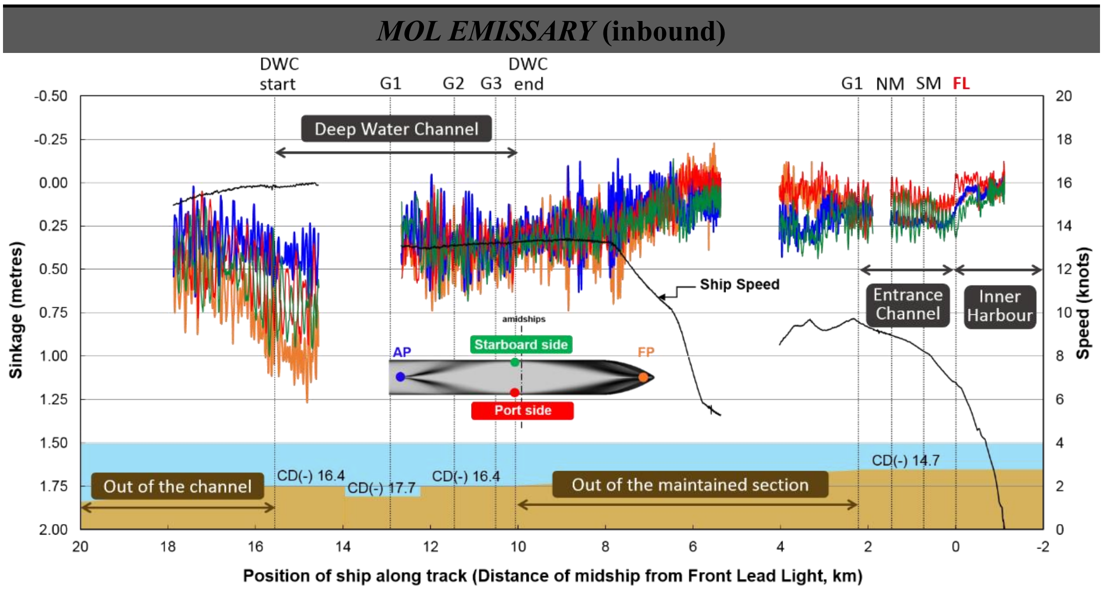

(a) Measured sinkage

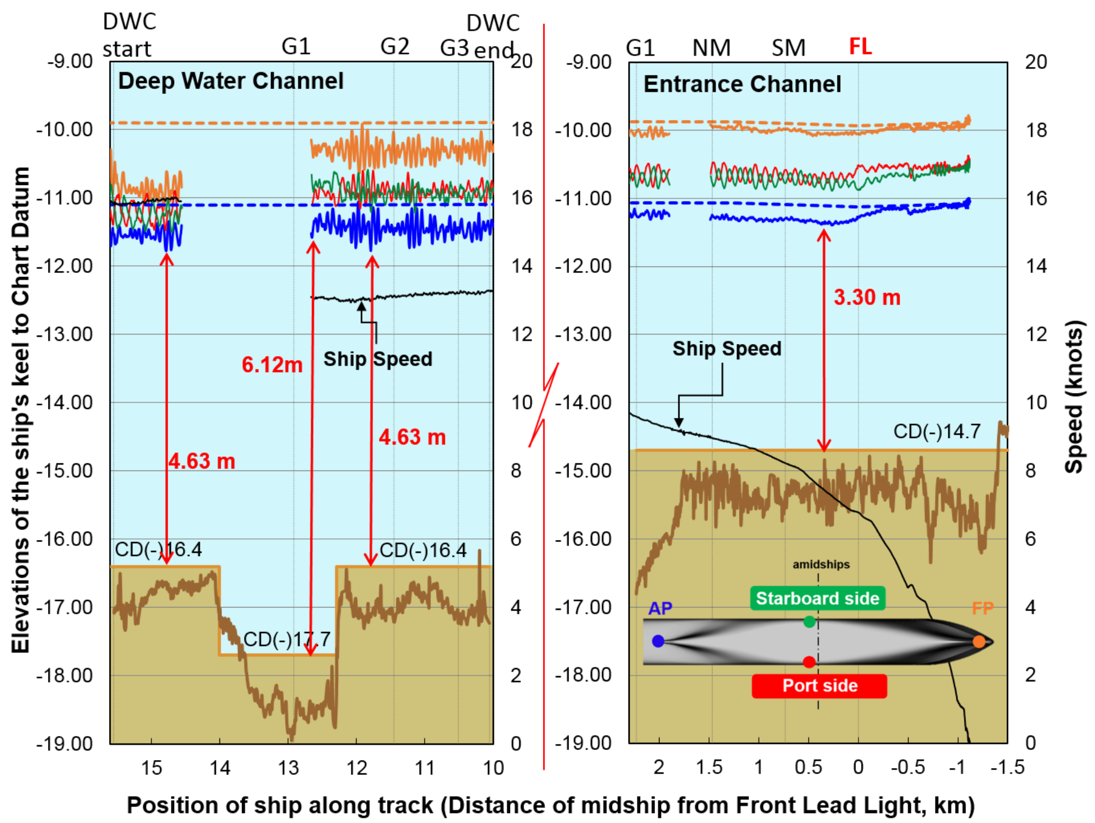

(b) Elevations of the ship's keel

Figure C.14. (a) Measured sinkage (positive downward) at four points [Note: Chart datum depths (not to scale) also shown]; (b) Elevations of the ship's keel relative to chart datum [Note: Dashed lines near the top of the figure are elevations of the FP (orange) and AP (blue), including changes in tide only; i.e., their static position, not including squat and wave-induced motions; the flat seabed line is based on the charted depth on AUS112; the fluctuating seabed line is the actual survey line provided by Fremantle Ports]

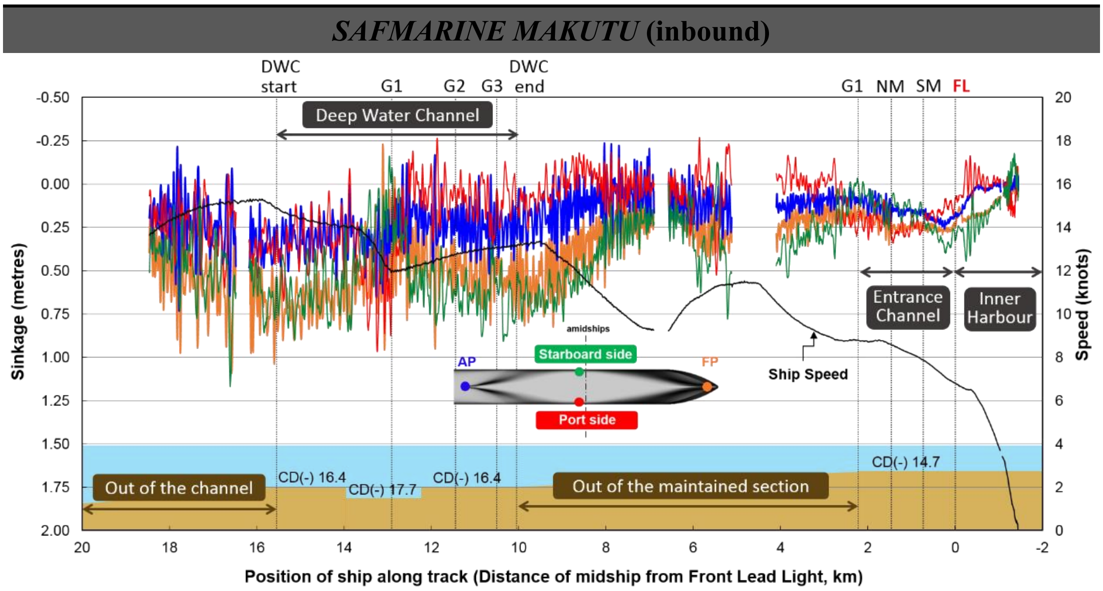

(a) Measured sinkage

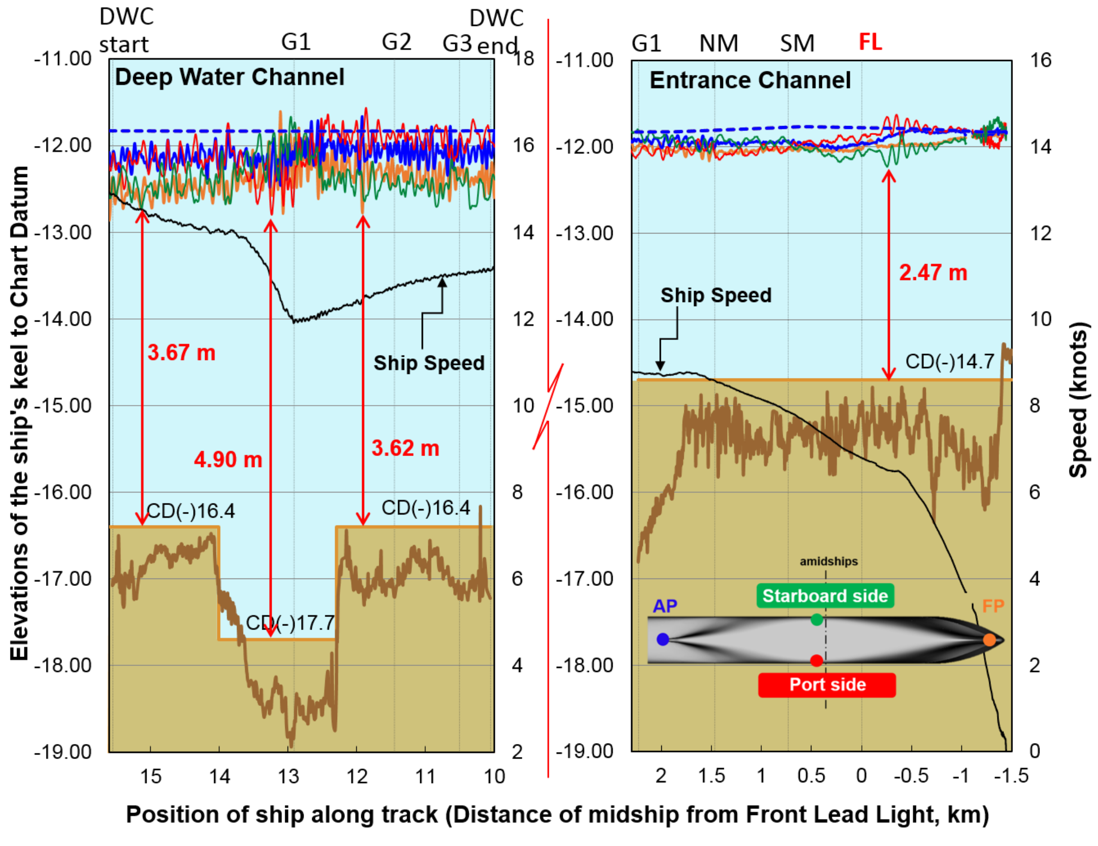

(b) Elevations of the ship's keel

Figure C.15. (a) Measured sinkage (positive downward) at four points [Note: Chart datum depths (not to scale) also shown]; (b) Elevations of the ship's keel relative to chart datum [Note: Dashed lines near the top of the figure are elevations of the FP (orange) and AP (blue), including changes in tide only; i.e., their static position, not including squat and wave-induced motions; the flat seabed line is based on the charted depth on AUS112; the fluctuating seabed line is the actual survey line provided by Fremantle Ports]

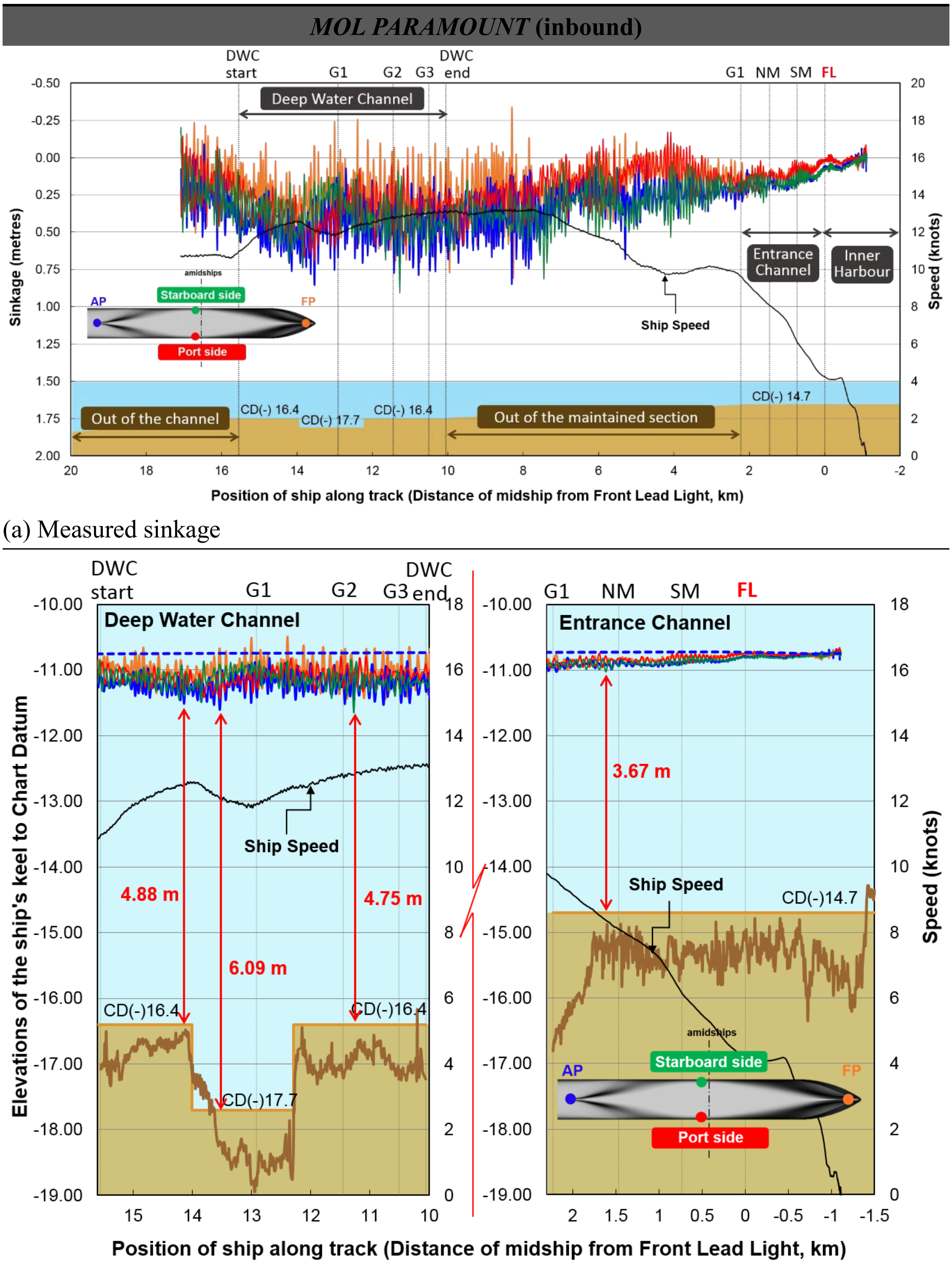

(a) Measured sinkage

(b) Elevations of the ship's keel

Figure C.16. (a) Measured sinkage (positive downward) at four points [Note: Chart datum depths (not to scale) also shown]; (b) Elevations of the ship's keel relative to chart datum [Note: Dashed lines near the top of the figure are elevations of the FP (orange) and AP (blue), including changes in tide only; i.e., their static position, not including squat and wave-induced motions; the flat seabed line is based on the charted depth on AUS112; the fluctuating seabed line is the actual survey line provided by Fremantle Ports]

OOCL BRISBANE **(inbound)**

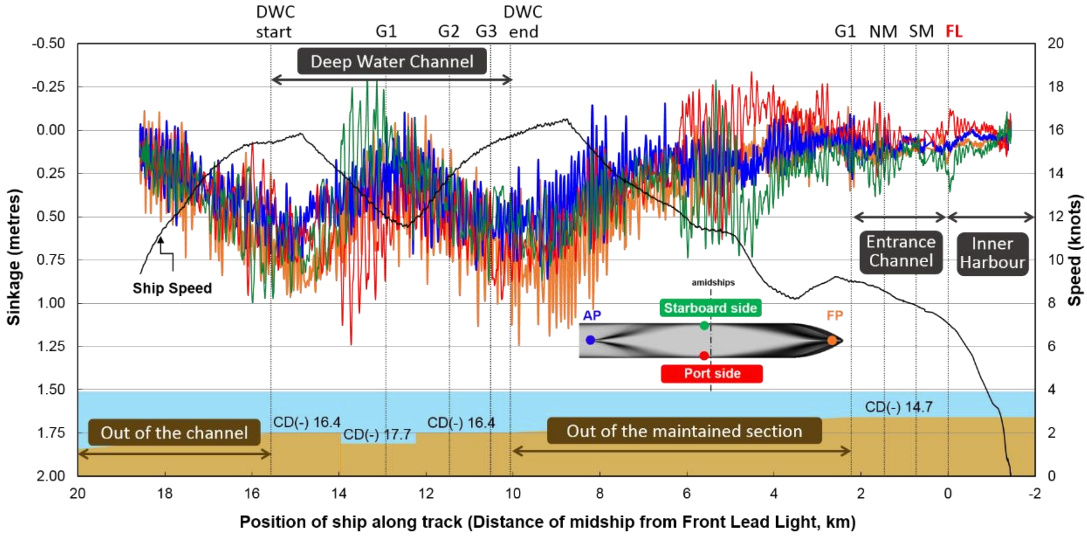

(a) Measured sinkage

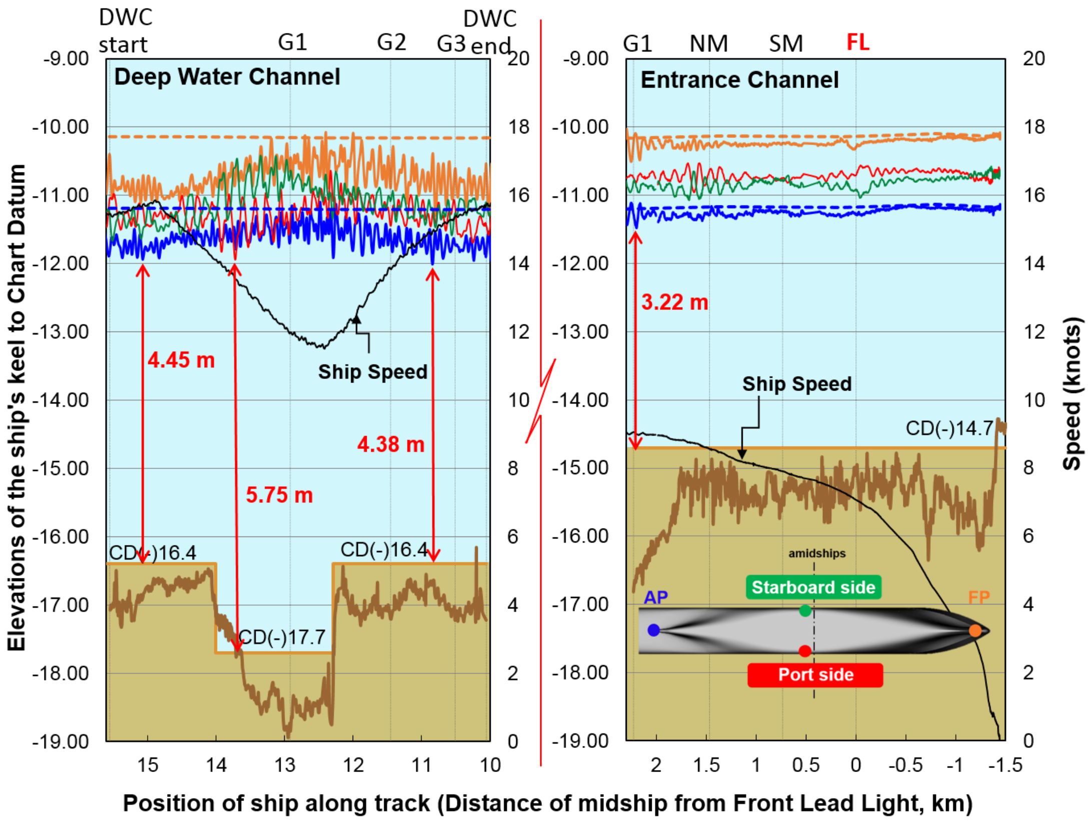

(b) Elevations of the ship's keel

Figure C.17. (a) Measured sinkage (positive downward) at four points [Note: Chart datum depths (not to scale) also shown]; (b) Elevations of the ship's keel relative to chart datum [Note: Dashed lines near the top of the figure are elevations of the FP (orange) and AP (blue), including changes in tide only; i.e., their static position, not including squat and wave-induced motions; the flat seabed line is based on the charted depth on AUS112; the fluctuating seabed line is the actual survey line provided by Fremantle Ports]

CMA CGM WAGNER (inbound)

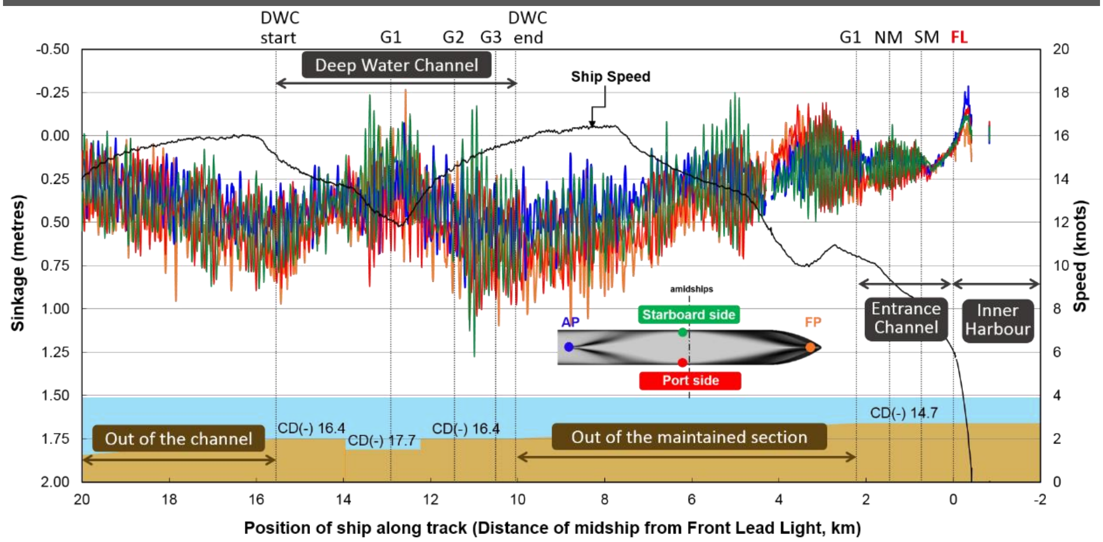

(a) Measured sinkage

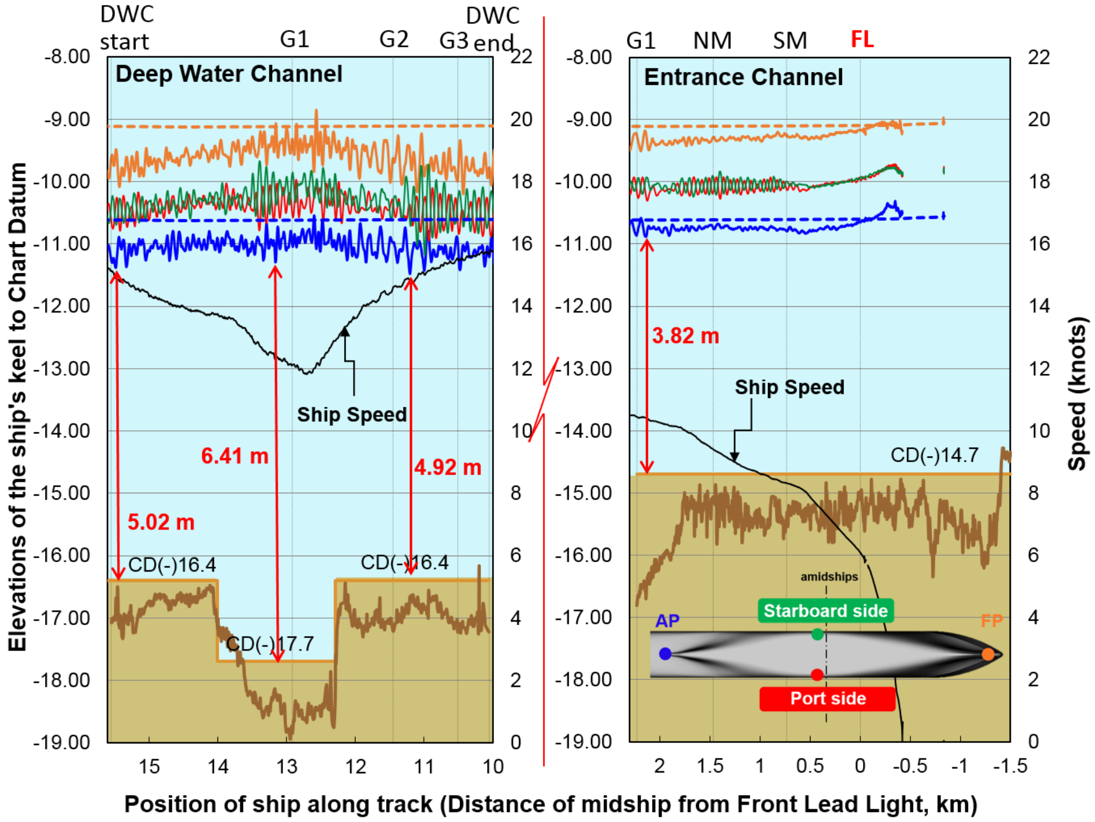

(b) Elevations of the ship's keel

Figure C.18. (a) Measured sinkage (positive downward) at four points [Note: Chart datum depths (not to scale) also shown]; (b) Elevations of the ship's keel relative to chart datum [Note: Dashed lines near the top of the figure are elevations of the FP (orange) and AP (blue), including changes in tide only; i.e., their static position, not including squat and wave-induced motions; the flat seabed line is based on the charted depth on AUS112; the fluctuating seabed line is the actual survey line provided by Fremantle Ports]

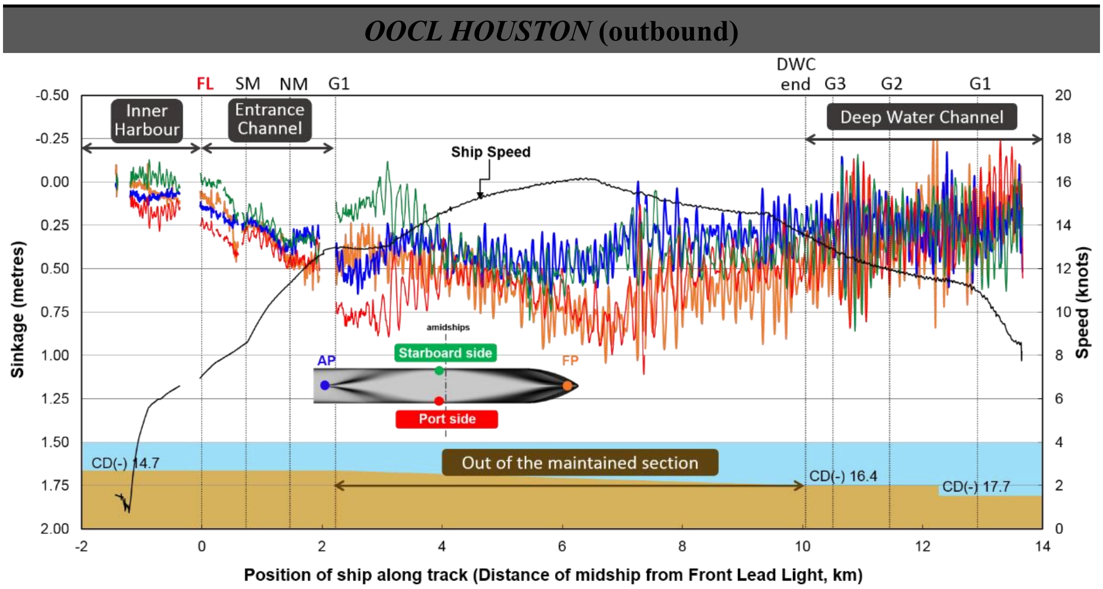

(a) Measured sinkage

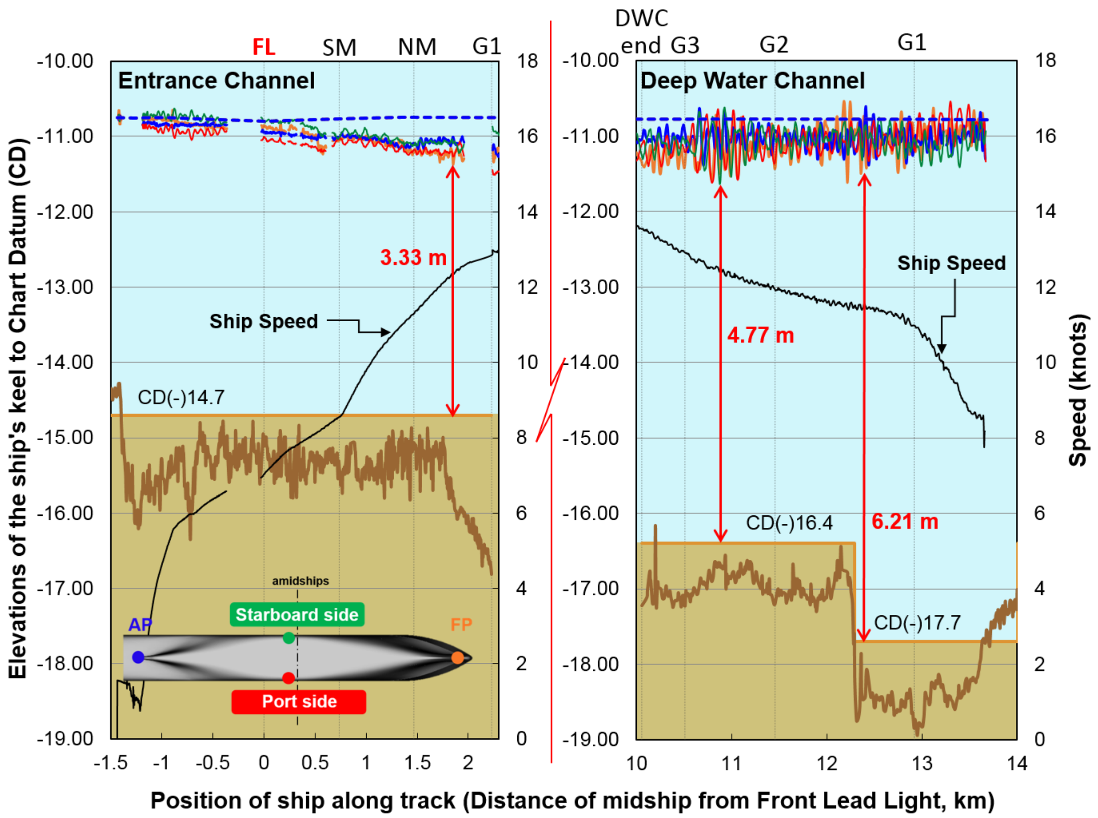

(b) Elevations of the ship's keel

Figure C.19. (a) Measured sinkage (positive downward) at four points [Note: Chart datum depths (not to scale) also shown]; (b) Elevations of the ship's keel relative to chart datum [Note: Dashed lines near the top of the figure are elevations of the FP (orange) and AP (blue), including changes in tide only; i.e., their static position, not including squat and wave-induced motions; the flat seabed line is based on the charted depth on AUS112; the fluctuating seabed line is the actual survey line provided by Fremantle Ports]

***CMA CGM CHOPIN* (outbound)**

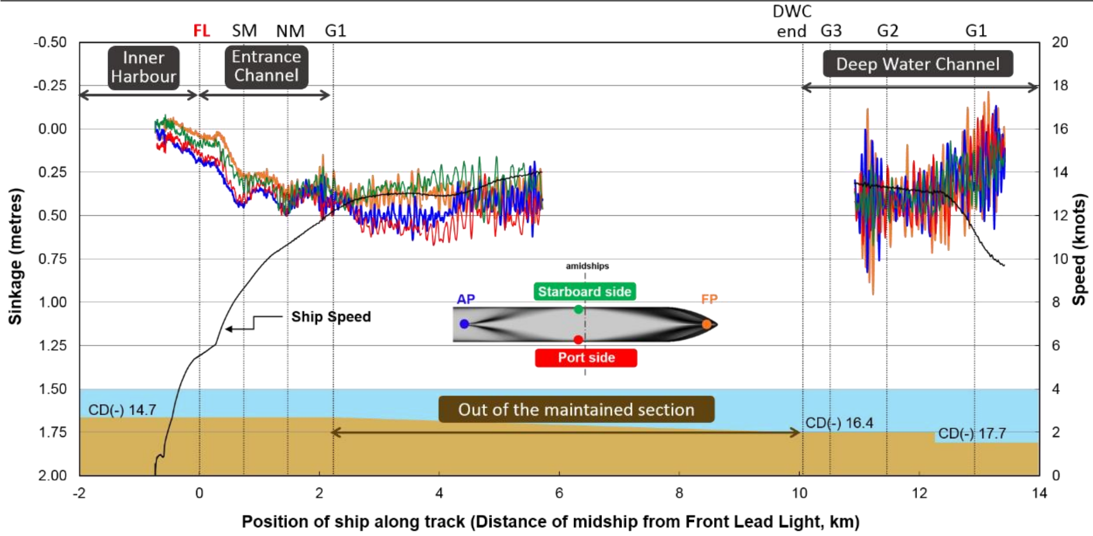

(a) Measured sinkage

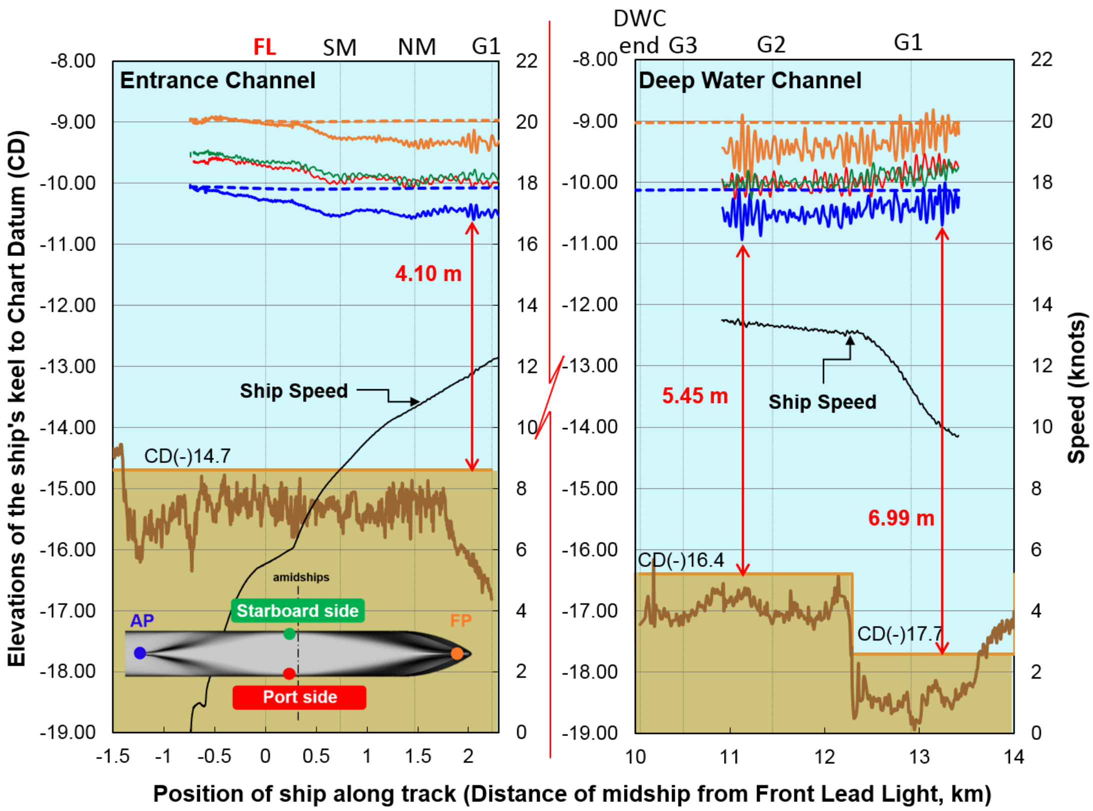

(b) Elevations of the ship's keel

Figure C.20. (a) Measured sinkage (positive downward) at four points [Note: Chart datum depths (not to scale) also shown]; (b) Elevations of the ship's keel relative to chart datum [Note: Dashed lines near the top of the figure are elevations of the FP (orange) and AP (blue), including changes in tide only; i.e., their static position, not including squat and wave-induced motions; the flat seabed line is based on the charted depth on AUS112; the fluctuating seabed line is the actual survey line provided by Fremantle Ports]

MOL EMISSARY **(outbound)**

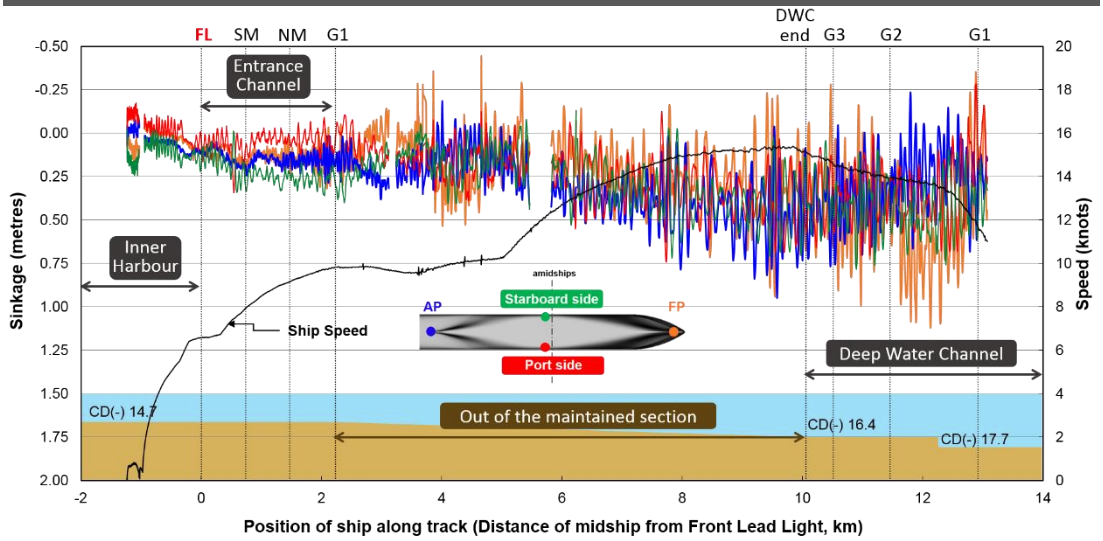

(a) Measured sinkage

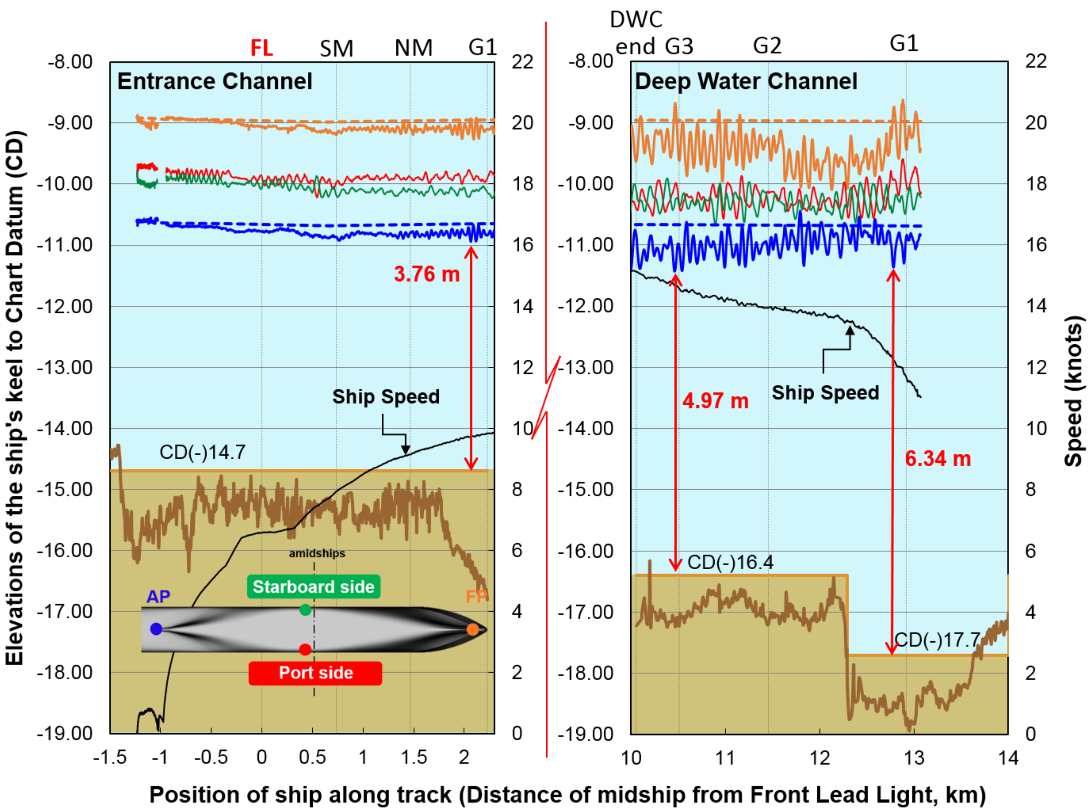

(b) Elevations of the ship's keel

Figure C.21. (a) Measured sinkage (positive downward) at four points [Note: Chart datum depths (not to scale) also shown]; (b) Elevations of the ship's keel relative to chart datum [Note: Dashed lines near the top of the figure are elevations of the FP (orange) and AP (blue), including changes in tide only; i.e., their static position, not including squat and wave-induced motions; the flat seabed line is based on the charted depth on AUS112; the fluctuating seabed line is the actual survey line provided by Fremantle Ports]

***SAFMARINE MAKUTU* (outbound)**

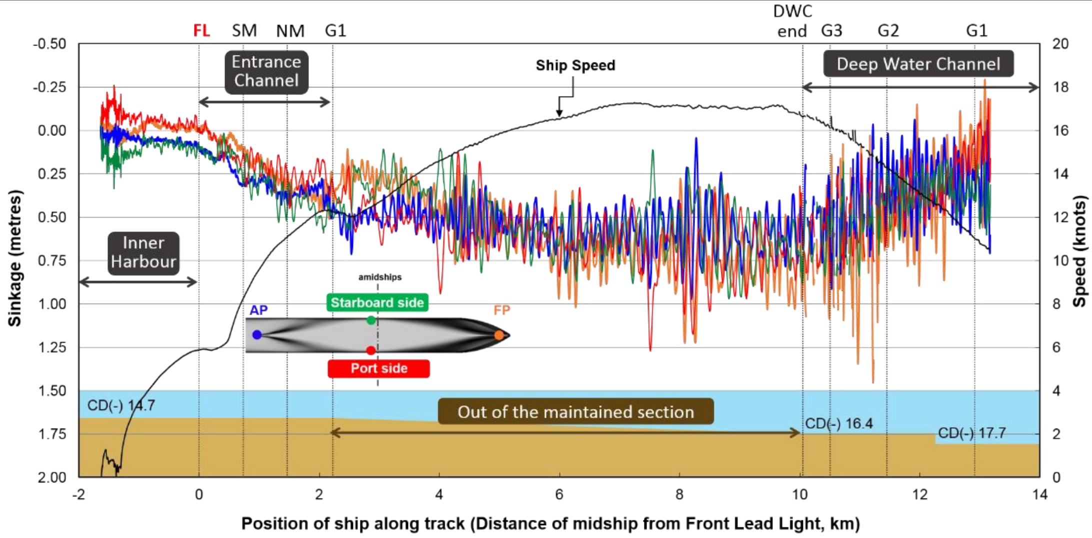

(a) Measured sinkage

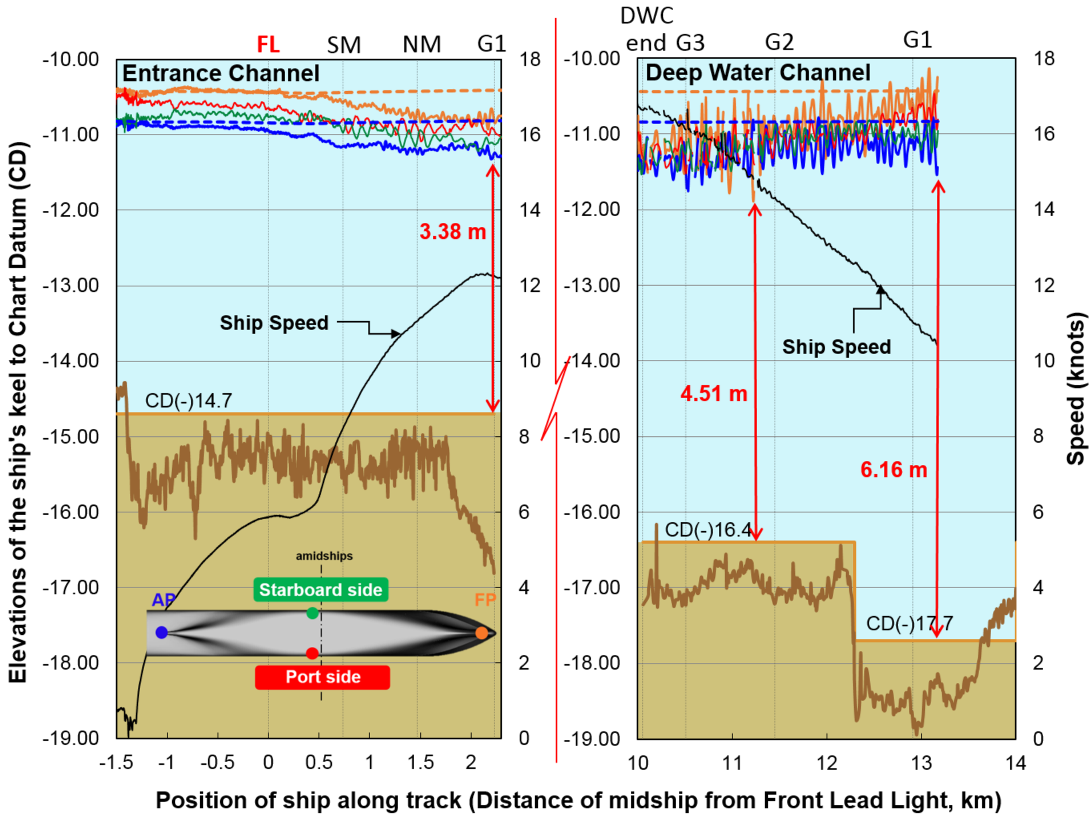

(b) Elevations of the ship's keel

Figure C.22. (a) Measured sinkage (positive downward) at four points [Note: Chart datum depths (not to scale) also shown]; (b) Elevations of the ship's keel relative to chart datum [Note: Dashed lines near the top of the figure are elevations of the FP (orange) and AP (blue), including changes in tide only; i.e., their static position, not including squat and wave-induced motions; the flat seabed line is based on the charted depth on AUS112; the fluctuating seabed line is the actual survey line provided by Fremantle Ports]

***CMA CGM LAMARTINE* (outbound)**

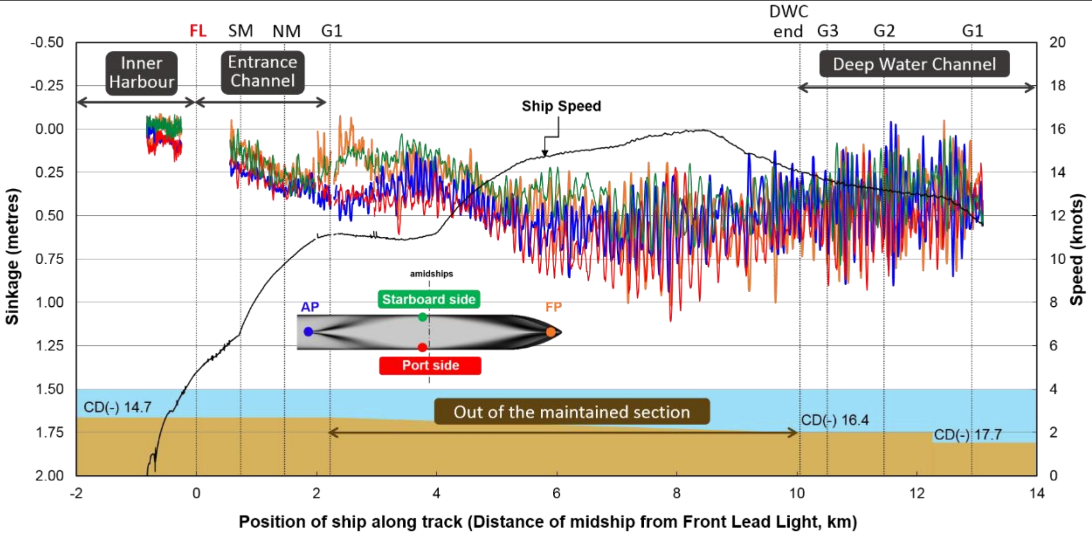

(a) Measured sinkage

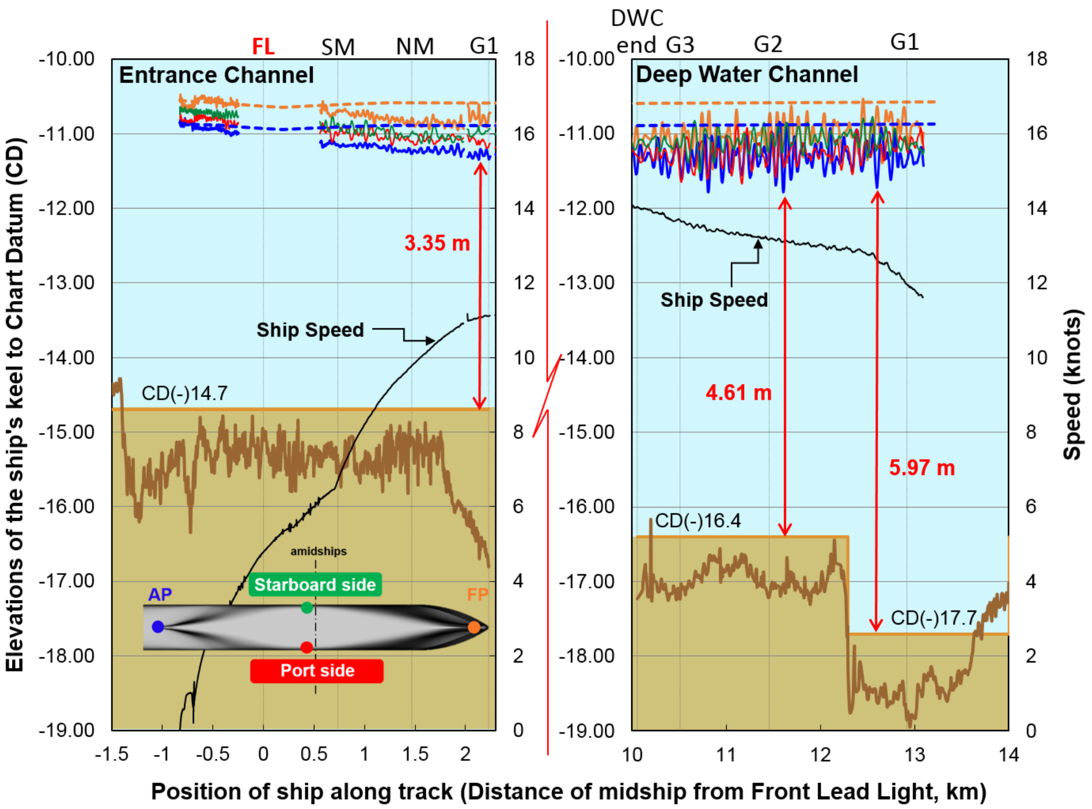

(b) Elevations of the ship's keel

Figure C.23. (a) Measured sinkage (positive downward) at four points [Note: Chart datum depths (not to scale) also shown]; (b) Elevations of the ship's keel relative to chart datum [Note: Dashed lines near the top of the figure are elevations of the FP (orange) and AP (blue), including changes in tide only; i.e., their static position, not including squat and wave-induced motions; the flat seabed line is based on the charted depth on AUS112; the fluctuating seabed line is the actual survey line provided by Fremantle Ports]

***MOL PARAMOUNT* (outbound)**

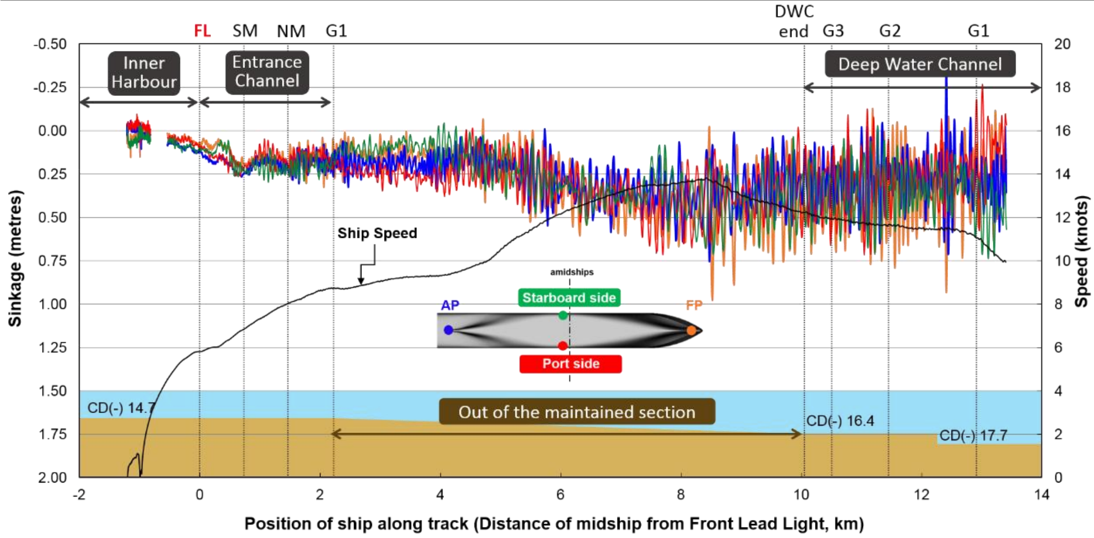

(a) Measured sinkage

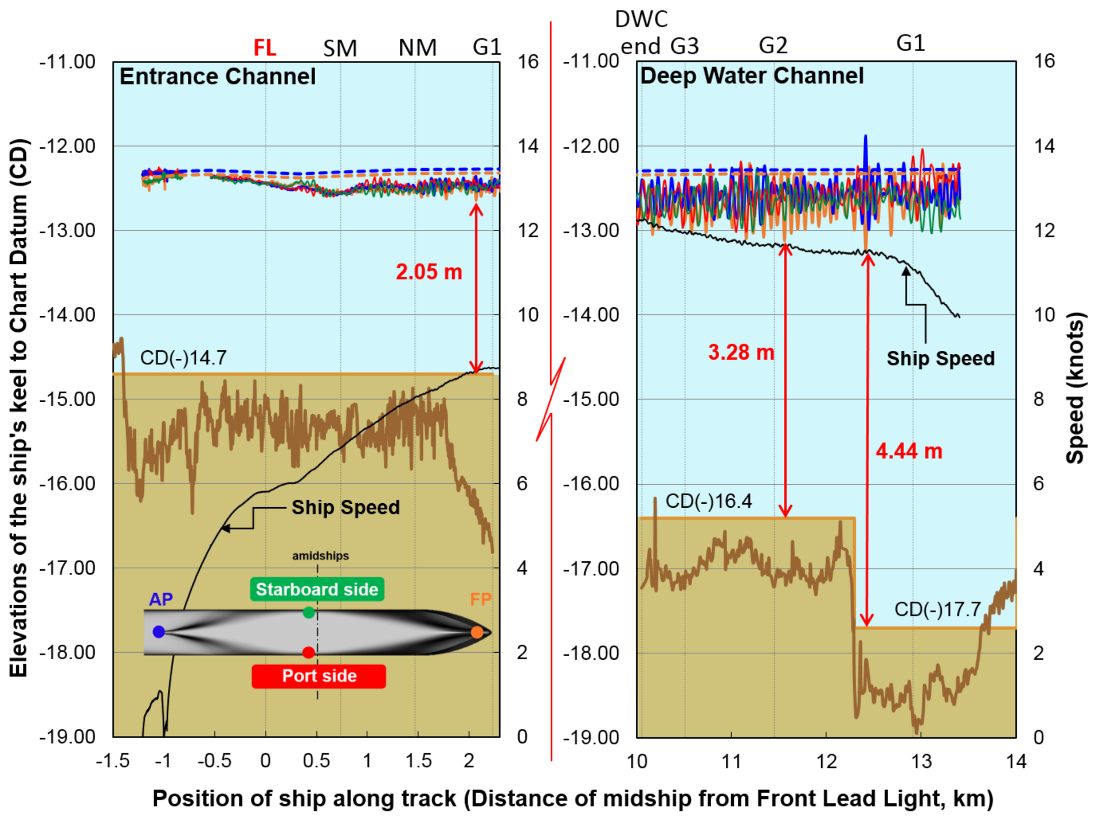

(b) Elevations of the ship's keel

Figure C.24. (a) Measured sinkage (positive downward) at four points [Note: Chart datum depths (not to scale) also shown]; (b) Elevations of the ship's keel relative to chart datum [Note: Dashed lines near the top of the figure are elevations of the FP (orange) and AP (blue), including changes in tide only; i.e., their static position, not including squat and wave-induced motions; the flat seabed line is based on the charted depth on AUS112; the fluctuating seabed line is the actual survey line provided by Fremantle Ports]

Appendix D - Ship Motion RAOs

The computer code *OCTOPUS* (www.abb.com), with its module *SEAWAY* (Journée, 2001; Journée & Adegeest, 2003), has been used to obtain motion RAOs for the ship transits. Calculated heave (at LCG), roll and pitch RAOs over the full range of wave directions and frequencies for all six container ship transits in the given conditions (see Table 6.3) are shown in Figure D.1. Note that the roll RAOs (middle, Figure D.1) are the results from the Ikeda method with no B_{44S} (see Figure 6.10(b)) by way of example.

Figure D.2 also shows the roll RAOs from the three approaches: the potential method, the Ikeda method with no B_{44S}, and the Ikeda method with all five components (see Figure 6.10(b)) for the container ship transits.

(a)
SEAMAX STAMFORD
(inbound)
15.35knots

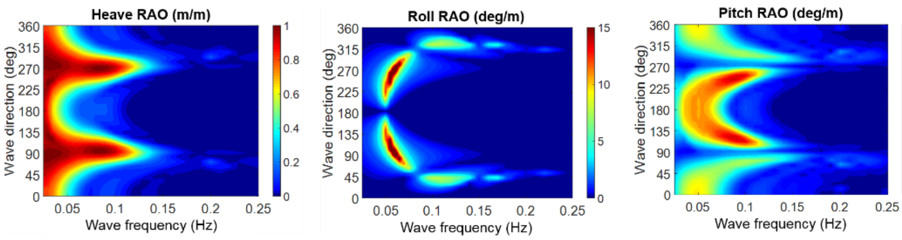

(b)
CMA CGM WAGNER
(inbound)
14.89 knots

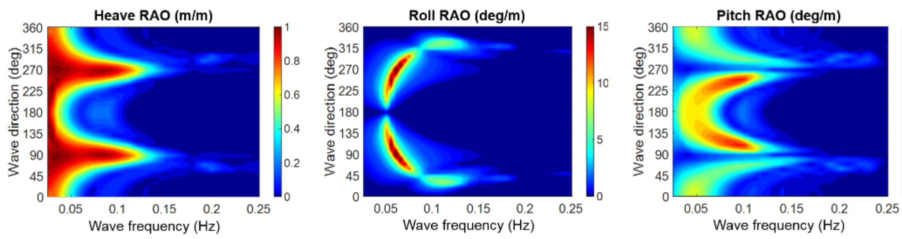

(c)
CMA CGM LAMARTINE
(outbound)
14.38 knots

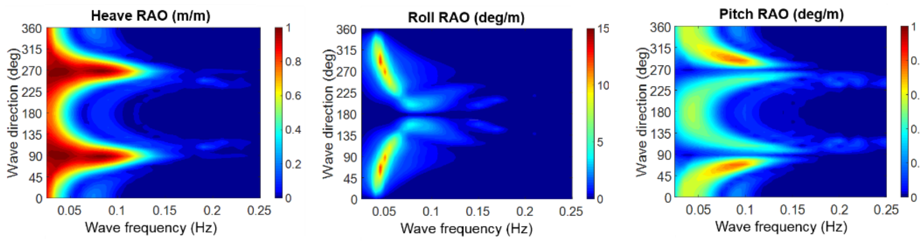

(d)
MOL EMISSARY
(inbound)
12.70 knots

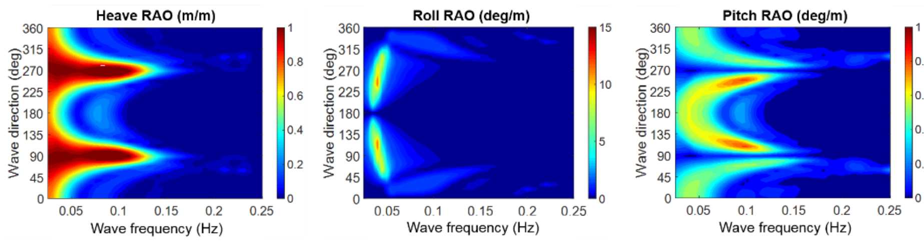

(e)
MOL EMISSARY
(outbound)
14.47 knots

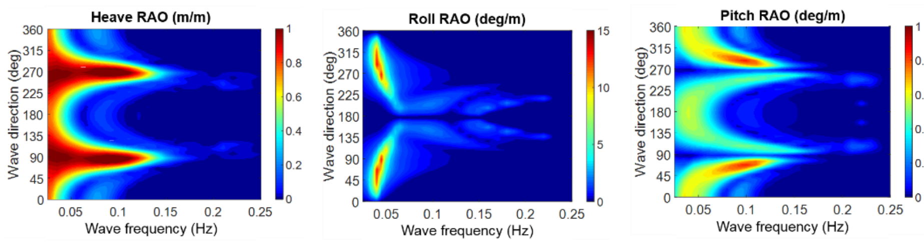

(f)
SAFMARINE MAKUTU
(inbound)
11.90 knots

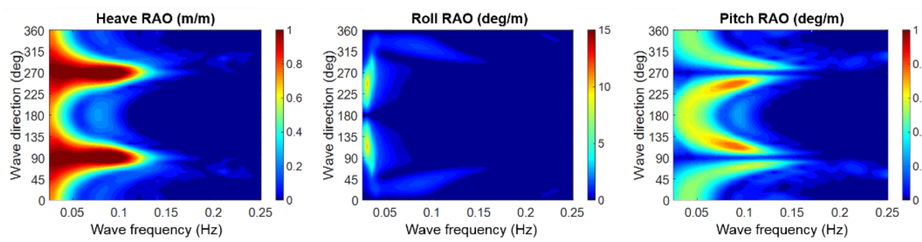

Figure D.1. Calculated motion RAOs: Heave (left); Roll (middle); Pitch (right)

(a)
SEAMAX STAMFORD
(inbound)
15.35knots

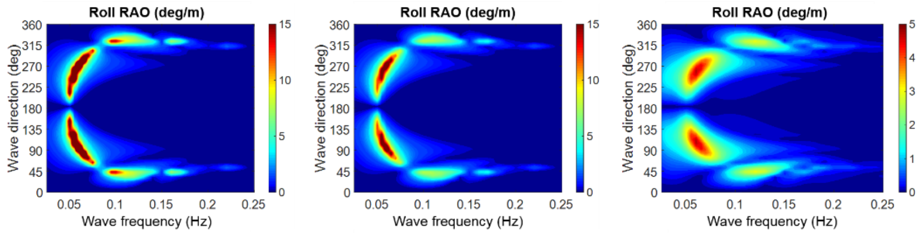

(b)
CMA CGM WAGNER
(inbound)
14.89 knots

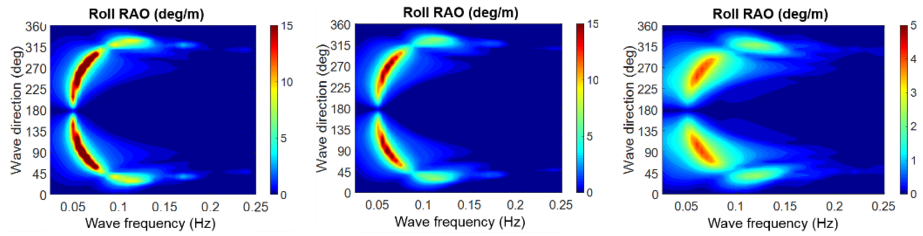

(c)
CMA CGM LAMARTINE
(outbound)
14.38 knots

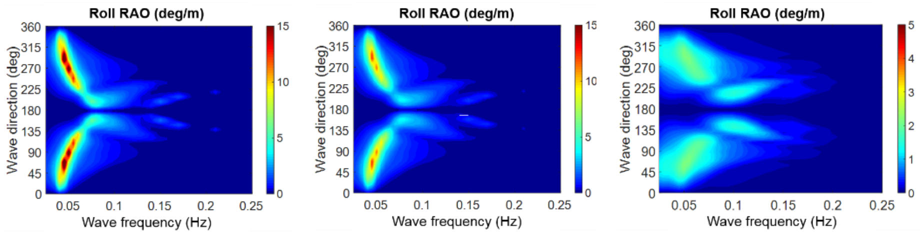

(d)
MOL EMISSARY
(inbound)
12.70 knots

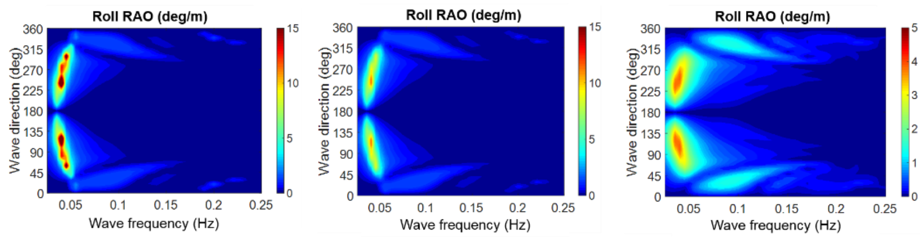

(e)
MOL EMISSARY
(outbound)
14.47 knots

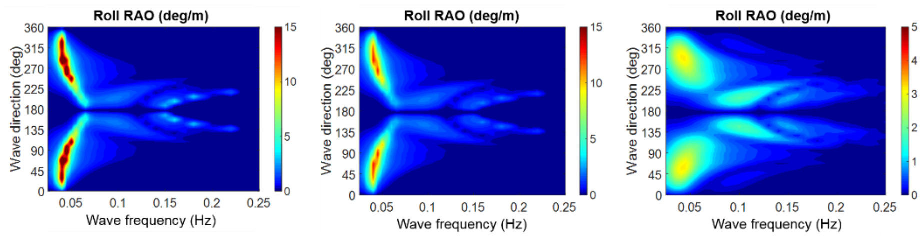

(f)
SAFMARINE MAKUTU
(inbound)
11.90 knots

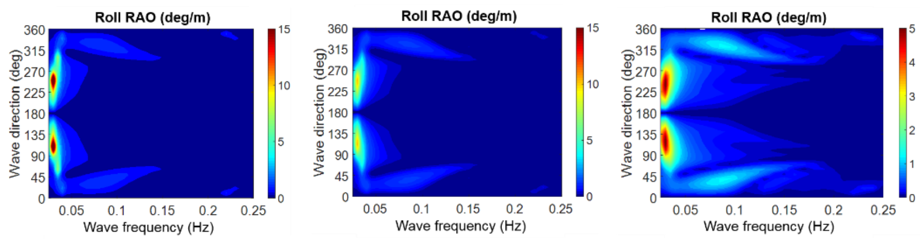

Figure D.2. Roll RAOs from three approaches: The potential method (left); the Ikeda method with no B_{44S} (middle); the Ikeda method with all five components (right)

Appendix E - Directional Motion Response Spectra

This appendix shows the directional motion response spectra together with the corresponding directional wave spectra and motion RAOs. Heave, roll and pitch response spectra for all six container ship transits are shown in Figure E.1, Figure E.2 and Figure E.3, respectively. Note that the Ikeda method with no B_{44S}, having the highest accuracy, has been used for the roll predictions (see Figure 6.14). These figures clearly show how each of the motion RAOs responds to the full range of wave directions and periods; and hence how the heave, roll and pitch response spectra are derived from the measured directional wave spectra and calculated motion RAOs.

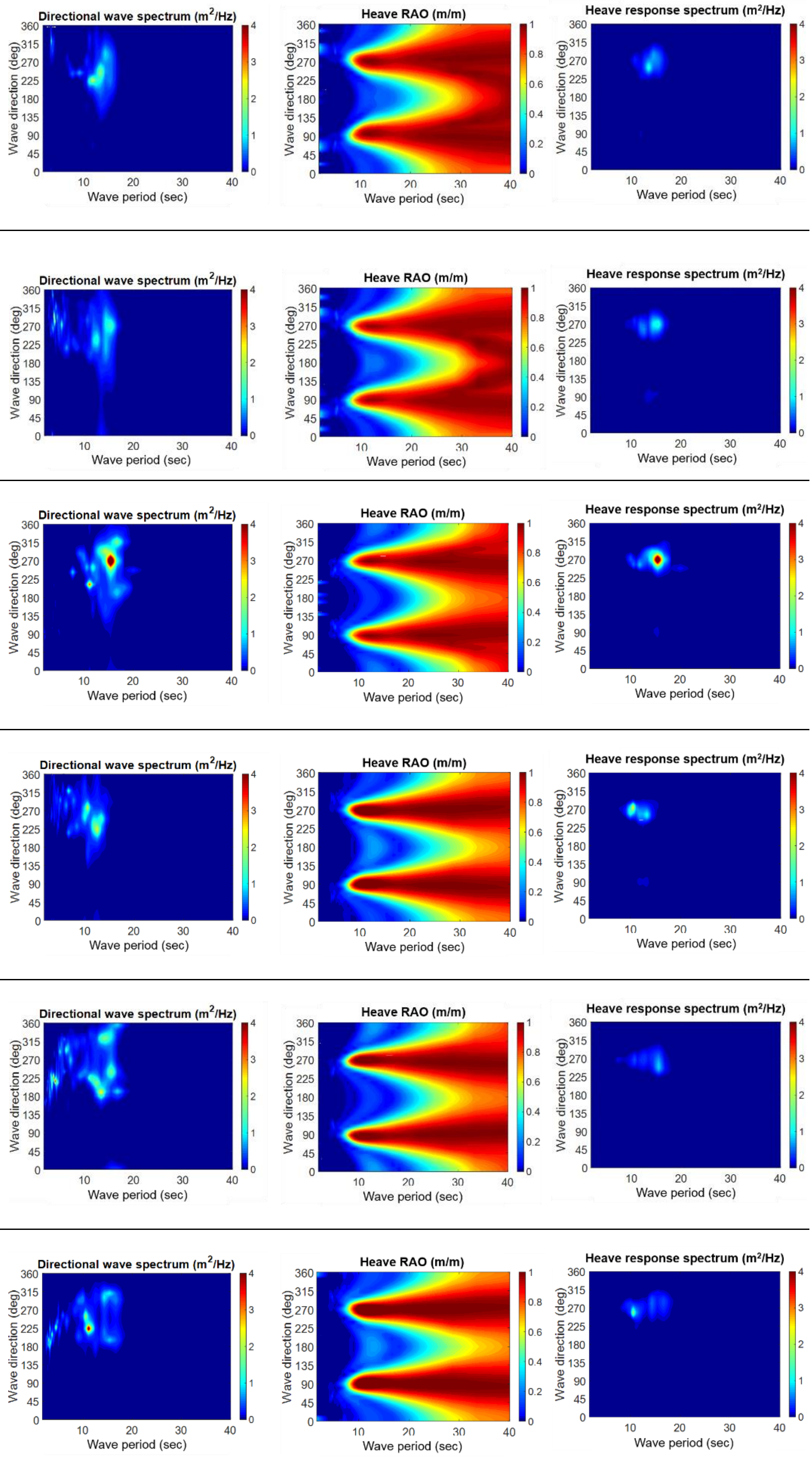

(a) *SEAMAX STAMFORD* (inbound) 15.35knots

(b) *CMA CGM WAGNER* (inbound) 14.89 knots

(c) *CMA CGM LAMARTINE* (outbound) 14.38 knots

(d) *MOL EMISSARY* (inbound) 12.70 knots

(e) *MOL EMISSARY* (outbound) 14.47 knots

(f) *SAFMARINE MAKUTU* (inbound) 11.90 knots

Figure E.1. Directional wave spectra (left); Calculated heave RAOs (middle); Resulting heave response spectra (right)

(a)
SEAMAX STAMFORD
(inbound)
15.35knots

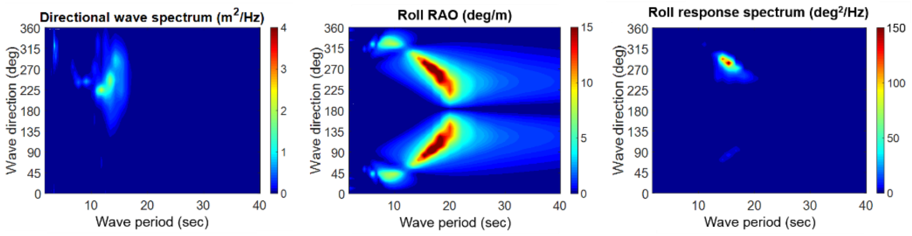

(b)
CMA CGM WAGNER
(inbound)
14.89 knots

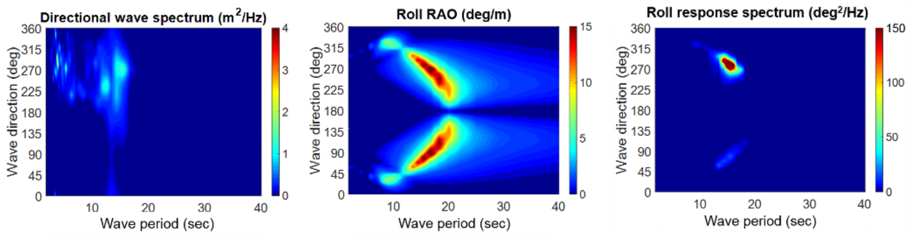

(c)
CMA CGM LAMARTINE
(outbound)
14.38 knots

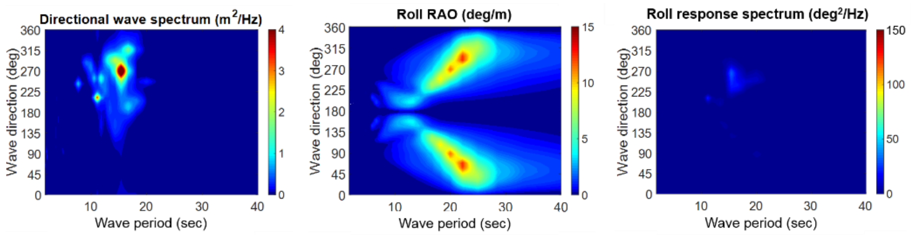

(d)
MOL EMISSARY
(inbound)
12.70 knots

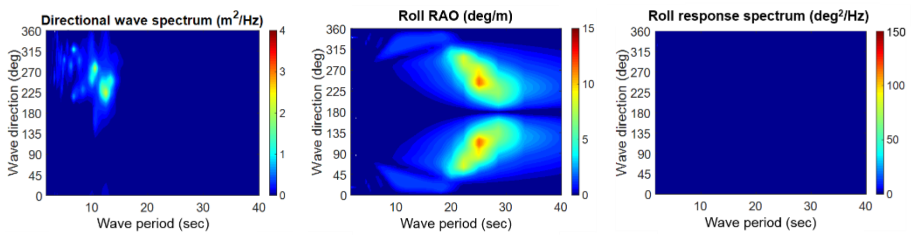

(e)
MOL EMISSARY
(outbound)
14.47 knots

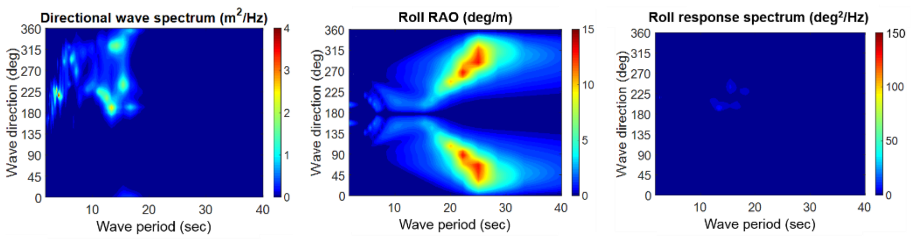

(f)
SAFMARINE MAKUTU
(inbound)
11.90 knots

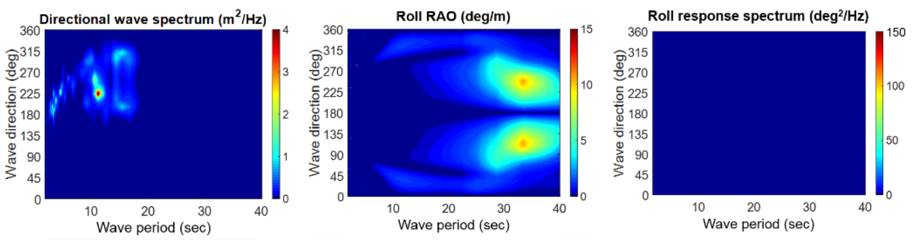

Figure E.2. Directional wave spectra (left); Calculated roll RAOs (middle); Resulting roll response spectra (right)

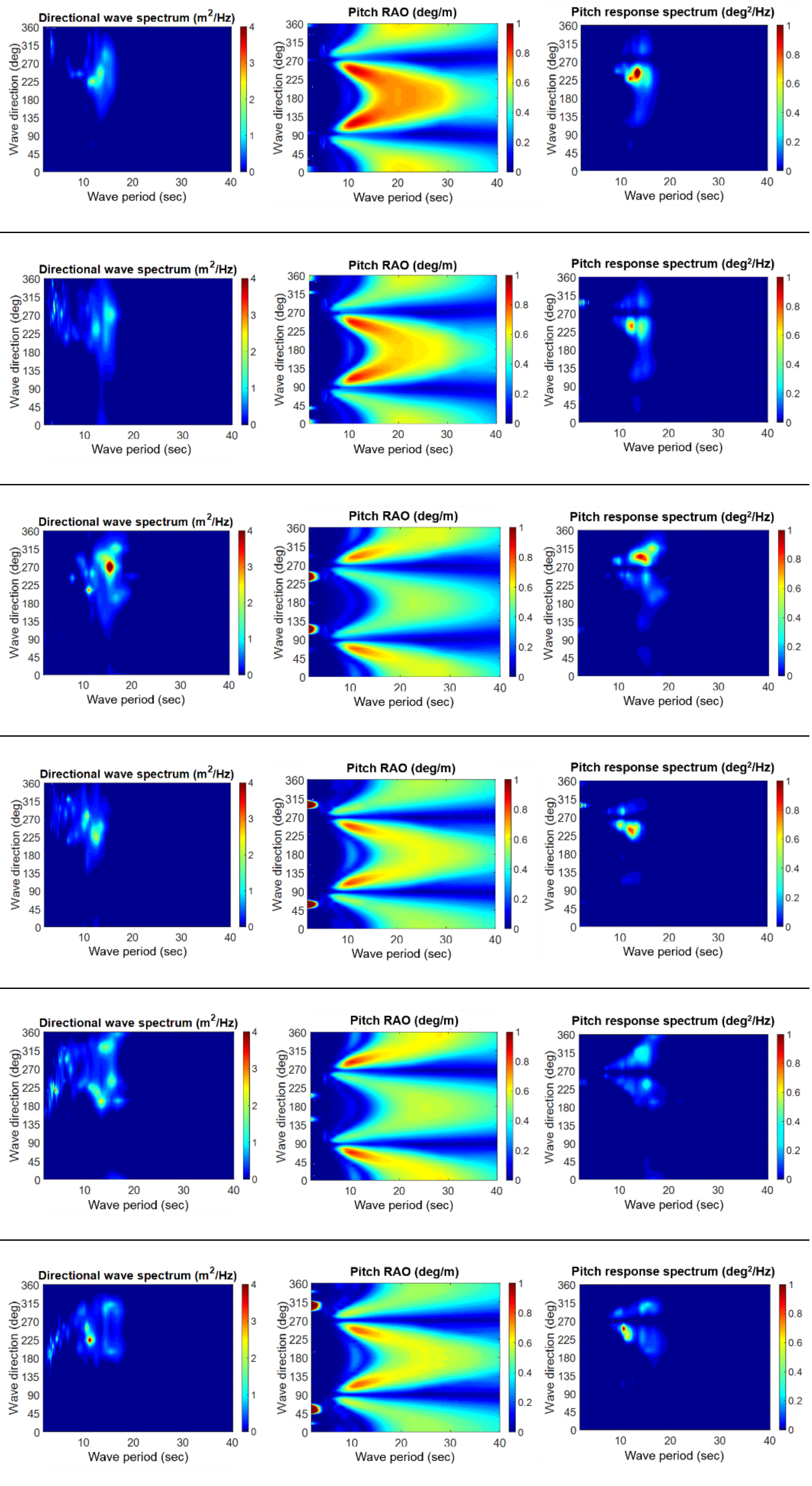

(a) *SEAMAX STAMFORD* (inbound) 15.35knots

(b) *CMA CGM WAGNER* (inbound) 14.89 knots

(c) *CMA CGM LAMARTINE* (outbound) 14.38 knots

(d) *MOL EMISSARY* (inbound) 12.70 knots

(e) *MOL EMISSARY* (outbound) 14.47 knots

(f) *SAFMARINE MAKUTU* (inbound) 11.90 knots

Figure E.3. Directional wave spectra (left); Calculated pitch RAOs (middle); Resulting pitch response spectra (right)

Appendix F - Copyright Permissions

I warrant that I have obtained, where necessary, permission from the copyright owners to use any third-party copyright material reproduced in the thesis, or to use any of my own published work (e.g. journal articles) in which the copyright is held by another party (e.g. publisher, co-author). See below for copyright permissions.

Chapter 1

PERMISSION TO USE COPYRIGHT MATERIAL AS SPECIFIED BELOW:

Two photos of Freight Ro-Ro at 10 knots and 20 knots, in Chapter 1 of the thesis with the caption:

Figure 1.5. An example of ship squat: (a) Freight Ro-Ro at draught of 6.5 m, speed of 10 knots and UKC of approximately 8 m; (b) The same ship at speed of 20 knots and UKC of 10 m [photos by John Clandillon-Baker FNI (United Kingdom Maritime Pilots' Association, 2008)]

3/21/2018 Mail - jeonghun.ha@postgrad.curtin.edu.au

Re: Request for permission to use your photos in The Pilot 292

John Clandillon-Baker <jclandillonbaker@gmail.com>

Fri 9/03/2018 5:50 PM

To: Scott Ha <jeonghun.ha@postgrad.curtin.edu.au>;

Hello Jeong,
By coincidence our emails must have crossed in cyberspace!! I replied to Tim just as your email arrived and yes, I'm happy for you to use my photos and wish you every success in your studies.
Best regards
John

Chapter 2

PERMISSION TO USE COPYRIGHT MATERIAL AS SPECIFIED BELOW:

Ha, J. H., & Gourlay, T. P. (2017). Bow and stern sinkage coefficients for cargo ships in shallow open water. *Third-place winner of the 2017 PIANC De Paepe-Willems Award*, *PIANC Yearbook 2017*. Brussels, Belgium: World Association for Waterborne Transport Infrastructure.

PIANC
The World Association for Waterborne Transport Infrastructure

Brussels, 13 March 2018

Subject: Permission to quote paper

Dear Mr Jeong Hun Ha,

With this letter, I hereby grant you full permission to quote the paper 'Bow and Stern Sinkage Coefficients for Cargo Ships in Shallow Open Water', winning paper of the PIANC De Paepe-Willems Award 2017.

Best regards,

Geert Van Cappellen

Geert Van Cappellen,
Secretary-General of PIANC

Chapter 3

PERMISSION TO USE COPYRIGHT MATERIAL AS SPECIFIED BELOW:

Gourlay, T. P., Ha, J. H., Mucha, P., & Uliczka, K. (2015). Sinkage and trim of modern container ships in shallow water. *Proceedings of the Coasts and Ports 2015 Conference*, *Auckland*, *New Zealand*.

Chapter 5

PERMISSION TO USE COPYRIGHT MATERIAL AS SPECIFIED BELOW:

Ha, J. H., Gourlay, T. P., & Nadarajah, N. (2016). Measured ship motions in Port of Geraldton approach channel. *Proceedings of the 4th International Conference on Ship Manoeuvring in Shallow and Confined Water, MASHCON 2016, Hamburg, Germany*, 236–250.

3/29/2018 Mail - jeonghun.ha@postgrad.curtin.edu.au

RE: Request for permission to use of a MASHCON2016 paper

Maxim Candries <Maxim.Candries@UGent.be>

Thu 29/03/2018 3:49 PM

To: Scott Ha <jeonghun.ha@postgrad.curtin.edu.au>;

Dear Scott,

Apologies for my late reply. This mail was written on 9/3/18 but somehow did not reach you.

Congratulations on (nearly) obtaining your PhD.
There is no problem: the 2016 proceedings are open access, so it's OK regarding copyright.

Best Regards,

Maxim

Maxim Candries

Ghent University
EA15 - Maritime Technology Division
Tech Lane Ghent Science Park – Campus A 904, B 9052 GENT (Belgium)
Tel +32 (0)9 2645558
Fax +32 (0)9 2645843
Mobile +32 (0) 486787597
maxim.candries@ugent.be

Scientific Advisor
Knowledge Centre "Manoeuvring in Shallow and Confined Water"
Flanders Hydraulics Research
Berchemlei 115, B 2140 ANTWERPEN (Belgium)
Tel + 32 (0)3 224 6956
Fax + 32 (0)3 224 6036
maxim.candries@mow.vlaanderen.be

PERMISSION TO USE COPYRIGHT MATERIAL AS SPECIFIED BELOW:

Ha, J. H., & Gourlay, T. P. (2018). Validation of container ship squat modelling using full-scale trials at the Port of Fremantle. *Journal of Waterway, Port, Coastal, and Ocean Engineering*, *144*(1). doi: 10.1061/(ASCE)WW.1943-5460.0000425

3/14/2018 Rightslink® by Copyright Clearance Center

Copyright Clearance Center RightsLink®

Home | Create Account | Help

ASCE AMERICAN SOCIETY OF CIVIL ENGINEERS

Title: Validation of Container Ship Squat Modeling Using Full-Scale Trials at the Port of Fremantle

Author: Jeong Hun Ha, Tim Gourlay

Publication: Journal of Waterway, Port, Coastal, and Ocean Engineering

Publisher: American Society of Civil Engineers

Date: 10/25/2017

LOGIN

If you're a copyright.com user, you can login to RightsLink using your copyright.com credentials.
Already **a RightsLink user** or want to learn more?

Permissions Request

As an author of an ASCE journal article, you are permitted to reuse the accepted manuscript version of your article for your thesis or dissertation.

BACK | CLOSE WINDOW

Chapter 6

PERMISSION TO USE COPYRIGHT MATERIAL AS SPECIFIED BELOW:

Ha, J. H., & Gourlay, T. P. (2018). Full-scale measurements and method validation of container ship wave-induced motion at the Port of Fremantle. *Journal of Waterway, Port, Coastal, and Ocean Engineering*, *144*(1). doi: 10.1061/(ASCE)WW.1943-5460.0000425